PolyPublie
Polytechnique Montréal

POLYTECHNIQUE MONTRÉAL
UNIVERSITÉ D'INGÉNIERIE

Titre: Title:	Fabric and Elastic Properties of Antigorite, Mica and Amphibole-Rich Rocks and Implications for the Tectonic Interprétation of Seismic Anisotropy
Auteur: Author:	Tongbin Shao
Date:	2015
Type:	Mémoire ou thèse / Dissertation or Thesis
Référence: Citation:	Shao, T. (2015). Fabric and Elastic Properties of Antigorite, Mica and Amphibole-Rich Rocks and Implications for the Tectonic Interprétation of Seismic Anisotropy [Thèse de doctorat, École Polytechnique de Montréal]. PolyPublie. https://publications.polymtl.ca/2042/

Document en libre accès dans PolyPublie
Open Access document in PolyPublie

URL de PolyPublie: PolyPublie URL:	https://publications.polymtl.ca/2042/
Directeurs de recherche: Advisors:	Shaocheng Ji
Programme: Program:	Génie minéral

Ce fichier a été téléchargé à partir de PolyPublie, le dépôt institutionnel de Polytechnique Montréal
This file has been downloaded from PolyPublie, the institutional repository of Polytechnique Montréal

https://publications.polymtl.ca

UNIVERSITÉ DE MONTRÉAL

FABRIC AND ELASTIC PROPERTIES OF ANTIGORITE, MICA AND AMPHIBOLE-RICH ROCKS AND IMPLICATIONS FOR THE TECTONIC INTERPRETATION OF SEISMIC ANISOTROPY

TONGBIN SHAO

DÉPARTEMENT DES GÉNIES CIVIL, GÉOLOGIQUE ET MINES

ÉCOLE POLYTECHNIQUE DE MONTRÉAL

THÈSE PRÉSENTÉE EN VUE DE L'OBTENTION

DU DIPLÔME DE PHILOSOPHIAE DOCTOR

(GÉNIE MINÉRAL)

DÉCEMBRE 2015

© Tongbin Shao, 2015.

UNIVERSITÉ DE MONTRÉAL

ÉCOLE POLYTECHNIQUE DE MONTRÉAL

Cette thèse intitulée :

FABRIC AND ELASTIC PROPERTIES OF ANTIGORITE, MICA AND AMPHIBOLE-RICH ROCKS AND IMPLICATIONS FOR THE TECTONIC INTERPRETATION OF SEISMIC ANISOTROPY

présentée par : SHAO Tongbin

en vue de l'obtention du diplôme de : Philosophiae Doctor

a été dûment acceptée par le jury d'examen constitué de :

M. LI Li, Doctorat, président

M. JI Shaocheng, Ph. D., membre et directeur de recherche

M. MARTIGNOLE Jacques, Ph. D., membre

M. GIROUX Bernard, Ph. D., membre externe

DEDICATION

To my mother Jinlian Cheng, my elder sisters Yuqin Shao and Yuzhen Shao, and my girlfriend Sofie Cheng for their unconditional love and support.

ACKNOWLEDGEMENTS

First and foremost, I feel privileged to have the most inspiring and supportive advisor, Prof. Shaocheng Ji, with whom I have been acquainted since 2010 when I was a postgraduate student in the Guangzhou Institute of Geochemistry, Chinese Academy of Sciences. Since I started my Ph.D. study in École Polytechnique de Montréal in September 2012, he guided me with his immense knowledge, great enthusiasm, and dedication to scientific research and teaching. The transition, from a Master graduate in the dark of seismic properties of rocks to a Ph.D. candidate in petrophysics, rock rheology, and structural geology, would not have been possible without his guidance, patience, and encouragement. I sincerely thank Prof. Ji for what have I learned from taking his classes, being his teaching assistant, collaborating on research projects, and most of all, for what he influences me on the attitude on a journey of scientific discovery.

I would like to thank the other three members of my dissertation committee, Professors Bernard Giroux, Li Li, and Jacques Martignole for their time and thought. My special thanks are also given to Prof. Chouteau Michel for his smile and encouragement since I took his course.

I am grateful to Prof. Matthew H. Salisbury for his support and kindness during the seismic velocity measurements and to Mr. Robert Iuliucci for his technical assistance and patience in the GSC/Dalhousie High Pressure Laboratory, which enriched my experiences in high pressure experiment. I would also like to thank Prof. Denis Marcotte for his help for the statistical analysis of the experimental data, and Dr. A-Wei Li for his assistance during my field work.

This dissertation contains a large amount of measurement of crystallographic preferred orientations that were performed at Shizuoka University (Japan) with the kind helps of Prof. Katsuyoshi Michibayashi and his graduate students (Yosuke Kondo and Shoma Oya), and at Macquarie University (Australia) with Dr. Takako Satsukawa. All their helps are much appreciated.

I would like to thank Mrs. Manon Latour, Mrs. Carole Giguère, Mrs. Manon Leduc, Mrs. Margareth Mompoint and Mr. Yvéric Rousseau for their support and smile. I acknowledge École Polytechnique de Montréal for the exemption of my foreign student tuition fees. I thank the Natural Sciences and Engineering Council of Canada and the Geological Survey of China for research grants to Prof. Shaocheng Ji.

I also would like to express my sincere appreciations to Prof. Maoshuang Song and Drs. Qian Wang and Jianfeng Li (Guangzhou Institute of Geochemistry, Chinese Academy of Sciences), Dr. Shengsi Sun (Northwest University, Xi'an, China), Prof. Yongsheng Zhou (Institute of Geology, China Earthquake Administration, Beijing, China), and Prof. Xinyue Chen (Hunan University of Science and Technology) for encouraging me to study in Canada and continuous help in these years. Many thanks to my friends Drs. Kai Zhang, Yutao Pang, Pengzhi Zhao, Xiaoyu Bai and Min Liang in Canada, and Mr. Xuwei Jia and Huan Liao and Drs. Yongfeng Cai, Yun Zhou and Jian Li in China for swapping academic and non-academic ideas that broadened my horizon and for sharing wonderful time together.

Last, but certainly not least I want to express my gratitude to, and love for my mother (Jinlian Cheng), elder sisters (Yuqin Shao and Yuzhen Shao) and my girlfriend (Sofie Cheng). Sixteen years ago, I began to leave home for studying and went back home from twice a week, through once a year, to once per two or three years. Being so far away from you was very hard at times and I am really looking forward to spending more time with you once I return to China.

RÉSUMÉ

La connaissance des propriétés sismiques et élastiques des agrégats polycristallins, qui sont représentatifs de roches actuellement déformées à haute pression et haute température, sert de base pour l'interprétation géologique des données sismiques *in situ* (profils sismiques de réflexion et de réfraction, fonctions télésismiques, tomographie, et biréfringence des ondes S). Les données sismiques ont ainsi permis d'établir des modèles de structure et de composition de la lithosphère. D'autre part, les propriétés sismiques et mécaniques [vitesse des ondes de compression et de cisaillement (V_p et V_s), anisotropie, module élastique] peuvent être déterminées expérimentalement sur des échantillons de roche orientés. Certaines des propriétés comme l'orientation cristallographique (CPO; pétro-fabrique) des minéraux peuvent aussi être déterminées sur des lames polies grâce à la rétro-diffraction d'électrons (Electron Back-scatter Diffraction, EBSD). On peut ainsi mieux comprendre comment les propriétés sismiques des roches sous pression de confinement sont influencées par leur composition modale et chimique, par leur structure (foliation et linéation) et par la fabrique des minéraux (CPO).

Cette thèse comprend cinq chapitres. Le Chapitre 1 aborde le calcul des propriétés sismiques, dans le cadre des principes de base de l'élasticité, des lois de mélange, et des propriétés sismiques des minéraux des roches. Dans ce chapitre on introduit trois groupes de technique de mesure des propriétés sismiques, en présentant les méthodes expérimentales utilisées. En outre, ce chapitre donne un aperçu sur la source de l'anisotropie sismique de la lithosphère.

Le Chapitre 2 traite des propriétés sismiques et élastiques de 15 échantillons de serpentinite à antigorite obtenues à des pressions hydrostatiques allant jusqu'à 650 MPa. Les propriétés sismiques en 3D ont également été obtenues pour 11 échantillons en se basant sur les données de petro-fabrique (CPO). Ces données fournissent un nouvel étalonnage pour les propriétés sismiques et la fabrique de l'antigorite qui est la seule serpentine stable dans les zones de subduction où la température dépasse ~300 °C. Les comparaisons des vitesses mesurées en laboratoire à haute pression avec les vitesses calculées en utilisant les données de pétro-fabrique, démontrent que l'anisotropie sismique dans les serpentinites à haute température est contrôlée par la CPO des axes c de l'antigorite. L'anisotropie est cependant indépendante du système de glissement, qui dépend du régime et de l'ampleur de la déformation finie subie par la roche. L'extrapolation des données expérimentales avec la pression et la température suggère que

l'anisotropie de V_p diminue alors que la biréfringence des ondes de cisaillement (ΔV_s) et le rapport de V_p/V_s augmentent avec l'augmentation de la pression dans les zones de subduction aussi bien froides que chaudes. Dans une plaque fortement plongeante, l'antigorite est probablement déformée par aplatissement quasi- coaxial ou par glissement parallèle à la fosse océanique, induisant une anisotropie sismique avec des vitesses rapides parallèles à la fosse océanique. Dans une plaque plongeante à faible pendage et température élevée, l'antigorite est probablement déformée par cisaillement simple ou transpression. L'anisotropie sismique normale à la fosse océanique peut être observée lorsque la pente de la subduction est inférieure à 30°. Les caractéristiques géophysiques du plateau tibétain, telles que la forte hétérogénéité des ondes V_p et V_s, la forte atténuation sismique, la forte biréfringence des ondes de cisaillement et la forte conductivité électrique peuvent s' expliquer par la présence de serpentinites très déformées dans les zones de cisaillement lithosphérique. Ces zones de cisaillement seraient réactivées le long d'anciennes zones de suture entre les blocs en collision, le long de zones hydratées dans le manteau lithosphérique en subduction et dans la zone de transition entre la croûte et le manteau supérieur si la température est inférieure à 700 °C.

Le Chapitre 3 fournit un étalonnage détaillé de l'ampleur et de la symétrie de l'anisotropie sismique pour 132 schistes. Ceci permet de d'évaluer la déviation par rapport à l'isotropie transversale (TI) qui est généralement assumée dans l'interprétation des données sismiques. L'anisotropie de V_P observée à 600 MPa pour les schistes à chlorite, les schistes à mica, les phyllites, les schistes à sillimanite-mica, les schistes à amphibole est en moyenne de 12,0%, 12,8%, 12,8%, 17,0% et 12,9%, respectivement. La plupart des schistes montre une anisotropie de V_p dans le plan de foliation qui est en moyenne de 2,4% pour les phyllites, 3,3% pour les schistes à mica, de 4,1% pour les schistes à chlorite, de 6,8% pour les schistes à sillimanite-mica, et de 5,2% pour les schistes à amphiboles. Cette déviation par rapport à TI est due à la présence d'amphibole, de sillimanite, et de quartz. L'amphibole et la sillimanite développent une forte CPO avec l'axe c rapide parallèle à la linéation, déterminant une anisotropie orthorhombique avec $V_p(X)>V_p(Y)>V_p(Z)$. Les effets du quartz sont complexes, variant en fonction de son volume relatif et du système de glissement en vigueur. La plupart des schistes et des mylonites sont quasi transversalement isotropes en termes de vitesse des ondes S et de biréfringence des ondes S, bien que les propriétés des ondes P puissent afficher une symétrie orthorhombique. Ces résultats s'appliquent à l'interprétation des données sismiques pour le sud-est du plateau tibétain.

L'anisotropie de la croûte avec polarisations orientées NS à NW-SE dans les blocs Sibumasu et Indochine est causée par des foliations subverticales dans les schistes riches en mica et en amphibole déformés par plissement de compression et par cisaillement décrochant. Ces blocs ont subi une rotation en sens horaire de 70-90° autour de la Syntaxe orientale de l'Himalaya, sans extrusion latérale vers l'est ou le sud-est, en réponse à l'indentation progressive de l'Inde en Asie.

Le Chapitre 4 rapporte de nouveaux résultats sur les vitesses des ondes P et S et sur l'anisotropie de 17 échantillons de roches riches en amphibole (34 à 80 vol. %), mesurée à la température ambiante et à des pressions hydrostatiques allant jusqu'à 650 MPa. Les études pétrophysiques combinées avec les analyses microstructurales et géochimiques fournissent un nouvel étalonnage pour la densité moyenne, les teneurs en éléments majeurs, les relations V_p-P et V_s-P, les anisotropies V_p et V_s , les coefficients de Poisson, le rapport logarithmique $R_{s/p}$, et les modules d'élasticité pour des roches riches en amphibole. Les vitesses des ondes P diminuent avec l'augmentation de SiO_2 et $Na_2O + K_2O$, mais augmentent avec MgO et CaO. La biréfringence des ondes S (≤0,38-0,40 km/s) est au maximum dans la direction de propagation parallèle à Y et au minimum dans la direction perpendiculaire à la foliation. L'amphibole joue un rôle essentiel dans la formation de l'anisotropie sismique alors que la présence de plagioclase, de quartz, de pyroxène, et de grenat diminue l'anisotropie induite par l'amphibole. Les variations de CPO se traduisent par différents modèles d'anisotropie clairement illustrés dans le diagramme de $V_p(X)/V_p(Y)$ - $V_p(Y)/V_p(Z)$. Ces résultats permettent de distinguer, en termes de propriétés sismiques, les amphibolites des autres types de roches comme les granites-granodiorites, les diorites, les gabbro-diabases, les gneiss felsiques, les gneiss mafiques, les éclogites et les péridotites. Par conséquent, l'amphibole, alignée par fluage de dislocations, par croissance anisotrope ou par rotation de cristaux rigides, est le facteur le plus important pour la formation de l'anisotropie sismique dans la croûte profonde, sous les continents ou sous les arcs insulaires océaniques.

Enfin, le Chapitre 5 décrit brièvement les principales conclusions et présente le travail envisagé pour de futures recherches.

ABSTRACT

The knowledge of seismic and elastic properties of polycrystalline rocks, which are representative of rocks currently being deformed at depth, under high pressure and temperature conditions is fundamental for geological interpretation of in-situ seismic data (e.g., reflections, refractions, received functions, tomography, and shear-wave splitting) and for establishing lithospheric structure and composition models. Through seismic properties measurements by directing high frequency waves at oriented rock samples and calculations from the crystallographic preferred orientation (CPO) measurements of minerals in polished rock samples using electron backscatter diffusion (EBSD) techniques, this thesis aims to better understand how the seismic and elastic properties [e.g., compressional and shear-wave velocities (V_p and V_s), anisotropy, and elastic moduli] of main rocks under confining pressure are influenced by their chemical and modal compositions, microstructures (e.g., foliation and lineation), and CPO of anisotropic minerals, and to interpret in situ seismic data observed in Tibetan Plateau and oceanic subduction zone using these data.

This thesis consists of five chapters. Chapter 1 addresses the framework of calculation of seismic properties, with focus on basic principles of elasticity, mixture rules, and seismic properties of rock-forming minerals. Then it introduces three main groups of techniques for measuring rock seismic property, and describes the experimental details used in this study. Also, this chapter provides an overview on the source of seismic anisotropy in the lithosphere.

Chapter 2 deals with seismic and elastic properties of 15 antigorite serpentinite samples measured at hydrostatic pressures up to 650 MPa, and with CPO-based calculation of 3D seismic properties of 11 samples. These data provide a new calibration for both seismic and fabric properties of antigorite, the only stable serpentine in subduction zones where temperature is above ~300 °C. Comparisons of laboratory velocities measured at high pressure with CPO data measured using EBSD techniques demonstrate that seismic anisotropy in high temperature serpentinites, which is essentially controlled by the antigorite c-axis fabric, is independent on the operating slip system but strongly dependent on the regime and magnitude of finite strain experienced by the rock. Extrapolation of experimental data with both pressure and temperature suggests that V_p anisotropy decreases but shear-wave splitting (ΔV_s) and V_p/V_s increase with increasing pressure in either cold or hot subduction zones. For a cold, steeply subducting slab, antigorite is most likely

deformed by nearly coaxial flattening or trench-parallel movement, forming trench-parallel seismic anisotropy. For a hot, shallowly subducting slab, however, antigorite is most likely deformed by simple shear or transpression. Trench-normal seismic anisotropy can be observed when the subducting dip angle is smaller than 30°. The geophysical characteristics of the Tibetan Plateau, such as strong heterogeneity in V_p, V_s and attenuation, shear-wave splitting and electric conductivity, may be explained by the presence of strongly deformed serpentinites in lithospheric shear zones reactivated along former suture zones between amalgamated blocks, hydrated zones of subducting lithospheric mantle, and the crust-mantle boundary if the temperature is below 700 °C in the region of interest.

Chapter 3 provides a detailed calibration on the magnitude and symmetry of seismic anisotropy for 132 schists to constrain their departures from transverse isotropy (TI) that is usually assumed in the interpretation of seismic data. The average bulk V_p anisotropy at 600 MPa for chlorite schists, mica schists, phyllites, sillimanite-mica schists, and amphibole schists examined is 12.0%, 12.8%, 12.8%, 17.0%, and 12.9%, respectively. Most of the schists show V_p anisotropy in the foliation plane which averages 2.4% for phyllites, 3.3% for mica schists, 4.1% for chlorite schists, 6.8% for sillimanite-mica schists, and 5.2% for amphibole schists. This departure from TI is due to the presence of amphibole, sillimanite, and quartz. Amphibole and sillimanite develop strong CPO with the fast c-axes parallel to the lineation, forming orthorhombic anisotropy with $V_p(X)>V_p(Y)>V_p(Z)$. Effects of quartz are complicated, depending on its volume fraction and prevailing slip system. Most of the mica- or amphibole-bearing schists and mylonites are approximately transversely isotropic in terms of S-wave velocities and splitting although their P-wave properties may display orthorhombic symmetry. The results provide insight for the interpretation of seismic data from the southeast Tibetan Plateau. The N-S to NW-SE polarized crustal anisotropy in the Sibumasu and Indochina blocks is caused by subvertically foliated metamorphic rocks deformed by predominantly compressional folding and subordinate strike-slip shear. These blocks have been rotated clockwise 70-90° around the east Himalayan Syntaxis, without finite eastward or southeastward extrusion, in responding to progressive indentation of India into Asia.

Chapter 4 reports new results on P- and S-wave velocities and anisotropy for 17 amphibole-rich rock samples containing 34-80 vol.% amphibole, measured at room temperature and hydrostatic pressures up to 650 MPa, and calculation of CPO-based seismic properties for 6 samples.

Combined petrophysical and geochemical analyses provide a new calibration for mean density, average major element contents, mean V_p-P and V_s-P coefficients, intrinsic V_p and V_s anisotropy, Poisson's ratios, the logarithmic ratio $R_{s/p}$, and elastic moduli of amphibole-rich rocks. The V_p values decrease with increasing SiO_2 and $Na_2O + K_2O$ contents but increase with increasing MgO and CaO contents. The maximum (≤0.38-0.40 km/s) and minimum S-wave birefringence values occur generally in the propagation direction parallel to Y and normal to foliation, respectively. Amphibole plays a critical role in the formation of seismic anisotropy, whereas the presence of plagioclase, quartz, pyroxene, and garnet diminishes the anisotropy induced by amphibole CPO. The CPO variations cause different anisotropy patterns illustrated in the Flinn diagram of $V_p(X)/V_p(Y)$-$V_p(Y)/V_p(Z)$ plots. The results make it possible to distinguish, in terms of seismic properties, the amphibolites from other categories of lithology such as granite-granodiorite, diorite, gabbro-diabase, felsic gneiss, mafic gneiss, eclogite, and peridotite within the Earth's crust. Hence, amphibole, aligned by dislocation creep, anisotropic growth, or rigid-body rotation, is the most important contributor to the seismic anisotropy of the deep crust beneath the continents and oceanic island arcs, which contains rather little phyllosilicates such as mica or chlorite.

Finally, Chapter 5 briefly outlines the main conclusions obtained from the present study and presents the further work which I am interested in.

TABLE OF CONTENTS

DEDICATION ..... **iii**

ACKNOWLEDGEMENTS ..... **iv**

RÉSUMÉ ..... **vi**

ABSTRACT ..... **ix**

TABLE OF CONTENTS ..... **xii**

LIST OF TABLES ..... **xvi**

LIST OF FIGURES ..... **xviii**

LIST OF INITIALS AND ABBREVIATIONS ..... **xxxii**

LIST OF RELATIONSHIPS AMONG THE ELASTIC CONSTANTS FOR ISOTROPIC MATERIALS AND ROCKS ..... **xxxiii**

CHAPTER 1 INTRODUCTION **1**

1.1 Objective and organization of the thesis 1

1.2 Calculations of rock seismic properties 3

1.2.1 Theory of elasticity 3

1.2.2 Mixture rules 8

1.2.3 Seismic properties of rock-forming minerals 12

1.2.4 Seismic properties of polycrystalline rocks 21

1.3 Laboratory techniques for measurement of seismic properties 23

1.4 Observation of seismic anisotropy 27

1.4.1 Propagation and polarization anisotropy 27

1.4.2 Laboratory measurement of anisotropy on rock samples 29

1.4.3 Field observation of seismic anisotropy 34

1.5 Sources of anisotropy in the Earth's interior 35

1.5.1 Layer-induced anisotropy 36

1.5.2 Fracture-induced anisotropy 37

1.5.3 CPO-induced anisotropy 39

CHAPTER 2 ANTIGORITE-INDUCED SEISMIC ANISOTROPY AND IMPLICATIONS FOR DEFORMATION IN OCEANIC SUBDUCTION ZONES AND THE TIBETAN PLATEAU 42

2.1 Introduction 42

2.2 Samples 45

2.3 Measured seismic velocities and anisotropy 50

2.3.1 Velocity-pressure relationship 50

2.3.2 P-wave velocity anisotropy 58

2.3.3 S-wave anisotropy and birefringence 60

2.4 CPO and calculated seismic velocities 61

2.5 Discussion 71

2.5.1 Comparison between single crystal and polycrystalline antigorite elasticity data 71

2.5.2 Effects of pressure on velocities and anisotropy 72

2.5.3 CPO-induced seismic anisotropy 77

2.5.4 Dependence of seismic velocities on the degree of serpentinization 81

2.5.5 Seismic anisotropy in subducting slabs and mantle wedge 84

2.5.6 Seismic anisotropy of the Tibetan Plateau 85

2.6 Conclusions 90

CHAPTER 3 MAGNITUDE AND SYMMETRY OF SEISMIC ANISOTROPY IN SCHISTS AND IMPLICATIONS FOR INTERPRETATION OF CRUSTAL STRUCTURE AND SHEAR-WAVE SPLITTING DATA FROM THE SOUTHEAST TIBETAN PLATEAU 92

3.1 Introduction 92
3.2 Samples 95
3.3 Laboratory-measured seismic velocities 101
3.4 EBSD-measured CPO and calculated seismic velocities 106
3.5 Discussion 127
3.5.1 Seismic properties of schists 127
3.5.2 Effects of quartz on seismic anisotropy of schists 134
3.5.3 Effects of prismatic minerals on seismic anisotropy of mica schists 141
3.5.4 Seismic properties of amphibole schists 143
3.5.5 Shear-wave velocity anisotropy 145
3.5.6 Implications for interpretation of crustal structure and seismic data from the southeast Tibetan Plateau 147
3.6 Conclusions 155
CHAPTER 4 A NEW CALIBRATION OF SEISMIC VELOCITIES, ANISOTROPY, FABRICS AND ELASTIC MODULI OF AMPHIBOLE-RICH ROCKS 158
4.1 Introduction 158
4.2 Samples 159
4.3 Measured seismic velocities and anisotropy 164
4.3.1 Velocity-pressure relationship 164
4.3.2 P-wave velocity anisotropy 171
4.3.3 S-wave anisotropy and splitting 175
4.4 CPO and calculated seismic velocities 178
4.5 Discussion 186
4.5.1 Seismic anisotropy 186
4.5.2 Dependence of seismic properties on chemical and modal compositions 191

4.5.3 V_p/V_s ratios and Poisson's ratios 196

4.5.4 Relationship between V_p and V_s 199

4.5.5 Elastic moduli 202

4.6 Conclusions 203

CHAPTER 5 CONCLUSION AND FUTURE WORK 205

5.1 Concluding summary 205

5.2 Future work 210

REFERENCES 213

LIST OF TABLES

Table 1.1 The stiffness C_{qr} for isotropic, cubic, hexagonal, and orthorhombic systems 6

Table 1.2 Density and anisotropic seismic properties of single crystals (Ji et al., 2002 and references therein; Bezacier et al., 2010) 15

Table 2.1 Description of the antigorite serpentinites studied* 47

Table 2.2 Chemical composition of each serpentinite sample studied 48

Table 2.3 Parameters of V_p-P curves and V_p anisotropy for 15 antigorite serpentinite samples studied 53

Table 2.4 Parameters of V_s-P curves and V_s anisotropy for 15 antigorite serpentinite samples studied 54

Table 2.5 Temperature derivatives of P- and S-wave velocities in an antigorite serpentinite[a] 73

Table 3.1 Description of the mica- or amphibole-bearing rock samples studied.....100

Table 3.2 Parameters of V_p-P curves and V_p anisotropy for 25 schist, gneiss and mylonite samples studied 102

Table 3.3 Parameters of V_s-P curves and V_s anisotropy for 10 mica- or amphobole-bearing samples studied 104

Table 3.4 Summary of seismic velocities and anisotropies calculated using the VRH averages for samples GLG132J, GLG133, GLG257, and YN1389[a] 122

Table 3.5 Calculated P-wave seismic properties based on EBSD-measured CPO and modal compositions for 15 quartz- and mica-bearing rock samples[a].....139

Table 4.1 Description of the amphibole-rich rock samples studied* 161

Table 4.2 Chemical compositions (wt.%) of amphibole-rich rock samples studied.....162

Table 4.3 Parameters of V_p-P curves and V_p anisotropy for 17 amphibole-rich samples studied[a] 167

Table 4.4 Parameters of V_s-P curves and V_s anisotropy for amphibole-rich rock samples studied[a] 169

Table 4.5 The arithmetic mean (M), the mode (Mo), and the median (Me) of V_p(X), V_p(Y), V_p(Z) and V_p(mean) values of 17 amphibole-rich rock samples studied 171

Table 4.6 Elastic constants in GPa of six amphibolite samples for which seismic velocities and anisotropy have been computed based on fabric data and modal compositions.....180

Table 4.7 Summary of crustal anisotropy measured worldwide*.....193

LIST OF FIGURES

Figure 1.1 Stress components acting on the faces of a unit cube.....4

Figure 1.2 Three-dimensional microstructures of two-phase composites. (a) The stress (σ_c) is applied in such a direction that both phases experience the same strains but different stresses (model of homogeneous strain). (b) The stress (σ_c) is applied in such a direction that both phases are subjected to same stresses but different strains (model of homogeneous stress). 10

Figure 1.3 Schematic comparison of isotropic and anisotropic wave propagation, in three dimensions. Isotropic propagation has linear P-wave particle motion parallel to the propagation direction and S-wave particle motion perpendicular to propagation, with two components arbitrarily defined as oriented horizontally (SH) and in the vertical plane (SV). Anisotropic propagation has a quasi-P (qP) wave with linear particle motion that is not quite parallel to the propagation direction, and two quasi-S waves (qS_1 and qS_2) with polarizations parallel and perpendicular to the fast direction for the propagation direction in question. The quasi-S waves are separated by a time δt. 13

Figure 1.4 Relative orientation between rock structural elements and seismic wave propagation (the first letter) and vibration directions (the second letter). X is parallel to the stretching lineation, Y is normal to the lineation and in the foliation plane, and Z is normal to the foliation plane.....14

Figure 1.5 P- and S-wave properties of 11 main minerals in the lithosphere. The P-wave phase velocities (V_p, up-left), the fast S-wave velocities (V_{s1}, up-right), the slow S-wave velocities (V_{s2}, low-left), and the S-wave birefringence or shear-wave splitting ($\Delta V_s=V_{s1}-V_{s2}$, low-right) are shown in equal area stereographic projection with respect to the crystallographic orientations of a, b, c, a^* and b^*, where a^* and b^* are the directions normal to (100) and (010) planes, respectively. Therein, one exception is present for biotite with the P-wave velocities (V_p, up-left), S-wave velocity anisotropy (AV_s, up-right) and the fast S-wave polarization (V_{s1}P). The maximum velocity (in km/s) is marked by a solid square and the minimum by an open circle. The anisotropy is in percent. Notice that the contour intervals are not the same for every diagram. Shaded areas correspond to directions of high P- or S-wave velocities. Except

antigorite and biotite which are cited from, respectively, Bezacier et al. (2010) and Aleksandrov and Ryzhova (1961), the left are modified after Ji et al. (2002). 21

Figure 1.6 Schematic illustration of sample assembly for measurement of seismic velocity at room temperature 27

Figure 1.7 Mean anisotropy of V_p [A_p(mean), %] for igneous, metamorphic and mantle rocks at 600 MPa and room temperature. The numbers of measurements (N) are also indicated. (Data from Ji et al., 2002). 33

Figure 1.8 Shear-wave splitting in layered rocks, with the faster polarized wave (V_{s1}) parallel to bedding and the slower polarized wave (V_{s2}) perpendicular to bedding. 37

Figure 1.9 Schematic illustration of shear-wave splitting through distributions of stress-aligned parallel vertical microcracks aligned normal to the direction of minimum horizontal stress (σ_h). 38

Figure 1.10 Temporal variations in normalized shear-wave delay time (ms/km) observed before earthquakes (modified after Crampin and Peacock, 2008). M_s 6 North Palm Springs Earthquake (Peacock et al., 1988). Left-hand-side: delay time with a least-squares line showing general increase before the earthquake. Right-hand-side: enlarged time scale for dotted box in left-hand-side, with dashed line showing precursory decrease in delay times before the earthquake. 39

Figure 2.1 (a) A weakly deformed antigorite serpentinite (Xiuyan Jade, sample A10) collected from (123.02383º E, 40.46767º N); (b) Three cylindrical minicores (diameter 2.54 cm) cut from an extremely deformed antigorite serpentinite (sample A1) in the X, Y, and Z directions. 44

Figure 2.2 Optical photomicrographs of antigorite serpentinites. (a) Undeformed serpentinite with cross-shaped interpenetrating texture. (b-c) Relict porphyroclasts in a highly sheared matrix with different crystallographic preferred orientations (b: sample A3; c: sample WZG2). (d) Ultramylonite of antigorite (sample A5). All images viewed in cross-polarized light with gypsum λ plate inserted. 46

Figure 2.3 Chemical variation diagrams showing the comparsion between serpentinites derived from metasomatism of dolomite (solid circles, this study and Ji et al., 2013a) and

serpentinization of peridotite (open circles, Ji et al., 2002; Sun et al., 2012; Wang et al., 2005; Wang and Ji, 2009). Weight percent plots of (a) MgO, (b) Al_2O_3, and (c) FeO + Fe_2O_3 versus SiO_2, and (d) Al_2O_3 versus CaO. 49

Figure 2.4 P-wave velocity (V_p) versus pressure in three orthogonal directions (X, Y, and Z) through samples (a) A5, (b) A1 and (c) WZG2, and seven directions (X, Y, Z, X45Y, X45Z, Y45Z, and X55Y55Z as defined in the text) through (d) sample A16. Samples A1, A5, and A16 (this study) and WZG2 (Ji et al., 2013a). 51

Figure 2.5 S-wave velocity (V_s) versus propagation and polarization directions in representative antigorite serpentinite samples (a) A5, (b) A1, (c) WZG2, and (d) A16. The orientations of wave propagation and polarization are defined in Table 2.4. Samples A1, A5, and A16 (this study) and WZG2 (Ji et al., 2013a). 52

Figure 2.6 Statistics of V_p-P curve parameters, defined by Eq. (2.1), for three structural directions (X, Y, and Z) and the equivalent isotropic aggregate (mean) of 32 antigorite serpentinite samples (15 from this study and 17 from Ji et al., 2013a). N: total number of samples; M: arithmetic mean; S.D.: standard deviation; M_o: mode (the most frequently occurring value in the distribution); Me: median (the fiftieth percentile in the distribution). 56

Figure 2.7 Statistics of V_s-P curve parameters, defined by Eq. (2.1), for six sets of propagation-polarization directions (XY, XZ, YX, YZ, ZX, and ZY) and the equivalent isotropic aggregate (mean) of 24 antigorite serpentinite samples on which V_s has been measured as a function of pressure in all six sets of propagation-polarization directions) (13 from this study, and 11 from Ji et al., 2013a). N, M, S.D., Mo, and Me as in Figure 2.6 caption. 57

Figure 2.8 Flinn-type diagram showing V_p anisotropy at 600 MPa. Solid dots indicate the data (15 samples) from this study and open dots (17 samples) from Ji et al. (2013a). The origin of the coordinate axes represents random CPO and thus zero anisotropy. Dashed lines indicate iso-anisotropy surfaces. 59

Figure 2.9 Shear-wave birefringence along the Y direction [V_s(YX)-V_s(YZ)] versus shear-wave birefringence along the X direction [V_s(XY)-V_s(XZ)]. 61

Figure 2.10 EBSD-measured pole figures for antigorite from 11 serpentinite samples (A5, A9, YSK5A, A1, A13, A15, YSK3B, WZG2, YSK2A, A3, and A16). Equal-area lower hemisphere projections. The maximum density and *J* index (*pfJ*), which are calculated from the orientation distribution function, are indicated for each sample. N: number of measured grains. Samples are arranged according to antigorite c-axis fabric pattern. 63

Figure 2.11 P-wave velocities, S-wave velocity anisotropy and fast polarization directions for 11 antigorite serpentinite samples (A5, A9, YSK5A, A1, A13, A15, YSK3B, WZG2, YSK2A, A3, and A16) calculated from CPO data and single crystal elastic constants of antigorite. Equal-area lower hemisphere projections. Samples are arranged in the same order as in Figure 2.10. 65

Figure 2.12 Variations of calculated P-wave velocity as a function of incidence angle in the XY, XZ, and YZ planes. (a) Sample A5 (extremely deformed), k_p=0.029 and $V_p(X) \approx V_p(Y) \gg V_p(Z)$; (b) Sample YSK3B (highly deformed), k_p=0.221 and $V_p(X) > V_p(Y) \gg V_p(Z)$; (c) Sample WZG2 (extremely deformed), k_p=0.742 and $V_p(X) > V_p(Y) > V_p(Z)$; (d) Sample A16 (moderately deformed), k_p=2.456 and $V_p(X) \gg V_p(Y) > V_p(Z)$. 67

Figure 2.13 Calculated split fast and slow S-wave velocities (V_{s1} and V_{s2}) as a function of incidence angle in the XY, XZ, and YZ planes of 4 representative antigorite serpentinite samples (A5, YSK3B, WZG2, and A16). For sample YSK3B (highly deformed) and samples A5 and WZG2 (extremely deformed), the largest birefringence occurs for the propagation in the foliation plane while little birefringence occurs in the direction normal to the foliation. For sample A16 (moderately deformed), however, the birefringence is relatively small (<0.18 km/s) but occurs almost equally in the X, Y, and Z directions. 68

Figure 2.14 Plots of P- and maximum S-wave velocity anisotropy (A_p and AV_s^{max}) as a function of the *J* index (*pfJ*) for antigorite a-, b-, and c-axis fabrics of serpentinites containing >91 vol.% antigorite.....69

Figure 2.15 Histograms showing the distribution of antigorite serpentinite intrinsic velocity V_0 for (a) P- and (b) S-waves and the comparison with the Reuss, Voigt, and Hill averages calculated from the single crystal elasticity data of antigorite (Bezacier et al., 2010). Data from this study

and Ji et al. (2013a) are shown in light grey shaded domains. Data from Christensen (2004) are also indicated. N, M, S.D., Mo, and Me as in Figure 2.6 caption. 72

Figure 2.16 Comparison of P-wave velocity (V_p) and anisotropy (A_p), S-wave velocity (V_s) and birefringence (ΔV_s) and V_p/V_s between hot and cold subduction zones. The lower boundary of the antigorite stability field is defined by P=7.750-0.0258T, where P is in GPa, and T in °C (Reynard, 2013). Antigorite turns to peridotite above 600 °C in the cold subduction zone but 700 °C in the hot subduction zone. The orientations of wave propagation and polarization are defined in Tables 2.3-2.4. 76

Figure 2.17 Mean (a) P- and (b) S-wave velocities and velocity ratios V_p/V_s measured at 600 MPa as a function of serpentine volume fraction (φ) for low temperature (LT, open dots) and high temperature (HT, solid squares from this study and Ji et al. (2013a), and open squares from the references) serpentinization. The LT data are from Ji et al. (2002, 2007), Sun (2011) and Wang et al. (2005) and the HT data are from Birch (1960), Christensen (1978), Ji et al. (2013a), Kern et al. (1997) and this study. 83

Figure 2.18 (a) Observations of shear-wave splitting in the Tibetan Plateau and its adjacent regions. (b) Lithospheric section of Himalaya-Tibet orogen (modified from Tapponnier et al., 2001). Dotted lines indicate potential serpentinized shear zones. 88

Figure 3.1 (a) Simplified geological map of the Tibetan Plateau and surrounding regions. Blue rectangle refers to Figure 3.1b. (b) Tectonic map of the east Tibetan Plateau and surrounding regions with the vectors of GPS (magenta arrows; Chen et al., 2000; Gan et al., 2007; Zhang et al., 2004), Pms- (blue bars) and XKS- (black bars) wave splitting (Chen et al., 2013; Huang et al., 2007; Lev et al., 2006; Shi et al., 2012; Xu et al., 2006), the maximum principal stress σ_1 (green bars; Wu et al., 2004; Zhao et al., 2013; Zhong and Cheng, 2006), and the APM (thick white arrows; Chen et al., 2013; DeMets et al., 1994). (c) Average orientations of GPS, Pms- and XKS-wave splitting, σ_1, and APM in three tectonic blocks. Red lines show main shear zones or fault zones: (1) Gaoligong shear zone; (2) Lancangjiang shear zone; (3) Ailao Shan-Red River shear zone; (4) Xianshuihe-Xiaojiang fault zone; (5) Nabang fault; (6) Nanting fault; (7) Longmen Shan fault; (8) Lijiang-Xiaojinhe fault. Half arrows refer to Tertiary shear sense. 94

Figure 3.2 Typical phyllosilicate-bearing rocks in the (a-b, e-f) Gaoligong, (c) Ailao Shan-Red River, and (d, g-h) Lancangjiang shear zones, Yunnan, China, where foliation is nearly vertical and stretching lineation is subhorizontal. (a) Chlorite-mica schist at site GLG31 (24°48′47.9″ N, 98°50′02.1″ E, altitude 1523 m). (b) Mica schist developed tight to isoclinal folds with upright axial surface and horizontal hinge line at site GLG 122 (27°55′32.9″ N, 98°39′56″ E, altitude 1543 m). (c) Mica schist at site YN1356 (27°07′10.6″ N, 99°10′11.7″ E, altitude 1514 m). (d) Schist split along its foliation planes in which the mica layers lie. Site YN1373 (25°55′2.5″ N, 99°07′56.6″ E, altitude 1656 m). (e) Mica-bearing dioritic mylonite at site GLG133 (26°49′37.5″ N, 98°53′02.4″ E, altitude 1164 m). (f) Dioritic gneiss and metapelitic schist at site GLG134 (26°48′57.4″ N, 98°53′07.1″ E, altitude 1164 m). (g) Quartz-mica schist at site GLG132 (26°59′5.3″ N, 98°51′50.8″ E, altitude 1204 m). (h) Quartz-mica schist at site YN1389 (26°51′31.3″ N, 98°52′33.6″ E, altitude 1153 m). Lineation is indicated by L. 97

Figure 3.3 Typical microstructures of schists from the Gaoligong, Lancangjiang, and Ailao Shan-Red River shear zones (west Yunnan, China). (a) Biotite-quartz schist from site GLG257 (26°21'12.2" N, 98°49'37.8" E, altitude 1840 m). (b) Muscovite-quartz schist, in which quartz c-axes are preferentially aligned parallel or subparrallel to Y (Figure 3.7c), from site GLG132J. (c) Muscovite-quartz-plagioclase schist from site YN1351 (28°27'42.8" N, 98°54'19.8" E, altitude 2902 m). (d) Metapelitic schist consisting of biotite, sillimanite, quartz, plagioclase and garnet from site GLG203 (26°57'28.3" N, 98°52'03.2" E, altitude 1174 m). (e) Phyllite consisting of fine-grained muscovite, quartz and feldspar from site GLG243 (28°04'58.5" N, 98°33'51.5" E, altitude 1564 m). (f) Amphibole schist consisting of hornblende, plagioclase and quartz from site GLG201 (26°35'43"N, 98°54'41" E, altitude 1181 m). (g) Dioritic mylonite from site GLG133. (h) Quartz-muscovite-biotite schist from site YN1389. Foliation is indicated by S..... 98

Figure 3.4 P-wave velocity (V_p) versus pressure in three orthogonal directions (X, Y, and Z) through samples (a) GLG237 (Qtz-Hbl-Bt schist), (b) GLG258 (Qtz-Bt schist), (c) GLG133 (dioritic mylonite), and (d) AM1 (amphibolitic gneiss)..... 105

Figure 3.5 S-wave velocity (V_s) versus propagation and polarization directions in samples (a) GLG237 (Qtz-Hbl-Bt schist), (b) GLG258 (Qtz-Bt schist), (c) GLG133 (dioritic mylonite),

and (d) AM1 (amphibolitic gneiss). The first letter signifies propagation direction and the second letter the polarization direction. 106

Figure 3.6 EBSD-measured pole figures for biotite from samples (a) GLG102, (b) GLG119, (c) GLG133, (d) GLG132J, (e) GLG203, (f) GLG237, (g) GLG257, (h) GLG134, (i) GLG258, and (j) YN1389, and for muscovite from samples (k) GLG132J, (l) YN1351, and (m) YN1389. Equal-area lower hemisphere projections. The maximum density and *J* index (*pfJ*), which are calculated from the orientation distribution function, are indicated for each sample. N: number of measured grains. 111

Figure 3.7 EBSD-measured pole figures for quartz from samples (a) GLG133, (b) GLG102, (c) GLG132J, (d) GLG134, (e) GLG203, (f) YN1389, (g) GLG110, (h) GLG119, (i) GLG237, (j) GLG258, (k) AM1, (l) YN1351, (m) GLG201B, and (n) GLG257. Equal-area lower hemisphere projections. The maximum density and *J* index (*pfJ*), which are calculated from the orientation distribution function, are indicated for each sample. N: number of measured grains. 113

Figure 3.8 EBSD-measured pole figures for plagioclase from samples (a) GLG102, (b) GLG110, (c) GLG119, (d) GLG132J, (e) GLG133, (f) GLG134, (g) AM1, (h) GLG201B, (i) GLG203, (j) GLG237, and (k) YN1351, and for K-feldspar from samples (l) GLG102 and (m) GLG110. Equal-area lower hemisphere projections. The maximum density and *J* index (*pfJ*), which are calculated from the orientation distribution function, are indicated for each sample. N: number of measured grains. 115

Figure 3.9 EBSD-measured pole figures for hornblende from samples (a) GLG110, (b) AM1, (c) GLG201B, and (d) GLG237. Equal-area lower hemisphere projections. The maximum density and *J* index (*pfJ*), which are calculated from the orientation distribution function, are indicated for each sample. N: number of measured grains. 117

Figure 3.10 EBSD-measured pole figures for sillimanite from metapelitic sample GLG203. Equal-area lower hemisphere projections. The maximum density and *J* index (*pfJ*), which are calculated from the orientation distribution function, are indicated for each sample. N: number of measured grains. 118

Figure 3.11 P-wave velocities, S-wave velocity anisotropy and fast polarization directions for mica schists (a) GLG257, (b) YN1389, (c) GLG132J, (d) YN1351, (e) GLG258, (f) GLG237, (g)

GLG119, and (h) GLG203, amphibolitic gneiss (i) AM1, amphibole schists (j) GLG201B and (k) GLG110, dioritic gneiss (l) GLG134 and mylonite (m) GLG133, and felsic mylonites (n) GLG102, calculated from CPO data, modal composition, and single crystal elastic constants of each rock-forming mineral. Equal-area lower hemisphere projections. 120

Figure 3.12 Variation of calculated P-wave velocity as a function of incidence angle in the XY, XZ, and YZ planes. (a) Sample GLG132J, k_p=-0.195 and $V_p(Y)>V_p(X)\gg V_p(Z)$; (b) Sample GLG133, k_p=-0.172 and $V_p(Y)>V_p(X)\gg V_p(Z)$; (c) Sample GLG257, k_p=0.118 and $V_p(X)>V_p(Y)\gg V_p(Z)$; (d) Sample YN1389, k_p=-0.116 and $V_p(Y)>V_p(X)\gg V_p(Z)$. 123

Figure 3.13 Calculated split fast and slow S-wave velocities (V_{s1} and V_{s2}) as a function of incidence angle in the XY, XZ, and YZ planes of three mica schists (samples GLG132J, GLG257, and YN1389) and one dioritic mylonite (sample GLG133). The largest birefringence ($\Delta V_s=V_{s1}-V_{s2}$) occurs for the propagation in the foliation plane while little birefringence takes place in the direction normal to the foliation. $\Delta V_s(X)\geq\Delta V_s(Y)\gg\Delta V_s(Z)$.....124

Figure 3.14 Variations of calculated S-wave velocity anisotropy as a function of incidence angle in the XY, XZ, and YZ planes. (a) Sample GLG132J; (b) Sample GLG133; (c) Sample GLG257; (d) Sample YN1389. All samples are characterized by $AV_s(X)>AV_s(Y)\gg AV_s(Z)$. 125

Figure 3.15 The ratios (V_p/V_s) of P-wave velocity to S-wave velocities (V_{s1} and V_{s2}) as a function of incidence angle in the XY, XZ, and YZ planes for (a, c and d) three mica schists and (b) one dioritic mylonite. The largest V_p/V_s occurs for propagation in the foliation plane whereas the minimum ratio appears in the direction at ~30° with the Z. 126

Figure 3.16 P- and S-wave properties of elastically anisotropic single crystals of 4 common rock-forming minerals (Quartz, plagioclase, muscovite, and biotite) making up some samples in this study are shown in equal-area lower hemisphere projections with respect to the crystal form and crystallographic orientations of **a**, **b**, **c**, $\mathbf{a}^*$ and $\mathbf{b}^*$, where $\mathbf{a}^*$ and $\mathbf{b}^*$ are the directions normal to (100) and (010) planes, respectively. V_p: P-wave velocities; AV_p: anisotropy of P-wave velocity; AV_s: direction-dependent shear-wave velocity (V_s) anisotropy; V_{s1}P: polarization direction of fast shear-wave. The maximum velocity (in km/s) and anisotropy (in percent) are marked by open square and the minimum by solid circle. The seismic properties are calculated using a suite of programs developed by Mainprice (1990) and appropriate

mineral single-crystal elastic constants (Quartz: McSkimin et al., 1965; Plagioclase: Aleksandrov et al., 1974; Muscovite: Vaughn and Guggenheim, 1986; Biotite: Aleksandrov et al., 1961).....128

Figure 3.17 Flinn-type diagram showing three possible end-member types of contoured CPO patterns of mica c-axes and corresponding P-wave velocity anisotropy. The origin of the coordinate axes (1, 1) represents random CPO and thus zero anisotropy. X, lineation; Y, direction normal to lineation and in foliation; Z, normal to foliation. The CPO strengths increase with increasing finite strains. 129

Figure 3.18 Flinn-type diagram showing P-wave velocities of 23 chlorite schists (open squares), 65 mica schists (solid dots), 19 phyllites (open dots) and 16 sillimanite-mica schists (open diamonds) at 600 MPa. Dashed lines signify iso-anisotropy surfaces. The shadowed zone indicates a quasi-transverse isotropy pattern.....131

Figure 3.19 Bulk anisotropy and foliation anisotropy of P-wave velocities as a function of hydrostatic pressure in a Qtz-Hb-Bt schist (sample GLG237) and a Qtz-Bt schist (sample GLG258) from the Gaoligong shear zone (Yunnan, China).....132

Figure 3.20 Histograms of the (a) bulk anisotropy and (b) foliation anisotropy of P-wave velocities for 23 chlorite schists, 65 mica schists, 19 phyllites, 16 sillimanite-mica schists, and 5 amphibole schists at 600 MPa.....133

Figure 3.21 Basic types of quartz c-axis fabrics and corresponding seismic anisotropy patterns in coaxially deformed rocks. 135

Figure 3.22 Cobweb diagram showing anisotropic patterns classified according to P-wave velocity ratios for 30 quartz-rich metamorphic rocks at 600 MPa. Dashed lines signify iso-anisotropy surfaces. The shadowed central zone indicates quasi-isotropy in seismic properties (bulk $A_p \leq 2\%$). See text for discussion. 137

Figure 3.23 Bulk (solid dot) and foliation (open dot) anisotropy of P-wave velocity as a function of volume fractions of (a) mica, (b) feldspar, and (c) quartz for 15 samples consisting of mica, quartz and feldspar (5 samples from this chapter; 8 samples from Erdman et al., 2013; 2 samples from Brownlee et al., 2011). Data used to build this figure are given in Table 3.5. 140

Figure 3.24 Ternary plots of (a) bulk and (b) foliation anisotropies as a function of normalized modal compositions of quartz (Q), feldspar (F), and mica (M). Each black diamond denotes data of each sample (Table 3.5). 141

Figure 3.25 Bulk anisotropy (solid dots) and foliation anisotropy (open dots) of P-wave velocities as a function of sillimanite content (vol.%) for metapelitic schists. 143

Figure 3.26 Flinn-type diagram showing P-wave velocities of four amphibole schists (samples AM2, AM3, P59, and S3570), an amphibolitic gneiss (sample AM1), a Hbl-Bt schist (sample S776.2) and a Qtz-Hbl-Bt schist (GLG237) at 600 MPa. Dashed lines indicating iso-anisotropy surfaces. The maximum anisotropy values are also illustrated for single crystal of hornblende, and S- and L-tectonites composed of amphibole. S- and L-tectonites, which deformed by coaxial flattening and coaxial constriction, develop only foliation and only lineation, respectively, whereas LS-tectonites develop both flattened foliation and stretching lineation under simple shear. S>L (foliation dominates over lineation) and L>S (lineation dominates over foliation). 144

Figure 3.27 (a) Bulk anisotropy and (b) foliation anisotropy of P-wave velocities as a function of hydrostatic pressure for four amphibole schists (samples AM2, AM3, P59, and S3570), an amphibolitic gneiss (sample AM1), a Hbl-Bt schist (sample S776.2) and a Qtz-Hbl-Bt schist (GLG237) at 600 MPa.....145

Figure 3.28 Plots of V_s(XY) versus V_s(YX), V_s(XZ) versus V_s(YZ), and V_s(ZX) versus V_s(ZY) in (a), (b), and (c), respectively, for 2 amphibole schists, 12 mica schists, 1 phyllite, 8 sil-mica schists and 10 mica-bearing felsic mylonites.....146

Figure 3.29 Histograms of V_s(XY)-V_s(YX), V_s(XZ)-V_s(YZ), and V_s(ZX)-V_s(ZY) values for 33 schists plotted in Figure 3.28. Data at 600 MPa.....147

Figure 3.30 Experiment of plasticene by Tapponnier et al. (1982), which emphasizes the eastward extrusion of the Indochina and South China lithospheric blocks bounded by major strike-slip faults as a result of the India-Eurasia convergence. 150

Figure 3.31 Dough experiment (Ji and Wang, unpublished data) suggesting that the post-collisional convergence by the northward indentation of India has been accomplished principally by crustal thickening through folding and vertical stretching in a northward-propagating zone

north of the Indian indenter and the clockwise rotation and northwestward displacement of the Sibumasu and Indochina blocks. 153

Figure 4.1 Densities (g/cm^3) of amphibole-rich rocks from this chapter (17 samples) and the references (44 samples). N, M, S.D., M_o, and Me as in Figure 2.6 caption. 160

Figure 4.2 Histograms of major element contents for amphibole-rich rocks from this chapter (17 samples) and the references (28 samples). The definitions of N, M, S.D, M_o, and Me as in Figure 2.6 caption. 162

Figure 4.3 P-wave velocity (V_p) versus pressure in three orthogonal directions (X, Y, and Z) through amphibolite samples (a) AM2, (b) AM4, (c) AM9, and (d) AM15. 165

Figure 4.4 S-wave velocity (V_s) versus propagation and polarization directions in representative amphibolite samples (a) AM2, (b) AM3, (c) AM4, (d) AM6, (e) AM9, and (f) AM15. The first letter signifies propagation direction and the second letter the polarization direction. 166

Figure 4.5 Statistics of V_p-P curve parameters, defined by Eq. (2.1), for three structural directions (X, Y, and Z) and the equivalent isotropic aggregate of the amphibolites consisting mainly of hornblende and plagioclase from this chapter (13 samples) and the references (35 samples). The definitions of N, M, S.D, M_o, and Me as in Figure 2.6 caption. 170

Figure 4.6 Three types of P-wave velocity anisotropy (A_p) versus pressure curves for amphibole-rich rock samples. See text for discussion. 172

Figure 4.7 (a) V_p-P and (b-c) V_s-P curves for various propagation and polarization directions (see Table 4.4 for their definitions) of amphibolite sample AM1 from the Gaoligong Mts, Yunnan, China. 174

Figure 4.8 Comparison of the theoretical P-wave velocities with those measured along 4 different propagating directions (X45Y, X45Z, Y45Z, and X55Y55Z) oblique to the principal axes of the finite strain ellipsoid (X, Y, and Z) in amphibolite sample AM1 from the Gaoligong Mts, Yunnan, China. 174

Figure 4.9 S-wave velocity anisotropy (A_s) versus pressure curves for five representative amphibole-rich rock samples (AM1, AM2, AM3, AM9, and AM15). 175

Figure 4.10 Shear-wave splitting along various propagating directions in amphibolite samples (a) AM1, (b) AM2, (c) AM6, and (d) AM9.....178

Figure 4.11 EBSD-measured pole figures for hornblende from samples AM1, AM2, AM3, AM4, AM7, and AM8. Equal-area lower hemisphere projections. The maximum density and *J* index (*pfJ*), which are calculated from the orientation distribution function, are indicated for each sample. N: number of measured grains.....181

Figure 4.12 EBSD-measured pole figures for plagioclase from samples AM1, AM2, AM3, AM4, AM7, and AM8. Equal-area lower hemisphere projections. The maximum density and *J* index (*pfJ*), which are calculated from the orientation distribution function, are indicated for each sample. N: number of measured grains.....182

Figure 4.13 EBSD-measured pole figures for quartz from samples AM1, AM3, AM4, AM7, and AM8. Equal-area lower hemisphere projections. The maximum density and *J* index (*pfJ*), which are calculated from the orientation distribution function, are indicated for each sample. N: number of measured grains. 183

Figure 4.14 P-wave velocities, S-wave velocity anisotropy and fast polarization directions for amphibolite samples AM1, AM2, AM3, AM4, AM7, and AM8, calculated from CPO data, modal composition, and single crystal elastic constants of each rock-forming mineral. Equal-area lower hemisphere projections. 185

Figure 4.15 Flinn-type diagram showing P-wave velocities of amphibole-rich rocks at 600 MPa. Dashed lines indicate iso-anisotropy surfaces. The maximum anisotropy values are also illustrated for single crystal of hornblende, and S- and L-tectonites. The solid dots indicate the data from this study.....187

Figure 4.16 Histograms of bulk P- and S-wave velocity anisotropy (A_p and A_s, %) for 48 amphibolites consisting mainly of hornblende and plagioclase at (a, c) 200 MPa and (b, d) 600 MPa from this chapter (13 samples) and the references (35 samples). The definitions of N, M, S.D, M_o, and Me as in Figure 2.6 caption. 189

Figure 4.17 Mean P- and S-wave velocities versus major element (SiO_2, MgO, CaO, and Na_2O+K_2O) contents for amphibole-rich rocks. Data from this chapter (solid circles) and those from previous studies (open circles, Burke and Fountain, 1990; Fountain, 1976;

Fountain et al., 1990; Kern et al., 1996, 1999, 2001, 2009; Miller and Christensen, 1994; Zhao et al., 2011; Zhou et al., 2011). 194

Figure 4.18 (a) V_p(X), (b) V_p(Y), (c) V_p(Z), (d) mean V_p, and (e) mean V_s measured at 600 MPa versus hornblende volume fraction (vol.%). Data from this chapter (solid circles) and those from previous studies (open circles, Barruol, 1993; Birch, 1960; Burke and Fountain, 1990; Christensen, 1965, 1978; Fountain, 1976; Fountain et al., 1990; Kern et al., 1996, 1997, 1999, 2001, 2009; Khazanehdari et al., 2000; McDonough and Fountain, 1988; Miller and Christensen, 1994; Punturo et al., 2005; Siegesmund et al., 1989; Zhao et al., 2011; Zhou et al., 2011).....195

Figure 4.19 P- and S-wave velocity anisotropy (A_p and A_s) versus hornblende volume fraction (vol.%). Data from this chapter (solid circles) and those from previous investigations (open circles, Barruol, 1993; Burke and Fountain, 1990; Christensen, 1965, 1978; Fountain, 1976; Fountain et al., 1990; Kern et al., 1996, 1997, 1999, 2001, 2009; Khazanehdari et al., 2000; McDonough and Fountain, 1988; Miller and Christensen, 1994; Punturo et al., 2005; Siegesmund et al., 1989; Zhao et al., 2011; Zhou et al., 2011).....196

Figure 4.20 Histogram of Poisson's ratios for 40 amphibole-rich rocks (9 from this chapter and 31 from Barruol, 1993; Christensen, 1965; Fountain, 1976; Fountain and Salisbury, 1996; Kern et al., 1996, 1997, 1999, 2001, 2009; Miller and Christensen, 1994; Punturo et al., 2005; Siegesmund et al., 1989; Zhao et al., 2011; Zhou et al., 2011) at 600 MPa. The statistical data (N, M, S.D, Mo and Me as in Figure 2.6 caption) are indicated only for amphibolites consisting mainly of hornblende and plagioclase (32 samples).....197

Figure 4.21 (a) Apparent V_p/V_{s1} ratio (β_{ij}) versus confining pressure for each propagation direction in amphibolite sample AM1 and (b) comparison of apparent ratios with the equivalent isotropic V_p/V_s ratio (β_0) calculated from the mean V_p and V_s velocities for sample AM1..199

Figure 4.22 (a) V_s-V_p and (b) lnV_s-lnV_p plots for 40 amphibole-rich rocks (9 from this chapter and 31 from the references) at 600 MPa. Predictions of the empirical equation (dashed curves) proposed by Brocher (2005) are also indicated.....200

Figure 4.23 Variation of $R_{s/p}$ versus density (g/cm^3) for amphibolite and other categories of lithology at a hydrostatic pressure of 600 MPa.....201

Figure 4.24 The μ-λ plots for amphibolite and other categories of lithology at a hydrostatic pressure of 600 MPa. 202

LIST OF INITIALS AND ABBREVIATIONS

P	Pressure
T	Temperature
HP	High pressure
UHP	Ultrahigh pressure
P-wave	Compressional wave
S-wave	Shear-wave
ρ	Density in g/cm^3
φ	Volume fraction in vol.%
λ	Lamé parameter
μ or G	Shear modulus
E	Young's modulus
K	Bulk modulus
υ	Poisson's ratio
$\boldsymbol{C}$	Stiffness tensor
$\boldsymbol{S}$	Compliance tensor
V_p	Compressional wave velocity
V_s	Shear-wave velocity
V_{s1}	Fast shear-wave velocity in shear-wave splitting
V_{s2}	Slow shear-wave velocity in shear-wave splitting
ΔV_s	Shear-wave birefringence (double refraction) ($\Delta V_s = V_{s1}-V_{s2}$)
ϕ or V_{s1}P	Fast polarization direction in shear-wave splitting
δt	Delay time in shear-wave splitting
X	Direction parallel to the stretching lineation
Y	Direction perpendicular to the lineation and in the foliation
Z	Direction normal to the foliation
Λ	Direction of wave propagation and polarization
A	Seismic velocity anisotropy
A_p or A_p(B)	Bulk P-wave velocity anisotropy
A_p(F)	P-wave velocity anisotropy within the foliation plane
A_s	S-wave velocity anisotropy
CPO	Crystallographic preferred orientation
SPO	Shape preferred orientation

LIST OF RELATIONSHIPS AMONG THE ELASTIC CONSTANTS FOR ISOTROPIC MATERIALS AND ROCKS

	K	E	λ	μ	υ
λ, μ	$\lambda + \frac{2\mu}{3}$	$\mu\frac{3\lambda + 2\mu}{\lambda + \mu}$			$\frac{\lambda}{2(\lambda + \mu)}$
K, λ		$9K\frac{K - \lambda}{3K - \lambda}$		$\frac{3(K - \lambda)}{2}$	$\frac{\lambda}{3K - \lambda}$
K, μ		$\frac{9K\mu}{3K + \mu}$	$K - \frac{2\mu}{3}$		$\frac{3K - 2\mu}{2(3K + \mu)}$
E, μ	$\frac{E\mu}{3(3\mu - E)}$		$\mu\frac{E - 2\mu}{3\mu - E}$		$\frac{E}{2\mu} - 1$
K, E			$3K\frac{(3K - E)}{9K - E}$	$\frac{3KE}{9K - E}$	$\frac{3K - E}{6K}$
λ, υ	$\lambda\frac{1 + \upsilon}{3\upsilon}$	$\lambda\frac{(1 + \upsilon)(1 - 2\upsilon)}{\upsilon}$		$\lambda\frac{1 - 2\upsilon}{2\upsilon}$	
μ, υ	$\mu\frac{2(1 + \upsilon)}{3(1 - 2\upsilon)}$	$2\mu(1 + \upsilon)$	$\mu\frac{2\upsilon}{1 - 2\upsilon}$		
K, υ		$3K(1 - 2\upsilon)$	$3K\frac{\upsilon}{1 + \upsilon}$	$\frac{3K(1 - 2\upsilon)}{2(1 + \upsilon)}$	
E, υ	$\frac{E}{3(1 - 2\upsilon)}$		$\frac{E\upsilon}{(1 + \upsilon)(1 - 2\upsilon)}$	$\frac{E}{2(1 + \upsilon)}$	
V_P, V_S, ρ	$\rho\left(V_P^2 - \frac{4}{3}V_S^2\right)$	$\frac{\rho V_S^2(3V_P^2 - 4V_S^2)}{V_P^2 - V_S^2}$	$\rho(V_P^2 - 2V_S^2)$	ρV_S^2	$\frac{V_P^2 - 2V_S^2}{2(V_P^2 - V_S^2)}$
V_P/V_S					$\sqrt{\frac{2(1 - \upsilon)}{1 - 2\upsilon}}$

CHAPTER 1 INTRODUCTION

1.1 Objective and organization of the thesis

In order to reconstruct the geodynamic history of the Earth's interior, geologists require to know the mineralogy and structure within the Earth, and to understand the deformational and kinematic processes that occur beneath the Earth's surface. So far, our knowledge on the interior of the Earth, which can be reflected by velocity distributions and anisotropy within the crust and mantle that are formed via these processes, mainly come from seismic data due to a fact that only the uppermost crust (<12 km) is accessible to geological sampling and mapping, especially in continental conditions. Interpretation of seismic data, however, is strongly dependent on the extrapolation of laboratory-measured seismic properties of relevant rocks, which are currently being deformed at certain depths, in a given geological setting. It is therefore necessary to obtain seismic properties (e.g., P- and S-wave velocities, anisotropy, and shear-wave splitting) of different rock types at different states of strain, through measurements by directing high frequency waves at oriented rock samples, or calculation from the crystallographic preferred orientations (CPO) of minerals measured in polished rock samples. The objective of this Ph.D. thesis is to better understand how the seismic compressional and shear-wave velocities (V_p and V_s), anisotropy, and elastic moduli of rocks in the Earth's middle and lower crust and subduction zones shallower than ~300 km are influenced by their chemical and modal compositions, microstructures (e.g., foliation and lineation), CPO of anisotropic minerals at various confining pressures and corresponding temperatures.

In order to facilitate the reading of this thesis, this chapter contains three aspects to be introduced: (1) the calculation of seismic properties of rocks, which contains basic principles of elasticity, mixture rules, and seismic properties of rock-forming minerals; and seismic properties of polycrystalline rocks; (2) laboratory measurement of rock seismic properties; and (3) the source of seismic anisotropy within the continental crust and upper mantle. In addition to simple description below, more detailed background information regarding the seismic properties of rocks used in this study can be found in the various chapters of this thesis.

Serpentinization is a key phenomenon, which occurs beneath mid-oceanic ridges, in oceanic subducting slabs, and the overlying mantle wedges, for understanding the geodynamics of

subduction zones in the 10-200 km depth range. Therein, anomalously low seismic velocities and high anisotropies in subducting oceanic slabs and forearc mantle wedges as well as suture zones between amalgamated continental lithospheric blocks are considered to be dominated by antigorite, the only serpentine stable above 300 °C in subduction zones and thus named as high temperature (HT) serpentine. In Chapter 2, a new calibration for both seismic and fabric properties of antigorite will be presented according to measurements of V_p, V_s, and anisotropy of 15 antigorite serpentinite samples at hydrostatic pressures up to 650 MPa, and to CPO-based calculation of 3D seismic properties of samples. The results of this chapter provides a basis to understand the critical role of antigorite c-axis fabric in the formation of different anisotropy patterns, which can equally be used to explain the variations of seismic velocities and anisotropy with depth in cold and hot subduction zones and the Tibetan Plateau.

Current interpretations of seismic data are generally based on an assumed simple symmetry in seismic properties of rocks in order to minimize the number of free parameters and guarantee stable and unique inversion. Thus, transverse isotropy (TI) or hexagonal symmetry in seismic waves is usually assumed to describe the elasticity of a rock body. In a TI material, P-wave velocities are virtually the same in all radial directions perpendicular to the axis of symmetry, along which the seismic velocity can be either higher (e.g., laminated anorthosite) or lower (e.g., mica schist) than the velocity normal to the axis. Shear-wave splitting is maximum and null for propagation perpendicular and parallel to the axis of symmetry, respectively. In Chapter 3, we calibrate the magnitude and symmetry of seismic anisotropy in various mica- and amphibole-bearing schists, gneisses, and mylonites, and evaluate whether the seismic properties of anisotropic metamorphic rocks can be reasonably approximated by a TI symmetry, and if not, how departures from TI may manifest in seismic data due to the application of seismic methods that force the symmetry of the resulting elastic tensor to be TI. This chapter also examines the factors that cause seismic symmetry of metamorphic rocks to deviate from TI. The results from measurements and CPO-based calculations of these seismic velocities will be used to help constrain the tectonic interpretation of seismic anisotropy and shear-wave splitting data from the southeast Tibetan Plateau, where the foliation (XY-plane) is subvertical and the stretching lineation (X) is subhorizontal, yielding strongly azimuthal anisotropy.

A large portion of the middle-to-lower crust beneath the continents and oceanic island arcs is probably composed of amphibolites dominated by hornblende and plagioclase. To determine the

volume fraction of amphibole-rich rocks in the continental crust beneath different tectonic regions is thus crucially important for constraining tectonic models of crustal evolution. Such information can currently be obtained only by comparing in situ observed seismic properties with those of amphibole-rich rock samples measured in laboratory. In Chapter 4, we deals with our new results on P- and S-wave velocities and anisotropy for 17 amphibole-rich rock samples containing 34-80 vol.% amphibole, measured at room temperature and hydrostatic pressures up to 650 MPa, and calculation of CPO-based seismic properties for 6 samples. The experimental results are combined with previously published experimental data to provide a systematic calibration of the seismic properties of amphibole-rich rocks, which serves as fundamental information for the interpretation of field seismic data from the continental and subducted oceanic crust.

Finally, Chapter 5 draws a succinct summary of the main conclusions and presents the work needed to perform in future.

1.2 Calculations of rock seismic properties

1.2.1 Theory of elasticity

Many solid materials such as crystalline rocks can be approximately regarded as perfectly linear elastic without appreciable erros when they are subjected to small strain, as is the case for seismic waves except near a seismic source. The theory of elasticity deals with the relations between the stress (σ_{ij}) and the resulting strain (ε_{ij}) on a body, where i and j may take the values 1, 2, or 3, parallel to the coordinate axes x_1, x_2, x_3, respectively, the first suffix denotes the direction of the stress component and the second indicates the direction of the normal to the plane upon which stress acts (Nye, 1957, Figure 1.1). Stresses of σ_{11}, σ_{22}, and σ_{33} are normal stresses, whereas the remaining six stress components which have different suffices are shear stresses (e.g., σ_{12}, σ_{23}, and σ_{32}).

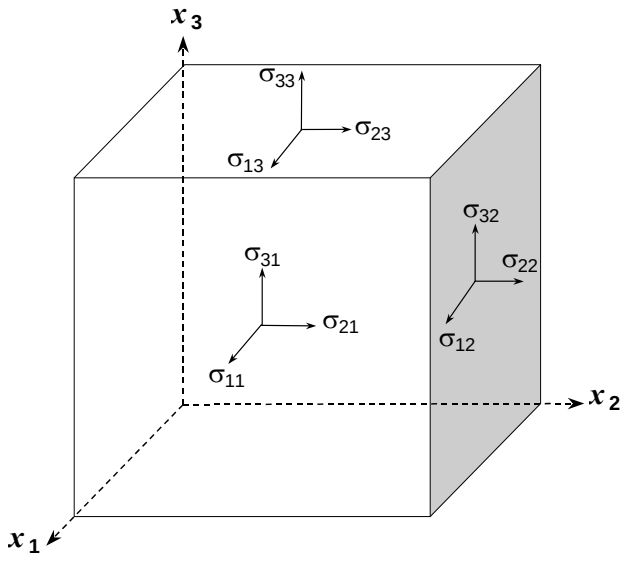


Figure 1.1 Stress components acting on the faces of a unit cube

The relation between stress and strain was first identified by Robert Hooke, a 17th century British physicist. A perfect elastic body deforms as linear elasticity, which is stated by Hooke's law:

$$\sigma_{ij} = C_{ijkl}\varepsilon_{kl} \tag{1.1}$$

or

$$\varepsilon_{ij} = S_{ijkl}\sigma_{kl} \tag{1.2}$$

where C_{ijkl} and S_{ijkl}, which are fourth-rank tensors and have the same symmetry, are the elastic stiffness and compliance, respectively, and i, j, k, l =1, 2, or 3. The elastic stiffness (C_{ijkl}) obeys the laws of tensor transformation and has a total of eighty-one components. However, not all eighty-one components are independent. The symmetry of stresses and strains implies

$$C_{ijkl}=C_{jikl}=C_{ijlk}=C_{jilk} \tag{1.3}$$

This symmetry reduces the number of independent constants to thirty-six. Furthermore, the existence of a unique strain energy potential requires that

$$C_{ijkl}=C_{klij} \tag{1.4}$$

This further reduces the number of independent constants to twenty-one, which is the maximum number of elastic constants that any medium can have. Specifically, since the conditions satisfying zero rotation of the body are $\sigma_{12}=\sigma_{21}$, $\sigma_{13}=\sigma_{31}$, and $\sigma_{23}=\sigma_{32}$, σ_{ij} contains only 6

independent components and the stiffness C_{ijkl} can be expressed by a 6×6 tensor. C_{ijkl} is usually written using two indices as C_{qr} when new indices are defined as 11→1, 22→2, 33→3, 23→4, 13→5, and 12→6. Thus C_{1111}=C_{11}, C_{1213}=C_{65}, etc.

$$C_{qr} = \begin{pmatrix} C_{11} & C_{12} & C_{13} & C_{14} & C_{15} & C_{16} \\ C_{21} & C_{22} & C_{23} & C_{24} & C_{25} & C_{26} \\ C_{31} & C_{32} & C_{33} & C_{34} & C_{35} & C_{36} \\ C_{41} & C_{42} & C_{43} & C_{44} & C_{45} & C_{46} \\ C_{51} & C_{52} & C_{53} & C_{54} & C_{55} & C_{56} \\ C_{61} & C_{62} & C_{63} & C_{64} & C_{65} & C_{66} \end{pmatrix} \tag{1.5}$$

The components of compliance S_{ijkl} can be specified in a similar way to the stiffness. The compatibility between C_{qr} and S_{qr} requires

$$C_{qr} \bullet S_{q_r} = I \tag{1.6}$$

where I is the unit tensor. As mentioned in Eq. (1.4), the reciprocal relations C_{qr}=C_{rq} imposed by thermodynamic requirements further reduce the stiffnesses C_{qr} into 21 independent elastic coefficients, which are used to describe the elastic behavior of a material with triclinic symmetry (e.g., plagioclase). The existence of symmetry will further reduce the number of independent elastic constants to 13 for monoclinic (e.g., antigorite, hornblende, clinopyroxene, coesite, and muscovite), 9 for orthorhombic (e.g., sillimanite, olivine, and orthopyroxene), 7 or 6 for trigonal (e.g., dolomite, α-quartz, and calcite) or tetragonal (e.g., rutile and zircon), 5 for hexagonal (e.g., graphite and nepheline), and 3 for cubic crystal systems (e.g., garnets, spinel, magnetite, halite, pyrite, and sphalerite). Isotropic, linear elastic materials (e.g., glass), which have the maximum symmetry, can be completely characterized by two independent elastic constants (Table 1.1).

Table 1.1 The stiffness C_{qr} for isotropic, cubic, hexagonal, and orthorhombic systems

Symmetry	$\boldsymbol{C_{qr}}$	**Symmetry**	$\boldsymbol{C_{qr}}$
Isotropic	$\begin{pmatrix} C_{11} & C_{12} & C_{12} & 0 & 0 & 0 \\ C_{12} & C_{11} & C_{12} & 0 & 0 & 0 \\ C_{12} & C_{12} & C_{11} & 0 & 0 & 0 \\ 0 & 0 & 0 & (C_{11}-C_{12})/2 & 0 & 0 \\ 0 & 0 & 0 & 0 & (C_{11}-C_{12})/2 & 0 \\ 0 & 0 & 0 & 0 & 0 & (C_{11}-C_{12})/2 \end{pmatrix}$	Hexagonal	$\begin{pmatrix} C_{11} & C_{12} & C_{13} & 0 & 0 & 0 \\ C_{12} & C_{11} & C_{13} & 0 & 0 & 0 \\ C_{13} & C_{13} & C_{33} & 0 & 0 & 0 \\ 0 & 0 & 0 & C_{44} & 0 & 0 \\ 0 & 0 & 0 & 0 & C_{44} & 0 \\ 0 & 0 & 0 & 0 & 0 & (C_{11}-C_{12})/2 \end{pmatrix}$
Cubic	$\begin{pmatrix} C_{11} & C_{12} & C_{12} & 0 & 0 & 0 \\ C_{12} & C_{11} & C_{12} & 0 & 0 & 0 \\ C_{12} & C_{12} & C_{11} & 0 & 0 & 0 \\ 0 & 0 & 0 & C_{44} & 0 & 0 \\ 0 & 0 & 0 & 0 & C_{44} & 0 \\ 0 & 0 & 0 & 0 & 0 & C_{44} \end{pmatrix}$	Orthorhombic	$\begin{pmatrix} C_{11} & C_{12} & C_{13} & 0 & 0 & 0 \\ C_{12} & C_{22} & C_{23} & 0 & 0 & 0 \\ C_{13} & C_{23} & C_{33} & 0 & 0 & 0 \\ 0 & 0 & 0 & C_{44} & 0 & 0 \\ 0 & 0 & 0 & 0 & C_{55} & 0 \\ 0 & 0 & 0 & 0 & 0 & C_{66} \end{pmatrix}$

For a statistically isotropic (e.g., fabric-free polycrystalline rocks and amorphous glasses), linearly elastic solid, only two among the following elastic constants are required to characterize the seismic and elastic properties: the Young's (E), shear (G) and bulk (K) moduli, Lamé parameter (λ), and Poisson's ratio (υ). All these constants are called dynamic moduli, which, by definition, are those calculated from the elastic wave velocities and density. In contrast, static moduli are those directly measured in a deformational experiment. Among these dynamic moduli, once two independent constants are known, other constants can be calculated according to the well-known equations in elastic mechanics. The magnitudes of the elastic constants reflect crystal interatomic bonding, grain boundary strength, and microstructural characteristics (e.g., microcracks, porosity, phase connectivity and continuity) of rocks during uniaxial extension/compression, simple shear, and hydrostatic compression.

Young's modulus (E) is defined as the ratio of compressional stress to the resultant longitudinal strain for a small cylinder under compression at both ends:

$$E = \frac{\sigma_{11}}{\varepsilon_{11}} \tag{1.7}$$

Bulk modulus (K), which measures the resistance of a substance to uniform compression, is defined as:

$$K = -V\frac{\partial P}{\partial V} \tag{1.8}$$

where P is pressure, V is volume, and $\partial P/\partial V$ denotes the partial derivative of pressure with respect to volume.

Poisson's ratio (υ) was defined by a French mathematician Siméon Poisson in 1829 as the negative of the ratio of transverse strain (ε_{jj}) to the axial strain (ε_{ii}) when an isotropic elastic solid is subjected to uniaxial stress (σ_{ii}) alone (Gercek, 2007; Wang and Ji, 2009).

$$\upsilon = -\frac{\varepsilon_{jj}}{\varepsilon_{ii}} \tag{1.9}$$

For an isotropic material at a given temperature and pressure, Poisson's ratio is a constant that does not depend on the choice of i and j, and ranges from -1 to 0.5. Liquids have no resistance to shear but are incompressible and hence υ=0.5. Materials with υ<0 are called auxetic materials (e.g., foams) as there is an increase in volume when compressed (Lakes, 1987). A negative value of Poisson's ratio implies that a cylinder undergoing compression along its axis would contract simultaneously in all directions, which has been observed for certain directions in single crystals of nickel base alloy (Svetlov et al., 1988). The values of Poisson's ratio vary from 0.05 for very hard, rigid rocks to about 0.45 for soft, poorly consolidated materials. For most rocks, Poisson's ratio is about 0.22-0.30.

Lambda (λ) and mu (μ), which are the first and second Lamé constants, respectively, were introduced and named after the 18th century French mathematician and engineer Gabriel Lamé (1795-1870) and can describe independently the elastic properties of an isotropic material or rock. In 1828, Lamé formulated the modern version of Hooke's law relating stress (σ_{ij}) to strain (ε_{ij}) in its general tensor form, thereby creating the basis for the material sciences and rock mechanics:

$$\sigma_{ij} = \delta_{ij}\lambda\Delta + 2\mu\varepsilon_{ij} \tag{1.10}$$

where the volume strain $\Delta=\varepsilon_{11}+\varepsilon_{22}+\varepsilon_{33}$, δ_{ij} is the Kronecker delta, δ_{ij}=1 when i=j, and δ_{ij}=0 when $i\neq j$. Lamé parameter (λ) varies with pressure and temperature and relates stresses and strains in perpendicular directions (Jaeger, 1969; Ji et al., 2010). Considering

$$K = -V\frac{\partial P}{\partial V} = -P\frac{V}{\Delta V} = \lambda + \frac{2}{3}\mu \tag{1.11}$$

Goodway (2001) believes that λ is closely related to material's incompressibility and contains a large proportion of information about the resistance to a change in volume caused by a change in pressure (λ=K-2μ/3). λ is negative if K<2μ/3 as K>0 and μ>0. The second Lamé constant μ is identical to the shear modulus (G) or rigidity, which reflects the resistance of a substance to a simple shear strain that generates a shape change without changing total volume. Thus, mu (μ) or shear modulus (G) can be expressed as:

$$\mu = G = \frac{\sigma_{12}}{2\varepsilon_{12}} \tag{1.12}$$

The elastic constants of an isotropic rock are usually determined from the measured compressional (P) and shear (S) wave velocities (V_p and V_s) using the pulse transmission technique (Birch, 1960; Christensen, 1974; Ji et al., 1993; Ji and Salisbury, 1993; Ji et al., 2007), along with the density (ρ), because they are the most common geophysical parameters measurable.

$$K = \rho\left(V_p^{\,2} - \frac{4}{3}V_s^{\,2}\right) \tag{1.13}$$

$$E = \frac{\rho V_s^{\,2}\left(3V_p^{\,2} - 4V_s^{\,2}\right)}{V_p^{\,2} - V_s^{\,2}} \tag{1.14}$$

$$G = \rho V_s^2 \tag{1.15}$$

$$\upsilon = \frac{0.5(V_p/V_s)^2 - 1}{(V_p/V_s)^2 - 1} \tag{1.16}$$

$$\lambda = \rho(V_p^2 - 2V_s^2) \tag{1.17}$$

1.2.2 Mixture rules

A terrestrial material consists of rocks made of different minerals and pores that can be filled with various gas and fluids. Each of the constitutents has its own physical properties, such as elastic moduli, flow strength, density, magnetic susceptibility, electrical conductivity, thermal conductivity, and heat generation in the Earth's crust and upper mantle. Hence, the bulk physical properties of the terrestrial material behave complexly, depending in some way on the relative abundance and physical property of each constituent mineral. This way can be generally

expressed by a rule of mixture or a mixing law, which describes the variation of a given physical property of polymineralic composite as a function of their end-member properties and volume fractions. In addition to measurement, these physical properties of polyphase rocks are generally calculated from laboratory-measured physical properties of constituent minerals and appropriate rules of mixture. The success of such a commonly practiced scientific approach relies not only on accurate information about the physical properties of the proposed minerals but also on the relevance of the mixture rule used. The application of different rules of mixture yields different results. It is thus very important to understand the physical meaning of each existing rule of mixture. Only those rules of mixture which are commonly used for statistically isotropic composite materials or rocks will be listed below.

(1) Voigt average

Voigt average, which was proposed by Voigt (1928) based on an assumption that strain is uniform through the rock and averaged over elastic stiffness (C_{ij}), is actually an arithmetic mean, that is,

$$M_c = \sum_{i=1}^{N} \left(f_i M_i \right) \tag{1.18}$$

where M is a given physical property (e.g., density, elastic modulus, electrical conductivity, and thermal conductivity), the subscript c stands for the composite which consists of N phases in total, f_i is the volume fraction of the ith phase.

$$\sum_{i=1}^{N} f_i = 1 \tag{1.19}$$

Eq. (1.18) yields a linear variation of M_c with any volume fraction f_i. For the elasticity (e.g., Young's modulus, shear modulus, and bulk modulus), and this equation suggests that the overall stress in the composite is equal to the arithmetic weight average of the stresses in the constituent phases and the weight factors are the volume fractions of the phases, but the strain is uniform in the composite (Figure 1.2a).

The density of a composite rock consisting of N components always obeys the mixing law given by Eq. (1.20):

$$\rho_c = \sum_{i=1}^{N} (f_i \rho_i) \tag{1.20}$$

(2) Reuss average

In contrast to Voigt's isostrain model, Reuss (1929) assumed that the average stress of each phase is identical to the applied stress, which yields the harmonic mean estimate for the effective properties, that is

$$\frac{1}{M_c} = \sum_{i=1}^{N} \frac{f_i}{M_i} \tag{1.21}$$

This equation yields a non-linear variation of M_c with any volume fraction f_i. For the elasticity of materials and rocks, Eq. (1.21) means that the overall strain is equal to the arithmetic weight average of the strains in the phases and the stress is uniform (Figure 1.2b).

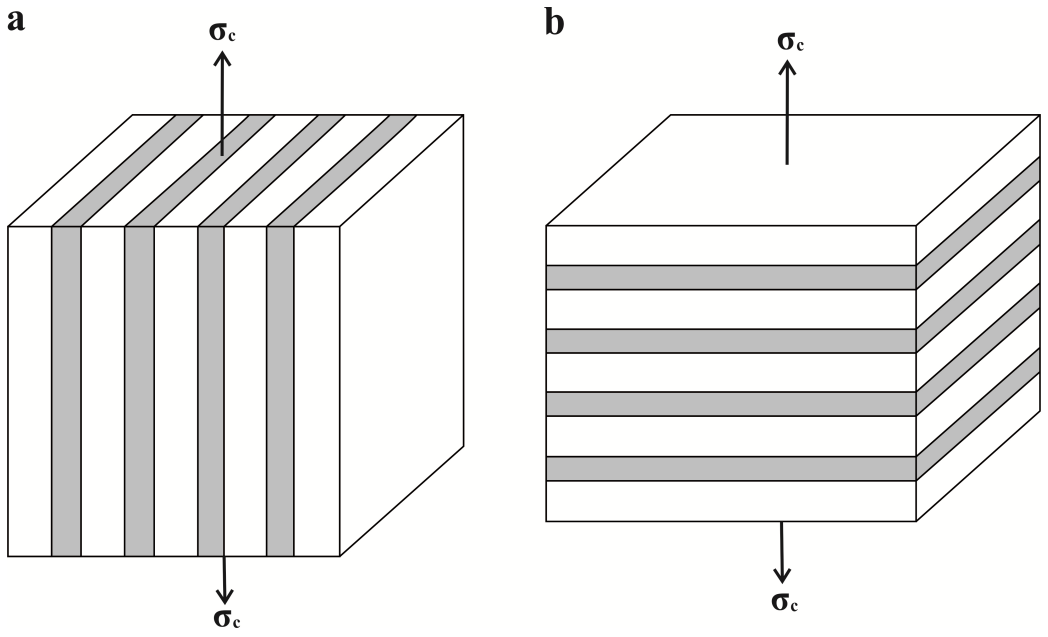


Figure 1.2 Three-dimensional microstructures of two-phase composites. (a) The stress (σ_c) is applied in such a direction that both phases experience the same strains but different stresses (model of homogeneous strain). (b) The stress (σ_c) is applied in such a direction that both phases are subjected to same stresses but different strains (model of homogeneous stress).

(3) Voigt-Reuss-Hill average

Given the composition, Voigt and Reuss averages give, respectively, the rigorous upper and lower bounds on the effective properties and bracket the permissible range in which the effective properties must lie. If the constituent phases have a significant difference in property, however, the range between them is then too large to be meaningful for estimating the effective elastic properties of rocks. Hill (1952) proved mathematically that the measured moduli of an aggregate of crystals invariably lie between the Voigt and Reuss values and proposed an empirical averaging relation−Voigt-Reuss-Hill or VRH average. The VRH average yields an arithmetic mean of the Voigt and Reuss bounds, that is

$$M_{\mathrm{VRH}} = \frac{1}{2}\left(M_{\mathrm{Voigt}} + M_{\mathrm{Reuss}}\right) \tag{1.22}$$

The Hill averaging or the VRH approximation has been widely used as the representation of the overall elastic or seismic properties of polymineralic aggregates in the interpretation of worldwide seismic data (e.g., Preliminary reference Earth model, Dziewonski and Anderson, 1981; Zhao and Anderson, 1994). However, the VRH average has no clear physical significance and does not give compatible elastic stiffness (C_{ij}) or compliance (S_{ij}) tensors (e.g., Ji and Xia, 2002; Mainprice and Humbert, 1994; Matthies and Humbert, 1993). Furthermore, the VRH average failed in the test by comparing with the experimental data in both the regimes of strong-phase-supported structure (SPSS) and weak-phase-supported structure (WPSS) (Ji et al., 2004).

(4) Geometric average

The geometric average yields

$$M_c = \prod_{i=1}^{N} M_i^{f_i} \tag{1.23}$$

which gives a result approximate to the very complicated iterative self-consistent micromechanical model in the prediction of the bulk elastic properties for composite materials (Mainprice and Humbert, 1994; Matthies and Humbert, 1993). As stated by Ji (2004), however, the geometrical average becomes physically meaningless when one of the constituent phases has a null property (e.g., pores have zero shear strength). In this case, the overall property of the composite materials or rocks determined by the geometric average will always vanish for any

finite volume fraction of the constituent that has a null property.

(5) Generalized mixture rule (GMR)

Ji (2004) and Ji et al. (2004) put the Voigt average, Reuss average, and geometric average into a unified model named the generalized mean:

$$M_c^{\,J} = \sum_{i=1}^{N} \left(V_i M_i^{\,J} \right) \tag{1.24}$$

where V_i is the volume fraction of the ith phase. J is a scaling, fractal parameter, reflecting the effects of microstructure on the physical properties of material studied. This parameter is mainly controlled by the shape and distribution (continuity and connectivity) of the phases. The case J=1 yields the arithmetic average or Voigt average. The case J=-1 yields the Reuss average. Variations of the composite properties with the volume fraction are nonlinear for all J values other than J=1. The GMR yields the geometric average as $J \rightarrow 0$.

By fitting the laboratory-measured M_c data with the predicted curves, Ji et al. (2004, 2006) found that the GMR with J=0.5 and J=-0.5 provides good agreement with experimental data of Young's modulus for the two-phase composites (including porous materials) in which inclusions are shaped like spheres isolated in a continuous, stronger (SPSS: strong-phase supported structure) and weaker (WPSS: weak-phase supported structure) host mediums, respectively. For most composite materials in which the inclusions are of somewhat arbitrary geometry, however, the GMR with J=-0.25 and J=0.25 does well at predicting the measured values of Young's modulus for those with WPSS (the volume fraction of strong phase $\varphi_s \leq 0.5$) and SPSS ($\varphi_s \geq 0.7$), respectively. In the intermediate range ($0.5 \leq \varphi_s \leq 0.7$), J value was found to vary progressively from -0.25 to 0.25 owing to the transition in microstructure.

For more specific mixing models for physical properties of rocks, the reader is referred to a comprehensive review by Berryman (1995), Ji (2008), and Schön (2011).

1.2.3 Seismic properties of rock-forming minerals

In isotropic elastic solids, linear P-wave particle motion is parallel to the propagation direction and S-wave particle motion is perpendicular to propagation, with two components arbitrarily defined as oriented horizontally and in the vertical plane. For anisotropic media, however, waves

are neither purely longitudinal nor transverse except in certain directions. The particle displacement has components both along and transverse to the direction of propagation. Since particle motions are no longer simply related to ray directions, the waves are called quasi-P wave with linear particle motion that is not quite parallel to the propagation direction, and two quasi-S waves (V_{s1} and V_{s2}, $V_{s1}>V_{s2}$) with polarization parallel and perpendicular to the fast direction for the propagation direction in question (Figure 1.3).

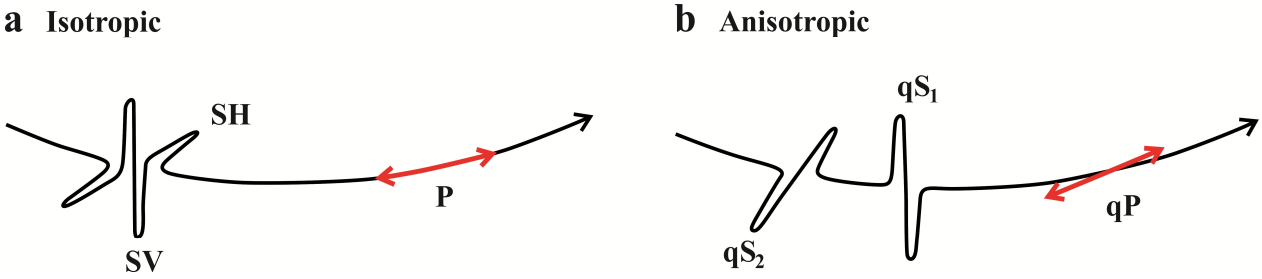


Figure 1.3 Schematic comparison of isotropic and anisotropic wave propagation, in three dimensions. Isotropic propagation has linear P-wave particle motion parallel to the propagation direction and S-wave particle motion perpendicular to propagation, with two components arbitrarily defined as oriented horizontally (SH) and in the vertical plane (SV). Anisotropic propagation has a quasi-P (qP) wave with linear particle motion that is not quite parallel to the propagation direction, and two quasi-S waves (qS_1 and qS_2) with polarizations parallel and perpendicular to the fast direction for the propagation direction in question. The quasi-S waves are separated by a time δt.

Calculations of seismic properties of rock-forming minerals are essential for understanding the relationship between the crystallographic preferred orientation (CPO) and volume fraction of each constituent mineral, and the overall seismic velocities and anisotropy of polycrystalline rocks (e.g., Ji et al., 1988). For each propagation direction, the P-wave velocity, the two shear-wave velocities, and shear-wave splitting (V_{s1}-V_{s2}) can be computed according to the elastic constants (the 6×6 symmetric matrix) and density of each mineral, the Christoffel equation and the Hill averaging scheme. The P-wave anisotropy, AV_p, is defined as $100\%\times(V_{max}-V_{min})/V_m$, where $V_m=[V_p(X)+V_p(Y)+V_p(Z)]/3$, X is parallel to the stretching lineation, Y perpendicular to the lineation and in the foliation, and Z normal to the foliation (Figure 1.4). In fact, $100\%\times(V_{max}-V_{min})/[(V_{max}+V_{min})/2]$ is usually applied in the calculation of both AV_p and S-wave anisotropy (AV_s). For shear-wave, V_{max} and V_{min}, are usually denoted as V_{s1} and V_{s2} that are the

fast and slow shear-wave velocities, respectively. Thus, AV_p is direction-independent and only reflects the relative difference between the maximum and minimum V_p values in a given rock body, whereas AV_s is a directional parameter.

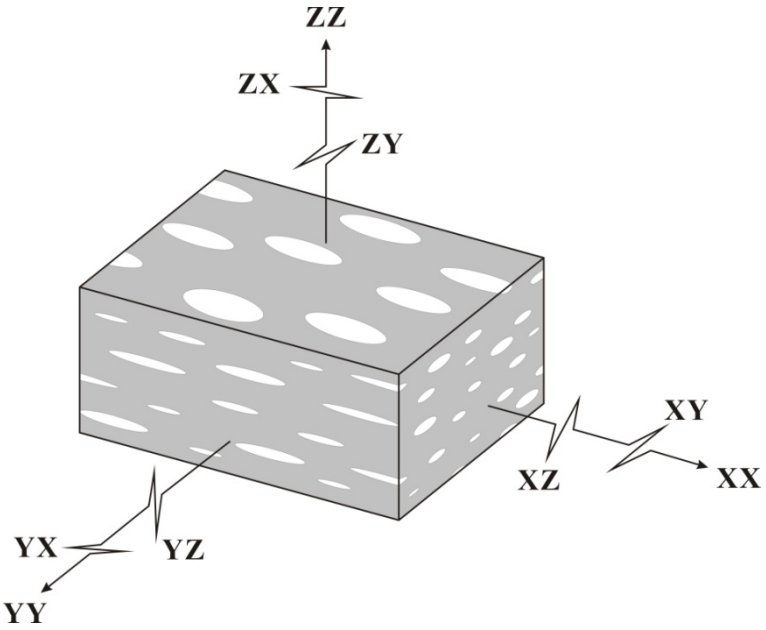


Figure 1.4 Relative orientation between rock structural elements and seismic wave propagation (the first letter) and vibration directions (the second letter). X is parallel to the stretching lineation, Y is normal to the lineation and in the foliation plane, and Z is normal to the foliation plane.

The single crystal symmetry of plagioclase is actually triclinic, while it has been treated as monoclinc so far due to lack of adequate single crystal elastic constants. The maximum V_p of plagioclase (Figure 1.5b) and K-feldspar (Figure 1.5a) occurs parallel to the b^*-axis [the direction perpendicular to the (010) plane] and their maximum shear-wave splitting concentrates around [011] direction. Also, plagioclase has both higher V_p and V_s values than K-feldspar. Quartz (Figure 1.5c) exhibits trigonal symmetry, with the maximum shear-wave splitting parallel to the a-axis. For hornblende (Figure 1.5h) the symmetry plane is defined by the a^*- [the direction perpendicular to the (100) plane] and c-axes. The maximum V_p is observed parallel to the c-axis and a pronounced shear-wave splitting occurs in the plane marked by the b^*- and c-axes with a maximum parallel to the c-axis. Muscovite (Figure 1.5f) can be treated as hexagonal since the velocity differences in the directions of the a- and b-axes are vanishing. A maximum V_p and shear-wave splitting occurs in the (001) plane, and the minimum parallel to the c-axis. Seismic

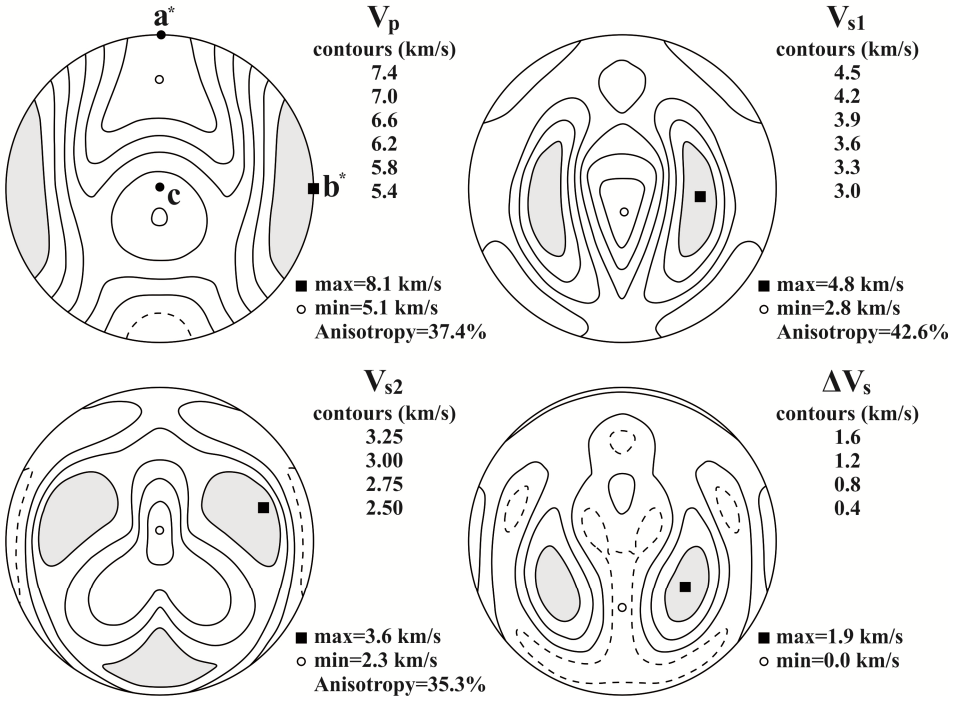
properties of muscovite can approximate those of biotite (Figure 1.5e), which possesses both greater V_p anisotropy and maximum V_s anisotropy than muscovite (Table 1.2).

The fastest V_p of antigorite lies parallel to the a-axis, while the maximum shear-wave splitting and the fastest V_s occur at the middle way between a- and b-axes (Figure 1.5d). For pyroxene, omphacite (30 vol.% diopside, 58 vol.% jadeite) displays the maximum V_p around [101] and pronounced shear-wave splitting in the plane defined by the b^*- and c-axes; while the fastest V_p of enstatite (Figure 1.5i) distributes subparallel to the a-axis and the maximum shear-wave splitting lies around [111]. For olivine [$(Fe,Mg)_2SiO_4$] (Figure 1.5j) that is dominant in the upper mantle, both V_p and V_s increase with increasing Mg_2SiO_4 (forsterite) content whereas ρ increases with increasing Fe_2SiO_4 (fayalite) content. The maximum shear-wave splitting of olivine is observed along [101] direction. Both the fastest V_p (9.89 km/s) and the minimum shear-wave splitting (0.02 km/s) are observed parallel to the a-axis. Sillimanite is characterized by the fastest and slowest V_p, respectively, parallel to the c- and b-axes. The fastest shear-wave velocity lies around [111], while the slowest shear-wave velocity is observed in the middle way between a- and b-axes (Figure 1.5k).

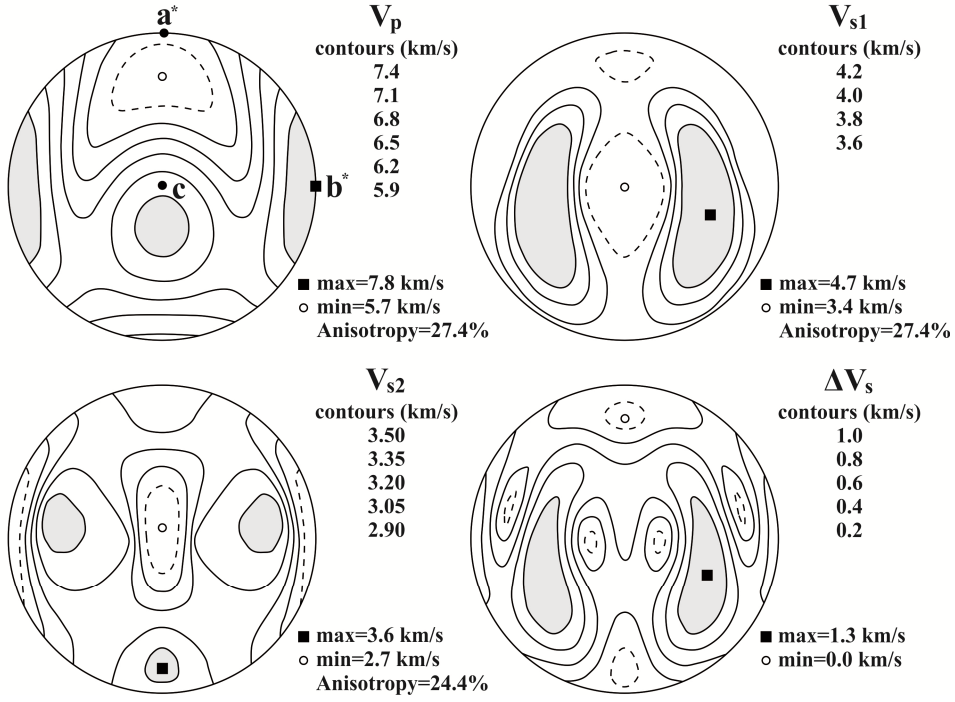
Table 1.2 Density and anisotropic seismic properties of single crystals (Ji et al., 2002 and references therein; Bezacier et al., 2010)

Mineral	Symmetry	Density	V_p (km/s)		V_{s1} (km/s)		V_{s2} (km/s)		ΔV_s	Anisotropy (%)		
		(g/cm^3)	max	min	max	min	max	min	(km/s)	AV_p	AV_{s1}	AV_{s2}
Albite	Triclinic	2.620	7.40	5.20	4.40	3.00	3.50	2.50	1.40	30.9	31.2	27.2
Anorthite	Triclinic	2.760	8.60	5.90	5.00	3.60	3.80	2.90	1.20	31.8	27.5	23.2
K-feldspar	Triclinic	2.540	8.10	5.10	4.80	2.80	3.60	2.30	1.90	37.4	42.6	35.3
Plagioclase (An53)	Triclinic	2.680	7.80	5.70	4.70	3.40	3.60	2.70	1.30	27.4	27.4	24.4
Quartz	Trigonal	2.640	7.00	5.30	5.10	3.70	4.70	3.30	1.80	24.3	26.8	29.5
Antigorite	Monoclic	2.620	8.91	5.58	5.15	2.65	4.21	2.54	2.57	46.0	64.2	49.7
Biotite	Monoclic	3.090	7.81	5.60	5.22			1.43		32.9	113.8	
Muscovite	Monoclic	2.840	8.10	4.50	5.00	2.50	3.50	2.40	2.70	44.2	50.7	32.9
Diopside	Monoclic	3.290	9.40	7.00	5.00	4.30	4.80	4.00	0.90	25.8	13.7	16.2
Hornblende	Monoclic	3.120	7.90	6.00	4.30	3.40	3.80	3.20	1.10	23.8	22.3	16.2
Jadeite	Monoclic	3.330	9.50	7.90	5.70	4.90	5.60	4.30	1.00	16.8	12.7	23.9
Omphacite	Monoclic	3.330	9.40	7.60	5.40	4.80	5.30	4.30	0.80	18.6	12.0	18.3
Enstate	Orthorhombic	3.200	8.40	7.50	5.10	4.90	5.00	4.40	0.50	11.3	4.1	11.4
Olivine (Fo93Fa7)	Orthorhombic	3.311	10.00	7.70	5.60	4.90	4.90	4.40	1.00	22.9	12.7	9.4
Sillimanite	Orthorhombic	3.240	10.90	8.50	6.30	5.00	5.80	3.90	1.90	22.7	19.5	33.2

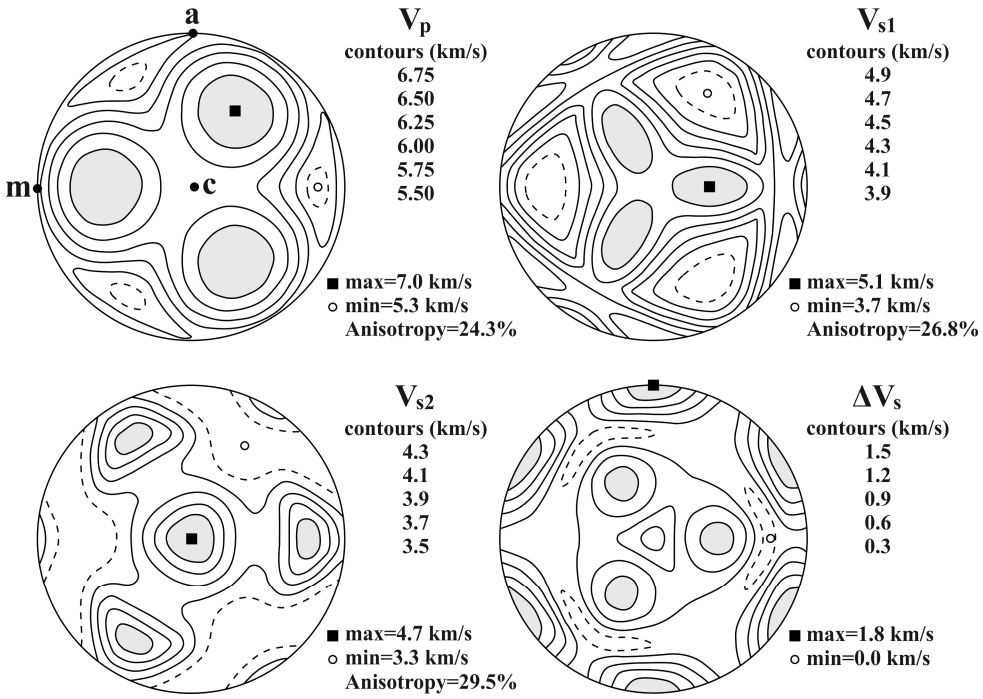
a K-feldspar $KAlSi_3O_8$



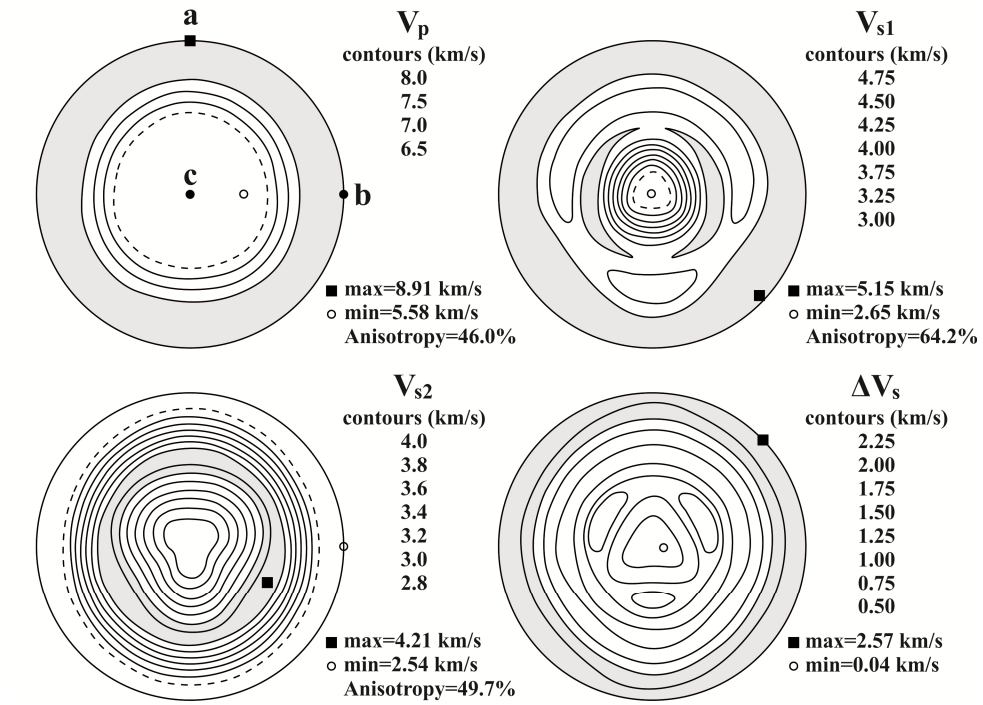
b Plagioclase An53



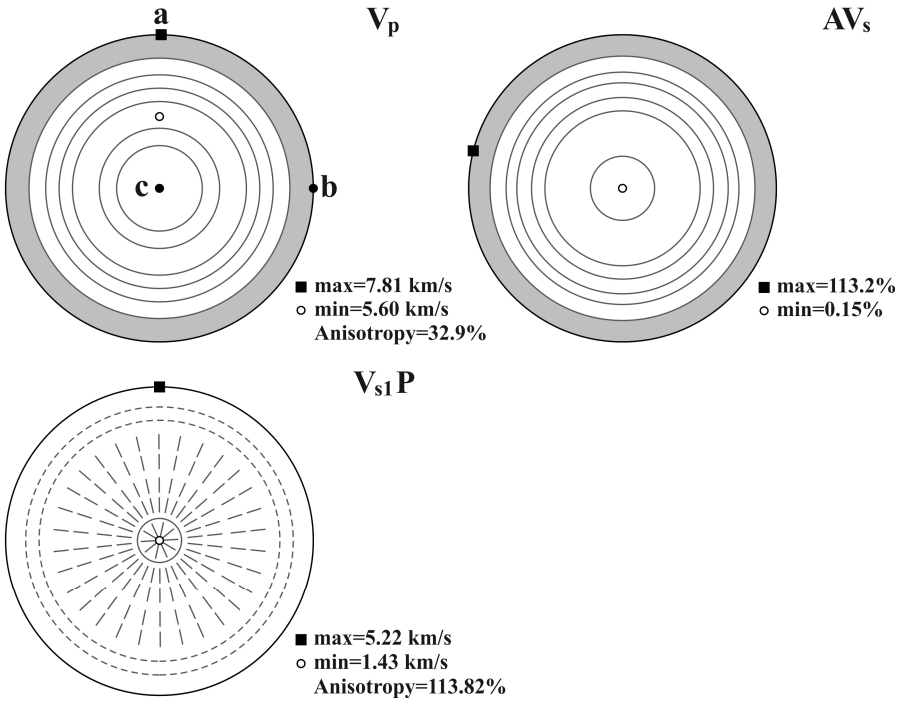
c Quartz SiO_2



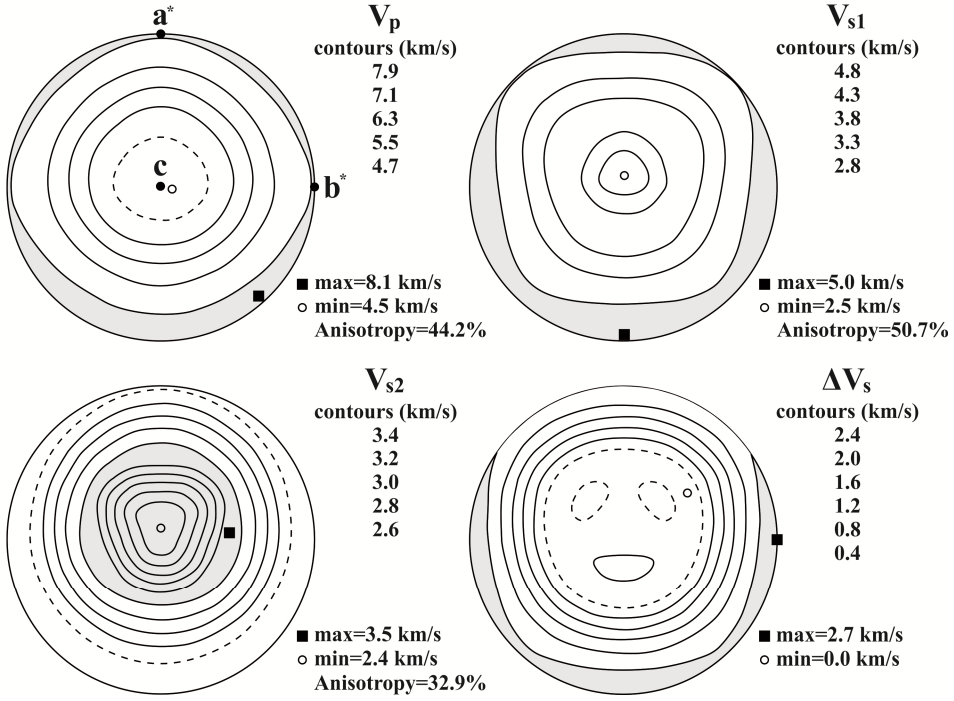
d Antigorite $Mg_3Si_2O_5(OH)_4$



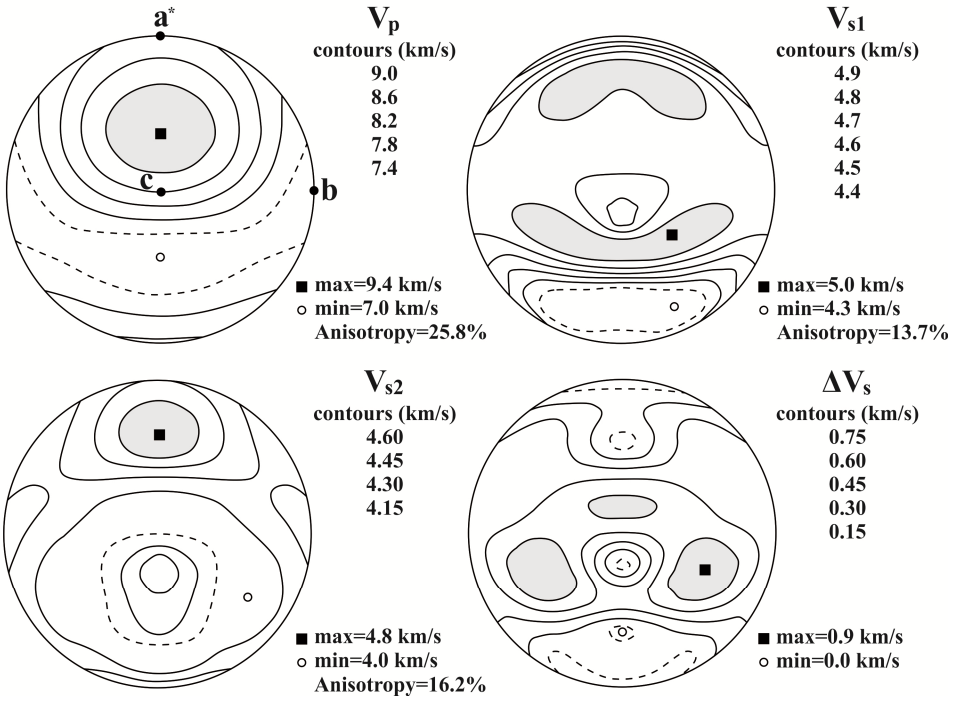
e Biotite $K(Mg,Fe)_3AlSi_3O_{10}(F,OH)_2$



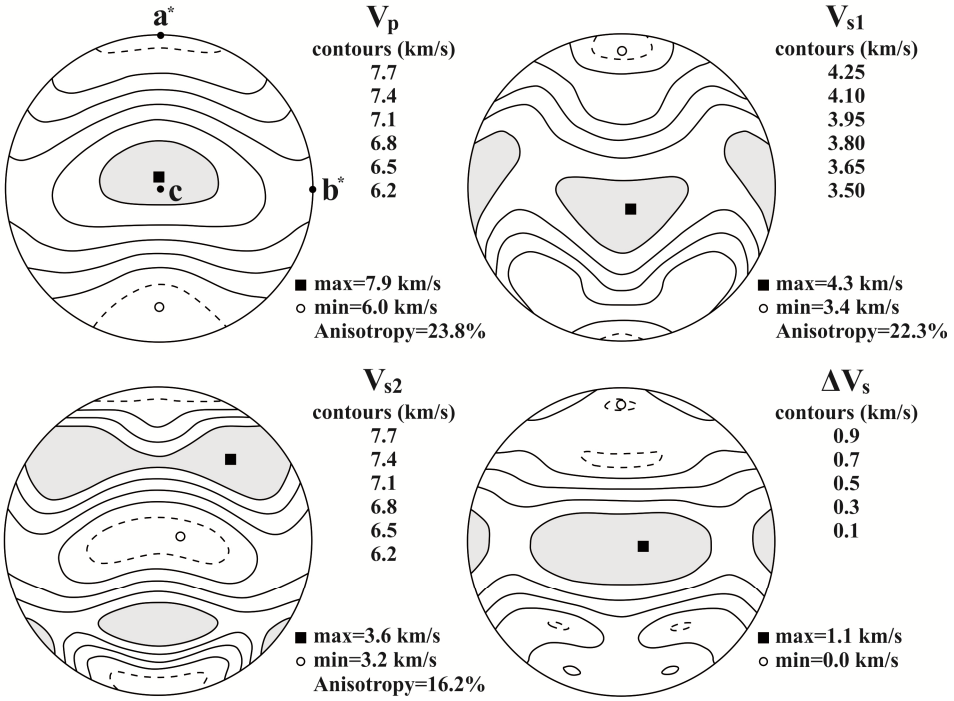
f Muscovite $KAl_3Si_3O_{10}(OH)_2$



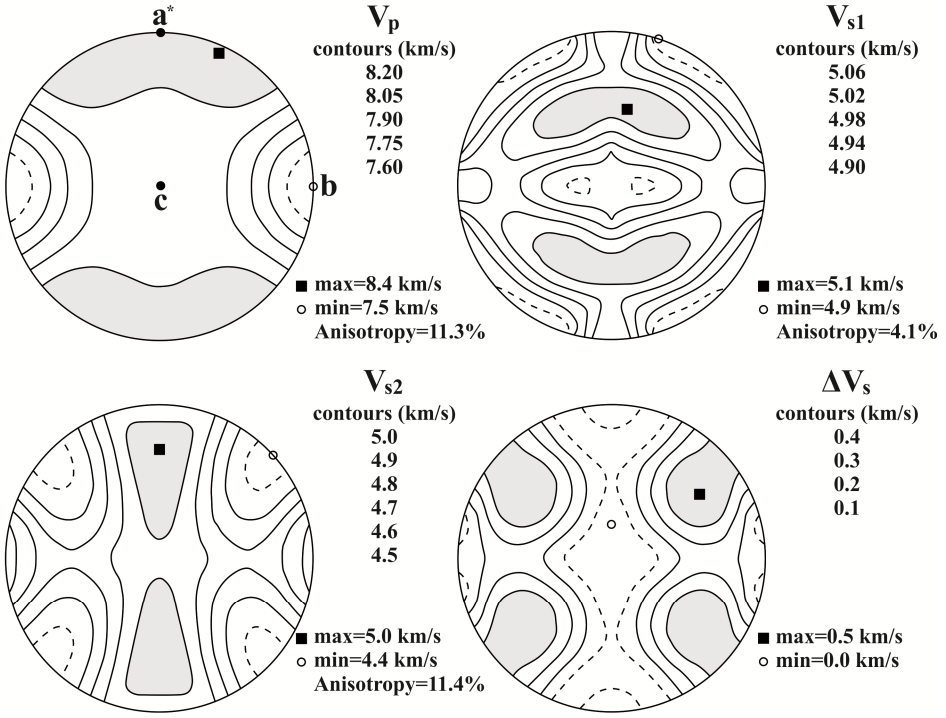
g Diopside $CaMgSi_2O_6$



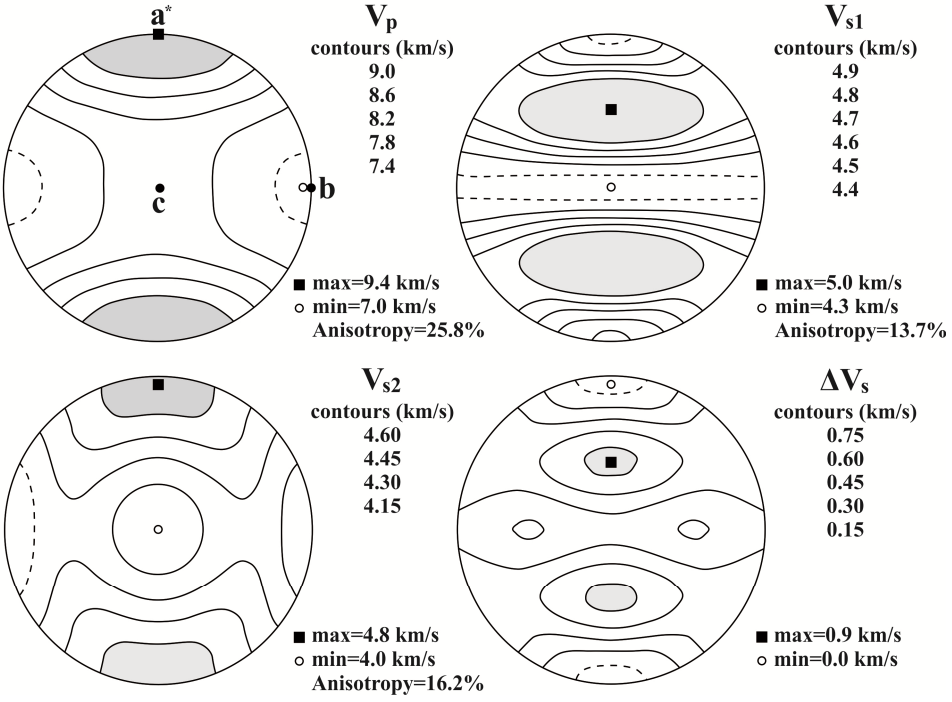
h Hornblende $(Ca,Na)_{2-3}(Mg,Fe,Al)_5(Al,Si)_8O_{22}(OH)_2$



i Enstatite $MgSiO_3$



j Olivine $Fo_{93}Fa_7$



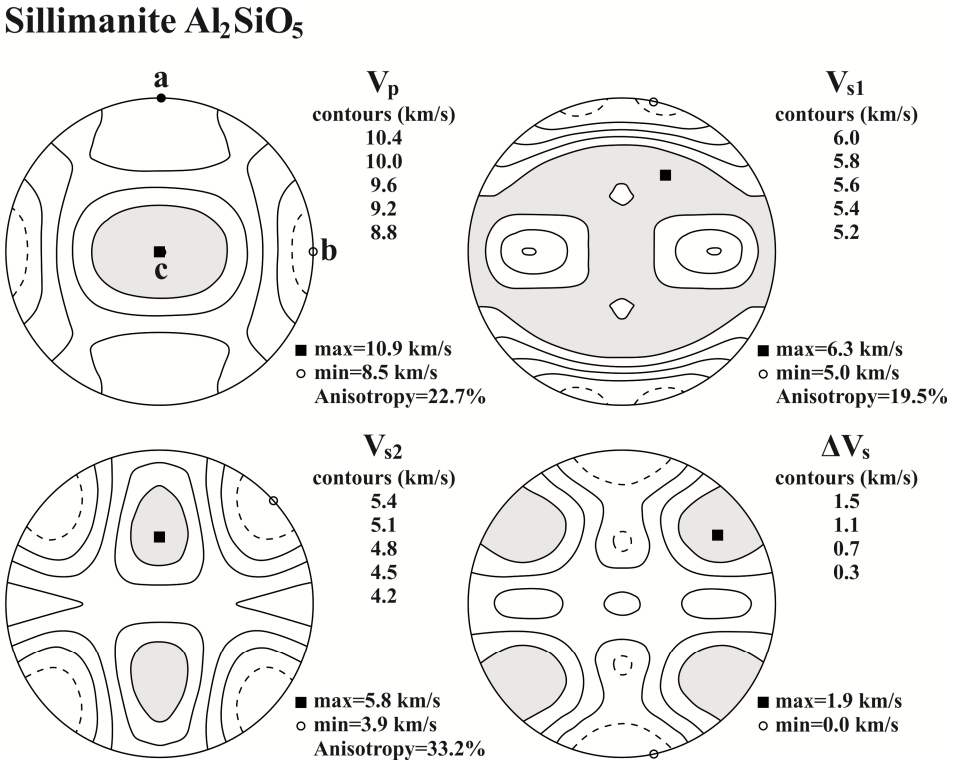


Figure 1.5 P- and S-wave properties of 11 main minerals in the lithosphere. The P-wave phase velocities (V_p, up-left), the fast S-wave velocities (V_{s1}, up-right), the slow S-wave velocities (V_{s2}, low-left), and the S-wave birefringence or shear-wave splitting ($\Delta V_s=V_{s1}-V_{s2}$, low-right) are shown in equal area stereographic projection with respect to the crystallographic orientations of a, b, c, a^* and b^*, where a^* and b^* are the directions normal to (100) and (010) planes, respectively. Therein, one exception is present for biotite with the P-wave velocities (V_p, up-left), S-wave velocity anisotropy (AV_s, up-right) and the fast S-wave polarization (V_{s1}P). The maximum velocity (in km/s) is marked by a solid square and the minimum by an open circle. The anisotropy is in percent. Notice that the contour intervals are not the same for every diagram. Shaded areas correspond to directions of high P- or S-wave velocities. Except antigorite and biotite which are cited from, respectively, Bezacier et al. (2010) and Aleksandrov and Ryzhova (1961), the left are modified after Ji et al. (2002).

1.2.4 Seismic properties of polycrystalline rocks

Seismic properties (i.e., P-wave velocities, fast and slow shear-wave velocities, direction-dependent shear-wave anisotropy, and polarization direction of fast shear waves) of the polycrystalline aggregates can be computed by averaging the elastic-constant tensors of

individual grains as a function of the CPO and modal composition of a sample (e.g., Mainprice, 1990) with the VRH averaging of related single crystal elastic constants at ambient conditions. Up to now, three main methods have been available for measuring the CPO of minerals: an optical microscope equipped with a five-axis universal stage (i.e., U-stage), an X-ray or neutron texture goniometer, or a scanning electron microscope (SEM) equipped with an electron backscatter diffraction (EBSD) system. Among these techniques, the EBSD is the most powerful and was employed to evaluate the mineral fabric characteristics of rocks in this study. In order to calculate composition-dependent seismic properties, the modal compositions were derived from microscopic observation of each sample. The gridded data were used to calculate the seismic properties of the samples that are corresponding to conditions of one atmosphere pressure, room temperature, and zero porosity. This method enables the calculation of the 3D distribution of seismic velocities in an anisotropic polycrystalline aggregate (Ji and Mainprice, 1988; Mainprice and Humbert, 1994). Moreover, given pressure and temperature derivatives of single crystal elastic constants, the CPO-derived seismic properties can be extrapolated to any pressure (P) and temperature (T):

$$C_{qr}(P,T) = (C_{qr})_0 + \left(\frac{dC_{qr}}{dP}\right)(P - P_0) + \left(\frac{dC_{qr}}{dT}\right)(T - T_0) \tag{1.25}$$

$$\rho(P,T) = \rho_0 + \left(\frac{\rho_0}{K}\right)(P - P_0) + \alpha\rho_0 (T - T_0) \tag{1.26}$$

where K is the bulk modulus; $(C_{qr})_0$ and ρ_0 are the elastic stiffness coefficient and density, respectively, at room temperature (T_0) and room pressure (P_0); dC_{qr}/dP and dC_{qr}/dT are the pressure and temperature derivatives, respectively; and α is the thermal expansion coefficient.

In this study, in order to understand the origin of seismic anisotropy in the antigorite-, mica-, and amphibole-rich rocks, we measured the CPOs of antigorite in 11 samples (A1, A3, A5, A9, A13, A15, and A16 and YSK2A, YSK5A, YSK3B, and WZG2), and those of biotite, muscovite, quartz, feldspar, amphibole, and sillimanite in 19 samples (GLG102, GLG110, GLG119, GLG132J, GLG133, GLG134, GLG201B, GLG237, GLG257, GLG258, YN1351, YN1389; AM1, AM2, AM3, AM4, AM7, and AM8) using EBSD with a HITACHI S-3400N SEM at Shizuoka University (Japan) and a Zeiss EVO MA15 SEM at Macquarie University (Australia). Operating conditions were as follows: 20 kV accelerating voltage, 8.2 nA (Macquarie) or 10 nA

(Shizuoka) probe current, 7.0-10.5 mm (Macquarie) or 28 mm (Shizuoka) working distance, and 70° specimen tilt. EBSD indexing of antigorite was performed using the HKL Channel 5 software package according to the structural data reported in Capitani and Mellini (2004). The EBSD data were collected by indexing in a given scanned area from each thin section with an interpoint spacing of 3-7 μm, depending on the mean grain size. Each scanned area in a highly polished thin-section cut parallel to the XZ plane is sufficiently representative of each homogeneous sample. All index data represent points with a mean angular deviation of <1°. The resulting CPO data are presented on equal-area, lower hemisphere projections in which the plane of projection contains the stretching lineation (X) and the pole to the foliation (Z). The CPO strength is described by the *J* index (*pfJ*) for each pole figure (Michibayashi and Mainprice, 2004), which denotes the alignment degree of crystal axes and is equal to 1 for a random fabric.

1.3 Laboratory techniques for measurement of seismic properties

Since 1960's, laboratory measurements of elastic constants and elastic wave velocities are performed with focus on natural rocks (e.g., Birch, 1960; Christensen, 1965; Ji and Salisbury, 1993; Ji et al., 1993, 2013a; Kern, 1993; Sun, 2011; Wang, 2005, 2009; Wang et al., 2009a), hot-pressed polycrystalline aggregates (e.g., Wang and Ji, 2001; Watt et al., 1976), and single crystals (e.g., Bezacier et al., 2010; Bhagat et al., 1992; Wang, 1966). The accuracy of laboratory velocities is generally related to the techniques employed, varying from 0.5-3% for the pulse transmission method commonly used for rocks (e.g., Birch, 1960; Kern, 1982) to approximately 0.01% with interferometric method for single crystal and polycrystalline specimens (e.g., Liu et al., 2000; McSkimin, 1950). A combined ultrasonic interferometry, X-ray diffraction, and X-radiography in multi-anvil apparatus was reported for measuring elasticity of polycrystalline Mg_2SiO_4 at pressure to 6.7 GPa and temperature to 1273 K (Li et al., 2004). Using dual-mode transducers, furthermore, this method can produce P- and S-wave data at same conditions in a single acoustic experiment, which enables simultaneous measurements on P- and S-wave velocities, sample lengths, and X-radiographic images. Recently, Kern et al. (2015) measured ultrasonic velocities of serpentinites both with a multi-anvil apparatus and a novel instrument to measure 3D velocities on spheres.

In general, seismic velocities of rocks are measured by the ultrasonic transmission method using piezoelectric transducers with frequencies of 1-2 MHz. Reported velocities are derived from

curves during decompression (depressurization) runs since these measurements can be reproduced whereas those determined during pressurization are not reproducible. Although the frequencies used in the laboratory experiments are much higher than those in field studies, laboratory-derived seismic velocities can be directly compared with field data due to negligible dispersion in the frequency range of 10^{-1} to 10^{7} Hz (Christensen, 1989). Three groups of experimental techniques can be distinguished according to the method of pressure generation, the preparation of specimen, and the position of transducers relative to specimen.

1) Measurements on jacketed cylindrical samples in internally heated fluid- or gas-medium apparatuses with the transducers placed directly onto the sealed speciments (e.g., Birch, 1960; Christensen, 1965; Ji and Salisbury, 1993; Wang et al., 2009a). Confining pressure is generated by advance of a piston over the pressure medium. Transmitting and receiving transducers are exposed to pressure and temperature during the experiment, which limits the working temperatures up to 450-500 °C because of the Curie temperature of the transducer material. The advantage of this technique is that truly hydrostatic pressure is obtained, especially in gas-medium apparatus, and that the sealing of the specimen allows the study of the effects of pores on velocities (e.g., Sun, 2011). Errors mainly result from inaccuracies in core length measurements, travel time determination, and sample length change at high pressure. The accuracy in V_p and V_s are estimated to be about 0.5% and 1%, respectively.

2) Experiments on unjacketed, cube-shaped specimens in a cubic anvil pressure apparatus (e.g., Kern, 1982; Kern et al., 1997, 2001). A state of near-hydrostatic stress is achieved by pressing six pyramidal pistons along the three mutually orthogonal directions onto a cube-shaped specimen. A furnace surrounds one end of each piston next to the specimen and heat is transmitted from pistons to the specimen. Transducers are placed on the low temperature side of the pistons, which allows measurements to be carried out at temperatures as high as 700 °C. This technique not only simultaneously measures P- and S-wave velocities on the three perpendicular directions, but also directly determines length changes (density change) of the specimen with increasing pressure and temperature. The cumulative error in V_p and V_s is estimated to be less than 1%. However, because the confining pressure is not exactly hydrostatic, the values of pressure derivative and seismic anisotropy could be potentially overestimated.

3) Laboratory measurements of the 3D velocity distribution of sphere-shaped sample coated with a thin layer of epoxy in an equipement that consists of a pressure vessel connected to a two-step pressure generator, a sample positioning unit equipped with ultrasonic piezoceramic transducers, and a device for generating ultrasonic pulses and travel time measurement and data acquisition (Kern et al., 2015; Lokajicek and Svitek, 2015; Lokajicek et al., 2014). An additional thin cover of a high-viscosity shear-wave gel provides the necessary point contact transducers with the sample during the measurements without any disturbance by the fluid. This technique allows measurements of P- and S-wave velocities on spherical samples with a diameter of 50 mm in 132 independent directions by using a pair of P-wave sensors (transmitter and receiver polarized along the radial direction) or two pairs of S-wave sensors (transmitter and receiver polarized tangentially to the spherical sample axis along the vertical and horizontal directions) [see Lokajicek and Svitek (2015) for details]. The sample can be exposed to hydrostatic pressures ranging from 0.1 up to 400 MPa for P-waves and currently up to 100 MPa for S-waves. The acoustic signals are excited and recorded by three piezoceramic sensor pairs with resonant frequency of 2 MHz and 700 kHz for measuring P- and S-waves, respectively. Because of the transducers being spaced at 15°, the current measuring system is only suitable for 15° measuring nets.

In my thesis, high pressure velocity measurements using standard pulse transmission methods (Birch, 1960) were carried out at the Geological Survey of Canada (GSC)/Dalhousie High Pressure Laboratory in Halifax, Nova Scotia (Ji et al., 2007; Sun et al., 2012; Wang and Ji, 2009). The pressure apparatus is a 7 ton, double-walled steel vessel with a 40 cm long by 10 cm diameter working chamber, which can operate to a pressure up to 1.4 GPa (Ji et al., 2007). The pressure was generated using an air-driven fluid pump in conjunction with a multi-stage fluid intensifier system. The pressure medium, which is an ester (Monoplex DOS: Di-2-ethylhexyl sebacate), has a viscosity of 0.15, 110, 400 Poises at 0.1, 600, and 800 MPa, respectively (ASME, 1953). Temperature rise due to adiabatic compression from 0.1 to 800 MPa is ~30 °C. This rise in temperature results in a reduction in the viscosity of ester by a factor of about 5. P-waves were generated and received by lead zirconate transducers with a 1 MHz resonance frequency, while S-waves were generated and received using lead zirconate-titanate transducers. In order to prevent the oil pressure medium from invading the samples during the pressure runs, the minicores were sheathed in impermeable thin copper foil and the entire sample/copper

paper/transducer/electrode assembly was enclosed in neoprene tubing (Figure 1.6). Once the sample assembly was sealed in the pressure vessel and the pressure was raised, a high voltage spike from a pulse generator excited the sending transducer and the time of flight to the receiving transducer was measured using a digital oscilloscope.

For each run, velocity measurements were performed first during pressurization and then depressurization in order to characterize the seismic hysteresis of rocks. Three cylindrical minicores, 2.54 cm in diameter and 4-6 cm in length, were cut in the X, Y, and Z directions of each sample except some special samples from each of which 7 minicores were taken in order to constrain the geometry of seismic anisotropy. These minicores are referred to as cores X, Y, Z, X45Y, X45Z, Y45Z, and X55Y55Z. The core X45Y is aligned at 45° with either the X or Y direction in the XY plane. The core X45Z is oriented at 45° with the X and Z directions in the XZ plane while the core Y45Z has its axis aligned 45° to the Y and Z directions in the YZ plane. The core X55Y55Z is oriented at an equal angle (54.7°) with each of the X, Y, and Z directions. These structural directions (Figure 1.3) are defined below: the X direction is parallel to the stretching lineation, the Y direction perpendicular to the lineation and in the foliation plane, and the Z direction normal to the foliation. For small samples, only one (usually the Z direction) or two directions (usually parallel to X and Z) were taken. Each minicore was grinded and polished to make the ends parallel within 0.01 mm.

Errors in velocity measurement may arise from several sources: (1) Errors in measuring core length and travel time. Core lengths are accurate to 0.0005 cm and travel time to 2.5 nanoseconds, which result in velocity measurements smaller than 0.4% for standard length cores (Burke, 1991). (2) Changes in sample length at elevated confining pressure. No corrections were made for this effect in this study because it is significant only at extremely high pressures (e.g., Brace, 1965). (3) The presence of compositional heterogeneity within a core measured could cause the real travel route of wave slightly longer than the length of core, thus resulting in a slightly lower velocity. Since the studied samples consist of relatively homogeneous composition in the longitudinal direction, this effect could be negligible. The confining pressure was determined to within 0.1 MPa by direct digital readout from a calibrated strain gauge. The accuracy is estimated to be 0.5% for V_p and 1% for V_s (Christensen, 1985; Ji et al., 1997).

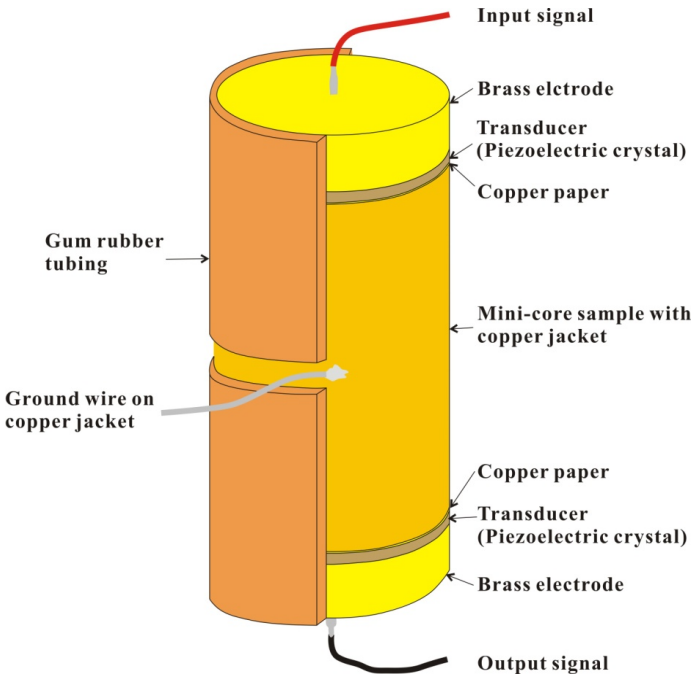


Figure 1.6 Schematic illustration of sample assembly for measurement of seismic velocity at room temperature

1.4 Observation of seismic anisotropy

Seismic observations of the dependency of P- and S-wave velocities on the direction of propagation and of shear-wave splitting in the Earth have made the study of anisotropy one of the most exciting and challenging research themes in Solid Earth Geophysics. Anisotropy carries a wealth of information about the structural and textural elastic properties of the medium through which the seismic wave propagates. In Geophysics this may be the only viable mean to access information on the elastic properties of the Earth's interior. In this section, the propagation and polarization anisotropy, and the evidence for the presence of seismic anisotropy in the Earth are briefly reviewed.

1.4.1 Propagation and polarization anisotropy

Seismic anisotropy is revealed as velocity variations both as a function of propagation and polarization direction of seismic waves. Propagation anisotropy, also called azimuthal anisotropy, reflects the variations in P-wave (or surface wave) velocity with propagation direction. The propagation anisotropy was firstly recongnized by Hess (1964) based on measurements of azimuthal dependence in seismic velocity of Pn phase that propagates subhorizontally beneath

the oceanic Moho discontinuity. P-waves are sensitive to a wide variety of phenomena, however, accurate measurements of travel times over a wide range of directions in a uniform homogeneous rock mass were therefore considered to be necessary for identifying P-wave velocity anisotropy (Crampin and Peacock, 2005). Currently, propagation anisotropy is observed usually by exploiting azimuthal variations in the seismic velocity of Pn phase (e.g., Barazangi and Ni, 1982; Liang and Song, 2006; Shearer and Orcutt, 1986) and of long-period surface waves (e.g., Montagner and Tanimoto, 1991; Smith and Dahlen, 1973; Tanimoto and Anderson, 1985).

Polarization anisotropy is defined as the differences in seismic velocity as a function of polarization (vibration) direction. The polarization anisotropy was early evidenced as a discrepancy between dispersion of slow Rayleigh waves (hybrid compressional and vertically polarized shear) and fast Love waves (horizontally polarized shear) (Anderson, 1961, 1989). This discrepancy is also the basis for assuming the upper 220 km of the mantle in the Preliminary reference Earth model (PREM) to be transversely isotropic (hexagonal symmetry anisotropic) with a vertical symmetry axis (Anderson and Dziewonski, 1982; Dziewonski and Anderson, 1981). The observations of quasi-Love waves (Love waves that have converted from Rayleigh waves along a path) were used to map locations of lateral gradients in anisotropy at 100-300 km depth (Park and Yu, 1993; Yu and Park, 1994). The polarization anisotropy is distinct in observations from propagation anisotropy. As propagation anisotropy results from seismic waves travelling different paths, there is always a tradeoff with laterally varying isotropic structures that also produce path-dependent velocity variations (Silver, 1996), thereby making the interpretation of propagation anisotropy observations difficult. For polarization anisotropy, in contrast, the tradeoff is much weaker in the case of surface waves and is absent regarding shear-wave splitting. Compared to propagation anisotropy, in other word, polarization anisotropy is less sensitive to heterogeneous isotropic structure. This difference should be responsible for the fact that data on polarization anisotropy are available around the world whereas those on propagation anisotropy are little. Herein, shear-wave birefringence or splitting in teleseismic shear waves such as Pns and XKS (including SKS, SKKS, and PKS) phases is the most popular and powerful tool for investigating polarization anisotropy, and has been used to study anisotropy throughout the Earth's crust and upper mantle (e.g., Long and Silver, 2009; Silver, 1996; Vinnik et al., 1992).

Two types of body waves, P- and S-waves, propagate in an isotropic, homogeneous medium with the particle displacement directions, respectively, parallel and perpendicular to the propagation

direction. However, there are three body waves, a quasi-P wave and two quasi-S waves, in a weakly anisotropic medium (such as the Earth's crust and upper mantle). As mentioned above, the particle displacement directions of quasi-P and quasi-S wave are still subparallel and subperpendicular to the propagation direction, respectively. The two shear waves are characterized by orthogonal polarization directions and different propagation velocities; such a phenomenon is known as shear-wave splitting (or seismic birefringence), which is analogous to the birefringence (double refraction) observed in an optically anisotropic medium (e.g., a calcite crystal). For a homogeneous elastic anisotropic medium, the velocities and displacement directions of the three seismic waves are given by the eigenvalues and eigenvectors of the polarization matrix V defined by the Christoffel equation (Backus, 1965),

$$\rho V_{il} \equiv C_{ijkl} \hat{p}_j \hat{p}_k \tag{1.27}$$

where ρ is density, C_{ijkl} is the elasticity tensor for the medium, and $\hat{p}$ is a unity vector defining the propagation directions. The two basic shear-wave splitting parameters obtained from seismic data are the fast polarization direction (ϕ), which is related to the orientation of strain field, and the delay time (δt) between the fast and slow shear waves. δt is proportional to effective path length L according to the approximate expression for small anisotropy (Silver, 1996),

$$\delta t = L \delta \hat{\beta} / \beta_0 \tag{1.28}$$

where β_0 is the isotropically averaged shear-wave velocity, $\delta \hat{\beta}$ is the dimensionless intrinsic anisotropy, which is a function of $\hat{p}$.

1.4.2 Laboratory measurement of anisotropy on rock samples

In the section 1.3, three groups of experimental techniques for measuring seismic properties of sample are briefly introduced. The relative simplicity of the experimental configuration and the close relationship of the observed elastic anisotropy to the physical properties of materials make the laboratory ultrasonic measurements of elastic wave velocities a basic technique for the fine-scale investigation of anisotropy in rocks. For the technique employed in this study, one P-wave velocity (V_p) and two shear-wave velocities (V_{s1} and V_{s2}, $V_{s1}>V_{s2}$) are usually measured from each of the three orthogonal directions in a cylindrical sample. For the rocks with both foliation and lineation, these directions are parallel to the X, Y, and Z axes of the tectonic

framework or the strain ellipsoid (Figure 1.4). If the sample is foliated but not lineated rock which was deformed by flattening strain, both X and Y directions are arbitrarily aligned in the foliation plane. However, the lineated but not foliated rock sample, which experienced constricting deformation, is characterized by X direction parallel to lineation and Y and Z directions arbitrarily aligned in the YZ plane. For samples that displayed neither foliation nor lineation (e.g., undeformed isotropic igneous rocks), all three directions are aligned in an arbitrary direction and thus only one direction is taken since such rocks are generally isotropic.

The average elastic properties of an anisotropic rock, which are equivalent to the properties of their isotropic counterparts, can be computed from the mean V_p and mean V_s values derived from the equations (1.29) and (1.30).

$$V_p(\text{mean})=[V_p(\text{X})+V_p(\text{Y})+V_p(\text{Z})]/3 \tag{1.29}$$

$$V_s(\text{mean})=[V_s(\text{XY})+V_s(\text{XZ})+V_s(\text{YX})+V_s(\text{YZ})+V_s(\text{ZX})+V_s(\text{ZY})]/6 \tag{1.30}$$

In Eq. (1.29), V_p(X), V_p(Y), and V_p(Z) are, respectively, the P-wave velocities along the propagation directions X, Y, and Z. In Eq. (1.30), V_s(XY), V_s(XZ), V_s(YX), V_s(YZ), V_s(ZX), and V_s(ZY) are the S-wave velocities with the first letter in the brackets to refer to the propagation direction and the second letter to the polarization direction. The mean V_p and V_s values calculated from Eqs. (1.29)-(1.30) generally give values very close to those of true isotropic rocks, even in highly anisotropic rocks (Christensen and Ramananantoandro, 1971; Ji et al., 2003; Wang and Ji, 2009).

Bulk V_p anisotropy [A_p(B)] or A_p is defined by Birch (1961) as:

$$A_p(\text{B}) = \left[V_p(\text{max}) - V_p(\text{min})\right] / V_p(\text{mean}) \times 100\% \tag{1.31}$$

where V_p(max) and V_p(min) are, respectively, the maximum and minimum values of the P-wave velocities measured in a given sample along different propagation directions. Thus, A_p(B) depends only on the maximum and minimum velocity values and does not carry any information about their orientations.

In order to characterise symmetry in seismic anisotropy, we define a V_p anisotropy within the foliation or simply a foliation anisotropy, A_p(F), as

$$A_{\mathrm{p}}(\mathrm{F}) = \frac{V_{\mathrm{p}}(\max) - V_{\mathrm{p}}(\min)}{\left[V_{\mathrm{p}}(\max) \cdot V_{\mathrm{p}}(\min)\right]^{0.5}} \times 100\% \tag{1.32}$$

where $V_{\mathrm{p}}(\max)$ and $V_{\mathrm{p}}(\min)$ are the maximum and minimum compressional wave velocities, respectively, within the foliation plane.

For each bulk sample, the V_{s} anisotropy (A_{s}) is defined as

$$A_{\mathrm{s}} = \left[V_{\mathrm{s}}(\max) - V_{\mathrm{s}}(\min)\right] / V_{\mathrm{s}}(\mathrm{mean}) \times 100\% \tag{1.33}$$

where $V_{\mathrm{s}}(\max)$ and $V_{\mathrm{s}}(\min)$ are the maximum and minimum V_{s} values measured in a given sample along different propagation-polarization directions, respectively.

Shear-wave splitting (ΔV_{s}) is defined as the difference in velocity between fast and slow split S-waves with the same propagation direction Λ:

$$\Delta V_s = V_{s1} - V_{s2} \tag{1.34}$$

The percentage shear-wave splitting (S_Λ or AV_{s}) is referred to the normalized difference between the fast and the slow S-wave velocities for a given propagation direction Λ:

$$AV_s = S_\Lambda = \frac{(V_{s1} - V_{s2})}{(V_{s1} + V_{s2})/2} \times 100\% \tag{1.35}$$

Thus, AV_{s} is a directional parameter, while A_{s} calculated from Eq. (1.33) does not carry any information about orientation.

Despite initial simplified assumptions that rocks are considered as isotropic polycrystalline aggregates (e.g., Simmons and Wang, 1971), laboratory measurements consistently revealed a more or less directional dependence of the elastic velocities in almost all naturally occurring rocks. Ji et al. (2002) summarized the available data on seismic velocities and anisotropies in rock samples. Therein, the distributions of V_{p} and V_{s} anisotropy at 600 MPa and 25 ºC, respectively, for 1438 and 467 rock samples were analyzed by Sun (2011). The result shows that ~ 45% of the studied samples have both A_{p} and A_{s} values less than 3%, and ~70% of those have anisotropy values no more than 6%. The mean V_{p} and V_{s} anisotropies are 5.29% and 5.73%, respectively. Figure 1.7 illustrates the mean V_{p} anisotropy [A_{p}(mean)] values for 31 common lithologies. The igneous rocks are, to a first approximation, isotropic [A_{p}(mean)≈2.5-3.5%], whereas many of the metamorphic rocks show significant anisotropy. Anisotropy is a particularly

important parameter in the low-grade pelitic rocks, for example, the mean V_p anisotropies of slate and phyllite are up to 10.36% and 11.89%, respectively. The medium-grade metamorphic rocks, such as gneiss [A_p(mean)≈4.5-5.5%] and amphibolite [A_p(mean)=9.15%] have higher anisotropies than those of high-grade metamorphic rocks. The mean V_p anisotropies of high grade granulite and eclogite facies rocks are relatively low, only about 2-3%. Thus seismic anisotropy is likely to be a more significant property of upper and middle crustal regions than the lower crust in which granulite-facies rocks are probably dominant. For mantle rocks, 82 peridotites and 18 pyroxenites have A_p(mean) of 5.92% and 3.61%, respectively. With predominant frequencies close to 1 MHz and P-wave velocities ranging from ~2 to ~8 km/s, the wavelength in a typical ultrasonic experiment is ~2-8 mm, allowing elastic wave to detect causes of millimeter-scale anisotropy (Cholach, 2005). The causes of seismic anisotropy in the Earth's interior will be discussed in the section 1.5. Seismic anisotropy in many rocks likely reflects the effect of compositional variation on wave velocity, thereby making the prediction of rock type from seismic velocity more complex.

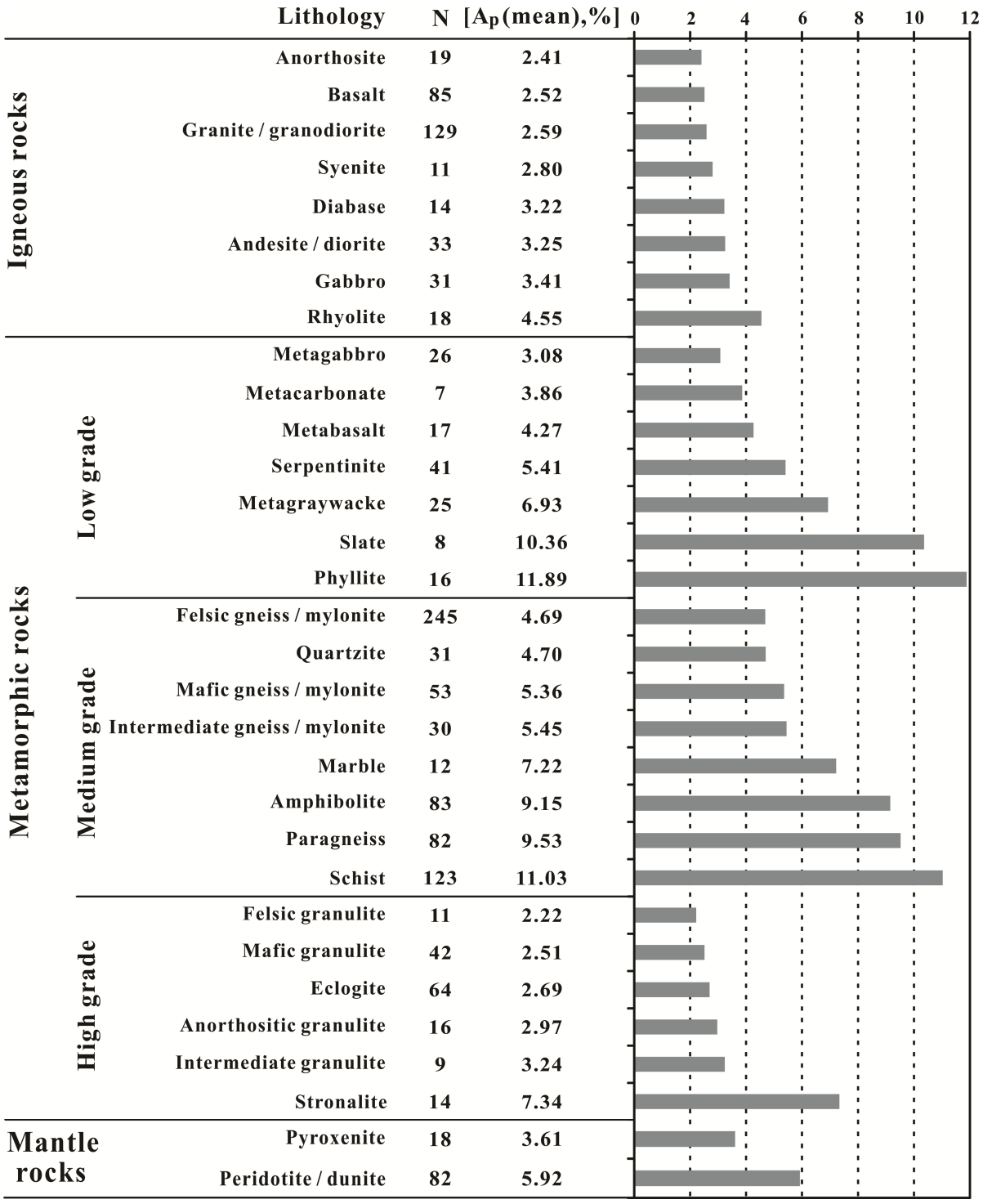


Figure 1.7 Mean anisotropy of V_p [A_p(mean), %] for igneous, metamorphic and mantle rocks at 600 MPa and room temperature. The numbers of measurements (N) are also indicated. (Data from Ji et al., 2002).

1.4.3 Field observation of seismic anisotropy

In addition to laboratory ultrasonic measurements, seismic anisotropy presence in both the crust and upper mantle has also been observed on several orders of magnitude larger scales during exploration seismic surveys (Helbig, 1994). In the uppermost crust, seismic anisotropy of geological strata can be sampled with a typical frequency range of 10-120 Hz and a wavelength of seismic wave in the range of 25-400 m. Also, a directional dependence of P-wave velocities was reported for seismic surveys of different geometries, including reflection (e.g., Grechka and Tsvankin, 1999; Thomsen et al., 1999), refraction surveys (Helbig, 1964; Leslie and Lawton, 1999), and vertical seismic profiling (VSP) (e.g., Kebaili and Schmitt, 1996; Leaney et al., 1999; Liu et al., 1993; Miller et al., 1994; Yardley and Crampin, 1991). The main objective of these exploration surveys was to determine the orientation of the predominant brittle fracture set forming anisotropy.

In the mid-lower crust and upper mantle, however, surface Rayleigh and Love waves and Pn, P, S, SKS, SKKS phases of body waves (e.g., Lay and Wallace, 1995) were employed to reveal anisotropy on a global scale. Seismic anisotropy can be inferred from the inversion of dispersion curves of Rayleigh and Love waves, which are horizontally and vertically polarized, respectively (Montagner, 1986). Since the original work of Smith and Dahlen (1973) on the azimuthal velocity dependence of Love and Rayleigh waves in an anisotropic medium, this approach has been widely used for studying the radial anisotropy in the crust (Chen et al., 2009; Duret et al., 2010; Moschetti et al., 2010; Shapiro et al., 2004) and upper mantle (e.g., Becker et al., 2008; Beghein et al., 2006; Chen et al., 2009; Ekstrom and Dziewonski, 1998; Shapiro and Ritzwoller, 2002). Following a method of inverting azimuthal variations of surface velocities (Smith and Dahlen, 1973), Montagner and Nataf (1986) provided functional dependence of anisotropy with depth. Thus, surface waves can offer an advantage over subvertically propagating teleseismic S-waves. Based on the inversion of a vast surface wave dataset, Shapiro et al. (2004) revealed 10-20% radial anisotropy throughout the middle crust (20-50 km depth) beneath the Tibetan Plateau. Large sets of Love and Rayleigh dispersion curves have also been inverted to better reconstruct the 3D variations of anisotropic parameters in the upper mantle. For example, some models of the Earth's interior are proposed to account for anisotropy in the upper mantle (e.g., Babuška et al., 1998; Beghein et al., 2006; Montagner, 1998).

Azimuthal and lateral anisotropy in the lower crust and upper mantle has been widely reported from observations of variations in Pn phase body wave. Azimuthal variations of Pn velocity provide information about subhorizontal properties of the mantle just beneath the Moho discontinuity. As mentioned before, Hess (1964) first reported azimuthal velocity variations of Pn phase in oceanic basins. Bamford (1977) analyzed large sets of Pn traveltimes from deep continental refraction profiles and suggested a 6-7% anisotropy of Pn in the continental lithosphere beneath western Germany. According to tomographic analysis, Hearn (1999) proposed that 5% of P-wave anisotropy is required to properly image the uppermost mantle from Pn wave observations.

Furthermore, observations of teleseismic P- and S-wave velocity anisotropy are likely to provide more complete information about the 3D structure of the Earth's interior. Mapping the lateral changes of P-wave anisotropy within the subcrustal lithosphere on teleseismic P-residual spheres allows detection of direction of the symmetry axis of the observed anisotropy (Babuška et al., 1993). Joint interpretation of P-wave delay times with polarization analysis of shear-wave splitting of SKS phase (Silver, 1996) resolved the ambiguity in the interpretation of vertical velocity anomalies in the mantle (Babuška et al., 1998; Babuška and Plomerova, 2001; Plomerova et al., 1996, 1998). Knowledge about the contributions of crustal anisotropy (Barruol and Mainprice, 1993; Weiss et al., 1999) and upper mantle anisotropy (e.g., Barruol and Kern, 1996; Ji et al., 1994a) to shear-wave splitting measured from teleseismic observations help to understand the style and magnitude of deformation in the crust and upper mantle and to explore the degree of crust-mantle coupling.

1.5 Sources of anisotropy in the Earth's interior

As mentioned above, anisotropy of the Earth's interior is observed on various scales and dominantly focuses in the lithosphere (Silver, 1996). This fact implies that sources of elastic anisotropy are non-unique and can contribute to overall observed anisotropy. Such a non-uniqueness of the origin of anisotropy imposes ambiguity on geological interpretation of observed variations in P- and S-wave velocities (e.g., Rasolofosaon et al., 2000; Werner and Shapior, 1998, 1999). Given specific geological settings, there are three commonest mechanisms responsible for the observed seismic anisotropy: (1) horizontal or inclined layering of rock units; (2) extensive networks of oriented cracks and microfractures (also incorporates oriented pore

space), which are usually further complicated by in situ stress state; and (3) textured rocks with a CPO of the constituent minerals.

In many cases, all three sources are superposed and contribute simultaneously to the anisotropy. On a global scale the correlation of the source of the seismic anisotropy observed on the Earth's surface is complex, depending on vertical (depth) and laterial variations in these sources (e.g., Montagner, 1998). Seismic anisotropy is generally attributed to the combined effect of compositional layering, CPO and aligned fractures in the upper crust (Crampin, 1991; Crampin and Atkinson, 1985; Crampin and Peacock, 2008; Mainprice and Nicolas, 1989), and predominantly to the CPO of mica in the mid-crust (Cossette et al., 2015; Dempsey et al., 2011; Erdman et al., 2013; Kern et al., 2008; Lloyd et al., 2009; Meltzer and Christensen, 2001; Ward et al., 2012), amphibole in the lower crust (Ji et al., 2013b; Tatham et al., 2008), and olivine and pyroxene in the upper mantle (Ji et al., 1994a; Karato et al., 2008; Mainprice et al., 2007; Saruwatari et al., 2001).

1.5.1 Layer-induced anisotropy

In many geological settings, especially in sedimentary basins with characteristic subhorizontal layering (named bedding) and subvertical symmetry axis, seismic P-wave propagates substantially faster parallel to the bedding plane than perpendicular to it, reflecting their transverse isotropy (TI) (Figure 1.8). Within a single layer of massive rocks such as sandstones, for example, seismic anisotropy is low due to slight variation in velocities as a function of propagation direction. However, the rocks interlayered with different lithological layers (e.g., sandstone with mudstone or limestone) exhibit strong anisotropy with faster velocities parallel to bedding and slower velocities perpendicular to bedding. Seismic waves in a TI medium behave similarly to elastic waves in the single crystals of hexagonal symmetry, with null shear-wave splitting and difference in P-wave velocity in the plane perpendicular to the symmetry axis. This property of a TI medium allows a better understanding of the direction-dependencies of velocities. According to a model of the solid consisting of thin isotropic horizontal layers, early theoretical studies were performed on the wave propagation in a TI medium (Backus, 1962; Krey and Helbig, 1956; Postma, 1955; Riznichenko, 1949; Rytov, 1956). Since then, the anisotropy of TI media has received extensive attention (Berryman, 1979; Byun, 1984; Daley and Hron, 1977; Hake et al., 1984; Helbig, 1981, 1984a, b; Helbig and Schoenberg, 1987; Levin, 1979; Thomsen, 1986),

resulting in more systematic characterization of TI media. Also, parameterizations of P- and S-wave behavior have been developed to significantly simplify the description of elastic wave velocities in a TI media. TI has been reported to result from thin layers (e.g., Cheadle et al., 1991; Kebaili and Schmitt, 1997; Mah and Schmitt, 2003; Melia and Carlson, 1984) in laboratory ultrasonic experiments on synthetic materials with well-controlled properties as well as in numerical experiments (e.g., Hovem, 1995; Schoenberg and Costa, 1991).

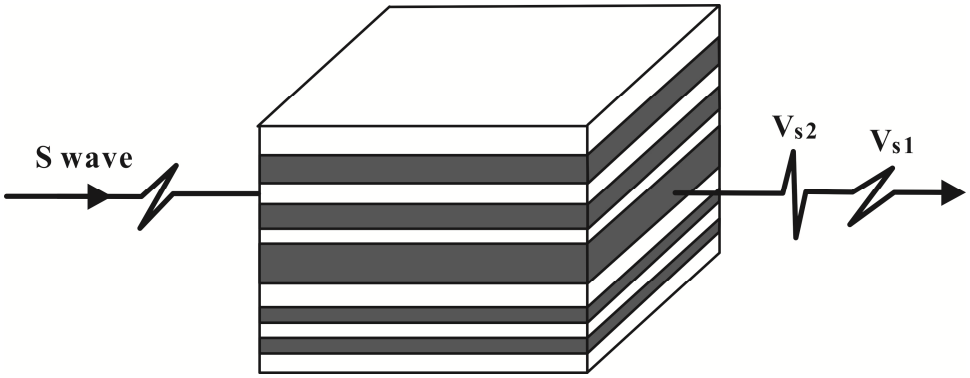


Figure 1.8 Shear-wave splitting in layered rocks, with the faster polarized wave (V_{s1}) parallel to bedding and the slower polarized wave (V_{s2}) perpendicular to bedding.

1.5.2 Fracture-induced anisotropy

In the upper crust, anisotropy can also be produced by the preferred orientations of discontinuities (e.g., cracks, microfractures, and mineral grain boundaries), and particularly stress-induced fluid-saturated microcracks, in an isotropic or anisotropic quasi-continuous solid. For example, Babuska and Pros (1984) attributed experimentally observed anisotropy of granodiorities and quartzites to a pervasive set of oriented microcracks. To a first approximation, such an anisotropic medium can be considered as TI with a symmetry axis normal to the microcrack plane that is perpendicular to the minimum principal stress (σ_3). Thus, the symmetry axis is parallel to the minimum principal stress. Figure 1.9 illustrates shear-wave splitting through distribution of stress-aligned parallel vertical microcracks. These parallel vertical cracks are generally found below the critical depth of 500-1000 m, where the increasing vertical stress (σ_V) becomes greater than the minimum horizontal stress (σ_h) (Crampin and Peacock, 2008). For propagation within 30º of the vertical, the faster shear waves (V_{s1}) are polarized parallel to both the strike of the cracks and the direction of maximum horizontal stress (σ_H), and the slower shear waves (V_{s2}) are polarized perpendicular to the microcrack plane and parallel to the direction of σ_h.

Such vertically aligned crack-induced anisotropy is confined within the brittle portion of the crust alone. That is to say, rocks with the maximum fracture-induced anisotropy are located less than 3-5 km of the uppermost crust (10-15 km) (Kaneshima, 1990; Kaneshima and Ando, 1988). This critical depth of crack-induced anisotropy corresponds to the depth of the brittle-ductile transition and decreases with increasing regional geothermal gradient.

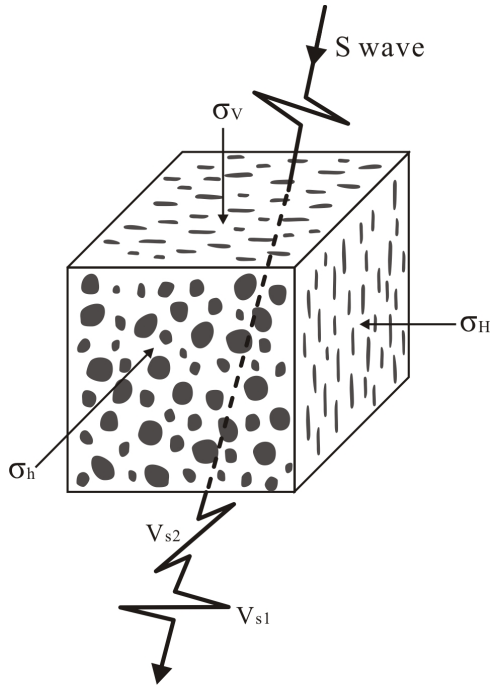


Figure 1.9 Schematic illustration of shear-wave splitting through distributions of stress-aligned parallel vertical microcracks aligned normal to the direction of minimum horizontal stress (σ_h).

Fracture-induced seismic anisotropy is well associated with the distribution of regional stress, e.g., in fault zones (Mizuno et al., 2001), orogenic belts (Lokmer and Herak, 1999), and fracturing reservoirs for oil and gas exploration (MacBeth et al., 1998). Fluids trapped in cracks and pores increase seismic velocity and play an important role in the spatial and temporal variations of seismic anisotropy. For example, Bokelmann and Harjes (2000) observed that a tectonic stress release and temporal anisotropy variation resulted from seismic events triggered by fluid injection, suggesting that changes in shear-wave splitting can be observed before and after large earthquakes. In fact, such chages are also likely to be detected prior to impending large earthquakes as they are the most sensitive diagnostic indicators of stress-induced variations in microcrack geometry. Given sufficient seismic events before the impending earthquake to provide effective shear-wave splitting data, the normalized delay time is observed to initially

increase and then abruptly decrease immediately before the larger earthquake (Figure 1.10). In general, the initial increase in delay time is interpreted as stress-accumulation, whereas the following abrupt decrease is attributed to stress relaxation caused by crack propagation and coalescence onto the eventual fault break. Both the logarithm of the duration of the increase and decrease in delay time is proportional to the magnitude of the impending earthquake (Crampin and Peacock, 2008; Gao and Crampin, 2004). Thus, it is possible to estimate the times and magnitudes of impending larger earthquakes by analyzing shear-wave splitting because characteristic temporal variations of shear-wave delay time (δt) can be available before earthquakes worldwide (Crampin and Peacock, 2008 and references therein).

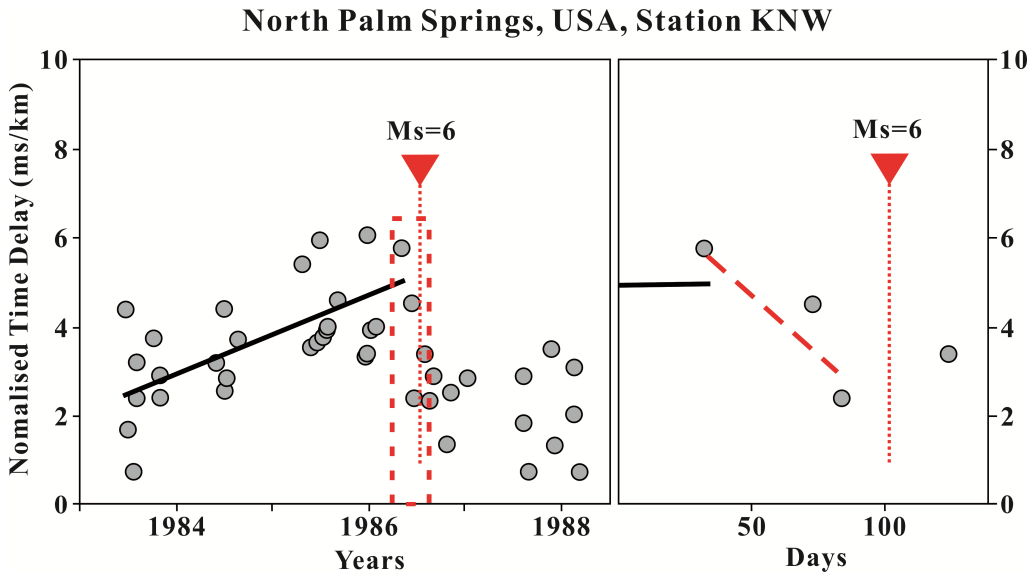


Figure 1.10 Temporal variations in normalized shear-wave delay time (ms/km) observed before earthquakes (modified after Crampin and Peacock, 2008). M_s 6 North Palm Springs Earthquake (Peacock et al., 1988). Left-hand-side: delay time with a least-squares line showing general increase before the earthquake. Right-hand-side: enlarged time scale for dotted box in left-hand-side, with dashed line showing precursory decrease in delay times before the earthquake.

1.5.3 CPO-induced anisotropy

In the middle-to-lower crust, most aligned microcracks are closed due to high confining pressure, thus seismic anisotropy is dominated by CPOs of main constitutent minerals and metamorphic/structural layering (Ji and Salisbury, 1993; Ji et al., 1993). The lower crust consists

of amphibolite-granulite facies metamorphic rocks, in which mica, amphibole, feldspar, pyroxene (clinopyroxene and orthopyroxene) are dominant minerals. Therein, mica and amphibole are considered to control seismic anisotropy in the middle-to-lower crust (Barruol and Mainprice, 1993a; Cholach et al., 2005; Ji and Salisbury, 1993; Ji et al., 1993, 2013b, 2015; Shao et al., 2015; Takanashi et al., 2001; Tatham et al., 2008). The amphibolitic mylonite and mica-rich mylonite often possess a seismic anisotropy greater than 8% (e.g., Ji et al., 1993, 2015; Chapter 3 in this thesis). At the deepest crust, however, the igneous rocks are quasi-isotropic with the exception of layered structures in mafic and ultramafic intrusions, which can result from fractional crystallization and crystal segregation controlled by setting or floating of minerals during the cooling of magma (Ji et al., 2014b), and high-grade granulite and eclogite facies rocks exhibit relatively low anisotropy. Hence, seismic anisotropy is more significant for the upper and middle crust than for the lowermost crust (Figure 1.7; Ji et al., 2002), and can be used as an indicator of shear zones or thrust faults and an extremely important proxy of ductile deformation of rocks in the deep crust (e.g., Ji et al., 1993, 2002; Jones and Nur, 1984; Meissner et al., 2002). For example, low-angle or even subhorizontal mylonitic zones, likely formed by crustal channel flow, can be distinguished by fabric-related seismic anisotropy; as such mylonites appear as low-velocity layers when the seismic wave propagates subvertically (Ji et al., 1993; Zorin et al., 2002). Again, in west Yunnan there are several crustal-scale strike-slip shear zones (e.g., the Gaoligong, Lancangjiang, and Ailaoshan-Red River shear zones), in which pervasively subvertical foliation and subhorizontal stretching lineation formed a quasi-TI with the slowest velocity perpendicular to the foliation and the fastest velocity always in the foliation plane (Ji and Salisbury, 1993; Ji et al., 2015; Shao et al., 2015; Chapter 3 in this thesis). Towards deeper crust, however, the shear zones penetrate into the granulite facies and may become quasi-isotropic (Ji and Salisbury, 1993). Therefore, the variation in anisotropy of a shear zone may imply change in metamorphic facies in a given crustal setting.

Hess (1964) suggested that the dependence of seismic velocities on propagation direction observed during refraction surveys of Pn phase can be attributed to the CPO of olivine in the upper mantle. Since then, numerous works have been devoted to the investigation of the relationship between elastic properties of upper mantle rocks and observed seismic anisotropy (Barruol and Kern, 1996; Christensen, 1984; Christensen and Crosson, 1968; Christensen and Salisbury, 1979; Christensen et al., 2001; Nicolas and Christensen, 1987; Peselnick et al., 1974;

Pselnick and Nicolas, 1978; Soedjatmiko and Christensen, 2000). Results suggest that the observed upper mantle seismic anisotropy results from the CPOs of constituent peridotite minerals, mainly olivine and secondly pyroxenes. The contribution of CPO of olivine in peridotites to shear-wave splitting of observed teleseismic SKS waves is evidenced significant (e.g., Ji et al., 1994a; Mainprice and Silver, 1993; Silver, 1996; Vauchez and Barruol, 1996). Like velocity structures of the crust, the relation between observed seismic anisotropy and CPO of plastically deformed peridotites also implies that the observed seismic anisotropy may be a direct manifestation of tectonic processes in the upper mantle related to plate motion (e.g., Carter et al., 1972; Fuchs, 1977; Karato, 1987, 1998; Vauchez et al., 2000). These processes primarily include cratonization, terrane accretion and continental collision or rifting (passive or active), subduction, and lithospheric basal erosion due to a relative motion of cratonic keels and the convective mantle. At convergent margins, for example, pure shear in the shallow mantle can interpret orogen-parallel fast polarization in the Pyreness (Barruol et al., 1998) and in South Island, New Zealand (Little et al., 2002). At the base of the North American plate, the fast a-axis of olivine crystals will align with the extension (flow) direction, which is parallel to the absolute plate movement (APM) and produces anisotropy with a plunging axis of symmetry (Barruol et al., 1997). The frozen fabrics of peridotite may control the deformation regime and impose a strong strike-slip shear component in tectonically active continental regions, although seismic anisotropy observed is well consistent with localized lithospheric flows during the most recent thermotectonic events (e.g., Barruol and Granet, 2002).

CHAPTER 2 ANTIGORITE-INDUCED SEISMIC ANISOTROPY AND IMPLICATIONS FOR DEFORMATION IN OCEANIC SUBDUCTION ZONES AND THE TIBETAN PLATEAU

2.1 Introduction

Serpentine, which is a phyllosilicate with stacking of tetrahedral-octahedral sheets bonded by hydroxyl groups, forms by hydration of peridotites beneath mid-oceanic ridges, in the subducting slabs and the overlying mantle wedge as well as in continental suture zones between amalgamated blocks. There are three forms of serpentine – lizardite, chrysotile and antigorite – all with approximate composition $Mg_3Si_2O_5(OH)_4$ but different structures (flat-layered lizardite, rolled-layered chrysotile, and antigorite with a wavelike structure parallel to the a-axis). In altered ultramafic rocks from surface outcrops, the serpentines are generally lizardite and chrysotile because both are stable only at temperatures below ~300 °C (Evans, 2004; Schwartz et al., 2013). The critical temperature for the lizardite-antigorite transition decreases with increasing pressure, enlarging the stability field of antigorite at high pressures (Reynard, 2013). Under water-present conditions, antigorite rich in Al_2O_3 and Cr_2O_3 is stable over a wide range of pressure up to 5-6 GPa below 650-720 °C (Bromiley and Pawley, 2003; Nestola et al., 2010; Ulmer and Trommsdorff, 1995) and thus should exist in the coldest portion of a subducting slab down to a depth of 150-200 km. Its low density (Guillot et al., 2009; Pilchin, 2005), low flow strength (e.g., Escartin et al., 1997; Hilairet et al., 2007), low friction coefficient (e.g., Hirth and Guillot, 2013; Moore and Lockner, 2007), high water content (~13 wt%, Schmidt and Poli, 1998; Ulmer and Trommsdorff, 1995), low seismic velocities and high anisotropy (e.g., Christensen, 2004; Ji et al., 2002, 2013a; Kern et al., 1997; Watanabe et al., 2007) are particularly important for understanding geodynamic processes within subducting oceanic slabs and the cold tip of mantle wedge (e.g., Guillot et al., 2000; Hilairet and Reynard, 2013; Hyndman and Peacock, 2003; Reynard, 2013; Wada et al., 2008).

Experimental investigations on the seismic properties of antigorite serpentinites are scarce. Birch (1960) measured, at confining pressures up to 1.0 GPa, direction-dependent P-wave velocities for a serpentinite sample (ρ=2.614 g/cm^3) from Ludlow, Vermont with an antigorite content of 86 vol.%. Christensen (1978) reported the mean P- and S-wave velocities of a serpentinite (95 vol.%

antigorite, 5 vol.% other minerals such as opaques and chlorite; ρ=2.665 g/cm^3) from Stonyford, California, measured at pressures up to 1.0 GPa. Kern et al. (1997) investigated both P- and S-wave velocities and anisotropy of a serpentinized peridotite (ρ=2.720 g/cm^3, 74.9 vol.% antigorite, 20.3 vol.% olivine, 3.8 vol.% opaque minerals, and 1.0 vol.% others) at pressures up to 600 MPa. Watanabe et al. (2007, 2011) studied the low pressure (≤200 MPa) seismic properties of 13 serpentinized peridotite samples with 42.1-88.8 vol.% antigorite, in which other minerals are olivine, tremolite, chlorite and magnetite. Bezacier et al. (2010) measured the elastic constants of a small (~0.150 mm) antigorite plate (ρ=2.62 g/cm^3) picked from a sample from the Escamray massif (Central Cuba), using Brillouin spectroscopy under ambient conditions (0.1 MPa and 20 °C). Using the Hill average, they obtained V_p=6.76 km/s, V_s=3.83 km/s, and V_p/V_s=1.77 for an isotropic aggregate of antigorite. The values are markedly different from the values of antigorite serpentinite reported by Christensen (2004) even at 200 MPa (V_p=6.54 km/s, V_s=3.58 km/s, and V_p/V_s=1.83). Recently, Ji et al. (2013a) measured the P- and S-wave velocities, anisotropy and shear-wave birefringence of 17 antigorite serpentinite samples containing >90 vol.% antigorite at pressures up to 650 MPa. Their experimental results revealed distinctly different effects of low and high temperature (LT and HT) serpentinization on the seismic properties of mantle rocks. At 600 MPa, for example, V_p=8.10-3.00φ_{LT}, V_s=4.51-2.19φ_{LT}, V_p=8.10-1.42φ_{HT}, and V_s=4.51-0.84φ_{HT}, where φ is the volume fraction of serpentine. These equations suggest that serpentine contents within subduction zones and fore-arc mantle wedges where temperature is >300 °C should be at least twice that of previous estimates based on LT serpentinization. Christensen's (1996) argument that serpentinites have an extremely high V_p/V_s ratio (2.120) or Poisson's ratio (0.352) at P < 1.0 GPa has been widely used during the last 15 years to the interpretation of seismic data from subduction zones and the mantle wedges (e.g., Bostock et al., 2002; Carlson and Miller, 2003; Hyndman and Peacock, 2003; Kamiya and Kobayashi, 2000; Matsubara et al., 2009; Nikulin et al., 2009; Tibi et al., 2008). However, the V_p/V_s ratio of 2.120 (Christensen, 1996) was obtained from a mixture of the data from many LT and few HT serpentinite samples. At 600 MPa, for instance, V_p=5.10 and 6.68 km/s, V_s=2.32 and 3.67 km/s, and V_p/V_s=2.15 and 1.81 for pure LT and HT serpentinites, respectively (Ji et al., 2013a). Recent high pressure measurements of antigorite elasticity at room temperature showed that V_p/V_s increases with increasing pressure: 1.82 at 2.99 GPa and 1.94 at 8.83 GPa (Bezacier et al., 2013).

In this chapter, we report new results on P- and S-wave velocities and anisotropy of 15 serpentinite samples consisting of almost pure antigorite (Figure 2.1), measured at hydrostatic pressures up to 650 MPa on core samples, together with CPO measurements using SEM-EBSD techniques, which allow computation of the 3D seismic properties of the sample. This double approach provides a good opportunity to understand the critical role of antigorite c-axis fabric in the formation of different anisotropy patterns. The antigorite c-axis fabric is controlled by the degree of shear strain and the extent of dynamic recrystallization. The results are used to explain the variations of seismic velocities and anisotropy with depth in cold and hot subduction zones and the Tibetan Plateau.

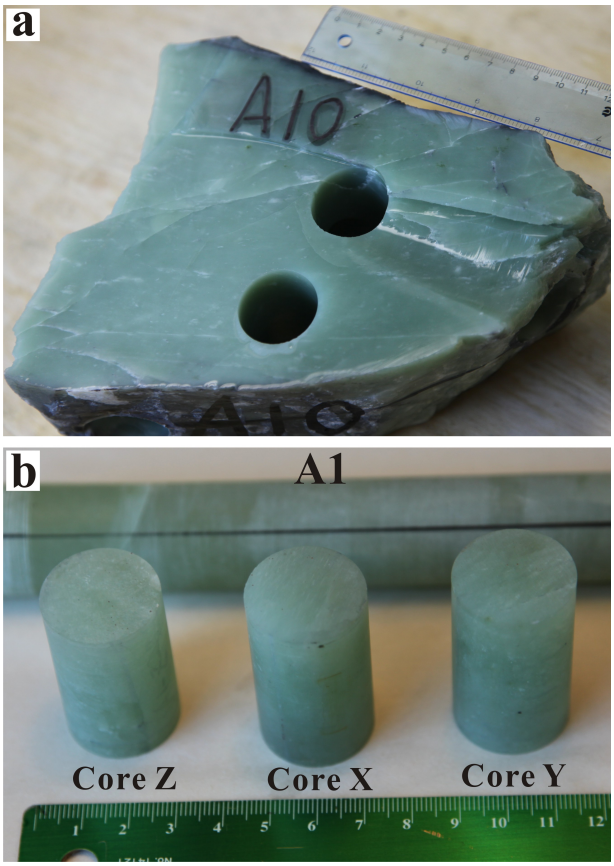


Figure 2.1 (a) A weakly deformed antigorite serpentinite (Xiuyan Jade, sample A10) collected from (123.02383º E, 40.46767º N); (b) Three cylindrical minicores (diameter 2.54 cm) cut from an extremely deformed antigorite serpentinite (sample A1) in the X, Y, and Z directions.

2.2 Samples

Fifteen serpentinite samples (Table 2.1), which consist mainly of antigorite (>91 vol.%) with generally minor to trace amounts of dolomite, magnesite, lizardite, and olivine, were collected from the 'Xiuyan Jade' deposits at Hadabei Town, Muniu Town and Pianling Town (Xiuyan County), and Gushan Town (Haicheng City) in Liaoning Province, China (Ji et al., 2013a). These fine-grained serpentinites or 'Xiuyan Jades' have been widely used for fashioning ornamental carvings or gems for ~8000 years (e.g., Zhang, 2002). The serpentinites, which occur as lens-shaped bodies (30-210 m long and 1-28 m thick) within magnesite-bearing dolomitic marbles of Paleoproterozoic age, were formed by metasomatic reactions between Si-rich aqueous fluids emanating from felsic plutons and dolomitic rocks at 400-550 °C and 300-500 MPa (Ma et al., 2007; Wang and Dong, 2011). For a detailed description of the geological setting, the reader is referred to Ji et al. (2013a) and references therein. The serpentinization occurred under near-static conditions as indicated by interpenetrating antigorite blades (Figure 2.2a). The metasomatic origin of these serpentinites is characterized by high contents of SiO_2, moderate contents of MgO, and significantly low contents of Al_2O_3, $FeO+Fe_2O_3$, Cr_2O_3, or TiO_2 compared with those derived from ultramafic rocks (Table 2.2 and Figure 2.3).

The studied samples display densities ranging from 2.576 to 2.669 g/cm^3 with an average value of 2.590 g/cm^3 under ambient conditions (Table 2.1), mainly reflecting the relative contents of antigorite (ρ=2.600 g/cm^3), lizardite (ρ=2.550 g/cm^3), dolomite (ρ=2.860 g/cm^3), magnesite (ρ=2.980 g/cm^3), and olivine (ρ=3.300 g/cm^3), and porosity (~0.5%). In undeformed serpentinites (Figure 2.2a), antigorite displays a typical interpenetrating texture and random CPO (Wicks and O'Hanley, 1988). In ductile shear zones, however, serpentinites with an initially interpenetrating texture have been transformed to LS mylonites with a well-developed flattening foliation (S) and stretching lineation (L). The content of porphyroclasts decreases with increasing shear strain (Figures 2.2b-2.2d). Optical observations suggest that the (001) planes of antigorite laths are aligned at high angles to the Y direction for the relict porphyroclasts while normal or subperpendicular to the Z direction in the highly deformed and recrystallized matrix (Figures 2.2b-2.2c). The mylonites generally display well-developed S-C-C' structures indicating a consistent simple shear (e.g., Passchier and Trouw, 2005). Sheared antigorite grains display abundant evidence of intracrystalline deformation such as undulatory extinction, lattice rotation, folding, kinking, subgrains, and recrystallization that significantly reduced the grain sizes (Ji et

al., 2013a). The recrystallized neograins are lath or leaf shaped with their short and long axes generally parallel to the c- and b-axes, respectively, probably reflecting their anisotropic growth during plastic flow in the presence of fluids.

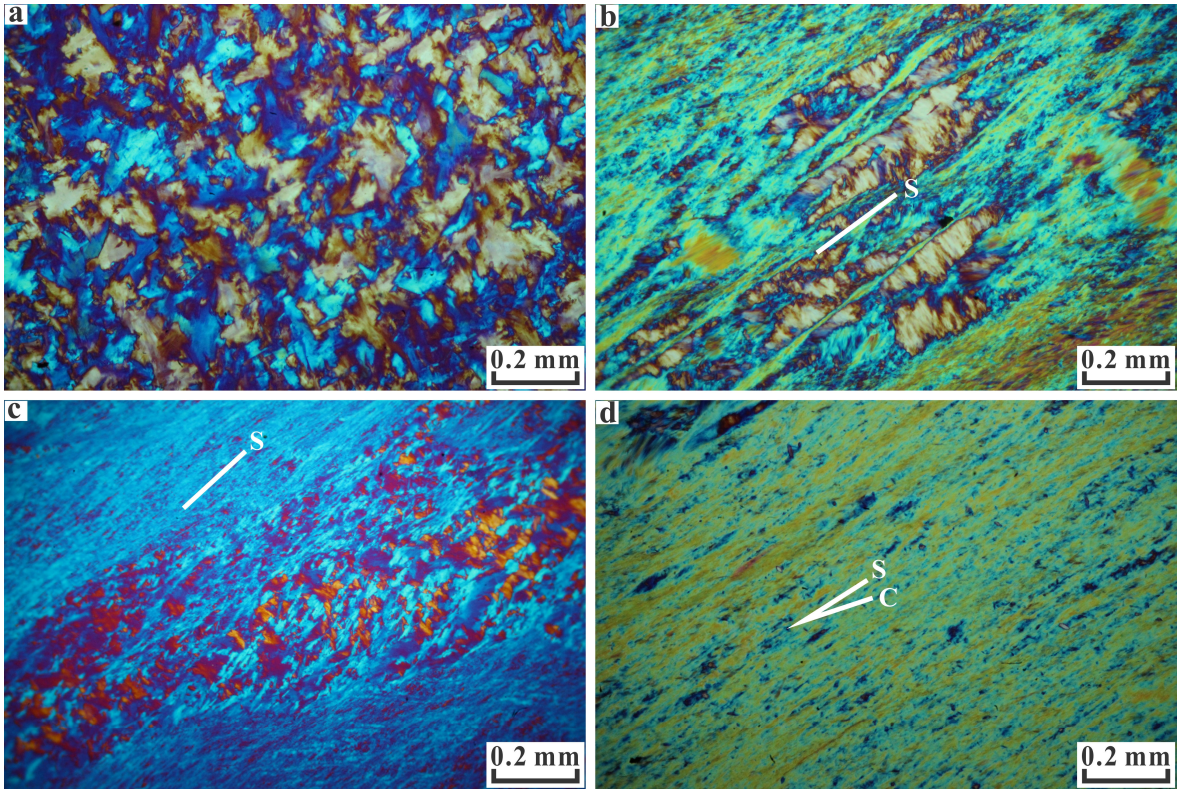


Figure 2.2 Optical photomicrographs of antigorite serpentinites. (a) Undeformed serpentinite with cross-shaped interpenetrating texture. (b-c) Relict porphyroclasts in a highly sheared matrix with different crystallographic preferred orientations (b: sample A3; c: sample WZG2). (d) Ultramylonite of antigorite (sample A5). All images viewed in cross-polarized light with gypsum λ plate inserted.

Table 2.1 Description of the antigorite serpentinites studied*

Sample	Location	GPS data			Density**	Modal composition	Degree of
		Latitude (°)	Longitude (°)	Altitude (m)	(g/cm^3)	(vol.%)	deformation
A1	1	40.46767	123.02383	414	2.591	Atg 99.0, Dol 1.0	Extremely deformed
A2	1	40.46767	123.02383	414	2.669	Atg 90.0, Dol 4.0, Mgs 1.0, Ol 5.0	Almost undeformed
A3	1	40.46767	123.02383	414	2.589	Atg 100.0	Extremely deformed
A4	1	40.46767	123.02383	414	2.583	Atg 100.0	Moderately deformed
A5	1	40.46767	123.02383	414	2.591	Atg 100.0	Extremely deformed
A6	1	40.46767	123.02383	414	2.591	Atg 100.0	Highly deformed
A8	4	40.51889	122.98728	499	2.577	Atg 93.0, Lz 7.0	Moderately deformed
A9	4	40.51889	122.98728	499	2.581	Atg 99.0, Lz 1.0	Highly deformed
A10	1	40.46767	123.02383	414	2.581	Atg 98.0, Dol 2.0	Weakly deformed
A11	1	40.46767	123.02383	414	2.592	Atg 96.0, Dol 4.0	Moderately deformed
A12	1	40.46767	123.02383	414	2.586	Atg 100.0	Weakly deformed
A13	4	40.51889	122.98728	499	2.583	Atg 99.0, Lz 1.0	Extremely deformed
A14	2	40.48058	123.24503	456	2.580	Atg 99.0, Lz 1.0	Highly deformed
A15	4	40.51889	122.98728	499	2.582	Atg 99.0, Lz 1.0	Extremely deformed
A16	3	40.63311	123.31161	456	2.587	Atg 99.0, Dol 1.0	Moderately deformed

*Mineral symbols and abbreviations according to Whitney and Evans (2010); **Samples contain about 0.5% porosity.

Sites 1, 2 and 3 are, respectively, Yushi (Hadabei Town), Dongsheng (Pianling Town) and Muniu (Muniu Town) deposits, Xiuyan County, Liaoning Province, China. Site 4 is Wazigou deposit (Gushan), Haicheng City in the same province.

Table 2.2 Chemical composition of each serpentinite sample studied

Sample	Chemical composition (wt.%)														
	SiO_2	**Al_2O_3**	**Fe_2O_3**	**CaO**	**MgO**	**Na_2O**	**K_2O**	**Cr_2O_3**	**TiO_2**	**MnO**	**P_2O_5**	**SrO**	**BaO**	**LOI**	**Total**
A1	43.94	0.07	0.92	0.17	40.97	0.08	<0.01	<0.01	<0.01	0.03	0.10	<0.01	<0.01	12.70	98.93
A2	50.92	0.09	0.95	0.35	36.82	0.07	<0.01	<0.01	<0.01	0.03	0.13	<0.01	<0.01	9.58	98.88
A3	44.09	0.09	0.75	0.31	41.38	0.08	<0.01	<0.01	<0.01	0.01	0.12	<0.01	<0.01	12.55	99.33
A4	44.41	0.04	0.24	0.03	41.93	0.08	<0.01	<0.01	<0.01	<0.01	0.03	<0.01	<0.01	12.50	99.21
A5	44.3	0.06	1.05	0.16	41.4	0.08	<0.01	<0.01	<0.01	0.03	0.02	<0.01	<0.01	12.70	99.76
A6	44.23	0.05	1.03	0.09	41.33	0.08	<0.01	<0.01	<0.01	0.03	0.06	<0.01	<0.01	12.40	99.26
A8	44.21	0.08	0.59	0.11	41.32	0.08	<0.01	<0.01	<0.01	<0.01	0.08	<0.01	<0.01	12.60	99.02
A9	44.38	0.17	0.34	0.07	41.74	0.08	<0.01	<0.01	<0.01	<0.01	0.06	<0.01	<0.01	12.55	99.33
A10	42.96	0.16	0.6	0.1	41.57	0.07	<0.01	<0.01	<0.01	<0.01	0.08	<0.01	<0.01	13.35	98.84
A11	43.72	0.06	0.71	0.56	41.11	0.08	<0.01	<0.01	<0.01	0.01	0.12	<0.01	<0.01	12.95	99.28
A12	44.62	0.09	0.52	0.1	41.79	0.11	<0.01	<0.01	<0.01	0.01	0.06	<0.01	<0.01	12.40	99.66
A13	43.73	0.16	0.37	0.61	41.25	0.08	<0.01	<0.01	<0.01	<0.01	0.45	<0.01	<0.01	12.30	98.90
A14	44.31	0.01	0.26	0.12	41.97	0.08	<0.01	<0.01	<0.01	<0.01	0.01	<0.01	<0.01	12.60	99.31
A15	44.36	0.03	0.37	0.08	41.82	0.08	<0.01	<0.01	<0.01	<0.01	0.06	<0.01	<0.01	12.40	99.16
A16	43.39	0.07	0.82	0.57	41.25	0.08	<0.01	<0.01	<0.01	<0.01	0.03	<0.01	<0.01	13.20	99.37

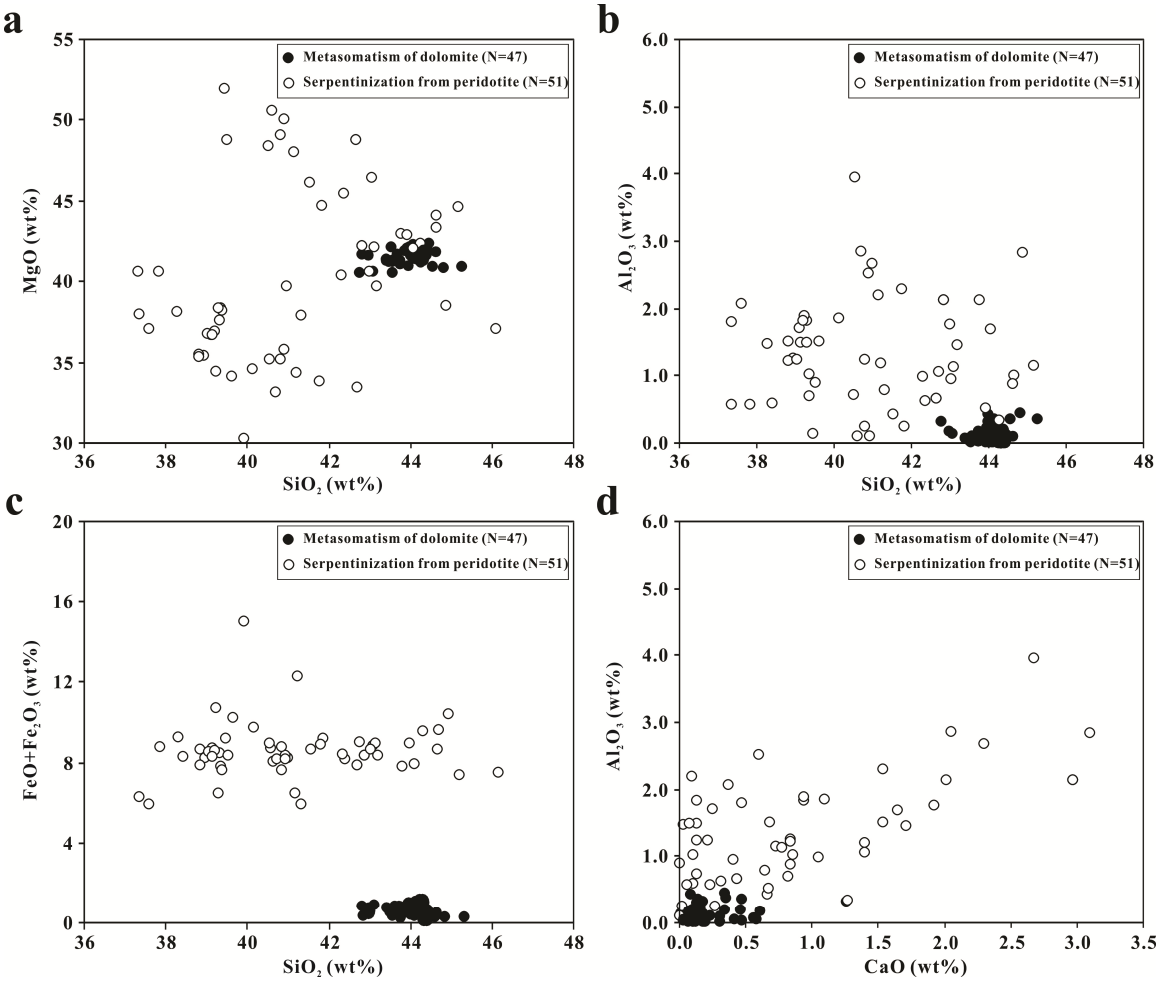


Figure 2.3 Chemical variation diagrams showing the comparsion between serpentinites derived from metasomatism of dolomite (solid circles, this study and Ji et al., 2013a) and serpentinization of peridotite (open circles, Ji et al., 2002; Sun et al., 2012; Wang et al., 2005; Wang and Ji, 2009). Weight percent plots of (a) MgO, (b) Al_2O_3, and (c) FeO + Fe_2O_3 versus SiO_2, and (d) Al_2O_3 versus CaO.

2.3 Measured seismic velocities and anisotropy

2.3.1 Velocity-pressure relationship

Typical V_p-P (Figure 2.4) and V_s-P curves (Figure 2.5) display a rapid, nonlinear increase in velocity with pressure at low pressures (generally <150 MPa) and then increase slowly and linearly in velocity at high pressures. P-wave velocities as a function of pressure were fitted to the following equation (e.g., Ji et al., 2007):

$$V(P) = V_0 + DP - B_0 \exp(-kP) \quad (2.1)$$

where V_0 is the reference velocity representing the intrinsic velocity of the nonporous or crack-free rock at zero pressure, which is determined by extrapolating the linear velocity-pressure relationship obtained at high pressures to zero pressure; D is the intrinsic pressure derivative of velocity in the linear elastic regime; B_0, which is the ambient velocity drop caused by the presence of pores/microcracks at zero pressure, determines the maximum value of the velocity increases due to the closure of pores and microcracks; and k, which is the decay constant of the velocity drop, controls the shape of the nonlinear segment of the velocity-pressure curve (Ji et al., 2007). In Eq. (2.1), V_0 and D are two parameters which describe the intrinsic seismic properties of the microcrack- or pore-free solid matrix, while B_0 and k are parameters which describe the extrinsic seismic properties related to the porosity and geometrical shape of pores (e.g., aspect ratio, spatial arrangement, orientation, and size distribution).

Parameters V_0, D, B_0, and k and their standard deviations determined for V_p and V_s as a function of propagation and polarization directions for each minicore sample during depressurization are given in Tables 2.3 and 2.4, respectively. The statistical results from P-wave velocities of total 32 antigorite serpentinites [15 samples from this study and 17 samples from Ji et al. (2013a), collected from Xiuyan County and Haicheng City, Liaoning Province, China] are shown in Figure 2.6. V_0(X) varies from 6.552 to 7.610 km/s with an average value of 7.075 km/s, V_0(Y) varies from 6.376 to 7.570 km/s with an average value of 6.727 km/s, and V_0(Z) varies from 5.286 to 6.839 km/s with an average value of 6.247 km/s. The V_0 values along the X, Y, and Z directions are significantly different, indicating the presence of strong seismic anisotropy. The average V_p-P parameters of the antigorite serpentinites studied, which are equivalent to the properties of their isotropic counterparts, are given below: V_0=6.681±0.165 km/s, D=1.817±0.390

$\times 10^{-4}$ km/s/MPa, B_0=0.428±0.191 km/s, and k=2.731±0.647$\times 10^{-2}$ MPa^{-1}. The histograms for the distributions of parameters V_0, D, B_0, and k for V_s data are presented in Figure 2.7.

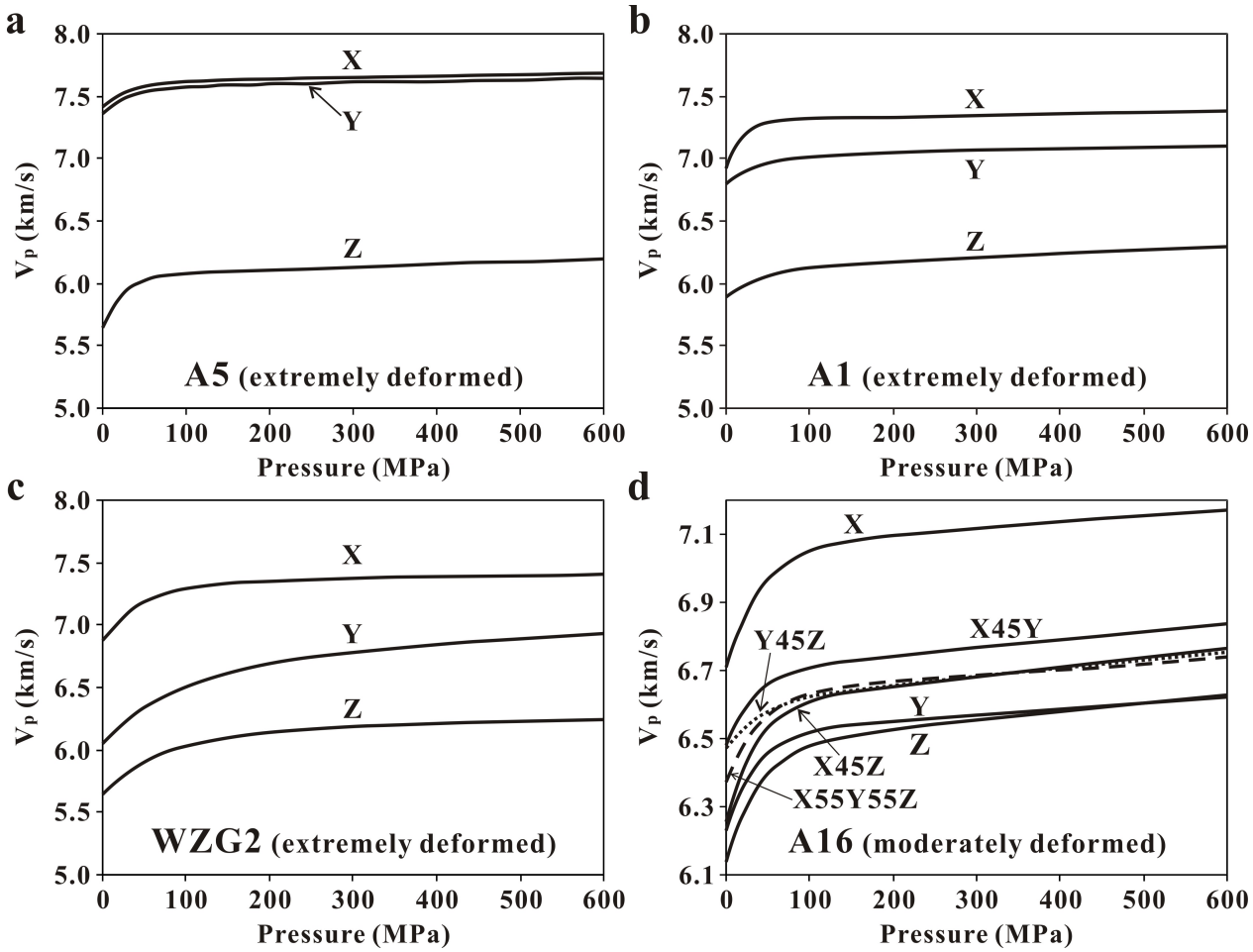


Figure 2.4 P-wave velocity (V_p) versus pressure in three orthogonal directions (X, Y, and Z) through samples (a) A5, (b) A1 and (c) WZG2, and seven directions (X, Y, Z, X45Y, X45Z, Y45Z, and X55Y55Z as defined in the text) through (d) sample A16. Samples A1, A5, and A16 (this study) and WZG2 (Ji et al., 2013a).

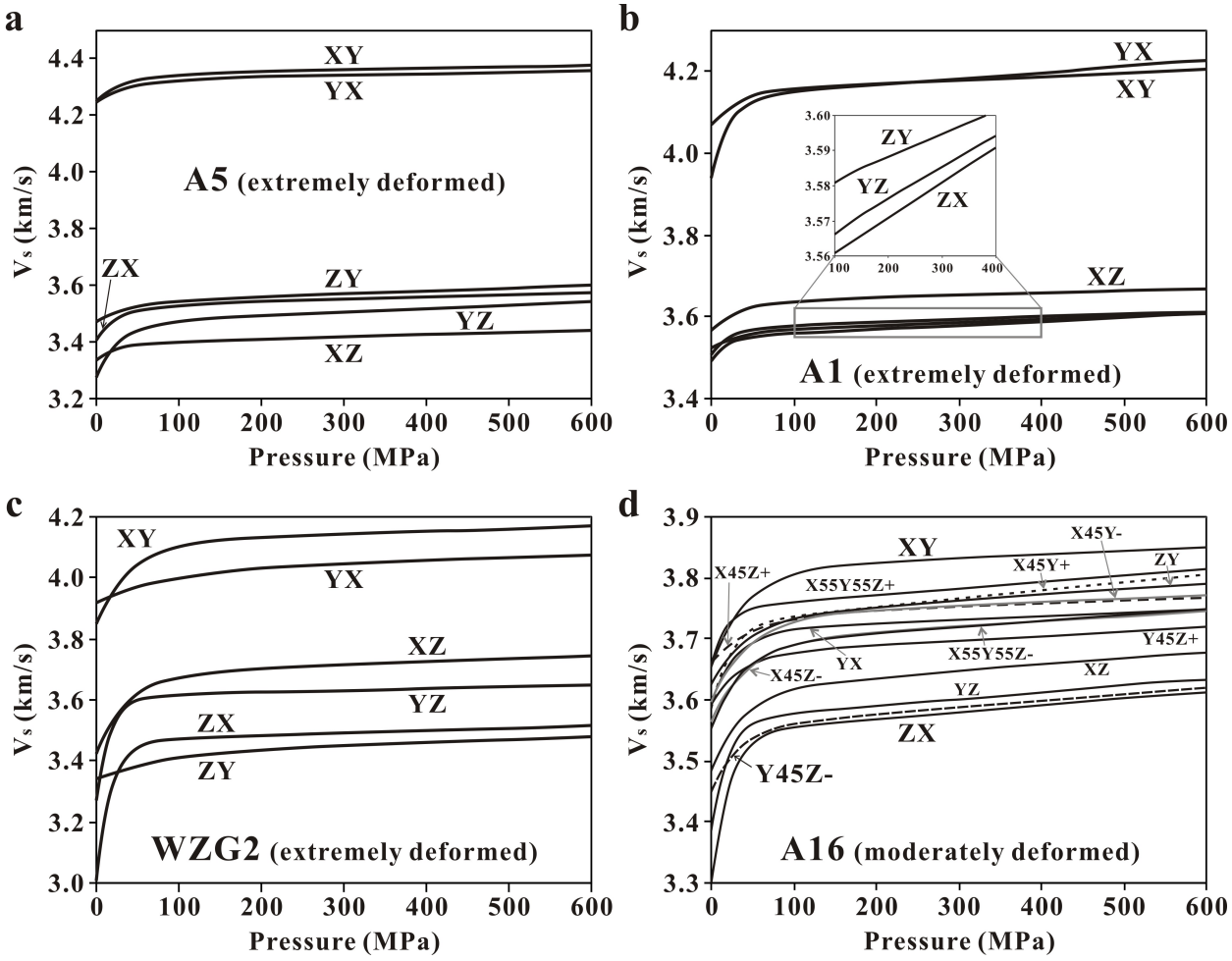


Figure 2.5 S-wave velocity (V_s) versus propagation and polarization directions in representative antigorite serpentinite samples (a) A5, (b) A1, (c) WZG2, and (d) A16. The orientations of wave propagation and polarization are defined in Table 2.4. Samples A1, A5, and A16 (this study) and WZG2 (Ji et al., 2013a).

Table 2.3 Parameters of V_p-P curves and V_p anisotropy for 15 antigorite serpentinite samples studied

Sample	λ[a]	Density	V_0	S.D.	D	S.D.	B_0	S.D.	k	S.D.	R^2	Mean V_p (km/s)	A_p (%)
		g/cm^3	km/s		10^{-4} km/s/MPa		km/s		10^{-2} MPa^{-1}			600 MPa	
A1	X	2.591	7.313	0.008	1.158	0.281	0.399	0.049	5.434	0.898	0.988	6.933	15.4
Extremely	Y		7.028	0.006	1.222	0.154	0.225	0.009	2.500	0.239	0.996		
deformed	Z		6.110	0.001	3.443	0.048	0.172	0.004	4.320	0.197	1.000		
	Mean		6.817	0.005	1.941	0.161	0.265	0.021	4.085	0.444	0.995		
A2	X	2.669	6.351	0.009	1.116	0.212	0.300	0.011	2.286	0.208	0.996	6.404	0.9
Almost	Y		6.311	0.006	1.913	0.152	0.300	0.018	4.306	0.447	0.995		
undeformed	Z		6.314	0.005	0.889	0.131	0.284	0.008	2.611	0.169	0.998		
	Mean		6.331	0.007	1.515	0.182	0.300	0.014	3.296	0.328	0.996		
A3	X	2.589	7.267	0.005	1.129	0.126	0.380	0.008	2.687	0.131	0.999	6.970	15.2
Extremely	Y		7.194	0.006	1.798	0.152	0.232	0.012	3.303	0.358	0.996		
deformed	Z		6.072	0.005	3.369	0.135	0.350	0.046	4.457	0.594	0.997		
	Mean		6.844	0.005	2.099	0.138	0.321	0.022	3.482	0.361	0.997		
A4	X	2.583	6.788	0.007	1.510	0.183	0.550	0.022	4.109	0.287	0.997	6.743	6.0
Moderately	Z		6.348	0.039	2.080	0.846	0.269	0.043	1.598	0.618	0.967		
deformed	Mean		6.641	0.017	1.700	0.404	0.456	0.029	3.272	0.397	0.987		
A5	X	2.591	7.610	0.002	1.219	0.048	0.196	0.004	3.113	0.130	0.999	7.174	20.8
Extremely	Y		7.570	0.002	1.253	0.058	0.206	0.005	3.120	0.149	0.999		
deformed	Z		6.059	0.006	2.237	0.211	0.422	0.035	4.279	0.394	0.998		
	Mean		7.080	0.003	1.570	0.106	0.275	0.014	3.504	0.225	0.999		
A6	X	2.591	7.327	0.005	1.246	0.131	0.213	0.015	2.730	0.317	0.995	6.987	13.8
Highly	Y		7.029	0.003	1.522	0.092	0.455	0.039	5.035	0.410	0.997		
deformed	Z		6.319	0.007	1.993	0.175	0.308	0.013	2.943	0.269	0.997		
	Mean		6.891	0.005	1.587	0.133	0.326	0.022	3.569	0.332	0.996		
A8	X	2.577	6.986	0.006	1.245	0.146	0.286	0.009	2.719	0.199	0.997	6.812	7.2
Moderately	Y		6.718	0.013	1.467	0.301	0.325	0.023	2.101	0.299	0.992		
deformed	Z		6.475	0.014	1.590	0.346	0.291	0.023	2.735	0.482	0.987		
	Mean		6.726	0.011	1.434	0.264	0.301	0.018	2.518	0.327	0.992		
A9	X	2.581	7.343	0.007	0.891	0.177	0.313	0.015	3.373	0.342	0.994	6.877	13.5
Highly	Y		6.634	0.004	2.281	0.098	0.370	0.009	3.576	0.178	0.999		
deformed	Z		6.348	0.012	1.934	0.298	0.299	0.017	2.388	0.330	0.993		
	Mean		6.775	0.008	1.702	0.191	0.327	0.014	3.112	0.283	0.995		
A10	X	2.581	6.580	0.004	2.327	0.096	0.195	0.023	3.840	0.531	0.997	6.525	5.0
Weakly	Y		6.600	0.003	1.455	0.092	0.242	0.006	2.934	0.166	0.999		
deformed	Z		6.199	0.004	2.721	0.095	0.163	0.018	3.491	0.495	0.998		
	Mean		6.400	0.004	2.088	0.093	0.202	0.012	3.212	0.331	0.998		
A11	X	2.592	6.878	0.003	2.460	0.079	0.122	0.005	2.854	0.282	0.999	6.871	6.3
Moderately	Y		6.822	0.006	2.888	0.147	0.254	0.009	2.664	0.226	0.998		
deformed	Z		6.450	0.009	2.356	0.217	0.206	0.012	2.408	0.345	0.995		
	Mean		6.717	0.006	2.568	0.148	0.194	0.009	2.642	0.284	0.997		
A12	X	2.586	6.929	0.005	2.235	0.130	0.343	0.009	2.790	0.162	0.999	6.978	2.1
Weakly	Y		6.849	0.010	1.764	0.240	0.216	0.011	1.934	0.259	0.995		
deformed	Z		6.839	0.007	1.307	0.204	0.459	0.013	3.290	0.203	0.998		
	Mean		6.872	0.007	1.769	0.191	0.339	0.011	2.671	0.208	0.997		
A13	X	2.583	7.418	0.005	1.773	0.115	0.085	0.007	2.730	0.540	0.995	6.924	16.2
Extremely	Y		6.682	0.004	2.654	0.118	0.120	0.030	4.228	1.215	0.995		
deformed	Z		6.291	0.003	1.911	0.078	0.144	0.006	3.232	0.300	0.998		
	Mean		6.797	0.004	2.113	0.104	0.117	0.014	3.397	0.685	0.996		
A14	X	2.580	6.908	0.007	1.342	0.166	0.335	0.021	2.713	0.267	0.996	6.743	10.2
Highly	Y		6.858	0.004	1.330	0.111	0.224	0.016	3.187	0.341	0.996		
deformed	Z		6.231	0.004	1.191	0.092	0.237	0.007	3.123	0.204	0.998		
	Mean		6.666	0.005	1.287	0.123	0.265	0.015	3.008	0.271	0.997		
A15	X	2.582	7.316	0.003	1.166	0.083	0.107	0.005	2.481	0.272	0.997	6.553	30.5
Extremely	Y		6.649	0.007	3.944	0.173	0.186	0.013	3.112	0.491	0.997		
deformed	Z		5.286	0.004	1.696	0.125	0.576	0.025	5.196	0.320	0.998		
	Mean		6.417	0.005	2.269	0.127	0.289	0.014	3.596	0.361	0.998		
A16	X	2.587	7.060	0.010	1.890	0.232	0.358	0.013	2.508	0.230	0.996	6.788	8.1
Moderately	Y		6.515	0.006	1.782	0.151	0.290	0.011	2.915	0.244	0.997		
deformed	Z		6.478	0.010	2.487	0.247	0.345	0.016	2.564	0.272	0.996		
	X45Y		6.693	0.003	2.395	0.072	0.219	0.005	3.105	0.164	0.999		
	X45Z		6.601	0.012	2.738	0.302	0.359	0.020	2.911	0.378	0.994		
	Y45Z		6.615	0.005	2.274	0.118	0.147	0.006	2.314	0.242	0.998		
	X55Y55Z		6.633	0.006	1.769	0.157	0.268	0.009	2.556	0.209	0.997		
	Mean		6.656	0.007	2.191	0.183	0.284	0.012	2.696	0.249	0.997		

[a]Direction of P-wave propagation

Table 2.4 Parameters of V_S-P curves and V_S anisotropy for 15 antigorite serpentinite samples studied

Sample	Density	λ	Propagation	Polarization	V_0	S.D.	D	S.D.	B_0	S.D.	k	S.D.	R^2	Mean V_s (km/s)	A_s (%)
	g/cm^3				km/s		10^{-4} km/s/MPa		km/s		10^{-2} MPa^{-1}			600 MPa	
A1	2.591	XY	X	Y	4.157	0.007	0.786	0.176	0.048	0.006	1.757	0.531	0.988	3.824	16.2
		XZ	X	Z	3.637	0.004	0.546	0.126	0.068	0.006	2.754	0.579	0.988		
		YX	Y	X	4.137	0.003	1.565	0.097	0.197	0.009	4.651	0.374	0.998		
		YZ	Y	Z	3.558	0.002	0.899	0.046	0.036	0.004	3.249	0.645	0.997		
		ZX	Z	X	3.551	0.001	1.000	0.050	0.054	0.006	5.468	0.952	0.995		
		ZY	Z	Y	3.575	0.001	0.643	0.036	0.066	0.003	4.128	0.355	0.998		
		Mean			3.769	0.003	0.907	0.088	0.078	0.006	3.668	0.573	0.994		
A2	2.669	XZ	X	Z	3.464	0.007	1.439	0.183	0.108	0.009	2.044	0.402	0.995	3.533	2.4
		YZ	Y	Z	3.442	0.003	0.781	0.105	0.486	0.044	5.783	0.438	0.997		
		ZX	Z	X	3.526	0.007	0.803	0.178	0.120	0.009	2.017	0.340	0.994		
		ZY	Z	Y	3.429	0.008	1.527	0.247	0.104	0.007	2.095	0.358	0.996		
		Mean			3.465	0.006	1.138	0.178	0.205	0.017	2.985	0.385	0.995		
A3	2.589	XY	X	Y	4.098	0.005	1.114	0.137	0.062	0.005	1.975	0.386	0.995	3.809	18.4
		XZ	X	Z	3.602	0.003	0.539	0.099	0.148	0.006	3.713	0.355	0.996		
		YX	Y	X	4.203	0.004	0.852	0.101	0.101	0.017	2.349	0.476	0.995		
		YZ	Y	Z	3.450	0.006	1.742	0.169	1.255	0.289	5.085	0.564	0.997		
		ZX	Z	X	3.579	0.003	0.735	0.080	0.088	0.005	3.352	0.399	0.995		
		ZY	Z	Y	3.581	0.003	0.699	0.090	0.057	0.004	2.605	0.472	0.993		
		Mean			3.752	0.004	0.947	0.113	0.285	0.054	3.180	0.442	0.995		
A4	2.583	XY	X	Y	4.058	0.003	0.528	0.090	0.085	0.005	3.201	0.419	0.993	3.886	11.0
		XZ	X	Z	4.015	0.004	0.650	0.101	0.092	0.004	2.487	0.301	0.995		
		ZX	Z	X	3.684	0.014	0.891	0.381	0.238	0.015	2.210	0.350	0.989		
		ZY	Z	Y	3.618	0.004	0.737	0.118	0.075	0.007	3.247	0.679	0.988		
		Mean			3.844	0.006	0.702	0.172	0.123	0.008	2.786	0.437	0.992		
A5	2.591	XY	X	Y	4.341	0.002	0.565	0.060	0.093	0.003	2.466	0.169	0.998	3.815	24.4
		XZ	X	Z	3.392	0.002	0.853	0.052	0.052	0.005	4.417	0.731	0.995		
		YX	Y	X	4.325	0.005	0.550	0.131	0.076	0.006	2.695	0.545	0.988		
		YZ	Y	Z	3.469	0.010	1.216	0.372	0.193	0.024	3.538	0.101	0.973		
		ZX	Z	X	3.536	0.002	0.602	0.057	0.127	0.003	3.273	0.202	0.998		
		ZY	Z	Y	3.534	0.003	1.094	0.099	0.063	0.005	2.660	0.487	0.995		
		Mean			3.766	0.004	0.813	0.128	0.101	0.008	3.175	0.372	0.991		
A6	2.591	XY	X	Y	4.015	0.003	0.702	0.095	0.054	0.004	2.274	0.403	0.994	3.867	10.7
		XZ	X	Z	3.852	0.003	1.239	0.086	0.057	0.004	2.196	0.376	0.998		
		YX	Y	X	4.039	0.003	0.811	0.074	0.076	0.004	3.022	0.367	0.996		
		YZ	Y	Z	3.647	0.002	1.566	0.077	0.152	0.033	8.908	1.664	0.994		
		ZX	Z	X	3.674	0.002	0.656	0.060	0.041	0.002	2.064	0.289	0.997		
		ZY	Z	Y	3.643	0.002	0.528	0.048	0.079	0.003	3.111	0.232	0.998		
		Mean			3.812	0.002	0.917	0.073	0.077	0.008	3.596	0.555	0.996		
A8	2.577	XY	X	Y	3.875	0.003	1.018	0.102	0.158	0.016	6.117	0.901	0.993	3.848	3.8
		XZ	X	Z	3.712	0.007	1.457	0.169	0.090	0.018	2.032	0.622	0.995		
		YX	Y	X	3.893	0.004	0.608	0.105	0.068	0.005	2.138	0.382	0.993		
		YZ	Y	Z	3.739	0.008	0.832	0.229	0.174	0.019	2.748	0.529	0.987		
		ZX	Z	X	3.809	0.002	0.428	0.067	0.081	0.003	2.329	0.205	0.997		
		ZY	Z	Y	3.697	0.002	1.733	0.076	0.366	0.028	9.376	0.671	0.998		
		Mean			3.787	0.004	1.013	0.125	0.156	0.015	4.123	0.552	0.994		
A9	2.581	XY	X	Y	4.022	0.003	0.435	0.089	0.078	0.004	2.494	0.315	0.995	3.801	12.0
		XZ	X	Z	3.700	0.013	0.946	0.367	0.159	0.014	2.347	0.544	0.983		
		YX	Y	X	3.964	0.004	0.816	0.123	0.109	0.006	2.790	0.372	0.995		
		YZ	Y	Z	3.544	0.002	0.805	0.069	0.057	0.005	2.700	0.458	0.996		
		ZX	Z	X	3.709	0.002	0.616	0.073	0.061	0.004	3.201	0.504	0.994		
		ZY	Z	Y	3.609	0.004	0.628	0.135	0.203	0.029	7.055	1.194	0.985		
		Mean			3.758	0.005	0.708	0.143	0.111	0.010	3.431	0.565	0.991		
A10	2.581	XY	X	Y	3.725	0.001	0.901	0.040	0.094	0.006	3.628	0.302	0.999	3.665	6.7
		XZ	X	Z	3.681	0.002	0.877	0.058	0.063	0.005	4.045	0.586	0.996		
		YX	Y	X	3.665	0.006	1.690	0.158	0.039	0.006	2.099	0.853	0.993		
		YZ	Y	Z	3.483	0.005	0.838	0.148	0.160	0.012	2.786	0.384	0.994		
		ZX	Z	X	3.557	0.006	1.064	0.180	0.134	0.007	2.302	0.307	0.994		
		ZY	Z	Y	3.513	0.002	0.725	0.056	0.037	0.005	2.932	0.686	0.995		
		Mean			3.604	0.004	1.016	0.107	0.088	0.007	2.965	0.519	0.995		
A11	2.592	XY	X	Y	3.957	0.003	0.688	0.096	0.080	0.004	2.567	0.333	0.995	3.861	6.8
		XZ	X	Z	3.679	0.006	0.946	0.184	0.126	0.020	4.305	1.170	0.980		
		YX	Y	X	3.780	0.004	0.768	0.109	0.049	0.004	1.828	0.346	0.995		
		YZ	Y	Z	3.779	0.001	0.496	0.043	0.155	0.009	6.946	0.473	0.997		
		ZX	Z	X	3.955	0.003	0.377	0.077	0.121	0.003	2.481	0.177	0.998		
		ZY	Z	Y	3.788	0.002	0.498	0.055	0.072	0.002	2.513	0.211	0.998		
		Mean			3.823	0.003	0.629	0.094	0.100	0.007	3.440	0.452	0.994		

Table 2.4 Continued

Sample	Density	λ	Propagation	Polarization	V_0	S.D.	D	S.D.	B_0	S.D.	k	S.D.	R^2	Mean V_s (km/s)	A_s (%)
	g/cm^3				km/s		10^{-4} km/s/MPa		km/s		10^{-2} MPa^{-1}			600 MPa	
A12	2.586	XY	X	Y	3.914	0.004	0.596	0.132	0.090	0.008	3.265	0.624	0.987	3.877	5.7
		XZ	X	Z	3.786	0.008	1.523	0.212	0.095	0.007	1.887	0.361	0.995		
		YX	Y	X	3.847	0.002	0.582	0.064	0.082	0.003	2.946	0.286	0.997		
		YZ	Y	Z	3.832	0.004	0.822	0.114	0.145	0.006	2.959	0.296	0.996		
		ZX	Z	X	3.896	0.002	0.767	0.067	0.097	0.006	4.117	0.450	0.996		
		ZY	Z	Y	3.666	0.006	1.065	0.169	0.081	0.008	2.712	0.650	0.988		
		Mean			3.823	0.004	0.892	0.126	0.099	0.006	2.981	0.445	0.993		
A13	2.583	XY	X	Y	4.066	0.002	0.812	0.070	0.058	0.004	3.201	0.523	0.995	3.961	19.1
		XZ	X	Z	4.053	0.022	0.894	0.667	0.191	0.044	3.517	1.689	0.917		
		YX	Y	X	4.025	0.001	0.581	0.037	0.066	0.003	3.838	0.324	0.998		
		YZ	Y	Z	3.508	0.002	0.660	0.066	0.150	0.011	5.933	0.566	0.996		
		ZX	Z	X	4.264	0.002	0.680	0.065	0.122	0.005	3.642	0.304	0.998		
		ZY	Z	Y	3.574	0.002	0.984	0.050	0.120	0.004	3.682	0.226	0.999		
		Mean			3.915	0.005	0.768	0.159	0.118	0.012	3.969	0.605	0.984		
A14	2.580	XY	X	Y	3.927	0.002	0.715	0.064	0.153	0.010	3.514	0.283	0.997	3.838	20.7
		XZ	X	Z	3.926	0.002	0.731	0.050	0.037	0.002	2.100	0.270	0.998		
		YX	Y	X	3.952	0.012	2.266	0.336	0.040	0.013	2.292	1.916	0.980		
		YZ	Y	Z	3.959	0.003	0.567	0.098	0.175	0.006	3.218	0.239	0.997		
		ZX	Z	X	3.678	0.004	0.590	0.098	0.088	0.006	2.450	0.351	0.994		
		ZY	Z	Y	3.255	0.002	0.644	0.045	0.072	0.003	3.177	0.271	0.998		
		Mean			3.783	0.004	0.919	0.115	0.094	0.007	2.792	0.555	0.994		
A15	2.582	XY	X	Y	4.063	0.002	0.533	0.059	0.062	0.003	2.849	0.316	0.996	3.752	14.8
		XZ	X	Z	3.502	0.002	0.655	0.051	0.109	0.005	4.694	0.394	0.997		
		YX	Y	X	4.000	0.005	0.519	0.129	0.073	0.005	2.028	0.336	0.992		
		YZ	Y	Z	3.452	0.004	1.728	0.112	0.117	0.009	3.923	0.591	0.996		
		ZX	Z	X	3.623	0.006	1.349	0.152	0.118	0.006	2.074	0.251	0.997		
		ZY	Z	Y	3.549	0.002	0.660	0.050	0.145	0.003	3.362	0.164	0.999		
		Mean			3.698	0.003	0.907	0.092	0.104	0.005	3.155	0.342	0.996		
A16	2.587	XY	X	Y	3.815	0.006	0.623	0.152	0.163	0.007	2.469	0.260	0.996	3.737	6.4
		XZ	X	Z	3.616	0.005	1.051	0.140	0.135	0.006	2.715	0.313	0.996		
		YX	Y	X	3.714	0.002	0.563	0.072	0.121	0.010	3.423	0.395	0.995		
		YZ	Y	Z	3.569	0.008	1.091	0.255	0.188	0.029	5.242	1.330	0.975		
		ZX	Z	X	3.546	0.003	1.121	0.090	0.256	0.011	4.798	0.335	0.998		
		ZY	Z	Y	3.734	0.004	0.971	0.109	0.109	0.004	2.402	0.248	0.997		
		X45Y+	X45Y	Z	3.725	0.001	1.352	0.033	0.141	0.003	4.077	0.147	1.000		
		X45Y-	X45Y	Normal to Z	3.735	0.006	0.626	0.179	0.141	0.007	2.242	0.275	0.994		
		X45Z+	X45Z	Y	3.738	0.005	0.494	0.126	0.078	0.005	1.998	0.304	0.994		
		X45Z-	X45Z	Normal to Y	3.696	0.007	0.818	0.204	0.132	0.008	2.184	0.325	0.993		
		Y45Z+	Y45Z	X	3.673	0.001	0.770	0.040	0.083	0.002	3.024	0.178	0.999		
		Y45Z-	Y45Z	Normal to X	3.553	0.003	1.127	0.105	0.106	0.006	3.132	0.393	0.996		
		X55Y55Z+	X55Y55Z	Parallel to foliation trace on the core end	3.750	0.001	1.068	0.037	0.095	0.005	5.584	0.458	0.998		
		X55Y55Z-	X55Y55Z	Normal to foliation trace on the core end	3.689	0.004	0.995	0.114	0.139	0.005	2.743	0.250	0.997		
		Mean			3.682	0.004	0.905	0.118	0.135	0.008	3.288	0.372	0.995		

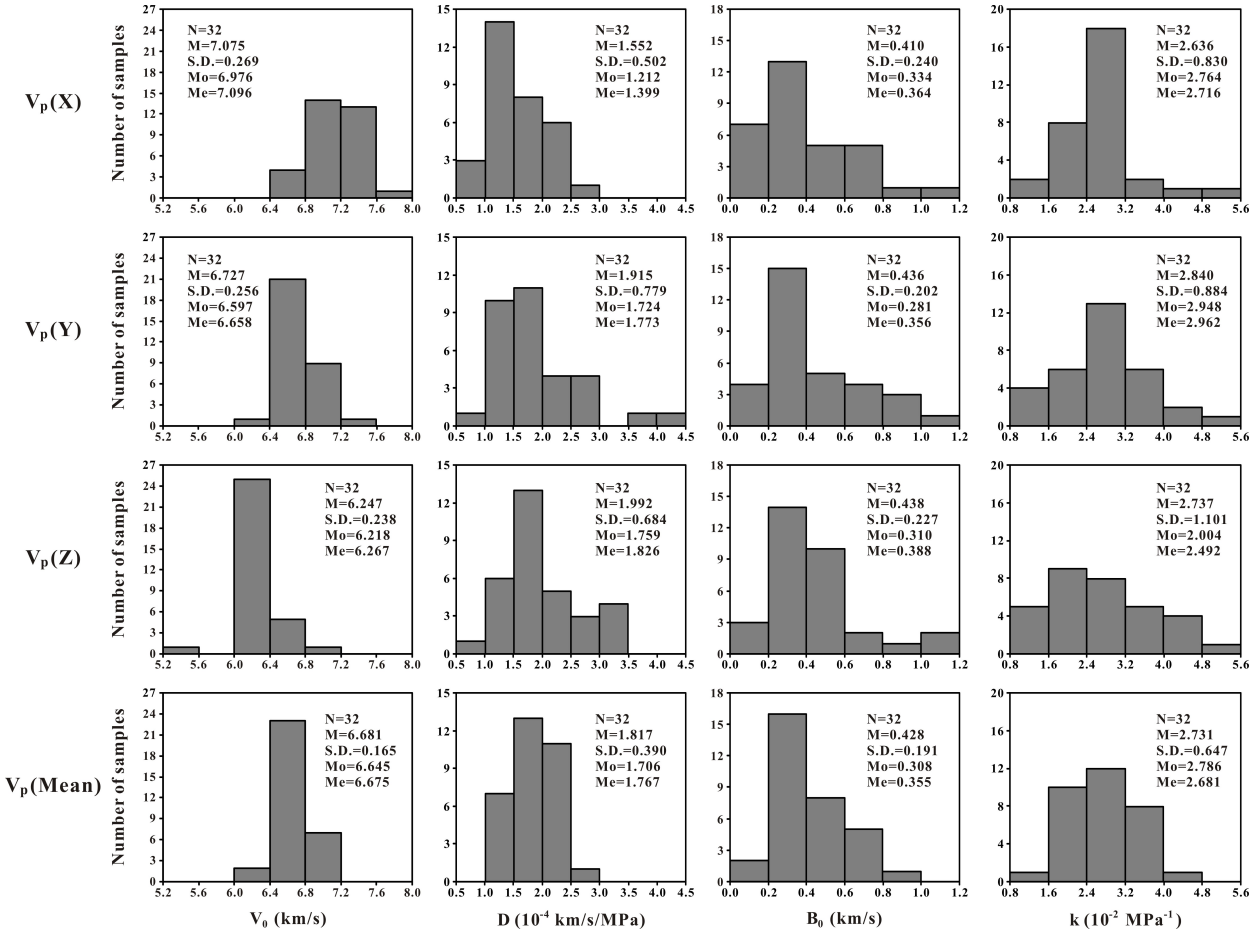


Figure 2.6 Statistics of V_p-P curve parameters, defined by Eq. (2.1), for three structural directions (X, Y, and Z) and the equivalent isotropic aggregate (mean) of 32 antigorite serpentinite samples (15 from this study and 17 from Ji et al., 2013a). N: total number of samples; M: arithmetic mean; S.D.: standard deviation; M_o: mode (the most frequently occurring value in the distribution); Me: median (the fiftieth percentile in the distribution).

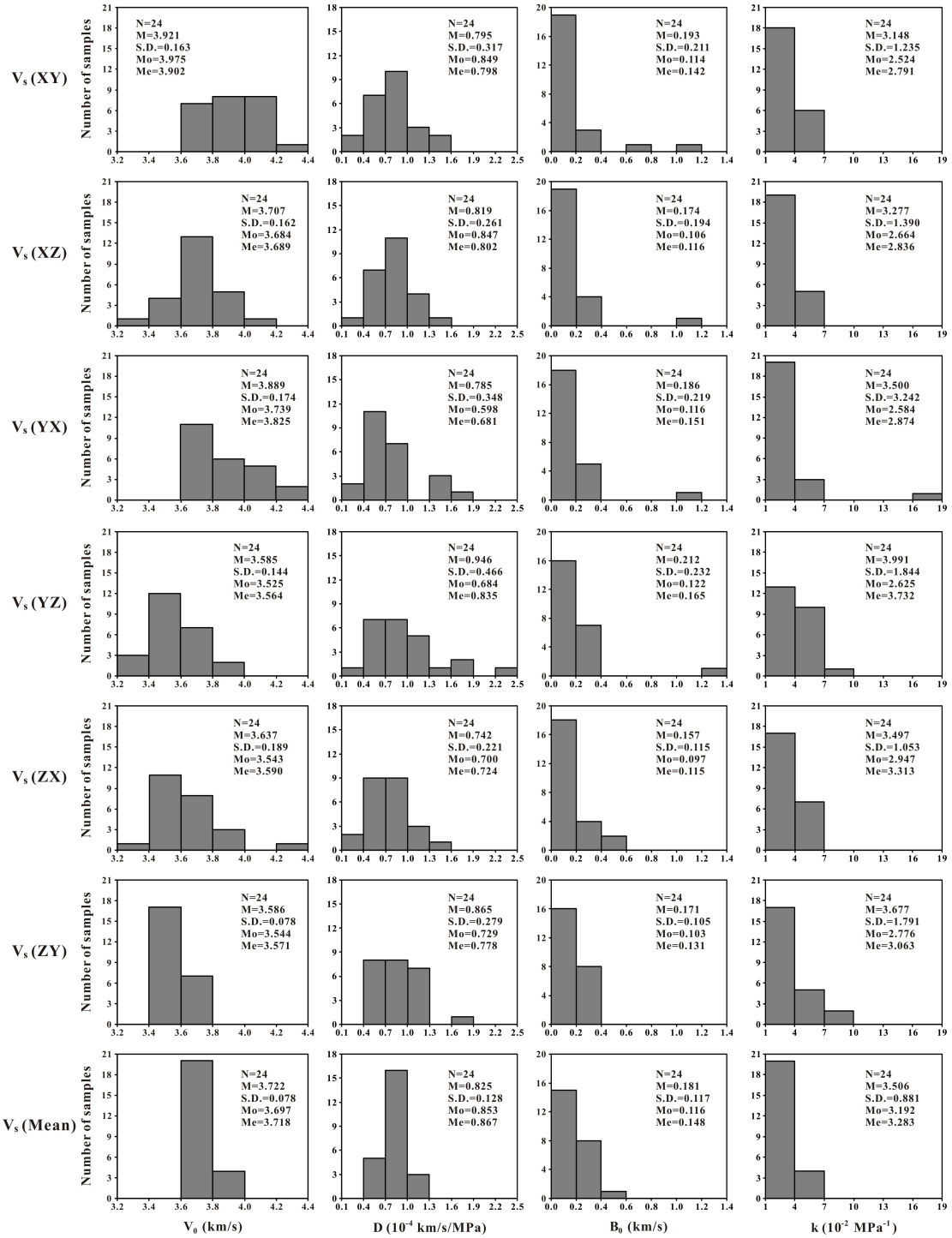


Figure 2.7 Statistics of V_S-P curve parameters, defined by Eq. (2.1), for six sets of propagation-polarization directions (XY, XZ, YX, YZ, ZX, and ZY) and the equivalent isotropic aggregate (mean) of 24 antigorite serpentinite samples on which V_S has been measured as a function of pressure in all six sets of propagation-polarization directions) (13 from this study, and 11 from Ji et al., 2013a). N, M, S.D., Mo, and Me as in Figure 2.6 caption.

2.3.2 P-wave velocity anisotropy

Bulk V_p anisotropy [A_p(B) or A_p] is defined in Eq. (1.31). The intrinsic anisotropy of the 32 serpentinite samples [15 from this study and 17 from Ji et al. (2013a)], calculated from the V_0 values measured in three orthogonal directions, ranges from 0.9% (sample A2, which is quasi-isotropic) to 30.5% (sample A15) with an average value of 12.4%. The A_p values calculated from the V_0 data are slightly higher than those measured at 600 MPa, which display an average value of 11.2%.

Figure 2.8, on which the $V_p(Y)/V_p(Z)$ and $V_p(X)/V_p(Y)$ values are, respectively, plotted on the abscissa and the ordinate of a Flinn-type diagram, is constructed to illustrate the categories of V_p anisotropy for the serpentinites studied. The origin of the coordinate axes for the diagram is (1, 1), representing antigorite serpentinites which are seismically isotropic. Any given V_p anisotropy plots at a particular point on the diagram, and the slope k_p of the line from the origin (1, 1) to that point is:

$$k_p = \frac{\left[V_p(X)/V_p(Y)\right]-1}{\left[V_p(Y)/V_p(Z)\right]-1} \tag{2.2}$$

The k_p value is a coefficient which can be used for classifying the types of intrinsic V_p anisotropy in the rocks. The three lines with k_p=0, k_p=1, and k_p=∞ correspond to three end-member types of anisotropy, A, B, and C, respectively. Type A (e.g., Figure 2.4a) is characterized by transverse isotropy (TI) with $V_p(X)=V_p(Y)\gg V_p(Z)$. Type B (e.g., Figure 2.4c) is characterized by an orthorhombic symmetry with $V_p(X)>V_p(Y)>V_p(Z)$ and $V_p(Y)=[V_p(X)V_p(Z)]^{0.5}$. Type C (Figure 2.4d) also shows TI but with $V_p(X)\gg V_p(Y)=V_p(Z)$. A_p (%), which is shown by a series of dotted lines in Figure 2.8, were calculated using the $V_p(X)/V_p(Y)$ and $V_p(Y)/V_p(Z)$ ratios. For single crystal antigorite, V_p(a-axis)=8.91 km/s, V_p(c-axis)=5.58 km/s, and Hill averaging yields a mean V_p value of 6.76 km/s (Bezacier et al., 2010). Thus, A_p=49% yields the upper limit for both S-type (only flattening foliation and no stretching lineation developed) and L-type (only stretching lineation and no flattening foliation developed) antigorite serpentinites because a single crystal of an anisotropic mineral always has much higher seismic anisotropy than its polycrystalline aggregate. S- and L-type tectonites are formed by coaxial flattening and constriction, respectively.

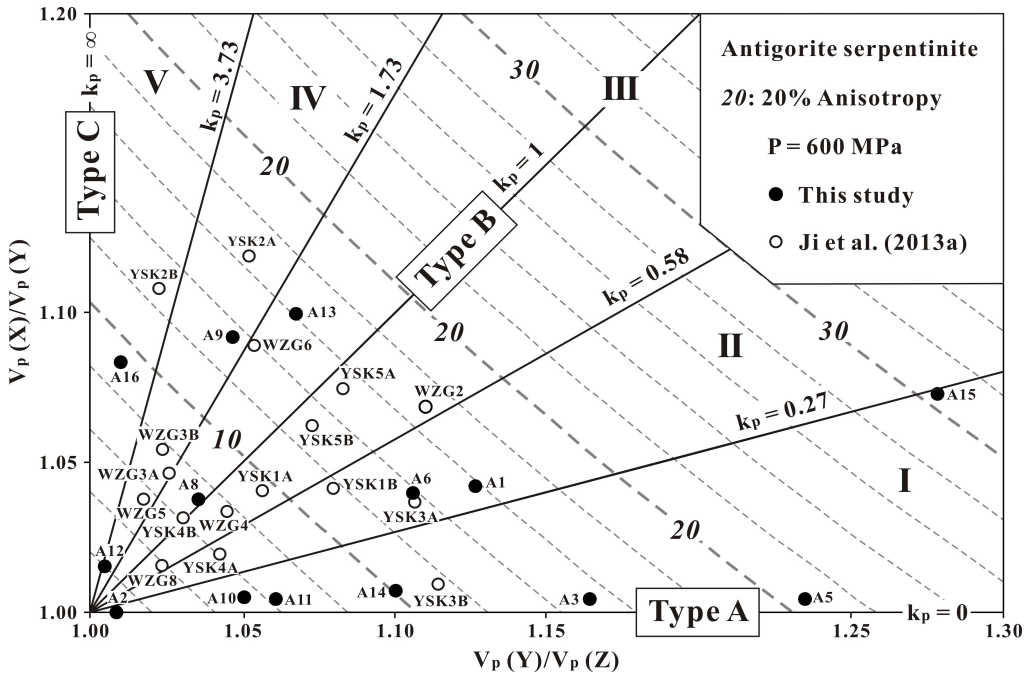


Figure 2.8 Flinn-type diagram showing V_p anisotropy at 600 MPa. Solid dots indicate the data (15 samples) from this study and open dots (17 samples) from Ji et al. (2013a). The origin of the coordinate axes represents random CPO and thus zero anisotropy. Dashed lines indicate iso-anisotropy surfaces.

The 32 antigorite serpentinite samples examined in this study and Ji et al. (2013a) can be classified into five categories according to their k_p values (Figure 2.8): (I) k_p=0-0.27; the serpentinites are quasi-transversely isotropic with $V_p(X)\approx V_p(Y)\gg V_p(Z)$ (e.g., samples A3, A5, A10, A11, A14, and YSK3B, Figure 2.4a). (II) k_p=0.27-0.58; the serpentinites are characterized by $V_p(X)>V_p(Y)\gg V_p(Z)$ (e.g., samples A1, A6, YSK1B, YSK3A, and YSK4A, Figure 2.4b). (III) k_p=0.58-1.73; the serpentinites in this group display quasi-orthorhombic anisotropy with $V_p(X)>V_p(Y)>V_p(Z)$ (Figure 2.4c). Ten samples belong to this category (samples A8, A13, WZG2, WZG4, WZG6, WZG8, YSK1A, YSK4B, YSK5A, and YSK5B). (IV) k_p=1.73-3.73; the V_p anisotropy of this group (samples A9, WZG3A, WZG3B, YSK2A, and WZG5) is characterized by $V_p(X)\gg V_p(Y)>V_p(Z)$. (V) k_p>3.73; the serpentinites in this group (samples A16 and YSK2B, Figure 2.4d) are quasi-transversely isotropic with $V_p(X)\gg V_p(Y)\approx V_p(Z)$. Samples A2 and A12 with $A_p\leq 2\%$ are quasi-isotropic.

2.3.3 S-wave anisotropy and birefringence

As shown in Figure 2.5, most of the antigorite serpentinites studied demonstrate pronounced variations of S-wave velocity with either propagation or vibration direction. In sample A5 (Figure 2.5a), for instance, the V_s at 600 MPa varies from 3.443 km/s (XZ) to 4.375 km/s (XY) with an average velocity of 3.815 km/s. This mean value was calculated from the six sets of propagation-polarization directions. For this sample, $V_s(XY) \approx V_s(YX)$, where $V_s(XY)$=4.375 km/s and $V_s(YX)$=4.358 km/s. Shear-wave splitting is the birefringence (ΔV_s) or difference in velocity between the fast and slow split, or polarized, S-waves propagating in the same propagation direction. For sample A5 at 600 MPa (Figure 2.5a), $\Delta V_s(X)$=0.932 km/s and $\Delta V_s(Y)$=0.816 km/s for propagation in the foliation plane while little birefringence occurs in the direction normal to the foliation [$\Delta V_s(Z)$=0.028 km/s]. Similar situations are observed in samples A1 (Figure 2.5b) and WZG2 (Figure 2.5c) as well as many other samples (e.g., A3, A6, and A10). For sample A16 at 600 MPa (Figure 2.5d), however, the shear-wave splitting is more complex with large birefringence in the propagation directions X (0.173 km/s) and Z (0.179 km/s) and moderate birefringence in the Y direction (0.114 km/s).

Plots of $\Delta V_s(Y)$ [i.e., $V_s(YX)$-$V_s(YZ)$] as a function of $\Delta V_s(X)$ [i.e., $V_s(XY)$-$V_s(XZ)$] are shown in Figure 2.9. Similarly, we can define the k_s coefficient for each serpentinite as

$$k_s = \Delta V_s(Y)/\Delta V_s(X) \qquad (2.3)$$

Most of the serpentinites, regardless of their V_p anisotropy patterns (Figure 2.8), lie directly on or near the line k_s=1. Only two among 36 samples fall below the line k_s=0.58. Thus, most of the serpentinites are systematically characterized by significant shear-wave splitting for propagation along the X and Y directions with the fast shear-wave polarized parallel to the foliation, but with little splitting in the propagation direction normal to the foliation. From the shear-wave splitting data, it is thus impossible to distinguish the serpentinites whose V_p anisotropy falls into the different domains I-V (Figure 2.8). The serpentinites with k_s>1 are characterized by shear-wave splitting that is stronger along the Y direction than the X direction (Figure 2.9).

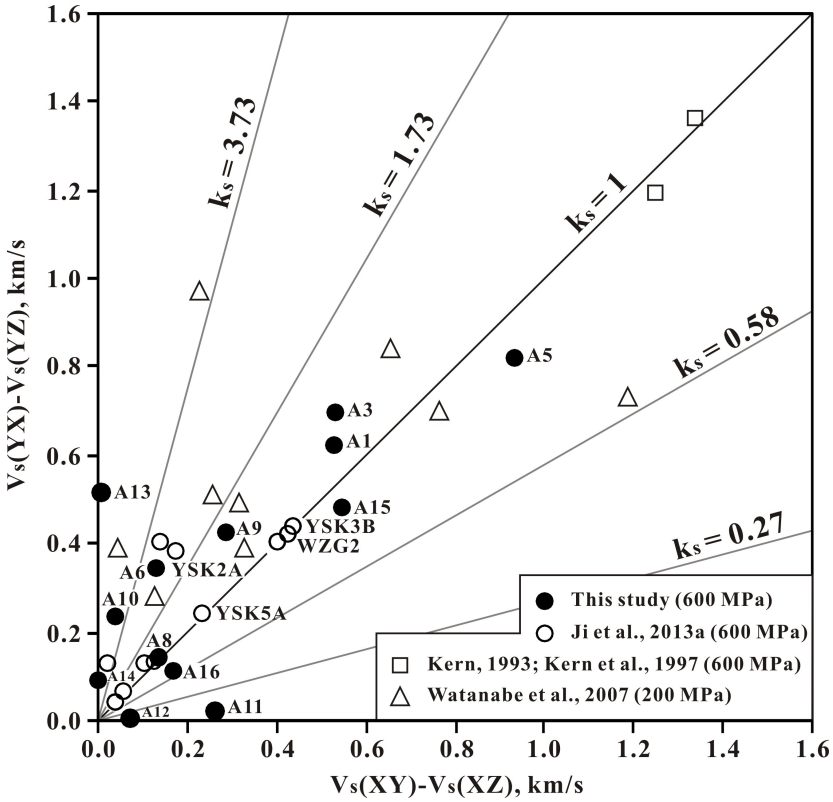


Figure 2.9 Shear-wave birefringence along the Y direction [V_s(YX)-V_s(YZ)] versus shear-wave birefringence along the X direction [V_s(XY)-V_s(XZ)].

2.4 CPO and calculated seismic velocities

As shown in Figure 2.10, the poles to the (001) planes or the [001] directions of antigorite display a strong, single concentration parallel or subparallel to Z in samples A5, A9, YSK5A, A1, and A13 while a partial girdle (samples A15 and YSK3B) or complete girdle (samples WZG2 and YSK2A) is sometimes developed perpendicular to X with a maximum close to Z. In sample A3, the [001] directions of antigorite developed two concentrations parallel or subparallel to Z and Y. In sample A16, which is moderately deformed, CPO is relatively weak and diffuse. The [010] directions form a partial (samples A1, A3 A5, A9, A13, A15, YSK3B, and WZG2) or complete (samples YSK2A and YSK5A) girdles parallel or subparallel to the flattening foliation (XY plane), in which the maximum concentration occurs generally at X. The distribution of [100] directions is more complicated: a wide girdle or partial girdle parallel to the foliation with the maximum concentration close to Y (e.g., samples A1, A3, A9, A15, YSK3B, and YSK5A). Generally speaking, the mean CPO strengths of antigorite [001], [010] and [100] are the strongest, moderate and weakest, respectively, in each sample.

P-wave velocities, direction-dependent V_s anisotropy (AV_s) and polarization directions of fast shear waves for the 11 antigorite serpentinite samples (Figures 2.11) were calculated on the basis of the CPO data (Figure 2.10) and elastic stiffness coefficients of single crystal antigorite (Bezacier et al., 2010) using software developed by Mainprice (1990). For a given propagation direction, AV_s is defined by Eq. (1.35). The Hill average was used for seismic velocity calculations. The calculated velocities and anisotropy (Figures 2.11-2.13) pertain to conditions of one atmosphere pressure, room temperature, and zero porosity, and must be compared with the intrinsic velocities (V_0) defined in Eq. (2.1).

Figures 2.12 and 2.13 show, respectively, the variations of calculated V_p and V_s as a function of the incidence angle of seismic rays in the XY, XZ, and YZ planes. In sample A5, for example, the calculated results are consistent with the measured values, and both indicate a quasi-hexagonal symmetry: $V_p(X) \approx V_p(Y) \gg V_p(Z)$, k_p=0.029 (category I in Figure 2.8). Both V_p (Figure 2.12a) and V_s (Figure 2.13a) of sample A5 display little variation with the incidence angle when propagating parallel to the foliation (XY) plane. When propagating in the XZ or YZ plane, however, V_p and V_s of this sample show pronounced variations with the maximum velocities and shear-wave splitting ($\Delta V_s = V_{s1} - V_{s2}$) near the X or Y direction, while the lowest velocities and shear-wave splitting are observed for directions within small angles (0-30º) with respect to Z.

In sample WZG2, large variations in V_p as a function of incidence angle occur in the XZ plane whereas moderate variations in V_p are observed in the XY or YZ plane (Figure 2.12c). The maximum V_p values are close to the X and Y directions when the P-waves propagate in the XZ and YZ planes, respectively. However, the V_p distribution in the foliation is asymmetrical with respect to the stretching lineation (X). The obliquity in seismic anisotropy is caused by shear-induced fabric asymmetry with respect to the structural framework (X-Y-Z). The results calculated from antigorite CPO data are in good agreement with the intrinsic velocities (V_0), and both indicate an orthorhombic symmetry for sample WZG2: $V_p(X) > V_p(Y) > V_p(Z)$ and k_p=0.742 (category III in Figure 2.8).

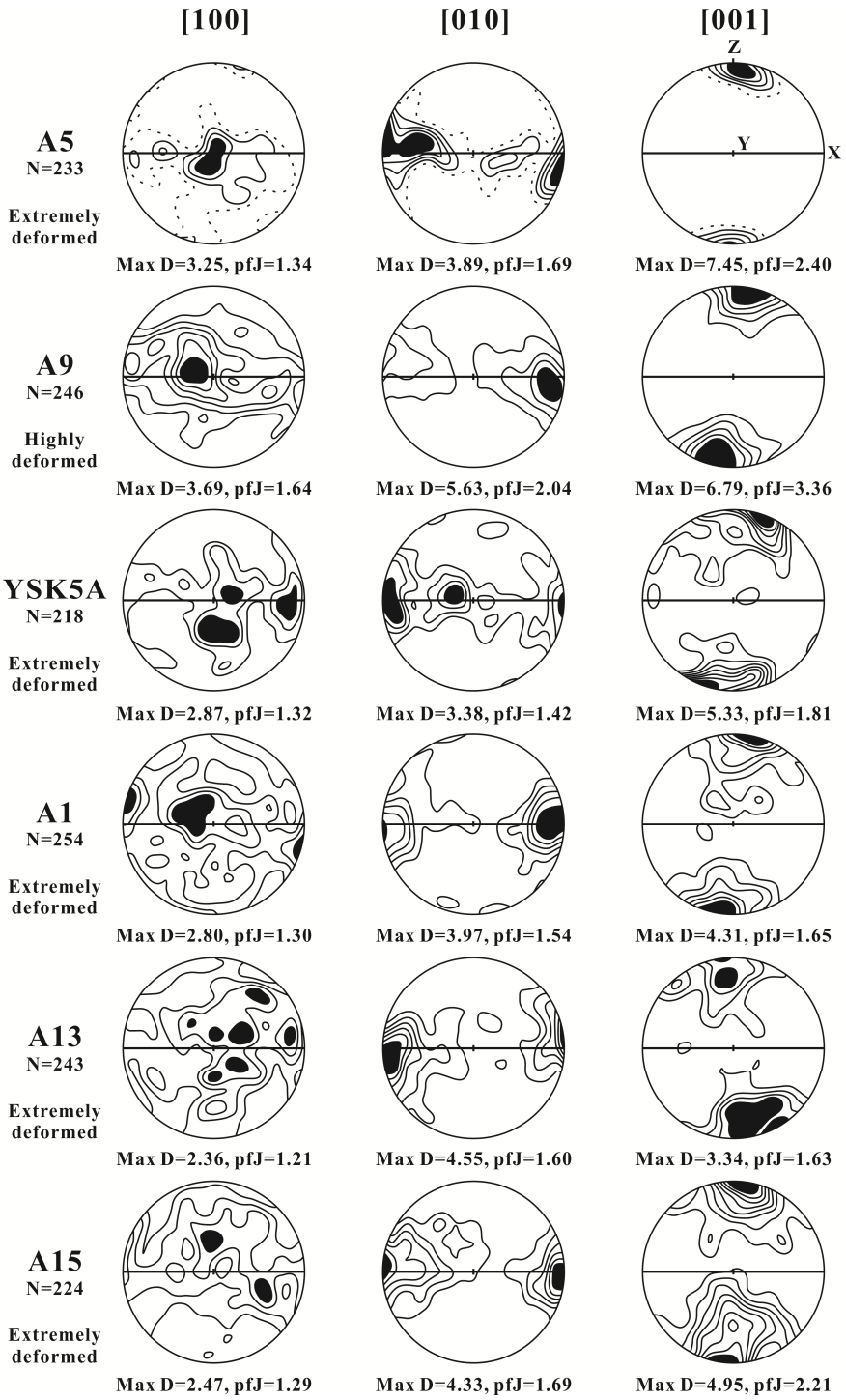


Figure 2.10 EBSD-measured pole figures for antigorite from 11 serpentinite samples (A5, A9, YSK5A, A1, A13, A15, YSK3B, WZG2, YSK2A, A3, and A16). Equal-area lower hemisphere projections. The maximum density and *J* index (*pfJ*), which are calculated from the orientation distribution function, are indicated for each sample. N: number of measured grains. Samples are arranged according to antigorite c-axis fabric pattern.

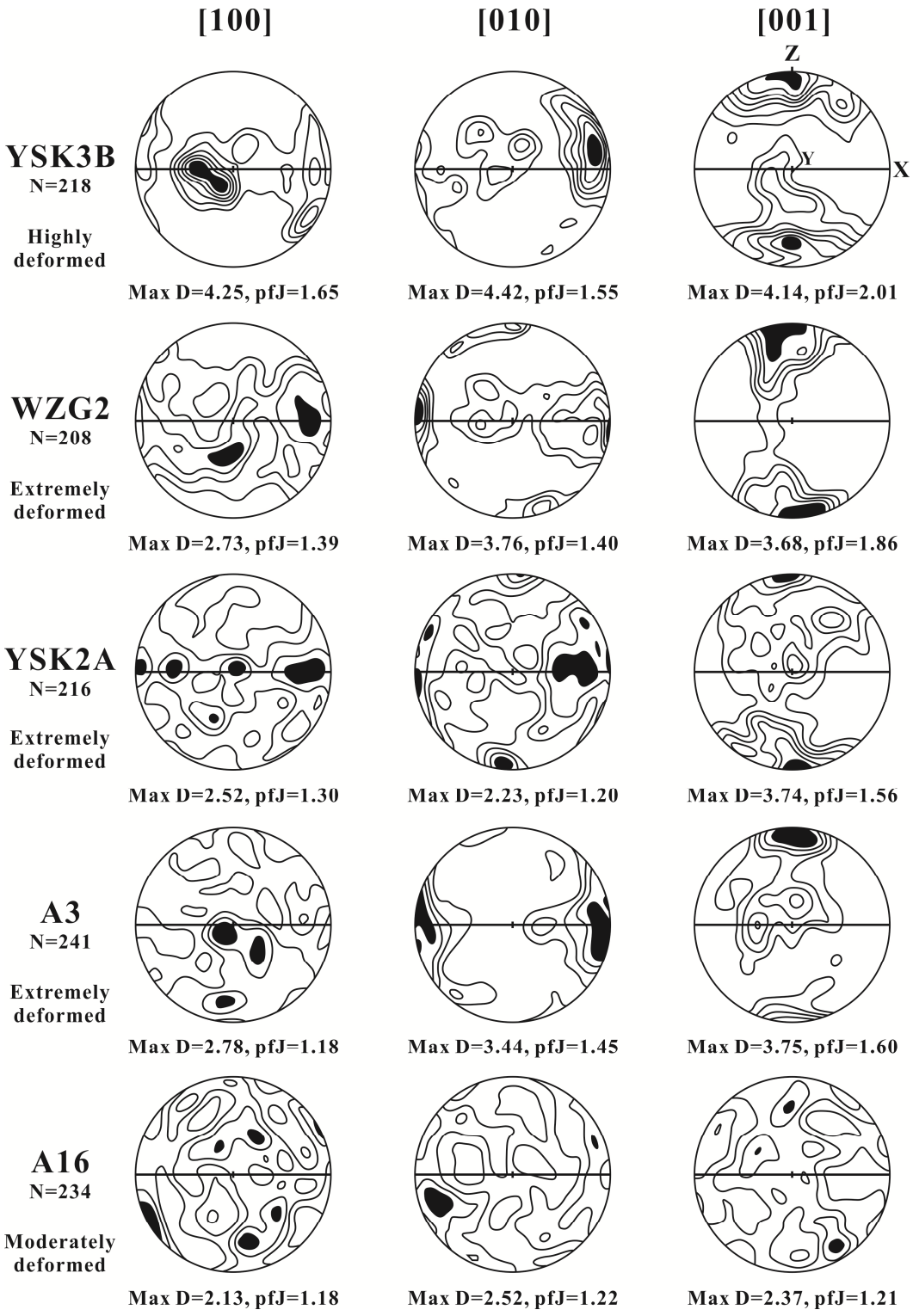


Figure 2.10 Continued

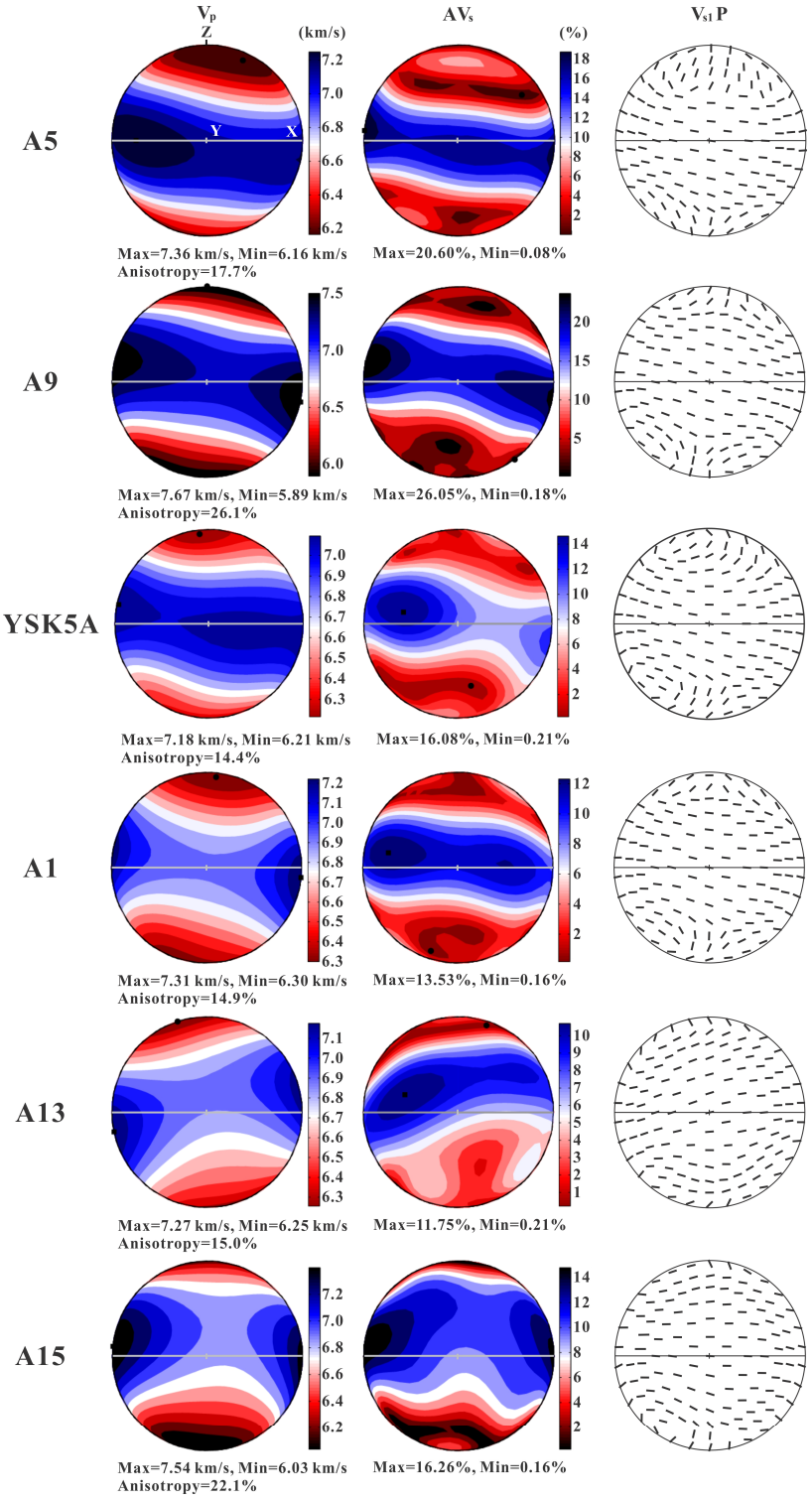


Figure 2.11 P-wave velocities, S-wave velocity anisotropy and fast polarization directions for 11 antigorite serpentinite samples (A5, A9, YSK5A, A1, A13, A15, YSK3B, WZG2, YSK2A, A3, and A16) calculated from CPO data and single crystal elastic constants of antigorite. Equal-area lower hemisphere projections. Samples are arranged in the same order as in Figure 2.10.

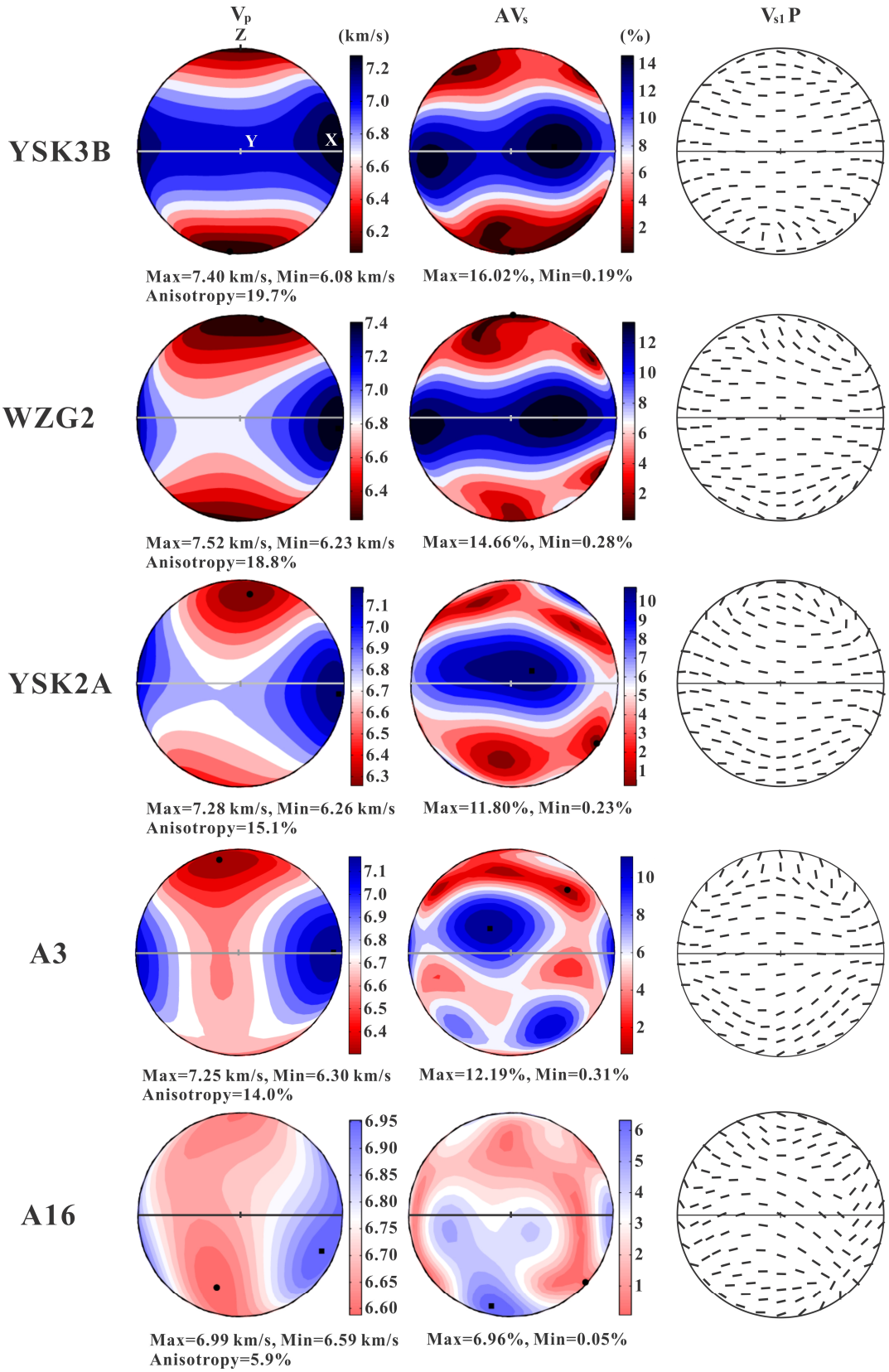


Figure 2.11 Continued

Sample YSK3B (Figure 2.12b) with k_p=0.221 is characterized by $V_p(X)>V_p(Y)\gg V_p(Z)$ and thus lies in a transitional regime between the hexagonal symmetry (e.g., sample A5) and orthorhombic symmetry (e.g., sample WZG2). Although the V_p symmetry patterns are clearly different among samples A5, YSK3B, and WZG2, their shear-wave splitting patterns are similar: ΔV_s is large and displays little variation for propagation parallel or subparallel to the foliation but very small for propagation normal or subperpendicular to the foliation.

Sample A16, which is a moderately deformed antigorite serpentinite, developed an anisotropic geometry: $V_p(X)\gg V_p(Y)>V_p(Z)$ with k_p=2.456 (Figure 2.12d). Both V_p and V_s anisotropy (A_p=5.9% and AV_s=6.6%) is small with the maximum V_p and ΔV_s at about 15° to the X or Y direction in the XZ, XY, or YZ plane (Figures 2.12d and 2.13d).

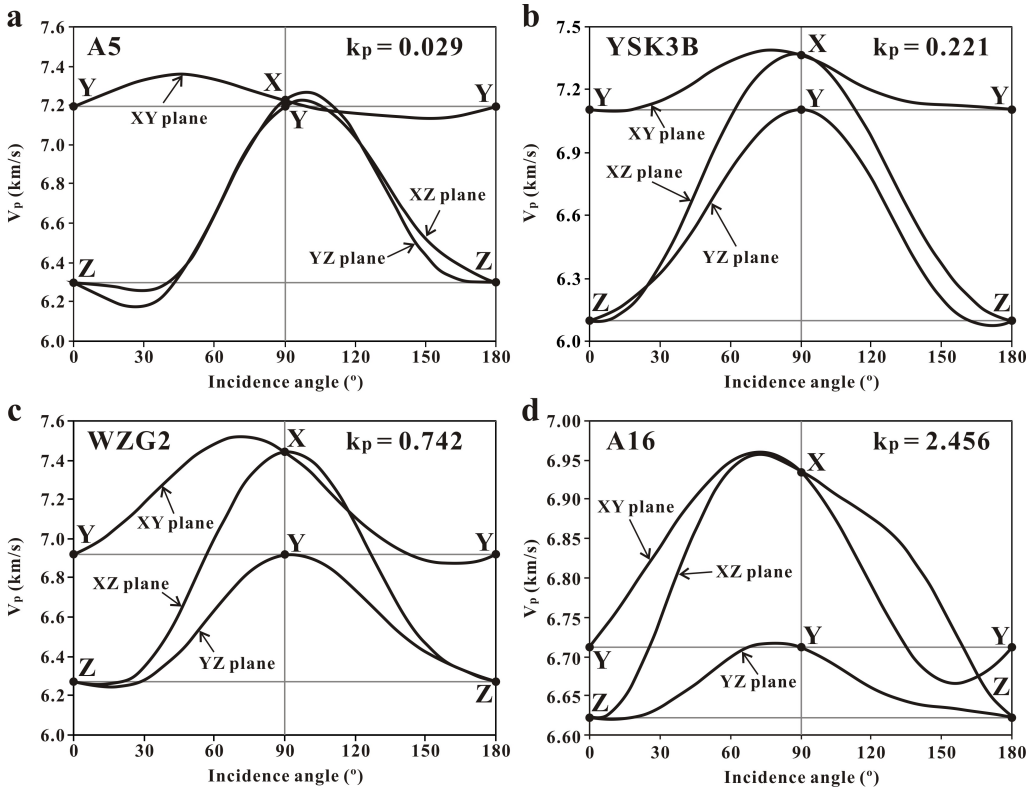


Figure 2.12 Variations of calculated P-wave velocity as a function of incidence angle in the XY, XZ, and YZ planes. (a) Sample A5 (extremely deformed), k_p=0.029 and $V_p(X)\approx V_p(Y)\gg V_p(Z)$; (b) Sample YSK3B (highly deformed), k_p=0.221 and $V_p(X)>V_p(Y)\gg V_p(Z)$; (c) Sample WZG2 (extremely deformed), k_p=0.742 and $V_p(X)>V_p(Y)>V_p(Z)$; (d) Sample A16 (moderately deformed), k_p=2.456 and $V_p(X)\gg V_p(Y)>V_p(Z)$.

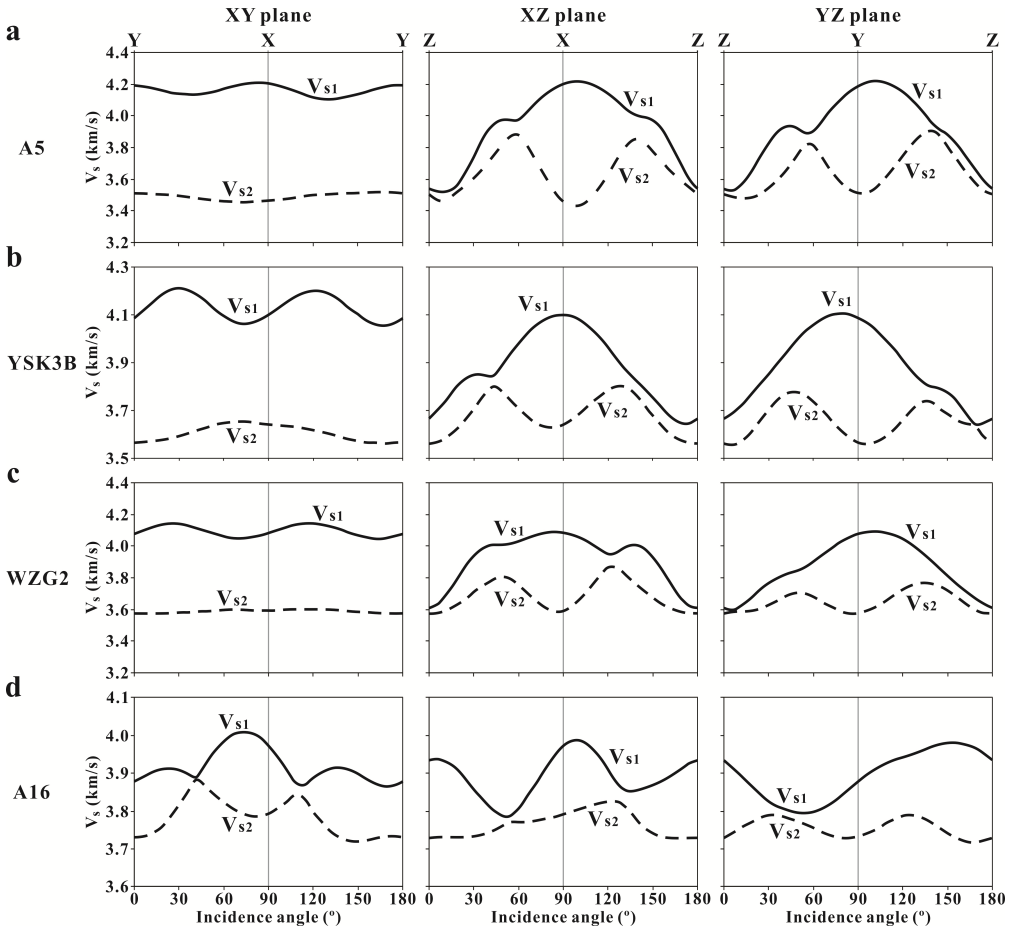


Figure 2.13 Calculated split fast and slow S-wave velocities (V_{s1} and V_{s2}) as a function of incidence angle in the XY, XZ, and YZ planes of 4 representative antigorite serpentinite samples (A5, YSK3B, WZG2, and A16). For sample YSK3B (highly deformed) and samples A5 and WZG2 (extremely deformed), the largest birefringence occurs for the propagation in the foliation plane while little birefringence occurs in the direction normal to the foliation. For sample A16 (moderately deformed), however, the birefringence is relatively small (<0.18 km/s) but occurs almost equally in the X, Y, and Z directions.

Figure 2.14 shows the plots of seismic anisotropy A_p (%) and the maximum AV_s (%) as a function of the J indexes (degree of alignment of crystal axes) for antigorite a-, b- and c-axis fabrics. For the a-axis fabric, $A_p(\%)=24.79\ln J+8.87$ ($R^2=0.75$) and $AV_s^{max}(\%)=35.88\ln J+5.05$ ($R^2=0.87$). For the b-axis fabric, $A_p(\%)=23.62\ln J+5.79$ ($R^2=0.80$) and $AV_s^{max}(\%)=34.03\ln J+0.66$ ($R^2=0.92$). For the c-axis fabric, $A_p(\%)=13.62\ln J+7.27$ ($R^2=0.92$) and $AV_s^{max}(\%)=19.08\ln J+3.17$ ($R^2=0.99$). As indicated by the goodness-of-fit coefficients (R^2), the correlations with the strength of the c-axis fabric are significantly stronger than those of either the a- or b-axis fabrics. Thus, the most

important factor controlling the seismic anisotropy of HT serpentinites is the fabric strength of the antigorite c-axes. This can be easily understood by taking into consideration the seismic properties of single crystal antigorite having quasi-hexagonal symmetry with fast P-wave velocities (8.9 km/s) along the a-b plane and slow P-wave velocities (5.6 km/s) parallel to the c-axis (Bezacier et al., 2010). The difference between the velocities along the a- and b-axes is only ~3%.

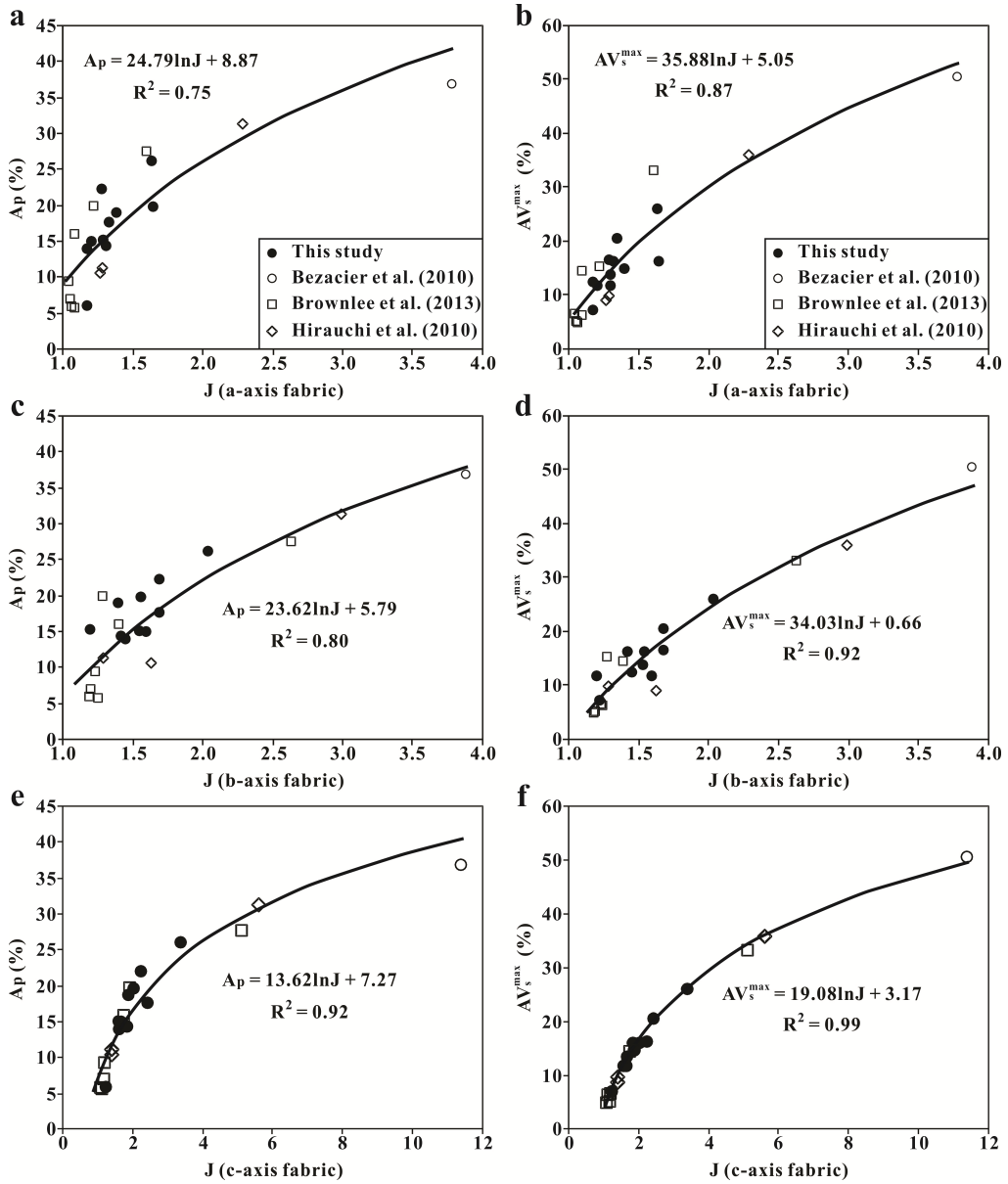


Figure 2.14 Plots of P- and maximum S-wave velocity anisotropy (A_p and AV_s^{max}) as a function of the *J* index (*pfJ*) for antigorite a-, b-, and c-axis fabrics of serpentinites containing >91 vol.% antigorite.

For most of the serpentinite samples studied, the P- and S-wave velocities and anisotropy calculated from the antigorite CPO and its single crystal elastic stiffness coefficients (Bezacier et al., 2010) and based on the Hill average (Figures 2.11-2.13) are very comparable to the intrinsic velocities (V_0) or those determined experimentally at ~200 MPa. The relative errors between the calculated and measured results are generally <2-3%. The discrepancies between the calculated and measured seismic velocities are caused mainly by the following four sources of errors: (1) The antigorite CPO was measured using the SEM-EBSD technique in a small domain on a thin section, from a very small volume of each sample, as compared with the volumes of the cylindrical minicores for which velocities are measured. As long as the strain is not fully homogeneous, the fabric may vary from place to place. The calculated results, which represent only the small domain from which the CPO was measured, may not be an accurate representation of the bulk rock. (2) The antigorite from the serpentinites studied does not have exactly the same chemical composition as the single crystal [$(Mg_{2.62}Fe_{0.16}Al_{0.15})(Si_{1.96}A1_{0.04})O_5(OH)_{3.57}$] for which the published elastic constants were determined (Bezacier et al., 2010). Additions of CaO, Al_2O_3, and FeO+Fe_2O_3 can not only increase the antigorite stability field to higher temperatures (Bromiley and Pawley, 2003; Hilairet et al., 2006) but also change its elastic constants. More laboratory measurements of single crystal elastic constants are needed for serpentinites of different compositions. (3) The contributions of minor and accessory minerals such as dolomite, lizardite and magnesite were not taken into account in the velocity calculations. (4) For serpentine minerals, not all grains can be indexed by the EBSD techniques due to their complex crystallographic structures, small grain sizes (usually several microns), radiation-induced surface amorphization and polishing problems. In the case of the antigorite schist examined by Brownlee et al. (2013), from the mélange adjacent to the Motagua fault system in central Guatemala, the indexing rate varies 21% to 81% in different samples. According to van de Moortele et al. (2010), however, most of the non-indexed points are along grain boundaries and holes where crystals were ripped off during polishing. Thus the indexation efficiency is controlled mainly by the quality of the sample surface. Padron-Navarta et al. (2012) reported that the indexing rates in XY sections are lower than in XZ sections. Hence it should be kept in mind that the CPOs are probably statistically imperfect representations of the bulk rocks. Although the calculations from the CPO data are quite robust for providing the 3D seismic properties of complex aggregates, calculated results cannot completely replace laboratory measurements of rock seismic properties

and should be verified by experiments.

2.5 Discussion

2.5.1 Comparison between single crystal and polycrystalline antigorite elasticity data

The elastic constants of the single crystal antigorite, measured by Bezacier et al. (2010), allowed calculating the equivalent isotropic properties of antigorite aggregate using the Reuss, Voigt, Hill, and geometrical averages: V_p=6.170, 7.300, 6.735, and 6.711 km/s, and V_s=3.320, 4.290, 3.805, and 3.774 km/s, respectively. The Reuss and Voigt bounds represent, respectively, equal stress and equal strain between grains while the Hill average is the arithmetic mean between the Reuss and Voigt values that are regarded as the lower and upper bounds for the bulk effective properties and bracket the permissible range in which the effective properties must lie (e.g., Ji, 2004; Ji et al., 2004). As shown in Figure 2.15, the V_0 values for both P- and S-wave velocities of the 26 antigorite serpentinite samples [15 from this study and 11 from Ji et al. (2013a)] all lie between the Reuss and Voigt bounds calculated from the single-crystal data (Bezacier et al., 2010) and are concentrated mainly around their arithmetic (V_p=6.668 km/s and V_s=3.717 km/s) and geometrical (V_p=6.666 km/s and V_s=3.715 km/s) means. The arithmetic and geometrical means of the V_0(P-wave) values from the 26 samples on which both V_p and V_s have been measured are only 0.95% and 0.63% lower than the Hill (6.735 km/s) and geometrical (6.711 km/s) means calculated using single crystal V_p data, respectively. However, the arithmetic and geometrical means of the V_0(S-wave) values from this set of samples are 2.31% and 1.56% lower than the Hill (3.805 km/s) and geometrical (3.774 km/s) means calculated using single crystal V_s data, respectively. In other words, most of the S-wave velocities lie between the Hill average and the Reuss bound but are much closer to the Hill average than the Reuss bound. These differences result probably from the fact that the antigorite on which the published elastic constants were determined (Bezacier et al., 2010) contains higher contents of Al_2O_3 and $FeO+Fe_2O_3$ (Ji et al., 2013a) and thus probably has higher seismic velocities than those "Xiuyan Jades" studied here (Hilairet et al., 2006). For both V_p and V_s, the geometrical mean yields a better prediction than the Hill average. It is interesting to note that the arithmetic and geometrical means of our measured V_0 values are the same, V_p/V_s=1.794, while the ratios computed from the single crystal antigorite elasticity data (Bezacier et al., 2010) using the Hill and geometrical schemes are slightly different, 1.780 and 1.778, respectively. These calculated values, which are similar to the data from this

study, are lower than those obtained by previous authors (1.84, Christensen, 1978; 1.83, Christensen, 2004; 1.98, Kern, 1993; 1.93, Kern et al., 1997).

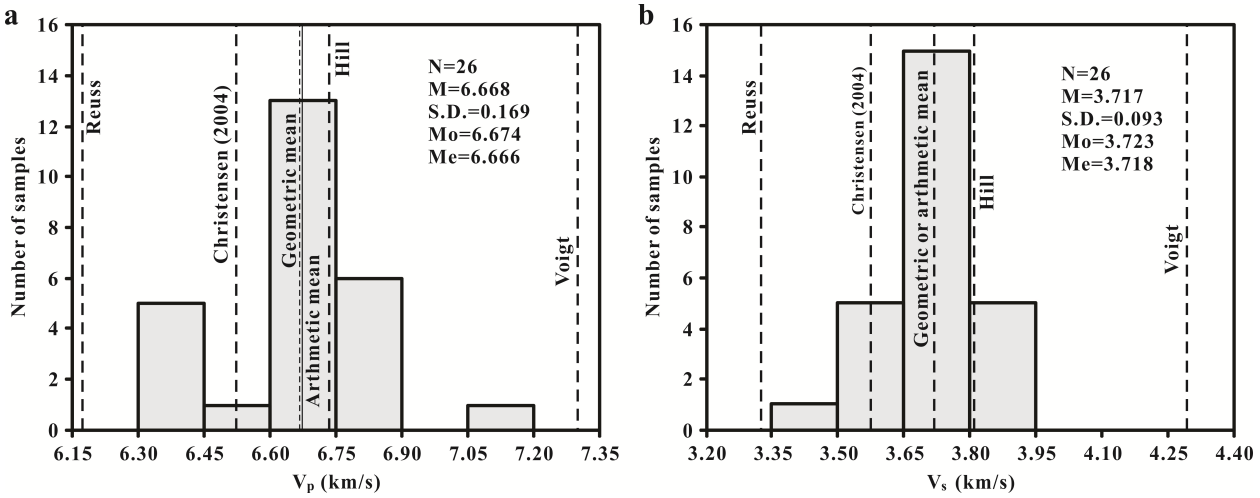


Figure 2.15 Histograms showing the distribution of antigorite serpentinite intrinsic velocity V_0 for (a) P- and (b) S-waves and the comparison with the Reuss, Voigt, and Hill averages calculated from the single crystal elasticity data of antigorite (Bezacier et al., 2010). Data from this study and Ji et al. (2013a) are shown in light grey shaded domains. Data from Christensen (2004) are also indicated. N, M, S.D., Mo, and Me as in Figure 2.6 caption.

2.5.2 Effects of pressure on velocities and anisotropy

Laboratory velocity data can be extrapolated to in situ *P*-*T* conditions according to the following equation:

$$V(P,T) = V_0 + DP - B_0 \exp[-kP] + (dV/dT)[T(P) - 20] \qquad (2.4)$$

where V is the seismic velocity; P and T are the lithostatic pressure (MPa) and temperature (°C) at a given depth; V_0, D, B_0, and k are defined in Eq. (2.1) and given in Tables 2.3 and 2.4 for the P- and S-wave velocities of each sample, respectively; and dV/dT, which is the temperature derivative of velocity, varies with the orientations of wave propagation and polarization (Table 2.5). As indicated by Eq. (2.4), seismic velocities increase with increasing P but decrease with increasing T. Here we used sample A1 as an example to illustrate the effects of hydrostatic pressure on the seismic velocities, anisotropy and shear-wave splitting of antigorite serpentinite by considering two types of geothermal structures: (1) Cold subduction with a linear relation between T (ºC) and P (GPa): T=96.67P+19.99. This simple equation assumes that T=600 ºC

when P=6 GPa, the assumedly highest P-T conditions in which Al_2O_3- and Cr_2O_3-bearing antigorite is stable in a water-saturated system and over which the breakdown of antigorite will take place (Ulmer and Trommsdorff, 1995). (2) Hot subduction with T=226.67P+19.98, assuming that T=700 ºC when P=3 GPa, over which antigorite is no longer stable and should break down by dehydration reactions. The pressures of 3 and 6 GPa correspond to depths of about 100 and 200 km, respectively, although the exact depths depend on the average density of the overlying rocks from surface to depth. Thus antigorite is assumed to be stable to depths of about 100 and 200 km in hot and cold subducting slabs, respectively (e.g., Bezacier et al., 2013).

Table 2.5 Temperature derivatives of P- and S-wave velocities in an antigorite serpentinite[a]

Propagation direction	Polarization direction	dV/dT	S.D.	Propagation direction	Polarization direction	dV/dT	S.D.
		10^{-4} km/s/ºC				10^{-4} km/s/ºC	
X	X	-7.117	2.239	X	Y	-3.811	0.588
Y	Y	-7.482	1.806	X	Z	-5.934	0.778
Z	Z	-10.225	2.032	Y	X	-5.761	0.632
				Y	Z	-5.974	1.113
				Z	X	-5.689	1.161
				Z	Y	-5.696	1.052

[a] Results derived from experimental data of Kern et al. (1997)

For sample A1, the intrinsic velocities (V_0) along X, Y, and Z equal 7.313, 7.028, and 6.110 km/s, respectively, reflecting the CPO-induced seismic anisotropy (Table 2.3). The temperature derivative of V_p in serpentinites (Table 2.5) is anisotropic: -7.1176×10^{-4}, -7.482×10^{-4}, and -1.023×10^{-3} km/s/°C along X, Y, and Z (Kern et al., 1997), reflecting the fact that thermal expansion is more pronounced in the direction normal to (001) than those parallel to this plane. The pressure derivatives (D) of V_p in this sample are also very anisotropic: 1.156×10^{-4}, 1.222×10^{-4}, and 3.443×10^{-4} km/s/MPa along X, Y, and Z. The anisotropy can be interpreted in terms of the elastic properties of single crystal antigorite and the CPO data of the serpentinite. In this sample, the a-, b-, and c-axes of antigorite cluster in the directions parallel to Y, X, and Z, respectively (Figure 2.10). Previous experiments up to 6 GPa (Nestola et al., 2010) showed that the compressibility of antigorite crystals is very anisotropic with ratios 1.11:1.00:3.24 along the a-, b-, and c-axes, respectively. These direction-dependent ratios of compressibility are comparable with but higher than those of the pressure derivatives of V_p: 1.06:1.00:2.97 along the X, Y, and Z directions of the serpentinite sample, which is a polycrystalline aggregate. The compressibility anisotropy is related to the direction–dependent bulk moduli: 98.1, 109.1, and

33.8 GPa along the a-, b-, and c-axes of antigorite, respectively (Nestola et al., 2010). The b-axis is less compressible than the a-axis, which is consistent with the sheet curvature parallel to the a-axis (Hilairet et al., 2006). This also explains why the dislocation slip along [010] is easier than along [100] in antigorite (Figure 2.10). The extremely high compressibility of antigorite may have an important bearing on the geodynamic processes of subduction zones. Antigorite density is 2.765 g/cm^3 (Hilairet et al., 2006) or 2.809 g/cm^3 (Holland and Powell, 1998) at 5.7 GPa and 470 °C but it is 2.600 g/cm^3 at the ambient conditions. Hydration or serpentinization of peridotites (3.300 g/cm^3) can lead to a significant reduction in density, generating a buoyancy force and a huge volume increase to produce high pressure within serpentinizing rocks. As long as they have sufficiently large volumes, antigorite bodies in subducted slabs or mantle wedges may form diapirs which flow upward (Guillot et al., 2009; Pilchin, 2005). With depressurization during progressive exhumation, antigorite expands and dilates, continuously increasing the buoyancy force which may speed up the exhumation of ultrahigh and high pressure (UHP and HP) metamorphic rocks.

In a hot subducting slab, the combined effect of pressure and temperature induces a decrease in V_p along either the X or Y direction but an increase along the Z direction with pressure/temperature or depth (Figure 2.16a). As a result, the V_p anisotropy decreases with pressure (A_p=17.4%, 15.3%, 13.0%, and 10.6% at 0.1, 1.0, 2.0, and 3.0 GPa, respectively, Figure 2.16b). The variations of V_s along different propagation-polarization directions with pressure in the hot subducting slab are shown in Figure 2.16c. Under the P and T conditions, for stable and metastable antigorite, V_s(XY) is almost equal to V_s(YX) while V_s(XZ), V_s(YZ), V_s(ZX), and V_s(ZY) have similar values. The shear-wave birefringence for wave propagation along either X or Y (Figure 2.16d) increases nearly linearly with pressure: ΔV_s(X)=0.592, 0.664, and 0.736 km/s, and ΔV_s(Y)=0.650, 0.721, and 0.793 km/s at P=1.0, 2.0, and 3.0 GPa and T=247, 473, and 700 °C, respectively. ΔV_s(Z) is ≤0.08 km/s in the whole range of P≤3 GPa and T≤700 °C. The V_p/V_s ratio of the antigorite serpentinite (Figure 2.16e) displays a linear increase from 1.81 to 1.86 with increasing pressure from 0.3 GPa (88 °C) to 3.0 GPa (700 °C). The elasticity data obtained at pressures up to 9 GPa and room temperature (Bezacier et al., 2013) yielded a relation for single crystal antigorite: V_p/V_s=1.7655+0.01952P, where P is in GPa. The calculations using this relation show that V_p/V_s=1.771 and 1.824 at 0.3 and 3.0 GPa and room temperature, respectively.

A comparison between the above two sets of data suggests that the effect of temperature is to increase the V_p/V_s values.

In the cold subducting slab, where the effect of pressure is more important than that of temperature on seismic properties, P-wave velocities along the X, Y, and particularly the Z directions increase remarkably with pressure (Figure 2.16f). At $P \geq 4.7$ GPa (corresponding to $T \geq 474$ °C), V_p(Z) surpasses V_p(Y) and approaches V_p(X) if the pressure and temperature derivatives determined in laboratory are also correct under natural conditions. Similar trends have been observed during measurements of antigorite single crystal elasticity using Brillouin scattering at high pressures up to 9 GPa and room temperature (Bezacier et al., 2013). The V_p anisotropy first decreases rapidly from 17.4% at 100 MPa (30 °C) to 4.7 GPa (474 °C), and then remains nearly constant (~3.7%) above 4.7 GPa (474 °C) (Figure 2.16g). As illustrated in Figure 2.16h, the difference between V_s(XY) and V_s(YX) increases with increasing pressure/temperature: V_s(XY)=V_s(YX) at 0.35 GPa and 54 °C; V_s(YX) is 0.157, 0.216, and 0.275 km/s higher than V_s(XY) at 3, 4, and 5 GPa, respectively. V_s(XZ), V_s(YZ), V_s(ZX), and V_s(ZY) display similar values below 3 GPa and 310 °C (Figure 2.16h). The shear-wave birefringence for the propagation along X, Y, and Z increases linearly with pressure in the stability field of antigorite: the maximum and minimum splitting occur in Y and Z, respectively. ΔV_s(X)=0.653, 0.698, and 0.742 km/s, ΔV_s(Y)=0.784, 0.853, and 0.922 km/s, ΔV_s(Z)=0.083, 0.118, and 0.154 km/s at P=3, 4, and 5 GPa and T=310, 407, and 503 °C, respectively (Figure 2.16i). In the cold subducting slab, the V_p/V_s ratio of antigorite serpentinite (Figure 2.16j) displays a linear increase from 1.81 to 1.88 with increasing pressure from 0.1 GPa (30 °C) to 6.0 GPa (600 °C).

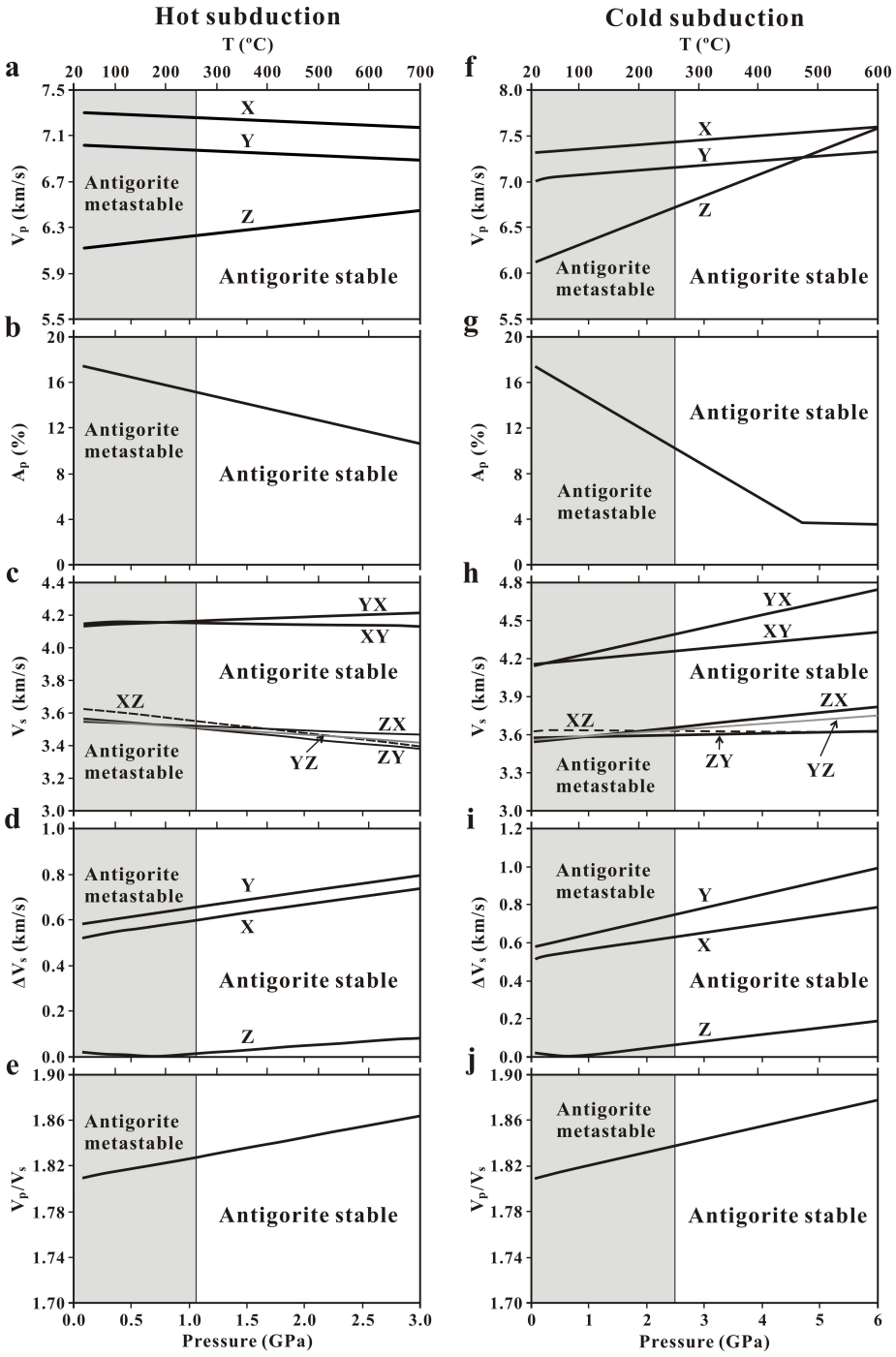


Figure 2.16 Comparison of P-wave velocity (V_p) and anisotropy (A_p), S-wave velocity (V_s) and birefringence (ΔV_s) and V_p/V_s between hot and cold subduction zones. The lower boundary of the antigorite stability field is defined by P=7.750-0.0258T, where P is in GPa, and T in °C (Reynard, 2013). Antigorite turns to peridotite above 600 °C in the cold subduction zone but 700 °C in the hot subduction zone. The orientations of wave propagation and polarization are defined in Tables 2.3-2.4.

2.5.3 CPO-induced seismic anisotropy

Serpentine CPO can result from various processes such as plastic deformation (e.g., Bezacier et al., 2010; Ji et al., 2013a; Padron-Navarta et al., 2012), metasomatism (e.g., Boudier et al., 2010; Faccenda et al., 2008), and dissolution-precipitation or pressure solution (e.g., Andreani et al., 2005; Auzende et al., 2006; Healy et al., 2009; Wassmann et al., 2011). The deformation processes include dislocation glide, lattice rotation (i.e., folding and kinking), dynamic recrystallization and fluid-assisted anisotropic growth under differential stresses. Both LT lizardite and HT antigorite have only a single slip plane [i.e, (001)], which certainly cannot produce homogenous deformation because the von Mises criterion for plasticity is not met. According to this criterion, for a crystal to undergo an arbitrary constant volume deformation, at least 5 independent slip systems are required to be active (e.g., Nicolas and Poirier, 1976). In order for antigorite to deform to large strain, it is necessary to have additional mechanisms such as lattice rotation, folding, kinking, recrystallization, pressure solution and anisotropic growth to accommodate intracrystalline dislocation slip.

Metasomatism processes include crack-seal mechanisms and topotactic growth. LT serpentinization usually starts from grain boundaries and develops multiple-oriented microfracture networks, forming a “mesh-texture” (Maltman, 1978; Wicks and Whittaker, 1977). The (001) planes of lizardite are commonly aligned parallel or perpendicular to the walls of original microcracks and grain boundaries (e.g., Boudier et al., 2010; Dewandel et al., 2003), forming an overall complex and random texture with no overall CPO at the scale of the samples (O’Hanley, 1996; Schmitt et al., 2007). In peridotites, the commonest fabric pattern is that in which (010) of olivine and (100) of pyroxene are preferentially parallel or subparallel to the foliation while [100] of olivine and [001] of pyroxene are preferentially parallel or subparallel to the lineation (e.g., Boudier et al., 2010; Ji et al., 1994a; Saruwatari et al., 2001). If serpentinization forms a penetrative network composed of three sets of serpentine-filled veins, each perpendicular to X, Y, or Z, and serpentine is aligned with (001) parallel to the fracture surfaces, lowering both V_p and V_s in the directions normal to the vein fractures, the serpentinization may not modify the velocity symmetry although the absolute velocity values decrease significantly. For these reasons, Kern and Tubia (1993) observed that V_p anisotropy declined from 6-8% in fresh lherzolite to <2% in more serpentinized samples. Horen et al. (1996) reported a remarkable decrease in both V_p and V_s anisotropy in peridotites from the Xigaze

ophiolite (Tibet) with increasing degrees of serpentinization from 3% to 70%. Schmitt et al. (2007) reported that V_p anisotropy decreases monotonically from over 12% to nearly zero with increasing serpentinization. If the serpentinization is characterized by only one set of serpentine-filling parallel veins, however, it may markedly increase the seismic anisotropy of peridotites (e.g., Boudier et al., 2010; Dewandel et al., 2003; Faccenda et al., 2008) because single crystal serpentine has much higher seismic anisotropy than olivine and orthopyroxene (Figure 1.5; Bezacier et al., 2010; Mookherjee and Capitani, 2011; Reynard et al., 2007). The above crack-seal mechanism takes place in the brittle deformation regime at low temperatures where serpentine grows in dilatational veins from fluid infiltration (e.g., Groppo and Compagnoni, 2007).

Boudier et al. (2010) reported a topotactic relationship between newly grown serpentine and precursor olivine during serpentinization: serpentine (010) and (001) are parallel to olivine (001) and (100), respectively. If (010) and [100] of olivine are preferentially parallel to the foliation and the lineation, respectively (e.g., Boudier et al., 2010; Ji et al., 1994a; Saruwatari et al., 2001), the a- and c-axes of serpentine are perpendicular to the foliation and parallel to the stretching lineation defined by HT deformed olivine, respectively. However, the formation mechanism of seismic anisotropy due to serpentine in-filling along mutually-parallel fractures (e.g., Boudier et al., 2010; Faccenda et al., 2008) can be eliminated in the samples we studied for the reasons below: (a) the CPO of antigorite is induced by dislocation creep as indicated by abundant microstructural evidence such as undulatory extinction, lattice rotation, folding, kinking, and dynamic recrystallization (Ji et al., 2013a); (b) the parallelism between antigorite c-axes and the lineation or between antigorite (100) and the foliation has not been observed; and (c) a fossil fabric of serpentine formed by the crack-seal mechanism can hardly survive and be preserved after intensive plastic deformation in a new strain field as serpentine is much weaker than the other minerals involved such as olivine and pyroxenes.

Serpentine is characterized by a layered structure with a pseudo-hexagonal network of linked SiO_4 tetrahedra. Consequently, a single crystal of antigorite displays a quasi-hexagonal symmetry with fast P-wave velocities (8.0-8.9 km/s) along the a-b plane perpendicular to the c-axis and slow P-wave velocities (5.58 km/s) parallel to the c-axis (Bezacier et al., 2010). The difference between the velocities along the a- and b-axes is only ~3%. The bulk V_p anisotropy (A_p) and the maximum directional V_s anisotropy in antigorite are 49% and 66%, respectively. The CPO

diagrams of antigorite (Figure 2.10) show that the dominant slip occurred along the [010] rather than [100] direction on the basal plane. Microstructural analyses from experimentally deformed antigorite serpentinite (T=500 °C, P=1.0 GPa, and strain rate of 1.5×10^{-5} s^{-1}) showed no prevailing slip systems other than (001)[010] (Ando et al., 2013). The CPO pattern can be explained by the corrugated sheet structure of antigorite which has b (0.925 nm) and c (0.725 nm) similar to those of lizardite and chrysotile but the a cell length ranges between 3.3 and 5.1 nm (Deer et al., 1992). Such a wave-like structure has a corollary that the b-axis is significantly stronger than the a-axis (Campione and Capitani, 2013; Nestola et al., 2010). In a crystal, the easiest slip direction should be the shortest Burgers vector on the easiest glide plane since dislocations with the lowest energy are the most stable and the energy of a dislocation is proportional to the square of the Burgers vector. On the basal plane of antigorite, thus b-slip should be significantly easier than a-slip (e.g., Banfield et al., 1995).

The seismic anisotropy pattern in serpentinites (Figure 2.11) is essentially controlled by the CPO of serpentine (001), but displays little dependence on the preferred orientation of [100], [010] or [hk0] because the velocities along these directions are almost the same (Bezacier et al., 2010, 2013). Therefore, the anisotropy patterns produced by serpentine deformed through intracrystalline slip on systems (001)[010] (Brownlee et al., 2013; Hirauchi et al., 2010; Jung et al., 2011; Nishi et al., 2011; Soda and Takagi, 2010; Vogler, 1987), (001)[100] (Katayama et al., 2009; Padron-Navarta et al., 2012; van de Moortèle et al., 2010) and mixed (001)[100] and (001)[010] slip (Bezacier et al., 2010; Brownlee et al., 2013) are all similar with the fastest and the slowest P-wave velocities and the maximum and minimum shear-wave birefringence values parallel and perpendicular to the foliation, respectively. The only difference between a- and b-slip in the (001) plane is the direction of the fast split shear-wave polarization (ϕ) when propagating normal to the foliation: ϕ parallel to the lineation for a-slip and normal to the lineation for b-slip. In the both cases, however, shear-wave splitting is very small because the propagation is normal to the foliation. The activation of nonbasal slip systems is almost impossible in serpentine and other sheet silicates such as mica. Thus, the seismic anisotropy pattern of serpentinite is independent on the operating slip system but strongly dependent on the regime and magnitude of finite strain experienced by the rock.

In serpentinites strongly deformed by coaxial flattening, the (001) planes of serpentine are preferentially aligned parallel to the foliation with the c-axis parallel to the Z direction, while

both a- and b-axes are randomly aligned in the foliation plane (Ji et al., 2013a). This is consistent with the results from the lower bound modeling (Padron-Navarta et al., 2012). The serpentinites deformed by axial shortening should develop uniaxial anisotropy or TI with $V_p(X) \approx V_p(Y) > V_p(Z)$ (e.g., sample A5 in Figure 2.12a) and the maximum and minimum shear-wave splitting observed for propagation in the foliation plane and normal to the foliation, respectively (e.g., sample A5 in Figure 2.13a). In serpentinites strongly deformed by coaxial constriction, (001) planes of serpentine are preferentially aligned parallel to the stretching lineation and the c-axes are randomly aligned in a complete girdle normal to the lineation. Both the [100] and [010] axes display a girdle parallel to the foliation. This type of antigorite CPO was indeed reported in Jung (2011), Nishii et al. (2011), and Soda and Takagi (2010). Seismic anisotropy of these serpentinites is quasi-transversely isotropic with $V_p(X) \gg V_p(Y) \approx V_p(Z)$.

In serpentinites which have been highly deformed by simple shear, the (001) planes of serpentine are preferentially aligned parallel to the bulk shear plane (this chapter). The obliquity between the foliation and the shear plane defined by the CPO of serpentine (001) planes decreases with increasing finite shear strain and finally these two planes become indiscernible. Such highly sheared serpentinites develop uniaxial anisotropy or TI with $V_p(X) \approx V_p(Y) > V_p(Z)$ and the maximum and minimum shear-wave splitting observed for propagation in the foliation plane and normal to the foliation, respectively. However, the serpentinites moderately deformed by simple shear are generally characterized by a bimodal distribution of serpentine grains (Ji et al., 2013a): (1) the strongly deformed matrix in which antigorite grains are aligned in an easy slip orientation with the (001) planes parallel or subparallel to the foliation; and (2) the poorly deformed porphyroclasts that are in an unfavorable orientation with the (001) planes perpendicular to the X and particularly to the Y direction. Increasing simple shear strain can progressively rotate the (001) planes aligned initially perpendicular to the X direction to the bulk shear plane, forming fish-shaped porphyroclasts. Nevertheless, it is difficult for progressive simple shear to eliminate the porphyroclasts whose c-axes cluster in the Y direction unless extensive dynamic recrystallization has taken place. As a result, strong and moderate concentrations of antigorite c-axes occur in the Z and Y directions in the YZ plane, respectively, forming an almost complete girdle in a plane subperpendicular to the lineation. The antigorite c-axis fabric in the regime of simple shear agrees approximately with the results of the lower bound modeling (Padron-Navarta et al., 2012) although their modeling predicts that both the a- and b-axes are equally concentrated

in the direction parallel to lineation, which is inconsistent with our measured results shown in Figure 2.10. The serpentinites deformed by simple shear generally produce an orthorhombic symmetry of seismic anisotropy with $V_p(X)>V_p(Y)>V_p(Z)$ and $k_p\approx1$ (e.g., sample WZG2, Figures 2.4c and 2.8).

2.5.4 Dependence of seismic velocities on the degree of serpentinization

Based on the experimental data from 12 HT serpentinized samples at 600 MPa, Ji et al. (2013a) determined the variations of mean P- and S-wave velocities (km/s) as a function of antigorite volume fraction (%):

$$V_p = 8.10 - 1.42\varphi_{HT} \quad (2.5)$$

$$V_s = 4.51 - 0.84\varphi_{HT} \quad (2.6)$$

$$V_p/V_s = 1.77 + 0.04\varphi_{HT} \quad (2.7)$$

The effect of HT serpentinization is significantly different from that of LT serpentinization. For LT serpentinization, they obtained:

$$V_p = 8.10 - 3.00\varphi_{LT} \quad (2.8)$$

$$V_s = 4.51 - 2.19\varphi_{LT} \quad (2.9)$$

$$V_p/V_s = 1.77 + 0.38\varphi_{LT} \quad (2.10)$$

An addition of the new data (600 MPa) from this study plus older data in the database (Figure 2.17) yields:

$$V_p = 8.10 - 1.37\varphi_{HT} \quad (2.11)$$

$$V_s = 4.51 - 0.77\varphi_{HT} \quad (2.12)$$

$$V_p/V_s = 1.77 + 0.03\varphi_{HT} \quad (2.13)$$

Equations (2.11)-(2.13) are only slightly different from Eqs. (2.5)-(2.7). For pure LT and HT serpentinites (φ=1) at 600 MPa, V_p=5.10 and 6.73 km/s, V_s=2.32 and 3.74 km/s and V_p/V_s=2.15 and 1.80 (corresponding Poisson's ratio υ=0.362 and 0.277), respectively. As shown in Figure 2.17, the velocity differences (ΔV) between HT and LT serpentinized peridotites increase linearly

with the degree of serpentinization: $\Delta V_p=1.63\varphi$ and $\Delta V_s=1.42\varphi$ at 600 MPa. For a given φ value, the HT serpentinized peridotites have significantly higher V_p and V_s than their LT counterparts. For a given measured V_p, the corresponding contents of HT and LT serpentines are very different: $\varphi_{HT}=2.19\varphi_{LT}$. This relationship indicates that serpentine contents in hydrous subducting slabs and mantle wedges where temperature is >300 °C, inferred from observed P-wave velocities, should be higher by a factor of 2.19 than the previous estimates based on LT serpentinization (e.g., Christensen, 1972, 1996; Horen et al., 1996; Wang et al., 2009). For the same V_s value, $\varphi_{HT}=2.84\varphi_{LT}$. These relations can be used to constrain the degree of serpentinization in the low-velocity zone at the plate interface and the cold nose of the mantle wedge, observed in subduction zones worldwide (Cascadian subduction zone: Abers et al., 2009; Bostock et al., 2002; Brocher et al., 2003; Nikulin et al., 2009; Park et al., 2004; Rondenay et al., 2001; Zhao et al., 2001; Mexican margin: Song et al., 2009; Nicoya Peninsula of Costa Rica: DeShon and Schwartz, 2004; Chile margin: Graeber and Asch, 1999; Central Japan: Kamiya and Kobayashi, 2000; Seno et al., 2001). For example, Zhao et al. (2001) and Ramachandran et al. (2006) reported that the upper fore-arc upper mantle (40-60 km depth) beneath the Strait of Georgia and Puget Lowland (the Northern Cascadian subduction zone) has P-wave velocities of 7.2-7.6 km/s. Antigorite should be dominant in the partially serpentinized peridotites at such depths. According to our results, these V_p values correspond to 36-66 vol.% HT serpentinization, which are much higher than the estimates (17-30 vol.%) based on LT serpentinization (Carlson and Miller, 2003; Hacker et al., 2003; Zhao et al., 2001).

DeShon and Schwartz (2004) detected a region with V_p/V_s=~1.85 within the hot fore-arc mantle wedge (32-60 km depth, P=1-2 GPa) along the Nicoya Peninsula, Costa Rica and interpreted it as a result of serpentinization. The relation between the V_p/V_s ratio and the volume fraction of LT serpentine yields ~21% serpentinization. However, temperatures within the fore-arc mantle wedge (320-600 °C) are too high for lizardite or chrysotile to be stable. Based on the seismic properties of HT serpentinized peridotites (Figure 2.16e), however, the velocity ratio of 1.85 may indicate almost complete serpentinization of the mantle rocks in the hot fore-arc mantle wedge at the depths of interest. As shown in Figure 2.16j, V_p/V_s values greater than 1.86 (van Keken et al., 2011) may be observed in the coldest core of the subducting slab at greater depths (P>4 GPa).

The Moho discontinuity is a lithological boundary that separates the mafic lower crust (gabbro for the oceanic crust and mafic granulites for the continental crust) from the ultramafic upper

mantle. Typical mafic granulites have an average V_p and V_s of 7.10 km/s and 3.92 km/s, respectively, at continental Moho depths (Ji et al., 2002). If the upper mantle is hydrated to contain >73 vol.% antigorite, V_p <7.10 km/s. The mantle beneath the Moho should have lower velocities than the lower crust above the Moho, causing the so-called inversion of the Moho (e.g., Bostock et al., 2002; Wang et al., 2013). However, the effects of seismic anisotropy and high pressure fluids should be also taken into account when interpreting mantle seismic data with V_p<7.10 km/s and V_s<3.92 km/s. For this reason, the inverted continental Moho reported by Bostock et al. (2002) may be equally explained by the presence of high pressure fluids (e.g., Audet et al., 2009; Peacock et al., 2011; Song et al., 2009).

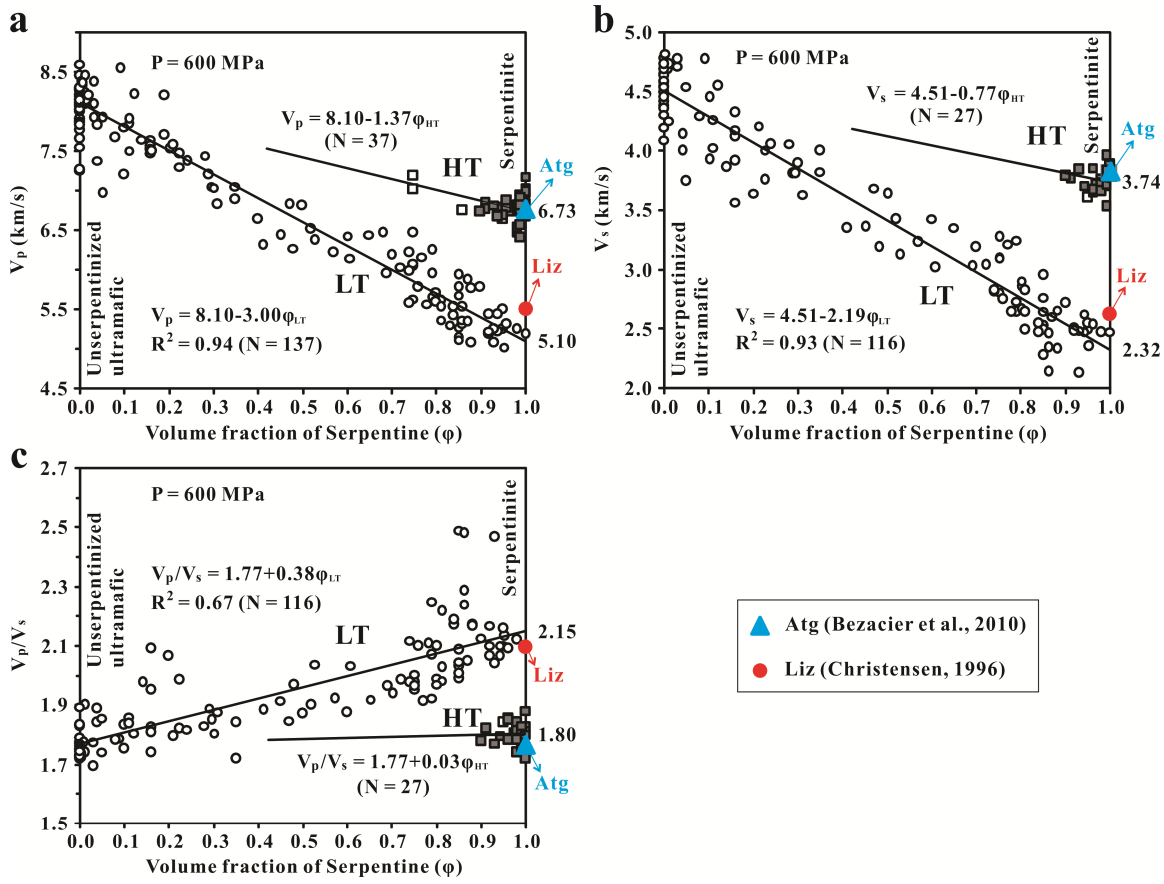


Figure 2.17 Mean (a) P- and (b) S-wave velocities and velocity ratios V_p/V_s measured at 600 MPa as a function of serpentine volume fraction (φ) for low temperature (LT, open dots) and high temperature (HT, solid squares from this study and Ji et al. (2013a), and open squares from the references) serpentinization. The LT data are from Ji et al. (2002, 2007), Sun (2011) and Wang et al. (2005) and the HT data are from Birch (1960), Christensen (1978), Ji et al. (2013a), Kern et al. (1997) and this study.

2.5.5 Seismic anisotropy in subducting slabs and mantle wedge

Seismic anisotropy has been observed in subduction zones worldwide (e.g., Long and Silver, 2008; Long and Becker, 2010; Savage, 1999). As pointed out by Ji et al. (2013a), the magnitude of detectable seismic anisotropy in a horizontal plane depends not only on the strain magnitude but also the strain geometry of serpentinite within the plate interface. Deformation of antigorite is caused by the movement of the subducting plate with respect to the overriding mantle wedge. According to their geometry and kinematics, plate boundaries can be classified into several categories:

(1) Steep-dipping subduction zones in which antigorite serpentine is deformed by nearly coaxial flattening and its (001) or foliation planes are orientated parallel to the plate interface, forming Type I seismic anisotropy with $k_p \approx 0$ [i.e., $V_p(X) \approx V_p(Y) > V_p(Z)$] and $k_s \approx 1$ (i.e., the polarization direction of the fast shear-wave component is trench-parallel and the largest delay time between the arrivals of the fast and slow shear waves occurs in the vertical or subvertical raypaths). Consequently, trench-parallel seismic anisotropy with fast V_p and V_s parallel to the trench, and large split shear-wave delay times (δt=1-2 s) are observed in steep subduction systems such as the Tonga-Kermadec-New Zealand, Aleutian and Ryukyu trenches (e.g., Long and van der Hilst, 2006; Long and Silver, 2008, 2009; Wiens et al., 2008; Wirth and Long, 2010).

(2) Shallow-dipping subduction zones in which antigorite is most likely deformed by simple shear. In serpentinized peridotites and serpentinites in this setting, strain should be heterogeneously distributed forming an anastomosing structure. Within the intensively strained zones, antigorite c-axes will be aligned normal or subnormal to the foliation, forming Type I seismic anisotropy with $k_p \approx 0$ [i.e., $V_p(X) \approx V_p(Y) > V_p(Z)$] and $k_s \approx 1$. Within the moderately sheared lozenges, however, antigorite c-axes will form a girdle normal or subperpendicular to the stretching lineation with the principal and secondary concentrations at the Z and Y axes, respectively, forming Type III seismic anisotropy with $k_p \approx 1$ [i.e., $V_p(X) > V_p(Y) > V_p(Z)$] but also $k_s \approx 1$. Within the horizontal plane, the seismic velocity in the trench-normal direction, which equals $V_p(X) \cdot \cos\theta$, where θ is the dip angle of the subducting slab, could be equal, less or greater than the value in the trench-parallel direction [i.e., $V_p(Y)$], depending on the values of k_p and θ. Assuming a subduction slab composed of antigorite serpentinite WZG2 (V_p=7.406, 6.933, and 6.246 km/s along X, Y, and Z at 600 MPa, respectively), the direction of the fast velocity rotates

from trench-normal when θ<21° to trench-parallel when θ≥21°. For sample YSK2A (V_p=7.408, 6.620, and 6.288 km/s along X, Y, and Z at 600 MPa, respectively), the critical angle for such a transition is 27°. Thus, trench-normal anisotropy with fast V_p normal to the trench can be detected along subducting slabs with a small θ (e.g., Cascadia, Currie et al., 2004; South America, Anderson et al., 2004; Polet et al., 2000). For the same reason, the polarization direction of the fast shear-wave could be normal to the trench but the shear-wave splitting could be small with short delay times [e.g., δt<0.3-0.5 s for the Chile-Argentina subduction zone (Anderson et al., 2004)] because seismic rays are at angles <30-35° with the foliation (Figure 2.13).

(3) In trench-parallel plate boundaries (Buttles and Olson, 1998; Hall et al., 2000; Savage, 1999), trench-parallel flow occurs in the fore-arc mantle where antigorite serpentinites develop steeply dipping foliation and horizontal lineation. In this tectonic setting, prominent shear-wave splitting occurs in both the horizontal and vertical propagation directions. The time delay for the latter may be as high as 1.0 s for S-waves propagating through a 30 km thick antigorite serpentinite section with the Y axis vertical (AV_s=12%) and an average V_s=3.658 km/s (sample YSK2A), and the fast polarization direction will be trench-parallel.

2.5.6 Seismic anisotropy of the Tibetan Plateau

The seismic properties of antigorite serpentinites can also be used to interpret tectonic and shear-wave splitting data from the Tibetan Plateau (Figure 2.18a). This is the Earth's largest and highest plateau, formed by successive amalgamation of 300-500 km wide crustal thrust wedges and sequential subduction of their underlying lithospheric mantle (Figure 2.18b, Tapponnier et al., 2001). The crustal thickness varies from south to north: 40 km beneath the Ganges basin on the Indian plate, 50 km beneath the Himalayas, 70 km beneath the Lhasa block between the Indus-Zangbo suture (IZS) and the Bangong-Nujiang suture (BNS), 60-80 km (Nabelek et al., 2009; Vergne et al., 2002) beneath the Qiangtang terrane, and ~50 km in the Qaidam basin. The thicknesses of the Indian and Asian lithospheres are ~200 km and 150 km, respectively (Guillot and Replumaz, 2013; Zhao et al., 2010). The tectonic model proposed by Tapponnier et al. (2001) contains two important tenets. (1) The crust has been thickened by transpressive folding and thrusting while the mantle beneath is decoupled at the Moho and has not been thickened. The decoupling requires an extremely weak material between the crust and mantle. Antigorite serpentinites derived from hydration of ultramafic rocks may be the most plausible candidate for

such a weakest lubricator (Guillot et al., 2000, 2001). (2) The lithospheric mantle beneath the crust is relatively strong without overall shortening and the strain is strongly localized into extremely weak, narrow shear zones between the lithospheric mantle blocks. This is the so-called plate tectonics hidden by thickening crust model (Tapponnier et al., 2001). The large fault zones (e.g., IZS, BNS, Tanggula-Red River fault, Jinsha-Xianshuihe fault, Kunlun fault, and Qilian fault), which are marked by the occurrence of extensively serpentinized ultramafic rocks, were initially suture zones along which continental blocks were amalgamated (e.g., Guillot and Replumaz, 2013; Yin and Harrison, 2000) or lithospheric fault zones in which ultramafic and mafic intrusions were emplaced. Hydration of the ultramafic and mafic rocks, which is due to reactions with circulating fluids, allowed these sutures or fault zones to be reactivated as weak, left-lateral strike-slip shear zones along which the lithospheric blocks have been laterally extruded northeastward, eastward and southeastward (e.g., Gan et al., 2007; Leloup et al., 1995; Tapponnier et al., 1990). Intensive deformation since the Tertiary caused the serpentinites (e.g., Ji et al., 2013a; this study), amphibolites (e.g., Gao and Liu, 2009; Ji et al., 2013b), schists, and phyllites (e.g., Mahan et al., 2006; Shapiro et al., 2004; Chapter 3 in this thesis) to develop strong subvertical foliation and horizontal lineation as well as strong CPOs. Thus, the CPOs of LT and HT serpentine as well as amphibole and mica should contribute to the observed seismic anisotropy and shear-wave splitting of the Tibetan Plateau.

Figure 2.18a is a comprehensive compilation of shear-wave splitting data (i.e, fast polarization direction ϕ and delay time δt), mostly from SKS and SKKS phases, from the Tibetan Plateau and its adjacent areas (e.g., Chen and Ozalaybey, 1998; Chen et al., 2010; Fu et al., 2008; Gao and Liu, 2009; Guilbert et al., 1996; Herquel and Tapponnier, 2005; Hirn et al., 1995; Huang et al., 2000; Li et al., 2011; Makeyeva et al., 1992; McNamara et al., 1994; Ozalaybey and Chen, 1999; Sandvol et al., 1994, 1997; Wang et al., 2010). It is generally observed that both teleseismic shear-wave splitting and crustal V_p/V_s ratios become higher from the interior of the blocks into the boundary fault zones. For example, SKS splitting on the BNS-Jiali fault, which is a 30 km wide left-lateral shear corridor, is characterized by E-W oriented, fast shear-wave polarization (parallel to the mountain range) and large δt ranging from 1.58 to 2.25 s with an average value of 1.95 s (Huang et al., 2000). Along the Tanggula-Red River fault zone, the fast polarization (i.e., 94º±3º) is aligned parallel to the surface trace of the fault zone and the delay times vary from 1.23 to 1.58 s with a mean value of 1.35 s. Similarly, on the Yushu-Gonghe profile, crustal V_p/V_s ratios are

low (1.65) north of the Kunlun fault, but become 1.84 in the Kunlun fault zone (Vergne et al., 2002). The low V_p/V_s ratios north of the fault imply the predominance of felsic composition and the absence of mafic composition within the crust (Ji et al., 2009), whereas the high values in the fault zone most likely indicate the presence of LT and HT serpentinites below and above the depth at which T=300°C, respectively, although hydrous fluids may also contribute to their origin.

There is a clear increase in δt (from 0.2 to 1.3 s), in less than 40 km from either the Tarim basin or the Qaidam basin, to the center of the Altyn Tagh fault zone, which bounds the north edge of the Tibetan Plateau for about 1800 km. The fast polarization directions are parallel to the fault trend within the fault zone but rotate counterclockwise 15-25° to become oblique to the fault trend beyond the fault zone (Dong et al., 1999; Herquel et al., 1999). Teleseismic tomography revealed that the Altyn Tagh fault zone is a steep, 40 km wide, 140 km deep, transpressive shear zone with a low V_p anomaly ($\leq$ 8%) with respect to adjacent regions (Wittlinger et al., 1998). Olivine CPO-induced anisotropy (3-4%) (Ji et al., 1994a; Mainprice et al., 2000) can hardly explain the sharp changes in seismic properties across the fault zone. However, the presence of deformed serpentine, amphibole, and phlogopite with strong CPOs is the best candidate to explain such a large low V_p anomaly and the observed shear-wave splitting.

A dramatic change in teleseismic shear-wave splitting or delay time δt over a distance of just 12-30 km is quite common in the Tibetan Plateau although the fast polarization directions are oriented quite consistently, that is, parallel to the mountain ranges. For example, station ST16 (Huang et al., 2000), which is located ~15 km south of the surface trace of the Jiali fault displays no splitting. Station ST17, which is located in the Lumpola valley, immediately next to the Bangong suture, has a delay time of 2.2 s with the fast polarization direction parallel to the Jiali fault. Such a sharp transition, which is hard to interpret in terms of olivine CPO in the lithospheric mantle (Ji et al., 1994a; Mainprice et al., 2000; Saruwatari et al., 2000; Silver, 1996) or in the asthenosphere (Fu et al., 2008; Vinnik et al., 1992; West et al., 2009), indicates that the anisotropy resides most likely shallower than 70-80 km in depth because the Fresnel zones of SKS phases at such close stations should overlap at depths of 70-80 km or less. Given that the crust beneath station ST17 is ~65 km thick, an anisotropic mantle layer of 5-15 km thickness absolutely cannot produce a delay time of 2.2 s because sheared peridotites generally have anisotropy of ~4% (Ji et al., 1994; Mainprice et al., 2000; Saruwatari et al., 2000). The most

likely cause is the CPO of LT and HT serpentine, which occurs in the strike-slip fault zone which reactivated previous suture zone between the lithospheric blocks.

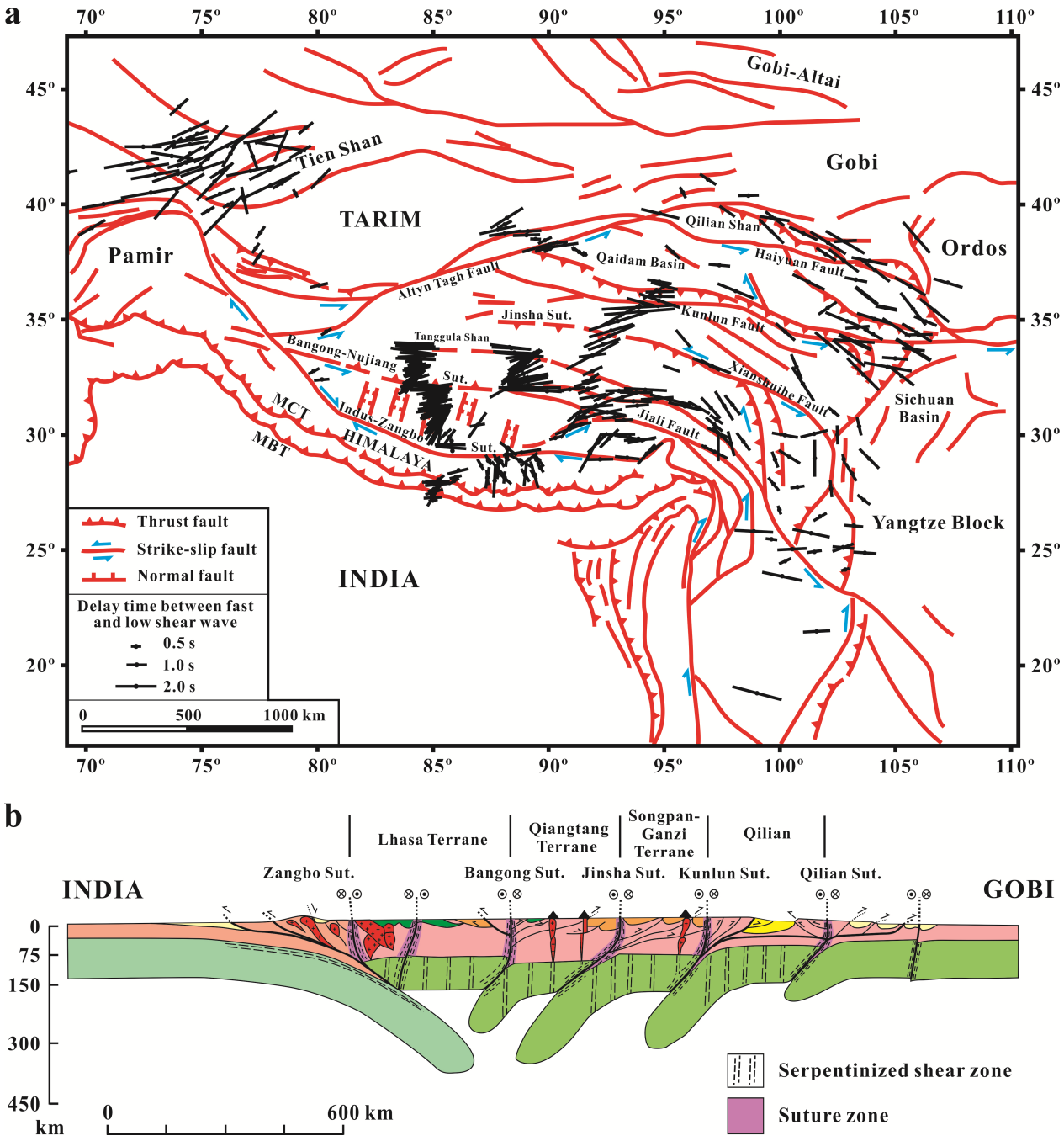


Figure 2.18 (a) Observations of shear-wave splitting in the Tibetan Plateau and its adjacent regions. (b) Lithospheric section of Himalaya-Tibet orogen (modified from Tapponnier et al., 2001). Dotted lines indicate potential serpentinized shear zones.

Extremely strong teleseismic shear-wave splitting, as high as 2.0-2.4 s, was observed between the Tanggula and Kunlun ranges (i.e., Qiangtang and Songpan-Ganzi terranes, Figure 2.18a). The lithospheric mantle beneath this region is characterized by low velocity (e.g., Wittlinger et al., 1996), high attenuation of Sn (e.g., McNamara et al., 1994; Ni and Barazangi, 1983) and Plio-Quaternary alkaline volcanism (e.g., Turner et al., 1993, 1996). All these data indicate the presence of hydrated mantle and possibly antigorite with strongly developed CPO. The hydration is due to percolation of fluids released from the subducting slab into the overlying lithospheric mantle (Figure 2.18b).

Kosarev et al. (1999) reported a continuous, north dipping P-to-S conversion boundary that can be traced from the Moho depth of ~70 km beneath southern Tibet to a depth of 200 km beneath station WNDO, 50 km north of the BNS, and corresponds to increases of 4-6% and 6-8% in V_p and V_s, respectively. This so-called Zangbo conversion boundary (ZCB) is interpreted by these authors as the boundary between the cold and depleted lithospheric mantle of India and the Asian lithospheric mantle. However, the velocity changes across the ZCB cannot be explained by assuming an extremely large temperature contrast (i.e., 500-650 °C at the top of the subducting Indian lithospheric mantle versus 1100-1300 °C in the overriding Asian lithospheric mantle immediately above the Indian mantle). Nor can it be explained by positing that the Indian lithospheric mantle is more depleted and has a higher Mg content than the Asian lithospheric mantle (e.g., Ji et al., 1994a; Nicolas et al., 1990). However, the velocity changes can be easily explained by the presence or absence of about 24-36 vol.% antigorite in the mantle rocks along the interface between the Asian and Indian lithospheric slabs. Such a rheologically weak subduction plane has played an important role for the exhumation of HP and UHP metamorphic rocks (Guillot et al., 2000, 2001). The temperature at the top of the Indian slab is 500-650 °C (Kosarev et al., 1999) where Al_2O_3- and Cr_2O_3-rich antigorite is stable. The ZCB disappears at the depth of 250 km, below which antigorite changes to forsterite and enstatite (Ulmer and Trommsdorff, 1995).

2.6 Conclusions

Antigorite is a main contributor to the formation of anomalously low seismic velocities and high anisotropy in subducting oceanic slabs and fore-arc mantle wedges as well as suture zones between amalgamated continental lithospheric blocks. We have measured P- and S-wave velocities (V_p and V_s), anisotropy, shear-wave birefringence (ΔV_s) and V_p/V_s in 15 HT serpentinite samples, which are nearly pure antigorite aggregates, at pressures up to 650 MPa. The high pressure experimental results combined with previous data (e.g., Christensen, 1978; Ji et al., 2013a; Kern et al., 1997) provide a new calibration for the effects of pressure on the seismic properties of HT serpentinites, suggesting that V_p anisotropy decreases but ΔV_s and V_p/V_s increase with increasing pressure in either cold or hot subduction zones. The variations in the seismic properties of antigorite serpentinites with increasing depth are due to the directional anisotropy of both the pressure and temperature derivatives of V_p and V_s. The experimental results, together with EBSD-CPO measurements, demonstrate the critical role of antigorite c-axis fabric, regardless of dislocation slip along [010], [100], or [hk0] within the (001) plane, in the formation of the different seismic anisotropy patterns for the serpentinites illustrated in Flinn diagrams. The antigorite c-axis fabric is believed to be controlled by the flow geometry (i.e., coaxial flattening, coaxial constriction, and simple shear), strain magnitude, and the degree of dynamic recrystallization. This study confirms the conclusions obtained by Ji et al. (2013a): (1) Coaxial flattening aligns the c-axes of antigorite parallel to the Z direction, forming transversely isotropic rocks with $V_p(X) \approx V_p(Y) \gg V_p(Z)$, almost equal shear-wave splitting in the X and Y directions but almost no splitting in the direction normal to foliation. (2) Coaxial constriction forms a nearly random distribution of antigorite c-axis in the YZ plane normal to the X direction, and thus $V_p(X) \gg V_p(Y) \approx V_p(Z)$ and shear-wave splitting is significantly larger along the Y direction than the X direction. (3) Simple shear aligns the c-axes of antigorite preferentially parallel to the shear plane whose angle with the foliation (XY) progressively decreases with increasing shear strain, but cannot rotate the grains with their c-axes oriented initially parallel or subparallel to the Y direction. As a result, moderately sheared antigorite serpentinites display orthorhombic symmetry with $V_p(X) > V_p(Y) > V_p(Z)$ and large shear-wave splitting for raypaths in the foliation plane. The antigorite grains with c-axes parallel or subparallel to the Y direction may be eliminated by dynamic recrystallization, producing a c-axis fabric indiscernible from those formed by coaxial flattening. This finding provides a new explanation for various anisotropy patterns observed in

subduction zones worldwide. For a cold, steeply subducting slab, antigorite is most likely deformed by nearly coaxial flattening or trench-parallel movements, forming trench-parallel seismic anisotropy with fast V_p and V_s parallel to the trench. For a hot, shallowly subducting slab, however, antigorite is most likely deformed by simple shear or transpression. Within the horizontal plane, the trench-normal velocity can be smaller, equal to, or larger than the trench-parallel velocity, depending on the subduction dip angle (θ). Trench-normal seismic anisotropy can be observed when $\theta<30°$. Interestingly, recent seismic data from the Tibetan Plateau such as strong heterogeneities in seismic velocity, attenuation, and shear-wave splitting can be well explained by the presence of strongly deformed HT serpentinites in lithospheric shear zones reactivated along former suture zones between amalgamated blocks, hydrated zones of subducting lithospheric mantle, and the crust-mantle boundary if the temperature is below 700 °C in the region of interest.

CHAPTER 3 MAGNITUDE AND SYMMETRY OF SEISMIC ANISOTROPY IN SCHISTS AND IMPLICATIONS FOR INTERPRETATION OF CRUSTAL STRUCTURE AND SHEAR-WAVE SPLITTING DATA FROM THE SOUTHEAST TIBETAN PLATEAU

3.1 Introduction

Current interpretations of seismic data are usually based on an assumed simple symmetry of rock seismic properties in order to minimize the number of free parameters and guarantee stable and unique inversion (e.g., Bostock and Christensen, 2012; Brocher and Christensen, 1990; Browaeys and Chevrot, 2004). The intrinsic seismic symmetry of a polyphase rock is controlled by the CPO, shape preferred orientation (SPO, foliation and lineation), composition layering, and elastic stiffness tensors and volume fraction of main constituent minerals (e.g., Ji and Mainprice, 1988; Mainprice, 2007). The CPO of each mineral, which is induced by differential stress and ductile deformation, depends on the prevailing deformation mechanism (e.g., dislocation slip system); the magnitude, geometry, and history of strain (e.g., coaxial or noncoaxial strain); and the conditions during deformation (e.g., temperature, pressure, differential stress, and fluid content) (e.g., Hansen et al., 2014; Miyazaki et al., 2013; Raterron et al., 2012). As a consequence, the seismic properties of naturally deformed rocks consisting dominantly of trigonal (e.g., α-quartz and calcite) or hexagonal (e.g., β-quartz) (Mainprice and Casey, 1990; Naus-Thijssen et al., 2011a; Ward et al., 2012; Zhao et al., 1997), orthorhombic [e.g., olivine and orthopyroxene (Ji et al., 1993, 1994a; Jung et al., 2013; Lee and Jung, 2015; Park and Jung, 2015; Nicolas and Christensen, 1987; Saruwatari et al., 2001)], monoclinic [e.g., amphibolite and clinopyroxene (Barberini et al., 2007; Barruol and Mainprice, 1993a; Ji et al., 1993, 2013b; Ko and Jung, 2015; Siegesmund et al., 1989; Tatham et al., 2008)], and triclinic [e.g., plagioclase (Ji and Mainprice, 1988; Ji and Salisbury, 1993; Ji et al., 2014b; Satsukawa et al., 2013)] minerals are often of complex geometry.

The interpretation of seismic data generally uses an assumption that the rock formations interrogated by seismic waves have a simple TI or hexagonal symmetry (e.g., Bostock and Christensen, 2012; Christensen and Okaya, 2007; Levin and Park, 1997; Okaya and Christensen, 2002; Porter et al., 2011). In a TI material, P-wave velocities are virtually the same in all radial

directions perpendicular to the axis of symmetry, along which the seismic velocity can be either higher [e.g., laminated anorthosite (Ji et al., 2014b)] or lower [e.g., mica schist (Brownlee et al., 2011; Dempsey et al., 2011; Erdman et al., 2013; Naus-Thijssen et al., 2011a; Ward et al., 2012; Wenk et al., 2012)] than the velocity normal to the axis. Shear-wave splitting is maximum and null for propagation perpendicular and parallel to the axis of symmetry, respectively. In the case where the symmetry axis is vertical, seismic velocities are sensitive to raypath inclination angles but not back-azimuths, inducing radial anisotropy (e.g., Becker et al., 2008; Wang et al., 2013). A horizontal or subhorizontal symmetry axis produces azimuthal anisotropy with the fast plane vertical or subvertical. A tilted symmetry axis makes the maximum and minimum velocities neither horizontal nor vertical (e.g., Frederiksen et al., 2003). Thus, different seismic methods, which sample the geological materials in different propagation and polarization directions, often yield different velocity and anisotropic values. For example, surface waves propagate horizontally along the surface of the Earth while teleseismic SKS and SKKS waves propagate with about 15-20° of the vertical direction. In regions where the symmetry axis is horizontal, receiver functions using shear waves could obtain significantly higher azimuthal anisotropy and shear-wave splitting (e.g., Porter et al., 2011). In regions where the symmetry axis is vertical, however, surface wave and shear-wave splitting methods detect hardly any seismic anisotropy (e.g., Lin et al., 2011; Moschetti et al., 2010). In this chapter, we measured and calculated both P- and S-wave velocities of representative mica- and amphibole-bearing schists, gneisses and mylonites in order to calibrate the magnitude and symmetry of seismic anisotropy in these crustal rocks. Special attention has been paid to evaluate whether seismic properties of the anisotropic metamorphic rocks can be reasonably well approximated by a TI symmetry, and if not, how departures from TI may manifest in seismic data due to the application of seismic methods that force the symmetry of the resulting elastic tensor to be TI. We will also examine the factors which cause the metamorphic rocks to deviate from TI. The results from seismic velocity measurements and calculations will be used to help constrain the tectonic interpretation of seismic data (e.g., Chen et al., 2013; Huang et al., 2007, 2011; Lev et al., 2006; Li et al., 2008; Shi et al., 2012; Sun et al., 2012, 2014; Wang et al., 2010; Xu et al., 2006; Yao et al., 2010) and regional stress field (Wu et al., 2004; Zhao et al., 2013; Zhong and Cheng, 2006) from the southeast Tibetan Plateau (Figure 3.1).

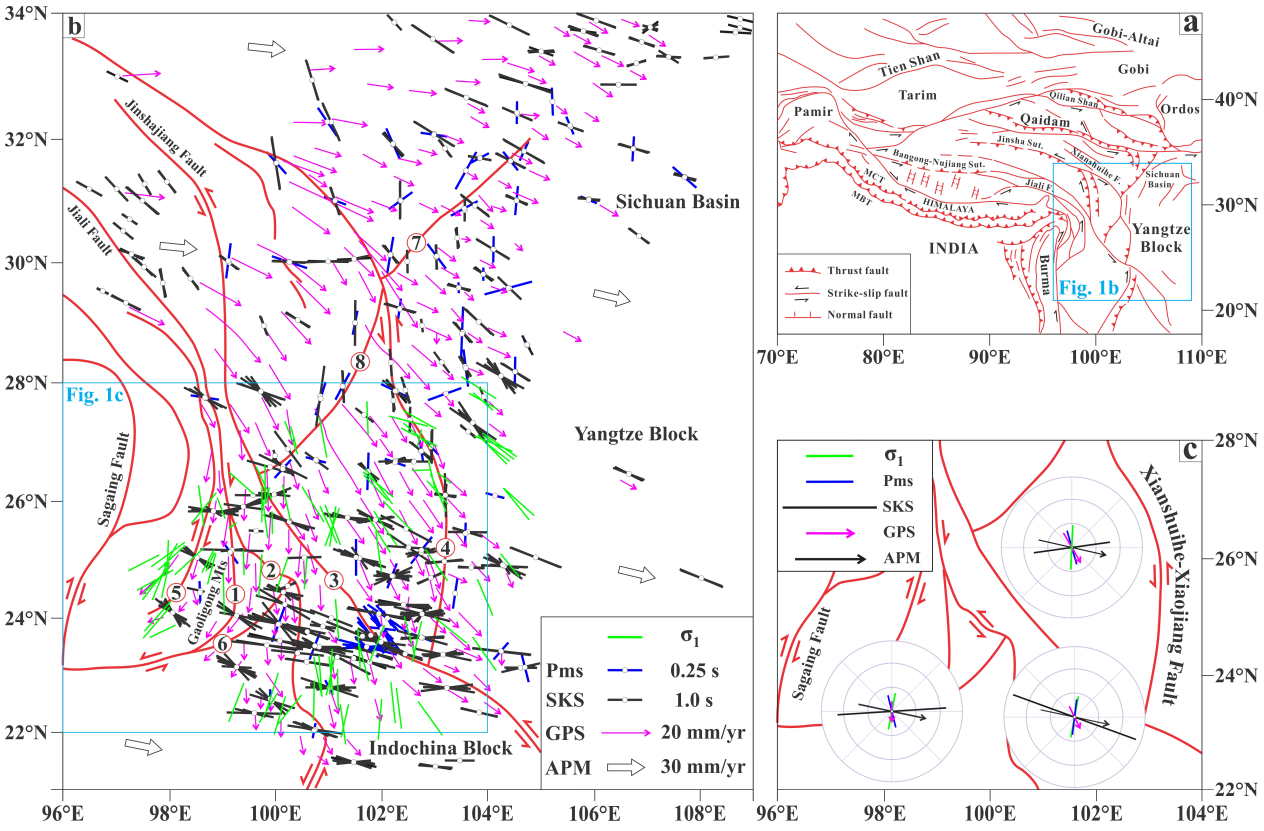


Figure 3.1 (a) Simplified geological map of the Tibetan Plateau and surrounding regions. Blue rectangle refers to Figure 3.1b. (b) Tectonic map of the east Tibetan Plateau and surrounding regions with the vectors of GPS (magenta arrows; Chen et al., 2000; Gan et al., 2007; Zhang et al., 2004), Pms- (blue bars) and XKS- (black bars) wave splitting (Chen et al., 2013; Huang et al., 2007; Lev et al., 2006; Shi et al., 2012; Xu et al., 2006), the maximum principal stress σ_1 (green bars; Wu et al., 2004; Zhao et al., 2013; Zhong and Cheng, 2006), and the APM (thick white arrows; Chen et al., 2013; DeMets et al., 1994). (c) Average orientations of GPS, Pms- and XKS-wave splitting, σ_1, and APM in three tectonic blocks. Red lines show main shear zones or fault zones: (1) Gaoligong shear zone; (2) Lancangjiang shear zone; (3) Ailao Shan-Red River shear zone; (4) Xianshuihe-Xiaojiang fault zone; (5) Nabang fault; (6) Nanting fault; (7) Longmen Shan fault; (8) Lijiang-Xiaojinhe fault. Half arrows refer to Tertiary shear sense.

3.2 Samples

Schists and gneisses, which are dominant in the exhumed middle continental crust (Figure 3.2), consist of flat, sheet-like minerals such as biotite, muscovite, chlorite, sericite, amphibole, talc, and graphite, interleaved with quartz and feldspar (Figure 3.3) and have been considered as typical examples of TI materials with minimum velocities for waves propagating perpendicular to the foliation (e.g., Brocher and Christensen, 1990; Burlini and Fountain, 1993; Cholach and Schmitt, 2006; Dempsey et al., 2011; Godfrey et al., 2000; Ji et al., 2002; Naus-Thijssen et al., 2011a; Shapiro et al., 2004). The word schist, which is derived ultimately from a Greek word meaning "to split" which reflects the ease with which schists can be split along their foliation planes in which the platy minerals lie (Figures 3.2d, 3.3), is a broad term. Phyllites are restricted to those schists with very fine phyllosilicates grains (Figure 3.3e), which usually result from mylonitization of schists. Most schists have been derived from pelitic materials such as clays and muds which have passed through a series of metamorphic processes involving the production of shales, slates, and phyllites as intermediate steps. Certain schists have been derived from fine-grained igneous rocks such as basalts, gabbros, tuffs, and granites. Most schists are mica (biotite, muscovite, or sericite) schists, but chlorite and amphibole schists are also common in orogenic belts (Figure 3.3f). The greenschists containing chlorite, actinolite, epidote, and albite are low grade metamorphic products from mafic igneous rocks or greywacke while the blueschists consisting of blue glaucophane and lawsonite are derived from metamorphism of mafic igneous rock or mafic graywacke at high pressures (corresponding to a depth of 15-30 km) and low temperatures (200-500 °C).

Schist, felsic gneiss, and amphibolite are three major constituents of the southeastern Tibet Plateau (Figures 3.1-3.3), occupying over 95% of the metamorphic terranes of the west Yunnan (i.e., the region of three rivers: Nujiang, Lancangjiang, and Red River). In this region (Figure 3.1), the Gaoligong shear zone (e.g., Ji et al., 2000; Lin et al., 2009; Socquet and Pubellier, 2005; Wang et al., 2008; Zhang et al., 2012), Lancangjiang shear zone (e.g., Akciz et al., 2008; Zhang et al., 2010), and Ailao Shan-Red River shear zone (e.g., Leloup et al., 1995; Tapponnier et al., 1990; Wu et al., 1990) have been the subject of many detailed investigations of the extrusion tectonics resulting from the collision of India with Eurasia (e.g., Dewey et al., 1989; Huchon et al., 1994; Tapponnier et al., 1982). The schists have protoliths ranging from shale, mudstone, and siltstone to mafic volcanics and volcanoclastic sediments which were folded into tight to isoclinal

folds with upright axial surfaces and horizontal to subhorizontal hinge lines (Figure 3.2). Metamorphic grade ranges from greenschist facies to amphibolite facies. The amphibolite-facies metapelitic schists (e.g., sample GLG203) are characterized by the assemblage quartz + muscovite + biotite + garnet + plagioclase ± sillimanite. The amphibolitic gneisses (e.g., sample AM1) occur generally as asymmetrical boudins that were originally joined and then separated along extensional shear zones or synthetic microfaults (R) oriented at ~15° to the foliation-parallel layering. The felsic gneisses and mylonites (e.g., samples GLG14, GLG97-2, and GLG133) were derived from granite, granodiorite, and diorite as well as felsic volcanics by metamorphism, deformation, and dynamic recrystallization. The metamorphic rocks in the west Yunnan are systematically characterized by planar structures such as slaty cleavage, schistosity, and foliation which are roughly vertical (Figure 3.2) with nearly horizontal lineation. Both foliation and lineation are pervasive and consistent at scales from centimeters to hundreds of kilometers.

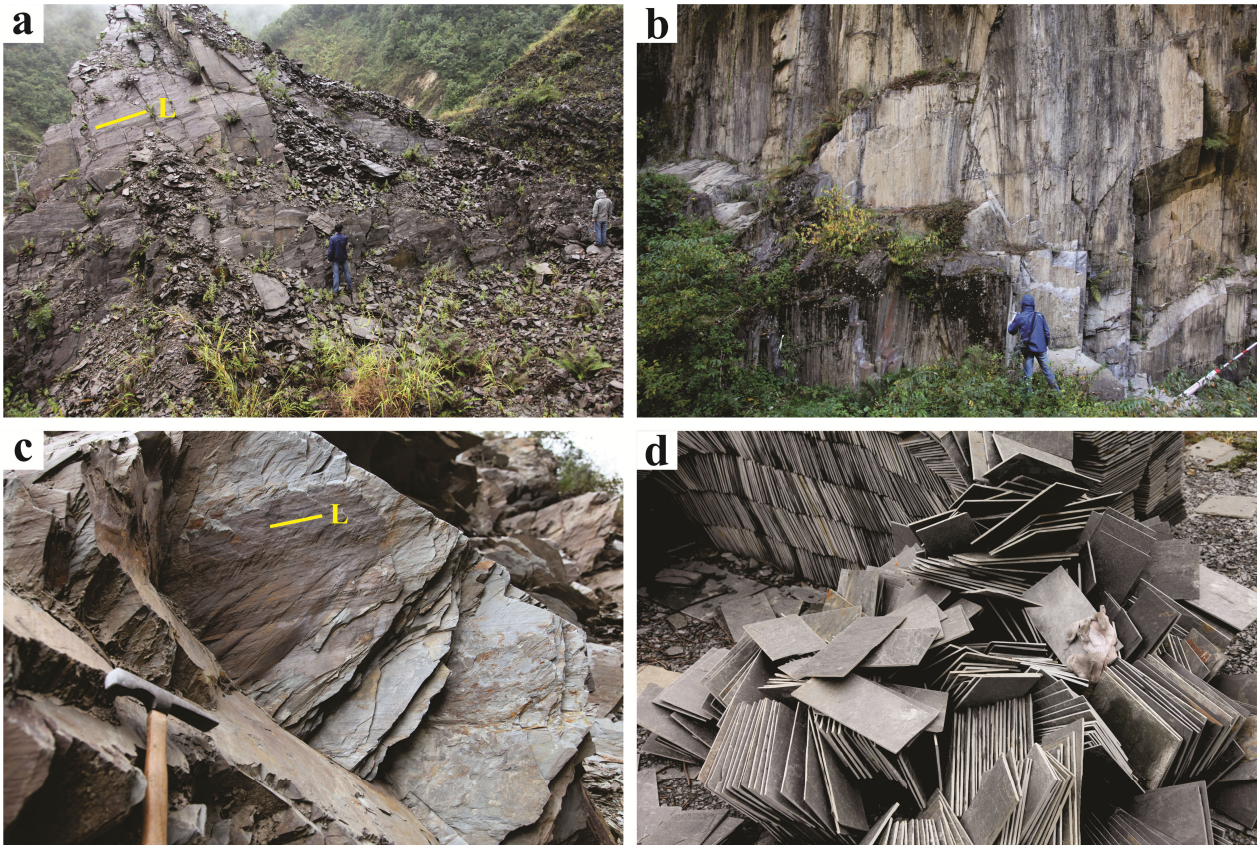


Figure 3.2

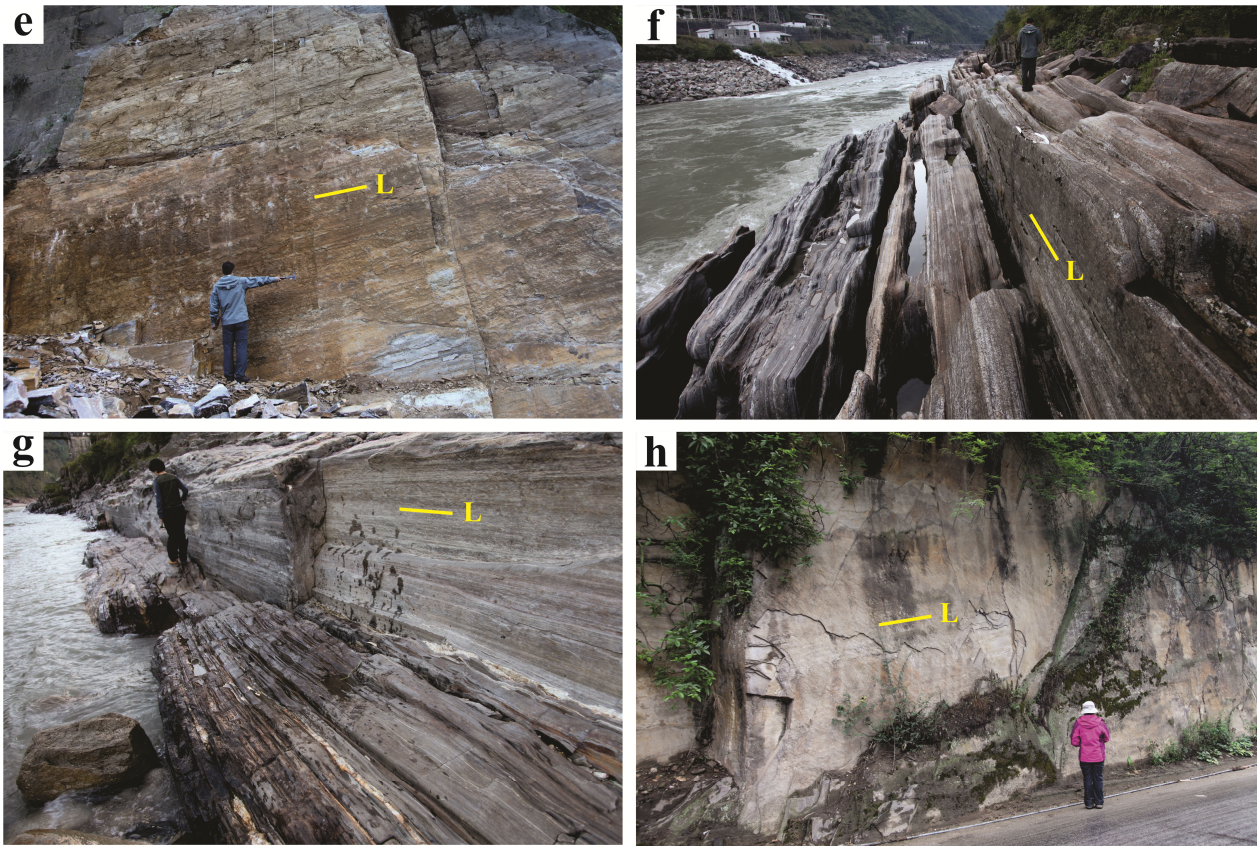


Figure 3.2 Typical phyllosilicate-bearing rocks in the (a-b, e-f) Gaoligong, (c) Ailao Shan-Red River, and (d, g-h) Lancangjiang shear zones, Yunnan, China, where foliation is nearly vertical and stretching lineation is subhorizontal. (a) Chlorite-mica schist at site GLG31 (24°48′47.9″ N, 98°50′02.1″ E, altitude 1523 m). (b) Mica schist developed tight to isoclinal folds with upright axial surface and horizontal hinge line at site GLG 122 (27°55′32.9″ N, 98°39′56″ E, altitude 1543 m). (c) Mica schist at site YN1356 (27°07′10.6″ N, 99°10′11.7″ E, altitude 1514 m). (d) Schist split along its foliation planes in which the mica layers lie. Site YN1373 (25°55′2.5″ N, 99°07′56.6″ E, altitude 1656 m). (e) Mica-bearing dioritic mylonite at site GLG133 (26°49′37.5″ N, 98°53′02.4″ E, altitude 1164 m). (f) Dioritic gneiss and metapelitic schist at site GLG134 (26°48′57.4″ N, 98°53′07.1″ E, altitude 1164 m). (g) Quartz-mica schist at site GLG132 (26°59′5.3″ N, 98°51′50.8″ E, altitude 1204 m). (h) Quartz-mica schist at site YN1389 (26°51′31.3″ N, 98°52′33.6″ E, altitude 1153 m). Lineation is indicated by L.

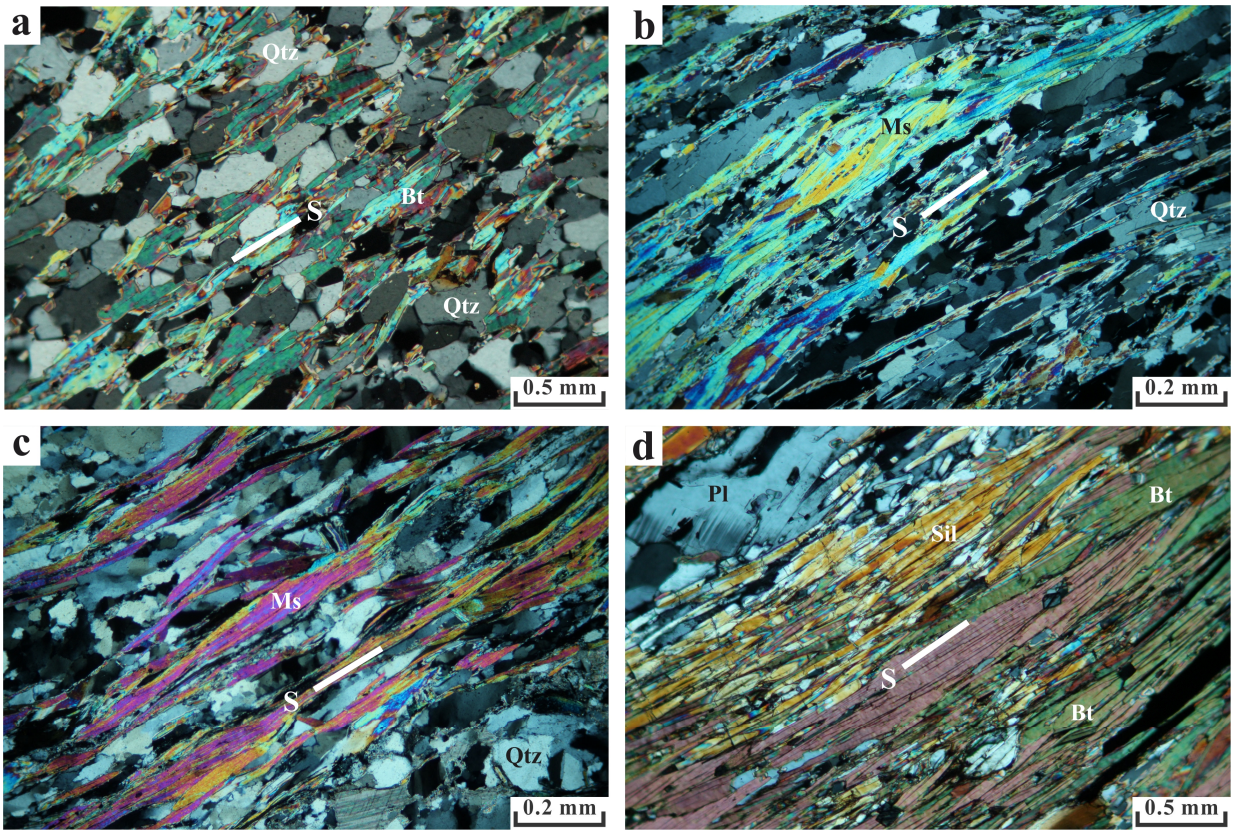


Figure 3.3 Typical microstructures of schists from the Gaoligong, Lancangjiang, and Ailao Shan-Red River shear zones (west Yunnan, China). (a) Biotite-quartz schist from site GLG257 (26°21'12.2" N, 98°49'37.8" E, altitude 1840 m). (b) Muscovite-quartz schist, in which quartz c-axes are preferentially aligned parallel or subparrallel to Y (Figure 3.7c), from site GLG132J. (c) Muscovite-quartz-plagioclase schist from site YN1351 (28°27'42.8" N, 98°54'19.8" E, altitude 2902 m). (d) Metapelitic schist consisting of biotite, sillimanite, quartz, plagioclase and garnet from site GLG203 (26°57'28.3" N, 98°52'03.2" E, altitude 1174 m). (e) Phyllite consisting of fine-grained muscovite, quartz and feldspar from site GLG243 (28°04'58.5" N, 98°33'51.5" E, altitude 1564 m). (f) Amphibole schist consisting of hornblende, plagioclase and quartz from site GLG201 (26°35'43"N, 98°54'41" E, altitude 1181 m). (g) Dioritic mylonite from site GLG133. (h) Quartz-muscovite-biotite schist from site YN1389. Foliation is indicated by S.

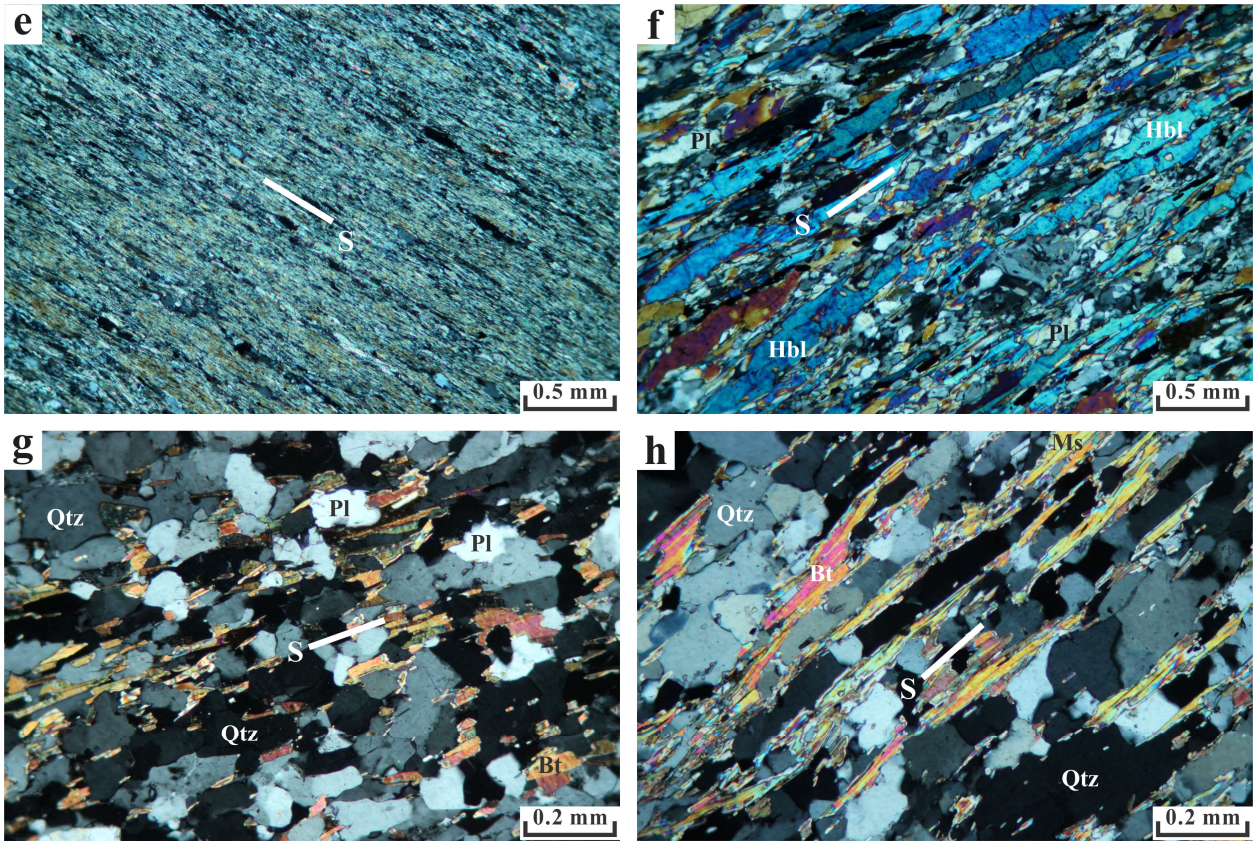


Figure 3.3 Continued

Table 3.1 Description of the mica- or amphibole-bearing rock samples studied

Sample	Measurement	Lithology	Locality	Latitude (°)	Longitude (°)	Modal composition (vol.%)	References for geological setting
Samples from China							
GLG14	Velocity	Granitic gneiss	Gaoligong shear zone, Yunnan	24.9795 N	98.7289 E	Qtz 28.0, Pl 32.0, Kfs 36.0, Bt 3.7, Ap 0.1, Mag 0.2	1, 2
GLG97-2	Velocity	Granitic gneiss	Gaoligong shear zone, Yunnan	26.2868 N	98.8309 E	Qtz 34.0, Pl 31.0, Kfs 33.0, Bt 1.8, Ap 0.1, Mag 0.1	1, 2
GLG102	CPO	Felsic mylonite	Lancangjiang shear zone, Yunnan	26.8760 N	98.8753 E	Qtz 42.8, Pl 23.3, Kfs 29.9, Bt 3.4, Ap 0.4, Mag 0.2	3, 4
GLG110	CPO	Hbl schist	Gaoligong shear zone, Yunnan	27.7144 N	98.7016 E	Qtz 22.4, Pl 34.2, Kfs 18.8, Hbl 22.8, Mag 1.5, Ap 0.3	1, 2
GLG119	CPO	Schist	Gaoligong shear zone, Yunnan	27.7756 N	98.5947 E	Qtz 33.0, Pl 38.0, Kfs 8.0, Bt 20.0, Mag 0.7, Ap 0.3	1, 2
GLG132J	CPO	Schist	Lancangjiang shear zone, Yunnan	26.9848 N	98.8641 E	Qtz 60.0, Fsp 14.0, Bt 10.0, Ms 16.0	3, 4
GLG133	CPO+Velocity	Dioritic mylonite	Lancangjiang shear zone, Yunnan	26.8271 N	98.8840 E	Qtz 50.0, Pl 33.0, Bt 15.0, Grt 2.0	3, 4
GLG134	CPO	Dioritic gneiss	Lancangjiang shear zone, Yunnan	26.8159 N	98.8853 E	Qtz 20.0, Pl 50.0, Bt 30.0	3, 4
AM1	CPO+Velocity	Amphibolitic gneiss	Lancangjiang shear zone, Yunnan	26.7620 N	98.8904 E	Qtz 6.0, Pl 10.0, Bt 4.0, Hbl 80.0	3, 4
GLG201B	CPO	Hbl schist	Lancangjiang shear zone, Yunnan	26.5953 N	98.9114 E	Qtz 30.0, Pl 17.0, Hbl 50.0, Mag 3.0	3, 4
GLG203	CPO+Velocity	Metapelitic schist	Lancangjiang shear zone, Yunnan	26.9579 N	98.8676 E	Qtz 20.0, Fsp 15.0, Bt 42.0, Sil 20.0, Grt 3.0	3, 4
GLG237	CPO+Velocity	Qtz-Hbl-Bt schist	Gaoligong shear zone, Yunnan	27.9591 N	98.6573 E	Qtz 55.0, Bt 30.0, Hbl 15.0	1, 2
GLG257	CPO	Qtz-Bt schist	Gaoligong shear zone, Yunnan	26.3537 N	98.8272 E	Qtz 60.0, Bt 40.0	1, 2
GLG258	CPO+Velocity	Qtz-Bt schist	Gaoligong shear zone, Yunnan	26.3650 N	98.8189 E	Qtz 55.0, Bt 45.0	1, 2
YN1351	CPO	Schist	Ailaoshan-Red River shear zone, Yunnan	28.4619 N	98.9055 E	Qtz 45.0, Fsp 10.0, Ms 35.0, Cal 10.0	5, 6
YN1389	CPO	Qtz-Bt-Ms schist	Lancangjiang shear zone, Yunnan	26.8587 N	98.8760 E	Qtz 67.0, Bt 7.0, Ms 25.0, Mag 1.0	3, 4
YK21A	Velocity	Pl-Bt schist	Yunkai Mts., South China	22.3300 N	111.3480 E	Qtz 6.0, Pl 39.0, Bt 47.0, Opq 4.8, Ap 0.2, Cal 2.0, Ser 1.0	7
Samples from Canada							
P5	Velocity	Qtz-Bt schist	Manitouwadge, ON			Qtz 75.0, Bt 22.0, Sil 3.0	8
S382	Velocity	Qtz-Bt schist	Manitouwadge, ON			Qtz 80.0, Bt 18.0, Sil 2.0	8
S19	Velocity	Qtz-Bt schist	Yellowknife, NT			Qtz 62.0, Kfs 13.0, Bt 25.0	9
CL10	Velocity	Chl schist	Flin Flon, MB			Hbl 15.0, Chl 80.0, Py5.0	10
CL11	Velocity	Ser schist	Flin Flon, MB			Qtz 30.0, Ser 70.0	10
CL12	Velocity	Ser schist	Flin Flon, MB			Qtz 5.0, Ser 93.0, Opq 1.0, Acc 1.0	10
CL13	Velocity	Py-Qtz-Chl schist	Flin Flon, MB			Qtz 35.0, Chl 9.0, Py 56.0	10
CL14	Velocity	Qtz-Ser schist	Flin Flon, MB			Qtz 60.0, Ser 30.0, Py 5.0, Sp 5.0	10
CWH13	Velocity	Ser schist	Tulks Valley, NL			Qtz 20.0, Ser 45.0, Py 15.0, Sp 20.0	11
DL20	Velocity	Qtz-Ser schist	Dessert Lake, NT			Qtz 48.0, Pl 11.0, Ser 32.0, Acc 1.0, Py 8.0	12
AM2	Velocity	Amp schist	Snowbird Shear Zone, SK			Qtz 0.2, Pl 28.9, Hbl 65.0, Opq 0.2, Chl 0.4, Ser 4.2, Acc 1.1	13
AM3	Velocity	Amp schist	Snowbird Shear Zone, SK			Pl 25.3, Hbl 69.2, Opq 3.2, Ser 1.5, Acc 0.8	13
P59	Velocity	Amp schist	God's Lake, MB			Qtz 2.0, Pl 27.5, Hbl 67.0, Opq 1.0, Chl 1.0, Ser 1.0, Acc 0.5	14
S3570	Velocity	Amp schist	Sudbury, ON			Qtz 12.0, Pl 54.0, Bt 13.0, Hbl 18.0, Opq 1.0, Chl 2.0	15
S3530	Velocity	Qtz-Fsp-Bt schist	Sudbury, ON			Qtz 40.0, Pl 20.0, Kfs 29.0, Bt 11.0	15
S776.2	Velocity	Hbl-Bt schist	Noranda, QC			Qtz 42.0, Pl 35.0, Bt 10.0, Hbl 9.0, Chl 4.0	16
S1132.1	Velocity	Qtz-Fsp-Bt schist	Noranda, QC			Qtz 35.0, Pl 5.0, Kfs 32.0, Bt 28.0	16

[a]Mineral symbols and abbreviations according to Whitney and Evans (2010). 1. Socquet and Pubellier (2005); 2. Zhang et al. (2012); 3. Akciz et al. (2008); 4. Zhang et al. (2010); 5. Tapponnier et al. (1990); 6. Leloup et al. (1995); 7. Wang et al. (2007); 8. Peterson and Zaleski (1999); 9. Helmstaedt et al. (1986); 10. Lucas et al. (1999); 11. Zagorevski et al. (2007); 12. Cook et al. (1998); 13. Hanmer et al. (1991); 14. Percival et al. (1992); 15. Milkereit et al. (2000); 16. Bellefleur et al. (2014).

3.3 Laboratory-measured seismic velocities

The analyses presented in this paper were mainly based on P-wave velocities measured experimentally along the X, Y, and Z directions in each of 132 schist and gneiss samples [25 from this study (Table 3.2) and 107 from the references (Barruol and Kern, 1996; Birch, 1960; Brocher et al., 1991; Burlini and Fountain, 1993; Christensen, 1965; Christensen and Okaya, 2007; Fountain, 1976; Fuis et al., 1991; Godfrey et al., 2000; Hughes et al., 1993; Kern and Wenk, 1990; Khazanehdari et al., 2000; McDonough and Fountain, 1988, 1993; Okaya et al., 1995; Punturo et al., 2005; Szymanski and Christensen, 1993)] and S-wave velocities measured for 6 pairs of propagation-vibration directions (XY, XZ, YX, YZ, ZX, and ZY) in each of 35 mica- or amphibole-bearing samples [10 from this study (Table 3.3) and 25 from the references (Barruol and Kern, 1996; Burke, 1991; Burlini and Fountain, 1993; Christensen, 1966; Fountain and Salisbury, 1996)], where the first letter refers to the propagation direction and the second to the polarization direction. Localities, densities, and modal compositions of the 25 samples, collected from metamorphic belts in Canada and China are listed in Table 3.1 along with one or two key references about the geological settings.

Typical V_p-P and V_s-P curves of the schist, gneiss, and mylonite samples measured during depressurization are shown in Figures 3.4 and 3.5, respectively. The curves display a rapid, nonlinear increase in velocity with pressure at low pressures (generally <200 MPa) and then increase slowly and linearly in velocity at high pressures. The seismic properties obtained at P=300-600 MPa, corresponding approximately to depths of 11-22 km, assuming an average density of 2.8 g/cm^3 for the crustal rocks, can be extrapolated to higher pressures unless metamorphic reactions, phase transition, or partial melting take place. Both the P- and S-wave velocities as a function of pressure were fitted to Eq. (2.1). Parameters V_0, D, B_0, and k and their standard deviations determined for V_p and V_s as a function of propagation and polarization directions for each sample during depressurization are given in Tables 3.2 and 3.3, respectively.

As shown in Figures 3.4 and 3.5, the schists (samples GLG237 and GLG258) are characterized by $V_p(X)>V_p(Y)\gg V_p(Z)$. These schists display a velocity symmetry deviating somewhat from TI but seismic anisotropy in the foliation plane (XY plane) is smaller than that in the YZ plane and particularly the XZ plane. The felsic mylonites (e.g., sample GLG133) display much smaller velocity anisotropy (Table 3.2) or shear-wave splitting (Table 3.3) than mica-rich schists (e.g.,

samples GLG237 and GLG258) and amphibolitic gneiss (e.g., sample AM1, Figures 3.4d and 3.5d). The amphibolitic gneiss is typical of orthorhombic velocity symmetry (Barberini et al., 2007; Barruol and Mainprice, 1993a; Ji et al., 1993, 2013b; Tatham et al., 2008). The shear-wave birefringence (ΔV_S) in the schists (e.g., samples GLG237 and GLG258) typically shows: $\Delta V_S(X) > \Delta V_S(Y) \gg \Delta V_S(Z) \approx 0$. Taking sample GLG237 as an example, $\Delta V_S(X)$=0.39 km/s, $\Delta V_S(Y)$=0.24 km/s, and $\Delta V_s(Z)$=0.02 km/s at 600 MPa (Figure 3.5a). For the amphibolitic gneiss (sample AM1), however, the maximum, intermediate, and minimum birefringence values occur in Y, Z, and X directions, respectively (Figure 3.5d). At 600 MPa, $\Delta V_S(Y)$=0.33 km/s, $\Delta V_S(Z)$=0.20 km/s, and $\Delta V_S(X)$=0.01 km/s, indicating almost no splitting for the propagation along the stretching lineation direction.

Table 3.2 Parameters of V_p-P curves and V_p anisotropy for 25 schist, gneiss and mylonite samples studied

Sample	Density	λ[a]	V_0	S.D.	D	S.D.	B_0	S.D.	k	S.D.	R^2	Mean V_p (km/s)	A_p (%)
	g/cm^3		(km/s)		(10^{-4} km/s/MPa)		(km/s)		(10^{-2} MPa^{-1})			600 MPa	
Samples from China													
AM1	3.061	X	7.386	0.016	2.447	0.439	0.453	0.020	2.525	0.277	0.996	6.977	14.5
AM1		Y	6.777	0.017	2.265	0.468	0.442	0.020	2.425	0.281	0.995		
AM1		Z	6.292	0.008	3.841	0.214	0.268	0.009	2.402	0.208	0.999		
AM1		Mean	6.818	0.014	2.851	0.374	0.388	0.016	2.451	0.255	0.997		
GLG133	2.651	X	5.928	0.032	3.560	0.510	0.796	0.039	2.178	0.261	0.995	6.071	7.2
GLG133		Y	6.086	0.023	2.872	0.362	1.042	0.029	2.237	0.149	0.998		
GLG133		Z	5.668	0.041	2.539	0.612	0.640	0.042	1.821	0.294	0.991		
GLG133		Mean	5.894	0.032	2.990	0.495	0.826	0.037	2.079	0.235	0.995		
GLG14	2.599	X	5.515	0.033	3.126	0.455	1.256	0.039	4.192	0.315	0.997	5.663	3.8
GLG14		Y	5.521	0.037	3.869	0.507	1.229	0.041	4.062	0.338	0.998		
GLG14		Z	5.307	0.039	3.829	0.508	1.335	0.034	4.081	0.235	0.999		
GLG14		Mean	5.448	0.036	3.608	0.490	1.273	0.038	4.112	0.296	0.998		
GLG97-2	2.595	X	5.497	0.117	3.194	1.411	1.028	0.091	2.902	0.617	0.989	5.677	0.4
GLG97-2		Y	5.399	0.113	4.434	1.333	1.372	0.089	2.720	0.393	0.996		
GLG97-2		Z	5.448	0.118	3.834	1.398	1.744	0.092	2.794	0.339	0.996		
GLG97-2		Mean	5.448	0.116	3.821	1.381	1.381	0.091	2.805	0.450	0.994		
GLG203	2.771	X	6.180	0.010	2.350	0.230	0.383	0.012	2.319	0.186	0.999	5.785	18.6
GLG203		Y	5.645	0.106	3.259	0.777	1.110	0.103	1.630	0.366	0.987		
GLG203		Z	5.040	0.086	3.419	0.629	0.776	0.083	1.611	0.413	0.988		
GLG203		Mean	5.622	0.067	3.009	0.545	0.756	0.066	1.853	0.322	0.991		
YK21A	2.853	X	6.124	0.002	1.207	0.037	0.523	0.002	1.423	0.014	1.000	6.004	7.8
YK21A		Y	5.992	0.003	1.819	0.059	0.415	0.004	1.235	0.023	1.000		
YK21A		Z	5.627	0.002	1.639	0.030	0.458	0.002	1.443	0.013	1.000		
YK21A		Mean	5.915	0.002	1.555	0.042	0.465	0.003	1.367	0.016	1.000		
GLG258	2.757	X	6.297	0.021	2.328	0.254	1.233	0.029	2.487	0.143	0.998	5.932	20.7
GLG258		Y	6.058	0.066	2.844	0.501	1.093	0.068	1.783	0.276	0.992		
GLG258		Z	5.019	0.049	3.143	0.381	1.201	0.057	2.086	0.244	0.995		
GLG258		Mean	5.791	0.045	2.772	0.379	1.176	0.051	2.119	0.221	0.995		
GLG237	2.768	X	6.283	0.076	2.939	0.926	1.429	0.108	2.550	0.467	0.985	6.158	12.1
GLG237		Y	6.125	0.031	3.353	0.370	1.652	0.039	2.292	0.134	0.998		
GLG237		Z	5.477	0.095	3.952	1.077	1.582	0.099	1.814	0.280	0.991		
GLG237		Mean	5.962	0.067	3.415	0.791	1.554	0.082	2.219	0.294	0.991		
Samples from Canada													
S3570	2.917	X	6.833	0.008	1.750	0.132	0.798	0.022	2.699	0.130	0.996	6.395	17.4
S3570		Y	6.337	0.008	2.250	0.129	0.962	0.039	4.653	0.282	0.994		
S3570		Z	5.673	0.011	2.500	0.177	1.960	0.069	5.462	0.265	0.995		
S3570		Mean	6.281	0.009	2.167	0.146	1.240	0.043	4.271	0.225	0.995		

[a]Direction of P-wave propagation.

Table 3.2 Continued

Sample	Density	λ[a]	V_0	S.D.	D	S.D.	B_0	S.D.	k	S.D.	R^2	Mean V_p (km/s)	A_p (%)
	g/cm^3		(km/s)		(10^{-4} km/s/MPa)		(km/s)		(10^{-2} MPa^{-1})			600 MPa	
Samples from Canada													
AM2	3.000	X	7.357	0.008	0.750	0.211	0.350	0.020	3.724	0.407	0.986	7.029	10.9
AM2		Y	6.983	0.010	1.500	0.243	0.375	0.014	2.305	0.192	0.994		
AM2		Z	6.513	0.011	2.000	0.247	0.385	0.013	1.881	0.138	0.996		
AM2		Mean	6.951	0.010	1.417	0.233	0.370	0.016	2.637	0.246	0.992		
AM3	3.020	X	7.383	0.006	1.250	0.134	0.119	0.007	1.876	0.244	0.993	7.033	10.6
AM3		Y	6.877	0.004	1.250	0.090	0.153	0.005	2.238	0.165	0.997		
AM3		Z	6.650	0.004	1.000	0.098	0.269	0.007	2.695	0.138	0.997		
AM3		Mean	6.970	0.005	1.167	0.107	0.180	0.006	2.270	0.182	0.996		
P59	2.893	X	7.280	0.006	2.250	0.136	0.272	0.008	2.438	0.162	0.997	7.048	10.4
P59		Y	6.943	0.003	2.000	0.083	0.229	0.005	2.314	0.107	0.999		
P59		Z	6.550	0.011	2.250	0.263	0.519	0.017	2.477	0.168	0.996		
P59		Mean	6.924	0.007	2.167	0.161	0.340	0.010	2.410	0.146	0.997		
CL10	3.150	X	7.365	0.018	2.786	0.474	1.357	0.057	4.353	0.320	0.993	7.171	10.1
CL10		Y	7.055	0.090	2.286	1.963	0.382	0.087	1.385	0.711	0.900		
CL10		Z	6.620	0.028	3.143	0.624	0.708	0.029	1.559	0.144	0.995		
CL10		Mean	7.013	0.045	2.738	1.020	0.816	0.058	2.432	0.392	0.963		
S776.2	3.010	X	6.973	0.027	4.214	0.681	0.984	0.051	2.982	0.313	0.990	6.809	15.0
S776.2		Y	6.868	0.018	2.929	0.442	1.404	0.086	3.616	0.270	0.993		
S776.2		Z	6.005	0.012	3.286	0.291	1.737	0.044	3.102	0.106	0.999		
S776.2		Mean	6.615	0.019	3.476	0.471	1.375	0.060	3.233	0.230	0.994		
S19	2.707	X	6.423	0.010	2.214	0.212	0.317	0.009	1.200	0.076	0.999	6.116	12.3
S19		Y	5.950	0.016	1.071	0.369	0.516	0.018	1.652	0.128	0.995		
S19		Z	5.680	0.018	2.071	0.362	0.366	0.016	1.120	0.101	0.998		
S19		Mean	6.018	0.015	1.786	0.315	0.400	0.014	1.324	0.102	0.997		
P5	2.660	X	6.420	0.010	3.250	0.155	0.574	0.028	3.002	0.254	0.993	6.332	9.4
P5		Y	6.167	0.008	3.500	0.120	0.626	0.022	3.050	0.185	0.996		
P5		Z	5.763	0.006	4.250	0.088	0.949	0.012	2.226	0.055	0.999		
P5		Mean	6.117	0.008	3.667	0.121	0.716	0.021	2.759	0.165	0.996		
S382	2.653	X	6.170	0.006	3.250	0.095	0.849	0.014	2.458	0.077	0.999	6.146	7.9
S382		Y	6.023	0.007	3.000	0.114	0.751	0.017	2.371	0.098	0.998		
S382		Z	5.670	0.007	3.500	0.108	0.769	0.017	2.540	0.101	0.998		
S382		Mean	5.954	0.007	3.250	0.106	0.789	0.016	2.457	0.092	0.998		
S3530	2.930	X	7.033	0.009	2.250	0.136	0.910	0.023	2.796	0.125	0.996	6.563	17.5
S3530		Y	6.417	0.003	2.250	0.053	1.290	0.020	5.406	0.117	0.999		
S3530		Z	5.853	0.017	2.750	0.279	1.336	0.064	3.794	0.297	0.988		
S3530		Mean	6.434	0.010	2.417	0.156	1.179	0.036	3.999	0.180	0.995		
S1132.1	2.720	X	6.003	0.032	2.214	0.782	0.604	0.047	2.337	0.391	0.975	5.878	11.1
S1132.1		Y	5.903	0.037	2.214	0.933	1.379	0.070	2.994	0.308	0.986		
S1132.1		Z	5.300	0.009	3.071	0.190	0.324	0.009	1.334	0.089	0.999		
S1132.1		Mean	5.735	0.026	2.500	0.635	0.769	0.042	2.222	0.263	0.987		
CL14	3.150	X	6.268	0.034	3.000	0.611	0.225	0.024	0.894	0.259	0.995	6.085	12.4
CL14		Y	6.065	0.011	1.286	0.254	0.846	0.105	2.903	0.307	0.992		
CL14		Z	5.605	0.030	1.429	0.584	0.463	0.024	1.064	0.163	0.995		
CL14		Mean	5.979	0.025	1.905	0.483	0.511	0.051	1.620	0.243	0.994		
DL20	3.030	X	6.793	0.005	1.643	0.116	0.191	0.006	1.930	0.137	0.998	6.543	10.0
DL20		Y	6.460	0.022	1.000	0.473	0.451	0.033	1.394	0.225	0.991		
DL20		Z	6.073	0.047	2.714	1.154	0.743	0.075	2.552	0.540	0.958		
DL20		Mean	6.442	0.025	1.786	0.581	0.462	0.038	1.959	0.301	0.982		
CWH13	3.867	X	6.515	0.025	6.857	0.609	2.271	0.075	2.737	0.134	0.998	6.921	4.2
CWH13		Y	6.698	0.053	6.143	1.082	0.652	0.046	1.137	0.198	0.995		
CWH13		Z	6.347	0.056	7.143	1.154	1.466	0.051	1.226	0.105	0.998		
CWH13		Mean	6.520	0.045	6.714	0.948	1.463	0.057	1.700	0.146	0.997		
CL11	2.850	X	7.210	0.031	1.500	0.570	0.544	0.046	1.057	0.191	0.996	6.948	8.4
CL11		Y	6.653	0.039	3.214	0.753	0.463	0.031	1.093	0.221	0.994		
CL11		Z	6.477	0.016	3.929	0.328	0.282	0.015	1.151	0.173	0.998		
CL11		Mean	6.780	0.029	2.881	0.551	0.430	0.031	1.100	0.195	0.996		
CL12	2.790	X	7.123	0.015	3.143	0.355	0.695	0.022	2.405	0.162	0.996	6.884	15.7
CL12		Y	7.055	0.012	1.786	0.250	0.697	0.180	1.981	0.354	0.994		
CL12		Z	5.990	0.000	4.000	0.000					1.000		
CL12		Mean	6.723	0.009	2.976	0.202	0.696	0.101	2.193	0.258	0.997		
CL13	3.070	X	6.728	0.014	2.929	0.305	0.543	0.015	1.367	0.089	0.998	6.225	27.1
CL13		Y	6.450	0.024	4.143	0.545	0.739	0.027	1.760	0.144	0.996		
CL13		Z	5.083	0.002	2.250	0.048					0.997		
CL13		Mean	6.087	0.013	3.107	0.299	0.641	0.021	1.563	0.117	0.997		

Table 3.3 Parameters of V_s-P curves and V_s anisotropy for 10 mica- or amphobole-bearing samples studied

Sample	Density	λ[a]	V_0	S.D.	D	S.D.	B_0	S.D.	k	S.D.	R^2	Mean V_s (km/s)	A_s (%)
	g/cm^3		(km/s)		(10^{-4} km/s/MPa)		(km/s)		(10^{-2} MPa^{-1})			600 MPa	
Sample from China													
AM1	3.061	XY	4.230	0.020	0.906	0.519	0.216	0.019	1.895	0.432	0.982	4.063	11.4
AM1		XZ	4.180	0.018	1.524	0.484	0.305	0.020	2.255	0.382	0.989		
AM1		YX	4.081	0.005	1.494	0.116	0.137	0.007	2.884	0.365	0.996		
AM1		YZ	3.748	0.016	1.578	0.454	0.274	0.035	2.568	0.598	0.984		
AM1		ZX	3.880	0.031	2.271	0.773	0.248	0.032	1.718	0.559	0.983		
AM1		ZY	3.708	0.017	1.887	0.449	0.294	0.019	2.222	0.356	0.992		
AM1		Mean	3.971	0.018	1.610	0.466	0.246	0.022	2.257	0.449	0.988		
GLG133	2.651	XY	3.673	0.007	4.878	0.191	0.923	0.015	2.784	0.088	0.998	3.791	7.4
GLG133		XZ	3.480	0.004	4.626	0.109	0.812	0.010	3.146	0.070	0.999		
GLG133		YX	3.714	0.006	3.836	0.165	0.985	0.015	3.003	0.081	0.998		
GLG133		YZ	3.497	0.006	3.675	0.178	0.986	0.016	3.041	0.090	0.998		
GLG133		ZX	3.517	0.004	2.866	0.116	0.966	0.011	3.230	0.066	0.999		
GLG133		ZY	3.496	0.007	3.134	0.210	0.933	0.018	2.860	0.101	0.997		
GLG133		Mean	3.563	0.006	3.836	0.162	0.934	0.014	3.011	0.083	0.998		
GLG14	2.599	XY	3.492	0.028	2.143	0.576	0.699	0.022	3.020	0.238	0.998	3.522	6.7
GLG14		XZ	3.299	0.018	2.990	0.388	0.650	0.015	3.446	0.217	0.999		
GLG14		YX	3.391	0.020	2.714	0.414	0.677	0.016	3.327	0.209	0.999		
GLG14		YZ	3.385	0.028	3.105	0.585	0.735	0.022	3.190	0.253	0.998		
GLG14		ZX	3.242	0.020	2.362	0.421	0.645	0.016	3.089	0.196	0.999		
GLG14		ZY	3.343	0.030	3.143	0.657	0.814	0.027	3.539	0.308	0.997		
GLG14		Mean	3.359	0.024	2.743	0.507	0.703	0.020	3.269	0.237	0.998		
GLG97-2	2.595	XY	3.345	0.078	3.371	1.570	0.578	0.061	2.880	0.724	0.986	3.525	3.5
GLG97-2		XZ	3.353	0.070	2.000	1.376	0.596	0.055	2.717	0.559	0.989		
GLG97-2		YX	3.430	0.067	2.524	1.350	0.711	0.052	2.925	0.519	0.991		
GLG97-2		YZ	3.353	0.066	3.762	1.283	0.750	0.052	2.681	0.405	0.995		
GLG97-2		ZX	3.326	0.064	2.181	1.282	0.891	0.050	2.852	0.378	0.994		
GLG97-2		ZY	3.301	0.041	3.581	0.843	0.884	0.032	2.990	0.271	0.998		
GLG97-2		Mean	3.351	0.064	2.903	1.284	0.735	0.050	2.841	0.476	0.992		
GLG203	2.771	XY	3.712	0.022	4.582	0.499	0.334	0.023	1.869	0.320	0.995	3.667	14.2
GLG203		XZ	3.201	0.023	5.264	0.536	0.448	0.026	1.994	0.286	0.995		
GLG203		YX	3.660	0.052	5.502	1.170	0.563	0.052	1.685	0.376	0.988		
GLG203		YZ	3.188	0.060	6.525	1.321	0.548	0.058	1.593	0.402	0.988		
GLG203		ZX	3.223	0.029	4.080	0.683	0.689	0.034	2.126	0.258	0.994		
GLG203		ZY	3.236	0.037	4.463	0.840	0.633	0.038	1.786	0.263	0.993		
GLG203		Mean	3.370	0.037	5.069	0.842	0.536	0.039	1.842	0.318	0.992		
YK21A	2.853	XY	3.522	0.001	0.898	0.015	0.234	0.001	2.420	0.025	1.000	3.350	13.1
YK21A		XZ	3.166	0.001	1.490	0.020	0.249	0.002	2.886	0.040	1.000		
YK21A		YX	3.543	0.001	0.589	0.016	0.198	0.001	2.912	0.041	1.000		
YK21A		YZ	3.064	0.001	1.228	0.022	0.288	0.002	2.771	0.036	1.000		
YK21A		ZX	3.203	0.003	2.783	0.048	1.047	0.003	1.846	0.012	1.000		
YK21A		ZY	3.129	0.001	1.385	0.029	0.223	0.003	4.096	0.109	0.999		
YK21A		Mean	3.271	0.001	1.396	0.025	0.373	0.002	2.822	0.044	1.000		
GLG258	2.744	XY	3.946	0.017	2.478	0.404	0.716	0.021	2.319	0.172	0.997	3.393	29.4
GLG258		XZ	2.978	0.021	2.968	0.496	0.552	0.024	2.002	0.224	0.996		
GLG258		YX	3.747	0.017	2.963	0.402	0.432	0.019	1.961	0.215	0.996		
GLG258		YZ	2.863	0.021	4.428	0.480	0.379	0.023	1.950	0.302	0.995		
GLG258		ZX	2.913	0.015	3.238	0.367	0.515	0.018	2.126	0.188	0.997		
GLG258		ZY	2.873	0.022	3.718	0.499	0.370	0.024	1.900	0.306	0.994		
GLG258		Mean	3.220	0.019	3.299	0.441	0.494	0.022	2.043	0.235	0.996		
GLG237	2.766	XY	3.812	0.020	2.009	0.480	0.952	0.028	2.467	0.174	0.997	3.632	15.3
GLG237		XZ	3.350	0.021	3.223	0.500	1.069	0.027	2.315	0.143	0.998		
GLG237		YX	3.767	0.019	2.398	0.458	0.777	0.025	2.278	0.177	0.997		
GLG237		YZ	3.503	0.038	2.799	0.885	1.106	0.044	2.107	0.209	0.995		
GLG237		ZX	3.195	0.034	3.368	0.773	0.565	0.036	1.809	0.283	0.991		
GLG237		ZY	3.217	0.017	2.646	0.386	0.505	0.019	2.041	0.189	0.997		
GLG237		Mean	3.474	0.025	2.741	0.580	0.829	0.030	2.170	0.196	0.996		

aThe propagation-polarization information with the first letter referring to the propagation direction and the second to the polarization direction.

Table 3.3 Continued

Sample	Density g/cm^3	λ[a]	V_0 (km/s)	S.D.	D (10^{-4} km/s/MPa)	S.D.	B_0 (km/s)	S.D.	k (10^{-2} MPa^{-1})	S.D.	R^2	Mean V_s (km/s) 600 MPa	A_s (%) 600 MPa
Sample from Canada													
AM2	3.000	XY	4.177	0.008	0.750	0.167	0.080	0.007	1.297	0.263	0.989	3.986	10.5
AM2		XZ	3.817	0.002	1.750	0.056	0.102	0.004	2.582	0.195	0.998		
AM2		YX	4.120	0.003	1.000	0.077	0.085	0.004	1.973	0.210	0.996		
AM2		YZ	3.743	0.003	1.000	0.071	0.126	0.004	1.916	0.125	0.998		
AM2		ZX	3.857	0.004	1.250	0.103	0.114	0.006	2.139	0.237	0.995		
AM2		ZY	3.783	0.003	1.500	0.063	0.101	0.003	1.874	0.134	0.999		
AM2		Mean	3.916	0.004	1.208	0.089	0.101	0.005	1.963	0.194	0.996		
AM3	3.020	XY	4.080	0.001	1.000	0.029	0.040	0.002	2.744	0.281	0.998	3.994	7.7
AM3		XZ	3.960	0.003	1.000	0.066	0.047	0.003	1.623	0.245	0.996		
AM3		YX	4.090	0.002	0.500	0.052	0.060	0.003	1.715	0.163	0.996		
AM3		YZ	3.840	0.003	0.500	0.074	0.059	0.004	1.862	0.267	0.990		
AM3		ZX	3.930	0.002	1.000	0.050	0.085	0.003	2.130	0.154	0.998		
AM3		ZY	3.787	0.004	0.750	0.090	0.121	0.004	1.767	0.148	0.996		
AM3		Mean	3.948	0.003	0.792	0.060	0.069	0.003	1.974	0.209	0.996		

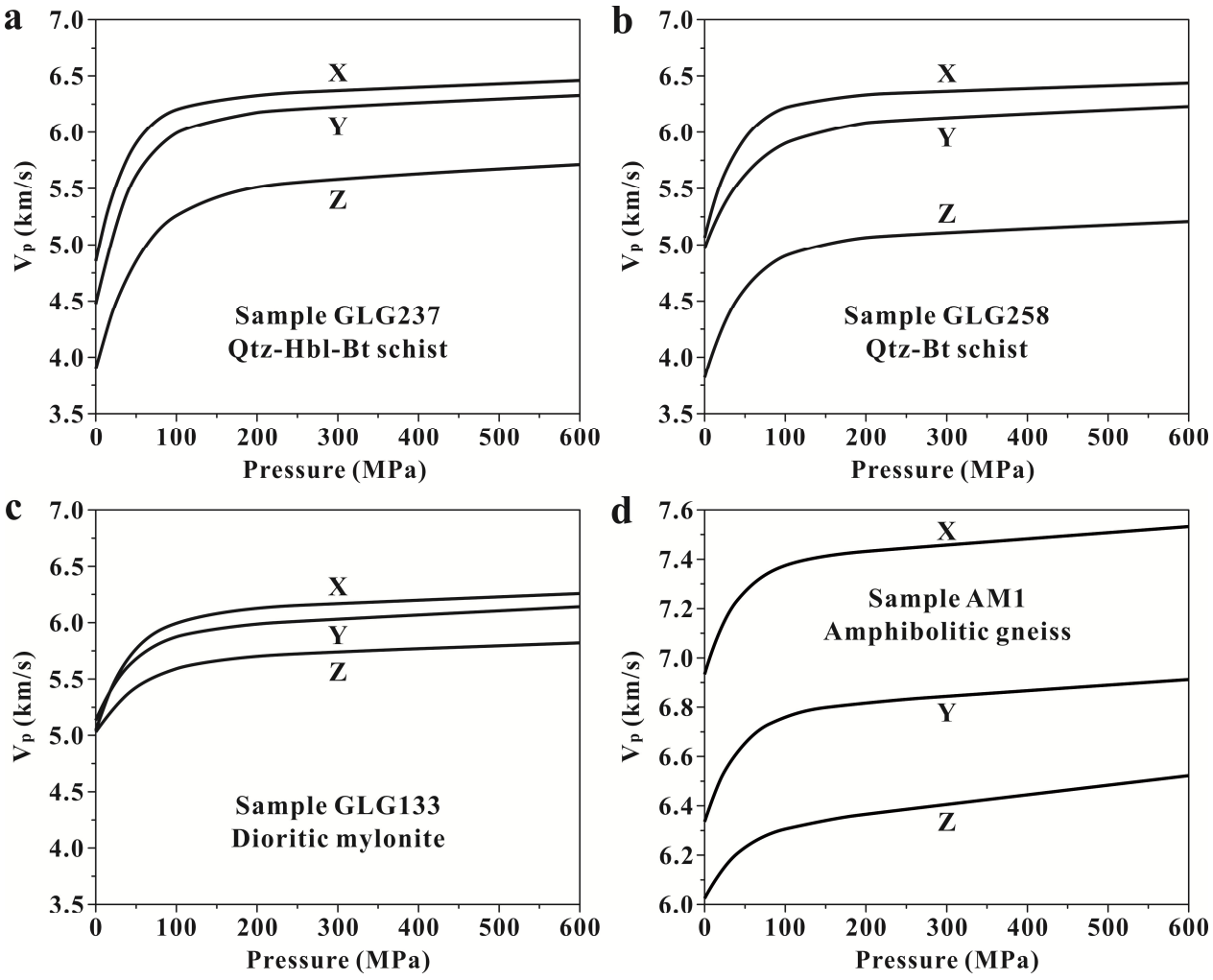


Figure 3.4 P-wave velocity (V_p) versus pressure in three orthogonal directions (X, Y, and Z) through samples (a) GLG237 (Qtz-Hbl-Bt schist), (b) GLG258 (Qtz-Bt schist), (c) GLG133 (dioritic mylonite), and (d) AM1 (amphibolitic gneiss).

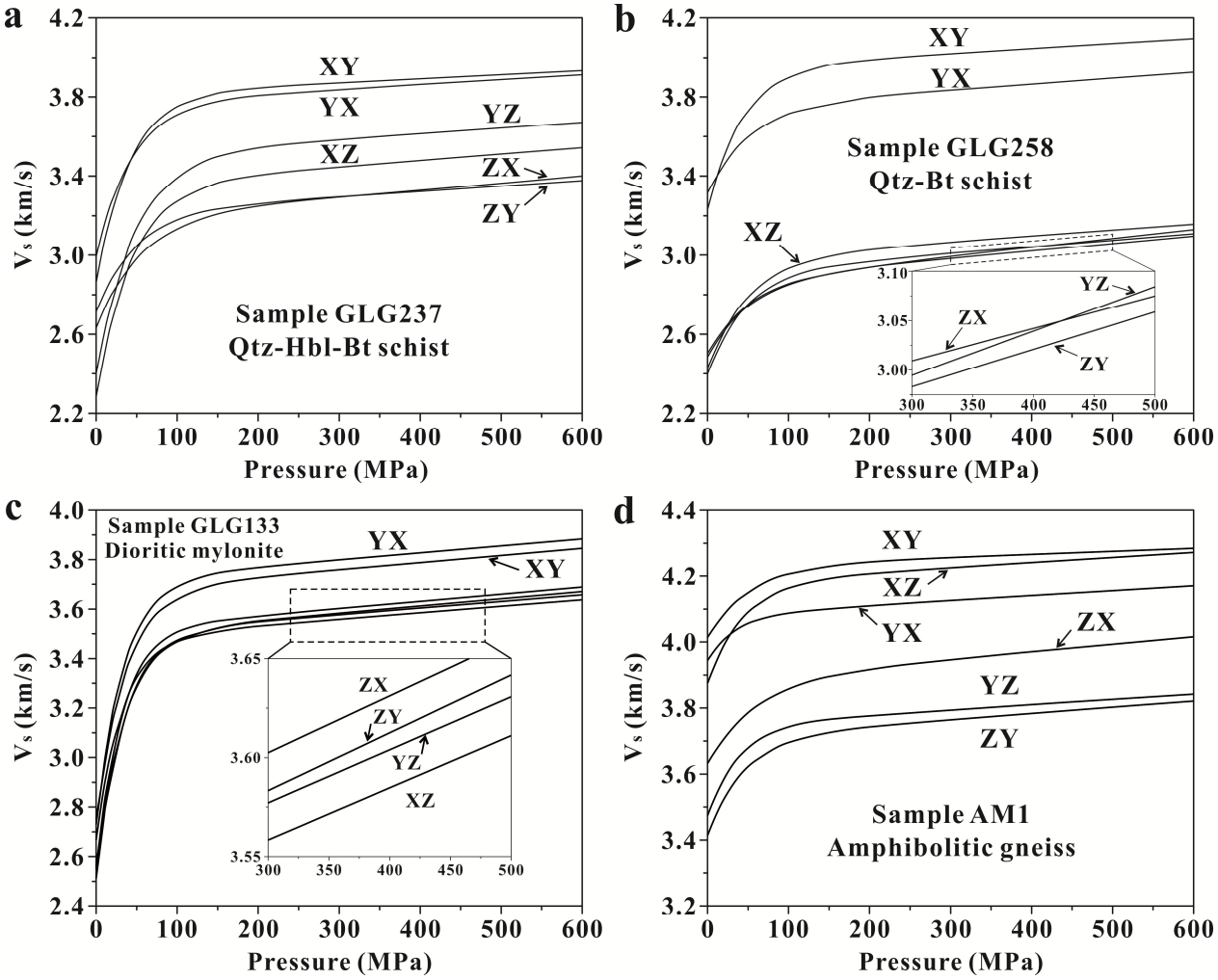


Figure 3.5 S-wave velocity (V_s) versus propagation and polarization directions in samples (a) GLG237 (Qtz-Hbl-Bt schist), (b) GLG258 (Qtz-Bt schist), (c) GLG133 (dioritic mylonite), and (d) AM1 (amphibolitic gneiss). The first letter signifies propagation direction and the second letter the polarization direction.

3.4 EBSD-measured CPO and calculated seismic velocities

As shown in Figure 3.6, biotite and muscovite from the same samples generally display very similar CPO patterns: the [001] directions of mica display a strong, single concentration parallel or subparallel to Z in the schists (samples GLG119, GLG132J, GLG203, GLG237, GLG257, GLG258, YN1351, and YN1389), felsic gneiss (sample GLG134) and mylonites (samples GLG102 and GLG133). Mica (100) poles lie in the foliation plane with the maximum concentrations around the X lineation (samples GLG102, GLG119, and GLG133) or the Y direction (samples GLG132J, GLG203, GLG237, and GLG257). The poles to (010) of mica are

also located in the foliation plane with the maximum concentrations at X (samples GLG132J, GLG203, GLG237, and GLG257) or Y (samples GLG102, GLG119, and GLG133). For samples GLG134, GLG258, YN1351, and YN1389, however, the poles to (100) or (010) are aligned almost equally to X and Y. It is interesting to note that the *pfJ* index for mica (001) is about 3.1 and 2.8 times as high as those for mica (100) and (010), respectively, in each sample. The *pfJ* index for (010) is only about 1.1 times as high as that for (100) in each sample.

Both biotite and muscovite consist of sheets of linked $(Si,Al)O_4$ tetrahedra bounding a layer of octahedrally coordinated cations. Their unit cell dimensions are characterized by the longest c-, intermediate b-, and shortest a-axes: a=5.30 Å, b=9.20 Å, and c=10.20 Å for biotite and a=5.19 Å, b=9.04 Å, and c=9.98 Å for muscovite (Deer et al., 1992). Only basal slip is active in either mica because the easiest glide plane is (001) which intersects the smallest number of strong bonds per unit area. Theoretically speaking, the easiest slip direction in mica should be [100] since this direction forms the shortest Burgers vector with which dislocations have the lowest energy and are thus the most stable. The [100](001) glide was dominant in the formation of mica CPO observed in samples GLG102, GLG119, and GLG133. However, the mica CPO patterns in samples GLG132J, GLG203, GLG237, and GLG257 suggest the dominance of dislocation glide using the 1/2[010](001) system. Furthermore, samples GLG134, GLG258, YN1351, and YN1389 indicate that mica deformed by simultaneous dislocation glide confined to the (001) plane with Burgers vectors [100], 1/2[010], and probably also 1/2[110] and 1/2[$\bar{1}$10]. These slip systems have been observed previously in experimentally deformed mica (e.g., Christoffersen and Kronenberg, 1993; Meike, 1989). The dominant a slip fabric has been reported for biotite in deformed rocks from the Basin and Range (e.g., Erdman et al., 2013). The dominant b slip fabric was reported for muscovite in a quartzite [sample CB-q, 95 vol.% quartz, 3 vol.% muscovite, and 2 vol.% kyanite (Ward et al., 2012)]. The a+b slip-induced fabric pattern was reported for biotite in quartzofeldspathic gneisses from the exhuming Papua New Guinea ultrahigh pressure terrane (Brownlee et al., 2011) and for a quartz-bearing amphibolite (sample GR-a), and muscovite in a quartzite (sample ISR-q consisting of 95 vol.% quartz, 3 vol.% muscovite, and 2 vol.% sillimanite) (Ward et al., 2012).

Quartz fabric patterns (Figure 3.7) vary considerably. In five samples (GLG102, GLG132J, GLG134, GLG203, and YN1389), quartz has a strong concentration of c-axes at Y while the a-axis is aligned parallel or subparallel to X, indicative of prism <a> slip (Mainprice and Casey,

1990; Zhao et al., 1997). In four samples (GLG110, GLG119, GLG237, and GLG258), quartz a-axis forms a broad partial girdle perpendicular to the stretching lineation whereas quartz c-axis has concentrations subparallel or at small angles to the lineation (Figure 3.7). This CPO pattern can be interpreted to be formed predominantly by prism <c> slip. In two fine-grained samples (GLG201B and GLG257), quartz CPOs are very weak, probably indicating diffusion-accommodated grain boundary glide as the dominant deformation mechanism for quartz. In two samples (AM1 and YN1351), quartz c-axis forms a complete girdle perpendicular to the lineation with the maximum near Z while quartz a-axis shows a girdle parallel to the foliation plane with the maximum at X (Figure 3.7). This CPO pattern is most likely produced by dislocation glide using base <a> slip as the predominant slip system and prism <a> and rhombohedron <a> slips as the subordinate slip systems.

Feldspar occurs not only in various mica-bearing schists, felsic gneisses, and mylonites but also in hornblende-rich amphibolitic gneisses. Unlike mica or hornblende in the same rock, plagioclase or K-feldspar developed nearly random or very weak CPOs with the *pfJ* index generally lower than 1.50 (Figure 3.8). Such weak or diffuse CPOs are less straightforward to interpret (e.g., Brownlee et al., 2011; Erdman et al., 2013; Ji and Mainprice, 1988; Ji and Salisbury, 1993; Ji et al., 1993). In samples GLG132J, GLG134, and AM1, the [100] direction of plagioclase developed a concentration near the X direction, and the poles to (001) form a girdle perpendicular to the lineation with some concentrations at Z. This CPO pattern indicates that plagioclase in these rocks was deformed dominantly by [100](001) slip. Plagioclase [100](010) slip was probably also active in samples GLG133 and YN1351. Combined slip using [100](010) and [100](001) probably occurred in plagioclase from samples GLG119 and K-feldspar in sample GLG110. Plagioclase [001] slip on (010) (samples GLG102 and GLG201B) or the (100) plane (GLG110) is also possible. Due to their random or weak CPO, the presence of feldspars consistently decreases the seismic anisotropy caused by CPO of mica or amphibole in the schists, gneisses, and mylonites (Figure 3.8).

The CPO of amphibole has been measured for 4 hornblende-bearing samples (amphibolitic gneiss AM1, amphibole schists GLG110 and GLG201B, and Qtz-Bt-Hbl schist GLG237). As shown in Figure 3.9, the CPO diagrams of amphibole are relatively simple and consistent. The [001] directions display a girdle parallel to the foliation plane with a maximum close to X (samples GLG237 and GLG201B) or a single strong concentration parallel to X (samples

GLG110 and AM1). The (100) and (010) poles form single maximum concentrations at Z and Y, respectively. For amphibole (100), the *pfJ* index varies from 3.11 (sample AM1) to 6.25 (sample GLG201B) with a mean value of 4.55. For amphibole (010), the *pfJ* index varies from 1.79 (sample GLG237) to 2.20 (sample GLG201B) with mean value of 1.94. For amphibole [001], the *pfJ* index varies from 3.52 (sample GLG237) to 5.12 (sample AM1) with a mean value of 4.24. Clearly, the mean CPO strengths of amphibole (100) and [001] are much stronger than that of (010). The amphibole fabric features of the samples from Yunnan are consistent with those measured previously in middle to high grade metamorphic rocks using an optical microscope equipped with a five-axis universal stage (Barberini et al., 2007; Barruol and Kern, 1996; Barruol and Mainprice, 1993a, 1993b; Christensen, 1965; Ji and Mainprice, 1989; Ji et al., 1993; Schwerdtner, 1964; Siegesmund et al., 1989) or EBSD techniques (Brownlee et al., 2011; Ji et al., 2013b; Kitamura, 2006; Tatham et al., 2008). The hornblende CPO pattern in sample GLG237 (Figure 3.9d) is similar to Type I fabric in a dry amphibolite (sample JH54) deformed experimentally at 1.0 GPa, 480 °C, and a shear strain rate of 5.0×10^{-5} s^{-1} (Ko and Jung, 2015). We interpret the CPO patterns of amphibole from Yunnan to have formed by either [001] slip along (100) and (110) planes (Barruol and Kern, 1996; Barruol and Mainprice, 1993a; Biermann and Van Roermund, 1983; Cumbest et al., 1989; Dollinger and Blacic, 1975; Ji and Mainprice, 1989; Ji et al., 1993, 2013b; Reynard et al., 1989; Skrotzki, 1990) or anisotropic growth (grain boundary migration) and passive rigid-body rotation under various different stresses (Díaz Azpiroz et al., 2007; Ji et al., 1993, 2013b; Shelley, 1994; Takeshita et al., 1999; Tatham et al., 2008). Type II fabric of Ko and Jung (2015), which is characterized by foliation-parallel girdles with the maximum [010] and [001] concentrations at X and Y, respectively, has not been observed in our amphibole-bearing rocks that have been plastically deformed. The type II fabric of amphibole sheared experimentally at high strain rates ($\geq10^{-5}$ s^{-1}) and differential stresses (≥100 MPa) was formed by mechanical rotation of brittle grains activated by cataclastic flow (Ko and Jung, 2015). Such a deformation process was not responsible for the formation of the amphibole fabrics reported in this chapter.

The CPO of sillimanite (Al_2SiO_5), which reveals abundant optical evidence of dislocation creep such as undulatory extinction and subgrain boundaries (Lambregts and van Roermund, 1990; Piazolo and Jaconelli, 2014), has been measured in a metapelitic schist (sample GLG203). As shown in Figure 3.10, [001] of sillimanite forms a single strong concentration at X whereas [010]

and particularly [100] form partial girdles perpendicular to the lineation with strong concentrations at Z and Y, respectively. This CPO pattern, which is similar to those reported from metapelitic mylonites from the Kangxiwar ductile strike-slip shear zone (west Kunlun, Tibetan Plateau, Xu et al., 2007), and the Basin and Range (USA, Erdman et al., 2013), can be interpreted in terms of dislocation glide using [001](010) as the dominant slip system and [001](100) as the subordinate slip system. Theoretical prediction suggests that the easiest slip system should be [001](010) with subordinate [001](100) slip system since the unit cell dimensions are a=7.48 Å, b=7.67 Å, and c=5.77 Å for prismatic sillimanite (Deer et al., 1992). The dominant [001](010) slip and resultant CPO were also observed in fine-grained sillimanite aggregates deformed by torsion at 1250 °C, 300 MPa, and a constant strain rate of 2×10^{-4} s^{-1} (Goergen et al., 2008).

The seismic properties of the polycrystalline aggregates were computed by averaging the elastic-constant tensors of individual grains as a function of the CPO and modal composition of each sample (e.g., Mainprice, 1990) using the VRH averaging of single crystal elastic constants at ambient conditions (Quartz: McSkimin et al., 1965; K-feldspar, hornblende, and plagioclase: Aleksandrov et al., 1974; Biotite: Belikov et al., 1970; Muscovite: Vaugham and Guggenheim, 1986; Sillimanite: Vaughan and Weidner, 1978). The bulk anisotropy of seismic velocities (AV_p and AV_s) is defined as $100\%\times(V_{max}-V_{min})/[(V_{max}+V_{min})/2]$, where V_{max} and V_{min} are the maximum and minimum velocities, respectively (Mainprice, 2011). The calculated velocities and anisotropy pertain to conditions of one atmosphere pressure, room temperature, and zero porosity, and must be compared with velocities measured at a pressure high enough to close microcracks (e.g., Barruol and Kern, 1996; Ji and Mainprice, 1988; Ji and Salisbury, 1993).

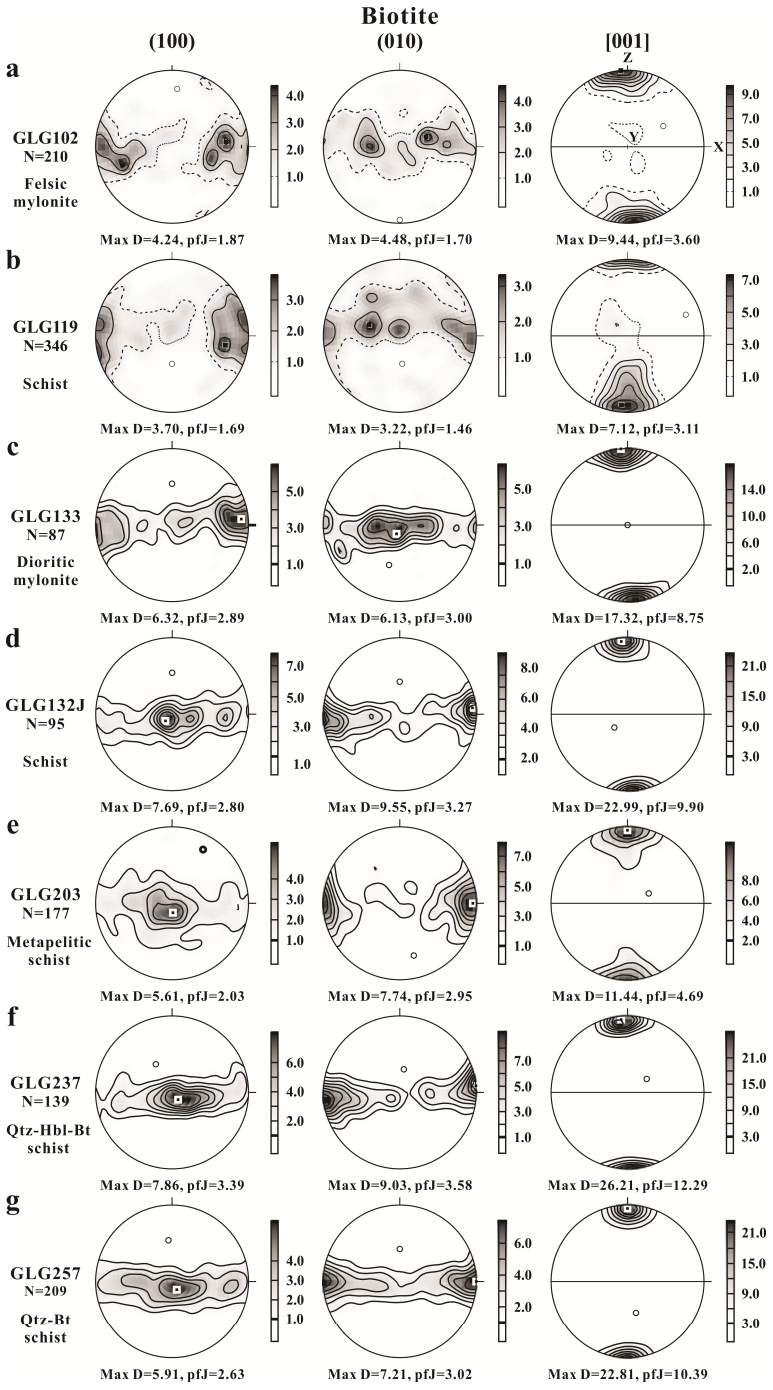


Figure 3.6 EBSD-measured pole figures for biotite from samples (a) GLG102, (b) GLG119, (c) GLG133, (d) GLG132J, (e) GLG203, (f) GLG237, (g) GLG257, (h) GLG134, (i) GLG258, and (j) YN1389, and for muscovite from samples (k) GLG132J, (l) YN1351, and (m) YN1389. Equal-area lower hemisphere projections. The maximum density and *J* index (*pfJ*), which are calculated from the orientation distribution function, are indicated for each sample. N: number of measured grains.

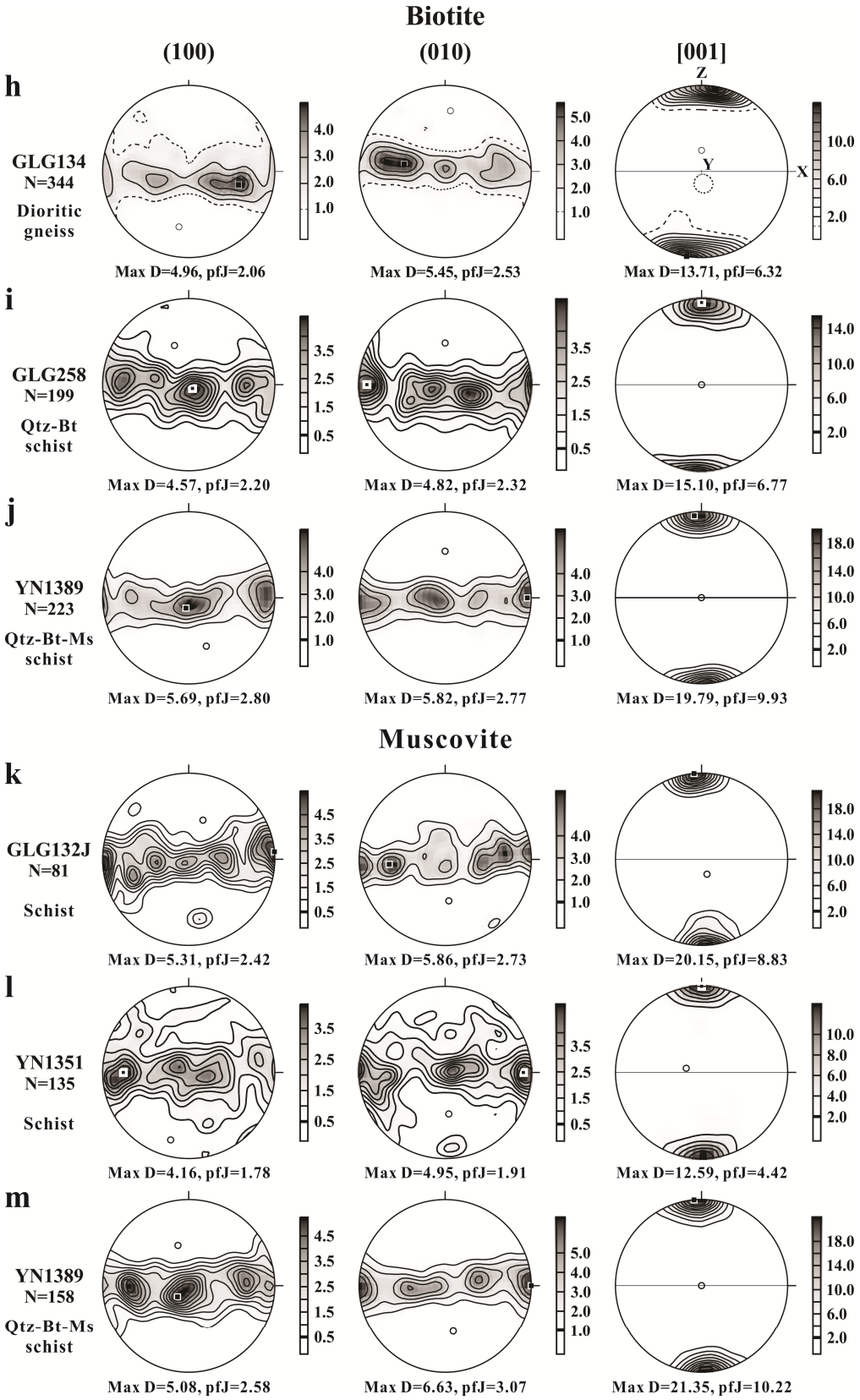


Figure 3.6 Continued

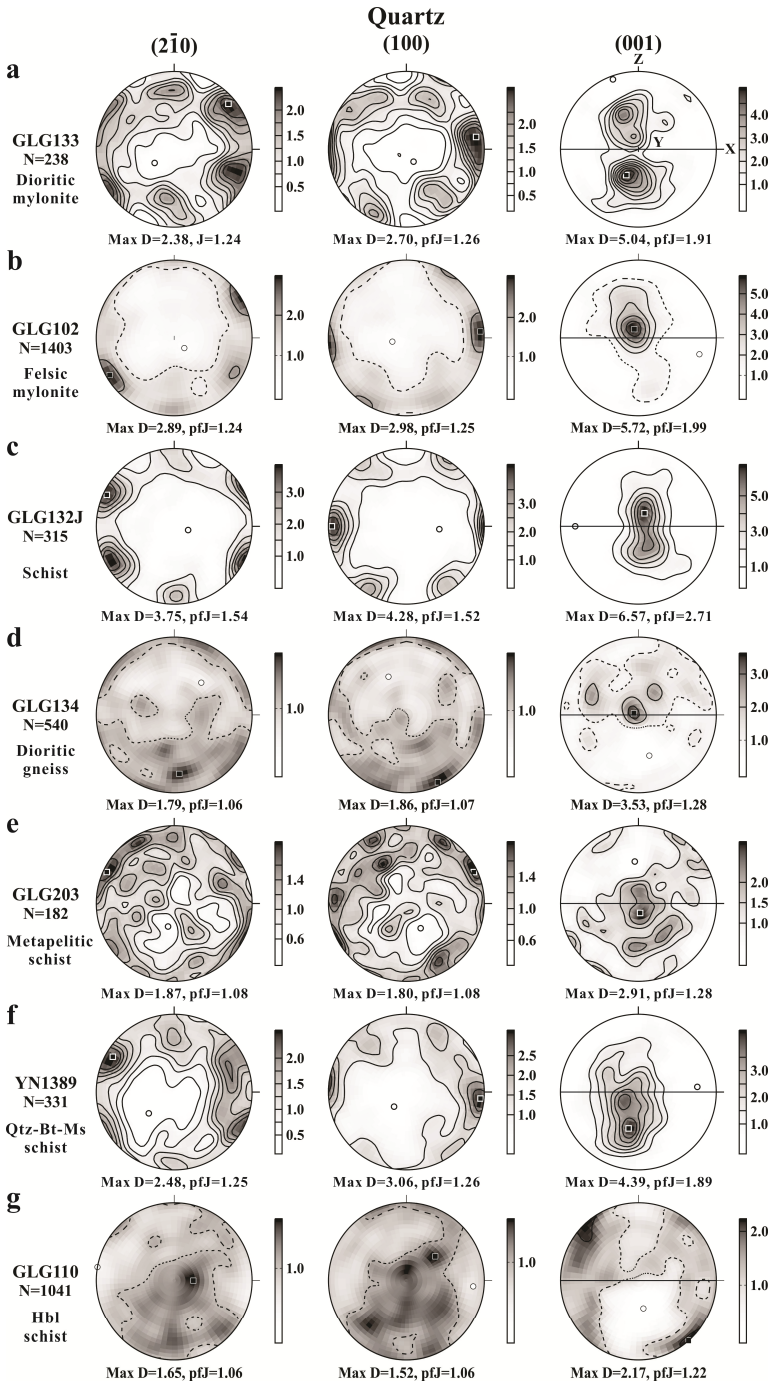


Figure 3.7 EBSD-measured pole figures for quartz from samples (a) GLG133, (b) GLG102, (c) GLG132J, (d) GLG134, (e) GLG203, (f) YN1389, (g) GLG110, (h) GLG119, (i) GLG237, (j) GLG258, (k) AM1, (l) YN1351, (m) GLG201B, and (n) GLG257. Equal-area lower hemisphere projections. The maximum density and *J* index (*pfJ*), which are calculated from the orientation distribution function, are indicated for each sample. N: number of measured grains.

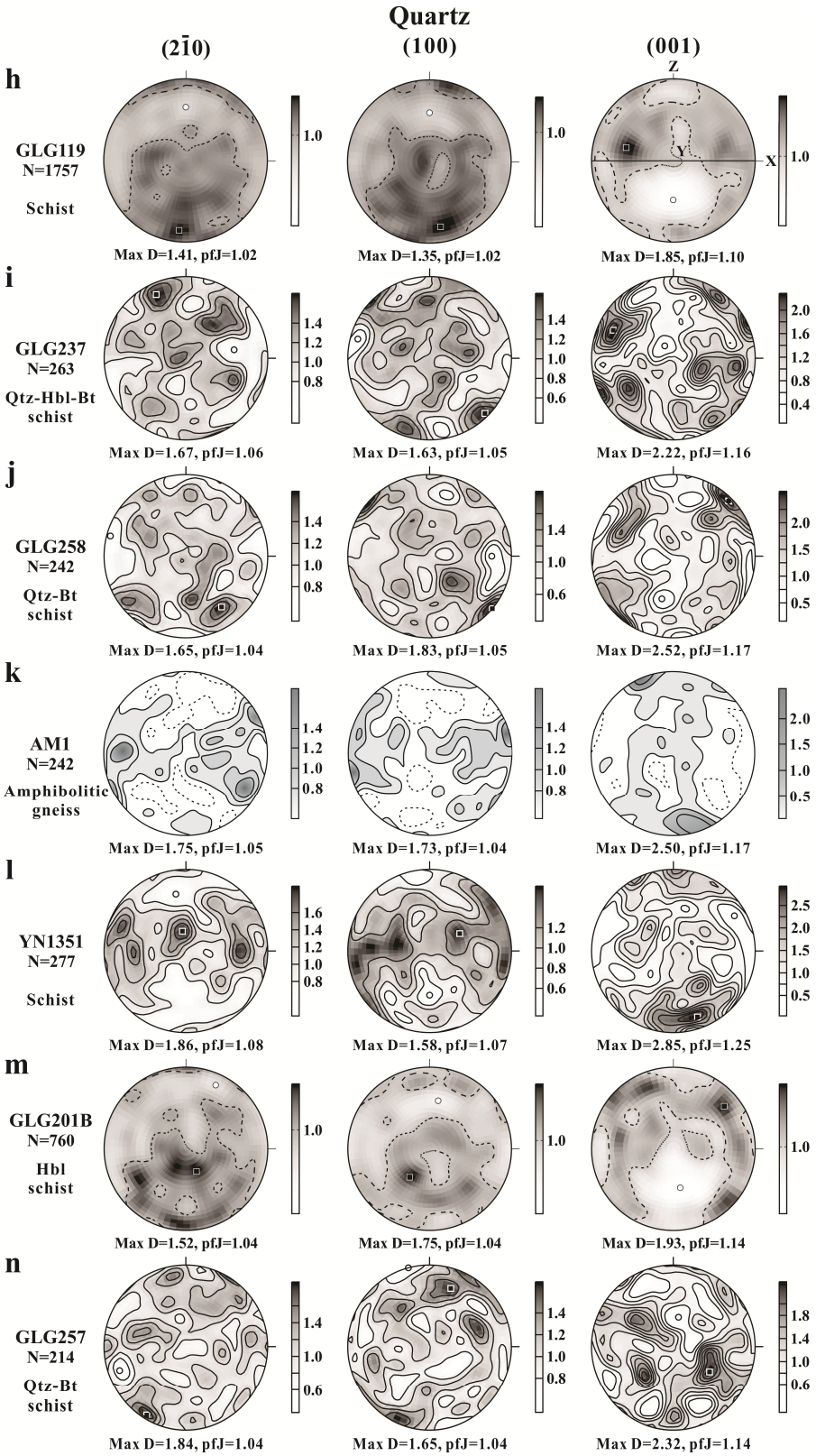


Figure 3.7 Continued

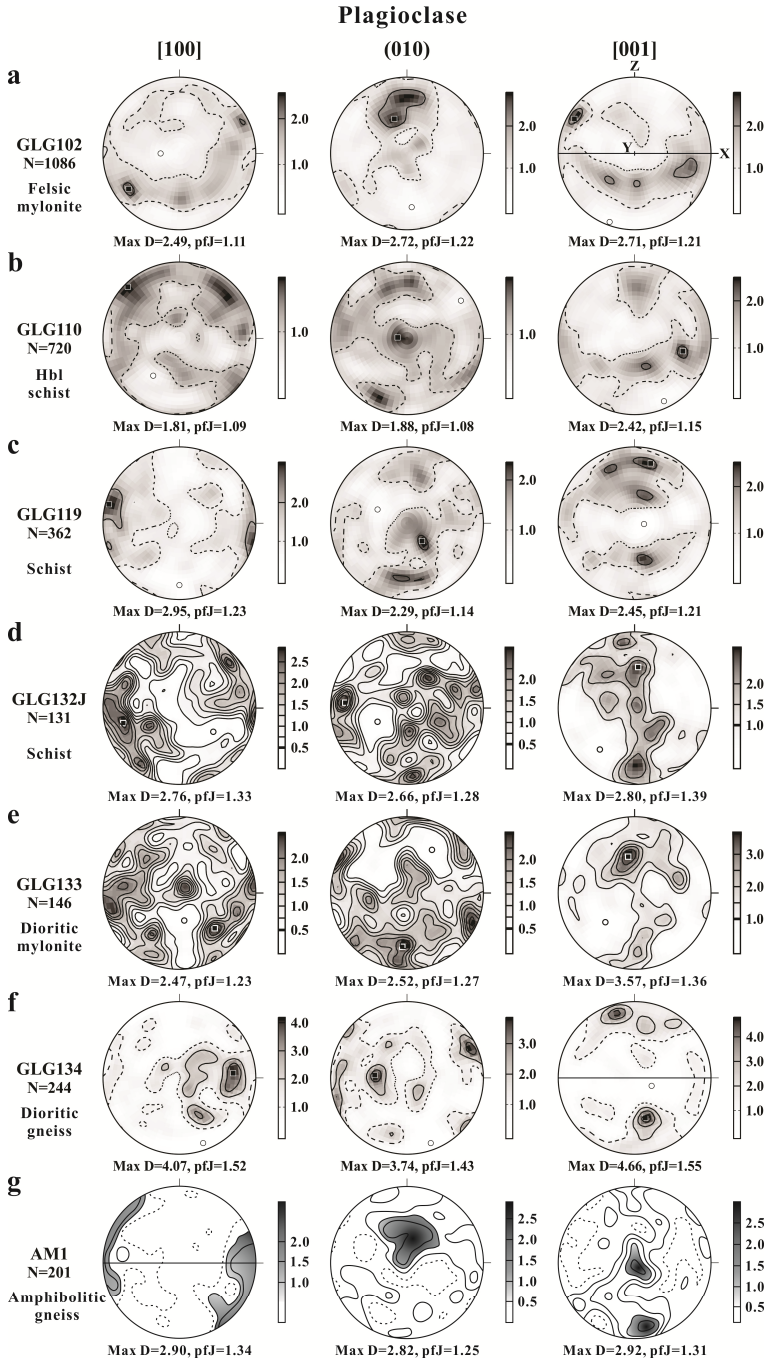


Figure 3.8 EBSD-measured pole figures for plagioclase from samples (a) GLG102, (b) GLG110, (c) GLG119, (d) GLG132J, (e) GLG133, (f) GLG134, (g) AM1, (h) GLG201B, (i) GLG203, (j) GLG237, and (k) YN1351, and for K-feldspar from samples (l) GLG102 and (m) GLG110. Equal-area lower hemisphere projections. The maximum density and *J* index (*pfJ*), which are calculated from the orientation distribution function, are indicated for each sample. N: number of measured grains.

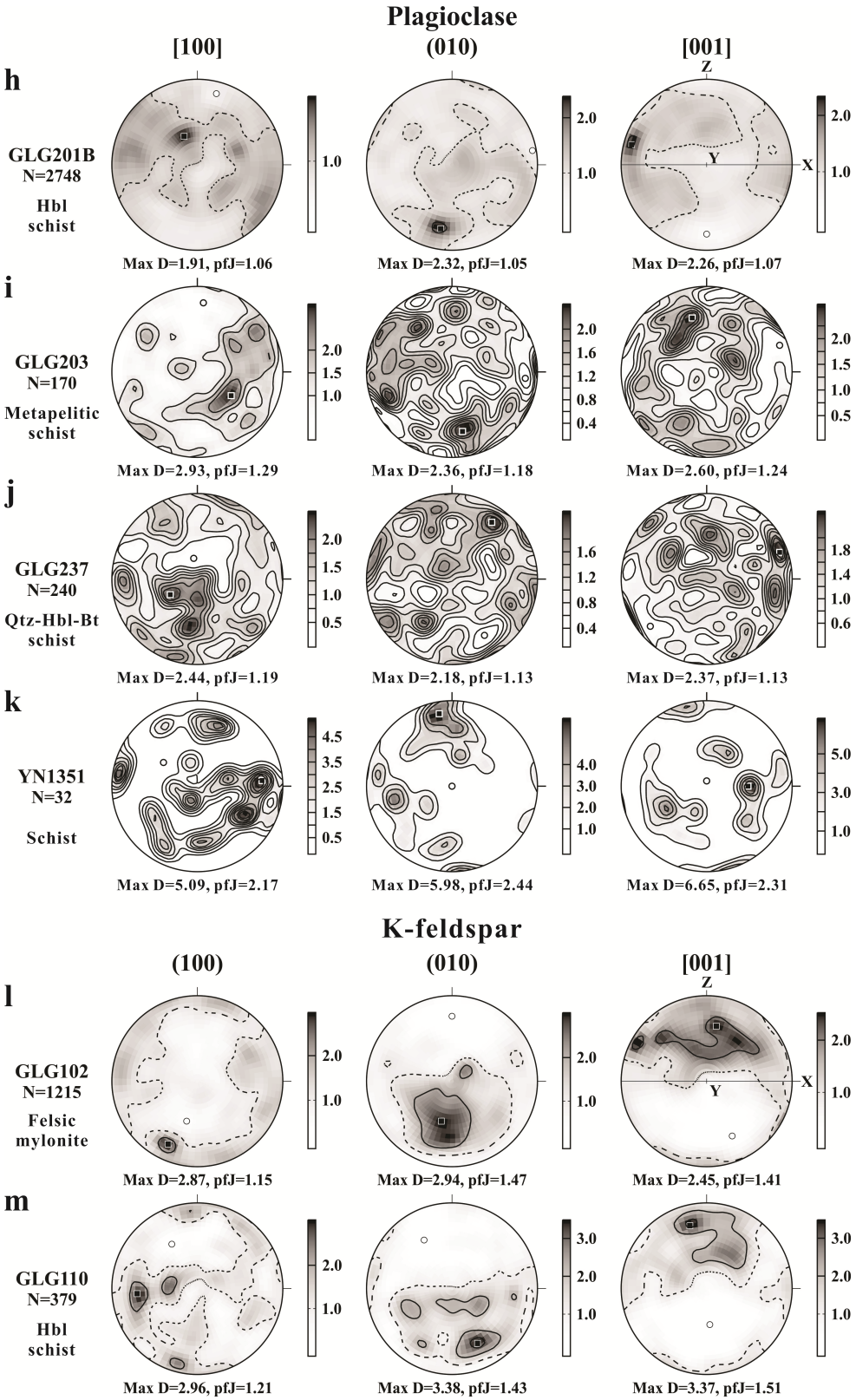


Figure 3.8 Continued

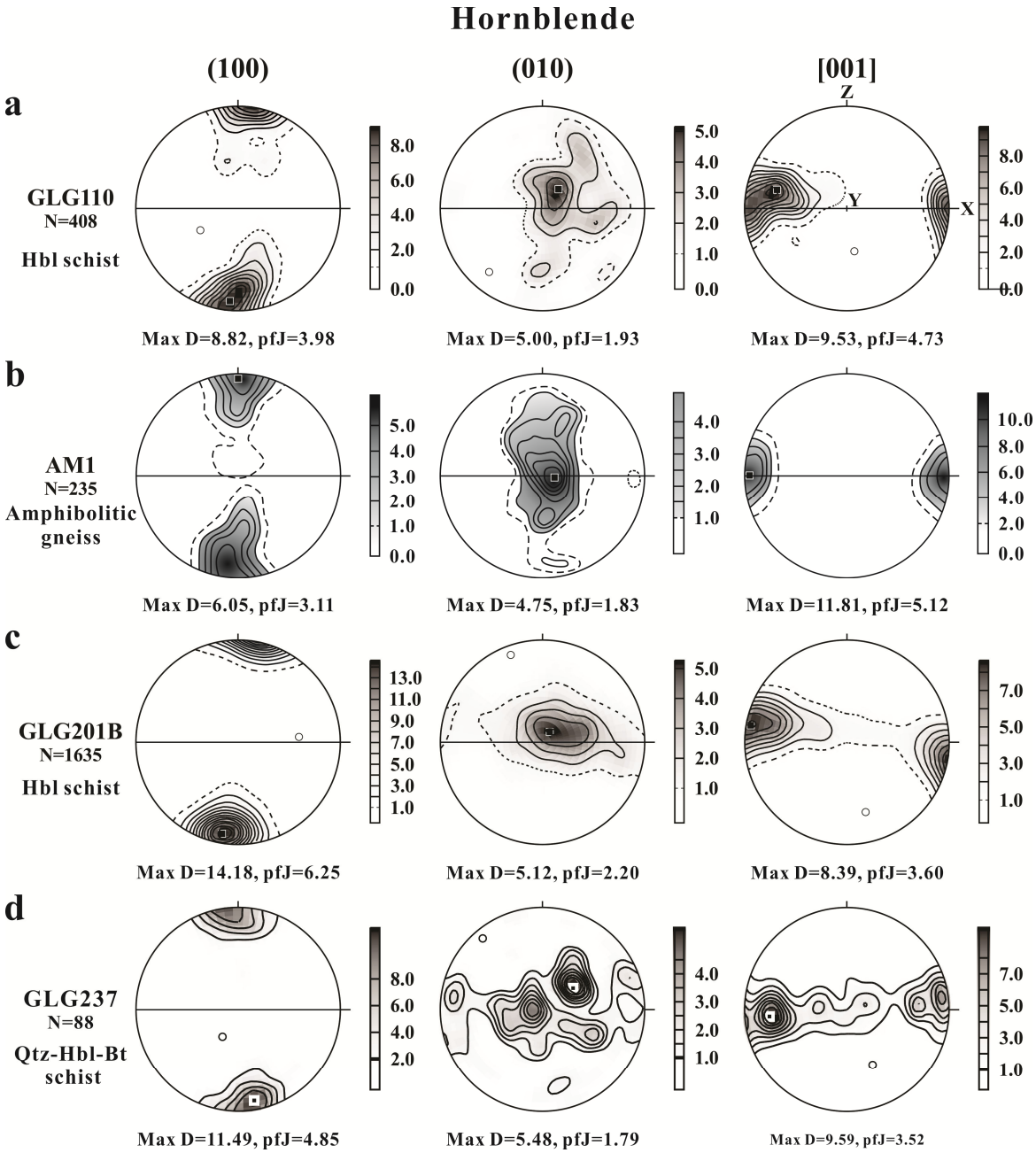


Figure 3.9 EBSD-measured pole figures for hornblende from samples (a) GLG110, (b) AM1, (c) GLG201B, and (d) GLG237. Equal-area lower hemisphere projections. The maximum density and *J* index (*pfJ*), which are calculated from the orientation distribution function, are indicated for each sample. N: number of measured grains.

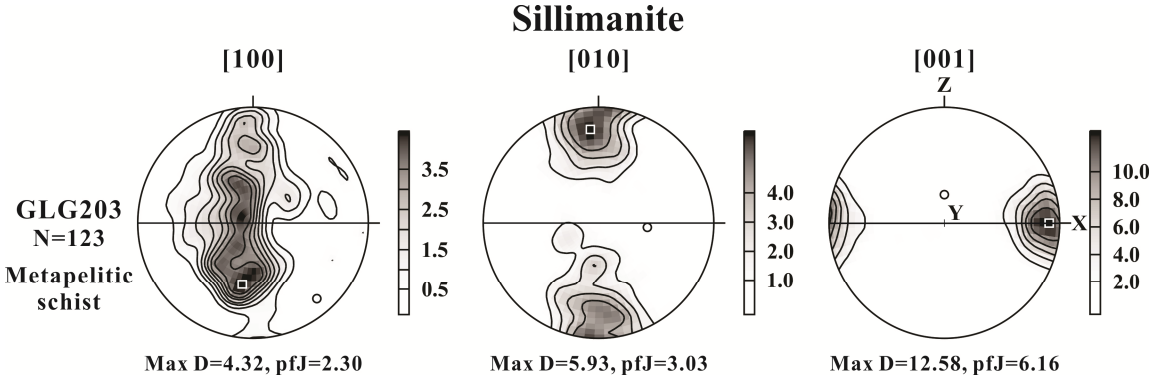


Figure 3.10 EBSD-measured pole figures for sillimanite from metapelitic sample GLG203. Equal-area lower hemisphere projections. The maximum density and *J* index (*pfJ*), which are calculated from the orientation distribution function, are indicated for each sample. N: number of measured grains.

As shown in Figures 3.11a-3.11f, the calculated results show that the 6 schist samples (GLG119, GLG132J, GLG257, GLG258, YN1389, and YN1351) consisting of 20-45 vol.% mica have bulk V_p anisotropy varying from 11.1% to 25.5%. The ratios of V_p(X) to V_p(Y) range from 0.97 to 1.09 while V_p(X)/V_p(Z)=1.08-1.25 and V_p(Y)/V_p(Z)=0.99-1.22. The above fact indicates that seismic properties of these schists are not exactly transversely isotropic. In order to describe quantitatively the departure of the seismic properties from TI, we define a coefficient for V_p anisotropy [A_p(F)] in the foliation plane as $A_p(F)=100\%(a^{0.5}-a^{-0.5})$, where $a=\left| V_p(max)/V_p(min) \right|$, and V_p(max) and V_p(min) are the maximum and minimum compressional wave velocities, respectively, within the foliation plane [also see Eq. (1.32)]. A_p(F) varies from 1.1% to 8.4% with a mean value of 4.2% for the six schist samples. Sample YN1351 with $A_p(F)\leq 2.0\%$ is considered as a quasi-transverse isotropic rock. The calculated V_s anisotropy results, which agree with the experimentally measured data, demonstrate a critical role of mica c-axis fabric, regardless of dislocation slip along [100], [010], or [hk0] within the (001) plane, in the formation of the maximum and minimum birefringence values in the foliation plane and in the direction normal to the foliation, respectively. In sample GLG257, for example, the intrinsic V_s anisotropy varies little in the foliation plane (32.5% at Y, and 32.9% at X) while the anisotropy value is only 1.7% for propagation parallel to Z. In other words, shear-wave splitting values of 1.34 km/s, 1.27 km/s, and 0.05 km/s occur in the X, Y, and Z directions with the fast shear-wave being polarized parallel to the foliation (Figure 3.11a).

As shown in Figures 3.11h-3.11k, the 4 hornblende-bearing samples (amphibolitic gneiss AM1, amphibole schists GLG110 and GLG201B, and Qtz-Hbl-Bt schist GLG237) display the fastest, intermediate, and slowest P-wave velocities in the X, Y, and Z directions, respectively. In amphibolitic gneiss AM1, the calculated P-wave velocities in the X, Y, and Z directions are 7.14, 6.52, and 6.21 km/s, respectively (Figure 3.11h). These values are in good agreement with the measured values at 40 MPa for V_p(X), V_p(Y), and V_p(Z) which are 7.23, 6.62, and 6.21 km/s, respectively. The V_p anisotropy coefficients calculated for samples AM1, GLG110, GLG201B, and GLG237 are 14.0%, 5.7%, 6.1%, and 20.0%, respectively. In sample AM1, for instance, the maximum shear-wave anisotropy (AV_s=8.4%) is observed for propagation in the foliation plane while almost no birefringence occur normal to foliation (Figure 3.11h). Similar features (Figures 3.11i-3.11j) are observed in amphibole schists (samples GLG110 and GLG201B) and Qtz-Hbl-Bt schist (sample GLG237). Clearly, the anisotropy of these rocks is controlled by the CPO of hornblende. The polarization direction of the fastest shear waves travelling parallel to foliation is located in the foliation plane, and controlled by the preferred orientation of hornblende (100) planes (e.g., Barruol and Kern, 1996; Ji and Salisbury, 1993; Ji et al., 2013b; Siegesmund et al., 1989).

Sample GLG203 (Figure 3.11g) is a metapelitic schist consisting of 20 vol.% Qtz, 15 vol.% Fsp, 42 vol.% Bt, 20 vol.% Sil, and 3 vol.% Grt (Figure 3.3d). The calculated P-wave velocities display orthorhombic symmetry with V_p(X)=7.13 km/s, V_p(Y)=6.56 km/s, and V_p(Z)=5.66 km/s, respectively. Such orthorhombic anisotropy cannot be interpreted in terms of the biotite CPO with its (001) planes parallel to the foliation (Figure 3.6e) and should be attributable to the strong CPO of sillimanite whose fast c-axes are preferentially aligned parallel to the lineation (Figure 3.10).

The calculated velocity results for 3 felsic rocks (Figures 3.11l-3.11n) illustrate clearly the role of mica in the formation of bulk seismic anisotropy. Samples GLG102 (felsic mylonites with 3.4 vol.% biotite), GLG133 (dioritic mylonite with 15 vol.% biotite), and GLG134 (dioritic gneiss with 30 vol.% biotite) have P-wave anisotropy of 3.3%, 13.2%, and 16.3%, respectively, reflecting their differences in mica volume fraction. Both samples GLG133 and GLG134 display a quasi-hexagonal symmetry with V_p(X)≈V_p(Y)≫V_p(Z). For instance, V_p(X)=6.09 km/s, V_p(Y)=6.17 km/s, and V_p(Z)=5.30 km/s in sample GLG134.

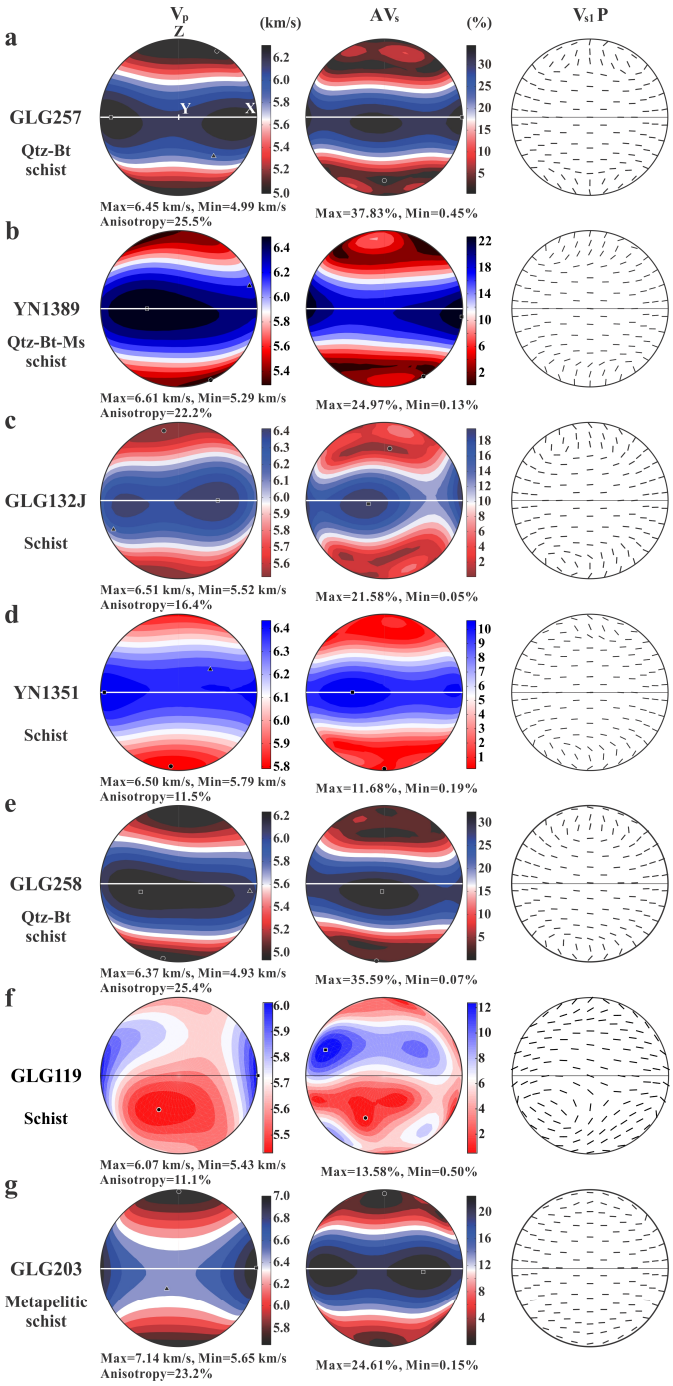


Figure 3.11 P-wave velocities, S-wave velocity anisotropy and fast polarization directions for mica schists (a) GLG257, (b) YN1389, (c) GLG132J, (d) YN1351, (e) GLG258, (f) GLG237, (g) GLG119, and (h) GLG203, amphibolitic gneiss (i) AM1, amphibole schists (j) GLG201B and (k) GLG110, dioritic gneiss (l) GLG134 and mylonite (m) GLG133, and felsic mylonites (n) GLG102, calculated from CPO data, modal composition, and single crystal elastic constants of each rock-forming mineral. Equal-area lower hemisphere projections.

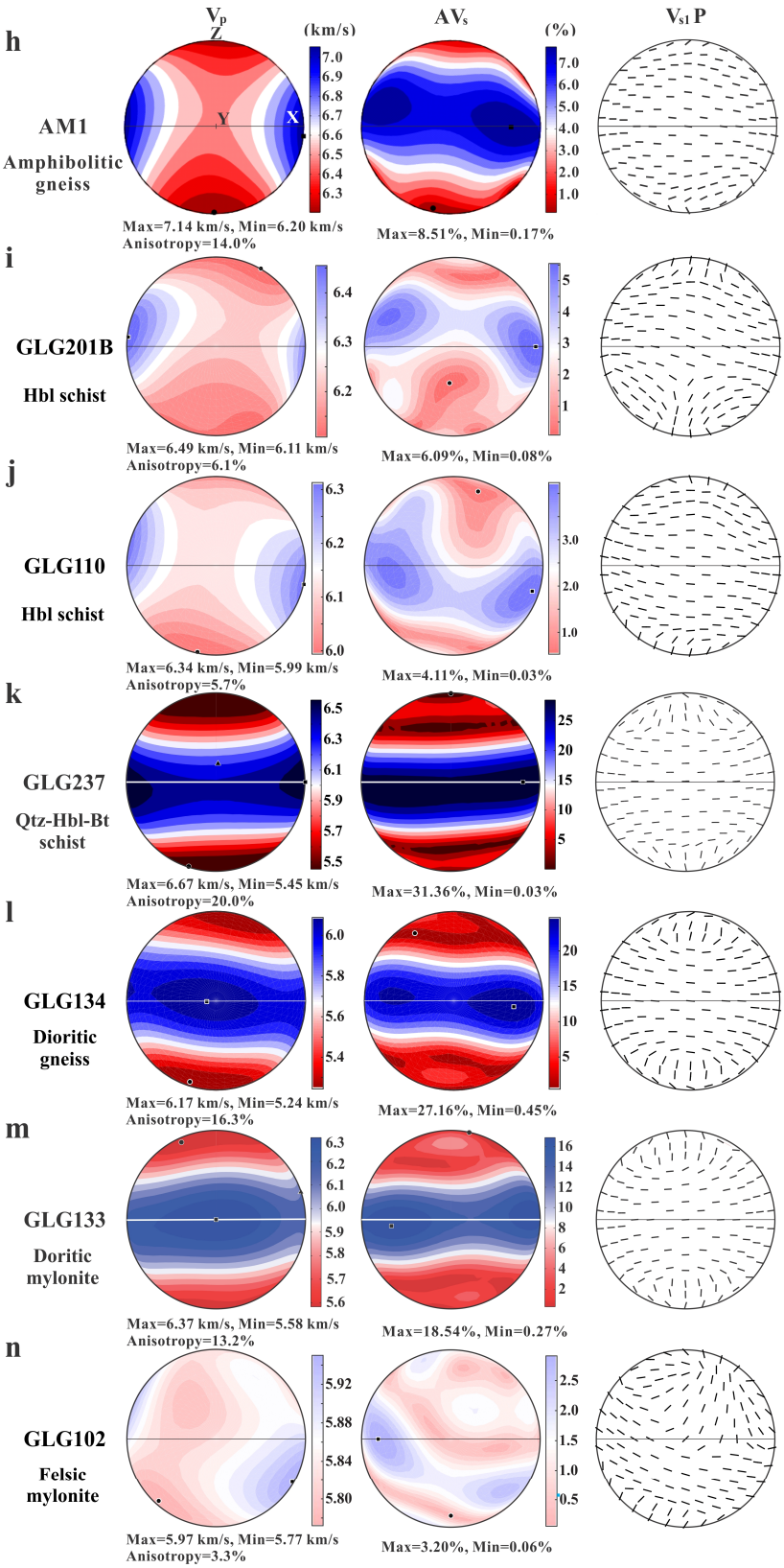


Figure 3.11 Continued

Here we take samples GLG132J, GLG133, GLG257, and YN1389 as examples to show the variation of V_p, V_s, AV_s, and V_p/V_s with incidence angle. Calculated seismic properties for these four samples are summarized in Table 3.4. V_p (Figure 3.12a), V_s (Figure 3.13a), AV_s (Figure 3.14a), and V_p/V_s (Figure 3.15a) in sample GLG132J display much less pronounced variations with incidence angle when propagating in the foliation (XY) plane than those along XZ and YZ planes where significant variations are observed with maximum values at or close to either X or Y. However, the minimum values in V_p (Figure 3.12a), V_s (Figure 3.13a), AV_s (Figure 3.14a), and V_p/V_s (Figure 3.15a) always occur in the directions within angles of ~0-45° with respect to Z. The V_p/V_s ratio can vary from 1.461 to 1.936 due to the presence of strong anisotropy (Table 3.4). For sample GLG133, little variations in V_p (Figure 3.12b), V_s (Figure 3.13b), AV_s (Figure 3.14b), and V_p/V_s (Figure 3.15b) are observed in the foliation plane. But significant changes in these parameters occur when propagating parallel to XZ and YZ planes. The maximum variations in V_p/V_s ratios (from 1.535 to 1.916) are observed in the foliation plane (Figure 3.15b). In sample GLG257, the largest variations in V_p (Figure 3.12c), V_s (Figure 3.13c), AV_s (Figure 3.14c), and V_p/V_s (Figure 3.15c) occur when propagating parallel to XZ and YZ planes. The V_p/V_s ratio varies from 1.372 to 2.207 (Table 3.4). Similar variations in those parameters occur for sample YN1389 and the V_p/V_s ratios vary from 1.392 to 1.918 (Figure 3.15d).

Table 3.4 Summary of seismic velocities and anisotropies calculated using the VRH averages for samples GLG132J, GLG133, GLG257, and YN1389[a]

Sample	Max	Min	X	Y	Z	AV_p	Max	Min	Max	Min	Max	Max	Min	Max	Min
	V_p	V_p	V_p	V_p	V_p		V_{s1}	V_{s1}	V_{s2}	V_{s2}	AV_s	V_p/V_{s1}	V_p/V_{s1}	V_p/V_{s2}	V_p/V_{s2}
GLG132J	6.506	5.521	6.230	6.424	5.563	16.4	4.221	3.481	3.799	3.331	21.6	1.630	1.461	1.936	1.501
GLG133	6.373	5.583	6.229	6.373	5.632	13.2	3.974	3.341	3.678	3.280	18.5	1.686	1.535	1.916	1.574
GLG257	6.445	4.985	6.381	6.223	5.120	25.5	4.259	2.961	3.648	2.904	37.8	1.727	1.372	2.207	1.433
YN1389	6.612	5.289	6.410	6.574	5.401	22.2	4.296	3.517	3.862	3.331	25.0	1.562	1.393	1.918	1.404

[a]All velocities are in km/s and anisotropies are in percent.

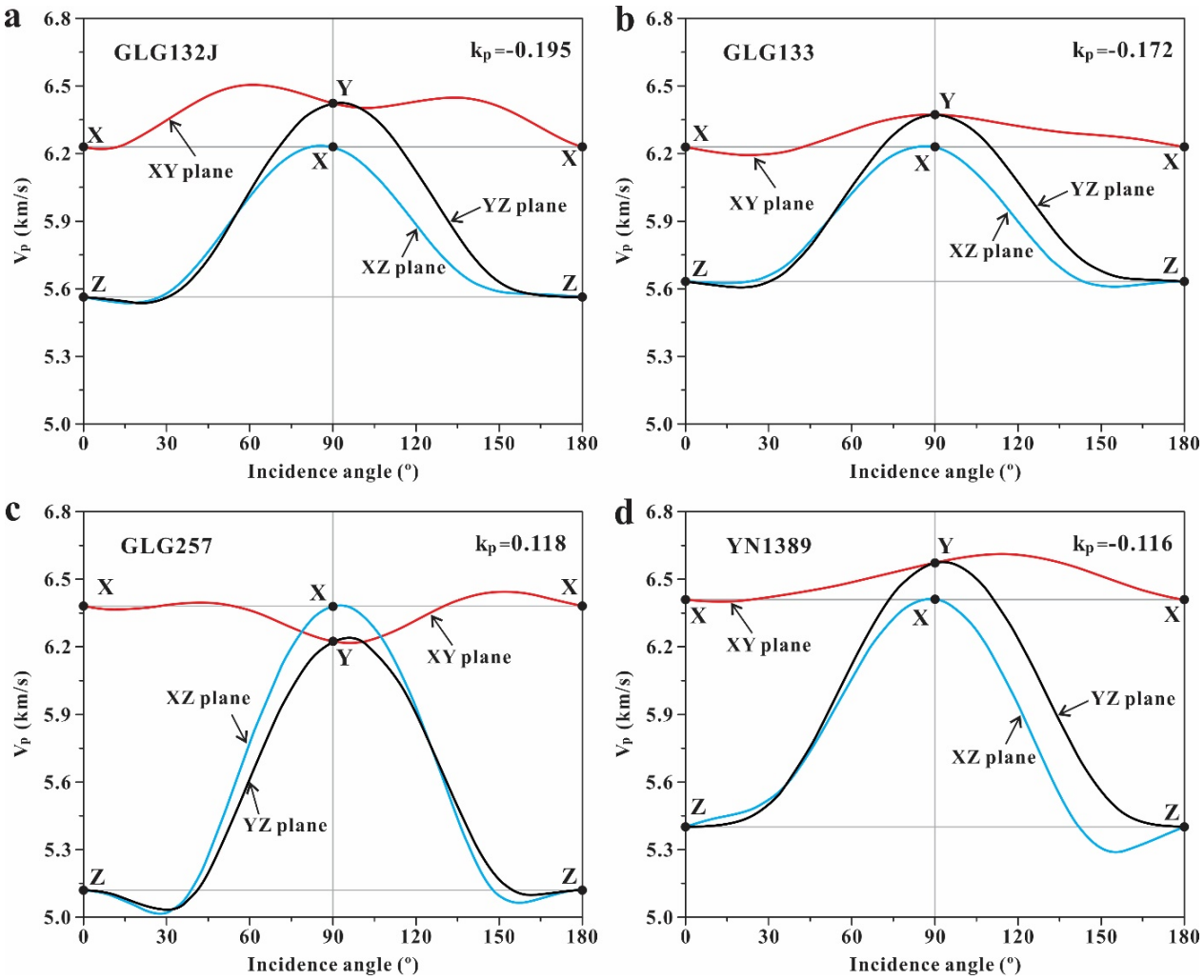


Figure 3.12 Variation of calculated P-wave velocity as a function of incidence angle in the XY, XZ, and YZ planes. (a) Sample GLG132J, k_p=-0.195 and $V_p(Y)>V_p(X)\gg V_p(Z)$; (b) Sample GLG133, k_p=-0.172 and $V_p(Y)>V_p(X)\gg V_p(Z)$; (c) Sample GLG257, k_p=0.118 and $V_p(X)>V_p(Y)\gg V_p(Z)$; (d) Sample YN1389, k_p=-0.116 and $V_p(Y)>V_p(X)\gg V_p(Z)$.

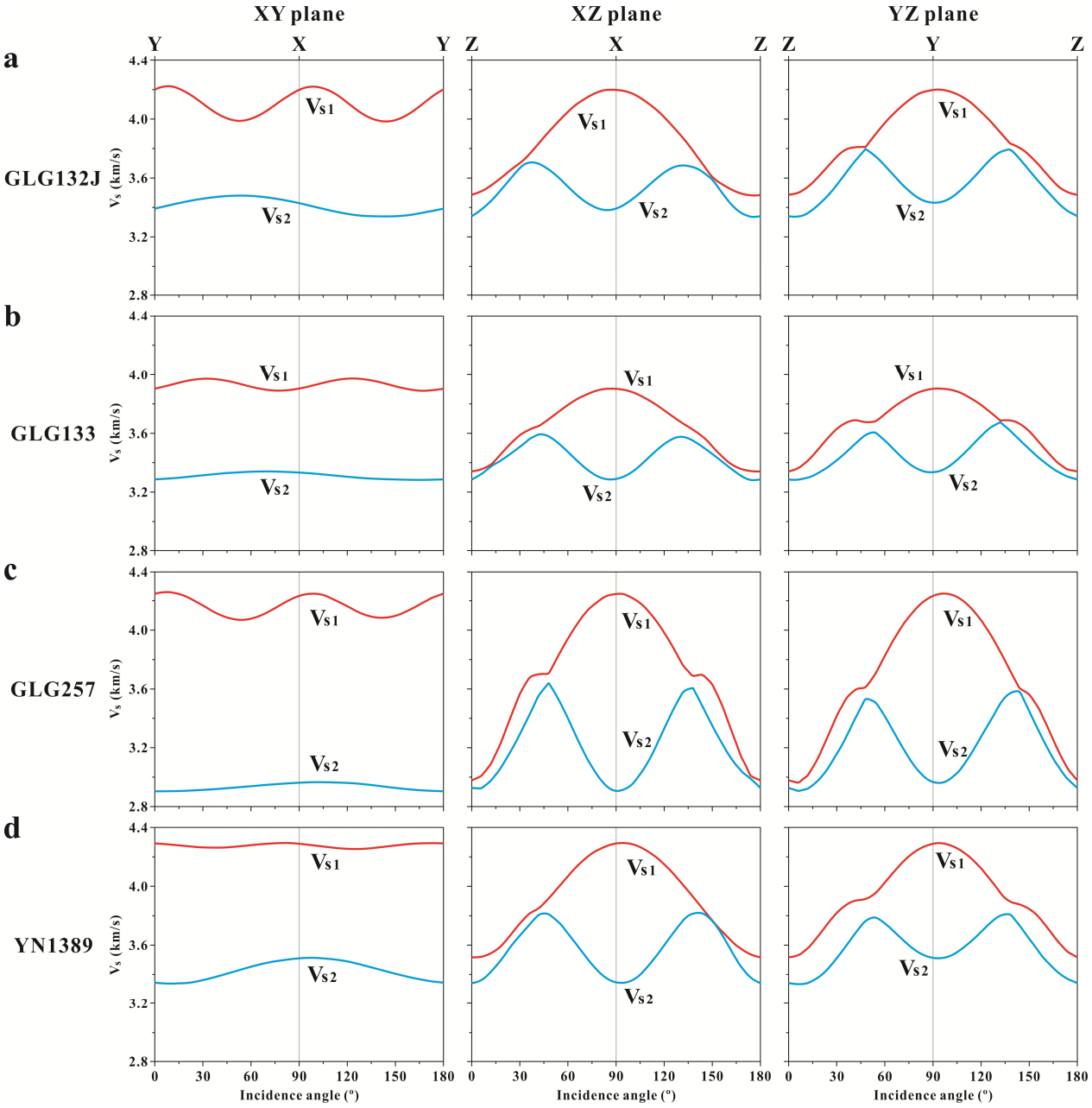


Figure 3.13 Calculated split fast and slow S-wave velocities (V_{s1} and V_{s2}) as a function of incidence angle in the XY, XZ, and YZ planes of three mica schists (samples GLG132J, GLG257, and YN1389) and one dioritic mylonite (sample GLG133). The largest birefringence ($\Delta V_s = V_{s1} - V_{s2}$) occurs for the propagation in the foliation plane while little birefringence takes place in the direction normal to the foliation. $\Delta V_s(X) \geq \Delta V_s(Y) \gg \Delta V_s(Z)$.

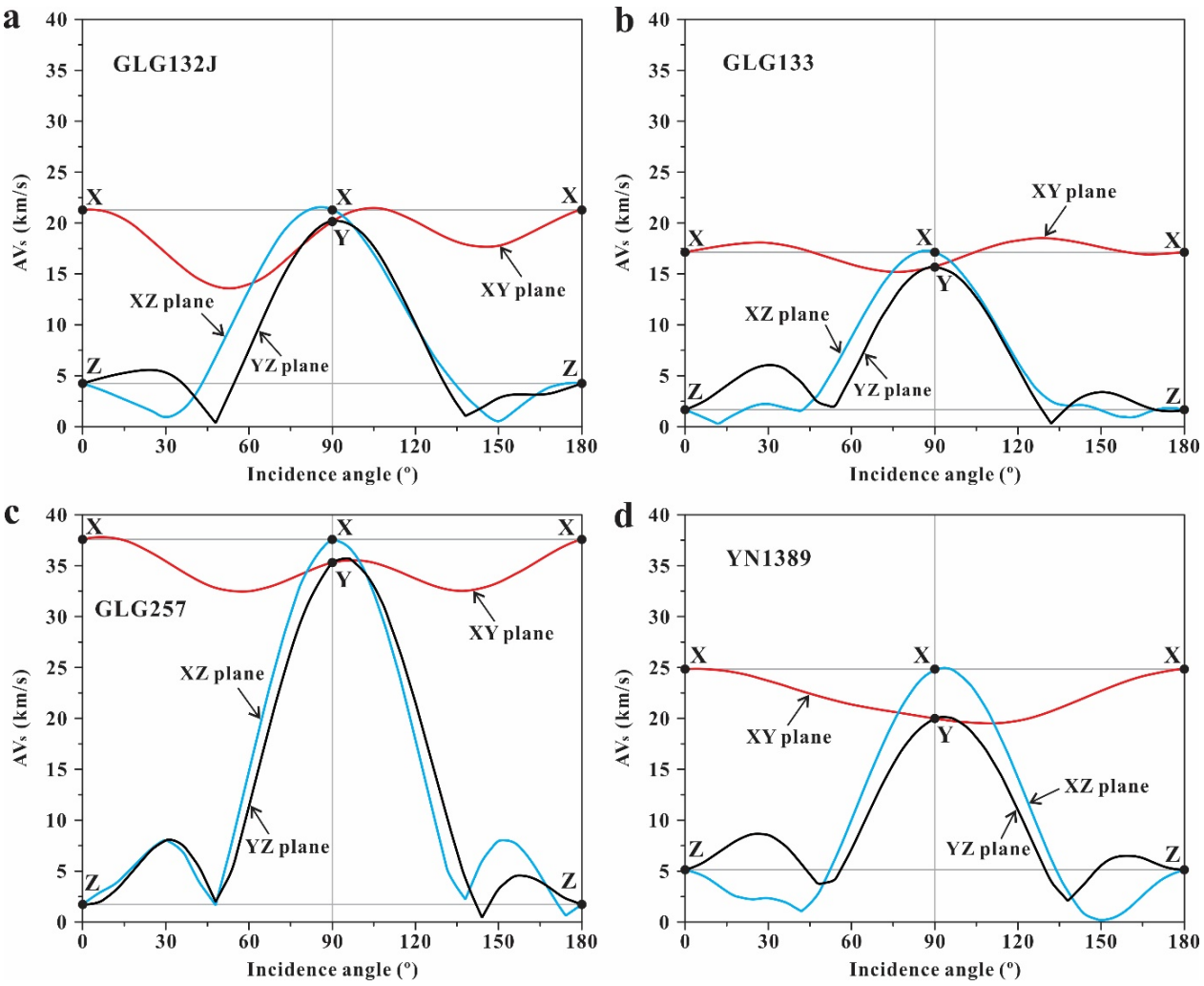


Figure 3.14 Variations of calculate d S-wave velocity an isotropy as a function of incidence angle in the XY, XZ, and YZ planes. (a) Sa mple GLG132J; (b) Sample GLG133; (c) Sample GLG257; (d) Sample YN1389. All samples are characterized by $AV_s(X)>AV_s(Y)\gg AV_s(Z)$.

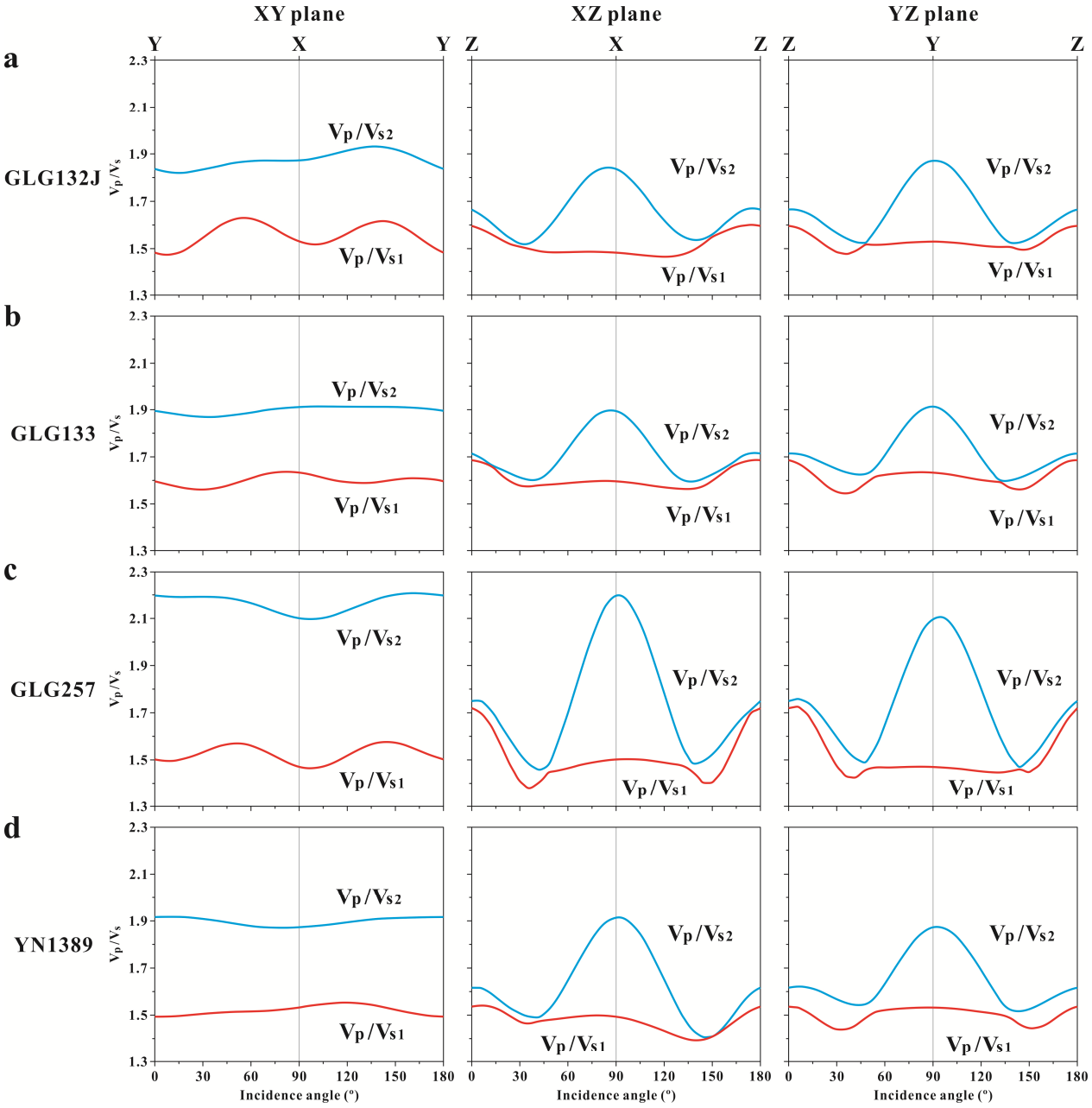


Figure 3.15 The ratios (V_p/V_s) of P-wave velocity to S-wave velocities (V_{s1} and V_{s2}) as a function of incidence angle in the XY, XZ, and YZ planes for (a, c and d) three mica schists and (b) one dioritic mylonite. The largest V_p/V_s occurs for propagation in the foliation plane whereas the minimum ratio appears in the direction at ~30° with the Z.

3.5 Discussion

We now discuss six issues that arise from our experimental measurements and CPO-based calculations of the seismic properties of mica- or amphibole-bearing schists, gneisses, and mylonites, and the analysis of previous data in the literature.

3.5.1 Seismic properties of schists

Elastic stiffness coefficients of single crystal biotite, muscovite (Figure 3.16), and chlorite have been measured by Alesandrov and Ryzhova (1961). Their work suggests that although phyllosilicate minerals have monoclinic symmetry, their elastic properties have nearly hexagonal symmetry with maximum and minimum P-wave velocities and shear-wave birefringence values parallel to and perpendicular to (001), respectively (e.g., Cholach and Schmitt, 2006; Ji et al., 1993, 2002; Kern and Wenk, 1990; Kim and Jung, 2015; Mahan, 2006; Mainprice and Ildefonse, 2009; Meltzer and Christensen, 2001; Shapiro et al., 2004; Wenk et al., 2012). Sericite is a fine-grained white mica which may be muscovite, paragonite, or some less-characterized mica which may deviate in some ways from typical muscovite composition (Deer et al., 1992). Sericite results from low temperature hydrothermal alteration of orthoclase or plagioclase feldspars. The elastic stiffnesses of sericite are not yet known, but it is often assumed that muscovite's elastic constants may instead be used. Thus, five sericite schists were included in the category of mica schists for the analysis. Phyllites are very fine-grained mica schists which have been extensively deformed and recrystallized in ductile shear zones.

In various schists, gneisses, and mylonites, mica are easily deformed by dislocation glide as indicated by abundant microstructural evidence such as undulatory extinction, lattice rotation, folding, sheared fish-shape, kinking, and dynamic recrystallization. Glide on any of the three plausible systems (001)[010], (001)[100], and (001)[hk0] produces the same seismic anisotropy pattern with the fastest and the lowest velocities parallel and perpendicular to the foliation, respectively, under a given strain geometry. This feature is similar to that for antigorite (Ji et al., 2013a; Jung, 2011; Katayama et al., 2009; Shao et al., 2014). Theoretically three main types of mica-induced V_p anisotropy, which are formed by three end-members of strain geometry (Figure 3.17), are possible in naturally deformed schists.

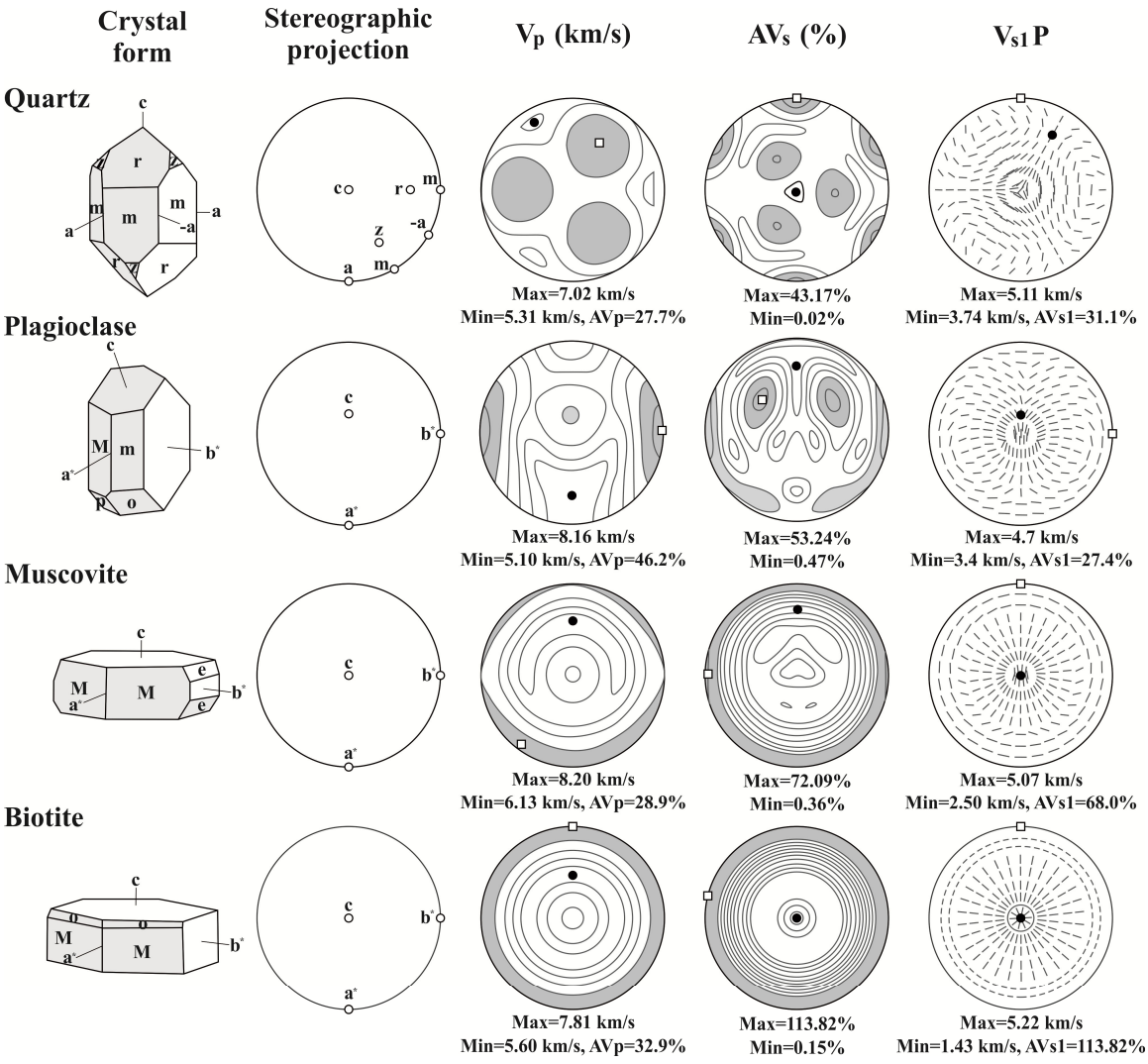


Figure 3.16 P- and S-wave properties of elastically anisotropic single crystals of 4 common rock-forming minerals (Quartz, plagioclase, muscovite, and biotite) making up some samples in this study are shown in equal-area lower hemisphere projections with respect to the crystal form and crystallographic orientations of **a**, **b**, **c**, $\mathbf{a}^*$ and $\mathbf{b}^*$, where $\mathbf{a}^*$ and $\mathbf{b}^*$ are the directions normal to (100) and (010) planes, respectively. V_p: P-wave velocities; AV_p: anisotropy of P-wave velocity; AV_s: direction-dependent shear-wave velocity (V_s) anisotropy; V_{s1}P: polarization direction of fast shear-wave. The maximum velocity (in km/s) and anisotropy (in percent) are marked by open square and the minimum by solid circle. The seismic properties are calculated using a suite of programs developed by Mainprice (1990) and appropriate mineral single-crystal elastic constants (Quartz: McSkimin et al., 1965; Plagioclase: Aleksandrov et al., 1974; Muscovite: Vaughn and Guggenheim, 1986; Biotite: Aleksandrov et al., 1961).

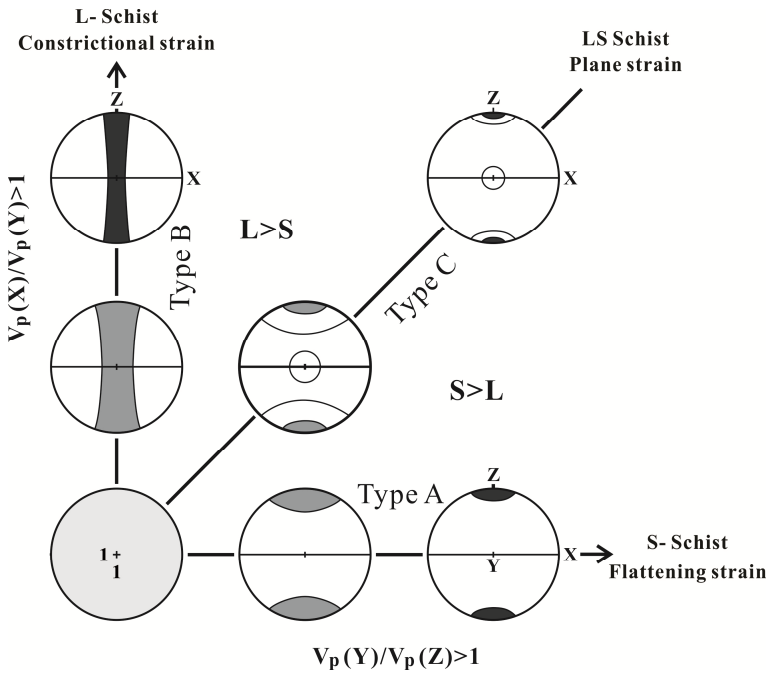


Figure 3.17 Flinn-type diagram showing three possible end-member types of contoured CPO patterns of mica c-axes and corresponding P-wave velocity anisotropy. The origin of the coordinate axes (1, 1) represents random CPO and thus zero anisotropy. X, lineation; Y, direction normal to lineation and in foliation; Z, normal to foliation. The CPO strengths increase with increasing finite strains.

Type A: transversely isotropic with $V_p(X) \approx V_p(Y) \gg V_p(Z)$, which is formed by the preferred orientation of mica (001) planes parallel to the foliation, the c-axis parallel to the Z direction (Figure 3.17), and the poles to (100) and (010) planes lying randomly in the foliation plane (e.g., Naus-Thijssen et al., 2011a). This type of mica CPO can be formed by coaxial flattening or anisotropic growth under differential stresses.

Type B: transversely isotropic with $V_p(X) \gg V_p(Y) \approx V_p(Z)$, which is related to a nearly random concentration of mica c-axis in the YZ plane perpendicular to the X direction (Figure 3.17). This type of mica CPO, which is characterized by girdle distributions of both the [100] and [010] axes within the foliation (i.e., the XY plane), can be formed by coaxial constriction.

Type C: orthorhombic symmetry with $V_p(X) > V_p(Y) > V_p(Z)$. This type of anisotropy, which is characterized by the largest, intermediate, and smallest V_p values in the X, Y, and Z directions, respectively, is caused by strong and moderate concentrations of mica c-axes in the Z and Y directions in the YZ plane, respectively (Figure 3.17). This pattern of mica CPO develops in

schists deformed in plane strain. Slip on (001) planes contributes mainly to c-axes near the Z direction while mica crystals aligned initially in unfavorable orientations for slip on (001) planes have their c-axes near the Y or X direction. Simple shear strain progressively rotates the (001) planes aligned initially perpendicular to the X direction to the bulk shear plane, forming fish-shaped porphyroclasts (mica fishes, Passchier and Trouw, 2005). Nevertheless, it is difficult for progressive simple shear to eliminate the porphyroclasts whose c-axes cluster in the Y direction unless extensive dynamic recrystallization has taken place (Figure 3.17).

Table 3.2 lists P-wave velocities along three principal orthogonal tectonic directions (i.e., X, Y, and Z) and bulk anisotropy as a function of hydrostatic pressure for 25 schist samples from this chapter. Several factors affect the bulk anisotropy [A_p(B), which is defined in Eq. (1.31)] of schists: (1) Mica content. The amount of bulk anisotropy in schists correlates generally with mica content. Anisotropy is typically less than 5% for rocks with mica contents of <10% but shows a wide range for rocks with mica contents of >15% (e.g., Fountain et al., 1984; McDonough and Fountain, 1988, 1993). (2) Mica CPO strength. Generally speaking, rocks in which mica are segregated, elongated, and strongly aligned parallel to the foliation have high anisotropy values whereas rocks in which mica are disseminated, equidimensional, and poorly oriented have low anisotropy values (e.g., Meltzer and Christensen, 2001). (3) Structure. The presence of multiple foliations (e.g., S-C structure, Lloyd et al., 2009), crenulations and folds (e.g., Naus-Thijssen et al., 2011b) can profoundly reduce bulk seismic anisotropy, depending on the angle between the S and C planes and the shape and tightness of the folds.

Figure 3.18, on which the V_p(Y)/V_p(Z) and V_p(X)/V_p(Y) values at 600 MPa (corresponding roughly to 22 km depth) are respectively plotted on the abscissa and the ordinate of a Flinn-type diagram, is constructed to illustrate how the V_p anisotropy of the 123 schists (except 4 amphibole schists and one Qtz-Hbl-Bt schist which are separately plotted in Figure 3.26) deviate from the TI geometry. Among these 123 schists, there are 65 mica schists, 23 chlorite schists, 16 sillimanite-bearing mica schists, and 19 phyllites. From Figure 3.18 alone, it is impossible to distinguish mica schists from phyllites or chlorite schists as the phyllites are in fact fine-grained mica schists and chlorite probably has deformation behavior and seismic properties similar to mica.

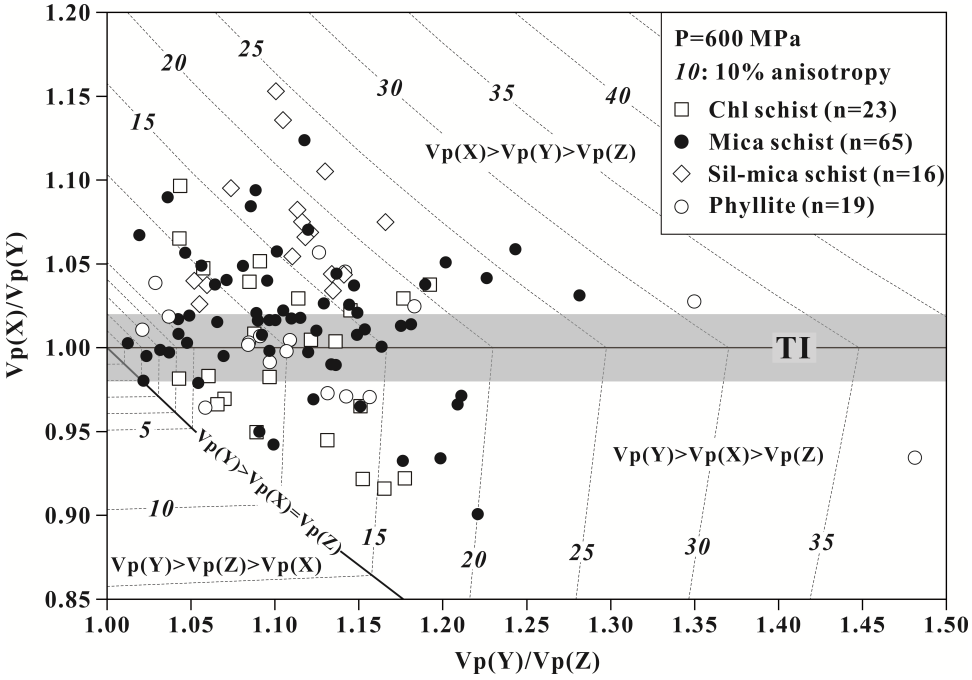


Figure 3.18 Flinn-type diagram showing P-wave velocities of 23 chlorite schists (open squares), 65 mica schists (solid dots), 19 phyllites (open dots) and 16 sillimanite-mica schists (open diamonds) at 600 MPa. Dashed lines signify iso-anisotropy surfaces. The shadowed zone indicates a quasi-transverse isotropy pattern.

As shown in Figure 3.18, all of the schist samples display consistently $V_p(Y) \geq V_p(Z)$ while their $V_p(X)$ values can be either larger [above line $V_p(X)/V_p(Y)=1$)] or smaller [below line $V_p(X)/V_p(Y)=1$] than $V_p(Y)$. The point (1, 1) represents elastically isotropic rocks. Dashed lines in Figure 3.18 represent iso-contours of V_p bulk anisotropy. Only 5 samples are nearly isotropic with $A_p(B) \leq 3\%$ and mica grains in these samples are disseminated, equidimensional, and poorly oriented (e.g., Meltzer and Christensen, 2001). Over one third of the 123 samples are located within the shadowed area in Figure 3.18 [i.e., $V_p(X)/V_p(Y)=1.00 \pm 0.02$] and can be regarded as quasi-transverse isotropic, reflecting the dominant role of mica or chlorite CPO, with the (001) planes subparallel to the foliation, on seismic anisotropy. The remaining samples lie either in the domain of $V_p(X)>V_p(Y)>V_p(Z)$ (above the TI zone) or that of $V_p(Y)>V_p(X)>V_p(Z)$, whereas no samples plot in the $V_p(Y)>V_p(Z)>V_p(X)$ domain. On the boundary between the $V_p(Y)>V_p(X)>V_p(Z)$ and $V_p(Y)>V_p(Z)>V_p(X)$ domains, $V_p(X)=V_p(Z)$. Seismic properties of the samples beyond the TI zone [$(V_p(X)/V_p(Y)>1.02$ or <0.98] have orthorhombic symmetry where seismic velocities are different in orthogonal directions within the foliation plane.

In Figure 3.19, we take two mica schist samples (GLG237 and GLG258) from the Gaoligong shear zone (Yunnan, China) as examples to illustrate the variations of the bulk anisotropy A_p(B) and the foliation anisotropy A_p(F) [defined in Eq. (1.32)] as a function of confining pressure. Both A_p(B) and A_p(F) decrease first rapidly with increasing confining pressure below 200 MPa, and then slowly above this pressure. The decreases in both A_p(B) and A_p(F) are presumably caused by progressive closure of microcracks in the schists with increasing hydrostatic pressure. At 600 MPa, A_p(B)=10.8% and 17.6%, and A_p(F)=1.6% and 1.4% for samples GLG237 and GLG258, respectively. Clearly, the anisotropy in the foliation plane is much smaller than the bulk anisotropy for these mica schists. As shown by Table 3.3, shear-wave birefringence in schist GLG258 displays an orthorhombic pattern with ΔV_s values of 0.939，0.796, and 0.011 km/s in the X, Y, and Z directions, respectively, at 600 MPa. When shear waves propagate within the foliation plane, V_s(XY)-V_s(YX)=0.171 km/s and V_s(XZ)-V_s(YZ)=0.028 km/s at 600 MPa.

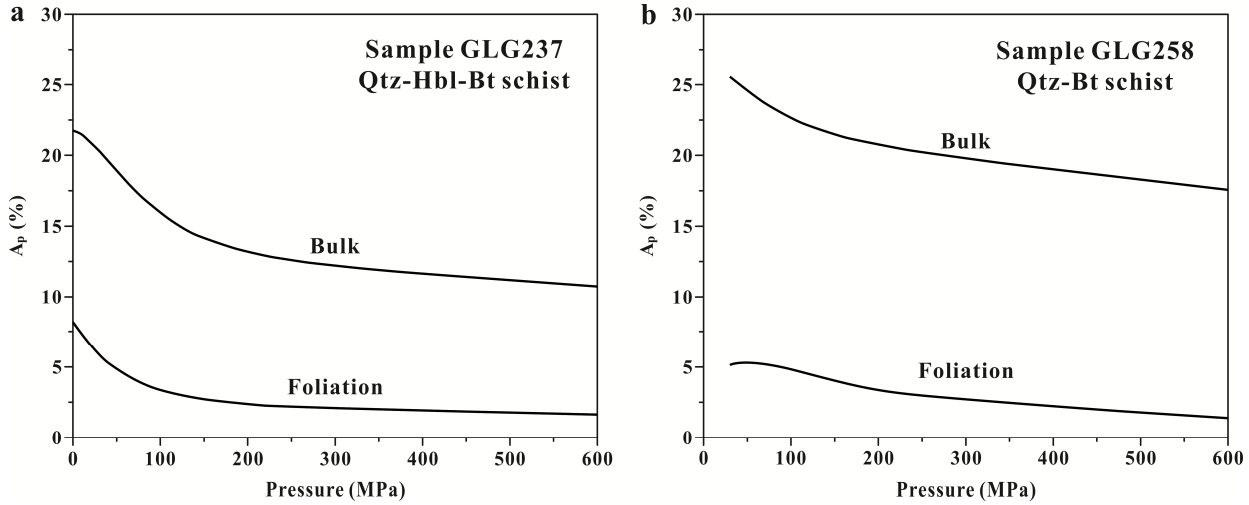


Figure 3.19 Bulk anisotropy and foliation anisotropy of P-wave velocities as a function of hydrostatic pressure in a Qtz-Hb-Bt schist (sample GLG237) and a Qtz-Bt schist (sample GLG258) from the Gaoligong shear zone (Yunnan, China).

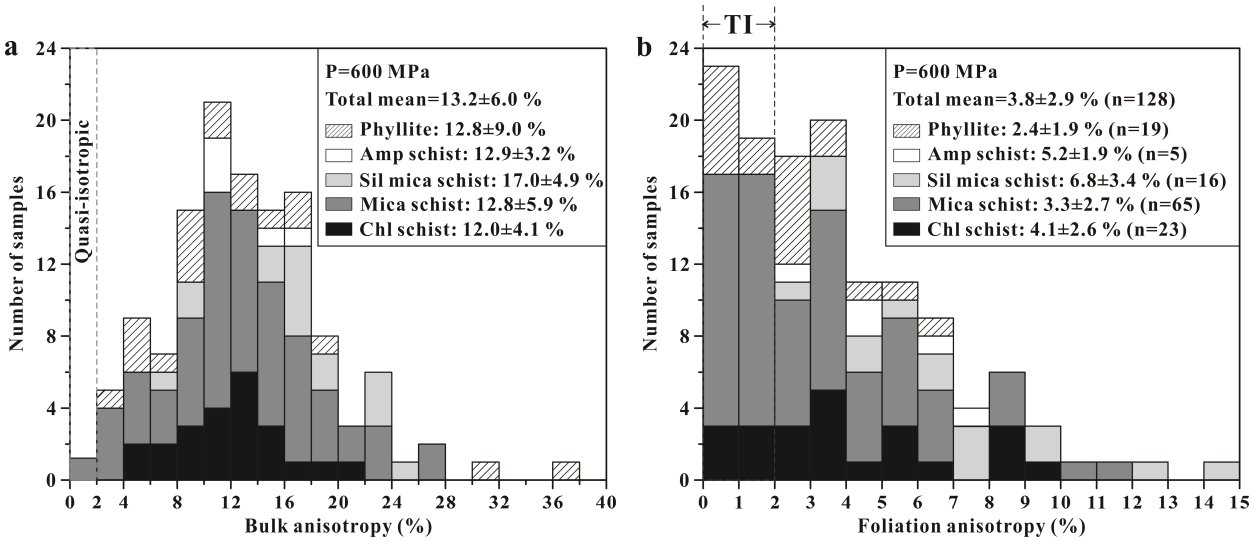


Figure 3.20 Histograms of the (a) bulk anisotropy and (b) foliation anisotropy of P-wave velocities for 23 chlorite schists, 65 mica schists, 19 phyllites, 16 sillimanite-mica schists, and 5 amphibole schists at 600 MPa.

Figure 3.20 shows the histograms of the bulk anisotropy and foliation anisotropy of P-wave velocities for 23 chlorite schists, 65 mica schists, 19 phyllites, 16 sillimanite-mica schists, and 5 amphibole schists at 600 MPa. The average bulk anisotropy values for chlorite schists, mica schists, phyllites, sillimanite-mica schists, and amphibole schists at 600 MPa are 12.0±4.1%, 12.8±5.9%, 12.8±9.0%, 17.0±4.9%, and 12.9±3.2%, respectively, indicating that such schists are much more anisotropic in V_p (13.2±6.0%) than other categories of metamorphic rocks such as granitic gneisses, felsic mylonites, granulites, and peridotites (e.g., Ji et al., 1993, 1994a; Mainprice and Silver, 1993; Saruwatari et al., 2001) in which the constituent minerals have geometrically complex seismic responses that interfere destructively to produce either low anisotropy or nearly isotropic properties. The characteristically high seismic anisotropy of the schists is attributed to strongly aligned phyllosilicates such as mica (Figure 3.6; also see Brownlee et al., 2011; Erdman et al., 2013; Ji et al., 1993; Kern and Wenk, 1990; Mahan, 2006; Meltzer and Christensen, 2001; Shapiro et al., 2004) as shown also by microstructural observations (e.g., Figure 3.3). However, the average V_p anisotropy values in the foliation plane or foliation anisotropy are much smaller than the bulk anisotropy values at the same pressure: 2.4±1.9% for phyllites, 3.3±2.7% for mica schists, 4.1±2.6% for chlorite schists, 6.8±3.4% for sillimanite-bearing mica schists, and 5.2±1.9% for amphibole schists. The proportions of the 128 schist samples having foliation anisotropy values larger than 2%, 4%, 6%, 8%, and 10% are

67.2%, 37.5%, 20.3%, 10.2%, and 3.1%, respectively. Statistical analysis of the 128 schists examined here yields an average foliation anisotropy of 3.8±2.9%.

3.5.2 Effects of quartz on seismic anisotropy of schists

Below the line $V_p(X)/V_p(Y)=0.98$ (Figure 3.18), $V_p(Y)$ becomes significantly larger than $V_p(X)$ in schists containing considerable volume fractions of quartz whose CPO is an important factor to move the anisotropic pattern from the TI zone to the $V_p(Y)>V_p(X)>V_p(Z)$ domain. Heyliger et al. (2003) and McSkimin et al. (1965) measured single crystal velocity properties of quartz (Figure 3.16) and showed that quartz has three maxima (7.02 km/s) and three minima (5.31 km/s) in V_p, which are subparrallel to the z and r directions, respectively. P-wave velocities along the <a>, <m>, and <c> directions are 5.749, 6.006, and 6.319 km/s, respectively, at room temperature and room pressure (Figure 3.16). The seismic properties of quartzites have been calculated by Lloyd et al. (2011), Mainprice and Casey (1990), Naus-Thijssen et al. (2011a), and Ward et al. (2012) based on quartz CPO data. As shown in Figure 3.21， there are essentially 6 types of quartz fabrics. Type 1 fabric, which is characterized by a point maxima of quartz c-axes at Z, which is a consequence of low temperature deformation, is produced by basal <a> slip and results in $V_p(Z)\gg V_p(Y)\approx V_p(X)$ (coaxial strain) or $V_p(Z)\gg V_p(Y)>V_p(X)$ (simple shear) anisotropy pattern. Type 2 fabric, which results from rhombohedral <a> slip and is characterized by a point maxima of quartz c-axes at the middle way between Y and Z in the plane perpendicular to X, forms $V_p(Y)>V_p(Z)>V_p(X)$ anisotropy pattern. Type 3 fabric, which results from prism <a> slip at moderate temperatures and is characterized by a point maxima of quartz c-axes at Y, forms $V_p(Y)\gg V_p(Z)>V_p(X)$ anisotropy pattern. Type 4 fabric, which is characterized by a point maxima of quartz c-axes at X, is produced by prism <c> slip at high temperatures (Mainprice et al., 1986) and results in $V_p(X)\gg V_p(Y)\approx V_p(Z)$ anisotropy pattern. Type 5 fabric, which is induced by a combination of prism <a> and rhombohedral <a> slips, and results in $V_p(Y)>V_p(Z)\gg V_p(X)$ anisotropy pattern. Type 6 fabric, which is characterized by a complete single girdle of c-axes perpendicular to X, is produced by a combination of basal <a>, rhombohedral <a>, and prism <a> slips, and results in $V_p(Z)\approx V_p(Y)\gg V_p(X)$ anisotropy pattern.

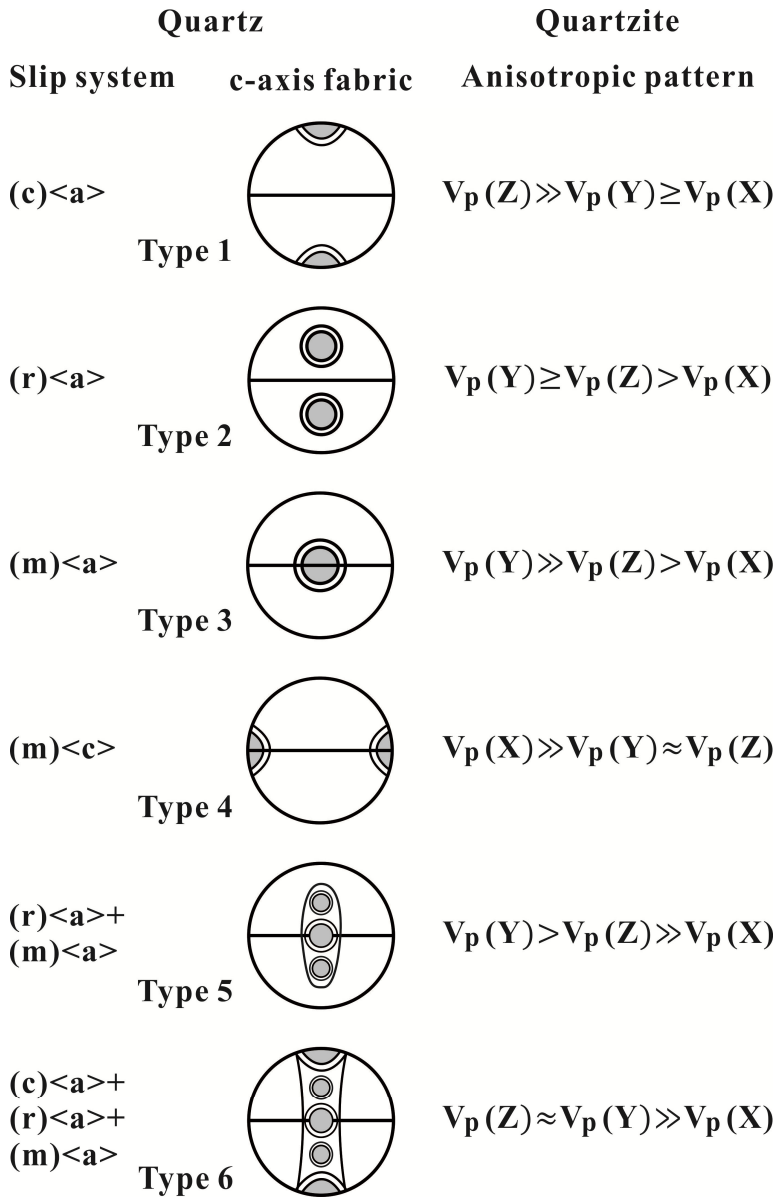


Figure 3.21 Basic types of quartz c-axis fabrics and corresponding seismic anisotropy patterns in coaxially deformed rocks.

Figure 3.22 plots the $V_p(X)/V_p(Y)$ versus $V_p(Y)/V_p(Z)$ data at 600 MPa to illustrate the categories of V_p anisotropy for 30 quartz-rich (>60 vol.%) rocks reported in this study (Table 3.2) and the literature (Barruol and Kern, 1996; Birch, 1960; Christensen, 1965; Fountain and Salisbury, 1996; Hughes et al., 1993; Ji et al., 1997; Kern et al., 1999; McDonough and Fountain, 1988, 1993; Punturo et al., 2005; Simons and Brace, 1965; Szymanski and Christensen, 1993; Zappone et al., 2000). Among these rocks, 7 samples [e.g., Granitic mylonite GLG97-2 from the Gaoligong shear zone from this chapter; Clarendon quartzite C8 from Christensen (1965); Pikwitonei

quartzite P33 from Fountain and Salisbury (1996); Upper Chihowee quartzites GMW24, GMW25, and GMW26 from Szymanski and Christensen (1993)] are quasi-isotropic with $A_p(B)$ ≤2% (the shadowed irregular hexagonal area in Figure 3.22) and located around point (1,1). Samples [e.g., Fuziling quartzite D9 from Kern et al. (1999), Iberian quartzite Z30 from Zappone et al. (2000), phyllitic quartzite F4 from Punturo et al. (2005), quartzite MT2 from Ji et al. (1997), and felsic mylonites GLG14 from this chapter] plot nearly on line $V_p(X)/V_p(Y)=1$, indicating a quasi-TI symmetry. Other samples which plot far from lines $V_p(X)/V_p(Y)=1$ and $V_p(Y)/V_p(Z)=1$ display orthorhombic symmetry. Samples [e.g., GLG237 and GLG258 from this chapter, Thomaston quartzite C6 from Christensen (1965), and Montana quartzite B9 from Birch (1960)] plot into domain $V_p(X)\geq V_p(Y)\gg V_p(Z)$ domain, reflecting the presence of a high temperature quartz fabric formed by prism <c> slip (Type 4 fabric in Figure 3.21). The effect of mica CPO [i.e., (001) planes aligned parallel to the foliation] tends to switch the anisotropy pattern from $V_p(X)>V_p(Y)>V_p(Z)$ toward $V_p(X)\approx V_p(Y)>V_p(Z)$. No samples lie in domain $V_p(X)>V_p(Y)<V_p(Z)$ (Figure 3.22). Sample RM8 from McDonough and Fountain (1993), which lies in domain $V_p(X)<V_p(Y)<V_p(Z)$, has an anisotropy pattern resulting from basal <a> slip (Type 1 fabric). The samples located in subdomain $V_p(Y)\geq V_p(Z)>V_p(X)$ contains nearly 100% quartz which deformed by prism <a> slip [Type 3 fabric, e.g., mylonitic quartzite RM9 from McDonough and Fountain (1993)] or rhomb <a> slip [e.g., ultramylonitic quartzite SB114a from Barruol et al. (1992)]. The samples containing 5-15 vol.% mica [e.g., sample RM19 from McDonough and Fountain (1993); samples KD5, KD9, KD12, and KD14 from McDonough and Fountain (1988)], plot in subdomain $V_p(Y)>V_p(X)\geq V_p(Z)$, indicating a combined effect from prism <a> slip in quartz and basal slip in mica. Clearly, adding mica into quartzites changes the bulk pattern of seismic anisotropy.

P-wave velocity anisotropy pattern of the schists shown in Figure 3.18 thus depends mainly on the interference effects between mica and quartz because these two main rock-forming minerals generally form strong CPOs. In a quartz-mica schist intensively deformed by simple shear, for example, the basal slip of mica causes $V_p(X)\approx V_p(Y)\gg V_p(Z)$ while the prism <a> slip of quartz, which develops a point maxima of quartz c-axes at Y and a strong concentration of <a> at X, respectively (e.g., Mainprice and Casey, 1990; McDonough and Fountain, 1988, 1993; Ward et al., 2012), will increase $V_p(Y)$ but decrease $V_p(X)$. As a result, this quartz-mica schist falls into the $V_p(Y)>V_p(X)>V_p(Z)$ domain (Figure 3.22). If quartz deforms by prism <c> slip, which

develops a point maxima or multiple concentrations of quartz c-axes parallel or subparallel to the lineation (Mainprice et al., 1986), a schist containing considerable volume fractions of quartz will move into the $V_p(X)>V_p(Y)>V_p(Z)$ domain (e.g., samples GLG237 and GLG258, Figure 3.22).

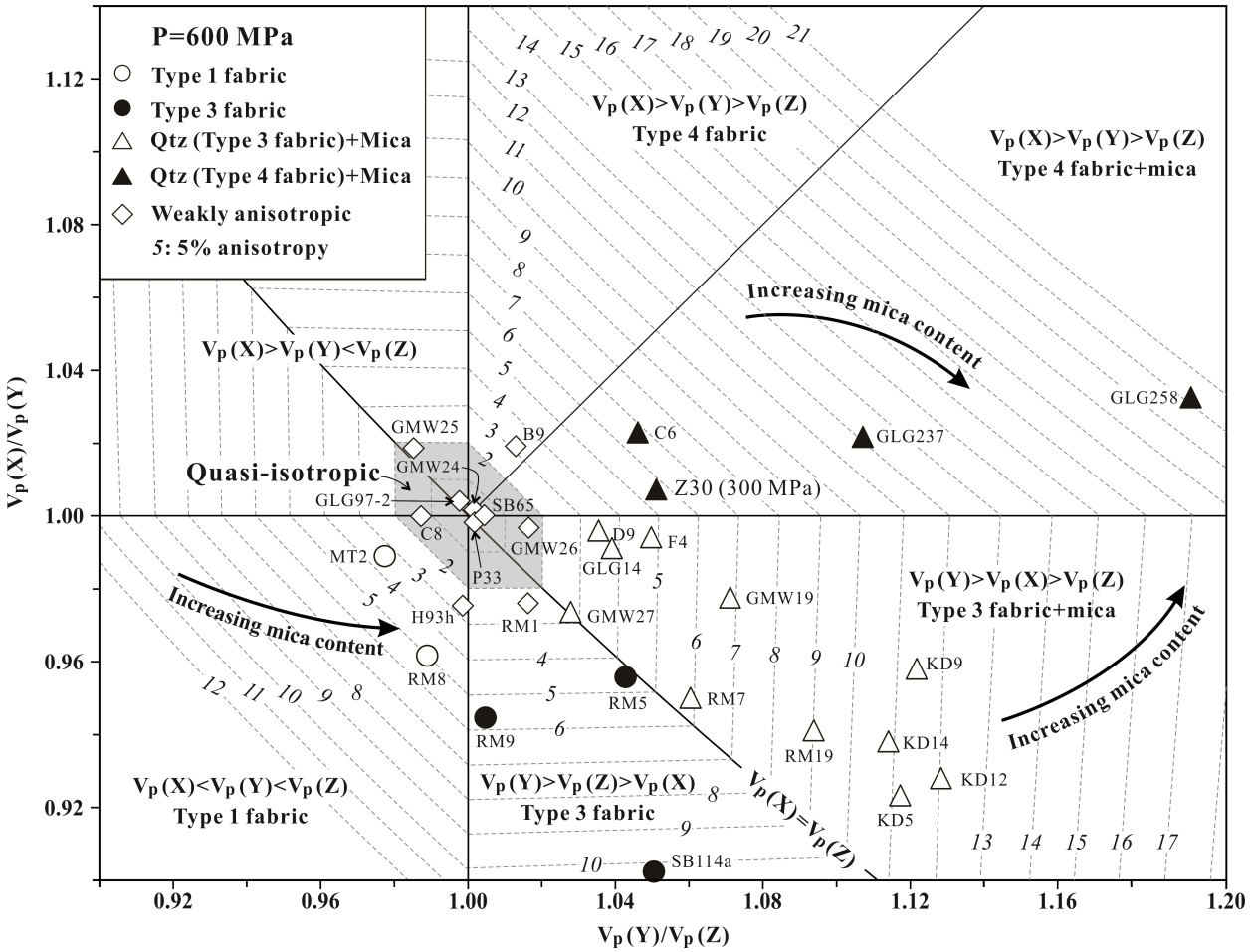


Figure 3.22 Cobweb diagram showing anisotropic patterns classified according to P-wave velocity ratios for 30 quartz-rich metamorphic rocks at 600 MPa. Dashed lines signify iso-anisotropy surfaces. The shadowed central zone indicates quasi-isotropy in seismic properties (bulk $A_p \leq 2\%$). See text for discussion.

Fifteen samples composed essentially of quartz, feldspar (plagioclase ± k-feldspar) and mica (biotite ± muscovite) (Table 3.5) were used to build Figures 3.23 and 3.24 in order to explore the mineralogy-dependence of the bulk and foliation seismic anisotropy. A_p(B) increases remarkably with increasing mica content when the latter is higher than ~12 vol.% (Figure 3.23a). However, A_p(F) shows little variations with mica content for this set of rocks. A_p(F) and particularly A_p(B) display a general tendency of decrease with increasing content of feldspar (Figure 3.23b). These

facts indicate a destructive interference between mica and feldspar in the formation of bulk seismic anisotropy. Interestingly, A_p(B) displays an increase with increasing quartz content until ~60 vol.%, followed by a decrease above this critical content, reflecting a competition between quartz and mica to the formation of the bulk anisotropy. The decrease in A_p(B) is attributed to the decrease in mica content (denoted by blue arrow in Figure 3.23c) when the quartz volume fraction is above ~60 vol.%. For example, from sample GLG258 (55 vol.% Qtz and 45 vol.% mica), through GLG257 (60 vol.% Qtz and 40 vol.% mica), to YN1389 (67.7 vol.% Qtz and 32.3 vol.% mica) (Table 3.5; Figure 3.23c), a consistent decrease in A_p(B) is observed, which should be attributed to the destructive interaction between quartz and mica on the bulk seismic anisotropy of rock. In contrast, a gentle increase in A_p(F) is observed in the full range of quartz content from 0 to 100%. It was previously reported that increasing quartz likely cancels the anisotropy caused by feldspar (e.g., Ji et al., 1993) because the fast V_p directions of the feldspar are aligned with the slow V_p directions of the mica or quartz, reducing the overall anisotropy of quartz-feldspar-mica rocks (e.g., Erdman et al., 2013; Ji et al., 1993). The effects of quartz-feldspar-mica (QFM) interaction on the bulk and foliation anisotropy are further illustrated by ternary plots (Figures 3.24a and 3.24b). A_p(B) is critically controlled by mica content while its corresponding A_p(F) is principally affected by quartz content for the rocks when their mica contents are higher than ~12 vol.%.

Table 3.5 Calculated P-wave seismic properties based on EBSD-measured CPO and modal compositions for 15 quartz- and mica-bearing rock samples[a]

Sample	Lithology	$V_p(X)$	$V_p(Y)$	$V_p(Z)$	V_p(mean)	$A_p(B)$	$A_p(F)$	$V_p(Y)/V_p(Z)$	$V_p(X)/V_p(Y)$	k_p	Modal composition (vol.%)	References
		km/s	km/s	km/s	km/s	%	%					
GLG132J	Qtz-Bt-Ms schist	6.230	6.424	5.563	6.061	14.21	3.07	1.155	0.970	-0.195	Qtz 60.0, Pl 14.0, Bt 10.0, Ms 16.0	This chapter
GLG133	Dioritic mylonite	6.229	6.373	5.632	6.069	12.21	2.29	1.132	0.977	-0.172	Qtz 50.0, Pl 33.0, Bt 15.0, Grt 2.0	This chapter
GLG257	Qtz-Bt schist	6.381	6.223	5.120	5.880	21.45	2.51	1.215	1.025	0.118	Qtz 60.0, Bt 40.0	This chapter
YN1389	Qtz-Bt-Ms schist	6.410	6.574	5.401	6.105	19.21	2.53	1.217	0.975	-0.115	Qtz 67.0, Bt 7.0, Ms 25.0, Mag 1.0	This chapter
GLG258	Qtz-Bt schist	6.104	6.275	4.976	5.755	22.57	2.76	1.261	0.973	-0.104	Qtz 55.0, Bt 45.0	This chapter
PNG/08-02	Quartzofeldspathic gneiss	6.080	6.070	6.020	6.057	0.99	0.16	1.008	1.002	0.198	Qtz 30.5, Fsp 65.4, Bt 3.8, Czo 0.3	Brownlee et al. (2011)
PNG/08-33	Quartzofeldspathic gneiss	6.160	6.070	6.010	6.080	2.47	1.47	1.010	1.015	1.485	Qtz 31.2, Fsp 58.6, Ms 6.1, Bt 3.4, Grt 0.6	Brownlee et al. (2011)
RM1	Gneiss	6.040	6.180	6.050	6.090	2.30	2.29	1.021	0.977	-1.054	Qtz 44.0, Pl 34.0, Kfs 15.0, Ms 7.0	Edrman et al. (2013)
RM6	Gneiss	6.010	6.050	6.140	6.066	2.14	0.66	0.985	0.993	0.451	Qtz 25.0, Pl 48.0, Kfs 16.0, Bt 11.0	Edrman et al. (2013)
RM7	Quartzite	5.820	6.200	6.020	6.011	6.32	6.33	1.030	0.939	-2.050	Qtz 85.0, Pl 3.0, Kfs 10.0, Bt 1.0, Ms 1.0	Edrman et al. (2013)
RM10	Gneiss	6.150	6.140	6.150	6.147	0.16	0.16	0.998	1.002	-1.002	Qtz 30.0, Pl 35.4, Kfs 24.0, Ms 10.0, Grt 0.6	Edrman et al. (2013)
RM16	Quartz monzonite	5.960	6.040	6.160	6.053	3.30	1.33	0.981	0.987	0.680	Qtz 29.0, Pl 46.0, Kfs 19.0, Bt 6.0	Edrman et al. (2013)
RM19	Quartzite	5.950	6.250	5.880	6.025	6.14	4.92	1.063	0.952	-0.763	Qtz 86.0, Pl 1.0, Kfs 10.0, Bt 3.0	Edrman et al. (2013)
RM28	Gneiss	6.040	6.130	5.930	6.033	3.32	1.48	1.034	0.985	-0.435	Qtz 36.0, Pl 32.0, Kfs 22.0, Bt 10.0	Edrman et al. (2013)
RM29	Micaceous quartzite	6.000	6.240	5.810	6.014	7.15	3.92	1.074	0.962	-0.520	Qtz 79.0, Pl 10.0, Bt 11.0	Edrman et al. (2013)

[a]Mineral symbols and abbreviations are according to Whitney and Evans (2010).

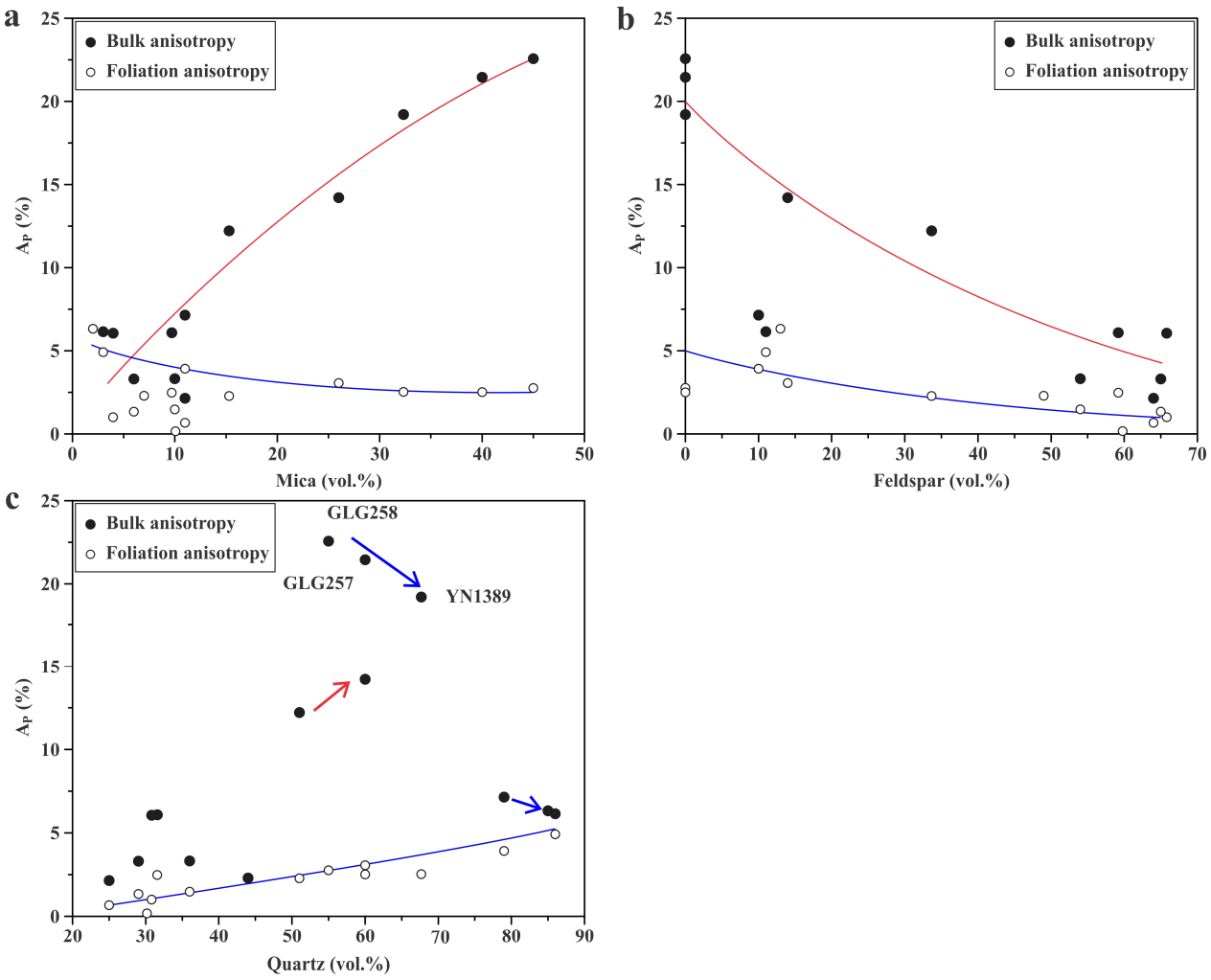


Figure 3.23 Bulk (solid dot) and foliation (open dot) anisotropy of P-wave velocity as a function of volume fractions of (a) mica, (b) feldspar, and (c) quartz for 15 samples consisting of mica, quartz and feldspar (5 samples from this chapter; 8 samples from Erdman et al., 2013; 2 samples from Brownlee et al., 2011). Data used to build this figure are given in Table 3.5.

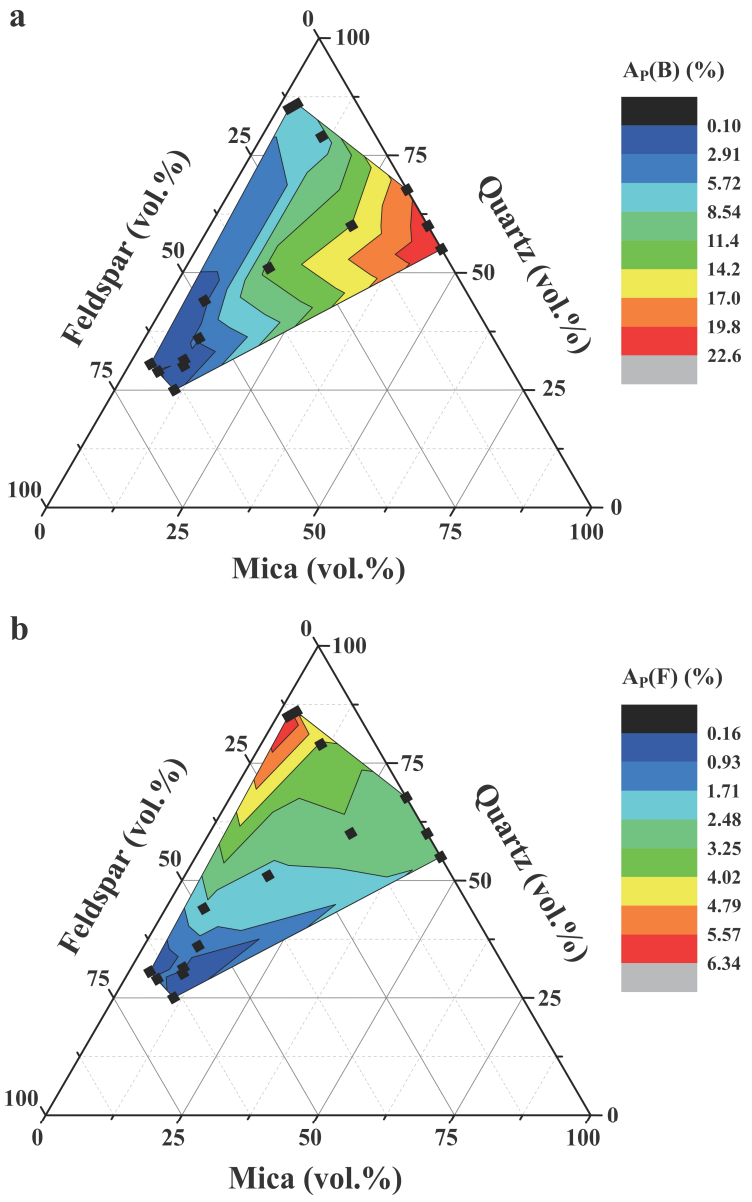


Figure 3.24 Ternary plots of (a) bulk and (b) foliation anisotropies as a function of normalized modal compositions of quartz (Q), feldspar (F), and mica (M). Each black diamond denotes data of each sample (Table 3.5).

3.5.3 Effects of prismatic minerals on seismic anisotropy of mica schists

The presence of amphibole, kyanite, and sillimanite whose common crystallographic habit is long prismatic, acicular, or fibrous along the c crystallographic axis, is also an important factor in causing the seismic anisotropy pattern of mica schists to depart from TI. Hornblende (Figure 1.5) has P-wave velocities of 6.0, 7.25, and 7.9 km/s along the directions normal to (100), (010), and parallel to the c-axis, respectively, with a bulk anisotropy of 23.8% (Hearmon, 1984). P-wave

velocities along the a-, b-, and c-axes of sillimanite (Figure 1.5) are 9.4, 8.5, and 10.9 km/s, respectively, giving the mineral an anisotropy of 22.7% (Vaughan and Weidner, 1978). Because fast c-axes of amphibole, kyanite, and sillimanite are generally aligned preferentially parallel to the lineation (Figures 3.9-3.10, also see Goergen et al., 2008; Ji et al., 2013b; Ko and Jung, 2015; Lambregts and van Roermund, 1990; Liu et al., 2012; Piazolo et al., 2014; Xu et al., 2007), V_p(X) values and V_p(X)/V_p(Y) ratios of the schists increase with prismatic mineral content. Accordingly, the anisotropic symmetry of prismatic minerals-bearing mica schists switches from TI to orthorhombic symmetry. As shown in Figure 3.18, the sillimanite-bearing mica schists have an obviously orthorhombic anisotropy pattern for P-wave velocities. These amphibolite-granulite facies metapelite samples, which were collected from the Lancangjiang shear zone of Yunnan (this chapter), the Ivrea-Verbano zone and Serie dei Laghi, northern Italy (Barruol and Mainprice, 1993a; Burlini and Fountain, 1993), and the Peloritani Mountains, Sicily, Italy (Punturo et al., 2005), contain 6-20 vol.% sillimanite, 25-50 vol.% biotite, 1-14 vol.% muscovite, 19-40 vol.% quartz, and 1-24 vol.% feldspar. Microstructural observations (e.g., Figure 3.6f) reveal that mica (001) planes are aligned parallel or subparallel to the foliation (Barruol and Kern, 1996; Burlini and Fountain, 1993; Khazanehdari et al., 2000; Punturo et al., 2005) and thus the observed orthorhombic symmetry cannot be caused by the CPO of mica. Figure 3.25 shows the variation of bulk V_p anisotropy [A_p(B, %)] as a function of the sillimanite volume fraction [φ_{sil}(%)]: A_p(B, %)=0.58φ_{sil}(%)+11.97 (R^2=0.75). This correlation suggests that the anisotropy caused by the CPO of mica would be 11.97% if sillimanite were absent. Both mica and sillimanite are thus the major contributors to the bulk anisotropy of the metapelitic schists. A clear tendency is also observed for the foliation anisotropy [A_p(F)] to increase with the volume fraction of sillimanite in the metapelitic samples (Figure 3.25). As indicated by the correlation A_p(F, %)=0.58φ_{sil}(%) (R^2=0.92), the mica schists will be transverse isotropic if no sillimanite is present. Hence the significant departure of the metapelites from being transversely isotropic results from the strong CPO of sillimanite whose fast c-axes are preferentially aligned parallel to the lineation (Figure 3.10). Similary, a kyanite schist (sample B11) from the Serie dei Laghi, northwest Italy (Khazanehdari et al., 2000) has an orthorhombic symmetry pattern with P-wave velocities along the X, Y, and Z directions of 6.941, 6.330, and 5.896 km/s, respectively, and an A_p(F) value is as high as 9.2% at 500 MPa.

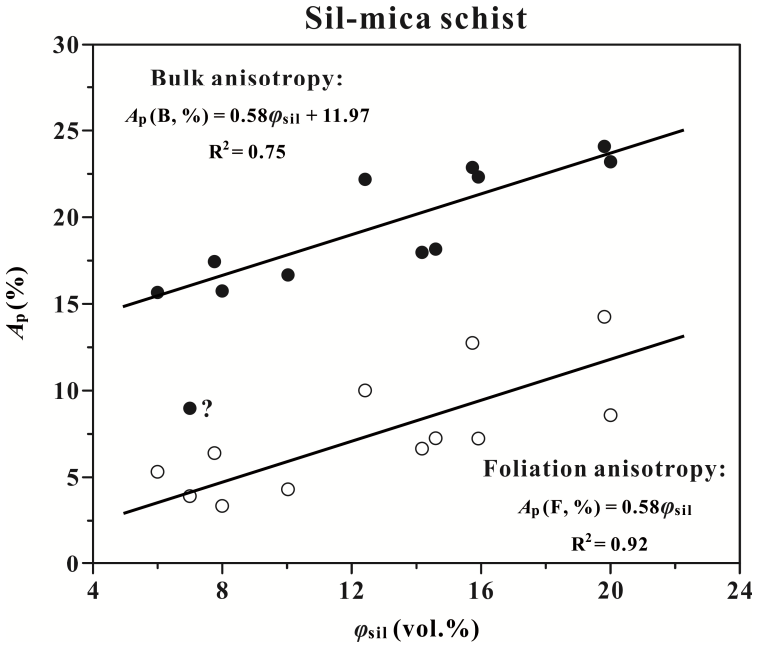


Figure 3.25 Bulk anisotropy (solid dots) and foliation anisotropy (open dots) of P-wave velocities as a function of sillimanite content (vol.%) for metapelitic schists.

3.5.4 Seismic properties of amphibole schists

Schists whose essential constituents are amphibole (e.g., hornblende, actinolite, and tremolite) and plagiocalse with lesser amounts of quartz, garnet, and mica are named amphibole schists. These schists, which deformed under the amphibolite facies metamorphic conditions, are equivalent to well-foliated, fine- to medium-grained amphibolites, whose protolith is usually a mafic igneous rock or greywacke (e.g., Winter, 2001). As shown in Figure 3.26, the seismic properties of 4 amphibole schists (samples AM2, AM3, P59, and S3570) and an amphibolitic gneiss (sample AM1) consistently display orthorhombic symmetry with $V_p(X)>V_p(Y)>V_p(Z)$ rather than TI symmetry. The orthorhombic symmetry is essentially controlled by the characteristic CPO of amphibole (Figure 3.9): the [001] directions are preferentially aligned parallel to X while the (100) planes are parallel or subparallel to the foliation because plagioclase displays nearly random or very weak CPO in the amphibole schists (Figure 3.8). In the foliation plane, P-waves along the X direction are 0.328, 0.352, 0.467, 0.507, and 0.620 km/s faster than those along the Y direction in samples AM2, P59, S3570, AM3, and AM1 at 600 MPa. For the amphibole schists, the bulk anisotropy of P-wave velocities [A_p(B)] decreases rapidly with increasing confining pressure below 200 MPa, and then reaches almost a constant value above this pressure (Figure 3.27a). At 600 MPa, the foliation anisotropy A_p(F)=4.54%, 4.86%, 6.96%, and 7.03% for amphibole schists P59, AM2,

S3570, and AM3 respectively (Figure 3.27b). For the amphibolitic gneiss AM1 at 600 MPa, the foliation anisotropy A_p(F) can be as high as 8.6% (Figure 3.27b). Assuming a TI symmetry for an amphibolitic gneiss like sample AM1 can underestimate and overestimate P-wave velocities in the X and Y directions, respectively, by 4.3%. As illustrated in Figure 3.26, samples S776.2 (42 vol.% Qtz, 35 vol.% Pl, 10 vol.% Bt, 9 vol.% Hbl, and 4 vol.% Chl) and GLG237 (55 vol.% Qtz, 30 vol.% Bt, and 15 vol.% Hbl) display their seismic properties switching from the orthorhombic symmetry towards the TI pattern due to an increase in biotite content.

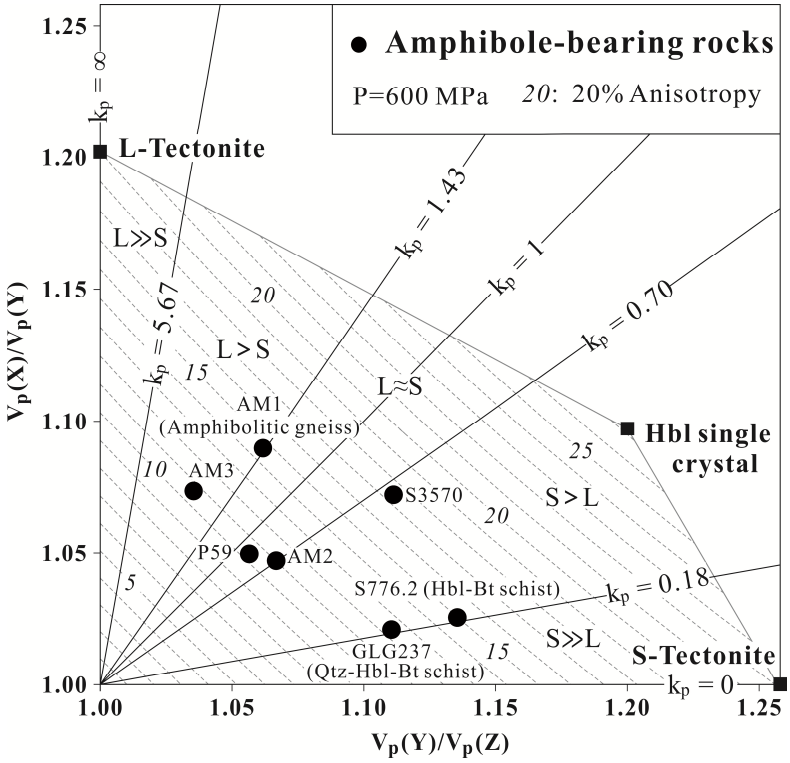


Figure 3.26 Flinn-type diagram showing P-wave velocities of four amphibole schists (samples AM2, AM3, P59, and S3570), an amphibolitic gneiss (sample AM1), a Hbl-Bt schist (sample S776.2) and a Qtz-Hbl-Bt schist (GLG237) at 600 MPa. Dashed lines indicating iso-anisotropy surfaces. The maximum anisotropy values are also illustrated for single crystal of hornblende, and S- and L-tectonites composed of amphibole. S- and L-tectonites, which deformed by coaxial flattening and coaxial constriction, develop only foliation and only lineation, respectively, whereas LS-tectonites develop both flattened foliation and stretching lineation under simple shear. S>L (foliation dominates over lineation) and L>S (lineation dominates over foliation).

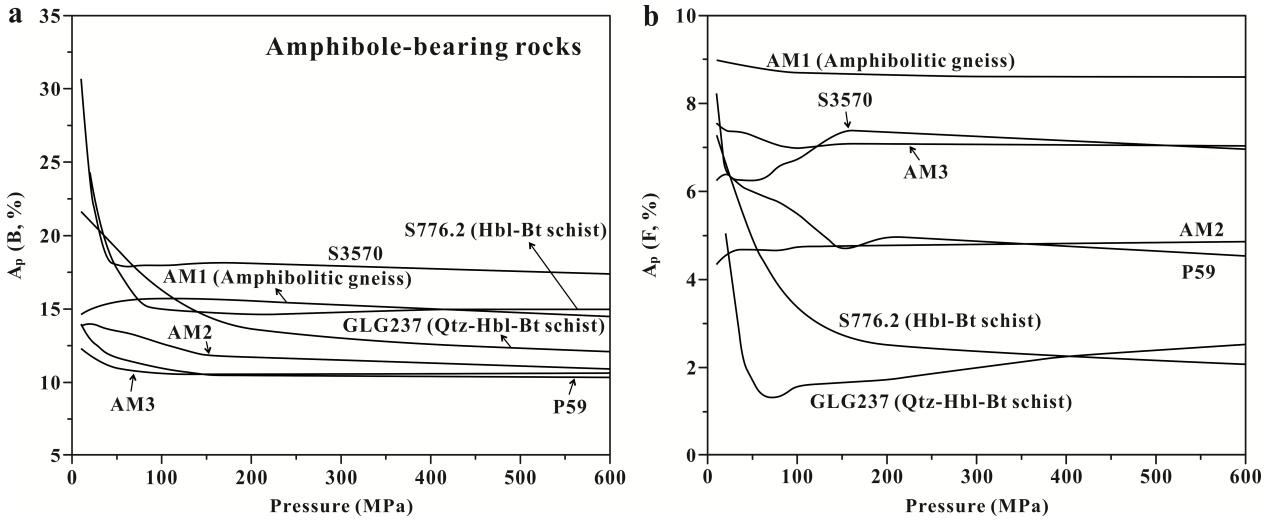


Figure 3.27 (a) Bulk anisotropy and (b) foliation anisotropy of P-wave velocities as a function of hydrostatic pressure for four amphibole schists (samples AM2, AM3, P59, and S3570), an amphibolitic gneiss (sample AM1), a Hbl-Bt schist (sample S776.2) and a Qtz-Hbl-Bt schist (GLG237) at 600 MPa.

3.5.5 Shear-wave velocity anisotropy

As noted above, for a fully TI material V_s(XY) should equal V_s(YX), V_s(XZ) should equal V_s(YZ), and V_s(ZX) should equal V_s(ZY). Plots of V_s(XY) versus V_s(YX), V_s(XZ) versus V_s(YZ), and V_s(ZX) versus V_s(ZY) are given in Figure 3.28 for 33 mica- or amphibole-bearing samples for which S-wave velocities were measured in six pairs of propagation-vibration directions (XY, XZ, YX, YZ, ZX, and ZY) at hydrostatic confining pressures up to 600 MPa [8 samples from this chapter and 25 from the references (Barruol and Kern, 1996; Builini and Fountain, 1993; Burke, 1991; Christensen, 1996; Fountain and Salisbury, 1996)]. The samples display a general trend: V_s(XY)≈V_s(YX), V_s(XZ)≈V_s(YZ), and V_s(ZX)≈V_s(ZY) with values of $|V_s(XY)-V_s(YX)|$, $|V_s(XZ)-V_s(YZ)|$, and $|V_s(ZX)-V_s(ZY)|\leq 0.1$ km/s (shadowed zone in Figure 3.28) for most samples (Figure 3.29). For example, amphibole schist AM2, whose V_p velocities display typically orthorhombic symmetry with V_p(X)=7.402 km/s, V_p(Y)=7.073 km/s, and V_p(Z)=6.633 km/s, is nearly transverse isotropic with V_s(XY)=4.222 km/s and V_s(YX)=4.180 km/s, V_s(XZ)=3.922 km/s and V_s(YZ)=3.803 km/s, and V_s(ZX)=3.932 km/s and V_s(ZY)=3.873 km/s at 600 MPa. Shear-wave birefringence values, which are 0.300, 0.377, and 0.058 km/s in the X, Y, and Z directions, respectively, at 600 MPa, display approximately the TI behavior. The above facts indicate that the mica- or amphibole-bearing schists and mylonites are essentially TI materials in

terms of S-wave velocities and splitting, although their P-wave properties may display orthorhombic symmetry.

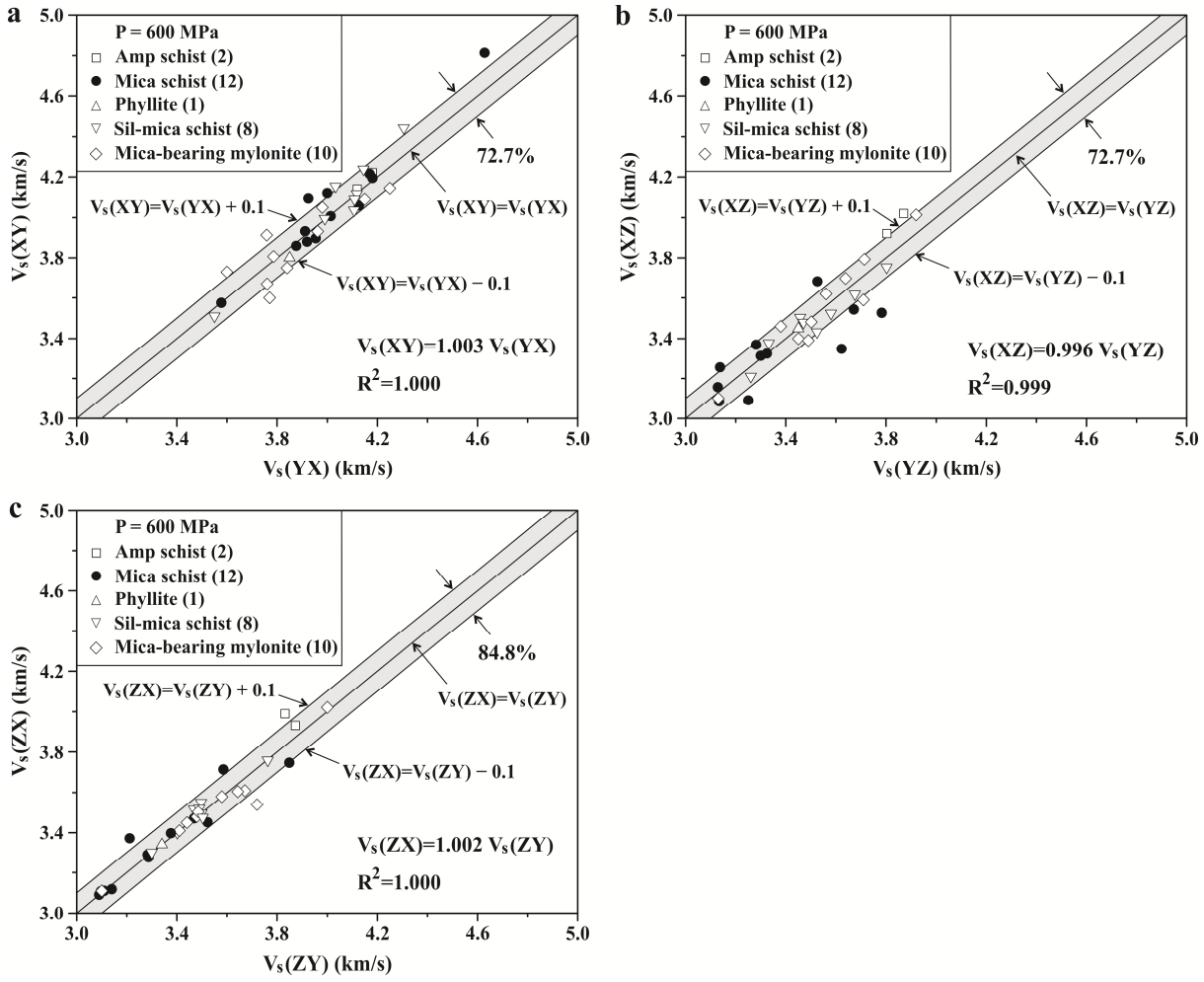


Figure 3.28 Plots of V_s(XY) versus V_s(YX), V_s(XZ) versus V_s(YZ), and V_s(ZX) versus V_s(ZY) in (a), (b), and (c), respectively, for 2 amphibole schists, 12 mica schists, 1 phyllite, 8 sil-mica schists and 10 mica-bearing felsic mylonites.

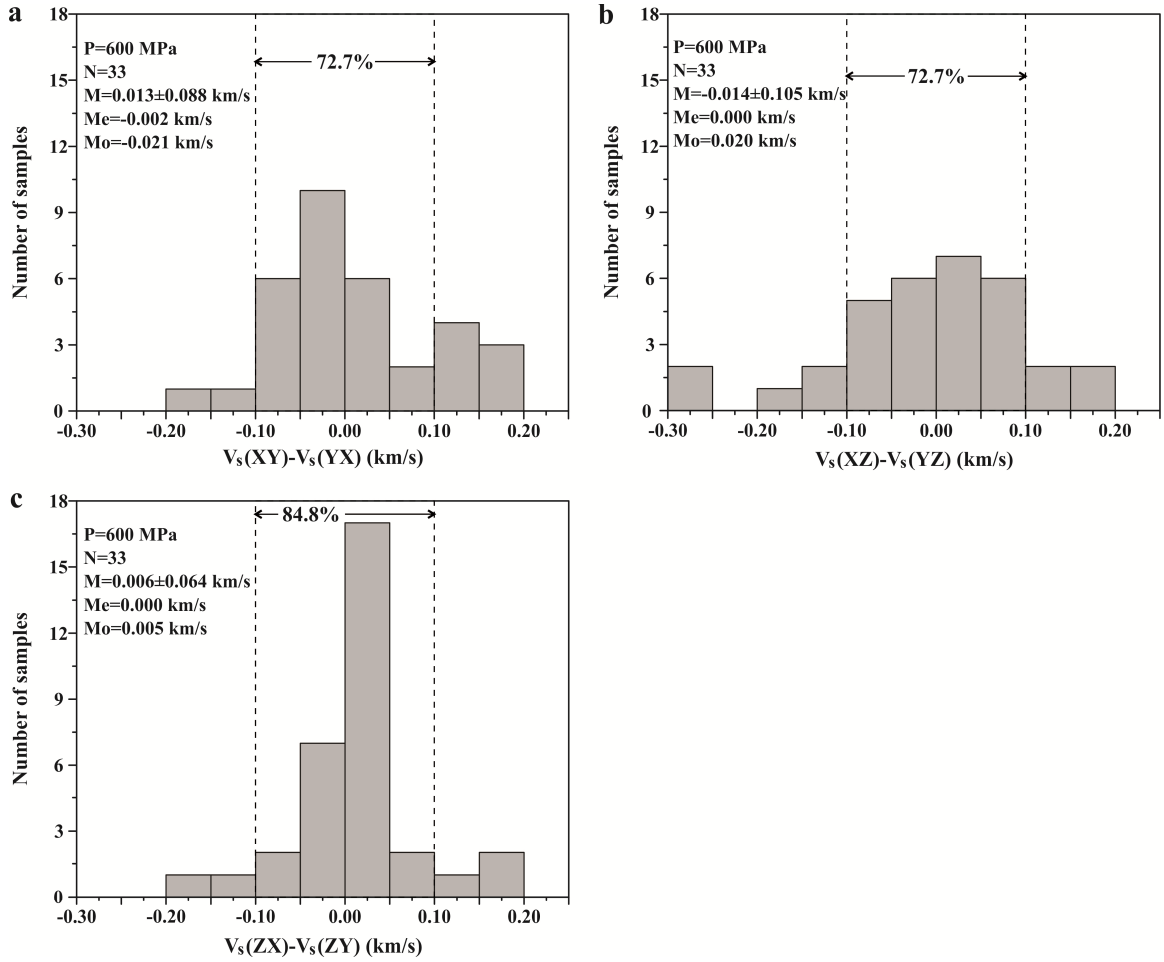


Figure 3.29 Histograms of V_s(XY)-V_s(YX), V_s(XZ)-V_s(YZ), and V_s(ZX)-V_s(ZY) values for 33 schists plotted in Figure 3.28. Data at 600 MPa.

3.5.6 Implications for interpretation of crustal structure and seismic data from the southeast Tibetan Plateau

Around the east Himalayan Syntaxis, the E-W structures in Tibet bend into the N-S or NW-SE direction in Yunnan, which has been rotated clockwise 70-90° with respect to the Tibet Plateau. The Ailao Shan-Red River fault zone is a tectonic boundary separating the Indochina block with an average crustal thickness of 36-37 km on the southwest and the Yangtze block with an average crustal thickness of 40-42 km on the northeast (Sun et al., 2014). The thickness of the crust beneath west Yunnan between the Ailao Shan-Red River fault zone and the Nabang fault zone increases northward (Sun et al., 2014; Wang et al., 2010). The average crustal Poisson's ratio in west Yunnan (≤0.280, V_p/V_s=1.81) is significantly higher than that in east Yunnan (≤0.245, V_p/V_s=1.72). In west Yunnan, the crustal Poisson's ratio decreases with increasing crustal

thickness (Chen et al., 2013; Ji et al., 2009; Sun et al., 2014), implying most likely thickening of felsic materials within the upper and middle crust and delamination of mafic materials from the lower crust. The high crustal Poisson's ratios have been interpreted to result from partial melting within the deep crust. Tomographic observations of a low-velocity column from the middle crust (15-30 km depth with V_s=2.9-3.3 km/s) down to 420 km depth in the upper mantle (Chen et al., 2010; Hu et al., 2014; Sun et al., 2014), regionally high electrical conductivity (Bai et al., 2010), high attenuation (Zhao et al., 2013), and high surface heat flow (Hu et al., 2000) are attributed to an upwelling of hot, flowing materials from the dehydration-induced partial melting of the eastward subducted Burma micro-plate. The thickness of the lithosphere beneath west Yunnan (Hu et al., 2014) is about 80-100 km, which is much thinner than that beneath Sichuan (140-180 km).

The shear-wave splitting parameters for SKS and SKKS phases in the southeast Tibetan Plateau have been investigated by Huang et al. (2007, 2011), Lev et al. (2006), and Shi et al. (2012). In the region between latitudes 30°N and 34°N, and longitudes 96°E and 99°E (Figure 3.1), the polarization directions of fast split shear waves (ϕ) are aligned almost parallel to the strike of fault zones (e.g., Jinshajiang fault and Jiali fault). Between latitudes 21°N and 27°N, however, the average polarization direction of fast split shear waves (ϕ) at stations between the Ailao Shan-Red River fault zone and the Nabang fault zone in the southwest Yunnan is 110±19°, which is approximately parallel to the absolute plate motion of the region but at high angles with the strikes of the fault zones. The observations are distinctly different from previous reports of parallelism between the fast polarization directions of SKS seismic waves and the strike of orogenic belts or suture zones in Tibet and Tian Shan (e.g., Chen et al., 2010; Fu et al., 2008; Gao and Liu, 2009; Huang et al., 2000; Li et al., 2011; McNamara et al., 1994; Wang et al., 2010) and many other orogenic belts (Heidbach et al., 2010; Nicolas et al., 1993; Savage, 1999). Tectonic implications of such a parallelism have been explored in terms of strike-parallel motion in the upper mantle (Nicolas, 1993). The average delay time is 1.58±0.44 s in the southwest Yunnan. However, Pms phases, which are the P-to-S waves converted at the Moho and extracted by receiver function analysis, display their fast polarization directions essentially parallel to the strikes of the fault zones and show splitting times of up to 0.45 s with typical values of 0.30 s (Figure 3.1, Chen et al., 2013; Sun et al., 2012, 2014; Xu et al., 2006). The wave paths of the Pms phases are confined within the crust. Station YUJ, for example, is located near the Red

River-Ailao Shan shear zone and showed a splitting delay time of 0.58 s. As the fast directions of the Pms phases are at quite high angles to the direction of the maximum horizontal compressional stress (σ_1) (Figure 3.1), the anisotropy cannot be interpreted by alignments of σ_1-parallel tensile cracks in the upper crust (above 15 km depth). Thus, the N-S to NW-SE polarized crustal anisotropy detected by Pms splitting in Yunnan should be attributed to the contribution of mica- and amphibole-bearing rocks such as schist, amphibolite, gneiss, and mylonite. In contrast, the SKS and SKKS splitting corresponds to seismic anisotropy caused primarily by the CPOs of olivine and pyroxenes (e.g., Ji et al., 1994a; Mainprice and Silver, 1993; Saruwatari et al., 2001) and preferred orientation of melt pockets (e.g., Kohlstedt and Zimmerman, 1996) in the hot flowing upper mantle. Hence, S-wave anisotropy in Yunnan is consistent with a model of two anisotropic layers: an upper layer related to frozen fabrics of mica- and amphibole-bearing rocks within the crust, which deformed during compressional folding and strike-slip shear, and a lower layer related to present-day APM-driven flow in the lithospheric mantle and asthenosphere. The most plausible interpretation for the discrepancy between the fast polarization directions of SKS and SKKS phases and GPS-measured surface velocity vectors (e.g., Gan et al., 2007) is the decoupling between the crust and mantle of the region. Temperature is probably high enough at the base of the crust to make the Moho or the crust-mantle transition zone as a decoupling interface between the crust and upper mantle. In this interpretation, the frozen fabrics of mica- and amphibole-bearing rocks within the crust beneath Yunnan, which formed by past ductile deformation (e.g., compressional folding and strike-slip shear), have been rotated almost 90° clockwise from initially E-W to the present-day N-S around the east Himalayan Syntaxis in response to progressive indentation of India into Asia.

The decoupled motion between the mantle and crust beneath the southeast Tibetan Plateau, as inferred by the discrepancies between SKS and Pms splitting data, is inconsistent with the tectonic escape model proposed by Tapponnier et al. (1982). In their plasticene analogue modeling experiments (Figure 3.30), vertical thickening, folding, and thrust faulting were strictly inhibited because the material is artificially maintained between two Perspex plates. Only horizontal plane strain was allowed and dominated by brittle faulting and lateral displacement and rotation of fractured blocks. Each of the fractured blocks (i.e., A and B in Figure 3.30, which are representative for Indochina and South China, respectively), which had almost no internal strain, was significantly extruded laterally southeastward or eastward and rotated rigidly up to

~40°. For example, points a, b, c, and d moved to a', b', c', and d', respectively (Figure 3.30). Deformation was localized along brittle faults that are always vertical from the upper and lower surfaces of the block that stands for the full lithosphere. Obviously, the analogue experiments of Tapponnier et al. (1982) cannot be representative for the generally-accepted concept that a rigid die (India) indents a plastic body (Asia) on the geological time scale. Although the block is initially composed of vertical layers of homogenous plasticene welded together by trichloroethane, the mechanical coupling between the layers prevented interlayer-slips. Moreover, the block contains no inherent weaknesses or discontinuities, analogue to faults, shear zones, and sutures in the lithosphere, so that they can be reworked or reactivated in response to progressive penetration of the indenter. Thus, the tectonic model of Tapponnier et al. (1982) could not predict any decoupling between the crust and the upper mantle.

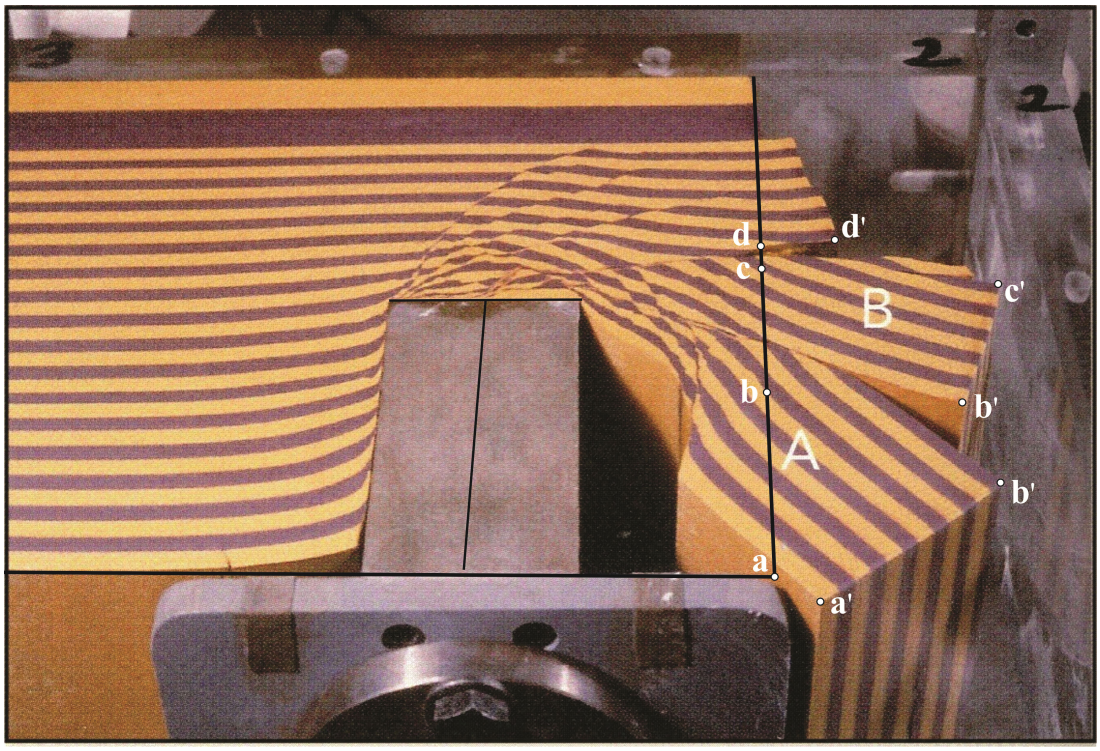


Figure 3.30 Experiment of plasticene by Tapponnier et al. (1982), which emphasizes the eastward extrusion of the Indochina and South China lithospheric blocks bounded by major strike-slip faults as a result of the India-Eurasia convergence.

The crustal deformation has been experimentally reconstructed by Ji and Wang (unpublished data) with simple dough analogue modeling experiments, producing insightful results (Figure 3.31). The rectangular indenter has the same thickness as the colorful dough layers before the

indentation so that the indenter is deep enough to indent the whole dough layers. The yellow, magenta, white, and green blocks are analogue to south Lhasa (Myanmar block), north Lhasa (Sibumasu block), Qiangtang (Indochina block), and Kunlan terranes, respectively (Figure 3.1). The indenter advanced at a steady speed. The deformation and displacements of the dough's upper surface marked by black grids were monitored using photographs taken from various directions. The dough deforms in a ductile manner, analogue to the ductile middle and lower crust while the upper crust deforms generally in a brittle fashion but has been removed by tectonic exhumation and erosion in the study region. It is reasonable to assume that the deformation behavior of the bulk crust is controlled by the ductility of the middle and lower crust while the upper crust is only to accommodate the deformation of the underlying middle and lower crust (Dewey et al., 1989).

An asymmetric tectonics is observed in all laboratory experiments of Ji and Wang (unpublished data) where the strain patterns are significantly different in the west and the east of India. Almost no deformation occurs in the regions west of line 12 (Figure 3.31). A mega, wide, left-lateral strike-slip shear zone occurs between lines 13 and 17. The strengths of lateral shear and stretching increase from line A to line R. The three dough blocks to represent the south Lhasa, north Lhasa, and Qiangtang terranes are extensively deformed: folding, lateral shear, subhorizontal stretching, and rotation around the Syntaxes. With successive indentation, the northern boundary of the plateau propagates northwards while the southern boundary of the plateau is thrust southwards upon the India plate. The northward advance of the indenter formed an arcuate folded belt around each Syntaxis. A bending occurs with a rotation to up to 75° about a vertical axis at each Syntaxis, which are clockwise in the east and counterclockwise in the west. The orogen-parallel extension results in E-W oriented horizontal stretching lineation in the plateau in front of the indenter and SE and SW oriented, subhorizontal stretching lineation in the parts east and west of the indenter, respectively. Wrench movements, as indicated by the change of marked squares to rhombuses, are originated from the differential stretching in the crust deformed by the indentation. The migration traces of points A and V, which were located at the original eastern margin of the south Lhasa terrane, are shown in Figure 3.31b. Clearly, no final lateral escape of rigid blocks as proposed by Tapponnier et al. (1982) has been observed. The analogue experiments also demonstrate the geomorphologic and geological features of the Tibetan Plateau: the highest plateau Tibet resulting from crustal thickening by folding and ductile

flow (e.g., Cohen and Morgan, 1987; England and Houseman, 1989; Houseman and England, 1986) occurs immediately north and the two corners of the India indenter while the ranges decrease their elevations from the east Syntaxis to the southeast or from the west Syntaxis to the southwest.

Between lines 17 and 24, the region in front of the rectangular indenter (India) soon becomes thickening by folding and ductile flow, forming an arcuately folded belt (Figure 3.31b). The N-S compression causes E-W extension which produces N-S trending normal faults in the brittle upper crust (e.g., Elliott et al., 2010) and stretching lineation (Brun et al., 1985; Xu et al., 2013) in the ductile middle and lower crust. The stretching lineation is parallel to the fold axis and aligned E-W and thus orogen-parallel. The fold axis is bended around the syntaxes and the intensity of its bending increases with the progressive northward penetration of the indenter. The folds in front of the indenter and around the corners of the indenter move northward along the indenter, indicating that considerable detachment has occurred on the dough-plate (crust-mantle) interface or the Moho. The longitudinal strain (ε) or extension was estimated by the comparison between the original and final lengths. The extension in the central Tibetan Plateau and the northwest Yunnan is 32% while that in the Chaman shear zone is as high as 158%. The regions between lines 24 and 31 are involved by folding, subhorizontal stretching, and clockwise rotation around the east Syntaxis. A minor left-lateral strike-slip movement is observed along the boundary between the yellow and magenta terranes, which corresponds to the Lancangjiang shear zone (Akciz et al., 2008; Zhang et al., 2010). The eastern boundary between the south and north Lhasa terranes, which was initially straight, becomes curved in order to accommodate the differential rotations of the blocks. The experiments show that both the Sibumasu and Indochina blocks have been rotated clockwise with respect to the Ordos and North China blocks (Avouac and Tapponnier, 1993). The migration path of the Sibumasu block, derived from the analogue model, is a curve with first southwestward displacement and then westward and finally northwestward movement (Figure 3.31b). The clockwise rotation results in a series of NE-SW oriented sinistral strike slip faults within the Sibumasu and Indochina blocks (e.g., Wanding fault, Nanting fault, Mengxing fault, Mam Ma fault, Mae Chan fault, and Dien Bien Phu fault).

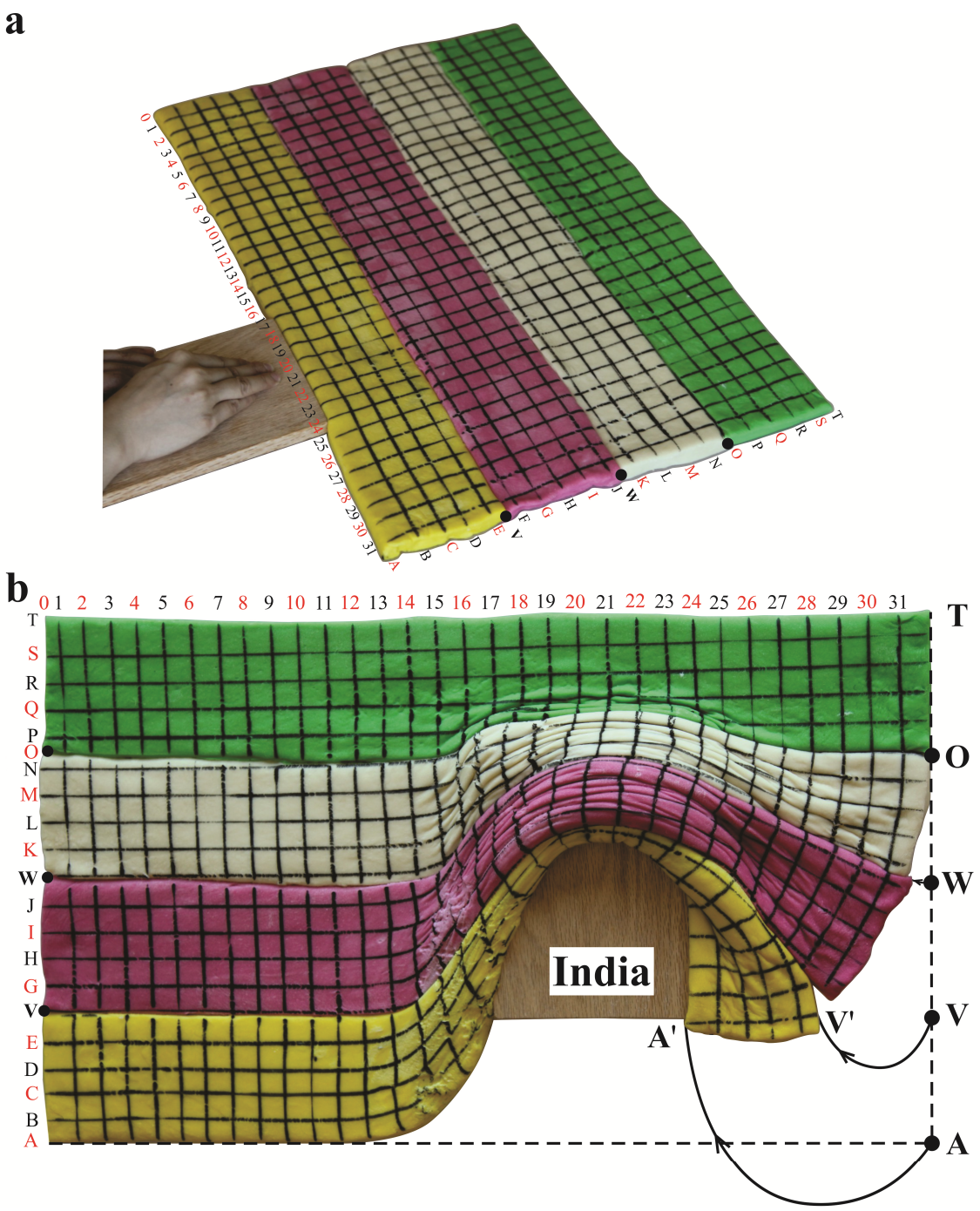


Figure 3.31 Dough experiment (Ji and Wang, unpublished data) suggesting that the post-collisional convergence by the northward indentation of India has been accomplished principally by crustal thickening through folding and vertical stretching in a northward-propagating zone north of the Indian indenter and the clockwise rotation and northwestward displacement of the Sibumasu and Indochina blocks.

Sun et al. (2012) proposed that the crustal seismic anisotropy in the southeast Tibetan Plateau is formed by horizontal channel flow of the lower crust from the centre of the Tibetan Plateau to its edge due to an elevation-induced pressure gradient between the plateau and its surroundings (Clark and Royden, 2000). Their interpretation disagrees with the structural observations in the exhumed metamorphic rocks in west Yunnan where foliation is consistently vertical or subvertical (Figure 3.2). Furthermore, there is almost no shear-wave splitting in the direction normal to the foliation in the mica or amphibole-bearing schists, gneisses, and mylonites (Table 3.3, and Figures 3.5 and 3.11). Thus, the crustal anisotropy as indicated by a splitting delay time of as much as 0.58 s cannot be produced by gravity-driven channel flow in the lower crust, which would result in a horizontal foliation.

In previous interpretation of teleseismic shear-wave splitting results, possible crustal contributions were ignored. We used Qtz-Bt schist samples GLG237 and GLG258 to calculate the amount of delay times (δt) caused by shear-wave splitting that would result from a vertically propagating shear-wave traveling along the Y direction in a 10 km thick schist belt with uniformly vertical foliation and horizontal lineation. In west Yunnan, vertical foliation-related crustal anisotropy is significant. The calculations suggest that δt=0.17 and 0.65 s for a 10 km thick schist layers consisting of materials equivalent to samples GLG237 (45 vol.% Qtz, 30 vol.% Bt, 15 vol.% Hbl, 10 vol.% Pl) and GLG258 (55 vol.% Qtz and 45 vol.% Bt), respectively. If the thickness of the anisotropic layers increases to 20 km, delay times of 0.34 and 1.30 s could occur in shear zones consisting of such materials. Certainly, the anisotropy of an actual schist belt would be significantly lower than that of sample GLG258, which is unusually anisotropic, because seismic methods such as teleseismic observations inherently sample material properties at a much larger length-scale than laboratory methods. The spatial heterogeneity in composition, structure (e.g., macro-scale folds), and CPO will be averaged by seismic observations, making the averaged anisotropy over a distance of 20-30 km (a typical diameter of the column sampled by SKS teleseismic waves) lower than the intrinsic anisotropy measured from a single sample. The presence of felsic gneisses and mylonites (e.g., samples GLG14 and GLG97-2) with lower seismic anisotropy will also decrease the splitting delay times. In addition, the effects of spatial variations in CPO strength and foliation orientation always dilute the values of seismic anisotropy observed at larger length scales of investigation. The present chapter suggests, however, that the crust, which contains 15-25 km thick schists, can easily contribute as much as

0.3-0.5 s to observed delay times caused by shear-wave splitting, consistent with the results from Pms splitting (Chen et al., 2013; Xu et al., 2006; Sun et al., 2012, 2014). Furthermore, the vertical foliation-related crustal anisotropy is parallel to the strikes of shear zones, which are at high angles with respect to the mantle anisotropy (Figure 3.1), in Yunnan. The crustal anisotropy contributes negatively to observed SKS and SKKS splitting values. Thus, if this is the case, then it is possible that the total anisotropy determined from teleseismic shear-wave splitting measurements is less than the actual amount of mantle anisotropy. If double splitting has occurred and δt values are anomalously small at certain stations (e.g., Luxi and Wanding in the Gaoligong shear zone, and Jinghong in the Lancangjiang shear zone), mantle strain beneath west Yunnan may be underestimated by teleseismic shear-wave splitting values (e.g., Chang et al., 2006; Huang et al., 2007; Lev et al., 2006; Shi et al., 2012).

3.6 Conclusions

Statistical analysis of the 132 samples shows that the average bulk V_p anisotropy [A_p(B)] for chlorite schists, mica schists, phyllites, sillimanite-mica schists, and amphibole schists at 600 MPa is 12.0±4.1%, 12.8±5.6%, 12.8±9.0%, 17.0±4.9%, and 12.9±3.2%, respectively. These schists show much higher V_p anisotropy (13.2±6.0%) than other categories of metamorphic rocks such as granitic gneisses, felsic mylonites, granulites, and peridotites in which the constituent minerals have geometrically complex seismic responses that interfere destructively to produce either low anisotropy or nearly isotropic properties. The degree of anisotropy for the schists is a function of phyllosilicate content, CPO strength, and strain geometry. Most of the schist samples show some P-wave velocity anisotropy in the foliation plane [A_p(F)], indicating that their seismic properties are orthorhombic rather than purely transversely isotropic. The average A_p(F), although much smaller than the bulk anisotropy at the same pressure, is 2.4±1.9% for phyllites, 3.3±2.7% for mica schists, 4.1±2.6% for chlorite schists, 6.8±3.4% for sillimanite-mica schists, and 5.2±1.9% for amphibole schists. The proportions of the 128 schist samples having A_p(F) values larger than 2%, 4%, 6%, 8%, and 10% are 67.2%, 37.5%, 20.3%, 10.2%, and 3.1%, respectively. These schists yield an average A_p(F) of 3.8±2.9%. In the schists studied, P-wave velocities along the foliation are always larger than in the Z direction. In situ seismic measurements from refracted rays with a substantial portion of their travel path in the foliation plane will systematically overestimate the average velocity of these rocks. Even in the foliation plane,

seismic velocities can vary with propagating direction, with the maximum velocity parallel to X or Y. Assuming a transverse isotropy (TI) pattern for all the schists, gneisses, and mylonites would systematically underestimate or overestimate the seismic velocities in the direction of lineation or in the Y direction. For the schists with purely TI seismic properties, it is impossible to determine the orientation of the lineation (transport direction) using seismic methods.

The departure of schists from TI seismic properties is mainly caused by the presence of non-phyllosilicate minerals (e.g., amphibole, sillimanite, and quartz). Amphibole, kyanite, and sillimanite generally developed strong CPOs with fast c-axes parallel to the lineation, which increases the velocity along the lineation (X) and causes the schists to switch from hexagonal to orthorhombic symmetry. Amphibole schists are characterized by orthorhombic anisotropy with $V_p(X)>V_p(Y)>V_p(Z)$, reflecting the CPO of amphibole [001] directions parallel to X while the (100) planes are parallel or subparrallel to the foliation. The sillimanite-bearing mica schists display significant foliation anisotropy of up to 14% with an average value of 6.8%. The foliation anisotropy increases linearly with the content of sillimanite in the schists. Increasing feldspar generally reduces the bulk anisotropy caused by mica or quartz via the fast-axis of the former aligned parallel to the slow-axis of the latter. Quartz affects the symmetry of seismic anisotropy of schists in a complex manner, depending on both the volume fraction and the prevailing slip system of quartz. The latter is further controlled by deformation conditions (e.g., temperature, pressure, differential stress, strain rate, magnitude and geometry of strain, and H_2O content). Moreover, strain geometry may also influence the symmetry of seismic properties in schists. Coaxial flattening makes their (001) planes parallel to the foliation, forming a TI pattern characterized by $V_p(X)=V_p(Y)\gg V_p(Z)$ with the lowest P-wave velocities normal to the foliation. Coaxial constriction forms a girdle distribution of phyllosilicate c-axis in the YZ plane perpendicular to the X direction, resulting in a TI pattern with $V_p(X)\gg V_p(Y)=V_p(Z)$. Simple shear may produce moderate and strong concentrations of phyllosilicate c-axes in the Z and Y directions in the YZ plane, respectively, causing an orthorhombic symmetry with $V_p(X)>V_p(Y)>V_p(Z)$.

However, most mica- or amphibole-bearing schists and mylonites approximate TI materials in terms of S-wave velocities and splitting although their P-wave properties may have weak orthorhombic symmetry. Our laboratory-measured and EBSD-based calculated seismic property data together with the analogue modeling experimental results help constrain the interpretation of

shear-wave splitting data from the southeast Tibetan Plateau. The N-S to NW-SE polarized crustal anisotropy detected by Pms splitting in the Sibumasu and Indochina blocks is caused by subvertically foliated mica- and amphibole-bearing rocks such as schists, amphibolites, gneisses, and mylonites. In contrast, the fast polarization direction of vertically propagating SKS and SKKS phases (110±19°), which is approximately parallel to the absolute plate motion of the region, principally reflects seismic anisotropy caused by CPOs of olivine and pyroxenes in the mantle and also possibly preferred orientation of vertically-aligned melt pockets, which are parallel to extensional shear bands (Kohlstedt and Zimmerman, 1996), in the hot flowing upper mantle (lithosphere and asthenosphere). The frozen fabrics of mica- and amphibole-bearing rocks within the crust of the Sibumasu and Indochina blocks, which formed by past ductile deformation (e.g., predominantly compressional folding and subordinately strike-slip shear), have been rotated 70-90° clockwise around the east Himalayan Syntaxis from initially E-W to a present-day nearly N-S orientation in response to the progressive indentation of India into Asia. Furthermore, the crustal anisotropy indicated by the Pms splitting delay times as high as 0.58 s cannot be produced by gravity-driven horizontal channel flow of the lower crust, since the latter should result in a horizontal foliation where vertically incident shear-wave will be hardly split. It is also inferred that no finite eastward or southeastward extrusion of the Sibumasu and Indochina blocks has occurred during progressive indentation of India into Asia.

CHAPTER 4 A NEW CALIBRATION OF SEISMIC VELOCITIES, ANISOTROPY, FABRICS AND ELASTIC MODULI OF AMPHIBOLE-RICH ROCKS

4.1 Introduction

Metamorphic rocks composed dominantly of amphiboles are referred to as amphibole-rich rocks. In such rocks, a second abundant constituent mineral can be orthopyroxene, clinopyroxene, garnet, plagioclase, biotite, epidote, or quartz. A hornblendite consists essentially of hornblende. Amphibole-rich rocks can be foliated or nonfoliated, depending on the degree of ductile deformation. Among the amphibole-rich rocks, amphibolite, which is composed mainly of amphibole and plagioclase with little or no quartz, is the most abundant. The protolith of amphibolite is either a mafic igneous rock or greywacke (e.g., Winter, 2001). An amphibolite can be retrograded into a greenschist which is a low-grade metamorphic rock that typically contains chlorite, muscovite, actinolite, epidote, and albite. An amphibolite can be transformed to an eclogite that contains omphacite and garnet under the conditions of low temperature and high pressure, or a mafic granulite that is predominantly composed of OH-free minerals such as orthopyroxene and plagioclase under the conditions of high temperature and moderate pressure.

Based on in situ seismic velocity data and petrological studies of xenoliths from volcanic eruptions and crustal sections of rock assemblages which were originated from great depth but now are exposed on the Earth's surface (e.g., the Ivrea zone, southern Alps, north Italy, Rutter et al., 2007), it is widely believed that amphibole-rich rocks (particularly amphibolite) become abundant (35-40 vol.%) in the middle crust (15-30 km) beneath the continents (e.g., Christensen and Mooney, 1995; Ji et al., 2009). For the same reason, layered amphibolite clusters within felsic rocks are considered as important candidates for the origin of deep crustal reflectivity (e.g., Barruol and Mainprice, 1993; Cholach et al., 2005; Ji et al., 1993, 1997; Ji and Long, 2006). At greater depths (30-40 km), amphibolite is transformed to mafic granulite. In the lowermost part of thickened crust beneath a high plateau, mafic granulite may then be transformed to eclogite which becomes denser than peridotite and is consequently detached from the crust and sink into the upper mantle. This process, which is referred to as delamination (Kay and Kay, 1993), is regarded as a mechanism that makes the continental crust more andesitic (e.g., Rudnick and

Fountain, 1995). Amphibolite is also thought to be abundant in the lower crust of oceanic arcs (Fliedner and Klempere, 2000; Kitamura et al., 2003; Nishimoto et al., 2005). The continents are believed to be a collage of oceanic arc blocks which accreted by serial coalescence according to the arc accretion model (e.g., Arculus, 1981; Condie, 1997). Amphibole and mica in amphibolites are important containers of water in the deep continental crust. Furthermore, partial melting of amphibolitic deep continental crust (Rushmer, 1991) or subducted oceanic crust (Hamilton, 1988) is the most likely source for the formation of plutonic bodies of tonalite-trondhjemite-granodiorites (TTG) and migmatites during orogenic events. The formation and growth of early (i.e. Archaean) continental crust are considered to have been controlled by melting of amphibolite in subduction zones (Foley et al., 2002).

To determine the volume fraction of amphibole-rich rocks in the continental crust beneath different tectonic regions is thus crucially important for constraining tectonic models of crustal evolution. Such information can currently be obtained only by comparing in situ observed seismic properties with those of amphibole-rich rock samples measured in laboratory. Here we report new results on P- and S-wave velocities and anisotropy of 17 amphibole-rich rock samples containing 34-80 vol.% amphibole, measured at room temperature and hydrostatic pressures up to 650 MPa (equivalent to ~24 km depth). The experimental results are combined with previous experimental data from the literature to provide a systematic calibration of seismic properties of amphibole-rich rocks, which serves as fundamental information for the interpretation of field seismic data from the continental and subducted oceanic crust.

4.2 Samples

The samples, containing 34-80 vol.% amphibole, were collected from the Gaoligong ductile shear zone of Yunnan, the Yunkai Mountains of Guangdong, and the Qinglong Massif in the Sulu ultrahigh-pressure (UHP) metamorphic belt (Jiangsu), China, the East Athabasca mylonite triangle in the Snowbird tectonic zone (northern Saskatchewan, Canada), and the Britt Domain of the southwestern Grenville Province (Ontario) of Canada. These amphibole-rich rocks display densities ranging from 2.81 to 3.20 g/cm^3 with a mean value of 3.01 g/cm^3 under ambient conditions (Table 4.1), mainly reflecting the relative contents of amphibole, plagioclase, and other minerals such as garnet, clino- and ortho-pyroxenes, mica, chlorite, quartz, and magnetite. The density distribution for this set of 17 samples (Figure 4.1) is comparable to that for the

amphibole-rich rocks reported in previous references (Barruol, 1993; Birch, 1960; Burke and Fountain, 1990; Christensen, 1965, 1978; Fountain, 1976; Fountain et al., 1990; Fountain and Salisbury, 1996; Ji et al., 2002; Kern and Fakhimi, 1975; Kern et al., 1996, 1997, 1999, 2001, 2009; Khazanehdari et al., 2000; McDonough and Fountain, 1988; Miller and Christensen, 1994; Punturo et al., 2005; Siegesmund et al., 1989; Zhao et al., 2011; Zhou et al., 2011). Figure 4.2 illustrates the histograms for the main chemical components of the studied samples, together with those of 28 amphibole-rich rock samples from previous references (Burke and Fountain, 1990; Fountain, 1976; Fountain et al., 1990; Kern et al., 1996, 1999, 2001, 2009; Miller and Christensen, 1994; Zhao et al., 2011; Zhou et al., 2011). Statistical analysis of these 45 samples yields an average composition (wt.%) for the amphibole-rich rocks: 49.50±4.05% SiO_2, 14.87±3.00% Al_2O_3, 11.33±3.13% $FeO+Fe_2O_3$, 9.78±2.16% CaO, 7.24±3.47% MgO, and 3.27±1.31% Na_2O+K_2O. In all of the amphibolites studied, flattened foliation and stretching lineation are clearly identified, allowing the minicores to be oriented with respect to an orthogonal reference system in which X lies parallel to the stretching lineation, Y is normal to the lineation and in the foliation plane, and Z is normal to the foliation plane. Modal and chemical compositions of the samples are given in Tables 4.1 and 4.2, respectively.

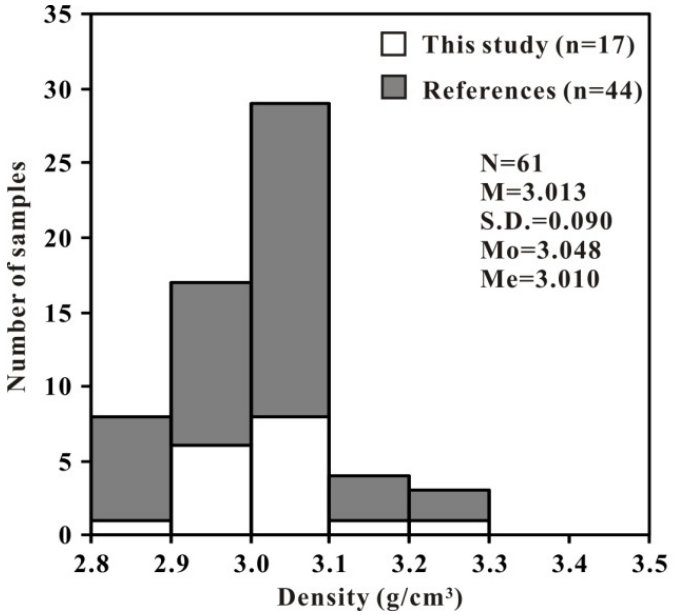


Figure 4.1 Densities (g/cm^3) of amphibole-rich rocks from this chapter (17 samples) and the references (44 samples). N, M, S.D., M_o, and Me as in Figure 2.6 caption.

Table 4.1 Description of the amphibole-rich rock samples studied*

Sample	Lithology	Location	Density g/cm^3	Modal composition (vol.%)
AM1	Amphibolite	Gaoligong Mts, Yunnan, China	3.063	Hbl 80.0, Pl 10.0, Qtz 6.0, Bt 4.0
AM2	Amphibolitic ultramylonite	East Athabasca mylonite triangle, Saskatchewan, Canada	3.000	Hbl 65.0, Pl 28.9, Ser 4.2, Acc 1.1, Chl 0.4, Qtz 0.2, Opq 0.2
AM3	Amphibolitic ultramylonite	East Athabasca mylonite triangle, Saskatchewan, Canada	3.020	Hbl 69.2, Pl 25.3, Opq 3.2, Ser 1.5, Acc 0.8
AM4	Cpx amphibolite	East Athabasca mylonite triangle, Saskatchewan, Canada	3.200	Hbl 61.8, Pl 19.2, Cpx 11.7, Grt 4.1, Opq 1.2, Ser 0.8, Chl 0.7, Czo 0.4, Ms 0.1
AM5	Serpentized hornblendite	East Athabasca mylonite triangle, Saskatchewan, Canada	3.080	Hbl 60.2, Srp 23.3 Opq 5.4, Spl 5.3, Tlc 3.3, Ol 2.5
AM6	Amphibolitic mylonite	East Athabasca mylonite triangle, Saskatchewan, Canada	2.970	Hbl 61.2, Pl 37.0, Bt 0.6, Cpx 0.6, Chl 0.6
AM7	Qtz-Chl amphibolite	East Athabasca mylonite triangle, Saskatchewan, Canada	2.970	Hbl 58.0, Pl 24.1, Chl 7.5, Qtz 5.6, Opq 2.1, Bt 1.4, Ser 1.2, Cal 0.1
AM8	Amphibolitic mylonite	East Athabasca mylonite triangle, Saskatchewan, Canada	3.010	Hbl 65.0, Pl 20.1, Qtz 6.1, Chl 5.3, Grt 1.5, Opq 1.1, Cpx 0.5, Ser 0.4
AM9	Amphibolite	Yunkai Mts, Guangdong, China	3.040	Hbl 46.0, Pl 43.5, Opq 3.0, Qtz 2.5, Bt 2.0, Chl 2.0, Ser 1.0
AM10	Qtz-Hbl gneiss	Sulu UHP mtamorphic terrane, Jiangsu, China	3.087	Hbl 80.0, Qtz 8.0, Pl 5.0, Opx 5.0, Opq 2.0
AM11	Cpx-Grt amphibolite	Central Gneiss Belt, Grenville Province, Ontario, Canada	3.083	Hbl 34.1, Pl 29.6, Grt 10.5, Cpx 10.1, Opq 5.6, Bt 5.3, Qtz 2.6, Ap 0.9, Chl 0.8, Kfs 0.5
AM12	Amphibolite	Central Gneiss Belt, Grenville Province, Ontario, Canada	2.910	Pl 48.3, Hbl 41.1, Bt 7.0, Qtz 3.1, Opq 2.0, Spn 0.2, Ap 0.1
AM13	Amphibolite	Central Gneiss Belt, Grenville Province, Ontario, Canada	2.930	Hbl 49.7, Pl 42.4, Pyx 2.2, Bt 1.9, Grt 1.7, Chl 1.1, Qtz 0.5, Kfs 0.3, Ap 0.2
AM14	Bt amphibolite	Central Gneiss Belt, Grenville Province, Ontario, Canada	2.810	Hbl 42.9, Pl 26.3, Bt 21.3, Qtz 8.1, Spn 0.5, Ms 0.5, Ap 0.2, Zrn 0.2
AM15	Amphibolite	Central Gneiss Belt, Grenville Province, Ontario, Canada	3.117	Pl 48.4, Hbl 45.1, Spn 4.9, Qtz 1.5, Ap 0.1
AM16	Cpx-Hbl gneiss	Sulu UHP mtamorphic terrane, Jiangsu, China	2.964	Hbl 50.0, Cpx 15.0, Chl 12.0, Pl 10.0, Qtz 5.0, Grt 3.0, Ep 2.0, Symp 2.0, Opq 1.0
AM17	Chloritized Cpx-Hbl gneiss	Sulu UHP mtamorphic terrane, Jiangsu, China	2.958	Hbl 45.0, Chl 30.0, Cpx 12.0, Opq 3.0, Ep 3.0, Symp 3.0, Qtz 2.0, Rt 2.0

*Mineral symbols and abbreviations according to Whitney and Evans (2010)

Table 4.2 Chemical compositions (wt.%) of amphibole-rich rock samples studied

Sample	SiO_2	TiO_2	Al_2O_3	Fe_2O_3	FeO	MnO	MgO	CaO	Na_2O	K_2O	P_2O_5	Cr_2O_3	BaO	SrO	LOI	Total
AM1	48.03	1.98	11.40	2.90	9.51	0.19	9.40	12.18	1.10	0.56	0.21	0.06	0.01	0.03	0.81	98.37
AM2	50.50	1.00	13.70	1.74	9.31	0.21	6.98	10.60	2.70	0.63	0.09	0.03	0.01	0.03	0.77	98.30
AM3	50.00	1.26	13.85	1.93	9.30	0.20	6.88	10.30	2.61	0.70	0.11	0.03	0.02	0.03	0.75	97.97
AM4	48.00	0.80	14.80	1.80	8.25	0.18	7.66	11.10	2.16	0.56	0.14	0.05	0.02	0.03	1.16	96.71
AM5	43.20	0.36	8.25	2.44	8.11	0.17	23.70	7.05	0.26	0.24	0.02	0.46	0.01	0.01	3.46	97.74
AM6	52.50	0.65	15.50	1.41	6.39	0.14	7.20	10.75	2.71	0.49	0.07	0.08	0.01	0.03	0.70	98.63
AM7	55.20	0.85	13.45	2.69	6.64	0.17	5.39	9.60	2.73	0.59	0.07	0.02	0.01	0.02	0.44	97.87
AM8	48.70	0.87	14.40	1.93	8.82	0.19	8.22	11.40	2.05	0.51	0.06	0.05	0.01	0.02	0.73	97.96
AM9	48.93	1.50	14.44	4.83	8.28	0.21	7.21	11.43	1.44	0.72	0.12	0.00	0.01	0.01	0.65	99.79
AM10	48.70	1.20	17.20	3.33	4.86	0.14	7.45	11.43	2.31	0.29	0.34	0.05	0.02	0.03	2.49	99.84
AM11	45.60	3.48	15.05	2.02	12.80	0.22	4.92	7.14	3.70	1.29	0.47	0.01	0.06	0.07	1.08	97.91
AM12	50.50	0.65	16.90	1.54	6.67	0.15	7.02	8.96	3.05	1.31	0.12	0.01	0.02	0.04	1.34	98.28
AM13	50.20	0.80	18.25	1.79	6.62	0.17	5.83	9.15	3.43	1.19	0.26	0.01	0.07	0.09	0.70	98.56
AM14	60.00	1.14	14.05	1.83	6.08	0.13	2.98	5.58	3.68	1.67	0.30	0.01	0.04	0.04	0.85	98.38
AM15	46.50	2.99	13.45	2.34	11.65	0.23	5.21	11.55	2.66	0.84	0.49	0.02	0.03	0.03	0.36	98.35
AM16	48.61	0.40	19.77	5.93	3.43	0.14	5.75	9.90	3.02	0.27	0.50	0.01	0.02	0.03	2.00	99.78
AM17	51.73	1.97	17.07	9.05	1.90	0.24	3.47	6.04	4.17	1.25	0.73	0.01	0.02	0.04	2.30	99.99

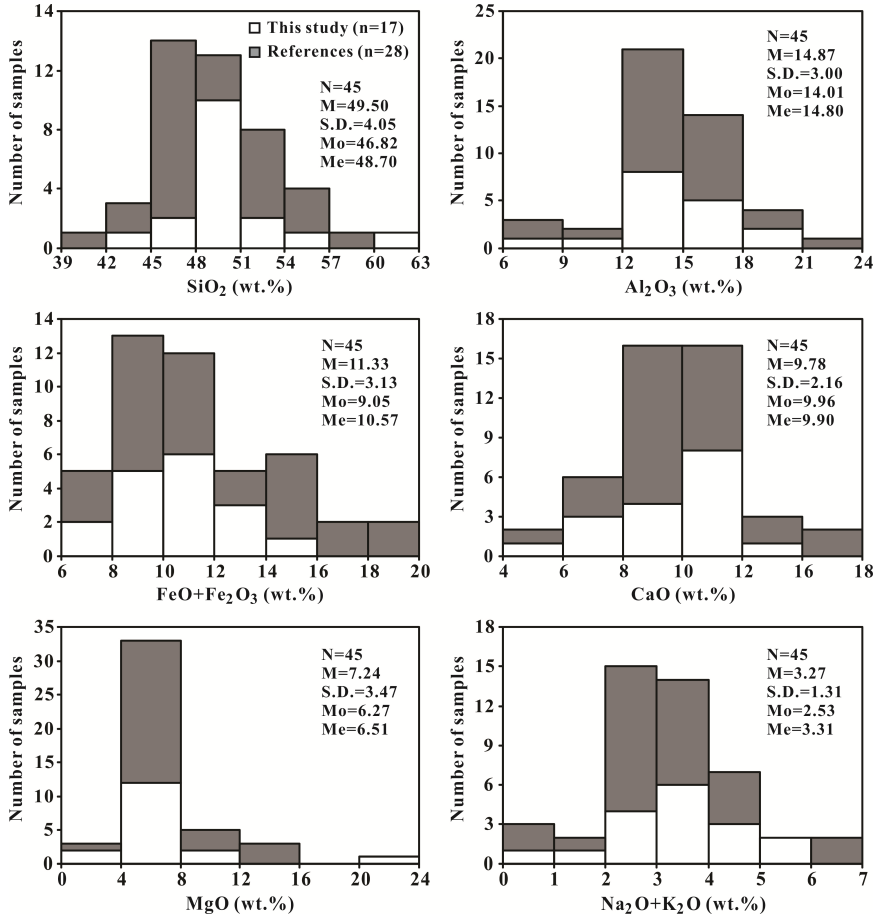


Figure 4.2 Histograms of major element contents for amphibole-rich rocks from this chapter (17 samples) and the references (28 samples). The definitions of N, M, S.D, M_o, and Me as in Figure 2.6 caption.

Brief descriptions of the geological context of each sample are given below; further information can be obtained from the references cited.

Sample AM1 is an amphibolite collected from a large polished outcrop (26.762° N, 98.890° E, altitude 1115 m) in the Nujiang Great Canyon (Yunnan, China) within the Gaoligong ductile shear zone which formed the western boundary of the southeastward extruding Indochina block in the Tertiary period (Leloup et al., 1995; Tapponnier et al., 1990). Foliation observed in outcrop is approximately vertical and lineation is nearly horizontal, both of which are consistent over several hundreds of kilometers. The amphibolite occurs as asymmetrical boudins that were originally joined and then separated along dextral extensional shear zones or synthetic microfaults (R) oriented at ~15° to the foliation-parallel layer. The amphibolitic boudins and particularly those with small length/width ratios were asymmetrically necked, back rotated, developing thin tails in the orientation of the R microfaults.

Samples AM2 to AM8 were collected from the East Athabasca mylonite triangle in the Snowbird tectonic zone (northern Saskatchewan, Canada) that has played a major role in the Neoarchean assembly and Paleoproterozoic reworking of the western Canadian Shield (Hanmer et al., 1991; Mahan and Williams, 2005). This mylonite triangle recorded a complex high pressure-high temperature metamorphism (>750 °C, 1.0 to >1.5 GPa), anatexis, ductile deformation, and fast exhumation history from 2.6 to 1.7 Ga (e.g., Baldwin et al., 2003, 2004). Samples AM2 and AM3 are fine-grained (0.05-0.15 mm) amphibolites from a deformed mafic dyke (1.9 Ga, Flowers et al., 2006) in the Chipman batholith which consists of annealed tonalitic straight gneisses, clinopyroxene-bearing tonalite ribbon mylonites, deformed or undeformed mafic dykes, and dispersed pyroxenite inclusions. Well-developed compositional banding is defined by alternating layers consisting predominantly of magnesiohornblende and plagioclase (An35-50). Lath-shaped hornblende and equant plagioclase microstructures suggest that the rock has been completely recrystallized. AM4, AM6, AM7, and AM8 are amphibole-rich tectonites in which magnesiohornblende occurs as both porphyroclasts and recrystallized fine-grained matrix, whereas plagioclase is completely recrystallized. AM5 is a serpentinized hornblendite from a large boudin in diatexitic mylonite. The sample displays a recrystallization-induced bimodal grain size distribution. Serpentinization took place along late brittle microfractures and produced Fe oxides.

Sample AM9 was collected from a plastically deformed mafic dyke (22.631° N, 110.700° E) within banded and granitic augen gneisses in the Yunkai Mountains, Guangdong (China). The metamorphic rocks are considered to be the Precambrian basement that was reworked during the Indosinian orogeny (zircon U/Pb age: 230±10 Ma) related to the collision between the South China and Indochina blocks (Wang et al., 2007).

Samples AM11 to AM15 were collected from the Britt Domain (between 81.333° W and 81.500° W, and between 44.667° N and 45.500° N) in the southwestern Grenville Province of the Canadian Shield. The Britt Domain is a subdivision of the Central Gneiss Belt extending along the northeast shore of the Georgian Bay from the southeast margin of the Grenville Front Tectonic Zone to the Parry Sound Domain. The regional deformation is characterized by southeast-northwest trending lineation that, together with kinematic indicators such as rolling porphyroclasts, S-C structures, and sheared dykes, suggests consistently southeast over northwest thrusting (Culshaw et al., 1994). This domain is regarded as a typical exposure of upper amphibolite facies midcrustal rocks of dominantly granitic and granodioritic gneisses, migmatites, and amphibolites (Long and Salisbury, 1996). Metamorphic data suggest that the present erosion surface represents a Grenvillian orogenic depth in excess of 20 km (e.g., Anovitz and Essene, 1990).

Samples AM16 and AM17 are clinopyroxene-hornblende (Cpx-Hbl) gneisses derived from retrogression of eclogites, collected from the Qinglong Shan (34.510° N, 118.890° E) in the Sulu UHP metamorphic belt. The UHP metamorphism (750-900 °C, 3.2-4.7 GPa), which corresponds to the final collision between the North China and Yangtze cratons, occurred at about 220-245 Ma. The amphibolite facies retrograde metamorphism overprinted the earlier UHP metamorphism during late exhumation within the middle crust at 210-180 Ma (e.g., Xu et al., 2009).

4.3 Measured seismic velocities and anisotropy

4.3.1 Velocity-pressure relationship

Typical V_p-P and V_s-P curves of the amphibolite samples measured during depressurization are shown in Figures 4.3 and 4.4, respectively. Three V_p measurements (i.e., for propagation along the X, Y, and Z directions) and six V_s measurements (i.e., for propagation and vibration

directions XY, XZ, YX, YZ, ZX, and ZY, where the first letter refers to the propagation direction and the second to the polarization direction) were performed for each sample using three orthogonal minicores. The curves display a rapid, nonlinear increase in velocity with pressure at low pressures (generally <200-250 MPa) and then increase slowly and linearly in velocity at high pressures. The critical pressure at which the transition from the nonlinear to the linear regime occurs is inferred as the microcrack closure pressure (P_c). The velocity-pressure curves above P_c can be reproduced in the laboratory while the curves below this pressure may vary slightly from run to run (Ji et al., 2007). This implies that the rocks become essentially crack-free, compact aggregates in the linear high pressure regime, while in the nonlinear low pressure regime, seismic velocities are still sensitive to the state of microcracks (e.g., the ratio of crack aperture to length), implying that the microcracks and pores have not been fully closed.

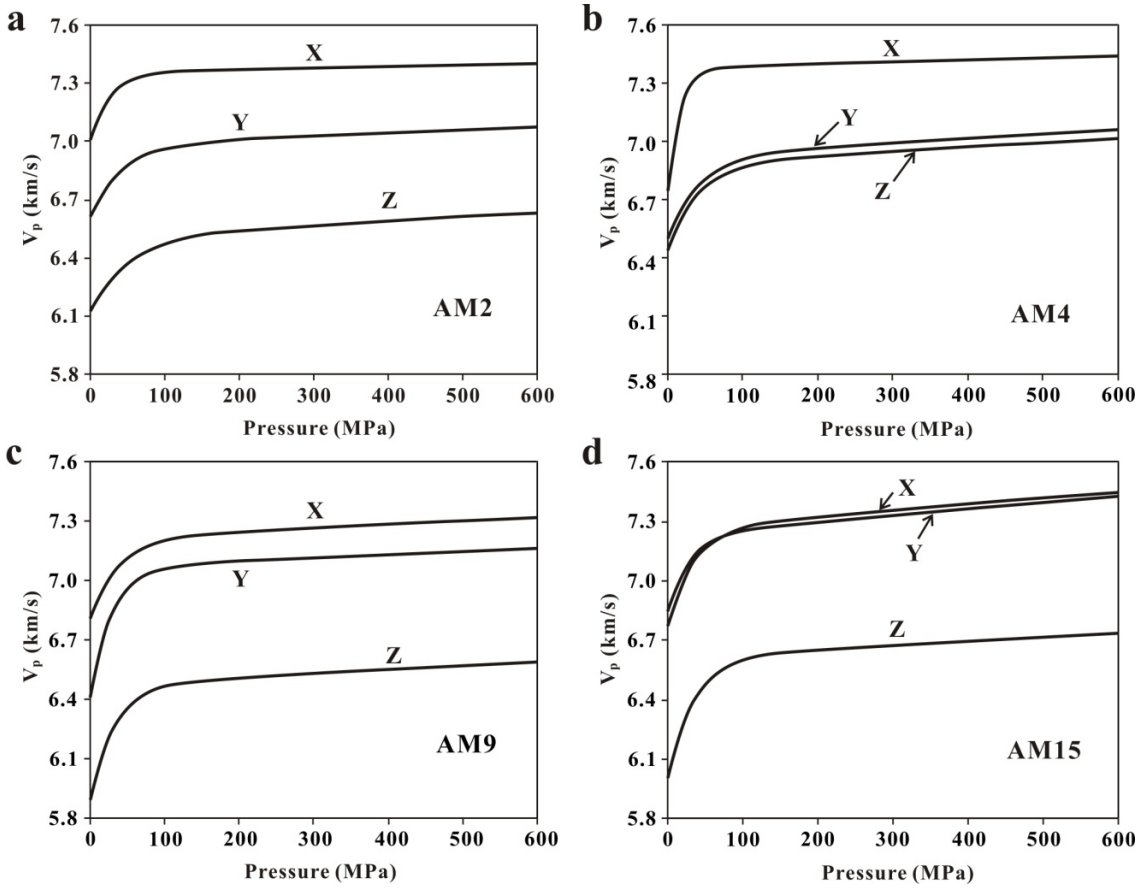


Figure 4.3 P-wave velocity (V_p) versus pressure in three orthogonal directions (X, Y, and Z) through amphibolite samples (a) AM2, (b) AM4, (c) AM9, and (d) AM15.

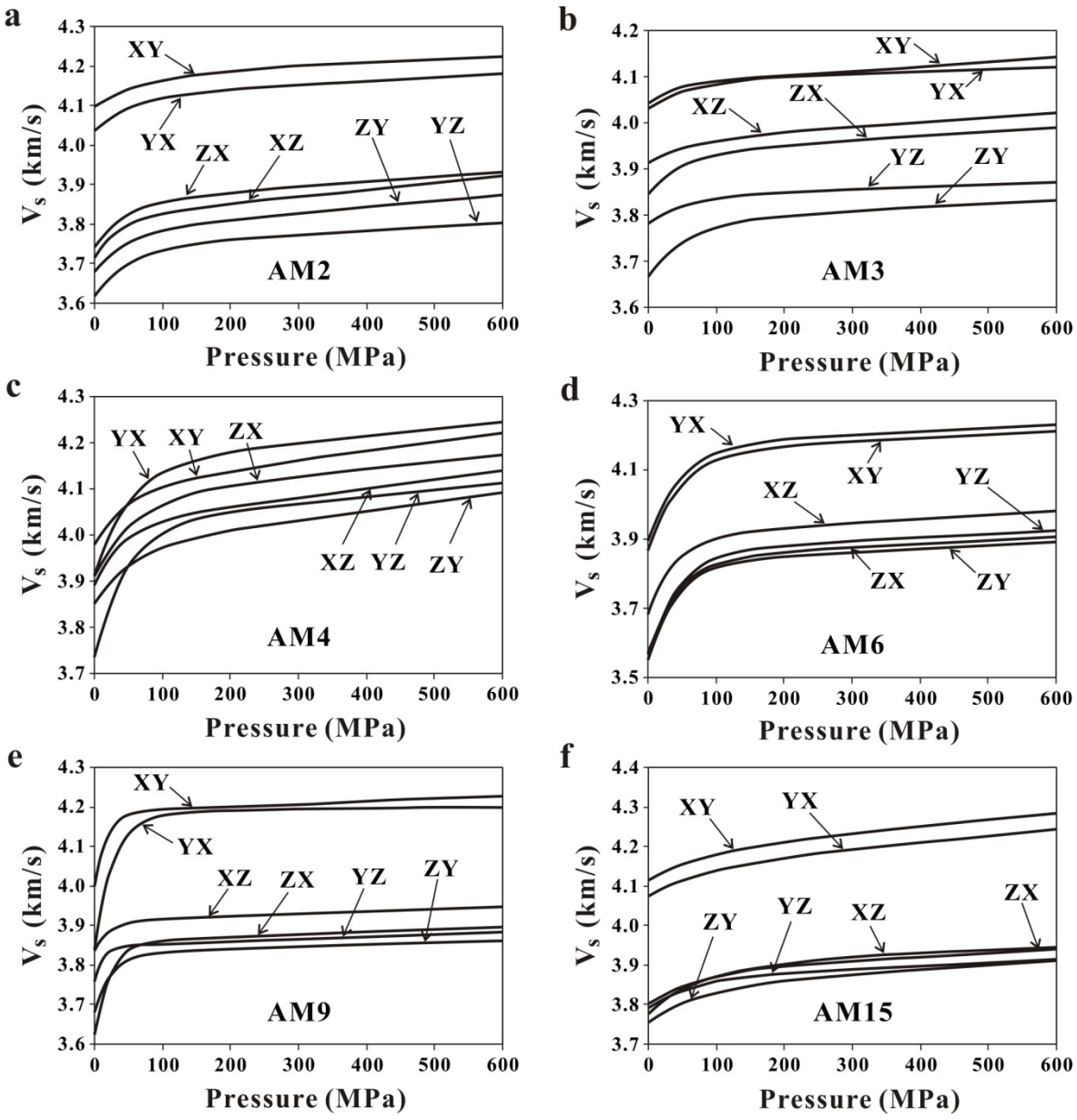


Figure 4.4 S-wave velocity (V_s) versus propagation and polarization directions in representative amphibolite samples (a) AM2, (b) AM3, (c) AM4, (d) AM6, (e) AM9, and (f) AM15. The first letter signifies propagation direction and the second letter the polarization direction.

As shown in Chapter 2, both P- and S-wave velocities as a function of confining pressure were fitted to Eq. (2.1). Parameters V_0, D, B_0, and k and their standard deviations were determined for the P- and S-wave velocities of each minicore of amphibole-rich rock sample during depressurization using a least square regression method and are given in Tables 4.3 and 4.4, respectively. As indicated by the goodness-of-fit coefficients ($R^2 \geq 0.98$), the pressure-velocity curves for P- and S-waves can be well represented by Eq. (2.1). The V_0, D, B_0, and k values for

P-wave velocity curves measured along each propagation direction (i.e., X, Y, and Z) are summarized in Figure 4.5 for the 13 amphibolites. These amphibolites are composed mainly of amphibole and plagioclase with little or no quartz (Table 4.3). The hornblendite and amphibolite-rich gneiss samples are not included in Figure 4.5. Table 4.5 lists the arithmetic mean (M), the mode (M_o, the most frequently occurring value in the distribution), and the median (M_e, the fiftieth percentile in the distribution) of V_p(X), V_p(Y), V_p(Z), and V_p(mean) values of all of the 17 amphibole-rich rock samples in this chapter. The V_p(mean) value of each sample corresponds to the seismic properties of an equivalent isotropic rock (Ji et al., 2003). For the V_p(mean) values of the 17 equivalent isotropic amphibole-rich rocks, V_0 varies from 6.052 to 7.064 km/s with an average value of 6.780 km/s, D ranges from 1.167×10^{-4} to 7.419×10^{-4} km/s/MPa with an average value of 2.379×10^{-4} km/s/MPa, B_0 lies between 0.180 km/s and 1.098 km/s with a mean value of 0.529 km/s, and k varies from 1.163×10^{-2} to 4.092×10^{-2} MPa^{-1} with an average of 2.653×10^{-2} MPa^{-1}.

Table 4.3 Parameters of V_p-P curves and V_p anisotropy for 17 amphibole-rich samples studied[a]

Sample	λ[b]	Density	V_0	S.D.	D	S.D.	B_0	S.D.	k	S.D.	R^2	A_p (%)
		g/cm^3	km/s		10^{-4} km/s/MPa		km/s		10^{-2} MPa^{-1}			600 MPa
AM1	X	3.063	7.386	0.016	2.447	0.439	0.453	0.020	2.525	0.277	0.996	14.5
	Y		6.777	0.017	2.265	0.468	0.442	0.020	2.425	0.281	0.995	
	Z		6.292	0.008	3.841	0.214	0.268	0.009	2.402	0.208	0.999	
	X45Y		7.220	0.014	2.066	0.377	0.399	0.016	2.468	0.258	0.996	
	X45Z		6.899	0.007	1.478	0.187	0.344	0.009	2.748	0.178	0.998	
	Y45Z		6.496	0.006	1.558	0.182	0.323	0.009	2.897	0.198	0.998	
	X55Y55Z		6.996	0.019	3.260	0.543	0.650	0.025	2.690	0.266	0.996	
	Mean		6.818	0.013	2.851	0.374	0.387	0.016	2.451	0.255	0.997	
AM2	X	3.000	7.357	0.008	0.750	0.211	0.350	0.020	3.724	0.407	0.986	10.9
	Y		6.983	0.010	1.500	0.243	0.375	0.014	2.305	0.192	0.994	
	Z		6.513	0.011	2.000	0.247	0.385	0.013	1.881	0.138	0.996	
	Mean		6.951	0.010	1.417	0.233	0.370	0.016	2.637	0.246	0.992	
AM3	X	3.020	7.383	0.006	1.250	0.134	0.119	0.007	1.876	0.244	0.993	10.6
	Y		6.877	0.004	1.250	0.090	0.153	0.005	2.238	0.165	0.997	
	Z		6.650	0.004	1.000	0.098	0.269	0.007	2.695	0.138	0.997	
	Mean		6.970	0.005	1.167	0.107	0.180	0.006	2.270	0.182	0.996	
AM4	X	3.200	7.380	0.009	1.000	0.253	0.634	0.060	6.337	0.799	0.982	5.8
	Y		6.927	0.007	2.250	0.176	0.431	0.011	2.357	0.125	0.998	
	Z		6.887	0.009	2.250	0.213	0.442	0.013	2.457	0.158	0.997	
	Mean		7.064	0.008	1.833	0.214	0.502	0.028	3.717	0.361	0.992	
AM5	X	3.080	7.227	0.003	2.750	0.075	0.201	0.004	2.240	0.106	0.999	10.1
	Y		7.013	0.003	1.750	0.081	0.234	0.006	3.031	0.160	0.998	
	Z		6.560	0.003	2.000	0.073	0.231	0.005	2.560	0.111	0.999	
	Mean		6.933	0.003	2.167	0.076	0.222	0.005	2.610	0.126	0.999	

[a] Parameters defined in text. [b] Direction of P-wave propagation.

Table 4.3 Continued

Sample	λ[b]	Density	V_0	S.D.	D	S.D.	B_0	S.D.	k	S.D.	R^2	A_p (%)
		g/cm^3	km/s		10^{-4} km/s/MPa		km/s		10^{-2} MPa^{-1}			600 MPa
AM6	X	2.970	7.467	0.013	1.750	0.328	0.802	0.036	4.070	0.328	0.992	12.8
	Y		7.000	0.009	2.000	0.232	0.691	0.029	4.403	0.314	0.995	
	Z		6.510	0.010	2.500	0.251	1.074	0.025	3.803	0.164	0.998	
	Mean		6.992	0.010	2.083	0.270	0.856	0.030	4.092	0.269	0.995	
AM7	X	2.970	7.310	0.003	1.000	0.064	0.191	0.004	2.523	0.115	0.998	12.3
	Y		7.050	0.011	1.500	0.269	0.360	0.022	3.241	0.391	0.986	
	Z		6.377	0.007	2.250	0.182	0.483	0.014	3.066	0.179	0.997	
	Mean		6.912	0.007	1.583	0.172	0.344	0.013	2.943	0.229	0.994	
AM8	X	3.010	7.257	0.006	1.250	0.153	0.500	0.010	2.497	0.103	0.998	9.6
	Y		7.057	0.011	1.250	0.270	0.870	0.016	2.366	0.095	0.998	
	Z		6.548	0.036	1.845	0.823	0.701	0.042	1.844	0.246	0.985	
	Mean		6.954	0.018	1.448	0.415	0.690	0.023	2.235	0.148	0.994	
AM9	X	3.040	7.215	0.000	1.651	0.002	0.407	0.000	2.598	0.002	1.000	10.3
	Y		7.062	0.000	1.610	0.001	0.665	0.000	3.482	0.001	1.000	
	Z		6.469	0.000	1.986	0.001	0.588	0.000	3.113	0.001	1.000	
	Mean		6.916	0.000	1.749	0.001	0.553	0.000	3.064	0.001	1.000	
AM10	X	3.087	7.225	0.004	1.826	0.068	0.321	0.004	1.292	0.038	0.999	3.9
	Y		6.935	0.006	3.291	0.101	0.475	0.006	1.291	0.038	0.999	
	Z		6.964	0.001	1.570	0.016	0.815	0.001	2.082	0.007	1.000	
	Mean		7.042	0.004	2.229	0.061	0.537	0.004	1.555	0.027	1.000	
AM11	X	3.083	7.153	0.006	1.500	0.158	1.095	0.028	3.431	0.111	0.999	9.8
	Y		6.623	0.002	2.500	0.055	0.397	0.009	3.250	0.096	0.999	
	Z		6.463	0.003	1.750	0.086	0.334	0.016	3.558	0.213	0.997	
	Mean		6.747	0.004	1.917	0.100	0.609	0.018	3.413	0.140	0.998	
AM12	X	2.910	7.180	0.004	1.500	0.100	0.410	0.019	3.605	0.208	0.997	13.3
	Y		6.867	0.008	2.250	0.185	0.478	0.015	2.090	0.121	0.998	
	Z		6.220	0.003	2.250	0.069	0.536	0.012	3.337	0.093	0.999	
	Mean		6.756	0.005	2.000	0.118	0.475	0.016	3.011	0.141	0.998	
AM13	X	2.930	6.996	0.009	2.708	0.213	0.370	0.018	2.148	0.188	0.996	11.2
	Y		6.810	0.004	2.500	0.141	0.396	0.013	3.248	0.163	0.999	
	Z		6.243	0.003	2.500	0.067	0.593	0.010	3.092	0.071	1.000	
	Mean		6.683	0.005	2.569	0.140	0.453	0.014	2.829	0.141	0.998	
AM14	X	2.810	6.593	0.023	2.500	0.542	0.501	0.048	2.200	0.369	0.982	9.3
	Y		6.430	0.005	2.000	0.119	0.510	0.017	2.956	0.135	0.998	
	Z		6.020	0.003	2.000	0.084	0.529	0.012	2.945	0.091	0.999	
	Mean		6.348	0.010	2.167	0.248	0.513	0.026	2.700	0.198	0.993	
AM15	X	3.117	7.263	0.004	3.000	0.089	0.477	0.012	2.892	0.103	0.999	9.8
	Y		7.237	0.006	3.250	0.162	0.405	0.028	3.353	0.293	0.996	
	Z		6.617	0.012	2.000	0.298	0.618	0.040	2.868	0.263	0.992	
	Mean		7.039	0.007	2.750	0.183	0.500	0.026	3.038	0.219	0.996	
AM16	X	2.964	6.251	0.019	6.285	0.322	0.996	0.020	1.174	0.050	0.999	2.8
	Y		6.081	0.028	7.271	0.476	1.135	0.029	1.105	0.061	0.998	
	Z		5.922	0.019	8.702	0.328	1.165	0.021	1.211	0.046	0.999	
	Mean		6.085	0.022	7.419	0.375	1.098	0.023	1.163	0.052	0.999	
AM17	X	2.958	6.503	0.004	2.727	0.076	0.448	0.005	1.358	0.032	1.000	17.0
	Y		6.249	0.006	3.055	0.099	0.600	0.006	1.365	0.032	1.000	
	Z		5.402	0.008	3.479	0.144	1.045	0.010	1.419	0.028	1.000	
	Mean		6.052	0.006	3.087	0.106	0.698	0.007	1.381	0.030	1.000	

Table 4.4 Parameters of V_s-P curves and V_s anisotropy for amphibole-rich rock samples studied[a]

Sample	Density	Property	Propagation	Polarization	V_0	S.D.	D	S.D.	B_0	S.D.	k	S.D.	R^2	A_s (%)
	g/cm^3				km/s		10^{-4} km/s/MPa		km/s		10^{-2} MPa^{-1}			600 MPa
AM1	3.063	Vs(XY)	X	Y	4.230	0.020	0.906	0.519	0.216	0.019	1.895	0.432	0.982	11.4
		Vs(XZ)	X	Z	4.180	0.018	1.524	0.484	0.305	0.020	2.255	0.382	0.989	
		Vs(YX)	Y	X	4.081	0.005	1.494	0.116	0.137	0.007	2.884	0.365	0.996	
		Vs(YZ)	Y	Z	3.748	0.016	1.578	0.454	0.274	0.035	2.568	0.598	0.984	
		Vs(ZX)	Z	X	3.880	0.031	2.271	0.773	0.248	0.032	1.718	0.559	0.983	
		Vs(ZY)	Z	Y	3.708	0.017	1.887	0.449	0.294	0.019	2.222	0.356	0.992	
		Vs(X45Y+)	X45Y	Z	4.211	0.007	1.101	0.210	0.190	0.009	2.457	0.288	0.995	
		Vs(X45Y-)	X45Y	Norma to Z	4.042	0.006	1.474	0.175	0.168	0.008	2.691	0.318	0.996	
		Vs(X45Z+)	X45Z	Y	4.062	0.021	1.608	0.536	0.294	0.020	1.952	0.343	0.990	
		Vs(X45Z-)	X45Z	Normal to Y	4.016	0.011	2.012	0.298	0.188	0.011	2.034	0.303	0.995	
		Vs(Y45Z+)	Y45Z	X	3.971	0.009	1.728	0.229	0.237	0.009	2.191	0.218	0.997	
		Vs(Y45Z-)	Y45Z	Normal to X	3.667	0.010	2.104	0.298	0.249	0.015	2.877	0.414	0.994	
		Vs(X55Y55Z+)	X55Y55Z	Parallel to foliation trace on the end surface	4.164	0.014	1.587	0.355	0.219	0.013	1.940	0.304	0.994	
		Vs(X55Y55Z-)	X55Y55Z	Normal to foliation trace on the end surface	3.802	0.011	1.292	0.287	0.271	0.011	2.172	0.227	0.996	
		M			3.971	0.018	1.610	0.466	0.246	0.022	2.257	0.449	0.988	
AM2	3.000	XY	X	Y	4.177	0.008	0.750	0.167	0.080	0.007	1.297	0.263	0.989	10.5
		XZ	X	Z	3.817	0.002	1.750	0.056	0.102	0.004	2.582	0.195	0.998	
		YX	Y	X	4.120	0.003	1.000	0.077	0.085	0.004	1.973	0.210	0.996	
		YZ	Y	Z	3.743	0.003	1.000	0.071	0.126	0.004	1.916	0.125	0.998	
		ZX	Z	X	3.857	0.004	1.250	0.103	0.114	0.006	2.139	0.237	0.995	
		ZY	Z	Y	3.783	0.003	1.500	0.063	0.101	0.003	1.874	0.134	0.999	
		M			3.916	0.004	1.208	0.089	0.101	0.005	1.963	0.194	0.996	
AM3	3.020	XY	X	Y	4.080	0.001	1.000	0.029	0.040	0.002	2.744	0.281	0.998	7.7
		XZ	X	Z	3.960	0.003	1.000	0.066	0.047	0.003	1.623	0.245	0.996	
		YX	Y	X	4.090	0.002	0.500	0.052	0.060	0.003	1.715	0.163	0.996	
		YZ	Y	Z	3.840	0.003	0.500	0.074	0.059	0.004	1.862	0.267	0.990	
		ZX	Z	X	3.930	0.002	1.000	0.050	0.085	0.003	2.130	0.154	0.998	
		ZY	Z	Y	3.787	0.004	0.750	0.090	0.121	0.004	1.767	0.148	0.996	
		M			3.948	0.003	0.792	0.060	0.069	0.003	1.974	0.209	0.996	
AM4	3.200	XY	X	Y	4.050	0.005	2.000	0.109	0.121	0.006	1.972	0.209	0.997	3.6
		XZ	X	Z	3.970	0.002	2.000	0.053	0.129	0.003	2.498	0.139	0.999	
		YX	Y	X	4.103	0.005	1.500	0.116	0.242	0.006	1.980	0.112	0.998	
		YZ	Y	Z	3.973	0.008	1.500	0.192	0.289	0.011	2.099	0.170	0.995	
		ZX	Z	X	4.033	0.008	1.500	0.172	0.169	0.008	1.631	0.179	0.995	
		ZY	Z	Y	3.923	0.005	2.000	0.108	0.122	0.005	1.800	0.178	0.998	
		M			4.009	0.005	1.750	0.125	0.179	0.007	1.997	0.164	0.997	
AM6	2.970	XY	X	Y	4.150	0.006	1.000	0.134	0.280	0.008	2.135	0.125	0.997	8.4
		XZ	X	Z	3.907	0.002	1.250	0.060	0.227	0.004	2.448	0.086	0.999	
		YX	Y	X	4.170	0.006	1.000	0.139	0.282	0.008	2.119	0.127	0.997	
		YZ	Y	Z	3.863	0.004	1.000	0.098	0.313	0.006	2.368	0.097	0.998	
		ZX	Z	X	3.843	0.004	1.000	0.091	0.280	0.005	2.254	0.093	0.999	
		ZY	Z	Y	3.833	0.004	1.000	0.098	0.282	0.006	2.437	0.112	0.998	
		M			3.961	0.004	1.042	0.103	0.277	0.006	2.293	0.107	0.998	
AM9	3.040	XY	X	Y	4.186	0.002	0.643	0.037	0.180	0.004	5.802	0.279	0.996	9.0
		XZ	X	Z	3.909	0.001	0.655	0.011	0.068	0.001	4.745	0.164	0.999	
		YX	Y	X	4.186	0.002	0.219	0.036	0.341	0.003	3.477	0.069	0.999	
		YZ	Y	Z	3.849	0.001	0.550	0.027	0.091	0.003	7.734	0.587	0.993	
		ZX	Z	X	3.859	0.002	0.584	0.035	0.239	0.003	4.423	0.135	0.998	
		ZY	Z	Y	3.829	0.001	0.564	0.020	0.151	0.002	4.134	0.112	0.999	
		M			3.970	0.001	0.536	0.028	0.178	0.003	5.052	0.224	0.997	
AM10	3.087	XY	X	Y	4.099	0.000	1.064	0.007	0.175	0.001	1.587	0.010	1.000	6.2
		XZ	X	Z	4.038	0.001	1.028	0.010	0.351	0.001	1.718	0.007	1.000	
		YX	Y	X	4.026	0.001	0.795	0.011	0.158	0.001	1.446	0.014	1.000	
		YZ	Y	Z	3.830	0.000	1.659	0.003	0.251	0.000	1.995	0.003	1.000	
		ZX	Z	X	4.019	0.001	1.087	0.017	0.186	0.001	1.361	0.018	1.000	
		ZY	Z	Y	3.806	0.001	1.780	0.011	0.286	0.001	1.615	0.009	1.000	
		M			3.970	0.001	1.236	0.010	0.235	0.001	1.620	0.010	1.000	

[a] Parameters defined in text

Table 4.4 Continued

Sample	Density g/cm^3	Property	Propagation	Polarization	V_0 km/s	S.D.	D 10^{-4} km/s/MPa	S.D.	B_0 km/s	S.D.	k 10^{-2} MPa^{-1}	S.D.	R^2	A_s (%) 600 MPa
AM15	3.117	XY	X	Y	4.183	0.003	1.643	0.061	0.068	0.005	1.230	0.192	0.999	9.2
		XZ	X	Z	3.895	0.008	0.786	0.145	0.097	0.008	1.078	0.242	0.996	
		YX	Y	X	4.143	0.003	1.643	0.061	0.068	0.005	1.230	0.192	0.999	
		YZ	Y	Z	3.865	0.008	0.786	0.159	0.072	0.008	1.042	0.330	0.994	
		ZX	Z	X	3.880	0.003	1.000	0.060	0.101	0.013	1.657	0.253	0.998	
		ZY	Z	Y	3.843	0.003	1.143	0.066	0.085	0.006	1.266	0.177	0.999	
		M			3.968	0.005	1.167	0.092	0.082	0.008	1.251	0.231	0.997	
AM16	2.964	XY	X	Y	3.473	0.006	2.346	0.106	0.573	0.007	1.182	0.029	1.000	2.6
		XZ	X	Z	3.462	0.004	3.568	0.077	0.606	0.005	1.280	0.022	1.000	
		YX	Y	X	3.528	0.001	2.162	0.012	1.041	0.001	1.989	0.004	1.000	
		YZ	Y	Z	3.482	0.006	2.665	0.109	0.695	0.007	1.225	0.026	1.000	
		ZX	Z	X	3.461	0.003	3.179	0.049	0.659	0.003	1.425	0.015	1.000	
		ZY	Z	Y	3.432	0.005	2.509	0.093	0.716	0.006	1.273	0.023	1.000	
		M			3.473	0.004	2.738	0.074	0.715	0.005	1.396	0.020	1.000	

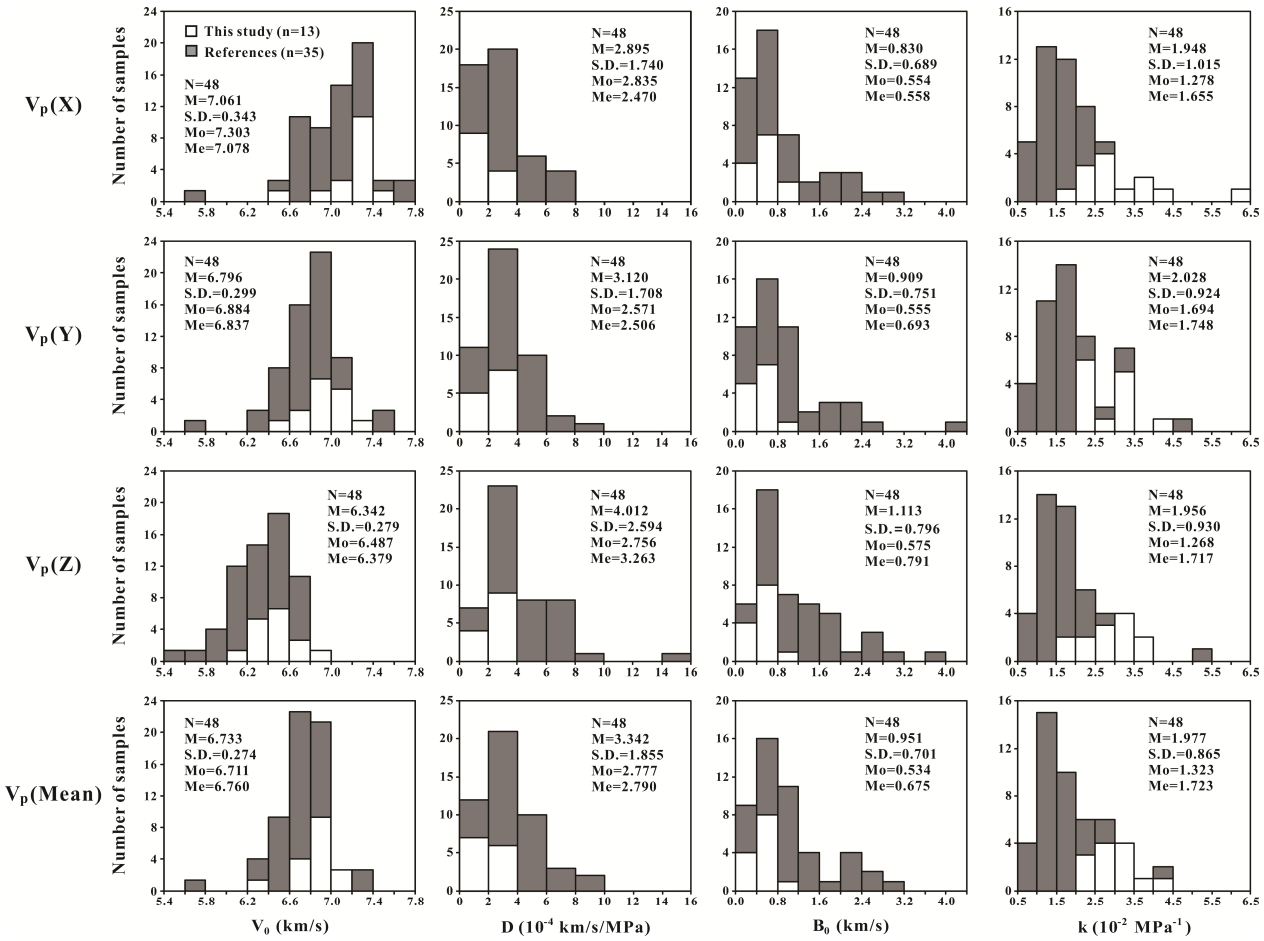


Figure 4.5 Statistics of V_p-P curve parameters, defined by Eq. (2.1), for three structural directions (X, Y, and Z) and the equivalent isotropic aggregate of the amphibolites consisting mainly of hornblende and plagioclase from this chapter (13 samples) and the references (35 samples). The definitions of N, M, S.D, M_o, and Me as in Figure 2.6 caption.

Table 4.5 The arithmetic mean (M), the mode (Mo), and the median (Me) of V_p(X), V_p(Y), V_p(Z) and V_p(mean) values of 17 amphibole-rich rock samples studied

V_p	V_0 (km/s)				D (10^{-4} km/s/MPa)				B_0 (km/s)				k (10^{-2} MPa^{-1})			
	M	S.D.	Mo	Me	M	S.D.	Mo	Me	M	S.D.	Mo	Me	M	S.D.	Mo	Me
V_p(X)	7.126	0.350	7.300	7.227	2.111	1.289	1.348	1.750	0.487	0.266	0.479	0.448	2.735	1.255	2.453	2.523
V_p(Y)	6.822	0.309	6.900	6.927	2.441	1.400	2.536	2.250	0.507	0.234	0.522	0.442	2.618	0.875	2.782	2.425
V_p(Z)	6.392	0.369	6.511	6.469	2.584	1.708	2.461	2.000	0.593	0.287	0.561	0.536	2.608	0.732	2.959	2.695
V_p(Mean)	6.780	0.319	6.931	6.916	2.379	1.402	2.434	2.083	0.529	0.223	0.553	0.502	2.653	0.781	2.744	2.700

Figure 4.5 also compares the P-wave velocity curve parameters (i.e., V_0, D, B_0, and k) between the 13 amphibolite samples used in this chapter and the 35 amphibolite samples reported in the previous references (Barberini et al., 2007; Birch, 1960; Burke et al., 1990; Christensen, 1965; 1978; Fountain, 1976; Fountain et al., 1990; Ji et al., 2002; Kern and Fakhimi, 1975; Kern et al., 1996, 1997, 1999, 2001, 2009; Khazanehdari et al., 2000; Miller and Christensen, 1994; Punturo et al., 2005; Siegesmund et al., 1989; Zhao et al., 2011, Zhou et al., 2011). For V_p values of the 48 equivalent isotropic amphibolites, V_0 varies from 5.635 to 7.308 km/s with an average value of 6.733 km/s, D ranges from 1.167×10^{-4} to 9.294×10^{-4} km/s/MPa with an average value of 3.342×10^{-4} km/s/MPa, B_0 lies between 0.136 km/s and 2.959 km/s with a mean value of 0.951 km/s, and k varies from 0.765×10^{-2} to 4.271×10^{-2} MPa^{-1} with an average of 1.977×10^{-2} MPa^{-1}.

4.3.2 P-wave velocity anisotropy

V_p anisotropy (A_p) is defined in Eq. (1.31). The intrinsic anisotropy of the 17 amphibole-rich rock samples, calculated from the V_0 values measured in three orthogonal directions, ranges from 4.1% (sample AM10) to 18.2% (sample AM17) with an average value of 10.9%. The values display slight differences from those at 600 MPa, which range from 2.8% (sample AM16) to 17.0% (sample AM17) with an average value of 10.2%.

For most of the studied amphibole-rich rock samples (Figure 4.6a), the anisotropy decreases rapidly with increasing the confining pressure below 100-150 MPa and then slowly decreases or reaches a constant value above this pressure (e.g., samples AM6, AM9, AM10 and AM17). This pattern, named as Pattern 1, can be attributed to the closure of aligned microcracks which reinforce the bulk P-wave anisotropy induced by the CPO of the constituent minerals, mainly amphibole (e.g., Barberini et al., 2007; Kern et al., 1997; Sun et al., 2012). However, other patterns for the dependence of V_p anisotropy on pressure are also observed in this set of 17 samples. In sample AM11 (Figure 4.6b), for instance, the anisotropy increases first with

increasing pressure in the low pressure range (<200 MPa) and then reaches a nearly constant value above this pressure. This pattern, named as Pattern 2, can be attributed to the rapid closure at low pressures of aligned microcracks which oppose the CPO-induced anisotropy (Ji et al., 2007). In sample AM5 (Figure 4.6b), surprisingly, the anisotropy remains almost unchanged with increasing pressure. This pattern (Pattern 3) can result from randomly oriented microcracks (e.g., Barruol and Kern, 1996) or the combination of Patterns 1 and 2. In the second case, two sets of orthogonal microcracks have opposite effects on velocity. For Pattern 3, the anisotropy is almost directly related to the contribution of amphibole CPO at each pressure.

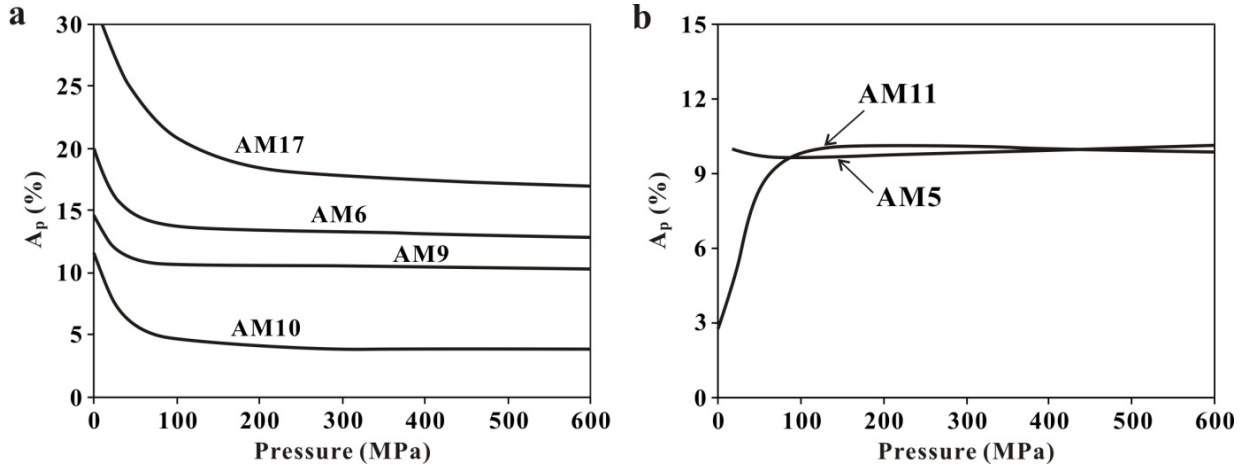


Figure 4.6 Three types of P-wave velocity anisotropy (A_p) versus pressure curves for amphibole-rich rock samples. See text for discussion.

P-wave velocities along seven propagating directions (i.e., X, Y, Z, X45Y, X45Z, Y45Z, and X55Y55Z) as a function of pressure for amphibolite sample AM1 are shown in Figure 4.7. Above 200 MPa, V_p(X)>V_p(X45Y)>V_p(X55Y55Z)>V_p(X45Z)>V_p(Y)>V_p(Y45Z)>V_p(Z). The relative differences between the arithmetic and geometrical means of P-wave velocities calculated from the three principal structural directions (X, Y, and Z) are very small (<0.2%). Furthermore, the arithmetic means of V_p values calculated from these principal structural directions (X, Y, and Z) and from the seven directions are almost the same at high pressures (>200 MPa) with relative errors less than 0.2%. At 500-600 MPa, these mean values are very close to V_p(X45Z) but significantly lower than V_p(X55Y55Z). If the three-dimensional distribution of P-wave velocities in a sample can be described by an ellipsoid whose three principal axes are parallel to those of the strain ellipsoid (i.e., X, Y, and Z), V_p(X55Y55Z) can be calculated from the following equation:

$$V_p\left(\text{X55Y55Z}\right)=\frac{\sqrt{3}abc}{\sqrt{a^2b^2+a^2c^2+b^2c^2}} \tag{4.1}$$

where a=V_p(X), b=V_p(Y), and c=V_p(Z) for amphibolites. For the same reason,

$$V_p\left(\text{X45Z}\right)=\frac{\sqrt{2}ac}{\sqrt{a^2+c^2}} \tag{4.2}$$

$$V_p\left(\text{X45Y}\right)=\frac{\sqrt{2}ab}{\sqrt{a^2+b^2}} \tag{4.3}$$

$$V_p\left(\text{Y45Z}\right)=\frac{\sqrt{2}bc}{\sqrt{b^2+c^2}} \tag{4.4}$$

The comparisons between the calculated and measured values for V_p(X45Y), V_p(X45Z), V_p(Y45Z), and V_p(X55Y55Z) are given in Figure 4.8. The relative error (R_e) is defined as $R_e(\%)=100\%(V_C-V_L)/V_L$, where V_C and V_L are the calculated and laboratory-measured velocities, respectively. As shown in Figure 4.8, $R_e \leq 2\%$ at 400-600 MPa for V_p(X45Y), V_p(X45Z), and V_p(Y45Z), but the calculated values for V_p(X55Y55Z) are 3.2-3.3% smaller than the corresponding measured values. The above comparison indicates that the three-dimensional distribution of P-wave velocities in amphibolite AM1 is nearly but not exactly ellipsoidal. The discrepancy is probably caused by small compositional difference among minicores drilled along different directions from a large sample.

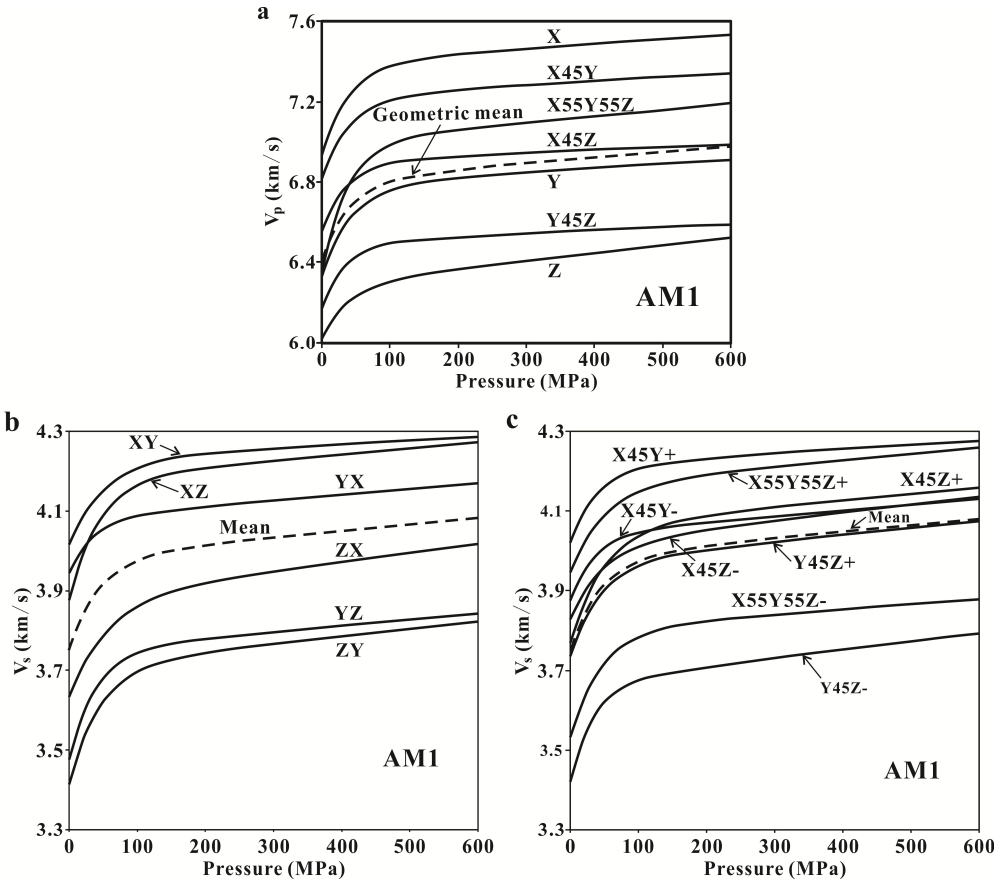


Figure 4.7 (a) V_p-P and (b-c) V_s-P curves for various propagation and polarization directions (see Table 4.4 for their definitions) of amphibolite sample AM1 from the Gaoligong Mts, Yunnan, China.

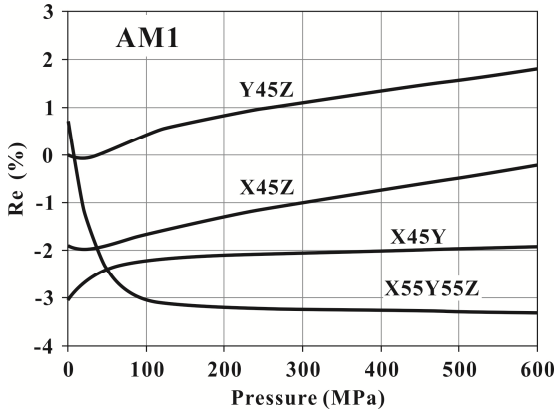


Figure 4.8 Comparison of the theoretical P-wave velocities with those measured along 4 different propagating directions (X45Y, X45Z, Y45Z, and X55Y55Z) oblique to the principal axes of the finite strain ellipsoid (X, Y, and Z) in amphibolite sample AM1 from the Gaoligong Mts, Yunnan, China.

4.3.3 S-wave anisotropy and splitting

As shown in Figures 4.4 and 4.7b-4.7c, the amphibole-rich rocks studied demonstrate pronounced variations of S-wave velocity with either propagation or vibration direction. In amphibolite AM1 from which seven minicores were drilled in different directions, for instance, the V_S at 600 MPa, varies from 3.793 km/s (Y45Z-) to 4.284 km/s (XY) with an average velocity of 4.080 km/s. This mean value calculated from the seven propagating directions is very close to the average value (4.068 km/s) calculated from the propagation directions along the three principal structural axes (X, Y, and Z). The shear-wave velocity at 600 MPa can be arranged in the following order: V_S(XY)>V_S(X45Y+)≈V_S(XZ)>V_S(X55Y55Z+)>V_S(YX)>V_S(X45Z+)>V_S(X45Z-)≈V_S(X45Y-)>V_S(Y45Z+)>V_S(ZX)>V_S(X55Y55Z-)>V_S(YZ)>V_S(ZY)>V_S(Y45Z-) (Figures 4.7b-4.7c and Table 4.4). V_S anisotropy (A_S) of each sample can also be defined as $A_S = (V_{max} - V_{min}) / V_m \times 100\%$ [also see Eq. (1.33)], where V_{max}, V_{min} and V_m are, respectively, the maximum, minimum and mean values of the S-wave velocities measured along three propagation directions and six polarization directions. A common feature is that A_S displays a rapid decrease with increasing pressure below ~150 MPa and then reaches a constant value above this pressure (Figure 4.9). This fact indicates that the V_S anisotropy is controlled by the intrinsic properties (i.e., CPO) of the rocks above the crack-closure pressure whereas microcracks make equally a contribution to the anisotropy below that critical pressure. The intrinsic V_S anisotropy of the amphibole-rich rocks measured at 600 MPa ranges from 2.6% (sample AM16) to 11.4% (sample AM1) with an average value of 7.6% (Table 4.4).

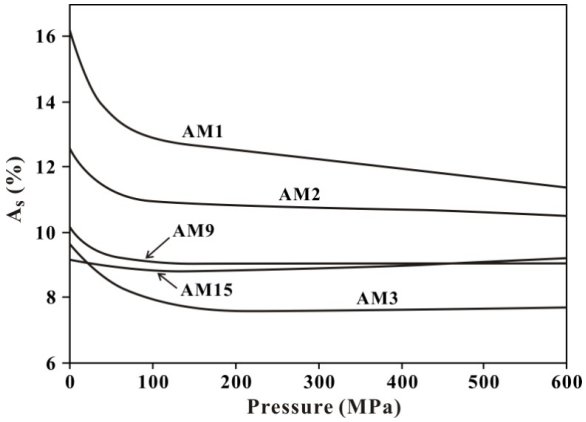


Figure 4.9 S-wave velocity anisotropy (A_S) versus pressure curves for five representative amphibole-rich rock samples (AM1, AM2, AM3, AM9, and AM15).

Shear-wave splitting is a phenomenon of birefringence (ΔV_s) that is quantified as the difference in velocity between the fast and slow split, or polarized, S-waves propagating in the same direction. The birefringence is both direction and pressure dependent. In the following, we define: $\Delta V_s(X)=V_s(XY)-V_s(XZ)$, $\Delta V_s(Y)=V_s(YX)-V_s(YZ)$, and $\Delta V_s(Z)=V_s(ZX)-V_s(ZY)$. For sample AM1 (Figure 4.10d), $\Delta V_s(X45Y)=V_s(X45Y+)-V_s(X45Y-)$, $\Delta V_s(X45Z)=V_s(X45Z+)-V_s(X45Z-)$, $\Delta V_s(Y45Z)=V_s(Y45Z+)-V_s(Y45Z-)$, and $\Delta V_s(X55Y55Z)=V_s(X55Y55Z+)-V_s(X55Y55Z-)$, where symbols "+" and "-" are defined in Table 4.4.

The most striking feature visible from Figure 4.10 is that the birefringence is almost constant and pressure insensitive above the crack closure pressure (>200 MPa). Previous studies showed that the effect of temperature on the birefringence is negligible as long as partial melting, metamorphic reaction, dehydration, or phase transformation does not occur (e.g., Barruol and Kern, 1996; Kern et al., 2001). Therefore, S-wave anisotropy within such crustal rocks becomes pressure and temperature independent at depths greater than 7-8 km.

The birefringence in anisotropic amphibole-rich rocks above 200 MPa when microcracks have been closed can be mainly classified into four categories: Type A: $\Delta V_s(Y)> \Delta V_s(X)>\Delta V_s(Z)\approx 0$ (samples AM2, AM6, and AM9, Figures 4.10b-4.10d); Type B: $\Delta V_s(Y)> \Delta V_s(Z)>\Delta V_s(X)\approx 0$ (sample AM1, Figure 4.10a); Type C: $\Delta V_s(Y)>\Delta V_s(X)\approx\Delta V_s(Z)>0$ (samples AM3 and AM4); Type D: $\Delta V_s(X)\approx\Delta V_s(Y)\gg\Delta V_s(Z)>0$ (sample AM15). Among these four categories, Type A is the most often observed. In other words, in most of the amphibole-rich rock samples, the maximum birefringence at high pressures occurs at the propagation direction parallel to Y, and the minimum birefringence is observed for propagation normal to foliation. Sample AM16 is quasi-isotropic with little birefringence (<0.06 km/s) in any propagation direction at 200-600 MPa. In amphibolite AM1 in which seven minicores were drilled in different directions, the birefringence above 200 MPa can be arranged in the following order: $\Delta V_s(X55Y55Z)>\Delta V_s(Y)>\Delta V_s(Y45Z)>\Delta V_s(Z)>\Delta V_s(X45Y)>\Delta V_s(X45Z)\approx\Delta V_s(X)\approx 0$ (Figure 4.10a). As can be seen in this figure, the maximum and minimum birefringence values occur when the propagation parallels to the directions X55Y55Z and X (or X45Z), respectively.

The variation of birefringence with pressure below 200 MPa (Figure 4.10) can be interpreted in terms of the preferential orientation of microcracks with respect to the propagation and polarization directions of the shear waves. In amphibolite AM9 (Figure 4.10d), for instance, both

ΔV_s(X) and ΔV_s(Y) increase rapidly at low pressures (<100 MPa) then become nearly constant at high pressures. This pattern of birefringence variation can be interpreted as destructive interference of the effects of oriented microcracks and mineral CPO of the amphibolite in which microcracks are preferentially oriented in such a manner that the microcrack-induced birefringence opposes the CPO-induced birefringence. Microcracks in sample AM9 are inferred to be orthogonally aligned and preferentially perpendicular to the X and particularly the Y directions. The presence of these microcracks causes a decrease in V_s(XY) and V_s(YX) but has little influence on V_s(XZ) or V_s(YZ) below 200 MPa. Accordingly, the progressive closure of these microcracks with increasing pressure increases the V_s(XY)-V_s(XZ) and V_s(YX)-V_s(YZ) birefringence values in the low pressure regime.

In amphibolite AM1 (Figure 4.10a), ΔV_s(X) displays an initial rapid decrease in birefringence with increasing pressure in the low pressure regime and then approaches zero in the high pressure regime. The rapid decrease in birefringence in the low pressure regime is caused by a progressive increase in V_s(XZ) due to the closure of the foliation-parallel cracks while V_s(XY) is not affected by the presence of these cracks. Interestingly, the birefringence (or shear-wave splitting) along the X direction in this amphibolite is induced almost entirely by the foliation-parallel microcracks, because it becomes nearly zero at pressures above ~200 MPa (Figure 4.10a). The variation of ΔV_s(Y) with pressure in the same sample can be attributed to the same cause.

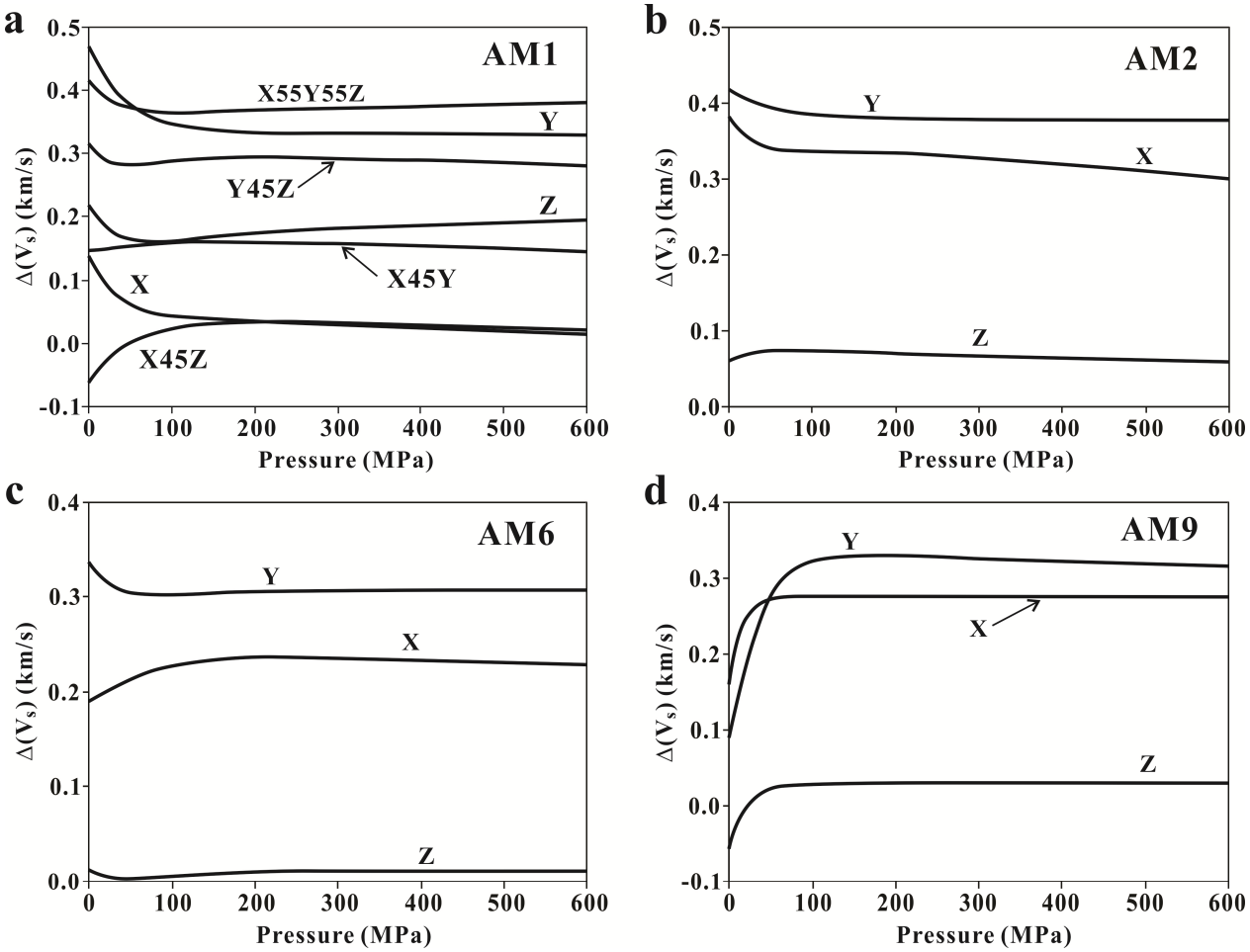


Figure 4.10 Shear-wave splitting along various propagating directions in amphibolite samples (a) AM1, (b) AM2, (c) AM6, and (d) AM9.

4.4 CPO and calculated seismic velocities

The CPO diagrams of amphibole, which are relatively simple and consistent, are shown in Figure 4.11. The [001] directions display a strong concentration parallel to X in these five samples (AM1, AM3, AM4, AM7, and AM8), while a girdle parallel to the foliation plane with a maximum close to X in sample AM2. The poles to the (100) planes form a partial girdle perpendicular to the stretching lineation (X), in which the maximum concentration occurs at Z. The distribution of (010) poles is more complicated: a partial girdle perpendicular to X with the maximum concentration at Y (samples AM1 and AM4) or in the middle way between Y and Z (sample AM3), a partial girdle parallel to the foliation with the maximum concentration at Y (sample AM2), or a single concentration at Y (samples AM7 and AM8). For amphibole (100), the *pfJ* index varies from 1.81 (sample AM4) to 3.48 (sample AM2) with a mean value of 2.67.

For amphibole (010), the *pfJ* index varies from 1.26 (sample AM3) to 1.83 (sample AM1) with a mean value of 1.54. For amphibole [001], the *pfJ* index varies from 2.19 (sample AM4) to 5.12 (sample AM1) with a mean value of 3.18. Clearly, the mean CPO strengths of amphibole [001], (100), and (010) are the strongest, moderate, and weakest, respectively. Unlike the other samples, sample AM2 displays the maximum *pfJ* index for (100) rather than [001]. The fabric features of our samples are consistent with those measured previously using an optical microscope equipped with a five-axis universal stage (Barberini et al., 2007; Christensen, 1965; Ji and Mainprice, 1989, Ji et al., 1993; Schwerdtner, 1964; Siegesmund et al., 1989) or EBSD techniques (Kitamura, 2006). However, it is impossible to compare the present CPO data with those reported in Christensen (1965) and Kern (1982) because they measured only the orientations of the {110} cleavage planes of hornblende. The CPO patterns of amphibole presented here can be interpreted by either [001] slip along (100) and (110) planes (Biermann and Van Roermund, 1983; Cumbest et al., 1989; Dollinger and Blacic, 1975; Ji et al., 1993; Reynard et al., 1989; Skrotzki, 1990) or anisotropic growth (grain boundary migration) and passive rigid-body rotation under various different stresses (Ji et al., 1993; Shelley, 1994; Takeshita, 1999). The CPO of plagioclase and quartz, which seems to be sensitive to their volume fractions in the rocks, is nearly random or very weak in all the samples except sample AM1 from the Gaoligong ductile shear zone (Yunnan, China). In this sample, the [100] direction in plagioclase developed a concentration near the X direction, the poles to (001) form a girdle perpendicular to the lineation with maxima near the Z and Y directions, and the poles to (010) are mainly concentrated near the Y directions. This CPO pattern indicates that the plagioclase in sample AM1 deformed by (001)[100] slip. In this sample, the quartz CPO indicates that a-slip operated along the basal planes in this mineral.

The P-wave velocities, direction-dependent V_s anisotropy (AV_s), and polarization directions of fast shear-wave for the six amphibolite samples were calculated on the basis of CPO, density, volume fraction, and elastic stiffness coefficients of each constituent minerals in the rocks (also see Figure 1.5) using the software developed by Mainprice (1990). For a given propagation direction, AV_s is defined by Eq. (1.35). The single crystal elastic stiffness coefficients of amphibole, plagioclase (An53), and quartz were taken from Hearmon (1984) and McSkimin et al. (1965). Table 4.6 lists the elastic constants of six amphibolitic samples for which seismic velocities and anisotropy have been calculated based on fabric data and modal compositions using the VRH average. The calculated velocities and anisotropy pertain to conditions of one

atmosphere pressure, room temperature, and zero porosity and must be compared with velocities measured at a pressure high enough to close microcracks (e.g., Barruol and Kern, 1996; Ji and Mainprice, 1988; Seront et al., 1993).

Table 4.6 Elastic constants in GPa of six amphibolite samples for which seismic velocities and anisotropy have been computed based on fabric data and modal compositions

Sample	**AM1**	**AM2**	**AM3**	**AM4**	**AM7**	**AM8**
Density (g/cm^3)	3.211	2.981	2.979	2.988	2.939	2.988
			Cij (GPa)			
C_{11}	123.9	123.8	126.0	126.4	121.5	122.7
C_{12}	55.1	56.7	54.1	53.5	53.1	53.2
C_{13}	50.7	55.5	51.7	51.0	50.9	50.6
C_{14}	-0.9	0.5	0.3	0.2	0.7	0.3
C_{15}	-1.0	-1.3	-0.6	0.1	0.4	0.5
C_{16}	0.0	-0.9	-0.5	1.6	-0.9	-0.2
C_{22}	163.6	149.6	149.2	145.6	146.9	149.1
C_{23}	56.9	59.5	54.6	54.0	55.0	54.4
C_{24}	0.3	1.1	1.4	0.0	2.4	0.2
C_{25}	-0.1	-0.4	-0.2	-0.1	0.6	-0.3
C_{26}	1.7	-2.3	-0.3	1.8	-1.2	-2.2
C_{33}	136.6	142.3	129.7	133.2	136.6	134.9
C_{34}	0.2	1.3	0.6	0.5	1.4	0.3
C_{35}	-1.2	-2.2	-0.7	0.0	0.0	0.4
C_{36}	0.6	-0.7	-0.2	-0.1	0.1	-0.5
C_{44}	45.4	43.2	41.6	42.3	43.4	43.8
C_{45}	0.7	-0.6	-0.1	0.1	-0.3	-0.1
C_{46}	-0.9	-0.9	0.0	-0.1	0.6	0.6
C_{55}	39.5	37.2	38.7	39.2	37.9	38.7
C_{56}	-0.3	-0.2	0.3	-0.1	0.1	-0.2
C_{66}	39.3	37.1	40.1	39.8	37.6	38.4

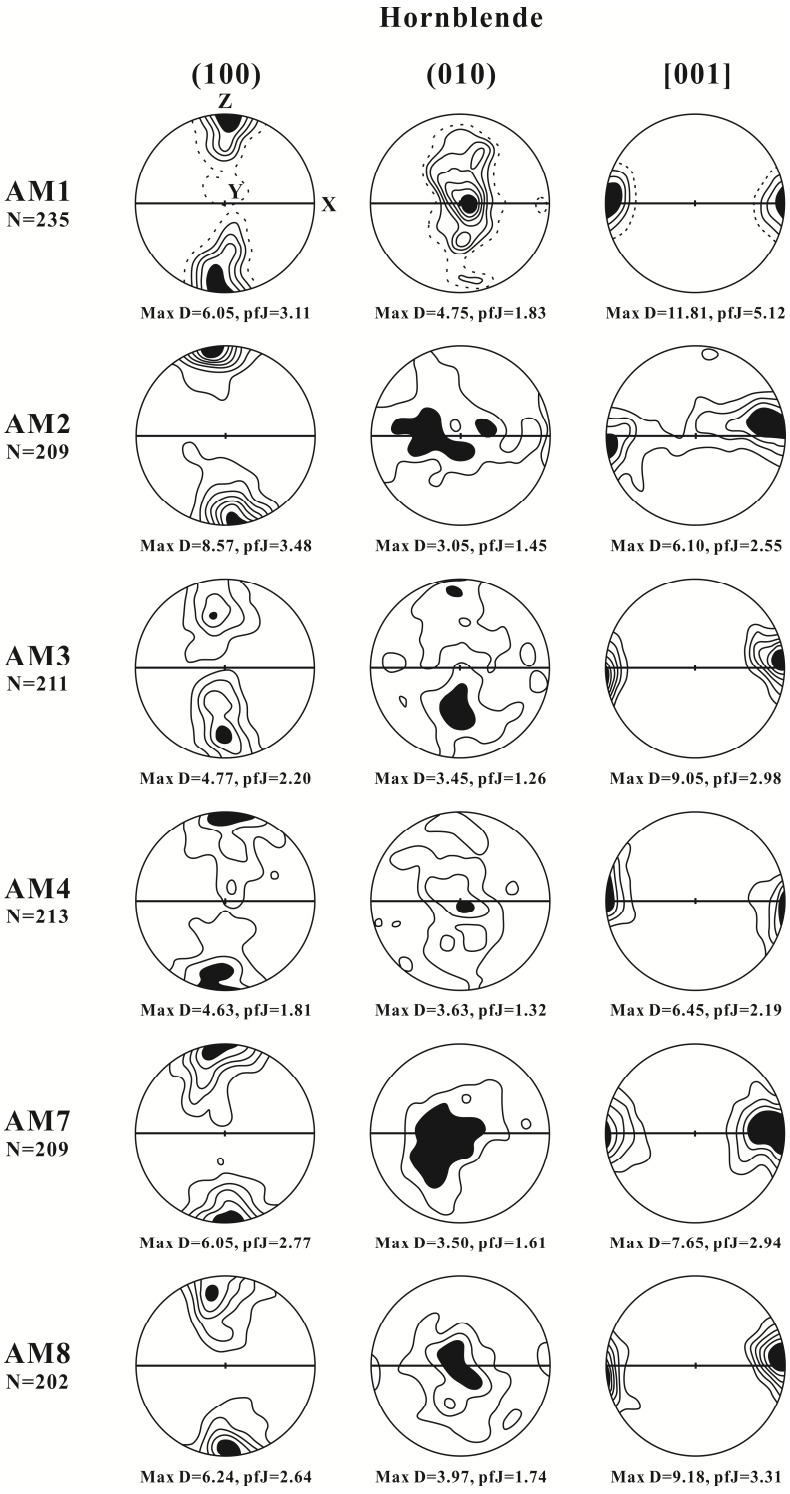


Figure 4.11 EBSD-measured pole figures for hornblende from samples AM1, AM2, AM3, AM4, AM7, and AM8. Equal-area lower hemisphere projections. The maximum density and *J* index (*pfJ*), which are calculated from the orientation distribution function, are indicated for each sample. N: number of measured grains.

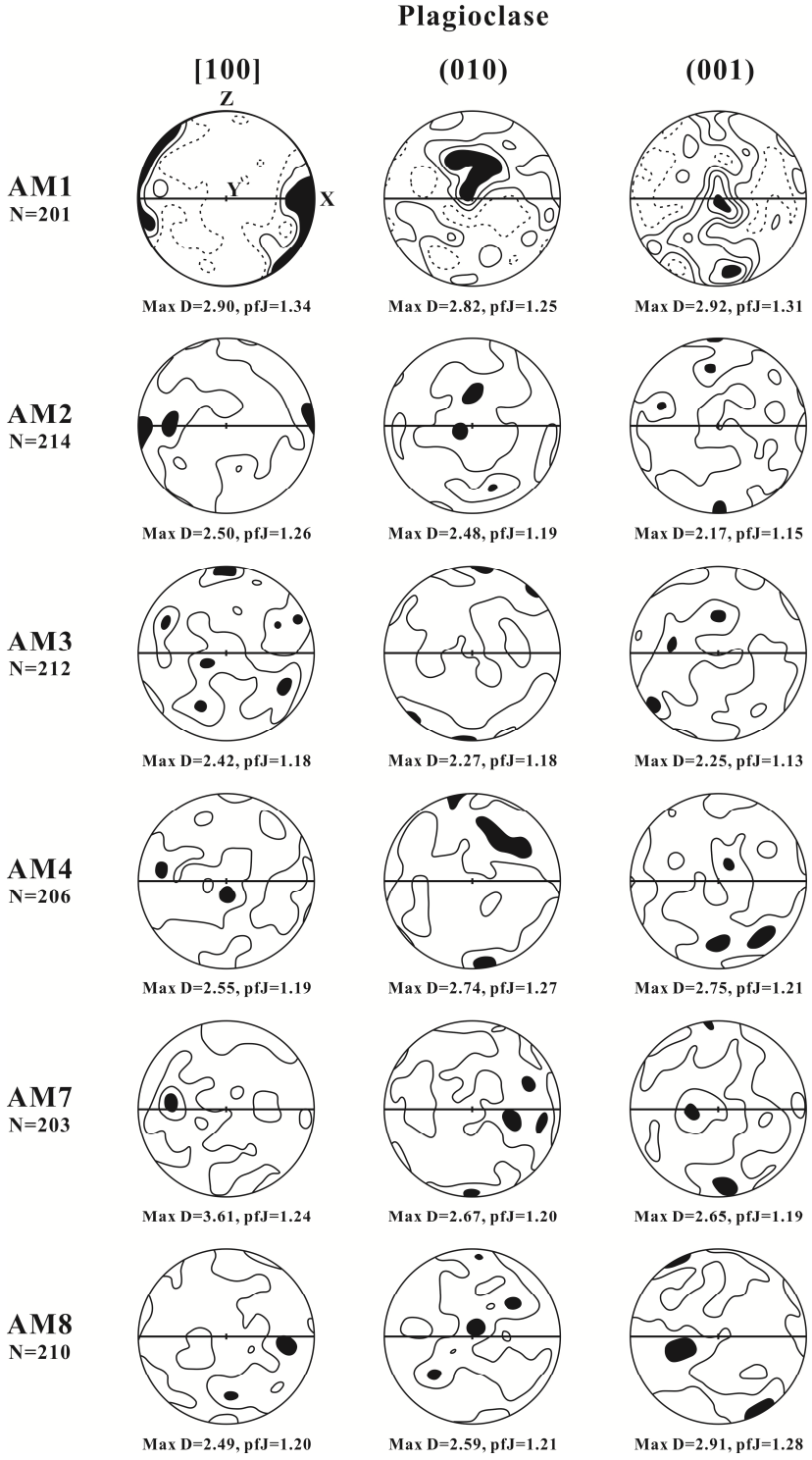


Figure 4.12 EBSD-measured pole figures for plagioclase from samples AM1, AM2, AM3, AM4, AM7, and AM8. Equal-area lower hemisphere projections. The maximum density and *J* index (*pfJ*), which are calculated from the orientation distribution function, are indicated for each sample. N: number of measured grains.

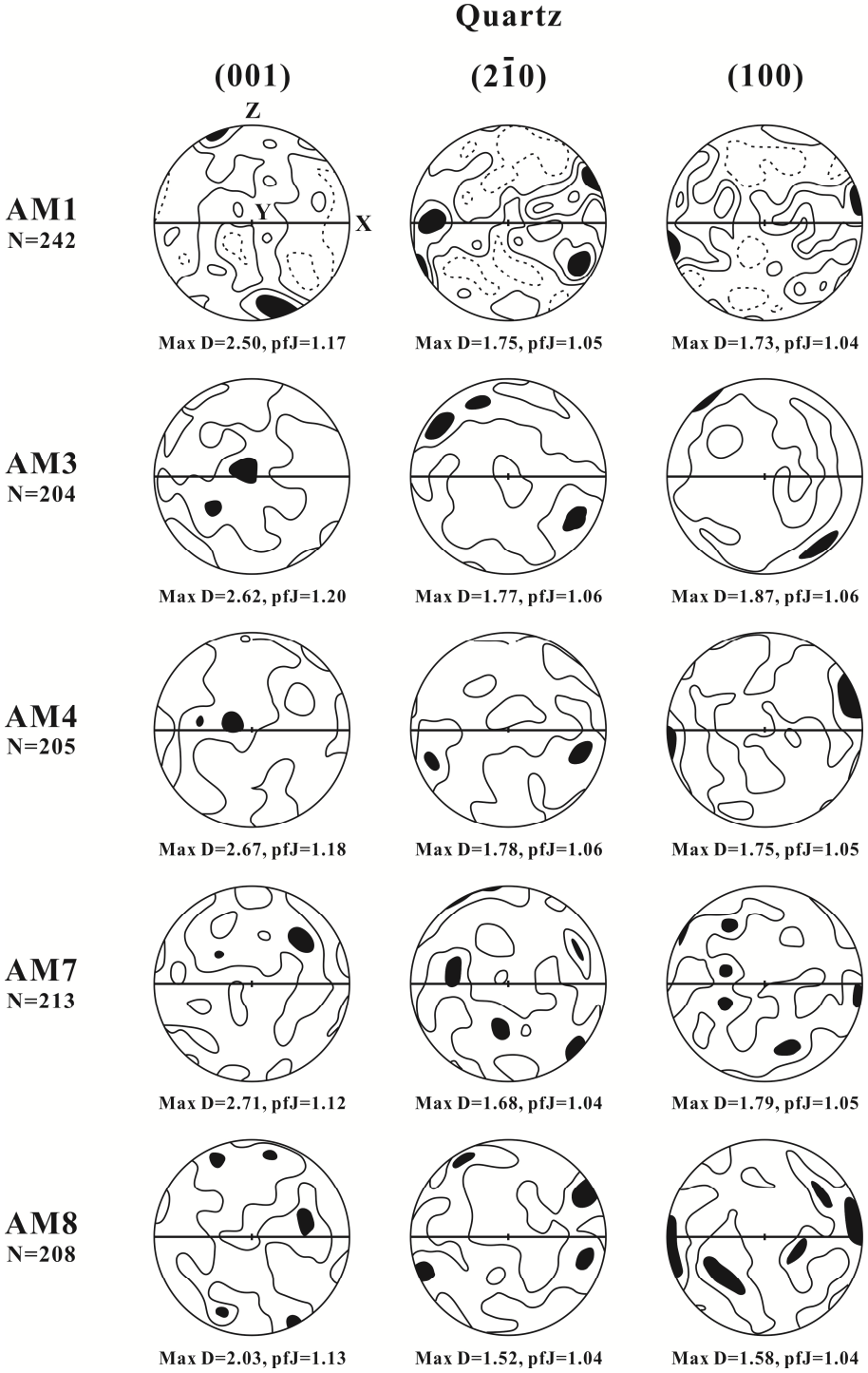


Figure 4.13 EBSD-measured pole figures for quartz from samples AM1, AM3, AM4, AM7, and AM8. Equal-area lower hemisphere projections. The maximum density and *J* index (*pfJ*), which are calculated from the orientation distribution function, are indicated for each sample. N: number of measured grains.

As shown in Figure 4.14, the calculated anisotropy patterns are very comparable to those determined experimentally above 200 MPa in the six amphibolite samples. The fastest, intermediate, and slowest P-wave velocities are in the X, Y, and Z directions, respectively. In sample AM1, for example, the calculated P-wave velocities in the X, Y, and Z directions are 7.33, 6.70, and 6.36 km/s, respectively (Figure 4.14). These values are in good agreement with the measured values at 200 MPa for V_p(X), V_p(Y), and V_p(Z) which are 7.37, 6.76, and 6.31 km/s, respectively. The V_p anisotropy coefficients calculated for samples AM1, AM2, AM3, AM4, AM7, and AM8 are 14.0%, 10.2%, 8.6%, 7.5%, 10.2%, and 9.9%, respectively, based on calculated velocities at zero porosity and room pressure, and 14.5%, 10.9%, 10.6%, 5.8%, 12.3%, and 9.6% using the measured values at 600 MPa (Table 4.3). The agreement between the calculated and measured A_p values is excellent for samples AM1, AM2, and AM8. The discrepancies between the calculated and measured A_p values for samples AM3, AM4, and AM7 may be attributed to the fact that the CPO data of fine-grained clinopyroxene, chlorite, mica, sericite, and other minor minerals such as opaque and garnet are unavailable, so their effects on the bulk seismic properties were not taken in consideration in the velocity calculations.

The variations of AV_s with propagation direction for the six amphibolites are shown in Figure 4.14. In sample AM2, for instance, the maximum shear-wave anisotropy (AV_s=8.4%) is observed for propagation in the foliation plane, while almost no birefringence occurs normal to foliation. The results are consistent with previous studies (Barruol and Kern, 1996; Ji and Salisbury, 1993; Siegesmund et al., 1989). It is found that the anisotropy is controlled by the CPO of hornblende. The polarization direction of the fastest shear waves travelling parallel to the foliation is located in the foliation plane and controlled by the preferred orientation of hornblende (100) planes. The calculated AV_s values are similar to those measured experimentally (Table 4.4 and Figure 4.10b). The slight differences between the calculated and measured velocities may be attributed to the presence of minor constituents such as accessory minerals and sericite. In sample AM3, which is anomalous, the calculated results，which are in good agreement with the measured values, showed that the $\Delta V_s(Y) \gg \Delta V_s(Z) > \Delta V_s(X) \approx 0$.

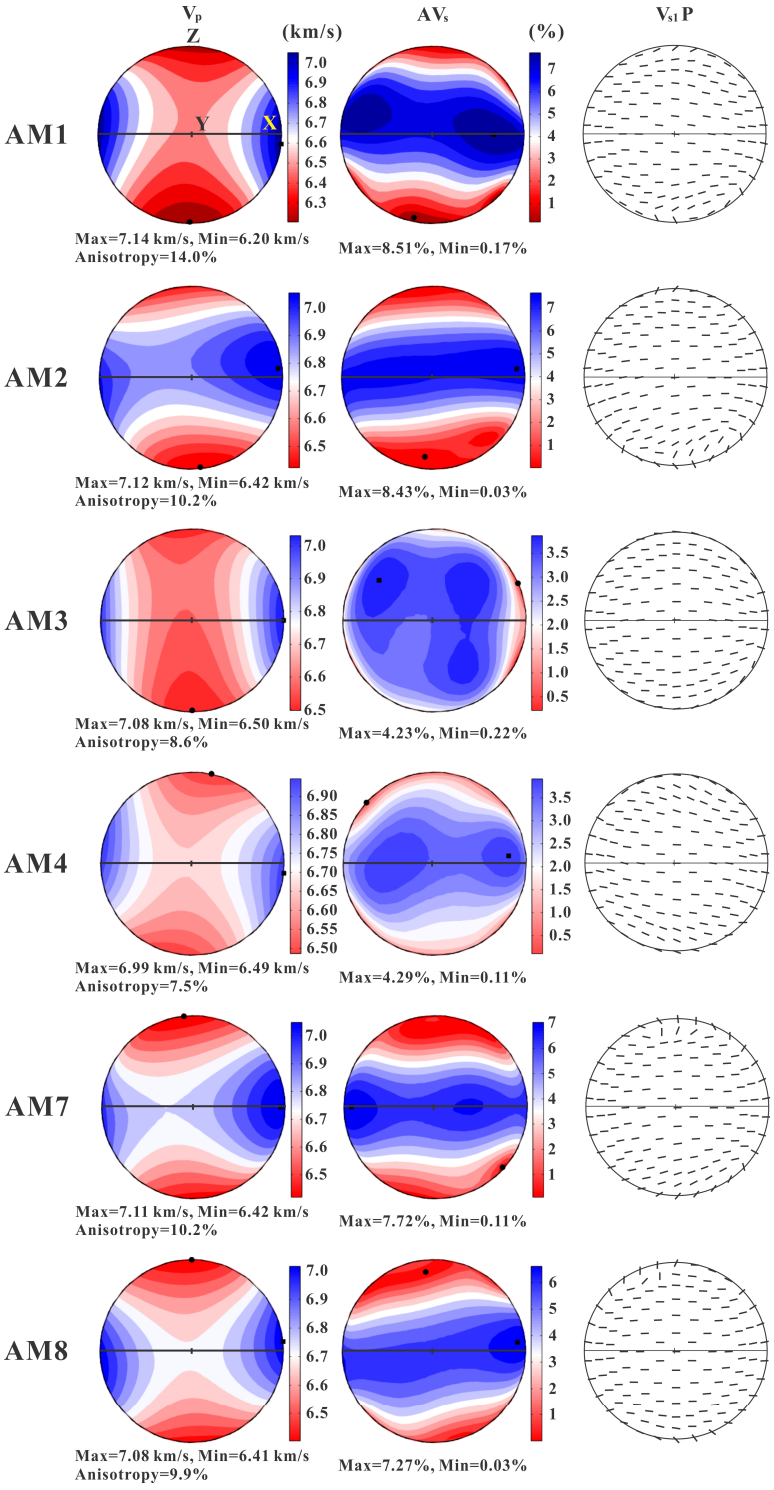


Figure 4.14 P-wave velocities, S-wave velocity anisotropy and fast polarization directions for amphibolite samples AM1, AM2, AM3, AM4, AM7, and AM8, calculated from CPO data, modal composition, and single crystal elastic constants of each rock-forming mineral. Equal-area lower hemisphere projections.

4.5 Discussion

We now discuss five issues that arise from our experimental measurements on the seismic properties of amphibole-rich rocks and the analysis of previous data in the literature.

4.5.1 Seismic anisotropy

Figure 4.15, on which the $V_p(Y)/V_p(Z)$ and $V_p(X)/V_p(Y)$ values are respectively plotted on the abscissa and the ordinate of a Flinn-type diagram, is constructed to illustrate the categories of V_p anisotropy for the amphibole-rich rocks examined in this study. The origin of the coordinate axes for the diagram is (1, 1), representing amphibole-rich rocks which are elastically isotropic. Any given V_p anisotropy plots at a particular point on the diagram, and the slope k_p of the line from the origin (1, 1) to that point is defined in Eq. (2.2).

The k_p value is a coefficient that can be used to classify the types of CPO-induced V_p anisotropy in the rocks. The three lines with k_p=0, k_p=1, and k_p=∞ correspond to three end-member Types A, B, and C of anisotropy for amphibole-rich rocks, respectively. Type A is characterized by transverse isotropy with $V_p(X)=V_p(Y)\gg V_p(Z)$. Type C also shows transverse isotropy but with $V_p(X)\gg V_p(Y)=V_p(Z)$, while Type B is characterized by an orthorhombic symmetry with $V_p(X)>V_p(Y)>V_p(Z)$ and $V_p(Y)=[V_p(X)\cdot V_p(Z)]^{0.5}$. A_p (%), which is shown by a series of dotted lines in Figure 4.15, were calculated using the values of both $V_p(X)/V_p(Y)$ and $V_p(Y)/V_p(Z)$ ratios. The V_p data of single crystal hornblende (Hearmon, 1984, Figure 1.5) and the maximum A_p values that can be formed in amphibole-rich S- and L-tectonites are also indicated in Figure 4.15. The above three extreme values (solid squares in Figure 4.15) form the theoretical upper bound for V_p anisotropy in amphibole-rich rocks.

The 17 amphibole-rich rock samples examined in this chapter can be classified into five categories according to their k_p values (Figure 4.15): (I) k_p=0-0.18; the rocks are quasi-transversely isotropic with $V_p(X)\approx V_p(Y)\gg V_p(Z)$ (e.g., sample AM15, Figure 4.3d). (II) k_p=0.18-0.70; the rocks are characterized by $V_p(X)>V_p(Y)\gg V_p(Z)$ (Figure 4.3c). Eight samples (AM5, AM7, AM8, AM9, AM12, AM13, AM14, and AM17) are classified into this category (Figure 4.15). (III) k_p=0.70-1.43; the rocks in this group (samples AM2, AM6, and AM16) display quasi-orthorhombic anisotropy with $V_p(X)>V_p(Y)>V_p(Z)$ (Figure 4.3a). (IV) k_p=1.43-5.67; the V_p anisotropy of this group (samples AM1, AM3, AM10, and AM11) is characterized by

$V_p(X) \gg V_p(Y) > V_p(Z)$. (V) $k_p > 5.67$; the rock in this group (sample AM4, Figure 4.3b) is quasi-transversely isotropic with $V_p(X) \gg V_p(Y) \approx V_p(Z)$. It is interesting to note that there are no samples with $V_p(Y)/V_p(Z) < 1$ or $V_p(X)/V_p(Y) < 1$. If plagioclase deforms by dislocation creep and develops a strong CPO with (010) parallel to the foliation and [001] parallel to the lineation, $V_p(Z)$ may exceed $V_p(Y)$ because in a single crystal of plagioclase, the fast P-wave velocities occur in the [001] and particularly the [010] directions, while low P-wave velocities occur near the [100] direction (Ji and Mainprice, 1988). As a result, strong CPO of plagioclase will increase $V_p(Z)$ and decrease $V_p(Y)$ in the amphibolite sample.

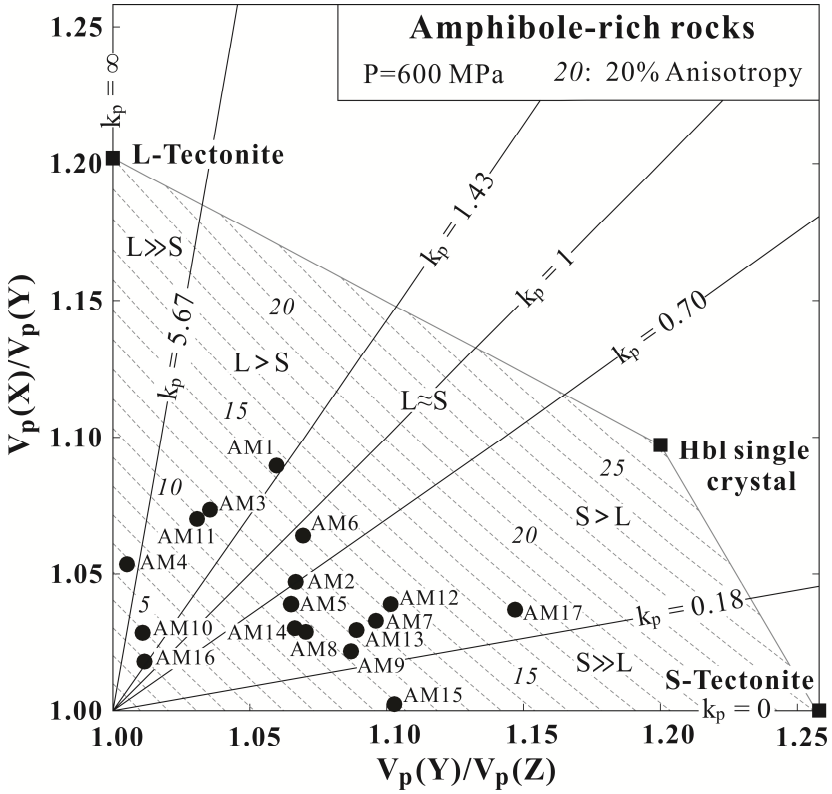


Figure 4.15 Flinn-type diagram showing P-wave velocities of amphibole-rich rocks at 600 MPa. Dashed lines indicate iso-anisotropy surfaces. The maximum anisotropy values are also illustrated for single crystal of hornblende, and S- and L-tectonites. The solid dots indicate the data from this study.

It is found that amphibole plays a critical role in the formation of seismic anisotropy, whereas the presence of plagioclase, quartz, pyroxene, garnet, and opaque minerals always diminishes the anisotropy induced by amphibole CPO in amphibolites. The presence of mica, chlorite, and sericite may reinforce the anisotropy induced by the CPO of amphibole. The highest V_p is parallel

to the lineation (X) because the [001] direction of hornblende, which is close to the fastest V_p direction in single crystal hornblende (Hearmon, 1984), is oriented parallel to the lineation in all six of the samples (Figure 4.11). The slowest V_p is normal to the foliation because the slowest P-wave direction in hornblende single crystals is normal to the (100) plane that is preferentially aligned parallel to the foliation. In a single crystal of hornblende, $V_p(b^*)=92\%V_p(<c>)=117\%V_p(a^*)$, where a^* and b^* are normal to (100) and (010), respectively, and c is the [001] direction. Thus, the V_p in the Y direction depends strongly on the degree of alignment of (010) planes in this structural direction. A weaker CPO of (010) at the Y direction will lower the V_p(Y) value and then make the V_p(Y)/V_p(Z) ratio smaller and the V_p(X)/V_p(Y) higher (e.g., samples AM3 and AM4). In contrast, a stronger CPO of (010) at the Y direction will increase the V_p(Y) value, making the V_p(Y)/V_p(Z) ratio higher and the V_p(X)/V_p(Y) smaller (e.g., samples AM7 and AM8). Thus, the Flinn diagram of V_p (Figure 4.15) can be explained essentially by the pattern and strength of amphibole fabric.

Figure 4.16 illustrates the histograms of bulk V_p and V_s anisotropy (A_p and A_s) at 200 and 600 MPa for the samples from this chapter and the literature (Barberini et al., 2007; Birch, 1960; Burke et al., 1990; Christensen, 1965; 1978; Fountain, 1976, 1990; Fountain et al., 1990; Fountain and Salisbury, 1996; Ji et al., 2002; Kern and Fakhimi, 1975; Kern et al., 1996, 1997, 1999, 2001, 2009; Khazanehdari et al., 2000; Miller and Christensen, 1994; Punturo et al., 2005; Siegesmund et al., 1989; Zhao et al., 2011, Zhou et al., 2011). The bulk V_p and V_s anisotropy is defined by Eqs. (1.31) and (1.33), respectively.

Unlike AV_s, A_s calculated from Eq. (1.33) is a constant for each sample and independent upon the propagation direction. The amphibole-rich rocks display an average A_p value (10.5% at 200 MPa, 9.5% at 600 MPa) higher than that of A_s (8.8% at 200 MPa, 8.5% at 600 MPa). These anisotropy values, which are comparable to those of mica-rich schists and phyllites (Godfrey et al., 2000; Kern and Wenk, 1990) as well as serpentinites (Ji et al., 2013a; Kern et al., 1997; Shao et al., 2014), are much larger than those for other categories of igneous and metamorphic rocks such as granite, diorite, gabbro, pyroxenite, peridotite, marble, felsic gneiss, and mafic granulite (Ji et al., 2002, p. 616). Metamorphic and deformed rocks that are anisotropic to ultrasonic waves should be also anisotropic at the scale of active and passive seismic experiments (lower-frequency waves) because the metamorphic and deformation fabrics are often pervasive for tens to hundreds of kilometers (Brocher and Christensen, 1990).

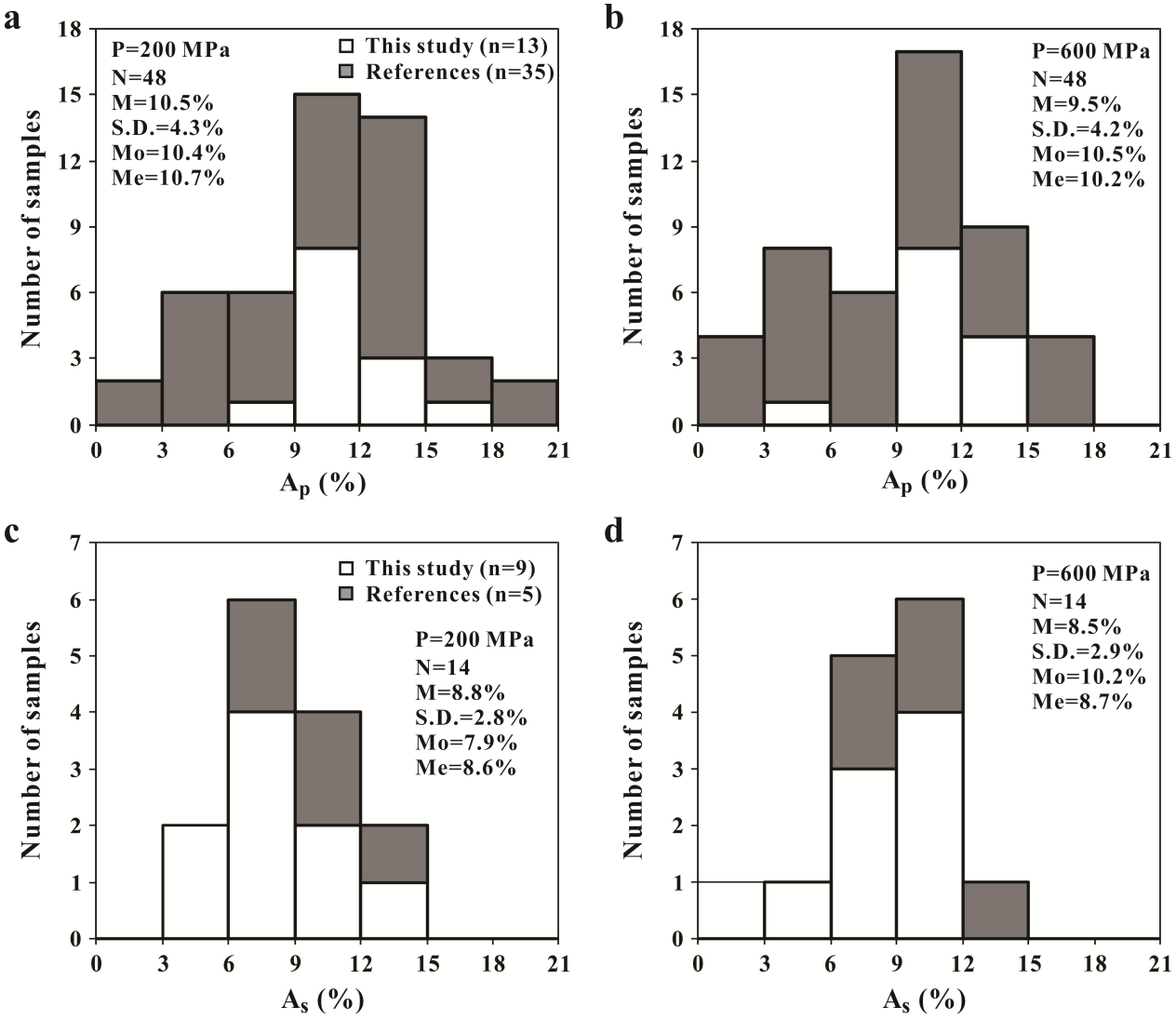


Figure 4.16 Histograms of bulk P- and S-wave velocity anisotropy (A_p and A_s, %) for 48 amphibolites consisting mainly of hornblende and plagioclase at (a, c) 200 MPa and (b, d) 600 MPa from this chapter (13 samples) and the references (35 samples). The definitions of N, M, S.D, M_o, and Me as in Figure 2.6 caption.

Crustal anisotropy has received increasing attention during the last two decades. Recent examples include seismological observations in the Tibetan Plateau and its tectonic extrusion system (e.g., Ozacar and Zandt, 2004; Gao and Liu, 2009; Xu et al., 2006); Chugoku, Kinki, Shikoku, and Kyushu districts in Japan (Nagaya et al., 2011); Marlborough and Wellington regions in New Zealand (Balfour et al., 2005; Savage, 1998); the San Andreas fault zone and the Basin and Range Province in the U.S. (McNamara and Owens, 1993; Zhang et al., 2007; Balfour et al., 2012); and the southern Vancouver Island in Canada (Bostock and Christensen, 2012). As listed

in Table 4.7, the source of anisotropy is generally located in the middle to lower crust where confining pressures are too high to allow cracks to open, and thus, the anisotropy should result from the CPO of anisotropic major constituent minerals such as amphibole and mica, formed by past and present crustal deformation. Even in the shallow crust, the anisotropy can originate jointly from both near-vertical, water-filled cracks in parallel alignment (e.g., Crampin, 1987) and fossil fabrics due to the CPO of amphibole, mica, and chlorite (Barruol and Mainprice, 1993a; Ji and Salisbury, 1993; Bostock and Christensen, 2012; Nagaya et al., 2011). Global compilations of compositions and seismic velocities of the continental crust and oceanic island arcs (e.g., Christensen and Mooney, 1995; Fliedner and Klemperer, 2000), volume fraction of lithologies in currently outcropping high-grade metamorphic terranes (e.g., Rutter et al., 2007), and evidence from deep-sourced xenoliths (e.g., Rudnick and Fountain, 1995) all indicate the dominance of amphibolite-to-granulite facies mafic rocks in the deep crust. In addition, most of the phyllosilicate-rich schists and phyllites exposed currently in the Earth's surface (Bostock and Christensen, 2012) were derived from retrograde metamorphism of initially deeper amphibolites during exhumation (Mahan, 2006).

In amphibole-rich rocks, the fastest shear-wave travels in the foliation plane with particle motion parallel to lineation and the slowest vibrates normal to foliation, causing shear-wave birefringence as high as 0.38-0.40 km/s. A 10-20 km thick section of amphibolites with steeply dipping foliation and horizontal lineation in large-scale strike-slip shear zones could contribute as much as 0.25-0.49 s of the time delay observed in the teleseismic shear-wave (SKS or SKKS) splitting experiments, making the crustal contributions significant. It should be kept in mind that the values calculated above are probably a maximum since it was assumed that the CPO of the amphibolite facies terrane is everywhere consistent. If the CPO pattern and strength vary at the scale of the seismic wavelength observed, the seismic anisotropy should be reduced. For example, a 25-31 km thick amphibolitic layer with an average anisotropy of 7% can well explain the splitting time of 0.45-0.55 s in the deep crust beneath southern Lhasa Terrane, Tibetan Plateau (Gao and Liu, 2009, Table 4.7). The fast polarization direction, which is controlled by the preferred orientation of amphibole c-axis, is thus parallel to the direction of topographically induced tectonic extrusion (e.g., Sherrington and Zandt, 2004). Similarly, the delay time of 0.24 s in Ps splitting from the Ailaoshan-Red River fault zone (Xu et al., 2006, Table 4.7) indicates AV_S=5.3-6.3% for a 15-18 km-thick amphibolitic layer with vertical foliation and horizontal

lineation within the middle-lower crust (Tapponnier et al., 1990). The so-called Ps converted wave is a seismic body wave resulting from the conversion of an incident parent P-wave at a boundary within the Earth's crust to a refracted shear-wave. Vergne et al. (2003) studied the radial and transverse receiver functions at two stations (BUDO and 121E) located on the Songpan-Ganze terrane, northeastern Tibet. Between 10 and 26 km depths, the seismic anisotropy is as high as 15-20% with V_p/V_s=1.73 (V_p=6.5 km/s and V_s=3.75 km/s). These characteristics are consistent with amphibole- and biotite-rich metasediments derived from a thick Triassic flysch complex but disagree with the assumption of partial melting in the middle crust beneath the northeastern Tibetan Plateau (Owens and Zandt, 1997). The fast azimuth of Ps-converted waves is parallel to the lineation formed by amphibole and the foliation defined by mica. Zhang et al. (2007) detected a highly anisotropic zone (3.5-4.5%) below 7 km depth to the northeast of the San Andreas Fault in the Parkfield, California. This highly anisotropic zone displays high V_p and V_s, indicating that the high anisotropy is caused most likely by the amphibole-rich rocks rather than serpentinite or mica-rich schists.

4.5.2 Dependence of seismic properties on chemical and modal compositions

In Figure 4.17, the mean V_p and V_s values of amphibole-rich rocks at 600 MPa are plotted versus their SiO_2, MgO, CaO, and Na_2O+K_2O contents. Although the data are scattered, clear trends can be seen for the P-wave velocities which decrease with increasing SiO_2 and Na_2O+K_2O contents but increase with increasing MgO and CaO contents. However, the correlations of V_s with increasing SiO_2, MgO, and CaO content are unclear although V_s seems to decrease with increasing Na_2O+K_2O contents. For the amphibole-rich rocks, the dependence of V_s on bulk chemical compositions is thus more complicated than that of V_p.

V_p(X), V_p(Y), V_p(Z), and mean V_p and V_s values at 600 MPa are plotted versus the volume fraction of hornblende in Figure 4.18. Mean V_p and V_s, V_p(Y), and particularly V_p(X) all show fairly clear trend of increasing velocity with amphibole abundance although there is considerable scatter in the data due most likely to variations in the contents of minor minerals such as garnet, pyroxene, epidote, biotite, chlorite, and magnetite. These trends can be primarily attributed to the following facts: (1) hornblende has higher mean V_p (7.10 km/s) and V_s (3.96 km/s) values than plagioclase (V_p=6.30 km/s and V_s=3.45 km/s for An29 and V_p=6.56 km/s and V_s=3.54 km/s for An53) (Hearmon, 1984), (2) the amphibole [001], which is coincident with the fastest V_p

direction in hornblende single crystal (Hearmon, 1984), develops generally a strong preferred orientation parallel to the lineation.

Figures 4.19a and 4.19b show plots of bulk V_p and V_s anisotropy (A_p and A_s) as a function of hornblende content. Although both plots show a great deal of scatter, it is apparent that metamorphic rocks containing higher contents of amphibole may develop stronger V_p and V_s anisotropy, depending on the CPO of amphibole. Only those rocks with high contents of amphibole (≥50 vol.%) and a well-developed amphibole fabric are strongly anisotropic (A_p≥15% and A_s≥10%). The rocks containing <20 vol.% amphibole cannot have A_p>4% and A_s>3% (Figure 4.19).

Table 4.7 Summary of crustal anisotropy measured worldwide*

Location	Method	φ (°)	δt (s) or AV_s(%)	Source of anisotropy	Note	Reference
Ailaoshan-Red River fault zone, Yunnan, China	1	132	0.24	15-18 km thick in middle-lower crust	Parallel to the strike of the crustal fault zone, but normal to the fast polarization direction in the upper mantle	Xu et al. (2006)
Bangong-Nujiang suture, Central Tibet, China	1	106	18%	Middle crust between 24 and 32 km depths	Parallel to the strike of the suture zone	Ozacar and Zandt (2004)
Kunlun fault zone, Tibetan Plateau, China	1	120	0.10-0.30	15-20 km thick layer in the crust	20° oblique to the strike-slip shear zone (100°)	Herquel et al. (1995)
Songpan-Ganze terrane, Northeastern Tibet	1	30	0.5	Upper crust between 10 and 26 km depths	Parallel to GPS-revealed direction of surface movement	Vergne et al. (2003)
Tibetan Plateau, China	4		0.5	Middle crust between 20 and 50 km depths	$V_{sh} > V_{sv}$	Shapiro et al. (2004)
Southern Lhasa terrane, Tibetan Plateau, China	5	40-59	0.45-0.55	30-40 km thick in middle-lower crust	Parallel to GPS-revealed direction of surface movement	Gao and Liu (2009)
Southern Tibet, China	6	N-NW	4-14%	Middle to lower crust (>25 km depth)	Combined influence from northward motion of India and lateral topographically driven flow	Sherrington and Zandt (2004)
Central Tibet, China	6	E-W	4-14%	Middle to lower crust (>25 km depth)	Parallel to the tectonic extrusion direction	Sherrington and Zandt (2004)
Eastern Tibet, China	6	NW	4-10%	Middle to lower crust (>25 km depth)	Parallel to the tectonic extrusion direction	Sherrington and Zandt (2004)
Shikoku and Kyushu districts, Japan	1	E-W to NW-SE	0.24-0.25	Both upper (0-20 km) and lower crust (20-35 km)	Parallel to the strike of metamorphic belts	Nagaya et al. (2011)
Chugoku and north Kinki districts, Japan	1	N-S to NE-SW	0.47-0.50	Lower crust between 20 and 35 km depths	Parallel to the strike of metamorphic belts	Nagaya et al. (2011)
Basin and Range Province, Nevada, USA	1	127	0.18-0.28	Lower crust between 15 and 30 km depths	Perpendicular to the strike of most regional normal fault traces	McNamara and Owens (1993)
San Andreas Fault Zone, Parkfield, California	2	130	0.15	Below 7 km depth	Parallel or subparrallel to the strike of the San Andreas Fault	Zhang et al. (2007)
Forearc of Northern Cascadia subduction zone, Southwest British Columbia, Canada	2	NW-SE	0.05-0.40	Upper crust shallower than 20 km	Parallel to the strike of the subduction margin	Balfour et al. (2012)
Southern Vancouver Island, Canada	3	113	0.2	<30 km in accretionary wedge	Parallel to the strike of the San Juan Fault and the dominant foliation of the Leech River Schist terrane	Bostock and Christensen (2012)
Marlborough, New Zealand	2	65	0.11-0.15	Upper crust shallower than 15 km	Parallel to the fault zone; structure rather than stress-controlled	Balfour et al. (2005)
Right-lateral, dip-slip fault zone at Wellington, New Zealand	1	57	12%	8 km-thick layer at the base of the crust (27-35 km depths)	Metamorphosed, subducted oceanic crust	Savage (1998)
Alborz Mountain Range, Iran	1	50	0.22-0.29	Both upper (0-18 km) and lower crust (18-30 km)	Subparallel to the NNE-SSW transpression direction	Sadidkhouy et al. (2008)

*1=Splitting of P-to-S converted phase; 2=S phase of local crustal earthquake; 3=Shear-wave splitting of tremor from the subduction zone beneath the accretionary wedge;
4=Velocity difference between intermediate-period Rayleigh (V_{sv}) and Love (V_{sh}) waves; 5=Two-layer modeling of teleseismic phases; 6=Inversion of receiver functions;
φ=the fast polarization direction (°) measured clockwise from the north; δt (s)=delay time (s); AV_s=the V_s aniostropy (%).

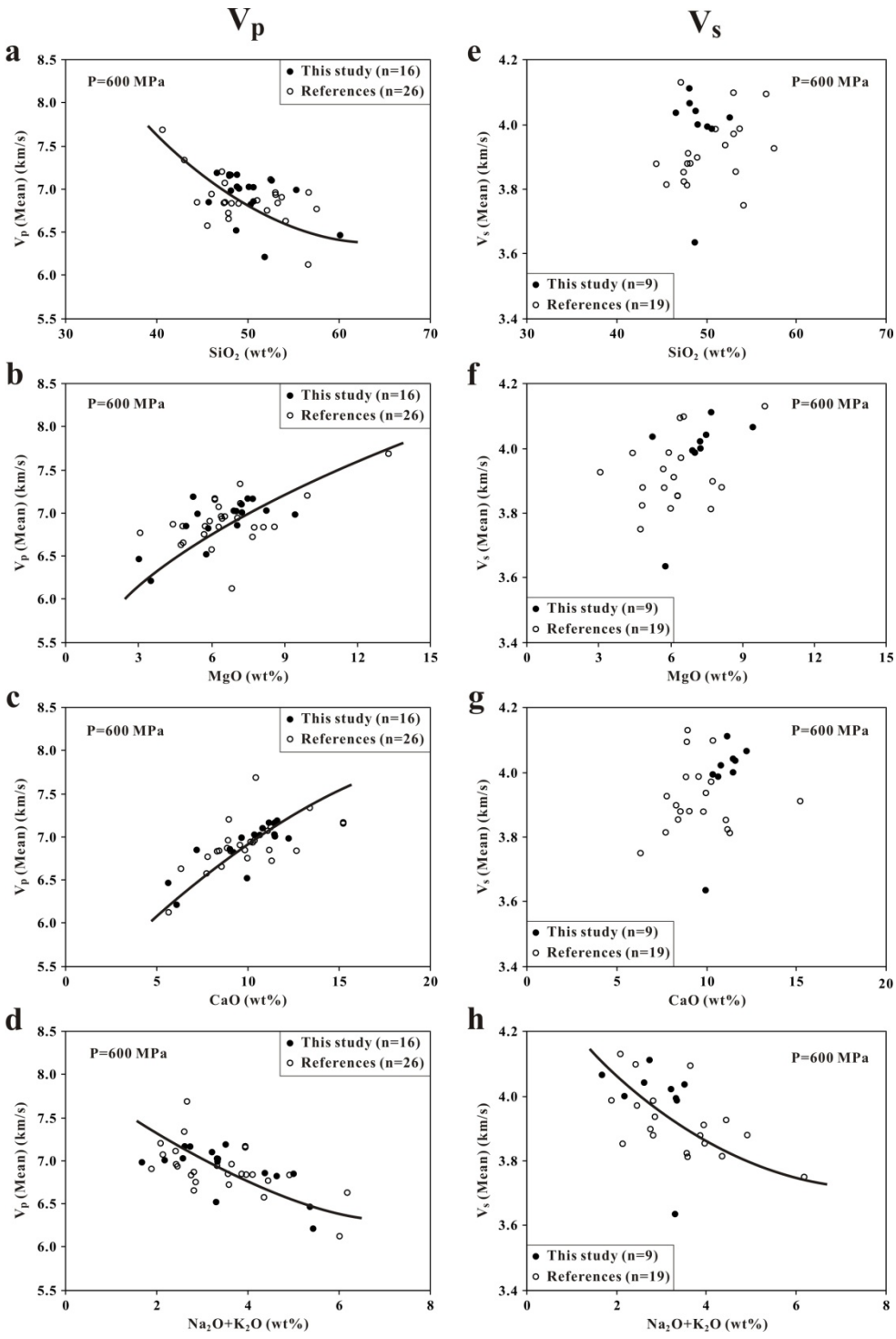


Figure 4.17 Mean P- and S-wave velocities versus major element (SiO_2, MgO, CaO, and Na_2O+K_2O) contents for amphibole-rich rocks. Data from this chapter (solid circles) and those from previous studies (open circles, Burke and Fountain, 1990; Fountain, 1976; Fountain et al., 1990; Kern et al., 1996, 1999, 2001, 2009; Miller and Christensen, 1994; Zhao et al., 2011; Zhou et al., 2011).

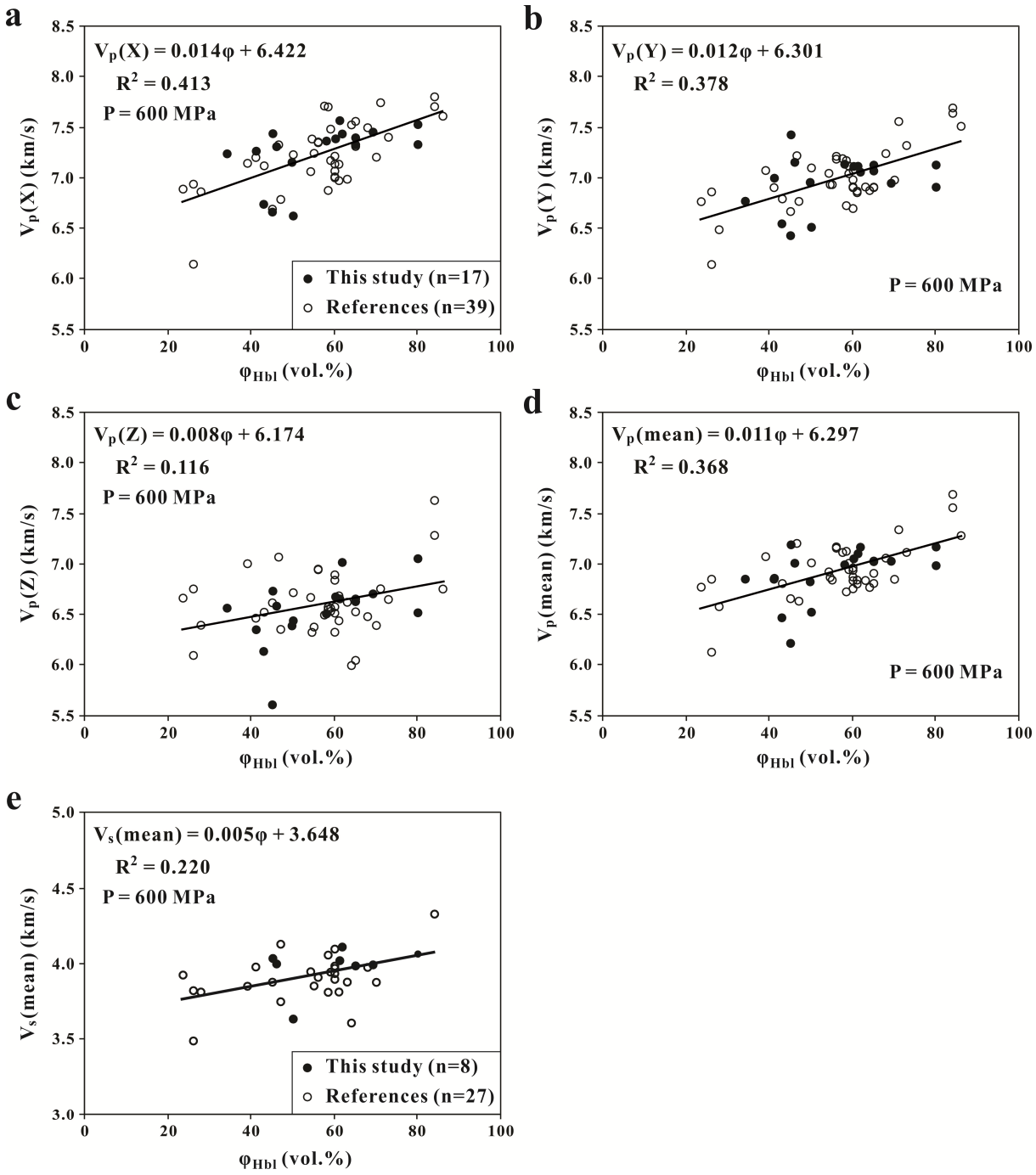


Figure 4.18 (a) V_p(X), (b) V_p(Y), (c) V_p(Z), (d) mean V_p, and (e) mean V_s measured at 600 MPa versus hornblende volume fraction (vol.%). Data from this chapter (solid circles) and those from previous studies (open circles, Barruol, 1993; Birch, 1960; Burke and Fountain, 1990; Christensen, 1965, 1978; Fountain, 1976; Fountain et al., 1990; Kern et al., 1996, 1997, 1999, 2001, 2009; Khazanehdari et al., 2000; McDonough and Fountain, 1988; Miller and Christensen, 1994; Punturo et al., 2005; Siegesmund et al., 1989; Zhao et al., 2011; Zhou et al., 2011).

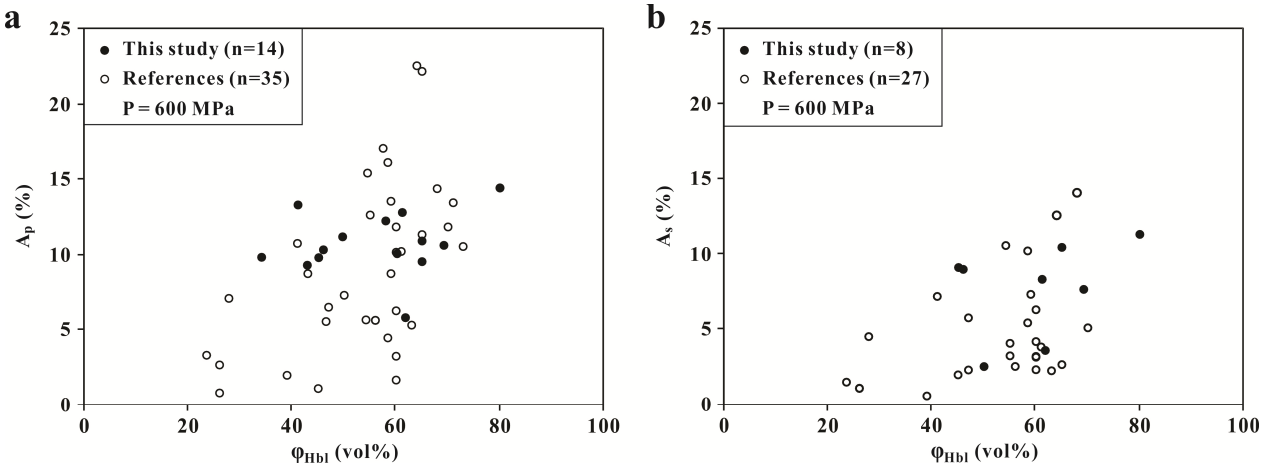


Figure 4.19 P- and S-wave velocity anisotropy (A_p and A_s) versus hornblende volume fraction (vol.%). Data from this chapter (solid circles) and those from previous investigations (open circles, Barruol, 1993; Burke and Fountain, 1990; Christensen, 1965, 1978; Fountain, 1976; Fountain et al., 1990; Kern et al., 1996, 1997, 1999, 2001, 2009; Khazanehdari et al., 2000; McDonough and Fountain, 1988; Miller and Christensen, 1994; Punturo et al., 2005; Siegesmund et al., 1989; Zhao et al., 2011; Zhou et al., 2011).

4.5.3 V_p/V_s ratios and Poisson's ratios

Poisson's ratio has been regarded as one of the most diagnostic properties of natural rocks (Christensen, 1996). It has been used as a discriminant of composition for the continental crust and provides valuable constraints on its formation and evolution (e.g., Ji et al., 2009). The Poisson's ratios of 32 amphibolite samples calculated from their average V_p and V_s data (i.e., equivalent isotropic velocities) measured at 600 MPa are given in Figure 4.20. Among them, 7 samples are from this chapter and 25 from the literature (Barruol, 1993; Christensen, 1965; Fountain, 1976; Fountain and Salisbury, 1996; Kern et al., 1996, 1997, 1999, 2001, 2009; Miller and Christensen, 1994; Punturo et al., 2005; Siegesmund et al., 1989; Zhou et al., 2011). The Poisson's ratios of these amphibolites composed mainly of amphibole and plagioclase with little or no quartz vary from 0.235 to 0.289 with a mean value of 0.260±0.012, corresponding to a ratio V_p/V_s=1.756±0.030. This Poisson's ratio value is only slightly smaller than that (0.263±0.017) calculated by Christensen (1996) from his unpublished velocity data. Also shown in Figure 4.20 are eight other amphibole-rich rocks with more varied compositions, including two mafic gneiss samples containing 64-65 vol.% hornblende, 31-32 vol.% biotite, and 4 vol.% opaque minerals (Kern et al., 2001) which display much higher Poisson's ratios (0.302-0.308), plus

garnet-hornblende, pyroxene-hornblende, and quartz-hornblende gneisses having mean Poisson's ratios of 0.249, 0.266, and 0.267, respectively (Figure 4.20).

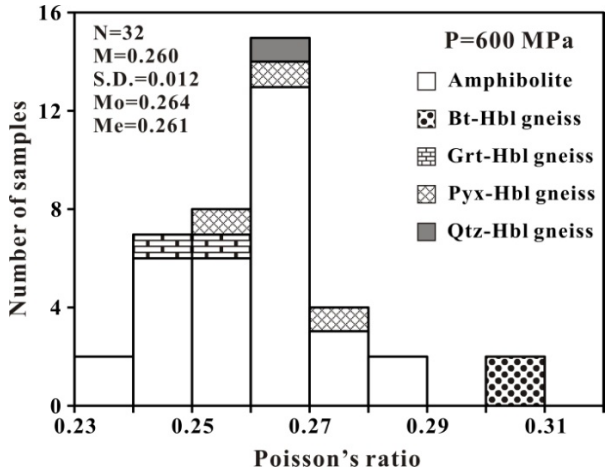


Figure 4.20 Histogram of Poisson's ratios for 40 amphibole-rich rocks (9 from this chapter and 31 from Barruol, 1993; Christensen, 1965; Fountain, 1976; Fountain and Salisbury, 1996; Kern et al., 1996, 1997, 1999, 2001, 2009; Miller and Christensen, 1994; Punturo et al., 2005; Siegesmund et al., 1989; Zhao et al., 2011; Zhou et al., 2011) at 600 MPa. The statistical data (N, M, S.D, Mo and Me as in Figure 2.6 caption) are indicated only for amphibolites consisting mainly of hornblende and plagioclase (32 samples).

Over the past decade, there has been a clear shift from the use of Poisson's ratio toward using the ratio V_p/V_s in petrophysical studies. The concept of Poisson's ratio is meaningful only for homogeneous isotropic media. However, most crustal rocks are elastically anisotropic due to the presence of compositional layering, CPO, SPO (i.e., foliation and lineation) of rock-forming minerals (e.g., Ji et al., 2002; Meissner et al., 2006), and the alignment of microcracks (e.g., Crampin and Peacock, 2005, 2008). Many people have used the term Poisson's ratio simply as a mathematical substitution for V_p/V_s. Here we suggest that V_p/V_s should be used instead of Poisson's ratio because the ratio of P- to S-wave velocities (V_p/V_s) is a physical property that can be really measured.

The V_p/V_s ratio is a constant (β_0) for an isotropic rock. In a given propagating direction through an anisotropic medium, however, there are generally three velocities (V_p, V_{s1}, and V_{s2}), where V_{s1} and V_{s2} are the velocities of the orthogonally polarized fast and slow split shear waves traveling in that directions. Usually, only the ratio V_p/V_{s1} is obtained because the first arriving shear-wave

phase is easily picked (Chevrot and van der Hilst, 2000; Owens and Zandt, 1997; Zandt and Ammon, 1995). The V_p/V_{s1} ratio of an anisotropic rock measured along a selected pair of propagation-vibration (i-j) directions is an apparent value (β_{ij}) that can be significantly different from the value for its isotropic counterpart (β_0). As an example, Figure 4.21 shows β_0 and the variations between β_0 and β_{ij} as a function of direction and confining pressure for amphibolite AM1. Clearly, the apparent V_p/V_{s1} ratio is strongly anisotropic and varies with the propagating direction (Figure 4.21a). At 600 MPa, the V_p/V_{s1} ratio is equal to 1.758, 1.657, 1.624, 1.717, 1.680, 1.617, and 1.689 for the propagating direction X, Y, Z, X45Y, X45Z, Y45Z, and X55Y55Z, respectively. At this pressure, the V_p/V_{s1} ratio in the direction X45Y (1.717) is close to the isotropic value (β_0=1.718), while the ratio in the direction X (1.758) is significantly higher than β_0, and those in the other directions (i.e., Y, Z, X45Z, Y45Z, and X55Y55Z) are clearly lower than β_0. At 600 MPa, V_p/V_{s1} ratios in the X direction is 2.34% larger than β_0 (1.718), while in the Y, Z, X45Y, X45Z, Y45Z, and X55Y55Z directions, the ratios are, respectively, 3.54%, 5.48%, 0.07%, 2.12%, 5.89%, and 1.73% lower than β_0 (1.718). The V_p/V_{s1} ratios measured along the Y, Z, X45Z, Y45Z, and X55Y55Z directions could be mistaken as indicative of felsic rocks.

So far, a full characterization of crustal V_p/V_{s1} anisotropy has not been achieved by in situ seismic observations due to the limitations of the raypath geometry. The crustal V_p/V_{s1} values reported in the literature were generally calculated from the V_p and V_{s1} data measured along a single propagation-vibration path through an anisotropic medium. The orientation of the path with respect to the structural framework (X-Y-Z) is generally unconstrained. The V_p and V_{s1} data used to calculate the V_p/V_{s1} values in some previous papers were even measured along different travel paths. For example, Musacchio et al. (1997) obtained a V_p/V_{s1} value (1.83) for the Tahawus complex of the Grenville Province using the P-wave velocity determined by seismic refraction modeling and the S-wave velocity from teleseismic modeling (Hughes and Luetgert, 1992). The reported V_p/V_{s1} ratios, which are extremely sensitive to the propagation and vibration directions, can be significantly different from the isotropic value (β_0). As the whole range of V_p/V_{s1} ratios displayed by a single rock can be as large as the range displayed by the entire spectrum of common rocks if the rock is strongly anisotropic, determinations of lithology using V_p/V_{s1} ratios alone are subject to considerable ambiguity. For example, if the deep crust subjected to tectonic extension is composed of amphibolite that developed regionally and pervasively horizontal foliation, the V_p/V_{s1} ratio can vary from 1.68 for steep propagation paths to 1.80 for horizontal

propagation path parallel to lineation. If velocities for the deep crust are determined from the wide-angle reflections and diving wave rays which turn in the deep crust due to gradients (e.g., Salisbury and Fountain, 1994), the V_p/V_{s1} ratio obtained should be biased toward higher values because the wave paths are aligned with subhorizontal to moderate (45º) dips. On the other hand, if velocities for the crust are obtained from the analysis of teleseismic receiver functions using single-station techniques (e.g., Chevrot and van der Hilst, 2000; Owens and Zandt, 1997; Zandt and Ammon, 1995), the wave propagation paths are oriented with subvertical to moderate (45º) dips, causing the V_p/V_{s1} ratio to be biased toward lower values.

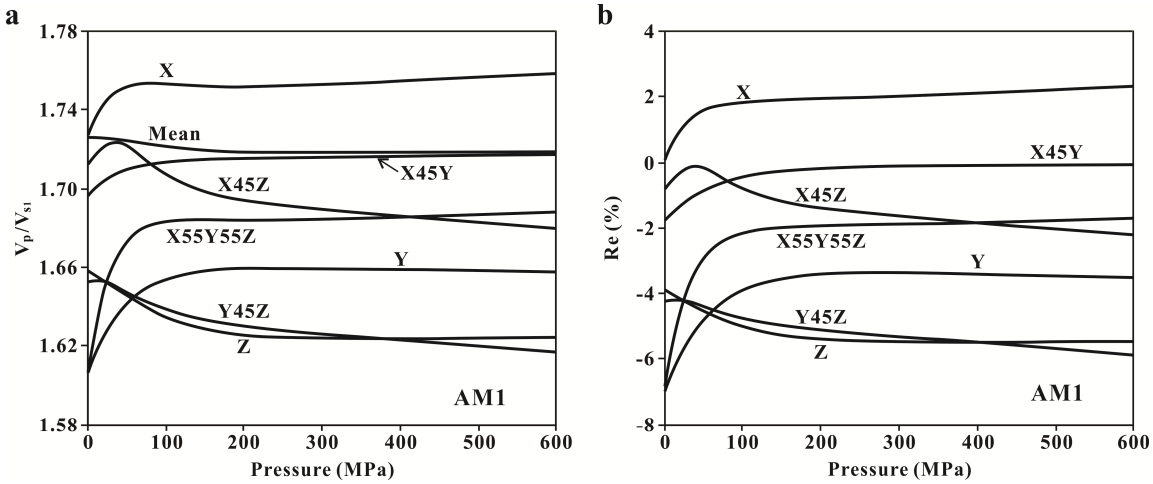


Figure 4.21 (a) Apparent V_p/V_{s1} ratio (β_{ij}) versus confining pressure for each propagation direction in amphibolite sample AM1 and (b) comparison of apparent ratios with the equivalent isotropic V_p/V_s ratio (β_0) calculated from the mean V_p and V_s velocities for sample AM1.

4.5.4 Relationship between V_p and V_s

Figures 4.22a and 4.22b show the V_s-V_p and lnV_s-lnV_p plots for 40 amphibole-rich rocks measured at a hydrostatic confining pressure of 600 MPa. Among them, 9 samples are from this chapter and 31 samples from the literature (Barruol, 1993; Christensen, 1965; Fountain, 1976; Fountain and Salisbury, 1996; Kern et al., 1996, 1997, 1999, 2001, 2009; Miller and Christensen, 1994; Punturo et al., 2005; Siegesmund et al., 1989; Zhao et al., 2011; Zhou et al., 2011). The least squares linear fit gives $V_s = 0.536V_p + 0.233$ (R^2=0.84), and $\ln V_s = 0.941 \ln V_p - 0.449$ (R^2=0.84). These relations are valid when V_p ranges from 6.1 to 8.0 km/s and V_s ranges from 3.4 to 4.6 km/s. The linear fit yields slightly better results than the nonlinear empirical equation proposed by Brocher (2005). The trend of velocity variation essentially reflects the relative

volume fractions of main constituent minerals. As noted by Wang et al. (2009), so far, there are many more laboratory measurements of V_p than V_s for rock samples in the literature (e.g., Handbook of Seismic Properties of Minerals, Rocks and Ores, Ji et al., 2002). This is in part because measurements of V_s met appreciable difficulties at low pressures, since the transfer of shear waves to the specimen requires a firm contact between the transducer and the end surfaces of the specimen. In situ seismic refraction experiments often report only V_p data because the experiments commonly use short-period vertical seismometers from which it is difficult to pick the S arrivals (e.g., Chevrot and van Hilst, 2000). Similarly, V_p and V_s structures of the Earth's interior beneath a given region are usually determined using seismic waves of different frequencies (~1 s for P-waves and ~20 s or longer for S-waves). Moreover, raypaths used to constrain these velocity structures may not be identical (e.g., Song and Helmberger, 2007). As pointed out by Brocher (2005), V_s data are more important for earthquake hazard analyses in a given region than V_p data because shear and surface waves have much larger amplitudes, excite strong ground motions, and consequently cause most of damage (Joyner, 2000). Thus, the empirical relation between V_s and V_p or between $\ln V_s$ and $\ln V_p$ can give a reasonable estimate for the V_s values when only V_p data exist.

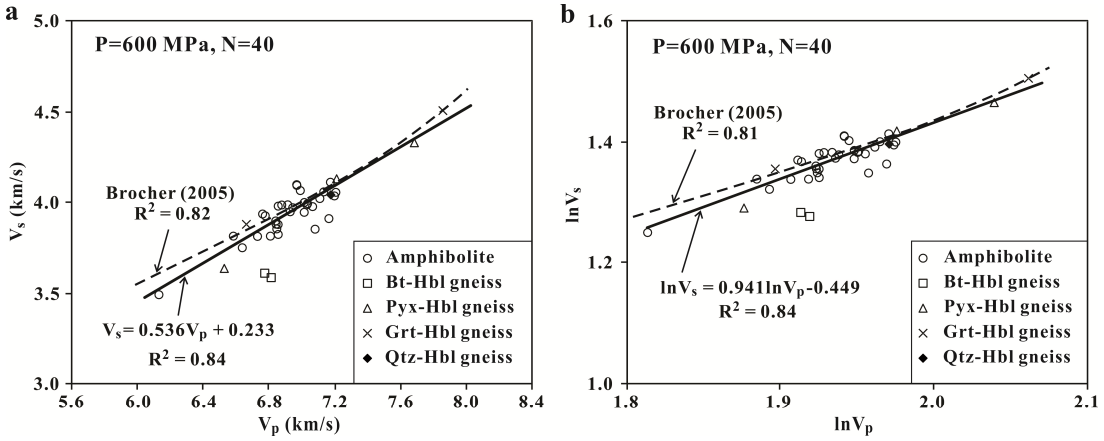


Figure 4.22 (a) V_s-V_p and (b) $\ln V_s$-$\ln V_p$ plots for 40 amphibole-rich rocks (9 from this chapter and 31 from the references) at 600 MPa. Predictions of the empirical equation (dashed curves) proposed by Brocher (2005) are also indicated.

From Figure 4.22b, we obtained $R_{s/p}$ =0.941. Here $R_{s/p}$ is a scaling factor which is defined as:

$$R_{s/p} = \frac{\partial V_s / V_s}{\partial V_p / V_p} = \frac{\partial \ln V_s}{\partial \ln V_p} \tag{4.5}$$

where $\partial V_s/V_s$ and $\partial V_p/V_p$ are the S- and P-wave velocity anomalies, respectively. For a given region, $R_{s/p}$ can be estimated from the P-wave travel time delay (∂t_p) and S-wave travel time delay (∂t_s) at a given depth: $R_{s/p} \approx (V_s/V_p)(\partial t_s/\partial t_p)$. The velocity heterogeneities in the Earth's interior, derived from seismic inversions, can be caused by variations in temperature, chemical composition, or phase transformation. As shown in Figure 4.23, $R_{s/p}$ varies with lithology: 0.567±0.175 for granite-granodiorite, 0.611±0.094 for felsic gneiss, 0.659±0.085 for diorite, 0.846±0.072 for eclogite, 0.926±0.084 for mafic gneiss, 0.941±0.069 for amphibolite and amphibole-rich rocks, 0.999±0.064 for gabbro-diabase, 1.285±0.064 for anorthosite, and 1.491±0.176 for peridotites. $R_{s/p}$ seems to increase globally with decreasing SiO_2 content from acidic to intermediate, through mafic to ultramafic rocks. $R_{s/p}$ is thus a potential diagnostic for the lithological composition of the continental crust and should be less ambiguous than the absolute values of the anomalies (e.g., Karato and Karki, 2001; Kennett et al., 1998). It is interesting to note that $R_{s/p}$ values for peridotite and eclogite are significantly different (Figure 4.23). A volumically important body of eclogite that was delaminated from the lowermost part of the thickened continental crust and had sunk into the upper mantle should be distinguishable from its surrounding peridotitic mantle in terms of its $R_{s/p}$. Otherwise, discrimination of eclogite from peridotite seems to be impossible using the absolute values of V_p or V_s.

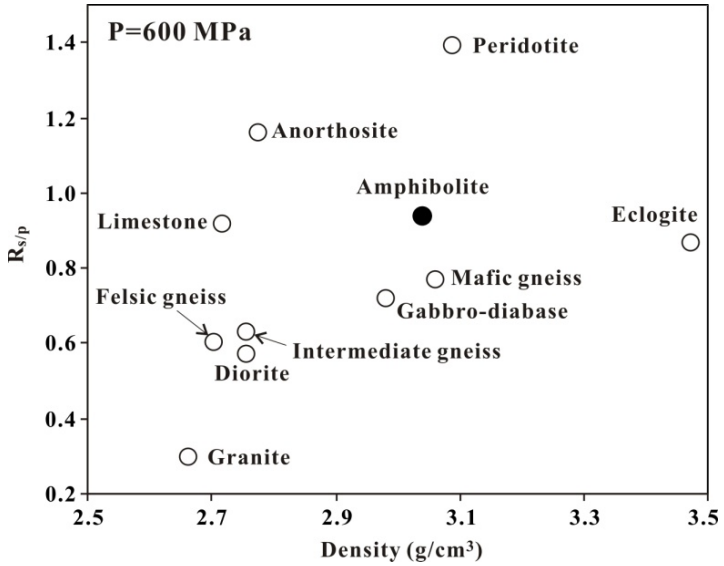


Figure 4.23 Variation of $R_{s/p}$ versus density (g/cm^3) for amphibolite and other categories of lithology at a hydrostatic pressure of 600 MPa.

4.5.5 Elastic moduli

The Lamé parameter (λ) and shear modulus (μ) form the most basic of all the intrinsic elastic properties of equivalent isotropic rocks (Goodway, 2001). The Lamé parameter, which relates stresses and strains in perpendicular directions, is closely related to incompressibility and contains a high proportion of information about the resistance to a change in volume caused by a change in pressure (Ji et al., 2010). Figure 4.24 illustrates the distribution of different lithologic categories in a μ-λ diagram built from the laboratory seismic data in the literature at 600 MPa. Amphibolite (32 samples) deviates clearly from eclogite (54 samples), peridotite (38 samples), low temperature (LT) serpentinite (lizardite and chrysotile, 29 samples), high temperature (HT) serpentinite (antigorite, 12 samples), anorthosite (8 samples), and felsic rocks (145 samples) such as granite, diorite, felsic gneiss, intermediate gneiss, and metasediments (Ji et al., 2010, 2013a). According to this μ-λ diagram, however, amphibolite is almost indistinguishable from the other mafic rocks (118 samples) such as gabbro, diabase, mafic gneiss, and mafic granulite. There is some overlapping between amphibolite and antigorite. Futhermore, the strong seismic reflectivity from middle to deep crustal sections with moderate refraction velocities (e.g., Ji et al., 1997; Ji and Long, 2006) may be due to the presence of amphibolite layers within the matrix of felsic rocks.

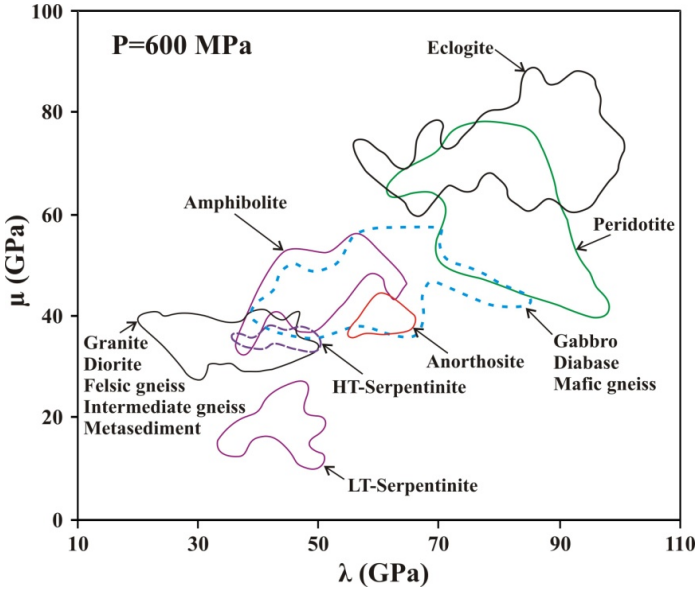


Figure 4.24 The μ-λ plots for amphibolite and other categories of lithology at a hydrostatic pressure of 600 MPa.

4.6 Conclusions

It is crucially important for constraining tectonic models of crustal evolution to determine the volume fraction of amphibole-rich rocks in the continental crust beneath different tectonic regions. Such information can be obtained almost only by comparing observed in situ seismic properties with those of amphibole-rich rock samples measured in laboratory. We have measured the P- and S-wave velocities, anisotropy, Poisson's ratios, and elastic moduli of 17 amphibole-rich rock samples containing 34-80 vol.% amphibole at room temperature and hydrostatic pressures up to 650 MPa. The results have been combined with previous experimental data from the literature to provide a systematic calibration for average density (3.013±0.090 g/cm^3), mean major element contents (wt.%) (49.50±4.05% SiO_2, 14.87±3.00% Al_2O_3, 11.33±3.13% FeO+Fe_2O_3, 9.78±2.16% CaO, 7.24±3.47% MgO, and 3.27±1.31% Na_2O+K_2O), mean P-wave velocity coefficients (V_0=6.733±0.274 km/s, D=3.342±1.855×10^{-4} km/s/MPa, B_0=0.951±0.701 km/s, and k=1.977±0.865×10^{-2} MPa^{-1}), mean S-wave velocity coefficients (V_0=3.851±0.201 km/s, D=1.549±0.791×10^{-4} km/s/MPa, B_0=0.535±0.366 km/s, and k=1.615±0.674×10^{-2} MPa^{-1}), P-wave velocity anisotropy (10.5±4.3% at 200 MPa, and 9.5±4.2% at 600 MPa), Poisson's ratios (0.260±0.012 at 600 MPa) or V_p/V_s=1.756±0.030, the logarithmic ratio $R_{s/p}$ (i.e., $\partial \ln V_s/\partial \ln V_p$=0.94±0.07), shear modulus (μ=46.97±4.40 GPa), bulk modulus (K=82.28±8.71 GPa), Young`s modulus (118.32±10.99 GPa), and Lamé coefficient (λ=50.97±6.57 GPa) of amphibole-rich rocks. The V_p values decrease with increasing SiO_2 and Na_2O+K_2O contents but increase with increasing MgO and CaO contents. The intrinsic shear-wave birefringence in the amphibole-rich rocks can be classified into four categories: Type A: $\Delta V_s(Y)>\Delta V_s(X)>\Delta V_s(Z)\approx 0$, Type B: $\Delta V_s(Y)>\Delta V_s(Z)>\Delta V_s(X)\approx 0$, Type C: $\Delta V_s(Y)>\Delta V_s(X)\approx\Delta V_s(Z)>0$, and Type D: $\Delta V_s(X)\approx\Delta V_s(Y)\gg\Delta V_s(Z)>0$. Type A is the most common with the maximum and minimum birefringence for the propagation directions parallel to Y and normal to foliation, respectively. The maximum birefringence can be as high as 0.38-0.40 km/s. The results provide a new calibration for the seismic properties of amphibole-rich rocks and make it possible to distinguish them from other lithologies such as granite, diorite, gabbro-diabase, felsic gneiss, intermediate gneiss, mafic gneiss, eclogite, and peridotite within the Earth's crust.

Measurements along seven key directions of an amphibolite with a particularly strong CPO (sample AM1) from the Gaoligong shear zone (Yunnan, China) suggest that the spatial

distribution of P-wave velocities can be represented by an ellipsoid whose longest, intermediate, and shortest axes are parallel to the X, Y, and Z axes of the strain ellipsoid, respectively. Thus, the P-wave velocity anisotropy of this amphibolite is approximately orthorhombic although it deformed in a nonaxial strain regime.

Although phyllosilicates (e.g., biotite and muscovite) may dominate the anisotropy of greenschist facies metamorphic rocks (Barruol and Mainprice, 1993b; Ji et al., 1993; Kern and Wenk, 1990; Mahan, 2006), amphibole plays a critical role in the formation of seismic anisotropy in the amphibole-rich deep crust which contains rather little mica. The presence of plagioclase, quartz, and clinopyroxene always diminishes the anisotropy induced by amphibole CPO in amphibolites. In the middle crust where amphibole and mica coexist, these minerals add their effects together through constructive interference of their own intrinsic anisotropies. EBSD analysis of six amphibolite samples showed the following characteristics: (1) The (100) poles of hornblende form a partial girdle perpendicular to the stretching lineation (X) with the maximum concentration at Z. (2) The [001] directions form a single maximum concentration parallel to X or a foliation-parallel girdle with a maximum concentration parallel to X. (3) The distribution of (010) poles is more complicated: a partial girdle perpendicular to X with the maximum concentration at Y or in the middle way between Y and Z, a partial girdle parallel to the foliation with the maximum concentration at Y, or a single concentration at Y. The above variations in hornblende CPO can explain the anisotropy patterns illustrated in the Flinn diagram of $V_p(X)/V_p(Y)$-$V_p(Y)/V_p(Z)$ plots. A weaker CPO of (010) in the Y direction will lower the $V_p(Y)$ value, making the $V_p(Y)/V_p(Z)$ ratio smaller and the $V_p(X)/V_p(Y)$ higher. In contrast, a stronger CPO of (010) in the Y direction will increase the $V_p(Y)$ value, making the $V_p(Y)/V_p(Z)$ ratio higher and the $V_p(X)/V_p(Y)$ smaller. Our data set allows for the future modelling of amphibolite facies metamorphic terranes using the results from active source seismic refraction/reflection experiments as well as passive seismological investigations.

CHAPTER 5 CONCLUSION AND FUTURE WORK

5.1 Concluding summary

So far, combined measurements by directing high frequency waves at oriented rock samples and calculations from the crystallographic preferred orientation (CPO) measurements of minerals in polished rock samples is the most powerful method to study seismic properties of rocks. This double approach has been employed throughout this dissertation, providing a good opportunity to understand the essential role of CPO in the formation of different anisotropy patterns.

Antigorite, which is a high temperature (HT) serpentine stable in subduction zones where temperature is above 300 °C, is believed to be responsible for anomalously low seismic velocities and high anisotropies in subducting oceanic slabs and forearc mantle wedges as well as suture zones between amalgamated continental lithospheric blocks. In Chapter 2, P- and S-wave velocities (V_p and V_s), anisotropy, shear-wave birefringence (ΔV_s), and V_p/V_s in 15 HT serpentinite samples have been measured at hydrostatic pressures up to 650 MPa. The high pressure experimental results combined with previous data (e.g., Christensen, 1978; Ji et al., 2013a; Kern et al., 1997) suggest that V_p anisotropy decreases but ΔV_s and V_p/V_s increase with increasing pressure in either cold or hot subduction zones. The variations in the seismic properties of antigorite serpentinites with increasing depth are caused by both the direction-dependent pressure and temperature derivatives of V_p and V_s. The experimental results, together with EBSD-measured CPOs, demonstrate the critical role of antigorite c-axis fabric, regardless of dislocation slip along [010], [100], or [hk0] within the (001) plane, in the formation of the different seismic anisotropy patterns for the serpentinites illustrated in Flinn diagrams. The antigorite c-axis fabric is believed to be controlled by the flow geometry (i.e., coaxial flattening, coaxial constriction, and simple shear), strain magnitude and the degree of dynamic recrystallization. This chapter confirms the conclusions obtained by Ji et al. (2013a): (1) Coaxial flattening aligns the c-axes of antigorite parallel to the Z direction, forming transversely isotropic rocks with $V_p(X) \approx V_p(Y) \gg V_p(Z)$, nearly equal shear-wave splitting in the X and Y directions but almost no splitting in the direction normal to foliation. (2) Coaxial constriction forms a nearly random distribution of antigorite c-axis in the YZ plane normal to the X direction, and thus $V_p(X) \gg V_p(Y) \approx V_p(Z)$ and shear-wave splitting is significantly larger along the Y direction than the X

direction. (3) Simple shear aligns the c-axes of antigorite preferentially parallel to the shear plane whose angle with the foliation (XY) plane progressively decreases with increasing shear strain, but cannot rotate the grains with their c-axes oriented initially parallel or subparallel to the Y direction. As a result, moderately sheared antigorite serpentinites display orthorhombic symmetry with $V_p(X)>V_p(Y)>V_p(Z)$ and large shear-wave splitting for raypaths in the foliation plane. The antigorite grains with c-axes parallel or subparallel to the Y direction may be eliminated by dynamic recrystallization, generating a c-axis fabric indiscernible from those formed by coaxial flattening. This finding provides a new explanation for various anisotropy patterns observed in subduction zones worldwide. For a cold, steeply subducting slab, antigorite is most likely deformed by nearly coaxial flattening or trench-parallel movements, forming trench-parallel seismic anisotropy with fast V_p and V_s parallel to the trench. For a hot, shallowly subducting slab, however, antigorite is most likely deformed by simple shear or transpression. Within the horizontal plane, the trench-normal P-wave velocity can be smaller, equal to, or larger than the trench-parallel velocity, depending on the subduction dip angle (θ). Trench-normal seismic anisotropy can be observed when $\theta<30°$. Interestingly, recent seismic data from the Tibetan Plateau such as strong heterogeneities in seismic velocity, attenuation and shear-wave splitting can be well explained by the presence of strongly deformed HT serpentinites in lithospheric shear zones reactivated along former suture zones between amalgamated blocks, hydrated zones of subducting lithospheric mantle, and the crust-mantle boundary if the temperature is below 700 °C in the region of interest.

Transverse isotropy (TI) or hexagonal symmetry in seismic wave is usually assumed to describe the elasticity of rock formations, thereby helpful to interpretations of seismic data. Statistical analysis of the 132 samples shows that the average bulk V_p anisotropy [A_p(B)] for chlorite schists, mica schists, phyllites, sillimanite-mica schists, and amphibole schists at 600 MPa is 12.0±4.1%, 12.8±5.6%, 12.8±9.0%, 17.0±4.9%, and 12.9±3.2%, respectively. These schists show much higher A_p(B) (13.2±6.0%) than other categories of metamorphic rocks such as granitic gneisses, felsic mylonites, granulites, and peridotites in which the constituent minerals have geometrically complex seismic responses that interfere destructively to produce either low anisotropy or nearly isotropic properties. The degree of anisotropy for the schists is a function of phyllosilicate content, CPO strength, and strain geometry. Most of the schist samples show some P-wave velocity anisotropy in the foliation plane [simply named foliation anisotropy, A_p(F)], indicating

that their seismic properties are orthorhombic rather than purely transversely isotropic. The average A_p(F), although much smaller than the A_p(B) at the same pressure, is 2.4±1.9% for phyllites, 3.3±2.7% for mica schists, 4.1±2.6% for chlorite schists, 6.8±3.4% for sillimanite-mica schists, and 5.2±1.9% for amphibole schists. The proportions of the 128 schist samples having A_p(F) values larger than 2%, 4%, 6%, 8%, and 10% are 67.2%, 37.5%, 20.3%, 10.2%, and 3.1%, respectively. These schists yield an average A_p(F) of 3.8±2.9%. In the schists studied, P-wave velocities along the foliation are always larger than in the Z direction. In situ seismic measurements from refracted rays with a substantial portion of their travel path in the foliation plane will systematically overestimate the average velocity of these rocks. Even in the foliation plane, seismic velocities can vary with propagating direction, with the maximum velocity parallel to X or Y. Assuming a TI pattern for all the schists, gneisses, and mylonites would systematically underestimate or overestimate the seismic velocities in the X (lineation) or Y direction. For the schists with purely TI seismic properties, it is impossible to determine the orientation of the lineation (transport direction) using seismic methods.

The departure of schists from TI seismic properties is dominated by the presence of non-phyllosilicate minerals (e.g., amphibole, sillimanite, and quartz). Amphibole, kyanite, and sillimanite generally developed strong CPOs with fast c-axes parallel to the lineation, which increases the velocity along the lineation (X) and causes the schists to switch from hexagonal to orthorhombic symmetry. Amphibole schists are characterized by orthorhombic anisotropy with $V_p(X)>V_p(Y)>V_p(Z)$, reflecting the CPO of amphibole with the [001] directions parallel to X while the (100) planes parallel or subparrallel to the foliation. The sillimanite-bearing mica schists display significant A_p(F) of up to 14% with an average value of 6.8%. The A_p(F) increases linearly with the content of sillimanite in the schists. Increasing feldspar generally reduces the bulk anisotropy caused by mica or quartz via the fast-axis of the former aligned parallel to the slow-axis of the latter. Quartz affects the symmetry of seismic anisotropy of schists in a complex manner, depending on both the volume fraction and the prevailing slip system of quartz. The latter is further controlled by deformation conditions (e.g., temperature, pressure, differential stress, strain rate, magnitude and geometry of strain, and H_2O content). Moreover, strain geometry may also influence the symmetry of seismic properties in schists. Coaxial flattening makes their (001) planes parallel to the foliation, forming a TI pattern characterized by $V_p(X)=V_p(Y)\gg V_p(Z)$ with the lowest P-wave velocities normal to the foliation. Coaxial

constriction forms a girdle distribution of phyllosilicate c-axis in the YZ plane perpendicular to the X direction, resulting in a TI pattern with $V_p(X) \gg V_p(Y)=V_p(Z)$. Simple shear may produce moderate and strong concentrations of phyllosilicate c-axes in the Z and Y directions in the YZ plane, respectively, causing an orthorhombic symmetry with $V_p(X)>V_p(Y)>V_p(Z)$.

However, most mica- or amphibole-bearing schists and mylonites approximate TI materials in terms of S-wave velocities and splitting although their P-wave properties may have weak orthorhombic symmetry. Our laboratory-measured and EBSD-based calculated seismic property data together with the analogue modeling experimental results help constrain the interpretation of shear-wave splitting and regional stress field data from the southeast Tibetan Plateau. The N-S to NW-SE polarized crustal anisotropy detected by Pms splitting in the Sibumasu and Indochina blocks is caused by subvertically foliated mica- and amphibole-bearing rocks such as schists, amphibolites, gneisses, and mylonites. In contrast, the fast polarization direction of vertically propagating SKS and SKKS phases (110±19°), which is approximately parallel to the absolute plate motion of the region, principally reflects seismic anisotropy caused by CPOs of olivine and pyroxenes and also possibly preferred orientation of vertically-aligned melt pockets, which are parallel to extensional shear bands (Kohlstedt and Zimmerman, 1996), in the hot flowing upper mantle (lithosphere and asthenosphere). The frozen fabrics of mica- and amphibole-bearing rocks within the crust of the Sibumasu and Indochina blocks, which formed by past ductile deformation (e.g., predominantly compressional folding and subordinately strike-slip shear), have been rotated 70-90° clockwise around the east Himalayan Syntaxis from initially E-W to present-day nearly N-S orientation in response to the progressive indentation of India into Asia. Furthermore, the crustal anisotropy indicated by the Pms splitting delay times as high as 0.58 s cannot be produced by gravity-driven horizontal channel flow of the lower crust, since the latter should result in a horizontal foliation where vertically incident shear-wave will be hardly split. It is also inferred that no finite eastward or southeastward extrusion of the Sibumasu and Indochina blocks has occurred during progressive indentation of India into Asia.

By comparing in situ observed seismic properties with those of amphibole-rich rock samples measured in laboratory, we can find out the volume fraction of amphibole-rich rocks in the continental crust beneath different tectonic regions, thereby providing constraint on tectonic models of crustal evolution. P- and S-wave velocities, anisotropy, Poisson's ratios, and elastic moduli were measured for 17 amphibole-rich rock samples containing 34-80 vol.% amphibole

at room temperature and hydrostatic pressures up to 650 MPa. The results have been combined with previous experimental data from the literature to provide a systematic calibration for density (3.013±0.090 g/cm^3), major element contents (wt.%) (49.50±4.05% SiO_2, 14.87±3.00% Al_2O_3, 11.33±3.13% FeO+Fe_2O_3, 9.78±2.16% CaO, 7.24±3.47% MgO, and 3.27±1.31% Na_2O+K_2O), mean P-wave velocity coefficients (V_0=6.733±0.274 km/s, D=3.342±1.855×10^{-4} km/s/MPa, B_0=0.951±0.701 km/s, and k=1.977±0.865×10^{-2} MPa^{-1}), mean S-wave velocity coefficients (V_0=3.851±0.201 km/s, D=1.549±0.791×10^{-4} km/s/MPa, B_0=0.535±0.366 km/s, and k=1.615±0.674×10^{-2} MPa^{-1}), P-wave velocity anisotropy (10.5±4.3% at 200 MPa, and 9.5±4.2% at 600 MPa), S-wave velocity anisotropy (8.8±2.8% at 200 MPa, and 8.5±2.9% at 600 MPa), Poisson's ratios (0.260±0.012 at 600 MPa) or V_p/V_s=1.756±0.030, the logarithmic ratio $R_{s/p}$ (i.e., $\partial \ln V_s/\partial \ln V_p$=0.94±0.07), shear modulus (μ=46.97±4.40 GPa) and Lamé coefficient (λ=50.97±6.57 GPa) of amphibole-rich rocks. The V_p values decrease with increasing SiO_2 and Na_2O+K_2O contents but increase with increasing MgO and CaO contents. The intrinsic shear-wave splitting (seismic birefringence) in the amphibole-rich rocks can be classified into four categories: Type A: $\Delta V_s(Y)>\Delta V_s(X)>\Delta V_s(Z)\approx 0$, Type B: $\Delta V_s(Y)>\Delta V_s(Z)>\Delta V_s(X)\approx 0$, Type C: $\Delta V_s(Y)>\Delta V_s(X)\approx\Delta V_s(Z)>0$, and Type D: $\Delta V_s(X)\approx\Delta V_s(Y)\gg\Delta V_s(Z)>0$. Type A is the most common with the maximum and minimum birefringence for the propagation directions parallel to Y and normal to foliation, respectively. The maximum birefringence can be as high as 0.38-0.40 km/s. The results provide a new calibration for the seismic properties of amphibole-rich rocks and make it possible to distinguish them from other lithologies such as granite, diorite, gabbro-diabase, felsic gneiss, intermediate gneiss, mafic gneiss, eclogite, and peridotite within the Earth's crust.

Measurements along seven key directions of an amphibolite with a particularly strong CPO (sample AM1) from the Gaoligong shear zone (Yunnan, China) suggest that the spatial distribution of P-wave velocities can be represented by an ellipsoid whose longest, intermediate, and shortest axes are parallel to the X, Y, and Z axes of the strain ellipsoid, respectively. Thus, the P-wave velocity anisotropy of this amphibolite is approximately orthorhombic although it deformed in a rotational strain regime.

It is found that amphibole plays a critical role in the formation of seismic anisotropy whereas the presence of plagioclase, quartz, and clinopyroxene always diminishes the anisotropy induced by amphibole CPO in amphibolites. EBSD measurements of 6 amphibolite samples showed the

following characteristics: (1) The (100) poles of hornblende form a partial girdle perpendicular to the stretching lineation (X) with the maximum concentration at Z. (2) The [001] directions form a single maximum concentration parallel to X or a foliation-parallel girdle with a maximum concentration parallel to X. (3) The distribution of (010) poles is more complicated: a partial girdle perpendicular to X with the maximum concentration at Y or in the middle way between Y and Z, a partial girdle parallel to the foliation with the maximum concentration at Y, or a single concentration at Y. The above variations in hornblende CPO can interpret the anisotropy patterns illustrated in the Flinn diagram of $V_p(X)/V_p(Y)$-$V_p(Y)/V_p(Z)$ plots. A weaker CPO of (010) at the Y direction will lower the $V_p(Y)$ value and then make the $V_p(Y)/V_p(Z)$ ratio smaller and the $V_p(X)/V_p(Y)$ higher. In contrast, a stronger CPO of (010) at the Y direction will increase the $V_p(Y)$ value and then make the $V_p(Y)/V_p(Z)$ ratio higher and the $V_p(X)/V_p(Y)$ smaller. Our data set allows for the future modelling of amphibolite-facies metamorphic terranes using the results from active source seismic refraction/reflection experiments as well as passive seismological investigations.

5.2 Future work

Thrusting shear of antigorite at the interface between the subducting slab and overlying mantle wedge generates non-coaxial deformation to cause c-axis and (001) plane aligned perpendicular to the foliation and parallel to the subducting direction, respectively (e.g., Hilairet et al., 2007; Katayama et al., 2009). The resultant CPO fabrics of antigorite have been proved to generate significant seismic anisotropy (Ji et al., 2013a; Katayama et al., 2009; Shao et al., 2014, Chapter 2) and permeability anisotropy (Kawano et al., 2011; Okazaki et al., 2013), and likely to affect slab-mantle coupling and thus seismicity (e.g., intermediate-depth earthquakes at depths of 60-300 km) in subduction zones. Hence, the objective of my future work is to improve our understanding of deformation behavior and tectonic significance of serpentine in subduction zones and oceanic lithosphere. Specifically, the proposed work should be focused on the following scientific problems.

(1) Origin of intermediate-depth earthquakes remains to be solved. Dehydration embrittlement, where fluid released from dehydration reactions causes brittle behavior within the dehydrating serpentinite itself, was proposed as a mechanism responsible for intermediate-depth earthquakes (Chollet et al., 2011; Dobson et al., 2002, 2004; Jung and Green, 2004; Jung et al., 2004, 2009;

Raleigh and Paterson, 1965; Xia, 2013). However, such a mechanism was challenged recently by the following studies. ① Stable fault slip and slow slip were observed (Chernak and Hirth, 2011); ② Weak correlation between the dehydration flux and seismicity rate was found at intermediate depths (Barcheck et al., 2012); ③ Dehydration embrittlement was thought to be invalid for generation of repeating seismicity in subduction zones (Prieto et al., 2012); ④ Stick-slip was considered to be responsible for intermediate-depth earthquake (Campione and Capitani, 2013), but their results cannot be extrapolated to subduction zones with confidence since their observations are performed during the experiments at room temperature and room pressure in the absence of fluid.

(2) How does the existent fabric affect the deformation behavior of antigorite in the subduction zones? Using atomic force microscopy, recently, Campione and Capitani (2013) revealed that antigorite single crystals possess strong frictional anisotropy on their basal slip surface: a- and b-axes are the high and low friction directions, respectively. Fault movements parallel to the preferred orientation of antigorite a-axis cause stick-slip behavior that generates earthquakes while those movements parallel to the preferred orientation of antigorite b-axis create aseismic stable sliding. However, this is opposite to the observations of Amiguet et al. (2014) for plastic deformation with easy glide along [100] and uneasy glide along [010]. Probably the opposite deformation behavior occurs in antigorite with A- and B-type CPOs, which are characterized by the dislocation slip using (001)[100] and (001)[010] systems, respectively.

(3) What is the effect of serpentinization degree on deformation of peridotite? Observations of both present seafloor and ancient seafloor obducted on land show that olivine alteration (e.g., serpentinization and carbonation) is an integrated part of the formation and evolution of the oceanic lithosphere. It is estimated that 10-30% of basement rocks found at crustal levels (depths<7 km below seafloor), which occur at slow and ultra-slow (<40 mm/year) spreading ridges, consist of serpentinized peridotite (Braga, 2014). Obviously, the serpentines contained in such peridotites are low temperature lizardite and chrysotile. Antigorite, however, is the dominant serpentine between 300-700 °C, and stable at pressures up to 5.0 GPa (Ulmer and Trommsdorff, 1995; Wunder and Schreyer, 1997), and thus records most of deformation history of a subduction zone. Different serpentine species have distinct mechanical properties (Reynard, 2013). So far, much work was performed to study mechanical properties of serpentine, but few refer to the

strength contrast between different species of serpentine and their protolith. For example, Escartin et al. (2001) found that lizardite/chrysotile dominates the strength of peridotite even if the volume fraction of lizardite/chrysotile is only ~10%. Recently, Hirauchi and Katayama (2013) observed that the viscosity contrast between lizardite/chrysotile and olivine is high ($\eta_{ol}/\eta_{liz/ctl}$=~10), indicating strong decoupling would occur between the low temperature serpentine layer and the overlying wedge. In contrast, a low viscosity contrast (η_{ol}/η_{atg}=~1-2) was observed between antigorite and olivine, suggesting that only weak decoupling would occur between the antigorite layer and the overlying wedge. The transition from strong-phase supported structure (SPSS) to weak-phase supported structure (WPSS) is considered to be critical phenomenon in the rheology of two-phase rocks (e.g., Ji and Xia, 2002) but is not investigated in detail for serpentinized peridotite, which certainly constrains the strength of oceanic lithosphere and geodynamics in subduction zones and have important implications on tectonic plate movement and fault activity.

(4) What is the effect of serpentinization on the transition from quartz to coesite? Serpentinite has a much lower density of ~2.6 g/cm^3 than peridotite with ~3.3 g/cm^3 in density, thus its formation can make serpentinized peridotite as buoyancy as continental crust and generate a huge volume expansion (~27%, O'Hanley, 1992) causing high to ultrahigh pressure within serpentinizing rocks, especially during exhumation since serpentine also has a huge compressibility of the c-axis under high pressures (e.g., Bezacier et al., 2013; Ji et al., 2013; Yang et al., 2014). Serpentine diapirs in subducted slabs or mantle wedges will form if sufficiently large volume is available for serpentine and flow up due to buoyancy, driving the exhumation of high- and ultrahigh-pressure (HP and UHP) metamorphic rocks (e.g., eclogite, Guillot et al., 2009; Pilchin, 2005). Indeed, the UHP eclogite usually contains coesite, a high pressure polymorph of quartz. I will use a high pressure high temperature apparatus (e.g., Piston-Cylinder apparatus) to investigate the probability of transition from quartz to coesite during serpentinization.

REFERENCES

A.S.M.E. (1953). Viscosity and density of over forty lubricating fluids of known composition at pressure to 150000 p.s.i. and temperatures to 425 °F. New York: *Amer. Soc. Mech. Engrs*.

Abers, G. A., Mackenzie, L. S., Rondenay, S., Zhang, Z., Wench, A. G., & Creager, K. C. (2009). Imaging the source region of Cascadia tremor and intermediate-depth earthquakes. *Geology, 37*, 1119-1122.

Akciz, S., Burchfiel, B. C., Crowley, J. L., Yin, J. Y., & Chen, L. Z. (2008). Geometry, kinematics, and regional significance of the Chong Shan shear zone, Eastern Himalayan Syntaxis, Yunnan, China. *Geosphere, 4*, 292-314, doi:10.1130/GES00111.1.

Aleksandrov, K. S., Alchikov, U. V., Belikov, B. P., Zaslavskii, B. I., & Krupnyi, A. I. (1974). Velocities of elastic waves in minerals at atmospheric pressure and increasing precision of elastic constants by means of EVM (in Russian). *Izv. Acad. Sci. USSR, Geol. Ser., 10*, 15-24.

Aleksandrov, K. S., & Ryzhova, T. V. (1961). The elastic properties of rock-forming minerals, II: layered silicates. Izvestiya of the Academy of Sciences USSR, Geophysics Series, 12, 186-189.

Amiguet, E., van de Moortele, B., Cordier, P., Hilairet, N., & Reynard, B. (2014). Deformation mechanisms and rheology of serpentines in experiments and in nature. *J. Geophys. Res., 119*, 4640-4655.

Anderson, D. L. (1961). Elastic wave propagation in layered anisotropic media. *J. Geophys. Res., 66*, 2953-2963.

Anderson, D. L. (1989). *Theory of the Earth*. Blackwell Sci., Cambridge, Massachusettes, 366 p.

Anderson, D. L., & Dziewonski, A. (1982). Upper mantle anisotropy: evidence from free oscillations. *Geophys. J. R. astr. Soc., 69*, 383-404.

Anderson, M., Zandt, G., Triep, E., Fouch, M., & Beck, S. (2004). Anisotropy and mantle flow in the Chile-Argentina subduction zone from shear wave splitting analysis. *Geophys. Res. Lett., 31*(23), L23608, doi:10.1029/2004GL020906.

Ando, J.-I., Urata, Y., Yamamoto, T., & Soda, Y. (2013). Strength of foliated antigorite serpentinite. Japan Geoscience Union Meeting, SCG07-P01.

Andreani, M., Boullier, A. M., & Gratier J. P. (2005). Development of schistosity by dissolution-crystallization in a Californian serpentinite gouge. *J. Struct. Geol., 27*, 2256-2267.

Anovitz, L. M., & Essene, E. J. (1990). Thermobarometry and pressure-temperature paths in the Grenville Province of Ontario. *J. Petrol., 31*, 197-241.

Arculus, R. J. (1981). Island arc magmatism in relation to the evolution of the crust and mantle. *Tectonophysics, 75*(1-2), 113-133.

Audet, P., Bostock, M. G., Christensen, N. I., & Peacock, S. M. (2009). Seismic evidence for overpressured subducted oceanic crust and megathrust fault sealing. *Nature, 457*, 76-78.

Auzende, A.-L., Guillot, S., Devouard, B., & Baronnet, A. (2006). Serpentinites in an Alpine convergent setting: effects of metamorphic grade and deformation on microstructures. *Eur. J.*

Mineral., 18, 21-33.

Avouac, J.-P., & Tapponnier, P. (1993). Kinematic model of active deformation in central Asia. *Geophys. Res. Lett., 20*, 895-898.

Babuška, V., Montagner, J. P., Plomerova, J., & Girardin, N. (1998). Age-dependent large-scale fabric of the mantle lithosphere as derived from surface-wave velocity anisotropy. *Pure Appl. Geophys., 151*, 257-280.

Babuška, V., & Plomerova, J. (2001). Subcrustal lithosphere around the Saxothuringian –Moldanubian Suture Zone – a model derived from anisotropy of seismic wave velocities. *Tectonophysics, 332*, 185-199.

Babuška, V., Plomerova, J., & Sileny, J. (1993). Models of seismic anisotropy in the deep continental lithosphere. *Phys. Earth Planet. Inter., 78*, 167-191.

Babuška, V., & Pros, Z. (1984). Velocity anisotropy in an granodiorite and quartzite due to the distribution of microcracks. *Geophys. J. R. Astr. Soc., 76*, 121-127.

Backus, G. E. (1962). Long-wave elastic anisotropy produced by horizontal layering. *J. Geophys. Res., 67*, 4427-4440.

Backus, G. E. (1965). Possible forms of seismic anisotropy of the uppermost mantle under oceans. *J. Geophys. Res., 70*, 3429-3439.

Bai, D., Unsworth, M. J., Meju, M. A., Ma, X. B., Teng, J. W., Kong, X. R., Sun, Y., Sun, J., Wang, L. F., Jiang, C. S., Zhao, C. Q., Xiao, P. F., & Liu, M. (2010). Crustal deformation of the eastern Tibetan plateau revealed by magnetotelluric imaging. *Nat. Geosci., 3*, 358-362, doi:10.1038/ngeo830.

Baldwin, J. A., Bowring, S. A., Williams, M. L., & Williams, I. S. (2004). Eclogites of the Snowbird tectonic zone: petrological and U-Pb geochronological evidence for Paleoproterozoic high-pressure metamorphism in the western Canadian Shield. *Contrib. Mineral. Petrol., 147*, 528-548.

Bamford, D. (1977). Pn velocity anisotropy in a continental upper mantle. *Geophys. J. R. Astr. Soc., 49*, 29-48.

Banfield, J. F., Bailey, S. W., Barker, W. W., & Smith, R. C. (1995). Complex polytypism: relationships between serpentine structural characteristics and deformation. *Am. Mineral., 80*, 1116-1131.

Barazangi, M., & Ni, J. (1982). Velocities and propagation characteristics of Pn and Sn waves beneath the Himalayan Arc and Tibetan Plateau: Possible evidence for underthrusting of India continental lithosphere beneath Tibet. *Geology, 10*, 179-185.

Barberini, V., Burlini, L., & Zappone, A. (2007). Elastic properties, fabric and seismic anisotropy of amphibolites and their contribution to the lower crust reflectivity. *Tectonophysics, 445*, 227-244.

Barcheck, C. G., Wiens, D. A., van Keken, P. E., & Hacker, B. R. (2012). The relationship of intermediate- and deep-focus seismicity to the hydration and dehydration of subducting slabs. *Earth Planet. Sci. Lett., 349*, 153-160.

Barruol, G. (1993). *Pétrophysique de la croûte inférieure. Rôle de l'anisotropie sismique sur la réflectivité et le déphasage des ondes S*. Ph.D. thesis. 239-258 pp., Université de Montpellier II, France.

Barruol, G., & Granet, M. (2002). A Tertiary asthenospheric flow beneath the southern French Massif Central indicated by upper mantle seismic anisotropy and related to the west Mediterranean extension. *Earth Planet. Sci. Lett., 202*, 31-47.

Barruol, G., & Kern H. (1996). Seismic anisotropy and shear-wave splitting in lower-crustal and upper-mantle rocks from the Ivrea Zone−Experimental and calculated data. *Phys. Earth Planet. Inter., 95*, 175-194.

Barruol, G., & Mainprice, D. (1993a). 3-D seismic velocities calculated from lattice-preferred orientation and reflectivity of a lower crustal section: examples of the Val Sesia section (Ivrea zone, northern Italy). *Geophys. J. Int., 115*, 1169-1188.

Barruol, G., & Mainprice D. (1993b). A quantitative evaluation of the contribution of crustal rocks to the shear-wave splitting of teleseismic SKS waves. *Phys. Earth Planet. Inter., 78*, 281-300.

Barruol, G., Mainprice, D., Kern, H., De Saint Blanquat, M., & Compte P. (1992). 3D seismic study of a ductile shear zone from laboratory and p etrofabric data (Saint Barthélémy Massif, Northern Pyrénées, France). *Terra Nova, 4*, 63-76.

Barruol, G., Silver, P. G., & Vauchez, A. (1997). Seismic anisotropy in the eastern US: deep structure of a complex continental plate. *J. Geophys. Res., 102*, 8329-8348.

Barruol, G., Souriau, A., Vauchez, A., Diaz, J., Gallart, J., Tubia, J., & Cuevas, J. (1998). Lithospheric anisotropy beneath the Pyrenees from shear wave splitting. *J. Geophys. Res., 103*, 30039-30053.

Becker, T. W., Kustowski, B., & Ekstrom, G. (2008). Radial seismic anisotropy as a constraint for upper mantle rheology. *Earth Planet. Sci. Lett., 267*, 213-227.

Beghein, C., Trampert, J., van Heijst, H. J. (2006). Radial anisotropy in seismic reference models of the mantle. *J. Geophys. Res., 111*, B02303, doi:10.1029/2005JB003728.

Bellefleur, G., de Kemp, E., Goutier, J., Allard, M., & Adam, E. (2014). Seismic imaging of the geologic framework and structures related to volcanogenic massive sulfide deposits in the Archean Rouyn-Noranda district, Quebec, Canada. *Economic Geology, 109*, 103-119.

Berryman, J. G. (1979). Long-wave elastic anisotropy in transversely isotropic media. *Geophysics, 44*, 896-917.

Berryman, J. G. (1995). Mixture theories for rock properties. In T. J. Ahrens (ed.), *Rock Physics and Phase Relations: A Handbook of Physics Constants* (pp. 205-228). AGU, Washington, D.C., USA.

Bezacier, L., Reynard, B., Bass, J. D., Sanchez-Valle, C., & Van de Moortèle, B. (2010). Elasticity of antigorite, seismic detection of serpentinites, and anisotropy in subduction zones. *Earth Planet. Sci. Lett., 289,* 198-208.

Bezacier, L., Reynard, B., Cardon, H., Montagnac, G., & Bass, J. D. (2013). High-pressure elasticity of serpentine and seismic properties of the hydrated mantle wedge. *J. Geophys. Res. 118*, 527-535, doi:10.1002/jgrb.50076.

Bhagat, S., Bass, J. D., & Smyth, J. (1992). Single-crystal elastic properties of omphacite-C2/c by Brillouin spectroscopy. *J. Geophys. Res., 97*, 6843-6848.

Biermann, C., & Van Roermund, H. L. M. (1983). Defect structures in naturally deformed clinoamphibole-A TEM study. *Tectonophysics, 95*, 267-278.

Birch, F. (1960). The velocity of compressional waves in rocks to 10 kilobars, Part 1. *J. Geophys. Res., 65*, 1083-1102.

Birch, F. (1961). The velocity of compressional waves in rocks to 10 kilobars, Part 2. *J. Geophys. Res., 66*, 2199-2224.

Bokelmann, G. H. R., & Harjes, H. P. (2000). Evidence for temporal variation of seismic velocity within the upper continental crust. *J. Geophys. Res., 105*, 23879-23894.

Bostock, M. G., & Christensen N. I. (2012). Split from slip and schist: Crustal anisotropy beneath northern Cascadia from non-volcanic tremor. *J. Geophys. Res., 117*, B08303, doi:10.1029/2011JB009095.

Bostock, B. C., Hyndman, R. D., Rondenay, S., & Peacock S. M. (2002). An inverted continental Moho and the serpentinization of the forearc mantle. *Nature, 417,* 536-538.

Boudier, F., Baronnet, A., & Mainprice, D. (2010). Serpentine mineral replacements of natural olivine and their seismic implications: Oceanic lizardite versus subduction-related antigorite. *J. Petrol., 51,* 495-512.

Braga, T. (2014). *Analyzing the Effect of Olivine Mineralization on the Strength of the Oceanic Lithosphere*. Senior thesis, 30 p., University of Maryland, MD., USA.

Brocher, T. M. (2005). Empirical relations between elastic wave speeds and density in the Earth's crust. *Bull. Seismol. Soc. Am., 95*(6), 2081-2092, doi:10.1758/0120050077.

Brocher, T. M., & Christensen, N. I. (1990). Seismic anisotropy due to preferred mineral orientation observed in shallow crustal rocks in southern Alaska. *Geology, 18*, 737-740.

Brocher, T. M., Nokleberg, W. J., Christensen, N. I., Lutter, W. J., Geist, E. L., & Fisher, M. A. (1991). Seismic reflection/refraction mapping of faulting and regional dips in the Eastern Alaska Range. *J. Geophys. Res., 96*, 10233-10249.

Brocher, T. M., Parsons, T., Tréhu, A. M., Snelson, C. M., & Fisher, M. A. (2003). Seismic evidence for widespread serpentinized forearc upper mantle along the Cascadia margin. *Geology, 31,* 267-270.

Bromiley, G. D., & Pawley, A. R. (2003). The stability of antigorite in the systems MgO-SiO_2-H_2O (MSH) and MgO-Al_2O_3-SiO_2-H_2O (MASH): The effects of Al^{3+} substitution on high-pressure stability. *Am. Mineral., 88,* 99-108.

Browaeys, T. J., & Chevrot, S. (2004). Decomposition of the elastic tensor and geophysical applications. *Geophys. J. Int., 159*, 667–678, doi:10.1111/j.1365-246X.2004.02415.x.

Brownlee, S. J., Hacker, B. R., Harlow, G. E., & Seward, G. (2013). Seismic signatures of a hydrated mantle wedge from antigorite crystal-preferred orientation (CPO). *Earth Planet. Sci. Lett., 375*, 395-407, doi:10.1016j.epsl.2013.06.003

Brownlee, S. J., Hacker, B. R., Salisbury, M., Seward, G., Little, T. A., Baldwin, S. L., & Abers G. A. (2011). Predicted velocity and density structure of the exhuming Papua New Guinea ultrahigh-pressure terrane. *J. Geophys. Res., 116*, B08206, doi:10.1029/2011JB008195.

Brun, J. P., Brug, J. P., & Chen, G. M. (1985). Strain trajectories above the Main Central Trust (Himalaya) in southern Tibet. *Nature, 313*, 388-391.

Burke, M. M. (1991). *Reflectivity of highly deformed terranes based on laboratory and in situ velocity measurements from the Grenville front tectonic zone, central Ontario, Canada*. PhD. Thesis. 46-50 pp., Dalhousie University.

Burke, M. M., & Fountain, D. M. (1990). Seismic properties of rocks from an exposure of extended continental crust - new laboratory measurements from the Ivrea zone. *Tectonophysics, 182*, 119-146.

Burlini, L., & Fountain, D. M. (1993). Seismic anisotropy of metapelites from the Ivrea-Verbano zone and Serie dei Laghi (northern Italy). *Phys. Earth Planet. Inter., 78*, 301-317.

Buttles, J., & Olson, P. (1998). A laboratory model of subduction zone anisotropy. *Earth Planet. Sci. Lett., 164*, 245-262.

Byun, B. S. (1984). Seismic parameters for transversely isotropic media. *Geophysics, 49*, 1908-1914.

Capitani, G. C., & Mellini, M. (2004). The modulated crystal structure of antigorite: the m=17 polysome. *Am. Mineral., 89*, 147-158.

Carbonell, R., Levander, A., & Kind, R. (2013). The Mohorovicic discontinuity beneath the continental crust: An overview of seismic constraints. *Tectonophysics, 609*, 353-376.

Carlson, R. L., & Miller, D. J. (2003). Mantle wedge water contents estimated from seismic velocities in partially serpentinized peridotites. *Geophys. Res. Lett.*, *30,* 1250, doi: 10.1029/2002GL016600.

Carter, N. L., Baker, D. W., & George, R. P. J. (1972). Seismic anisotropy, flow, and constitution of the upper mantle, in Flow and Fracture of Rocks, edited by H. C. Heard, I. Y. Borg, N. L. Carter, & C. B. Raleigh. *Geophysical Monograph, 16*, 167-190, AGU, Washington, D. C.

Chang, L. J., Wang, C. Y., & Ding, Z. F. (2006). A study on SKS splitting beneath the Yunnan region, southwestern China. *Chin. J. Geophys., 49*, 167-175.

Cheadle, S. P., Brown, R. J., & Lawton, D. C. (1991). Orthorhombic anisotropy: a physical seismic modeling study. *Geophysics, 56*, 1603-1613.

Chen W. P., Martin, M., Tseng, T. L., Nowack, R. L., Hung, S. H., & Huang, B. S. (2010). Shear-wave birefringence and current configuration of converging lithosphere under Tibet. *Earth Planet. Sci. Lett., 295*: 297-304.

Chen, W. P. & Özalaybey, S. (1998). Correlation between seismic anisotropy and Bouguer gravity anomalies in Tibet and its implications for lithospheric structures. *Geophys. J. Int., 135*, 93-101.

Chen, Y., Badal, J., & Zhang, Z. J. (2009). Radial anisotropy in the crust and upper mantle beneath the Qinghai-Tibet plateau and surrounding regions. *J. Asian Earth Sci., 36*, 289-302.

Chen, Y., Zhang, Z. J., Sun, C. Q., & Badal J. (2013). Crustal anisotropy from Moho converted Ps wave splitting analysis and geodynamic implications beneath the eastern margin of Tibet and surrounding regions. *Gondwana Research, 24*, 946-957.

Chen, Z., Burchfiel, B. C., Liu, Y., King, R. W., Royden, L. H., Tang, W., Wang, E., Zhao, J., & Zhang X. (2000), Global Positioning System measurements from eastern Tibet and their implications for India/Eurasia intercontinental deformation. *J. Geophys. Res., 105*, 16215-16227.

Chevrot, S., & van der Hilst, R. D. (2000). The Poisson ratio of the Australian crust: geological and geophysical implications. *Earth Planet. Sci. Lett., 183*(1-2), 121-132.

Cholach, P. Y. (2005). *The Elasticity of Intrinsically Anisotropic Rocks*. Ph.D. thesis, 153 p., University of Alberta, Alberta, Canada.

Cholach, P. Y., Molyneux, J. B., & Schmitt, D. R. (2005). Flin Flon Belt seismic anisotropy: elastic symmetry, heterogeneity, and shear-wave splitting. *Can. J. Earth Sci., 42*, 533-554.

Cholach, P. Y., & Schmitt, D. R. (2006). Intrinsic elasticity of a textured transversely isotropic muscovite aggregate: Comparisons to the seismic anisotropy of schists and shales. *J. Geophys. Res., 111*, B09410, doi:10.1029/2005JB004158.

Chollet, M., Daniel, I., Koga, K. T., Morard, G., van de Moortele, B. (2011). Kinetics and mechanism of antigorite dehydration: Implications for subduction zone seismicity. *J. Geophys. Res., 116*, B04203, doi:10.1029/2010JB007739.

Christensen, N. I. (1965). Compressional wave velocities in metamorphic rocks at pressures to 10 kilobars. *J. Geophys. Res., 70*, 6147-6164.

Christensen, N. I. (1966). Shear wave velocities in metamorphic rocks at pressures to 10 kilobars. *J. Geophys. Res., 74*, 3549-3556.

Christensen, N. I. (1972). The abundance of serpentinites in the oceanic crust. *J. Geol., 80,* 709-719.

Christensen, N. I. (1974). Compressional wave velocities in possible mantle rocks to pressures of 30 kilobars. *J. Geophys. Res., 79*, 407-412.

Christensen, N. I. (1978). Ophiolites, seismic velocities, and oceanic crustal structure. *Tectonophysics, 47,* 131-157.

Christensen, N. I. (1984). The magnitude, symmetry and origin of upper mantle anisotropy based on fabric analyses of ultramafic tectonites. *Geophys. J. R. Astr. Soc., 76*, 89-111.

Christensen, N. I. (1985). Measurement of dynamic properties of rock at elevated temperatures and pressures, In ASTM STP 869. American Society of Testing and Materials, Philadelphia, 93-107.

Christensen, N. I. (1989). Seismic velocities. In P*ractical Handbook of Physical Properties of Rocks and Minerals*. R. S. Carmichael (ed.). Boca Raton, Florida, US, CRC Press Inc. 429-546 p.

Christensen, N. I. (1996). Poisson's ratio and crustal seismology. *J. Geophys. Res., 101,* 3139-3156.

Christensen, N. I. (2004). Serpentine, peridotites and seismology. *Int. Geol. Rev., 46,* 795-816.

Christensen, N. I., & Crosson, R. (1968). Seismic anisotropy in the upper mantle. *Tectonophysics, 6*, 63-107.

Christensen, N. L., Medaris, L. G., Wang, H. F., & Jelinek, E. (2001). Depth variation of seismic anisotropy and petrology in central European lithosphere: A tectonothermal synthesis from spinel lherzolite. *J. Geophys. Res., 106*, 645-664.

Christensen, N. I., & Mooney, W. D. (1995). Seismic velocity structure and composition of the continental crust: A global view. *J. Geophys. Res., 100*(B7), 9761-9788.

Christensen, N. I., & Okaya, D. A. (2007). Compressional and shear wave velocities in South Island, New Zealand rocks and their applications to the interpretation of seismological models of the New Zealand crust, A Continental Plate Boundary: Tectonics at South Island. New Zealand Geophysical Monograph Series, 175, American Geophysical Union, 123-155, doi:10.1029/175GM08.

Christensen, N. I., & Ramananantoandro, R. (1971). Elastic moduli and anisotropy of dunite to 10 kilobars. *J. Geophys. Res., 76*, 4003-4010.

Christensen, N. I., & Salisbury, M. H. (1975). Structure and constitution of the lower oceanic crust. *Rev.Geophys. Space Phys., 13*, 58-86.

Christensen, N. I., & Salisbury, M. H. (1979). Seismic anisotropy in the oceanic upper mantle: evidence from the Bay of Islands Ophiolite Complex. *J. Geophys. Res., 84*, 4601-4610.

Christoffersen, R., & Kronenberg, A. K. (1993). Dislocation interactions in experimentally deformed biotite. *J. Struct. Geol., 15*, 1077-1095.

Clark, M. K., & Royden, L. H. (2000). Topographic ooze: building the eastern margin of Tibet by lower crustal flow. *Geology, 28*, 703-706.

Cohen, S., & Morgan, R. C. (1987). Propagating and quasi-static compressional straining in continental collisions. *Tectonophysics, 142*, 155-162.

Condie, K. C. (1997). Contrasting sources for upper and lower continental crust: the greenstone connection. *J. Geol., 105*, 729-736.

Cook, F. A., van der Velden, A. J., & Hall, K. W. (1999). Frozen subduction in Canada's Northwest Territories: Lithoprobe deep lithospheric reflection profiling of the western Canadian Shield. *Tectonics, 18*, 1-24.

Cossette, E., Schneider, D. A., Audet, P., Graseman, B., & Habler, G. (2015). Seismic properties and mineral crystallographic preferred orientations from EBSD data: Results from a crustal-scale detachment system, Aegean region. *Tectonophysics, 651*, 66-78.

Crampin, S. (1991). Effects of point singularities on shear wave propagation in sedimentary basins. *Geophys. J. Int., 107*, 531-543.

Crampin, S., & Atkinson, B. K. (1985). Microcracks in the Earth's crust. *First Break, 3*, 16-20.

Crampin, S., & Peacock, S. (2005). A review of shear-wave splitting in the compliant crack-critical anisotropic Earth. *Wave Motion, 41*, 59-77.

Crampin, S., & Peacock, S. (2008). A review of the current understanding of seismic shear-wave splitting in the Earth's crust and common fallacies in interpretation. *Wave Motion, 45*, 675-722.

Culshaw, N. G., Ketchum, J. W. F., Wodicka, N., & Wallace, P. (1994). Deep crustal ductile extension following thrusting in the southwestern Grenville Province, Ontario. *Can. J. Earth Sci., 31*, 160-175.

Cumbest, R. J., van Roermund, H. L. M., Drury, M. R., & Simpson, C. (1989). Burgers vector determination in clinoamphibole by computer simulation. *Am. Mineral., 74*:586–592

Currie, C. A., Cassidy, J. F., Hyndman, R. D., & Bostock, M. G. (2004). Shear wave anisotropy beneath the Cascadia subduction zone and western North American craton. *Geophys. J. Int., 157,* 341-353.

Daley, P. F., & Hron, F. (1977). Reflection and transmission coeffitients for transversely isotropic media. *Bull. Seism. Soc. Am., 67*, 661-675.

Deer, W. A., Howie, R. A., & Zussman, J. (1992). An introduction to the rock-forming minerals, 2nd edition. Longman Scientific and Technical, Harlow, Esses, UK, 696 pp.

DeMets, C., Gordon, R. G., Argus, D. F., & Stein, S. (1994). Effect of recent revisions to the geomagnetic reversal time scale on estimates of current plate motions. *Geophys. Res. Lett., 21*, 2191-2194.

Dempsey, E. D., Prior, D. J., Mariani, E., Toy, V. G., & Tatham, D. J. (2011). Mica-controlled anisotropy within mid-to-upper crustal mylonites: an EBSD study of mica fabrics in the Alpine Fault Zone, New Zealand. *Geol. Soc. London Spec. Publ., 360*, 33-47.

DeShon, H. R., & Schwartz, S. Y. (2004). Evidence for serpentinization of the forearc mantle wedge along the Nicoya Peninsula, Costa Rica. *Geophys. Res. Lett., 31*(21), L21611, doi:10.1029/2004GL021179.

Dewandel, B., Boudier, F., Kern, H., Warsi, W. K., & Mainprice, D. (2003). Seismic wave velocity and anisotropy of serpentinized peridotite in the Oman ophiolite. *Tectonophysics, 370,* 77-94.

Dewey, J. F., Cande, S., & Pitman III, W. C. (1989). Tectonic evolution of the India/Eurasia collision zone. *Eclogae Geol. Helv., 82*, 717-734.

Díaz Azpiroz, M., Lloyd, G. E., & Fernández, C. (2007). Development of lattice preferred orientation in clinoamphiboles deformed under low-pressure metamorphic conditions — A SEM/EBSD study of metabasites from the Aracena metamorphic belt (SW Spain). *J. Struct. Geol., 29*, 629-645.

Dollinger, G., & Blacic, J. D. (1975). Deformation mechanisms in experimentally and naturally deformed amphiboles. *Earth Planet. Sci. Lett., 26* (3), 409-416.

Dobson, D. P., Meredith, P. G., & Boon, S. A. (2002). Simulation of subduction zone seismicity by dehydration of serpentine. *Science, 298*, 1407-1410.

Dobson, D. P., Meredith, P. G., & Boon, S. A. (2004). Detection and analysis of microseismicity in multi anvil experiments. *Phys. Earth Planet. Inter., 143*, 337-346.

Dong, Y. J., Xue, G. Q., Ma, K. Y., & Jiang, M. (1999). Studies on shear wave anisotropy beneath Altyn fault system and its adjacent area. *Progress in Geophys., 14*, 58-65.

Duret, F., Shapiro, N. M., Cao, Z., Levin, V., Molnar, P., & Roecker, S. (2010). Surface wave dispersion across Tibet: direct evidence for radial anisotropy in the crust. *Geophys. Res. Lett.,*

37, L16306, doi:10.1029/2010GL043811.

Dziewonski, A. M., & Anderson, D. L. (1981). Preliminary reference Earth model. *Phys. Earth Planet. Inter., 25*, 297-356.

Ekstrom, G., & Dziewonski, A. M. (1998). The unique anisotropy in the Pacific upper mantle. *Nature, 394*, 168-172.

Elliott, J. R., Walters, R. J., England, P. C., Jackson, J. A., Li, Z., & Parsons, B. (2010). Extension on the Tibetan plateau: recent normal faulting measured by InSAR and body wave seismology. *Geophys. J. Int., 183*, 503-555.

England, P., & Houseman, G. (1989). Extension during continental convergence, with application to the Tibetan Plateau. *J. Geophys. Res., 94*, 17561-17579.

Erdman, M. E., Hacker, B. R., Zandt, G., & Seward, G. (2013). Seismic anisotropy of the crust: electron-backscatter diffraction measurements from the Basin and Range. *Geophys. J. Int*., 1-19, doi:10.1093/gji/ggt287.

Escartín, J., Hirth, G., & Evans B. (1997). Nondilatant brittle deformation of serpentinites: Implications for Mohr-Coulomb theory and the strength of faults. *J. Geophys. Res.*, *102*(B2), 2897-2913, doi:10.1029/96JB02792.

Escartín, J., Hirth, G., & Evans B. (2001). Strength of slightly serpentinized peridotites: implications for the tectonics of oceanic lithosphere. *Geology, 29*(11), 1023-1026.

Evans, B. W. (2004). The serpentinite multisystem revisited: chrysotile is metastable. *Inter. Geol. Rev.*, *46,* 479-506.

Faccenda, M., Burlini, L., Gerya, T. V., & Mainprice, D. (2008). Fault-induced seismic anisotropy by hydration in subducting oceanic plates. *Nature, 455,* 1097-1100, doi:10.1038/nature07376.

Fliedner, M. M., & Klemperer, S. L. (2000). Crustal structure transition from oceanic arc to continental arc, eastern Aleutian Islands and Alaska Peninsula. *Earth Planet. Sci. Lett., 179*, 567-579.

Flowers, R. M., Bowring, S. A., & Williams, M. L. (2006). Timescales and significance of high-pressure, high-temperature metamorphism and mafic dike anatexis, Snowbird tectonic zone, Canada. *Contrib. Mineral. Petrol., 151*, 558-581.

Foley, S., Tiepolo, M., & Vannucci, R. (2002). Growth of early continental crust controlled by melting of amphibolites in subduction zones. *Nature, 147*, 837-840.

Fountain, D. M. (1976). The Ivrea-Verbano and Strona-Ceneri zones, northern Italy: a cross section of the continental crust - new evidence from seismic velocities of rock samples. *Tectonophysics, 33*, 145-165.

Fountain, D. M., Hurich, C. A., & Smithson, S. B. (1984). Seismic reflectivity of mylonite zones in the crust. *Geology, 12*, 195-198.

Fountain, D. M., & Salisbury, M. H. (1996). Seismic properties of rock samples from the Pikwitonei granulite belt – God's Lake domain crustal cross section, Manitoba. *Can. J. Earth Sci., 33*, 757-768.

Fountain, D. M., Salisbury, M. H., & Percival, J. (1990). Seismic structure of the continental crust based on rock velocity measurements from the Kapuskasing uplift. *J. Geophys. Res., 95*, 1167-1186.

Frederiksen, A. W., Folsom, H., & Zandt, G. (2003). Neighbourhood inversion of teleseismic Ps conversions for anisotropy and layer dip. *Geophys. J. Int., 155*, 200-212.

Frohlich, C. (2006). Deep earthquakes. Cambridge University Press, Cambridge, United Kingdom, 574p.

Fu, Y. Y. V., Chen, Y. J., Li, A. B., Zhou, S. Y., Liang, X. F., Ye, G. Y., Jin, G., Jiang, M. M., & Ning, J. Y. (2008). Indian mantle corner flow at southern Tibet revealed by shear wave splitting measurements. *Geophys. Res. Lett., 35*, L02308, doi:10.1029/2007GL031753.

Fuchs, K. (1977). Seismic anisotropy of the subcontinental lithosphere as evidence for dynamic processes in the upper mantle. *Geophys. J. R. Astr. Soc., 49*, 167-179.

Fuis, G. S., Ambos, E. L., Mooney, W. D., Christensen, N. I., & Geist, E. (1991). Crustal structure of accreted terranes in southern Alaska, Chugach Mountains and Copper River basin, from seismic refraction results. *J. Geophys. Res., 96*, 4187-4227.

Gan, W.J., Zhang, P.Z., Shen, Z. K., Niu, Z., Wang, M., Wan, Y., Zhou, D., & Cheng, J. (2007), Present-day crustal motion within the Tibetan Plateau inferred from GPS measurements. *J. Geophys. Res., 112*, B08416, doi:10.1029/2005JB004120.

Gao, Y., & Crampin, S. (2004). Observations of stress relaxation before earthquakes. *Geophys. J. Int., 157*, 578-582.

Gao, S. S., & Liu K. H. (2009). Significant seismic anisotropy beneath the southern Lhasa Terrane, Tibetan Plateau. *Geochem. Geophys. Geosyst., 10*, Q02008, doi: 10.1029/2008GC002227.

Gercek, H. (2007). Poisson's ratio values for rocks. *International Journal of Rock Mechanics and Mining Sciences, 44*, 1-13.

Godfrey, N. J., Christensen, N. I., & Okaya, D. A. (2000). Anisotropy of schists: contribution of crustal anisotropy to active source seismic experiments and shear wave splitting observations. *J. Geophys. Res., 105*, 27991-28007.

Goergen, E. T., Whitney, D. L., Zimmerman, M. E., & Hiraga T. (2008). Deformation-induced polymorphic transformation: experimental deformation of kyanite, andalusite, and sillimanite. *Tectonophysics, 454*, 23-35.

Goodway, W. (2001). AVO and Lame constants for rock parameterization and fluid detection. *Recorder, 26*, 39-60.

Graeber, F. M., & Asch, G. (1999). Three-dimensional models of P wave velocity and P-to-S velocity ratio in the southern central Andes by simultaneous inversion of local earthquake data. *J. Geophys. Res. 104*(B9), 20237-20256.

Grechka, V., & Tsvankin, I. (1999). 3-D moveout inversion in azimuthally anisotropic media with lateral velocity variation: Theory and a case of study. *Geophysics, 64*, 1202-1218.

Groppo, C., & Compagnoni, R. (2007). Ubiquitous fibrous antigorite veins from the Lanzo Ultramafic Massif, Internal Western Alps (Italy): characterization and genetic conditions.

Per. Mineral., 76, 169-181.

Guilbert, J., Poupinet, G., & Jiang, M. (1996). A study of azimuthal P wave residuals and shear-wave splitting across the Kunlun range (Northern Tibetan Plateau). *Phys. Earth Planet. Inter., 95*, 167-174.

Guillot, S., Hattori, K., Agard, P., Schwartz, S., & Vidal O. (2009). Exhumation processes in oceanic and continental subduction contexts: a review, In *Subduction Zone Geodynamics*, edited by S. Lallemand, F. Funiciello, pp. 175-206, Springer-Verlag, Berlin Heidelberg.

Guillot, S., Harttori, K., & de Sigoyer, J. (2000). Mantle wedge serpentinization and exhumation of eclogites: insights from eastern Ladakh, northwest Himalaya. *Geology, 28* (3), 199-202.

Guillot, S., Harttori, K., de Sigoyer, J., Nägler, T., & Auzende, A. L. (2001). Evidence of hydration of the mantle wedge and its role in the exhumation of eclogites. *Earth Planet. Sci. Lett., 193*, 115-127.

Guillot, S., & Replumaz, A. (2013). Importance of continental subductions for the growth of the Tibetan plateau. *Bull. Soc. géol. France, 184*, 199-223.

Hacker, B. R., Peacock, S. M., Abers, G. A., & Holloway, S. D. (2003). Subduction factory 2, Are intermediate-depth earthquakes in subducting slabs linked to metamorphic dehydration reactions? *J. Geophys. Res., 108,* 2030, doi:10.1029/2001JB001129.

Hake, H., Helbig, K., & Mesdag, C. (1984). Three-term Taylor series for $t^2 - x^2$ curves of P- and S-waves over layered transversely isotropic ground. *Geophys. Prosp., 32*, 828-850.

Hall, C. E., Fischer, K. M., Parmentier, E. M., & Blackman, D. K. (2000). The influence of plate motions on three-dimensional back arc mantle flow and shear wave splitting. *J. Geophys. Res., 105*, 28009-28033.

Hamilton, W. B. (1988). Plate tectonics and island arcs. *Geol. Soc. Am. Bull., 100*, 1503-1527.

Hanmer, S., Ji, S., Darrach, M., & Kopf, C. (1991). Tantato domain, northern Saskatchewan: A segment of the Snowbird tectonic zone. In Current research, part C, pp. 121-133, Geological Survey of Canada, Paper 91-C.

Hansen, L. N., Zhao, Y. H., Zimmerman, M. E., & Kohlstedt, D. (2014). Protracted fabric evolution in olivine: Implications for the relationship among strain, crystallographic fabric, and seismic anisotropy. *Earth Planet. Sci. Lett., 387*, 157-168.

Healy, D., Reddy, S. M., Timms, N. E., Gray, E. M., & Brovarone, A. V. (2009). Trench-parallel fast axes of seismic anisotropy due to fluid-filled cracks in subducting slabs. *Earth Planet. Sci. Lett., 283*, 75-86.

Hearmon, R. F. S. (1984). The elastic constants of crystals and other anisotropic materials, *Landolt-Börnstein-Numerical Data and Functional Relationships in Science and Technology*, Group Ⅲ. Springer-Verlag, Berlin, Vol. 18.

Hearn, T. (1999). Uppermost mantle velocities and anisotropy beneath Europe. *J. Geophys. Res., 104*, 15123-14139.

Heidbach, O., Tingay, M., Barth, A., Reinecker, J., Kurfeb, D., & Müller B. (2010). Global crustal stress pattern based on the World Stress Map database release 2008. *Tectonophysics, 482*, 3-15.

Helbig, K. (1964). Refraction seismic with an anisotropic overburden: a graphical method of interpretation. *Geophys. Prosp., 12*, 383-396.

Helbig, K. (1981). Systematic classification of layer-induced transverse isotropy. *Geophys. Prosp., 29*, 550-577.

Helbig, K. (1984a). Transverse isotropy in exploration seismics. *Geophys. J. R. Astr. Soc., 76*, 79-88.

Helbig, K. (1984b). Anisotropy and dispertion in periodically layered media. *Geophysics, 49*, 364-373.

Helbig, K. (1994). *Foundations of anisotropy for exploration seismics*, Handbook of Geophysical Exploration – Section I: Seismic exploration. Elsevier Science Ltd., Oxford.

Helbig, K., & Schoenberg, M. (1987). Anomalous polarization of elastic waves in transversely isotropic media. *J. Acoust. Soc. Am., 81*, 1235-1245.

Herquel, G., & Tapponnier, P. (2005). Seismic anisotropy in western Tibet. *Geophys. Res. Lett., 32*, L17306, doi:10.1029/2005GL023561.

Herquel, G., Tapponnier, P., Wittlinger, G., Mei, J., & Danian, S. (1999). Teleseismic shear wave splitting and lithospheric anisotropy beneath and across the Altyn Tagh fault. *Geophys. Res. Lett., 26*, 3225-3228, doi:10.1029/1999GL005387.

Hess, H. (1964). Seismic anisotropy of the uppermost mantle under oceans. *Nature, 203*, 629-631.

Heyliger, P., Ledbetter, H., Kim, S. (2003). Elastic constants of natural quartz. *J. Acoust. Soc. Am., 114*, 644-650.

Hilairet, N., Daniel, I., & Reynard, B. (2006). Equation of state of antigorite, stability field of serpentines, and seismicity in subduction zones. *Geophys. Res. Lett., 33*, L02302, doi:10.1029/2005GL024728.

Hilairet, N., & Reynard, B. (2009). Stability and dynamics of serpentinite layer in subduction zone. *Tectonophysics, 465*(1–4), 24-29.

Hilairet, N., Reynard, B., Wang, Y., Daniel, I., Markel, S., Nishiyama, N., & Petitgirard, S. (2007). High-pressure creep of serpentine, interseismic deformation, and initiation of subduction. *Science, 318*, 1910-1913.

Hill, R. (1952). The elastic behavior of a crystalline aggregate. *Physical Society – Proccedings, 65*, 349-354.

Hirauchi, K., & Katayama, I. (2013). Rheological contrast between serpentine species and implications for slab-mantle wedge decoupling. *Tectonophysics, 608*, 545-551.

Hirauchi, K., Michibayashi, K., Ueda, H., & Katayama, I. (2010). Spatial variations in antigorite fabric across a serpentinite subduction channel: insights from the Ohmachi Seamount, Izu-Bonin frontal arc. *Earth Planet. Sci. Lett., 299*(1–2), 196-206.

Hirn, A., Jiang, M., Sapin, M., Diaz, J., Nercessian, A., Lu, Q. T., Lepine, J. C., Shi, D. N., Sachpazi, M., Pandey, M. R., Ma, K., & Gallart, J. (1995). Seismic anisotropy as an indicator of mantle flow beneath the Himalayas and Tibet. *Nature, 375*, 571-574.

Hirth, G., & Guillot, S. (2013). Rheology and tectonic significance of serpentinite. *Elements, 9*, 107-113.

Holland, T. J. B., & Powell, R. (1998). An internally consistent thermodynamic data set for phases of petrological interest. *J. Metamorph. Geol., 16*, 309-343.

Horen, H., Zamora, M., & Dubuisson, G. (1996). Seismic waves velocities and anisotropy in serpentinized peridotites from Xigaze ophiolite: abundance of serpentine in slow spreading ridge. *Geophys. Res. Lett., 23,* 9-12.

Houseman, G., & England, P. (1986). Finite strain calculations of continental deformation 1. Method and general results for convergent zones. *J. Geophys. Res., 91*, 3651-3663.

Hovem, J. M. (1995). Acoustic waves in finely layered media. *Geophysics, 60*, 1217-1221.

Hu, J. F., Yang, H. Y., Li, G. Q., & Peng, H. C. (2014). Seismic upper mantle discontinuities beneath Southeast Tibet and geodynamic implications. *Gondwana Research*, http://dx.doi.org/10.1016/j.gr.2014.08.016.

Hu, S. B., He, L. J., & Wang, J. Y. (2000). Heat flow in the continental area of China: a new data set. *Earth Planet. Sci. Lett., 179*, 407-419, doi:10.1016/S0012-821x(00)00126-6.

Huang, W.-C., Ni, J. F., Tilmann, F., Nelson, D., Guo, J. R., Zhao, W. J., Mechie, J., Kind, R., Saul, J., Rapine, R., & Hearn, T. M. (2000). Seismic polarization anisotropy beneath the central Tibetan Plateau. *J. Geophys. Res., 105*(B12), 27979-27989.

Huang, Z. C., Wang, L. S., Xu, M. J., Liu, J. H., Mi, N., & Liu, S. W. (2007). Shear wave splitting across the Ailao Shan-Red River fault zone, SW China. *Geophys. Res. Lett., 34*, L20301, doi:10.1029/2007GL031236.

Huang, Z. C., Wang, L. S., Zhao, D. P., Mi, N., & Xu, M. J. (2011). Seismic anisotropy and mantle dynamics beneath China. *Earth Planet. Sci. Lett., 306*, 105-117, doi:10.1016/j.epsl.2011.03.038.

Huchon, P., Le Pichon, X., & Rangin, C. (1994). Indochina Peninsula and the collision of India and Eurasia. *Geology, 22*, 27-30.

Hughes, S., & Luetgert, J. H. (1992). Crustal structure of the southeastern Grenville province northern New York state and eastern Ontario. *J. Geophys. Res., 97*, 17455-17479.

Hughes, S., Luetgert, J. H., & Christensen, N. I. (1993). Reconciling deep seismic refraction and reflection data from the Grenvillian-Appalachian boundary in western New England. *Tectonophysics, 225*, 255-269.

Hyndman, R. D., & Peacock, S. M. (2003). Serpentinization of the forearc mantle. *Earth Planet. Sci. Lett., 212*, 417-432.

Jaeger, J. C. (1969). *Elasticity, Fracture and Flow, with Engineering and Geological Applications*. London, Methuen & Co.

Ji, J. Q., Zhong, D. L., Sang, H. Q., & Zhang, L. S. (2000). The western boundary of extrusion blocks in the southeastern Tibetan Plateau. *Chin. Sci. Bull., 45*, 876-881.

Ji, S. (2004). A generalized mixture rule for estimating the viscosity of solid-liquid suspensions and mechanical properties of polyphase rocks and composite materials. *J. Geophys. Res., 109*, B10207, doi:10.1029/2004JB003124.

Ji, S. (2008). *Deformation Mechanisms, Rheology, and Seismic Properties of Rocks*, Continental Dynamics Series Volume 1. Geological Publishing House, Beijing, 539 p.

Ji, S., Gu, Q., & Xia, B. (2006). Porosity dependence of mechanical properties of solid materials. *Journal of Materials Science, 41*(6), 1757-1768.

Ji, S., Jiang, Z., Rybacki, E., Wirth, R., Prior, D., & Xia, B. (2004). Strain softening and microstructural evolution of anorthite aggregates and quartz-anorthite layered composites deformed in torsion. *Earth Planet. Sci. Lett., 222*, 377-390.

Ji, S., Li, A. W., Wang, Q., Long, C. X., Wang, H. C., Marcotte, D., & Salisbury, M. (2013a). Seismic velocity, anisotropy, and shear-wave splitting of antigorite serpentinites and tectonic implications for subduction zones. *J. Geophys. Res., 118*, 1015-1037, doi:10.1002/jgrb50110.

Ji, S., & Long, C. (2006). Seismic reflection response of folded structures and implications for the interpretation of deep seismic reflection profiles. *J. Struct. Geol., 28*, 1380-1387.

Ji, S., Long, C., Martignole, J., & Salisbury, M. (1997). Seismic reflectivity of a finely layered, granulite-facies ductile shear zone in the southern Grenville Province (Québec). *Tectonophysics, 279*, 113-133.

Ji, S., & Mainprice, D. (1988). Natural deformation fabrics of plagioclase: Implications for slip systems and seismic anisotropy. *Tectonophysics, 147*, 145-163.

Ji, S., & Mainprice, D. (1989). Seismic anisotropy in the lower crust induced by the lattice-preferred orientations of minerals. *Seismology and Geology, 4*, 15-30.

Ji, S., & Mainprice, D. (1990). Recrystallization and fabric development in plagioclase. *J. Geol., 98*, 65-79.

Ji, S., Mainprice, D., & Boudier, F. (1988). Sense of shear in high-temperature movement zones from the fabric asymmetry of plagioclase feldspars. *J. Struct. Geol., 10*, 73-81.

Ji, S., & Salisbury, M. H. (1993). Shear-wave velocities, anisotropy and splitting in high-grade mylonites. *Tectonophysics, 221*, 453-473.

Ji, S., Salisbury, M. H., & Hanmer, S. (1993). Petrofabric, P-wave anisotropy and seismic reflectivity of high-grade tectonites. *Tectonophysics, 222*, 195-226.

Ji, S., Shao, T., Michibayashi, K., Long, C. X., Wang, Q., Kondo, Y., Zhao, W. H., Wang, H. C., & Salisbury, M. H. (2013b). A new calibration of seismic velocities, anisotropy, fabrics, and elastic moduli of amphibole-rich rocks. *J. Geophys. Res., 118*, 4699-4728, doi:10.1002/jgrb.50352.

Ji, S., Shao, T., Michibayashi, K., Oya, S., Satsukawa, T., Wang, Q., Zhao, W. H., & Salisbury, M. H. (2015). Magnitude and symmetry of seismic anisotropy in mica- and amphibole-bearing metamorphic rocks and implications for tectonic interpretation of seismic data from the southeast Tibetan Plateau. *J. Geophys. Res., 120*, doi:10.1002/2015JB012209

Ji S., Shao, T., Salisbury, M. H., Sun, S. S., Michibayashi, K., Zhao, W. H., Long, C. X., Liang, F. H., & Satsukawa, T. (2014b). Plagioclase crystal preferred orientation and induced seismic anisotropy. *J. Geophys. Res., 119*, 8064-8088, doi:10.1002/2014JB011352.

Ji, S., Sun, S. S., Wang, Q., & Marcotte, D. (2010). Lame parameters of common rocks in the

Earth's crust and upper mantle. *J. Geophys. Res., 115* (B6), p. B06314.1-B06314.15.

Ji, S., Wang, Q., Marcotte, D., Salisbury, M. H., & Xu, Z. Q. (2007). P-wave velocities, anisotropy and hysteresis in ultrahigh-pressure metamorphic rocks as a function of confining pressure. *J. Geophys. Res., 112*, B09204, doi: 10.1029/2006JB004867.

Ji, S., Wang, Q., Shao, T., Sun, S. S., Li, A. W., Michibayashi, K., Kondo, Y., & Li, J. F. (2014a). The Yushugou granulite-peridotite terrane as a Paleozoic continental crust-mantle transition zone exposed at the northern margin of the southern Tianshan (Xinjiang). *Geotectonica et Metallogenia, 38*(3), 473-494.

Ji, S., Wang, Q., & Xia, B. (2002). *Handbook of Seismic Properties of Minerals, Rocks and Ores*, 630 pp., Polytechnic International Press, Montreal.

Ji, S., Wang, Q., & Xia, B. (2003). P-wave velocities of polymineralic rocks: comparision of theory and experiment and test of elastic mixture rules. *Tectonophysics, 366*, 165-185.

Ji S., Wang, Q., Xia, B., & Marcotte, D. (2004). Mechanical properties of multiphase materials and rocks: a phenomenological approach using generalized means. *J. Struct. Geol*., 26, 1377-1390.

Ji, S., Wang, Q., & Salisbury, M. H. (2009). Composition and tectonic evolution of the Chinese continental crust constrained by Poisson's ratio. *Tectonophysics, 463,* 15-30.

Ji, S., Wirth, R., Rybacki, E., & Jiang, Z. (2000). High-temperature plastic deformation of quartz-plagioclase multilayers by layer-normal compression. *J. Geophys. Res., 105*, 16651-16664.

Ji, S., & Xia, B. (2002). *Rheology of polyphase earth materials*, 259 pp., Polytechnic International Press, Montréal.

Ji, S., Zhao, X., & Francis, D. (1994a). Calibration of shear-wave splitting in subcontinental upper mantle beneath active orogenic belts using ultramafic xenoliths from the Canadian Cordillera and Alaska. *Tectonophysics, 239*, 1-28.

Ji, S., Zhao, X., & Zhao, P. (1994b). On the measurement of plagioclase lattice preferred orientations. *J. Struct. Geol., 16*, 1711-1718.

Jones, T. D., & Nur, A. (1984). The nature of seismic reflections from deep crustal fault zones. *J. Geophys. Res., 89*, 3153-3171.

Joyner, W. B. (2000). Strong motion from surface waves in deep sedimentary basins. *Bull. Seism. Soc. Am., 90*, S95-S112

Jung, H. (2011). Seismic anisotropy produced by serpentine in mantle wedge. *Earth Planet. Sci. Lett., 307,* 535-543.

Jung, H., Fei, Y., Silver, P. G., & Green, H. W. (2009). Frictional sliding in serpentine at very high pressure. *Earth Planet. Sci. Lett., 277*, 273-279.

Jung, H., & Green, H. W. (2004). Experimental faulting of serpentinite during dehydration: Implications for earthquakes, seismic low-velocity zones, and anomalous hypocenter distributions in subduction zones. *Int. Geol. Rev., 46*, 1089-1102.

Jung, H., Green, H. W., & Dobrzhinetskaya, L. F. (2004). Intermediate-depth earthquake faulting by dehydration embrittlement with negative volume change. *Nature, 428*, 545-549.

Jung, H., Lee, J., Ko, B., Jung, S., Park, M., Cao, Y., & Song, S. (2013). Natural type-C olivine fabrics in garnet peridotites in North Qaidam UHP collision belt, NW China. *Tectonophysics, 594*, 91-102.

Kamiya, S., & Kobayashi, Y. (2000). Seismological evidence for the existence of serpentinized wedge mantle. *Geophys. Res. Lett., 27*(6), 819-822.

Kaneshima, S. (1990). Origin of crustal anisotropy: shear wave splitting studies in Japan. *J. Geophys. Res., 95*, 121-133.

Kaneshima, S., & Ando, M. (1988). Crustal anisotropy inferred from shear-wave splitting. The Third International Workshop on Seismic Anisotropy, Berkeley, USA.

Karato, S. I. (1987). Seismic anisotropy due to lattice preferred orientation of minerals: kinematic or dynamic? in *High Pressure Research in Mineral Physics*, edited by M. H. Manghnani & Y. Syono, pp. 455-471, AGU, Washington, D. C.

Karato, S. I. (1998). Seismic anisotropy in the deep mantle, boundary layers and the geometry of the mantle convection. *Pure Appl. Geophys., 151*, 565-587.

Karato, S. I., Jung, H., Katayama, I., & Skemer, P. (2008). Geodynamic significance of seismic anisotropy of the upper mantle: New insights from laboratory studies. *Annu. Rev. Earth Planet. Sci., 36*, 59-95.

Karato, S. I., & Karki, B. B. (2001). Origin of lateral variation of seismic wave velocities and density in the deep mantle. *J. Geophys. Res., 106*, B10, 21771-21783.

Katayama, I., Hirauchi, K. I., Michibayashi, K., & Ando, J. I. (2009). Trench-parallel anisotropy produced by serpentine deformation in the hydrated mantle wedge. *Nature, 461,* 1114-1118.

Kawano, S., Katayama, I., & Okazaki, K. (2011). Permeability anisotropy of serpentinite and fluid pathways in a subduction zone. *Geology, 39*, 939-942.

Kay, R. W., & Kay, S. M. (1993). Delamination and delamination magmatism. *Tectonophysics, 219* (1-3), 177-189.

Kebaili, A., & Schmitt, D. R. (1996). Velocity anisotropy observed in wellbore seismic arrivals: combined effect of intrinsic properties and layering. *Geophysics, 61*, 12-20.

Kebaili, A., & Schmitt, D. R. (1997). Ultrasonic anisotropy phase velocity determination with the Radon transformation. *J. Acoust. Soc. Am., 101*, 3278-3286.

Kennett, B. L. N., Widiyantoro, S., & van der Hilst, R. D. (1998). Joint seismic tomography for bulk-sound and shear wave speed in the Earth's mantle. *J. Geophys. Res., 103*, 12469-12493.

Kern, H. (1982). P- and S-wave velocities in crustal and mantle rocks under the simultaneous action of high confining pressure and high temperature and the effect of the rock microstructure, In High-Pressure Research in Geosciences, edited by W. Schreyer et al., pp. 15-45.

Kern, H. (1993). P- and S-wave anisotropy and shear-wave splitting at pressure and temperature in possible mantle rocks and their relation to the rock fabric. *Phys. Earth. Planet. Inter., 78,* 245-256.

Kern, H., & Fakhimi, M. (1975). Effect of fabric anisotropy on compressional-wave propagation in various metamorphic rocks for the range 20-700℃ at 2 kb. *Tectonophysics, 28*, 227-244.

Kern, H., Gao, S., Jin, Z., Popp, T., & Jin, S. (1999). Petrophysical studies on rocks from the Dabie ultrahigh-pressure (UHP) metamorphic belt, central China: implication for the composition and delamination of the lower crust. *Tectonophysics, 301*, 191-215.

Kern, H., Gao, S., & Lui, Q. (1996). Seismic properties and densities of middle and lower crustal rocks exposed along the North China Geoscience Transect. *Earth Planet. Sci. Lett., 139*, 439-455.

Kern, H., Ivankina, T. I., Nikitin, A. N., Lokajicek, T., & Pros, Z. (2008). The effect of oriented microcracks and crystallographic and shape preferred orientation on bulk elastic anisotropy of a foliated biotite gneiss from Outokumpo. *Tectonophysics, 457*, 143-149.

Kern, H., Lokajicek, T., Svitek, T., & Wenk, H.-R. (2015). Seismic anisotropy of serpentinite from Val Malenco, Italy. *J. Geophys. Res., 120*, 4113-4129.

Kern, H., Lui, B., & Popp T. (1997). Relationship between anisotropy of P and S wave velocities and anisotropy of attenuation in serpentinite and amphibolites. *J. Geophys. Res., 102,* 3051-3065.

Kern, H., Mengel, K., Stauss, K. W., Ivankina, T. I., Nikitin, A.N., & Kukkonen, I. T. (2009). Elastic wave velocities, chemistry and modal mineralogy of crustal rocks sampled by the Outokumpu scientific drill hole: evidence from lab measurements and modeling. *Phys. Earth Planet. Int., 175*, 151-166.

Kern, H., Popp, T., Gorbatsevich, F., Zharikov, A., Lobanov, K. V., & Smirnov, Yu. P. (2001). Pressure and temperature dependence of Vp and Vs in rocks from the superdeep well and from surface analogues at Kola and the nature of velocity anisotropy. *Tectonophysics, 338*, 113-134.

Kern, H., & Tubia, J. M. (1993). Pressure and temperature dependence of P- and S-wave velocities, seismic anisotropy and density of sheared rocks from Sierra Alpujata massif (Ronda peridotites, southern Spain). *Earth Planet. Sci. Lett., 119*, 191-205.

Kern, H., & Wenk, H. R. (1990). Fabric-related velocity anisotropy and shear wave splitting in rocks from Santa Rosa Mylonite Zone, California. *J. Geophys. Res., 95*(B7), 11213-11223.

Khazanehdari, J., Rutter, E. H., & Brodie, K. H. (2000). High-pressure-high-temperature seismic velocity structure of the midcrustal and low crustal rocks of the Ivrea-Verbano zone and Serie dei Laghi, NW Italy. *J. Geophys. Res., 105*, 13843-13858.

Kim, D., & Jung, H. (2015). Deformation microstructures of olivine and chlorite in chlorite peridotites from Almklovdalen in the Western Gneiss Region, southwest Norway, and implications for seismic anisotropy. *Int. Geol. Rev., 57*, 650-668.

Kind, R., et al (1996). Evidence from earthquake data for a partially molten crustal layer in southern Tibet. *Science, 274*, 1692-1694.

Kitamura, K. (2006). Constraint of lattice-preferred orientation (LPO) on Vp anisotropy of amphibole-rich rocks. *Geophys. J. Int., 165* (3), 1058-1065.

Kitamura, K., Ishikawa, M., & Arima, M. (2003). Petrological model of the northern Izu-Bonin-Mariana arc crust: constraints from high-pressure measurements of elastic wave velocities of the Tanzawa plutonic rocks, central Japan. *Tectonophysics, 371*, 213-221.

Ko, B., & Jung, H. (2015), Crystal preferred orientation of an amphibole experimentally deformed by simple shear. *Nature Communications, 6*, 6586, doi:10.1038/ncomms7586.

Kohlstedt, D. L., & Zimmerman, M. E. (1996). Rheology of partially molten mantle rocks. *Ann. Rev. Earth Planet. Sci., 24*, 41-62.

Kosarev, G., Kind, R., Sobolev, S. V., Yuan, X., Hanka, W., & Oreshin, S. (1999). Seismic evidence for a detached Indian lithospheric mantle beneath Tibet. *Science, 283*, 1306-1309.

Krey, T., & Helbig, K. (1956). A theorem concerning anisotropy of stratified media and its significance for reflection seismics. *Geophys. Prosp., 4*, 294-302.

Lakes, R. S. (1987). Foam structures with a negative Poisson's ratio. *Science, 235*, 1038-1040.

Lambregts, P. J., & van Roermund, H. L. M. (1990). Deformation and recrystallization mechanisms in naturally deformed sillimanites. *Tectonophysics, 179*, 371-378.

Lay, T., & Wallace, T. C. (1995). *Modern Global Seismology*, volume 58 of International Geophysical Series (1st ed.). Academic Press, San Diego.

Leaney, W. S., Sayers, C. M., & Miller, D. E. (1999). Analysis of multiazimuthal VSP data for anisotropy and AVO. *Geophysics, 64*, 1172-1180.

Lee, J., & Jung, H. (2015). Lattice-preferred orientation of olivine found in diamond-bearing garnet peridotites in Finsch, South Africa and implications for seismic anisotropy. *J. Struct. Geol., 70*, 12-22.

Leloup, P. H., Lacassin, R., Tapponnier, P., Scharer, U., Zhong, D. L., Liu, X. H., Zhang, L. S., Ji, S., & Trinh, P. T. (1995). The Ailao Shan-Red River shear zone (Yunnan, China), Tertiary transform boundary of Indochina. *Tectonophysics, 251*, 3-84.

Leslie, J. M., & Lawton, D. C. (1999). A refraction-seismic field study to determine the anisotropic parameters of shales. *Geophysics, 64*, 1247-1252.

Lev, E., Long, M. D., & van der Hilst, R. D. (2006). Seismic anisotropy in Eastern Tibet from shear wave splitting reveals changes in lithospheric deformation. *Earth Planet. Sci. Lett., 251*, 293-304, doi:10.1016/j.epsl.2006.09.018.

Levin, F. K. (1979). Seismic velocities in transversely isotropic media. *Geophysics, 44*, 918-936.

Levin, V., & Park, J. (1997). P-SH conversions in a flat-layered medium with anisotropy of arbitrary orientation. *Geophys. J. Int., 131*, 253-266.

Li, B., Kung, J., & Liebermann, R. C. (2004). Modern techniques in measuring elasticity of Earth materials at high pressure and high temperature using ultrasonic interferometry in conjunction with synchrotron X-radiation in multi-anvil apparatus. *Phys. Earth Planet. Inter., 143-144*, 559-574.

Li Y. H., Wu, Q. J., Zhang, F. X., Feng, Q. Q., & Zhang, R. Q. (2011). Seismic anisotropy of the Northeastern Tibetan plateau from shear wave splitting analysis. *Earth Planet. Sci. Lett., 304*, 147-157.

Li, Y. H., Wu, Q. J., Zhang, R. Q., Tian, X. B., & Zeng, R. S. (2008). The crust and upper mantle structure beneath Yunnan from joint inversion of receiver functions and Rayleigh wave dispersion data. *Phys. Earth Planet. Inter., 170*, 134-146.

Liang, C., & Song, X. (2006). A low velocity belt beneath northern and eastern Tibet Plateau from Pn tomography. *Geophys. Res. Lett., 33*, L22306, doi:10.1029/2006GL027926.

Liu, J., Chen, G., Gwanmesia, G. D., Liebermann, R. C. (2000). Elastic wave velocities of pyrope-majorite garnets ($Py_{62}Mj_{38}$ and $Py_{50}Mj_{50}$) to 9 GPa. *Phys. Earth Planet. Inter., 120*, 153-163.

Liu, E., Crampin, S., Queen, J. H., & Rizer, W. D. (1993). Velocity and attenuation anisotropy caused by microcracks and microfractures in a multiazimuthal reverse VSP. *Can. J. Expl. Geophys., 29*, 177-188.

Lin, S., Davis, D. W., Rotenberg, E., Corkery, M. T., & Bailes, A. H. (2006). Geological evolution of the northwestern Superior Province: Clues from geology, kinematics, and geochronology in the Gods Lake Narrows area, Oxford-Stull terrane, Manitoba. *Can. J. Earth Sci., 43*, 749-765.

Lin, F.-C., Ritzwoller, M. H., Yang, Y. J., Moschetti, M. P., & Fouch, M. J. (2011). Complex and variable crustal and uppermost mantle seismic anisotropy in the western United States. *Nat. Geosci., 4*, 55-61, doi:10.1038/negeo1036.

Lin, T. H., Lo, C. H., Chung, S. L., Hsu, F. J., Yeh, M. W., Lee, T. Y., Ji, J. Q., Wang, Y. Z., & Liu, D. Y. (2009). 40Ar/39Ar dating of the Jiali and Gaoligong shear zones: Implications for crustal deformation around the Eastern Himalayan Syntaxis. *J. Asian Earth Sci., 34*, 674-685.

Little, T. A., Savage, M. K., Tikoff, B. (2002). Relationship between crustal finite strain and seismic anisotropy in the mantle, Pacific-Australia plate boundary zone, South Island, New Zealand. *Geophys. J. Int., 151*, 106-116.

Liu, J. L., Tang, Y., Tran, M.-D., Cao, S. Y., Zhao, L., Zhang, Z. C., Zhao, Z. D., & Chen, W. (2012). The nature of the Ailao Shan-Red River (ASRR) shear zone: Constraints from structural, microstructural and fabric analyses of metamorphic rocks from the Diancang Shan, Ailao Shan and Day Nui Con Voi massifs. *J. Asian Earth Sci., 47*, 231-251.

Lloyd, G. E., Butler, R. W. H., Casey, M., & Mainprice, D. (2009). Mica, deformation fabrics and the seismic properties of the continental crust. *Earth Planet. Sci. Lett., 288*, 320-328, doi:10.1016/j.epsl.2009.09.035.

Lloyd, G. E., Butler, R. W. H., Casey, M., Tatham, D. J., & Mainprice, D. (2011). Constraints on the seismic properties of the middle and lower continental crust, in Deformation Mechanisms, Rheology and Tectonics: Microstructures, Mechanics and Anisotropy. *Geol. Soc. Lond. Spec. Pub*. Vol., 360, pp. 7-32, doi: 10.1144/SP360.2, eds Prior, D. J., E. H. Rutter & D. J. Tatham, Geological Society, London.

Lokajicek, T., Kern, H., Svitek, T., & Ivankina, T. (2014). 3D velocity distribution of P- and S-waves in a biotite gneiss, measured in oil as the pressure medium: Comparison with velocity measurements in a multi-anvil pressure apparatus and with texture-based calculated data. *Phys. Earth Planet. Int., 231*, 1-15.

Lokajicek, T., & Svitek, T. (2015). Laboratory measurement of elastic anisotropy on spherical rock samples by longitudinal and transverse sounding under confining pressure. *Ultrasonics, 56*, 294-302.

Lokmer, I., & Herak, M. (1999). Anisotropy of P-wave velocity in the upper crust of the central External Dinarides. *Studia Geophysica et Geodetica, 43*, 345-356.

Long, M. D., & Becker, T. W. (2010). Mantle dynamics and seismic anisotropy. *Earth Planet. Sci. Lett., 297*, 341-354.

Long, M. D., & Silver, P. G. (2008). The subduction zone flow field from seismic anisotropy: a global view. *Science, 319,* 315-318.

Long, M. D., & Silver, P. G. (2009). Mantle flow in subduction systems: the subslab flow field and implications for mantle dynamics. *J. Geophys. Res., 114,* B10312, doi:10.1029/ 2008JB006200

Long, M. D., & van der Hilst, R. D. (2006). Shear wave splitting from local events beneath the Ryukyu arc: trench-parallel anisotropy in the mantle wedge. *Phys. Earth Planet. Inter., 155,* 300-312.

Long, C., & Salisbury, M. H. (1996). The velocity structure of the Britt Domain, southwestern Grenville Province, from laboratory and refraction experiments. *Can. J. Earth Sci., 33*, 729-745.

Ma, T. T., Liao, Z. T., & Zhou, Z. Y. (2007). The current research of Xiuyan nephrite ore genesis. *Shanghai Geol., 4*, 64-66.

MacBeth, C., Boyd, M., Rizer, W., & Queen, J. (1988). Estimation of reservoir fracturing from marine VSP using local shear-wave conversion. *Geophys. Prosp., 46*, 29-50.

Mah, M., & Schmitt, D. R. (2003). Determination of the complete elastic stiffnesses from ultrasonic phase velocity measurements. *J. Geophys. Res., 108*(B1), 2016, doi:10.1029/2001JB001586.

Mahan, K. (2006). Retrograde mica in deep crustal granulites: implications for crustal seismic anisotropy. *Geophys. Res. Lett., 33*, L24301, doi:10.1029/2006GL028130.

Mahan, K. H., & Williams, M. L. (2005). Reconstruction of a large deep-crustal terrane: Implications for the Snowbird tectonic zone and early growth of Laurentia. *Geology, 33* (5), 385-388.

Mainprice, D. (1990), A FORTRAN program to calculate seismic anisotropy from the lattice preferred orientation of minerals, *Computer Geoscience, 16*, 385-393.

Mainprice, D. (2007). Seismic anisotropy of the deep earth from a mineral and rock physics perspective, edited by Schubert, G. *Treatise on Geophysics, 2*, 437-491.

Mainprice, D., Barruol, G., & Ben Ismaìl, W. (2000). The anisotropy of the Earth's mantle: From single crystal to polycrystal, in Mineral Physics and Seismic Tomography: From Atomic to Global. *Geophys. Monogr. Ser., vol.117*, edited by S. Karato et al., pp.237-264, AGU, Washington, D. C.

Mainprice, D., Bouchez, J.-L., Blumenfeld, P., & Tubià, J. M. (1986). Dominant c slip in naturally deformed quartz: Implications for dramatic plastic softening at high temperature. *Geology, 14*, 819-822.

Mainprice, D., & Casey, M. (1990). The calculated seismic properties of quartz mylonites with typical fabrics: relationship to kinematics and temperature. *Geophys. J. Int., 103*, 599-608.

Mainprice, D., & Humbert, M. (1994). Methods of calculating petrophysical properties from lattice preferred orientation data. *Surveys in Geophysics, 15*, 575-592.

Mainprice, D., & Ildefonse, B. (2009). Seismic anisotropy of subduction zone minerals-contribution of hydrous phases, In Subduction Zone Geodynamics, pp. 63-84, Springer Berlin Heidelberg.

Mainprice, D., & Nicolas, A. (1989). Development of shear and lattice preferred orientations: application to the seismic anisotropy of the lower crust. *J. Struct. Geol., 11*, 175-189.

Mainprice, D., & Silver, P. G. (1993). Interpretation of SKS-waves using samples from the subcontinental lithosphere. *Phys. Earth Planet. Inter., 78*, 257-280.

Makeyeva, L. I., Vinnik, L. P., & Roecher S. W. (1992). Shear-wave splitting and small-scale convection in the continental upper mantle. *Nature, 358*, 144-147.

Makovsky, Y., Klemperer, S. L., Ratschbacher, L., Brown, L. D., Li, M., Zhao, W. J., & Meng, F. L. (1996). INDEPTH wide-angle reflection observation of P-wave-to-S-wave conversion from crustal bright spots in Tibet. *Science, 274*, 1690-1691, doi:10.1126/science.274.5293.1690.

Maltman, A. J. (1978). Serpentinite textures in Anglesey, North Wales, United Kingdom. *Geol. Soc. Amer. Bull., 89*(7), 972-980, doi: 10.1130/0016-7606.

Matsubara, M., Obara, K., & Kasahara, K. (2009). High-V_P/V_S zone accompanying non-volcanic tremors and slow-slip events beneath southwestern Japan. *Tectonophysics, 472* (1–4), 6-17.

Matthies, S., & Humbert, M. (1993). The realization of the concept of a geometric mean for calculating physical constants of polycrystalline materials. *Physica Status Solidi (b), 177*, K47-K50.

McDonough, D. T., & Fountain, D. M. (1988). Reflection characteristics of a mylonite zone based on compressional wave velocities of rock samples. *Geophys. J., 93*, 547-558.

McDonough, D. T., & Fountain, D. M. (1993). P-wave anisotropy of mylonitic and infrastructural rocks from a Cordilleran core complex. *Phys. Earth Planet. Inter., 78*, 319-336.

McNamara, D. E., Owens, T. J., Silver, P. G., & Wu, F. T. (1994). Shear-wave anisotropy beneath the Tibetan Plateau. *J. Geophys. Res., 99*, 13655-13665.

McNamara, D. E., & Thomas, J. O. (1995). Observations of regional phase propagation across the Tibetan Plateau. *J. Geophys. Res., 100*, B11, 22215-22229.

McSkimin, H. J. (1950). Ultrasonic measurement technique applicable to small solid specimens. *J. Acoust. Soc. Am., 22*, 413-418.

McSkimin, H. J., Andreatch, P., & Thurston, Jr. R. N. (1965). Elastic moduli of quartz versus hydrostatic pressure at 25° and -195.8 ℃. *J. Appl. Phys., 36*, 347-352.

Meike, A. (1989). In situ deformation of micas: A high-voltage electron-microscope study. *Am. Mineral., 74*, 780-796.

Meissner, R., Mooney, W. D., & Artemieva, I. (2002). Seismic anisotropy and mantle creep in young orogens. *Geophys. J. Int., 149*, 1-14.

Meissner, R., Rabbel, W., & Kern, H. (2006). Seismic lamination and anisotropy of the lower continental crust. *Tectonophysics, 416*, 81-99.

Melia, P. J., & Carlson, R. L. (1984). An experimental test of P-wave anisotropy in stratified media. *Geophysics, 49*, 374-378.

Meltzer, A., & Christensen, N. I. (2001). Nanga Parbat crustal anisotropy: Implications for interpretation of crustal velocity structure and shear-wave splitting. *Geophys. Res. Lett., 28*, 2129-2132.

Michibayashi, K., & Mainprice, D. (2004). The role of pre-existing mechanical anisotropy on shear zone development within oceanic mantle lithosphere: an example from the Oman ophiolite. *J. Petrol., 45*, 405-414.

Miller, D. J., & Christensen, N. I. (1994). Seismic signature and geochemistry of an island arc: a multidisciplinary study of the Kohistan accreted terrane, northern Pakistan. *J. Geophys. Res., 99*, 11623-11642.

Miller, D. E., Leaney, S., & Borland, W. H. (1994). An in situ estimation of anisotropic elastic moduli for a submarine shale. *J. Geophys. Res., 99*, 21659-21665.

Miyazaki, T., Sueyoshi, K., & Hiraga, T. (2013). Olivine crystals align during diffusion creep of Earth's upper mantle. *Nature, 502*,321-326.

Mizuno, T., Yomogida, K., Ito, H., & Kuwahara, Y. (2001). Spatial distribution of shear wave anisotropy in the crust of the southern Hyogo region by borehole observations. *Geophys. J. Int., 147*, 528-542.

Montagner, J. P. (1986). Regional three-dimentional structures using long-period surface waves. *Ann. Geophys., 4*, 283-294.

Montagner, J. P. (1998). Where can seismic anisotropy be detected in the earth's mantle? In boundary layers…. *Pure Appl. Geophys., 151*, 223-256.

Montagner, J. P., & Nataf, H. C. (1986). A simple method for inverting the azimuthal anisotropy of surface waves. *J. Geophys. Res., 91*, 511-520.

Montagner, J. P., & Tanimoto, T. (1991). Global upper mantle tomography of seismic velocities and anisotropies. *J. Geophys. Res., 96*, 20337-20351.

Mookherjee, M., & Capitani, G. C. (2011). Trench parallel anisotropy and large delay times: elasticity and anisotropy of antigorite at high pressures. *Geophys. Res. Lett., 38,* L09315, doi:10.1029/2011GL047160.

Moore, D. E., & Lockner, D. A. (2007). Comparative deformation behavior of minerals in serpentinized ultramafic rock: application to the slab-mantle interface in subduction zones. *Int. Geol. Rev*., 49, 401-415.

Moschetti, M. P., Ritzwoller, M. H., Lin, F., & Yang, Y. (2010). Seismic evidence for widespread western-US deep-crustal deformation caused by extension. *Nature, 464*, 885-889, doi:10.1038/nature08951.

Musacchio, G., Mooney, W. D., & Luetgert, J. H. (1997). Composition of the crust in the Grenville and Appalachian Provinces of North America inferred from V_p/V_s ratios. *J. Geophys. Res., 102*(B7), 15225-15241.

Nábělek, J., et al. (2009). Underplating in the Himalaya-Tibet collision zone revealed by the Hi-CLIMB experiment. *Science, 325*, 1371, doi:10.1126/science.1167719.

Naus-Thijssen, F. M. J., Goupee, A. J., Vel, S. S., & Johnson, S. E. (2011a). The influence of microstructure on seismic wave speed anisotropy in the crust: computational analysis of quartz-muscovite rocks. *Geophys. J. Int., 185*, 609-621.

Naus-Thijssen, F. M. J., Goupee, A. J., Johnson, S. E., Vel, S. S., & Gerbi, C. (2011b). The influence of crenulation cleavage development on the bulk elastic and seismic properties of phyllosilicate-rich rocks. *Earth Planet. Sci. Lett., 311*, 212-224.

Nelson, K. D., et al. (1996). Partially molten middle crust beneath southern Tibet: Synthesis of project INDEPTH results. *Science, 274*, 1684-1688.

Nestola, F., Angel, R. J., Zhao, J., Garrido, C. J., Sánchez-Vizcaíno, V. L., Capitani, G., & Mellini, M. (2010). Antigorite equation of state and anomalous softening at 6 GPa: an in situ single-crystal X-ray diffraction study. *Contrib. Mineral. Petrol., 160*, 33-43, doi:10.1007/s00410-009-0463-9.

Ni, J., & Barazangi, M. (1983). High frequency seismic wave propagation beneath the Indian shied, Himalayan arc, Tibetan Plateau and surrounding regions: High uppermost mantle velocities and efficient propagation beneath Tibet. *Geophys. J. R. Astron. Soc., 72*, 665-689.

Nicolas, A. (1993). Why fast polarization directions of SKS seismic waves are parallel to mountain belts. *Phys. Earth Planet. Inter., 78*, 337-342.

Nicolas, A., Boudier, F., Ildefonse, B., & Ball, B. (2000). Accretion of Oman and United Arab Emirates ophiolite: Discussion of a new structural map. *Mar. Geophys. Res., 21*, 147-179.

Nicolas, A., & Christensen, N. I. (1987). Formation of anisotropy in upper mantle peridotites-a review, in *The Composition, Structure and Dynamics of the Lithosphere-Asthenosphere System, American Geophysical Union Geodynamics Series,* edited by C. Froidevaux and K. Fuchs, pp. 111-123.

Nicolas, A., Hirn, A., Nicolich, R., & Polino, R. (1990). Lithospheric wedging in the western Alps inferred from the ECORS-CROP traverse. *Geology, 18*, 587-590.

Nicolas, A., & Poirier, J. P. (1976). Crystalline Plasticity and Solid-State Flow in Metamorphic Rocks. Wiley, Chichester.

Nikulin, A., Levin, V., & Park, J. (2009). Receiver function study of the Cascadia megarthrust: evidence for localized serpentinization. *Geochem. Geophys. Geosyst., 10*, Q07004, doi:10.1029/2009GC002376.

Nishii, A., Wallisa, S. R., Mizukamib, T., & Michibayashi, K. (2011). Subduction related antigorite CPO patterns from forearc mantle in the Sanbagawa belt, southwest Japan. *J. Struct. Geol., 33(10*), 1436-1445.

Nishimoto, S., Ishikawa, M., Arima, M., & Yoshida, T. (2005). Laboratory measurement of P-wave velocity in crustal and upper mantle xenoliths from Ichino-megata, NE Japan: ultrabasic hydrous lower crust beneath the NE Honshu arc. *Tectonophysics, 396*, 245-259.

Nye, J. F. (1957). *Physical Properties of Crystals: Their Representation by Tensors and Matrices*. London, Oxford University Press, Amen House.

O'Hanley, D. S. (1992). Solution to the volume problem in serpentinization. *Geology, 20*, 705-708.

O'Hanley, D. S. (1996). Serpentinites: Records of tectonic and petrologic history. Oxford, UK, Oxford University Press, 277 pp.

Okaya, D. A., & Christensen, N. I. (2002). Anisotropic effects of non-axial seismic wave propagation in foliated crustal rocks. *Geophys. Res. Lett., 29*, 1507, doi:10.1029/2001GL014285.

Okaya, D., Christensen, N. I., Stanley, D., Stern, T., & South Island Geophysical Transect Working Group (1995). Crustal anisotropy in the vicinity of the Alpine Fault Zone, South Island. *New Zealand J. Geol. Geophys., 38*, 579-583.

Okazaki, K., Katayama, I., & Noda, H. (2013). Shear-induced permeability anisotropy of simulated serpentinite gouge produced by triaxial deformation experiments. *Geophys. Res. Lett., 40*, 1290-1294.

Owens, T. J., & Zandt, G. (1997). Implications of crustal property variations for models of Tibetan Plateau evolution. *Nature, 387*, 37-43.

Özalaybey, S., & Chen, W. P. (1999). Frequency-dependent analysis of SKS/SKKS waveforms observed in Australia: evidence for null birefringence. *Phys. Earth Planet. Inter., 114*, 197-210.

Padrón-Navarta, J. A., Tommasi, A., Garrido, C. J., & Sanchez-Vizcaíno, V. L. (2012). Plastic deformation and development of antigorite crystal preferred orientation in high pressure serpentinites. *Earth Planet. Sci. Lett., 349-350*, 75-86.

Park, Y., & Jung, H. (2015). Deformation microstructures of olivine and pyroxene in mantle xenoliths in Shanwang, eastern China, near the convergent plate margin, and implications for seismic anisotropy. *Int. Geol. Rev., 57*, 629-649.

Park, J., & Yu, Y. (1993). Seismic determination of elastic anisotropy and mantle flow. *Science, 261*, 1159-1162.

Park, J., Yuan, H. Y., & Levin, V. (2004). Subduction zone anisotropy beneath Corvallis, Oregon: a serpentinite skid mark of trench-parallel terrane migration? *J. Geophys. Res., 109*, B10306, doi:1029/2003JB002718.

Passchier, C. W., & Trouw, R. A. J. (2005). Microtectonics (2nd). 353 pp., Springer Verlag, Berlin Heidelberg, Berlin.

Peacock, S. M., Christensen, N. I., Bostock, M. G., & Audet, P. (2011). High pore pressure and porosity at 35 km depth in the Cascadia subduction zone. *Geology, 39*, 471-474.

Peacock, S. M., Crampin, S., Booth, D. C., & Fletcher, J. B. (1988). Shear-wave splitting in the Anza seismic gap, Southern California: temporal variations as possible precursors. *J. Geophys. Res., 93*, 3339-3356.

Peselnick, L., & Nicolas, A. (1978). Seismic anisotropy in an ophiolite peridotite: Application to oceanic upper mantle. *J. Geophys. Res., 83*, 1227-1235.

Pselnick, L., Nicolas, A., & Stevenson, P. R. (1974). Velocity anisotropy in a mantle peridotite from the Ivrea zone: Application to upper mantle anisotropy. *J. Geophys. Res., 79*, 1175-1182.

Piazolo, S., & Jaconelli, P. (2014). Sillimanite deformation mechanisms within a Grt-Sil-Bt gneiss: effect of pre-deformation grain orientations and characteristics on mechanism, slip-system activation and rheology. *Geol. Soc. London Spec. Publ., 394*(1), 189-213.

Pilchin, A. (2005). The role of serpentinization in exhumation of high- to ultra-high-pressure metamorphic rocks. *Earth Planet. Sci. Lett., 237,* 815-828.

Plomerova, J., Babuška, S., & Sileny, J. (1998). Seismic anisotropy and velocity variations in the mantle beneath the Saxothuringicum-Moldanubicum Contact in the central Europe. *Pure Appl. Geophys., 151*, 365-394.

Plomerova, J., Sileny, J., & Babuška, S. (1996). Joint interpretation of upper-mantle anisotropy based on teleseismic P-travel time delays and inversion of shear-wave splitting parameters. *Phys. Earth Planet. Inter., 95*, 293-309.

Polet, J., Silver, P. G., & Beck, S. (2000). Shear wave anisotropy beneath the Andes from the BANJO, SEDA, and PISCO experiments. *J. Geophys. Res., 105,* 6287-6304.

Porter, R., Zandt, G., & McQuarrie, N. (2011). Pervasive lower-crustal seismic anisotropy in Southern California: Evidence for underplated schists and active tectonics. *Lithosphere, 3*, 201-220, doi:10.1130/L126.1.

Postma, G. W. (1955). Wave propagation in a stratified medium. *Geophysics, 20*, 780-806.

Prieto, G. A., Beroza, G. C., Barrett, S. A., Lopez, G. A., & Florez, M. (2012). Earthquake nests as natural laboratories for the study of intermediate-depth earthquake mechanics. *Tectonophysics, 570-571*, 42-56.

Punturo, R., Kern, H., Cirrincione, R., Mazzoleni, P., & Pezzino, A. (2005). P- and S-wave velocities and densities in silicate and calcite rocks from the Peloritani Mountains, Sicily (Italy): The effort of pressure, temperature and the direction of wave propagation. *Tectonophysics, 409*, 55-72.

Raleigh, C., & Paterson, M. (1965). Experimental deformation of serpentinite and its tectonic implications. *J. Geophys. Res., 70*, 3965-3985.

Ramachandran, K., Hyndman, R. D., & Brocher, T. M. (2006). Regional P-wave velocity structure of the Northern Cascadia, subduction zone. *J. Geophys. Res., 111,* B12301, doi:101029/2005Jb00408J.

Rasolofosaon, P. N. J., Rabbel, W., Siegesmund, S., & Vollbrecht, A. (2000). Characterization of crack distribution: fabric analysis versus ultrasonic inversion. *Geophys. J. Int., 141*, 413-424.

Raterron, P., Girard, J., & Chen, J. H. (2012). Activities of olivine slip systems in the upper mantle. *Phys. Earth Planet. Int., 200-201*, 105-112.

Reuss, A. (1929). Berechnung der Fliessgrenze von Mischkristallen (Calculation of flow limits of mixed crystals on basis of plasticity of monocrystals). *Zeitschrift fuer Angewandte Mathematik und Mechanik, 9*(1), 49-58.

Reynard, B. (2013). Serpentine in active subduction zones. *Lithos, 178*, 171-185, doi.org/10.1016/j.lithos.2012.10.012.

Reynard, B., Gillet, P., & Willaime, C. (1989). Deformation mechanisms in naturally deformed glaucophanes: a TEM and HREM study. *Eur. J. Miner., 1*, 611–624.

Reynard, B., Hilairet, N., Balan, E., & Lazzeri, M. (2007). Elasticity of serpentines and extensive serpentinization in subduction. *Geophys. Res. Lett., 34,* L13307, doi:10.1029/2007GL030176.

Riznichenko, Y. W. (1949). On seismic quasi-anisotropy. *Izu, Akad. Naud. Nauk SSSR, Ser. Geograf. i Geof., 13*, 518-540.

Rondenay, S., Bostock, M. G., & Shragge, J. (2001). Multiparameter two-dimensional inversion of scattered teleseismic body waves, 3: Application to the Cascadia 1993 data set. *J. Geophys. Res.,* 106, 30,795-30,808, doi: 10.1029/2000JB000039.

Rudnick, R. L., & Fountain, D. M. (1995). Nature and composition of the continental crust: A lower crustal perspective. *Reviews of Geophysics, 33*, 267-309.

Rushmer, T. (1991). Partial melting of two amphibolites: contrasting experimental results under fluid-absent conditions. *Contrib. Mineral. Petrol.,117*, 394-409.

Rutter, E., Brodie, K., James, T., & Luigi, B. (2007). Large-scale folding in the upper part of the Ivrea-Verbano zone, NW Italy. *J. Struct. Geol., 29*, 1-17.

Rytov, S. (1956). Acoustic properties of a thinly laminated medium. *Sov. Phys. Acous., 2*, 68-80.

Salisbury, M. H., & Fountain, D. M. (1994). The seismic velocity and poisons ratio structure of the Kapuskasing uplift from laboratory measurements. *Can. J. Earth Sci., 31*, 1052-1063.

Sandvol, E. A., Ni, J. F., Hearn, T. M., & Roecker, S. (1994). Seismic anisotropy beneath the Pakistan Himalayas. *Geophys. Res. Lett., 21*, 1635-1638.

Sandvol, E., Ni, J., Kind, R., & Zhao, W. J. (1997). Seismic anisotropy beneath the southern Himalayas-Tibet collision zone. *J. Geophys. Res., 102*, B8, 17813-17823.

Saruwatari, K., Ji, S., Long, C. X., & Salisbury, M. H. (2001). Seismic anisotropies of mantle xenoliths and constraints on the upper mantle structures beneath the southern Canadian Cordillera. *Tectonophysics, 339*, 399-422.

Satsukawa, T., Ildefonse, B., Mainprice, D., Morales, L. F. G., Michibayashi, K., & Barou, F. (2013). A database of plagioclase crystal preferred orientations (CPO) and microstructures-implications for CPO origin, strength, symmetry and seismic anisotropy in gabbroic rocks. *Solid Earth, 4*, 511-542, doi:10.5194/se-4-511-2013.

Savage, M. K. (1999). Seismic Anisotropy and mantle deformation: What have we learned from shear-wave splitting? *Rev. Geophys., 37* (1), 65-106.

Schmidt, M. W, & Poli, S. (1998). Experimentally based water budgets for dehydrating slabs and consequences for arc magma generation. *Earth Planet. Sci. Lett., 163,* 361-379.

Schmitt, D. R., Han, Z., Kravchinsky, V., & Escartin, J. (2007). Seismic and magnetic anisotropy of serpentinized ophiolite: implications for oceanic spreading rate dependent anisotropy. *Earth planet. Sci. Lett., 261*(3–4), 590-601.

Schön, J. H. (2011). *Physical Properties of Rocks*. Elsevier, 481 p.

Schoenberg, M., & Costa, J. (1991). The insensitivity of reflected SH waves to anisotropy in an underlying layered medium. *Geophys. Prosp., 39*, 985-1003.

Schwartz, S., Guillot, S., Reynard, B., Lafay, R., Debret, B., Nicollet, C., Lanari, P., & Auzende, A. L. (2013). Pressure-temperature estimates of the lizardite/antigorite transition in high pressure serpentinites. *Lithos*, 178, 197-210.

Schwerdtner, W. M. (1964). Preferred orientation of hornblende in a banded hornblende gneiss. *Am. J. Sci., 262*, 1212-1229.

Seno, T., Zhao, D., Kobayashi, Y., & Nakamura, M. (2001). Dehydration of serpentinized slab mantle: Seismic evidence from southwest Japan. *Earth Planets Space, 53,* 861-871.

Seront, B., Mainprice, D., & Christensen, N. I. (1993). A determination of the three-dimensional seismic properties of anorthosite: comparison between values calculated from the petrofabric and direct laboratory measurements. *J. Geophys. Res., 98*, 2209-2221.

Shao, T., & Ji, S. (2015). Earthquake mechanisms of subduction zones: A state-of-the-art overview. *Geological Review, 61*, 245-268.

Shao, T., Ji, S., Kondo, Y., Michibayashi, K., Wang, Q., Xu, Z., Sun, S., Marcotte, D., & Salisbury, M. H. (2014). Antigorite-induced seismic anisotropy and implications for deformation in subduction zones and the Tibetan Plateau. *J. Geophys. Res., 119*, 2068-2099, doi:10.1002/2013JB010661.

Shao, T., Ji, S., Michibayashi, K., & Wang, Q. (2015). Mica-dominated seismic properties of mid-crust beneath west Yunnan, China and geodynamic implications. *Tectonophysics, under review*.

Shapiro, N. M., Ritzwoller, M. H., Molnar, P., & Levin, V. (2004). Thinning and flow of Tibetan crust constrained by seismic anisotropy. *Science*, 305, 233-206.

Shapiro, N. M., & Ritzwoller, M. H. (2002). Monte-carlo inversion for a global shear-velocity model of the crust and the upper mantle. *Geophys. J. Int., 151*, 88-105.

Shearer, P. M., & Orcutt, J. A. (1986). Compressional and shear wave anisotropy in the oceanic lithosphere – The Ngendei seismic refraction experiment. *Geophys. J. R. Astron. Soc., 87*, 967-1003.

Shelley, D. (1994). Spider texture and amphibolite preferred orientations. *J. Struct. Geol., 16*:709–717

Shi, Y. T., Gao, Y., Su, Y. J., & Wang, Q. (2012). Shear-wave splitting beneath Yunnan area of Southwest China. *Earthq. Sci., 25*, 25-34, doi:10.1007/s11589-012-0828-4.

Siegesmund, S., Takeshita, T., & Kern, H. (1989). Anisotropy of Vp and Vs in an amphibolite of the deeper crust and its relationship to the mineralogical, microstructural and textural characteristics of the rock. *Tectonophysics, 157*, 25-38.

Silver, P. G. (1996). Seismic anisotropy beneath the continents: Probing the depths of geology. *Annual Rev. Earth Planet. Sci., 24*, 385-432, doi:10.1146/annurev.earth.24.1.385.

Simons, G., & Brace, W. F. (1965). Comparison of static and dynamic measurements of compressibility of rocks. *J. Geophys. Res., 70*, 5649-5656.

Simmons, G., & Wang, H. (1971). *Single crystal elastic constants and calculated aggregate properties: A handbook* (2nd ed.). MIT Press, Cambridge, Massachusetts, 354 p.

Skrotzki, W. (1990). Microstructure in hornblende of a mylonitic amphibolites, In Deformation Mechanisms, Rheology and Tectonics, edited by R. J. Knipe, and E. H. Rutter. *J. Geol. Soc. Spec. Pub., 54*: 321 - 325.

Smith, M. L., & Dahlen, F. A. (1973). The azimuthal dependence of Love and Rayleigh wave propagation in a slightly anisotropic medium. *J. Geophys. Res., 78*, 3321-3333.

Socquet, A., & Pubellier, M. (2005). Cenozoic deformation in western Yunnan (China-Myanmar border). *J. Asian Earth Sci., 24*, 495-515.

Soda, Y., & Takagi, H. (2010). Sequential deformation from serpentinite mylonite to metasomatic rocks along the Sashu Fault, SW Japan. *J. Struct. Geol., 32,* 792-802.

Soedjatmiko, B., & Christensen, N. I. (2000). Seismic anisotropy uder extended crust: evidence from upper mantle xenoliths, Cima Volcanic Field, California. *Tectonophysics, 321*, 279-296.

Song, T. R., & Helmberger, D. V. (2007). Validating tomographic model with broadband wave form modeling: An example from the LA RISTRA transect in the southwestern United States. *Geophys. J. Int., 171*, 244-258, doi:10.1111/j.1365-246X.2007.03508.x.

Song, T. R. A., Helmberger, D. V., Brudzinski, M. R., Clayton, R. W., Davis, P., Perez-Campos, X., & Singh, S. K. (2009). Subducting slab ultra-slow velocity layer coincident with silent earthquakes in Southern Mexico. *Science, 324*, 502-506.

Sun, S. S. (2011). *Seismic velocities, anisotropy and elastic properties of crystalline rocks and implications for interpretation of seismic data*. Ph.D. thesis. 210 p., Université de Montréal, QC., Canada.

Sun, S. S., Ji, S., Wang, Q., Xu, Z. Q., Salisbury, M. H., & Long, C. X. (2012). Seismic velocities and anisotropy of core samples from the Chinese Continental Scientific Drilling borehole in the Sulu UHP terrane, eastern China. *J. Geophys. Res., 117*, B01206, doi:10.1029/2011JB008672.

Sun, X. X., Bao, X. W., Xu, M. J., Eaton, D. W., Song, X. D., Wang, L. S., Ding, Z. F., Mi, N., Yu, D. Y., & Li, H. (2014). Crustal structure beneath SE Tibet from joint analysis of receiver functions and Rayleigh wave dispersion. *Geophys. Res. Lett., 41*, 1479-1481, doi:10.1002/2014GL059269.

Sun, Y., Niu, F. L., Liu, H. F., Chen, Y. L., & Liu, J. X. (2012). Crustal structure and deformation of the SE Tibetan plateau revealed by receiver function data. *Earth Planet. Sci. Lett., 349-350*, 186-197, doi:10.1016/j.epsl.2012.07.007.

Svetlov, I. L., Epishin, A. I., Krivko, A. I., Samoilov, A. I., Odintsev, I. N., & Andreev, A. P. (1988). Anisotropy of Poisson's ratio of nickel base alloy single crystals. *Soviet Physics Doklady, 302*(6), 1372-1375.

Szymanski, D. L., & Christensen, N. I. (1993). The origin of reflections beneath the Blue Ridge-Piedmont Allochthon: A view through the Grandfather Mountain window. *Tectonics, 12*, 265-278.

Takanashi, M., Nishizawa, O., Kanagawa, K., & Yasunaga, K. (2001). Laboratory measurements of elastic anisotropy parameters for the exposed crustal rocks from the Hidaka Metamorphic Belt, Central Hokkaido, Japan. *Geophys. J. Int., 145*, 33-47.

Takeshita, T., Wenk, H.-R., & Lebensohn, R. (1999). Development of preferred orientation and microstructure in sheared quartzite: comparison of natural data and simulated results. *Tectonophysics, 312*, 133-155.

Tanimoto, T., & Anderson, D. L. (1985). Lateral heterogeneity and azimuthal anisotropy of the Upper mantle: Love and Rayleigh waves 100-205 s. *J. Geophys. Res., 90*, 1842-1858.

Tapponnier, P., Lacassin, R., Leloup, P. H., Scharer, U., Zhong, D. L., Wu, H. W., Liu, X. H., Ji, S. C., Zhang, L. S., & Zhong, J. Y. (1990). The Ailao Shan/Red River metamorphic belt: Tertiary left-lateral shear between Indochina and South China. *Nature, 343*, 431-437.

Tapponnier, P., Peltzer, G., Le Dain, A. Y., & Armijo, R., & Cobbold, P. (1982). Propagating extrusion tectonics in Asia: New insights from simple experiments with plasticine. *Geology, 10*, 611-616.

Tapponnier, P., Xu, Z. Q., Roger, F., Meyer, B., Arnaud, N., Wittlinger, G., & Yang, J. S. (2001), Oblique stepwise rise and growth of the Tibet Plateau. *Science, 294*, 1671-1677.

Tatham, D. J., Lloyd, G. E., Butler, R. W. H., & Casey, M. (2008). Amphibole and lower crustal seismic properties. *Earth Planet. Sci. Lett., 267*, 118-128.

Thomsen, L. (1986). Weak elastic anisotropy. *Geophysics, 51*, 1954-1966.

Thomsen, L., Tsvankin, I., & Mueller, M. (1999). Coarse-layer tripping of vertically variable azimuthal anisotropy from shear-wave data. *Geophysics, 64*, 1129-1138.

Tibi, R., Wiens, D. A., & Yuan, X. H. (2008). Seismic evidence for widespread serpentinized forearc mantle along the Mariana convergence margin. *Geophys. Res. Lett., 35,* L13303, doi:10.1029/2008GL034163.

Turner, S., Arnaud, N., Liu, J., Hawkesworth, C. J., Harris, N., Kelley, S., van Calsteren, P., & Peng, W. (1996). Post-collision, shoshonitic volcanism on the Tibetan Plateau: implications for convective thinning of the lithosphere and the source of oceanic basalts. *J. Petrol., 37*, 45-71.

Turner, S., Hawkesworth, C. J., Liu, J., Rogers, N., Kelley, S., & van Calsteren, P. (1993). Timing of Tibetan uplift constrained by analysis of volcanic rocks. *Nature, 364*, 50-53.

Ulmer, P., & Trommsdorff, V. (1995). Serpentine stability to mantle depths and subduction-related magmatism. *Science, 268,* 858-861.

van de Moortèle, B., Bezacier, L., Trullenque, G., & Reynard, B. (2010). Electron back-scattering diffraction (EBSD) measurements of antigorite lattice-preferred orientations (LPO). *J. Microscopy, 239,* 245-248.

van Keken, P. E., Hacker, B. R., Syracuse, E. M., & Abers, G. A. (2011). Subduction factory: 4. Depth-dependent flux of H_2O from subducting slabs worldwide. *J. Geophys. Res., 116*, B01401, doi:10.1029/2010JB007922.

Vauchez, A., & Barruol, G. (1996). Shear-wave splitting in the Appalachians and the Pyrenees: importance of the inherited tectonic fabric of the lithosphere. *Phys. Earth Planet. Inter., 95*,

127-138.

Vauchez, A., Tommasi, A., Barruol, G., & Maumus, J. (2000). Upper mantle deformation and seismic anisotropy in continental rifts. *Phys. Chem. Earth (A), 25*, 111-117.

Vaughan, M. T., & Guggenheim, S. (1986). Elasticity of muscovite and its relationship to crystal structure. *J. Geophys. Res., 91*, 4657-4664.

Vaughan, M. T., & Weidner, D. J. (1978). The relationship of elasticity and crystal structure in andalusite and sillimanite. *Phys. Chem. Minerals., 3*, 133-144.

Vergne, J., Wittlinger, G., Hui, Q., Tapponnier, P., Poupinet, G., Jiang, M., Herquel, G., & Paul, A. (2002). Seismic evidence for stepwise thickening of the crust across the NE Tibetan plateau. *Earth Planet, Sci. Lett., 203*, 25-33, doi:10.1016/S0012-821X(02)00853-1.

Vinnik, L., Makeyeva, L. I., Milev, A., & Usenko, Y. (1992). Global patterns of azimuthal anisotropy and deformations in the continental mantle. *Geophys. J. Int., 111*, 433-447.

Vogler, W. S. (1987). Fabric development in a fragment of tethyan oceanic lithosphere from the piemonte ophiolite nappe of the western Alps, Valtournanche, Italy. *J. Struct. Geol., 9*, 935-953.

Voigt, W. (1928). *Lehrbuch der Kristallphysik (Textbook on crystal physics)*. Berlin-Leipzig, Teubner Verlag, 962 p.

Wada, I., Wang, K. L., He, J. G., & Hyndman, R. D. (2008). Weakening of the subduction interface and its effects on surface heat flow, slab dehydration, and mantle wedge serpentinization. *J. Geophys. Res., 113*(B4), B04402, doi:10.1029/2007JB005190.

Wang, C. (1966). Velocity of compressional waves in limestones, marbles and a single crystal of calcite to 20 kilobars. *J. Geophys. Res., 71*, 3543-3547.

Wang, C. Y., Flesch, L. M., Silver, P. G., Chang, L. J., & Chan, W. W. (2010). Evidence for mechanically coupled lithosphere in central Asia and resulting implications. *Geology, 36*, 363-366.

Wang, G., Wan, J. L., Wang, E. C., Zheng, D. W., & Li, F. (2008). Late Cenozoic to recent transtensional deformation across the Southern part of the Gaoligong shear zone between the Indian plate and SE margin of the Tibetan Plateau and its tectonic origin. *Tectonophysics, 460*, 1-20.

Wang, P., Wang, L. S., Mi, N., Liu, J. H., Li, H., Yu, D. Y., Xu, M. J., Wang, X. C., & Guo, Z. W. (2010). Crustal thickness and average Vp/Vs ratio variations in southwest Yunnan, China, from teleseismic receiver functions. *J. Geophys. Res., 115*, B11308, doi:10.1029/2009JB006651.

Wang, Y. J., Fan, W. M., Zhao, G. C., Ji, S., & Peng, T. P. (2007). Zircon U-Pb geochronology of gneissic rocks in the Yunkai massif and its implications on the Caledonian event in the South China Block. *Gondwana Research, 12*, 404-416.

Wang, Q. (2005). *Seismic Properties of Polyphase Rocks*. Ph.D. thesis, 270 p., Université de Montréal, QC., Canada.

Wang, Q. (2009). *Seismic Velocities, Anisotropy, Hysterisis and Poisson's ratio of Ultrahigh Pressure (UHP) Metamorphic Rocks*. Ph.D. thesis, 296 p., Université de Montréal, QC., Canada.

Wang, Q., & Ji, S. (2009). Poisson's ratio of crystalline rocks as a function of hydrostatic confining pressure. *J. Geophys. Res., 114*, B09202, doi:10.1029/2008JB006167.

Wang, Q., Ji, S., Sun, S. S., & Marcotte, D. (2009b). Correlations between Poisson's ratio and seismic wave velocities for some common rocks and sulfide ores. *Tectonophysics, 469,* 61-72.

Wang, Q., Bagdassarov, N., & Ji, S. (2013). The Moho as a transition zone: A revisit from seismic and electrical properties of minerals and rocks. *Tectonophysics, 609*, 395-422.

Wang, Q., Burlini, L., Mainprice, D., & Xu, Z. Q. (2009a). Geochemistry, petrofabrics and seismic properties of eclogites from the Chinese Continental Scientific Drilling boreholes in the Sulu UHP terrane, eastern China. *Tectonophysics, 475*, 251-266.

Wang, Q., Ji, S., Salisbury, M. H., Pan, M. B., Xia, B., & Xu, Z. Q. (2005). Pressure dependence and anisotropy of P-wave velocities in ultrahigh-pressure metamorphic rocks from the Dabie-Sulu orogenic belt (China): implications for seismic properties of subducted slabs and origin of mantle reflections. *Tectonophysics, 398*, 67-99.

Wang, Z. C., & Ji, S. (2001). Elasticity of six polycrystalline silicate garnets at pressure up to 3.0 GPa. *American Mineralogist, 86*, 1209-1218.

Wang, S. Q., & Dong, P. X. (2011). Classification, geologic characteristics and origin of the jade from Xiuyan, Liaoning Province, China. *Geology and Resources, 20*, 321-331.

Ward, D., Mahan, K., & Schulte-Pelkum, V. (2012). Roles of quartz and mica in seismic anisotropy of mylonites. *Geophys. J. Int., 190*, 1123-1134.

Wassmann, S., Stockhert, B., & Trepmann, C. A. (2011). Dissolution precipitation creep versus crystalline plasticity in high-pressure metamorphic serpentinites. *Geol. Soc. London, Spec.Publ., 360*, 129-149.

Watanabe, T., Kasami, H., & Ohshima, S. (2007). Compressional and shear wave velocities of serpentinized peridotites up to 200 MPa. *Earth Planets Space, 59*(4), 233-244.

Watanabe, T., Shirasugi, Y., Yano, H., & Michibayashi, K. (2011). Seismic velocity in antigorite-bearing serpentinite mylonites. *Geol. Soc. London, Spec.Publ., 360*, 97-112, doi:10.1144/SP360.6.

Watt, J. P., Davies, G. F., & O'Connell, R. J. (1976). The elastic properties of composite materials. *Rev. Geophys. Space Phys., 14*, 541-563.

Weiss, T., Siegesmund, S., Rabbel, W., Bohlen, T., & Pohl, M. (1999). Seismic velocities and anisotropy of the lower continental crust: a review. *Pure Appl. Geophys., 156*, 97-122.

Wenk, H.-R., Vasin, R. N., Kern, H., Matthies, S., Vogel, S. C., & Ivankina, T. I. (2012). Revisiting elastic anisotropy of biotite gneiss from the Outokumpu scientific drill hole based on new texture measurements and texture-based velocity calculations. *Tectonophysics, 570-571*, 123-134, doi:10.1016/j.tecto.2012.06.023.

Werner, U., & Shapior, S. A. (1998). Intrinsic anisotropy and thin multilayering – two anisotropy

effects combined. *Geophys. J. Int., 132*, 363-373.

Werner, U., & Shapior, S. A. (1999). Frequency-dependent shear-wave splitting in thinly layered media with intrinsic anisotropy. *Geophysics, 64*, 604-608.

West, J. D., Fouch, M. J., Roth, J. B., & Elkins-Tanton, L. T. (2009). Vertical mantle flow associated with a lithospheric drip beneath the Great Basin. *Nat. Geosci., 2*, 439-444.

Whitney, D. L., & Evans, B. W. (2010). Abbreviations for names of rock-forming minerals. *Am. Mineral., 95*, 185-187.

Wicks, F. J., & O'Hanley, D. (1988). Serpentine minerals: structure and pertrology, in Hydrous phyllosilicates. *Reviews in Mineralogy, Mineralogical Society of America*, vol. 19, edited by S. W. Bailey, pp. 91-167, Washington D. C.

Wicks, F. J. & Whittaker, E. J. W. (1977). Serpentine textures and serpentinization. *Can. Mineral., 15,* 459-488.

Wiens, D. A., Conder, J. A., & Faul, U. H. (2008). The Seismic Structure and Dynamics of the Mantle Wedge. *Annu. Rev. Earth Planet. Sci., 36,* 421-455.

Winter, J. D. (2001). An Introduction to Igneous and Metamorphic Petrology, Prentice Hall Inc., Upper Saddle River, New Jersey.

Wirth, E., & Long, M. D. (2010). Frequency-dependent shear wave splitting beneath the Japan and Izu-Bonin subduction zones. *Phys. Earth Planet. Inter., 181,* 141-154.

Wissinger, E. S., Levander, A., & Christensen, N. I. (1997). Seismic images of crustal duplexing and continental subduction in the Brooks Range. *J. Geophys. Res., 102*, 20847-20871.

Wittlinger, G., Masson, F., Poupinet, G., Tapponnier, P., Jiang, M., Herquel, G., Guilbert, J., Achauer, U., Xue, G., Shi, D., & Team, L. K. (1996). Seismic tomography of northern Tibet and Kunlun: evidence for crustal blocks and mantle velocity contrasts. *Earth Planet. Sci. Lett., 139*, 263-279.

Wittlinger, G., Tapponnier, P., Poupinet, G., Jiang, M., Shi, D. N., Herquel, G., & Masson, F. (1998). Tomographic evidence for localized lithospheric shear along the Altyn Tagh fault. *Science, 287*, 74, doi:10.1126/science.282.5386.74.

Wu, H., Zhang, L., & Ji, S. (1989). The Red-River-Ailao Shan fault zone - Himalayan large sinistral strike-slip intracontinental shear zone. *Scientia Geologica Sinica, 1*, 1-8.

Wunder, B., Wirth, R., & Gottschalk, M. (2001). Antigorite: Pressure and temperature dependence of polysomatism and water content. *Eur. J. Mineral., 13*, 485-495.

Xia, G. (2013). *Experimental Studies on Dehydration Embrittlement of Serpentinized Peridotite and the Effect of Pressure on Creep of Olivine*. Ph.D., thesis, 121 p., University of California, Riverside, USA.

Xu, Z., Xu, M. J., Wang, L. S., Liu, J. H., Zhong, K., & Tong, W. W. (2006). A study on crustal anisotropy using P to S converted phase of the receiver function: Application to Ailao Shan-Red River fault zone. *Chin. J. Geophys., 49*, 438-448 (in Chinese with English abstract).

Xu, Z. Q., Qi, X. X., Yang, J. S., Ji, S., Li, H. B., & Chen, F. Y. (2007). Senses and timings of two kinds of shear in the Kangxiwar strike-slip shear zone, West Kunlun, and their tectonic significance. *Geol. Bull. China, 26*, 1252-1261.

Xu, Z. Q., Yang, W. C., Ji, S., Zhang, Z. M., Yang, J. S., Wang, Q., & Tang, Z. M. (2009). Deep root of a continent-continent collision belt: Evidence from the Chinese Continental Scientific Drilling (CCSD) deep borehole in the Sulu ultrahigh-pressure (HP-UHP) metamorphic terrane, China. *Tectonophysics, 475*, 204-219.

Xu, Z. Q., Wang, Q., Pecher, A., Liang, F. H., Qi, X. X., Cai, Z. H., Li, H. Q., Zeng, L. S., & Cao, H. (2013). Orogen-parallel ductile extension and extrusion of the Greater Himalaya in the late Oligocene and Miocene, *Tectonics, 32*, 191-215.

Yang, C. P., Inoue, T., Yamada, A., Kikegawa, T., & Ando, J.-I. (2014). Equation state and phase transition of antigorite under high pressure and high temperature. *Phys. Earth Planet. Inter., 228*, 56-62.

Yao, H. J., van der Hilst, R. D., & Montagner, J.-P. (2010). Heterogeneity and anisotropy of the lithosphere of SE Tibet from surface wave array tomography. *J. Geophys. Res., 115*, B12307, doi:10.1029/2009JB007142.

Yardley, G. S., & Crampin, S. (1991). Extensive-dilatancy anisotropy: relative information in VSPs and reflection surveys. *Geophys. Prosp., 39*, 337-355.

Yin, A., & Harrison, T. M. (2000). Geologic evolution of the Himalayan-Tibetan orogen. *Annu. Rev. Earth Planet. Sci., 28*, 211-280.

Yu, Y., & Park, J. (1994). Hunting for azimuthal anisotropy beneath the Pacific Ocean region. *J. Geophys. Res., 99*, 15399-15421.

Zagorevski, A., van Staal, C. R., & McNicoll, V. J. (2007). Distinct Taconic, Salinic and Acadian deformation along the lapetus suture zone, Newfoundland Appalachians. *Can. J. Earth Sci., 44*, 1567-1585.

Zandt, G., & Ammon, C. J. (1995). Continental crust composition constrained by measurements of crustal Poisson's ratio. *Nature, 374*, 152-155.

Zappone, A., Fernàndez, M., García-Dueñas, V., & Burlini, L. (2000). Laboratory measurement of seismic P-wave velocities on rocks from the Betic chain (southern Iberian Peninsula). *Tectonophysics, 317*, 259-272.

Zhang, B., Zhang, J. J., & Zhong, D. L. (2010). Structure, kinematics and ages of transpression during strain partitioning in the Chongshan shear zone, western Yunnan, China. *J. Struct. Geol., 32*, 445-463.

Zhang, B., Zhang, J. J., Zhong, D. L., Yang, L. K., Yue, Y. H., & Yan, S. Y. (2012). Polystage deformation of the Gaoligong metamorphic zone: Structures, 40Ar/39Ar mica ages, and tectonic implications. *J. Struct. Geol., 37*, 1-18.

Zhao, L.-F., Xie, X.-B., He, J.-K., Tian, X., & Yao, Z.-X. (2013). Crustal flow pattern beneath the Tibetan Plateau constrained by regional Lg-wave Q tomography. *Earth Planet. Sci. Lett., 383*, 113-122, doi:10.1016/j.epsl.2013.09.038.

Zhang, L. J. (2002). Charcateristics and quality of Xiuyan jade in Liaoning Province. *Acta Petrologica et Mineralogica, 21,* 134-142.

Zhao, Y., & Anderson, D. L. (1994). Mineral physics constraints on the chemical composition of the Earth's lower mantle. *Phys. Earth Planet. Inter., 85*, 273-292.

Zhao, X., Ji, S., & Martignole, J. (1997). Quartz c-axis fabrics and their tectonic implications for high temperature deformation of the Morin Granulite Complex, Grenville Province. *Can. J. Earth Sci., 34*, 819-832.

Zhao, Z. D., Niu, Y., Christensen, N. I., Zhou, W., Hou, Q., Zhang, Z. M., Xie, H., Zhang, Z. C., & Liu, J. (2011). Delamination and ultra-deep subduction of continental crust: constraints from elastic wave velocity and density measurements in ultrahigh-pressure metamorphic rocks. *J. Metamorphic Geol., 29*, 781-801.

Zhao, D., Wang, K., Rogers, G. C., & Peacock, S. M. (2001). Tomographic image of low P velocity anomalies above slab in northern Cascadia subduction zone. *Earth Planets Space, 53,* 285-293.

Zhao, J. M., Yuan, X. H., Liu, H. B., Kumar, P., Pei, S. P., Kind, R., Zhang, Z. J., Teng, J. W., Ding, L., Gao, X., Xu, Q., & Wang, W. (2010). The boundary between the Indian and Asian tectonic plates below Tibet. *Proc. Natl. Acad. Sci.*, 107, 11229-11233, doi:10.1073/pnas.1001921107.

Zhou, W. G., Fan, D. W., Liu, Y. G., & Xie, H. S. (2011). Measurements of wave velocity and electrical conductivity of an amphibolite from southwestern margin of the Tarim basin at pressures to 1.0 GPa and temperatures to 700°C: comparison with field observations. *Phys. J. Int., 187*, 1393-1404.

Zorin, Y. A., Mordvinova, V. V., Turutanov, E. K., Belichenko, B. G., Artemyev, A. A., Kosarev, G. L., & Gao, S. S. (2002). Low seismic velocity layers in the Earth's crust beneath Eastern Siberia (Russia) and Centra Mongolia: receiver function data and their possible geological implication. *Tectonophysics, 359*, 307-327.